Preface

Dear reader,

This special issue of the "Bulgarian Chemical Communications" comprises most of the studies, presented at the Scientific Session on "Advanced Materials and Technologies", that was held in Sofia on October 10-11, 2016.

The Scientific Session was organized by the Institute for Optical Materials and Technologies "Acad. Jordan Malinowski" at the Bulgarian Academy of Sciences. The program involved invited lectures and poster presentations in three contemporary scientific directions in material science: optical characterization and monitoring of processes; materials for biomedical and environmental applications; thin films and multilayer systems for applications in photonics, optoelectronics and sensor technique. The testimony for the vivid interest this event provoked was the really high response rate materializing into more than 60 participants. The presentation of the invited distinguished lecturers in the above key research fields along with the participation of prominent Bulgarian scientists, working together with colleagues from leading international Institutes was highly appreciated by all present. The significant attendance of young scientists and PhD students indisputably added to the attractiveness of the session. Moreover, the continuous face-to-face communication during the session days provided valuable opportunities to the attendees to share knowledge and exchange experience, to network actively and confer on the latest developments in the fields of research and technologies in the corresponding areas of interest, that in fact was session's core mission. For those who didn't have the chance to be there – we hope that this reading will serve as a teaser to attend the next round.

Wishing you an exciting and beneficial experience,

Guest editors of the special issue:

S. Kitova

J. Dikova

Sol – Gel Synthesis, Characterization and Optical Properties of TiO₂/TeO₂ powders

A. D. Bachvarova-Nedelcheva[1]*, R. S. Iordanova[1], R. D. Gegova[1], P. V. Markov[1],
D. D. Nihtianova[1,2] and Y. B. Dimitriev[3]

[1]*Institute of General and Inorganic Chemistry, Bulgarian Academy of Sciences,
"Acad. G. Bonchev" str., bld. 11, 1113 Sofia, Bulgaria. E-mail: albenadb@svr.igic.bas.bg*
[2] *Institute of Mineralogy and Crystallography, Bulgarian Academy of Sciences, "Acad. G. Bonchev" str., bld. 107,
1113 Sofia, Bulgaria*
[3] *University of Chemical Technology and Metallurgy - Sofia,"Kl. Ohridski" blvd, 8,
1756 Sofia, Bulgaria*

The present investigation deals with the sol-gel synthesis and optical characterization of gels in the binary TiO₂ – TeO₂ system. Titanium butoxide and telluric (VI) acid (H₆TeO₆) were used as main precursors for preparation of the rich in TiO₂ (above 35 mol %) compositions. The heat treated up to 300°C gels are predominantly amorphous and contain small amount of metallic tellurium. Several crystalline phases TiTe₃O₈, TeO₂, TiO₂ (anatase) and TiO₂ (rutile) simultaneously exist above this temperature. Two maxima about 230 – 250 nm and 290 – 330 nm related to the isolated TiO₄ units and condensed TiO₆ groups, respectively were observed in the UV – Vis spectra. The heating of all samples above 500°C led to an increase of the UV absorption peak at 330 nm (instead of that at 230 nm) which is related to the greater condensation processes. In comparison to the pure Ti butoxide gel, a red shifting of the absorption edge for samples containing up to 50 mol % TeO₂ was observed, while composition containing higher TeO₂ amount (above 50 mol %) exhibited blue shifting.

Keywords: sol-gel, telluric (VI) acid, crystallization

INTRODUCTION

In the past decade much attention has been paid on the binary TiO₂ - TeO₂ system. From one side, TiO₂-based materials have always been of primary research interest for the materials chemists driven by the unique properties of TiO₂ and its ability to create high surface area structures for photocatalysis and sensing [1]. On the other side, the binary TiO₂-TeO₂ system is of special interest, as it has been shown that TiO₂ inhibits structural changes of the Te polyhedra and maintains a continuous amorphous network [2, 3]. It was found that the addition of TiO₂ increases the thermal stability of TeO₂-based glasses by replacing Te-O-Te linkages by more rigid Te-O-Ti ones [4]. However, it was established that the Ti⁴⁺ as an additive is the most influential ion for improving the optical properties of TeO₂ among all transition metal ions due to effect of its d orbital [5]. The pioneer's investigations with reference to sol-gel obtaining of TiO₂/TeO₂ thin films started by Weng and Hodgson [6]. In their earlier research the sol –

gel technique was applied as an alternative of the melt quenching method for synthesis of TeO₂ based thin films but the uncontrolled hydrolysis of tellurium isopropoxide was found as a problem. That question was widely discussed in several papers [4, 7 - 13]. Most of the authors reported that during the heat treatment of TeO₂ thin films highly dispersed metallic tellurium is present up to 340°C [7 - 9, 14]. The α-TeO₂ occurred when the heat treatment temperature was further increased. Addition of TiO₂ retard the crystallization of α-TeO₂ but promote the formation of other TiO₂ or TiTe₃O₈ phases [9, 15]. Recently, similar results in that system have been described in several papers [13, 16, 17]. Up to now, dense and transparent thin films were obtained by these methods in the TiO₂-TeO₂ system containing 10 mol % TiO₂ and in a more complex TiO₂ – TeO₂ – PbO system [18, 19].

The TiO₂/TeO₂ glasses, rich in TeO₂ (> 70 mol %) have been obtained by sol-gel techniques [10, 17] and the optical properties of the obtained materials were also verified. Melt quenched glasses in the TiO₂ - TeO₂ system were obtained in a narrow concentration range above 75 % TeO₂ [2, 20, 21]. Generally, it is difficult to be prepared

* To whom all correspondence should be sent:
E-mail: albenadb@svr.igic.bas.bg

glasses rich in TiO_2 by conventional melt – quenching route due to its high melting temperature (1843°C). We have chosen the sol – gel method as an alternative one for obtaining of rich in TiO_2 amorphous materials. Our earlier investigations in that binary system started with the phase transformations and photocatalytical properties of sol – gel derived TiO_2/TeO_2 powders containing from 70 to 90 mol % TiO_2 [13, 15]. Data on optical characterization of sol – gel derived TiO_2/TeO_2 powders containing higher TiO_2 content were not found in the literature that motivates our present study.

The purpose of this paper is to synthesize rich in titania TiO_2/TeO_2 powders applying a sol – gel technique and to characterize optically the prepared samples as well as to verify the morphology of the obtained products.

EXPERIMENTAL

Samples preparation

Various samples containing different TiO_2 content (above 40 mol %) were prepared and some of them were selected for detailed phase and optical investigations: $80TiO_2.20TeO_2$ (*sample A*), $50TiO_2.50TeO_2$ (*sample B*), $40TiO_2.60TeO_2$ (*sample C*). In order to overcome the problem with high hydrolysis rate of tellurium (VI) alkoxides we used Te(VI) acid (Aldrich) [6, 22, 23] in combination with Ti butoxide (Fluka AG) and ethylene glycol ($C_2H_6O_2$) (99% Aldrich). Solutions (A and B) were prepared via dissolving of the precursors in ethylene glycol by means of vigorous magnetic stirring. Thus, transparent gels were obtained. For comparison, pure TiO_2 gel was obtained from Ti butoxide without addition of water or ethylene glycol (EG) and it is denoted as TBT. The as – prepared gels were subjected to heating at ~ 150°C and subsequently to calcination in the temperature range 200-700⁰C. The stepwise heating of the samples from 200 to 700°C for one hour exposure time in air was performed, until obtaining powders. The calcination temperature was selected on the basis of our previous investigations [13, 15]. The pH during the experiments was measured to be about 7.

Samples characterization

Powder XRD patterns were registered at room temperature with a Bruker D8 Advance diffractometer using Cu-K_α radiation. It has to be noted that the XRD patterns obtained below 200°C are complicated due to the presence of organic complexes and they are not discussed. The morphology of the samples was examined by scanning electron microscopy (SEM) using a JEOL JSM 6390 electron microscope (Japan), equipped with ultrahigh resolution scanning system (ASID-3D). The accelerating voltage was 20kV, I~65 μA. Transmission Electron Microscopy (TEM) investigations were performed on a JEOL JEM 2100 instrument (Japan) at an accelerating voltage of 200 kV. The specimens were prepared by grinding and dispersing them in ethanol by ultrasonic treatment for 6 mins. The suspensions were dripped on standard carbon/Cu grids. The measurements of lattice fringe spacings recorded in HRTEM micrographs were made using digital image analysis of real space parameters. The analysis was carried out by the Digital Micrograph software. Additional support for the existence of all participated elements in the investigated samples was performed by X-ray energy dispersive spectrometry (XEDS) elemental mapping studies. The optical absorption spectra of the powdered samples in the wavelength range 200 – 800 nm were recorded by a UV–VIS diffused reflectance Spectrophotometer "Evolution 300" using a magnesium oxide reflectance standard as the baseline. The absorption edge and the optical band gap were determined following Dharma et al. instructions [24]. The bandgap energies (E_g) of the samples were calculated by the Planck's equation:

$$E_g = \frac{h.c}{\lambda} = \frac{1240}{\lambda}$$

where E_g is the bandgap energy (eV), h is the Planck's constant, c is the light velocity (m/s), and λ is the wavelength (nm).

RESULTS AND DISCUSSION

X – ray diffraction

Transparent and monolithic gels were obtained and the gel formation region determined at room temperature is situated between 35 - 100 mol % TiO_2 and up to 65 mol % TeO_2. According to the X-ray diffraction patterns heat treated gels up to 300°C consist of amorphous part and metallic tellurium only (JCPDS 78-2312) (Fig. 1, samples A, B, C). The residual organic component plays an important role in promoting the formation of tellurium [12]. According to Wei et al. [12] the samples heated at 300°C with preheated treatment at 200°C in O_2 showed great decrease in the metallic tellurium content and clearer amorphous phase in the XRD pattern. Looking at our results, at 400°C only tellurium was found in the XRD pattern

for sample A (80TiO$_2$.20TeO$_2$), while for samples B and C containing higher TeO$_2$ content (50, 60 mol %) partially oxidation of tellurium to paratellurite (α-TeO$_2$, JCPDS 42-1365) was registered. Further increasing of the temperature (500°C) led to fully oxidation of tellurium to TeO$_2$ and at this temperature it exists simultaneously with TiO$_2$ (anatase) (JCPDS 78-2486) and crystalline TiTe$_3$O$_8$ phase (JCPDS 50-0250). At higher temperatures (600, 700°C) all these phase coexist in the prepared composite materials (Fig. 1a). The The TiO$_2$ (anatase) to TiO$_2$ (rutile) (JCPDS 21-1276)

transformation is observed at 700°C for all samples. Irrespective of using different precursor (Te^{VI} acid) in our experiments, the observed phase transformations are in good accordance with those obtained by other teams [7, 9, 14, 17]. For comparison, the XRD patterns of Ti butoxide gel, showed that it is amorphous up to 300°C and the first TiO$_2$ (anatase) crystals appeared at 400°C (Fig. 1b). The addition of TeO$_2$ (samples A, B, C) to Ti butoxide preserved the amorphous titania up to 400°C and first TiO$_2$ (anatase) crystals appeared at 500°C.

($\blacksquare$) Te, ($\blacklozenge$) α-TeO$_2$, ($\blacktriangle$) TiO$_2$-anatase, ($\ast$) TiO$_2$-rutile, ($\bullet$) TiTe$_3$O$_8$, ($\odot$) H$_3$BO$_3$, ($\diamondsuit$) ZnTiO$_3$ (rhomb).
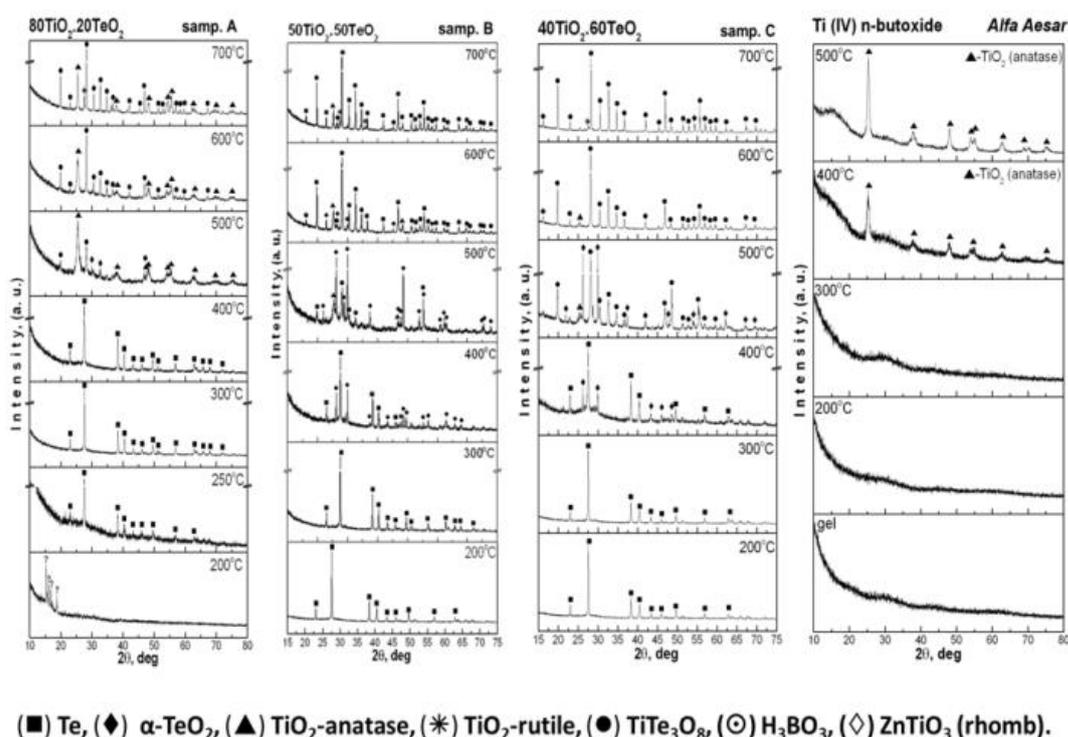
Fig. 1. XRD patterns of the: (a) investigated samples A (80TiO$_2$.20TeO$_2$), B (50TiO$_2$.50TeO$_2$) and C (40TiO$_2$.60TeO$_2$) and (b) pure Ti butoxide (TBT).

Electron microscopy

Sample C (40TiO$_2$.60TeO$_2$) heat treated at 400°C was subjected to SEM observations with microprobe analysis (Fig. 2). The sample morphology revealed shapeless agglomerates with a size around 50 - 100 μm, that are probably a result of the crashing of the monolithic gels during the drying process. The microprobe analysis was performed in different points of the sample surface and the obtained data are summarized in Table 1. As it is seen there are aggregates with composition corresponding to TeO$_2$ (spectrum 1), other pieces with composition equivalent to the initial one

(spectrum 2) and regions with segregated Ti on the surface (spectrum 3).

The HRTEM images performed in different parts of sample C heat treated at 400°C confirmed the inhomogeneous nature of the sample at unit cell level (Fig. 3a). The SAED data exhibited presence of tetragonal TeO$_2$ (SG P4$_1$2$_1$2) with the lattice parameters a = 4.810 Å and c = 7.612 Å (Fig. 3b). This implies that the crystal is viewed along the [122] zone axis. The composition map via STEM-XEDS analysis was carried out to examine the distribution of elements in the composite sample. The results of mapping studies (Fig. 4) portray the coexistence of Ti, O, Te and C elements and their

7

homogeneous distribution. The TEM images of another part of the sample rich in carbon are shown in Fig. 5. Several pods fill up with smooth and spherical particles are observed with size between 20 nm to 2 μm. Elemental mapping studies in this part of the composite illustrate mainly existence of carbon and oxygen (Fig. 6).

Table 1. Electron probe microanalysis (EPMA) performed in different points on the surface of sample C ($40TiO_2.60TeO_2$).

| Elements	Microprobe analysis (at %) $40TiO_2.60TeO_2$ (mol %)			
	initial composition, at %	400°C		
		sp. 1	sp. 2	sp. 3
Ti	13	-	11	23
Te	20	33	22	10
O	67	67	67	67
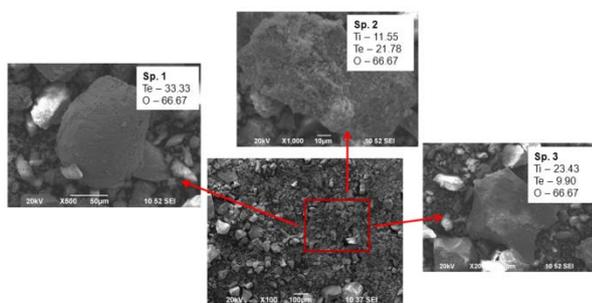
**Fig. 2.** SEM images of sample C ($40TiO_2.60TeO_2$) heat treated at 400°C.
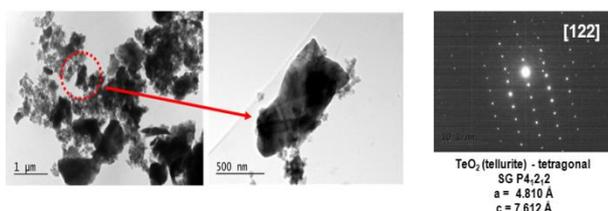
Fig. 3 (a, b). (a) Bright field TEM micrographs of sample C heat treated at 400°C and (b) SAED pattern of TeO_2 (paratellurite) particle from sample C, oriented along [122] direction.
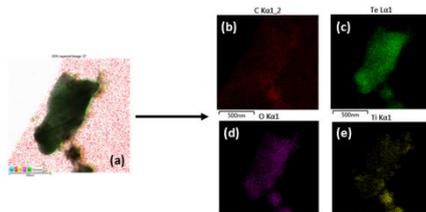
Fig. 4 (a,b,c,d,e). (a) Integral XEDS-STEM composition map of sample C heat treated at 400°C; **(b)** composition map of C; **(c)** composition map of Te; **(d)** composition map of O; **(e)** composition map of Ti.
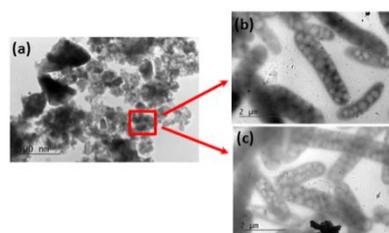
Fig. 5 (a,b,c). Bright field TEM micrographs from carbon rich areas of sample C heat treated at 400°C.
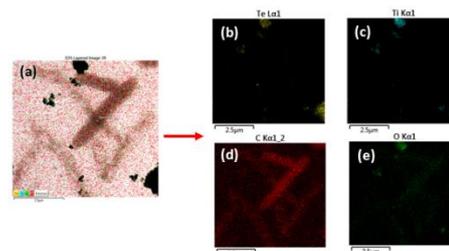

Fig. 6. (a,b,c,d,e). (a) Integral XEDS-STEM composition map from carbon rich area of sample C heat treated at 400°C; (b) composition map of Te; (c) composition map of Ti; (d) composition map of C; (e) composition map of O.

UV – Vis DRS characterization

The diffuse reflectance spectroscopy (DRS) studies were executed in order to determine the absorption edge (cut - off) as well as to calculate the band gap energy (E_g) of the binary and pure TBT gels (aged at room temperature) as well as of the heat treated at 600°C samples (Fig. 7a, b; Table 2). Generally, for the heated samples (200 - 400°C) these optical characteristics could not be determined because of the high absorption above 400 nm caused by the presence of carbon. Such absorption is illustrated by the UV – Vis spectra of pure TBT (Fig. 7c). The UV – Vis spectra of the investigated binary gels were compared to those of pure Ti butoxide gel (TBT). All spectra of the gels (samples A, B, C and TBT) are characterized with good transparency in the visible region. Useful structural information on the coordination number of Ti atoms was additionally obtained by UV–Vis spectroscopy. The appearance of two absorption bands below and above 300 nm, could be related to the charge transfer of electrons from O to Ti. The main building units in the unhydrolyzed Ti butoxide are isolated TiO_4 groups with absorption band in the region 240-260 nm. These groups change their coordination geometry to TiO_6 (300 – 330 nm) as a result of the polymerization processes (Ti–O–Ti links between TiO_6 units) [25, 26]. The UV – Vis spectra of as-prepared binary gels showed more intensive absorption peak about 300 - 310 nm that

could be associated with greater degree of hydrolysis and condensation processes (samples A, B) in comparison to pure TBT. It is also evident that TeO_2 increased the absorption in the UV region (samples A, B, C).
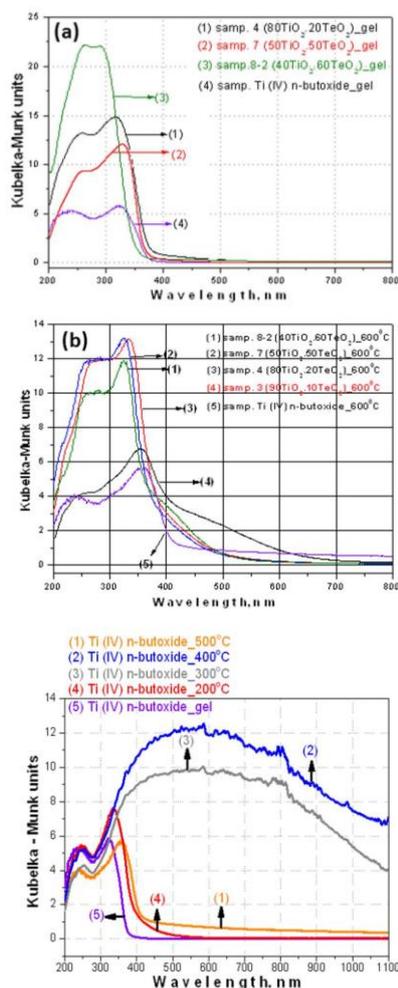
Fig. 7. UV-Vis DRS of samples: (a) gels, (b) heat treated at 600°C powders and (c) pure Ti butoxide.

It is clearly observed that the gel (sample A) containing lowest TeO_2 content (20 mol %) showed shifting of the absorption edge towards a longer wavelength (red shift) (~ 403 nm) compared to pure TBT gel (~ 390 nm). The highest TeO_2 content (60 mol %, sample C) led to shifting of the absorption edge towards a lower wavelength (blue shift) in respect to TBT gel (sample C, ~ 381 nm, Table 2). It is well known that Eg depends on many factors: generally, disordered systems cause blue shift; increasing the covalency of the bonds and the degree of polymerisation shift the absorption to the visible range [27]. Obviously, the binary gel $80TiO_2.20TeO_2$ with more completed polymerization processes exhibited red shifting of the

absorption edge, while the gel $40TiO_2.60TeO_2$ with uncompleted polymerization showed blue shifting.

Table 2. Investigated binary gels, observed cut-off and calculated optical band gap values (Eg).

Compositions, mol %	as prepared gels (25 °C)	
	E_g, eV	cut-off, nm
TiO_2 (Ti (IV) n-butoxide)	3.18	389.71
$80TiO_2.20TeO_2$	3.08	402.86
$50TiO_2.50TeO_2$	3.39	365.55
$40TiO_2.60TeO_2$	3.25	381.58

The UV-Vis spectra of the investigated samples (A, B and C) heat treated at 600°C possessing two – edge absorption (Fig. 7b) that could be related to the simultaneous existence of different crystalline phases [$TiTe_3O_8$, TeO_2 and TiO_2 (anatase)] (Fig. 1) and probably the absorption curves contain the contributions from each of the components. Similar explanations are made by other authors [28]. It was also stated [28] that in such cases the dominant is the influence of the compound with smaller E_g.

CONCLUSIONS

By the new combination of organic and inorganic precursors a simple route for obtaining of complex homogeneous gels in the TiO_2 – TeO_2 system is offered. The crystallization process started about 400°C and above this temperature sol – gel derived composite powders containing TiO_2 (anatase), α-TeO_2 (paratellurite) and $TiTe_3O_8$ were obtained depending on composition. By UV – Vis spectroscopy was established that the gels are characterized with good transparency in the visible region. It is also found that the low TeO_2 content (20 mol %) causes red shifting of the absorption edge while higher TeO_2 (60 mol %) amount leds to the blue shifting, both cases compared to pure Ti butoxide gel. It was found that the sol-gel method is suitable for obtaining of amorphous samples which are difficult to be prepared by conventional melt quenching route due to the high melting temperature of TiO_2.

REFERENCES

1. G. Arrachart, D. J. Cassidy, I. Karatchevtseva & G. Triani, *J. Am. Ceram. Soc.*, **92**, 2109 (2009).

2. M. Arnaudov, V. Dimitrov, Y. Dimitriev & L. Markova, *Mater. Res. Bull.*, **17**, 1121 (1982).

3. R. Iordanova, R. Gegova, A. Bachvarova-Nedelcheva, Y. Dimitriev, Europ. J. Glass Sci. Techn., Part B: Phys. Chem. *Glasses*, **56** (4), 128 (2015).

4. M. Udovic, P. Thomas, A. Mirgorodsky, O. Durand, M. Soulis, O. Masson, T. Merle-Méjean, J. C. Champarnaud-Mesjard, *J. Solid State Chem.*, **179**, 3252 (2006).

5. M. E. Lines, *J. Appl. Phys.*, **69**, 6876 (1991).

6. S. N. B. Hodgson, L. Weng, *J. Non-Cryst. Sol.*, **276**, 195 (2000).

7. L. Weng and S. N. B. Hodgson, J. Mater. Sci., 36, 4955 (2001).

8. L. Weng, S. N. B. Hodgson, X. Bao, K. Sagoe - Krentsil, *Mater. Sci. Engineer.*, **B107**, 89 (2004).

9. S. N. B. Hodgson and L. Weng, *J. Mater. Sci.*, **37**, 3059 (2002).

10. L. Weng, S. N. B. Hodgson, *Mater. Sci. Engineer. B*, **87**, 77 (2001).

11. S. Coste, A. Lecomte, P. Thomas, T. Merle-Mejean, J. C. Champarnaud-Mesjard , J. Sol-Gel Sci. Techn., 41, 79 (2007).

12. H-Y. Wei, W-H. Huang, Z-B. Feng, D-W. Li, *Mater. Sci. Engineer. B*, **164**, 51 (2009).

13. R. Iordanova, R. Gegova, A. Bachvarova-Nedelcheva, Y. Dimitriev, *Bulg. Chem. Commun.*, **45** (4), 485 (2013).

14. L. Weng, S. N. B. Hodgson, *Opt. Mater.*, **19**, 313 (2002).

15. A. Bachvarova-Nedelcheva, R. Gegova, R. Iordanova, A. Stoyanova, Y. Dimitriev, and N. Ivanova, *Nanoscience and Nanotechnology*, **13**, 56 (2013).

16. J.-N. Beaudry, S. Grenier, S. Amrate, M. Mazzera, A. Zappettini, *Mater. Chem. Phys.*, **133**, 804 (2012).

17. T. Hayakawa, H. Koyama, M. Nogami, Ph. Thomas, *J. Univ. Chem. Technol. Metall.*, **47** (4), 381 (2012).

18. S. Hodgson, L. Weng, *J. Non – Cryst. Sol.*, **297**, 18 (2006).

19. S. Hodgson, L. Weng, *J. Mater Sci: Mater Electron.*, **17**, 723 (2002).

20. W. Kingery, H. Bowen & D. Uhlmann, "*Introduction to Ceramics*", 2-nd ed., John Wiley, NY, 1976, p. 669.

21. J.-C. Sabadel, P. Armand, P. E. Lippens, D. C. Herreillat & E. Philippot, *J. Non-Cryst. Sol.*, **244**, 143 (1999).

22. A. Lecomte, F. Bamiere, S. Coste et al., *J. Europ. Cer. Soc.*, **27**, 1151 (2007).

23. L. Weng, S. N. B. Hodgson, *J. Non-Cryst. Sol.*, **297**, 18 (2002).

24. J. Dharma, A. Pisal, Simple method of measuring the band gap energy value of TiO2 in the powder form using a UV/Vis/NIR spectrometer. Application note. PerkinElmer, Shelton, CT, (2009).

25. V. Barlier, V. Bounor-Legare, G. Boiteux, J. Davenas, *Appl. Surf. Sci.*, **254**, 5408 (2008).

26. S. Klein, B. M. Weckhuysent, J. Martens, W. Maier, P. Jacobs, *J. Catal.*, **163**, 489 (1996).

27. R. Iordanova, R. Gegova, A. Bachvarova-Nedelcheva, Y. Dimitriev, Phys. Chem. Glasses: Eur. J. Glass *Sci*. Technol. B, 56 (4) 128 (2015).

28. El. Ross-Medgaarden and I. E. Wachs, J. Phys. Chem. C, 111, 15089 (2007).

ЗОЛ- ГЕЛЕН СИНТЕЗ, ХАРАКТЕРИЗИРАНЕ И ОПТИЧНИ СВОЙСТВА НА TiO$_2$/TeO$_2$ ПРАХОВЕ

А. Д. Бъчварова-Неделчева[1], Р. С. Йорданова[1], Р. Д. Гегова[1], П. В. Марков[1], Д. Д. Нихтянова[1,2] и Я. Б. Димитриев[3]

[1] *Институт по Обща и Неорганична Химия, БАН, ул. "Акад. Г. Бончев", бл. 11, 1113 София, България*
[2] *Институт по Минералогия и Кристалография, БАН, ул. "Акад. Г. Бончев", бл. 107, 1113 София, България*
[3] *Химикотехнологичен и Металургичен Университет, бул. "Кл. Охридски", 1756 София, България.*

(Резюме)

В настоящото изследване са обсъдени зол – гелният синтез и оптичното характеризиране на гели от двукомпонентната TiO$_2$ – TeO$_2$ система. Телурова (VI) киселина и титанов бутоксид са използвани за синтеза на богати на TiO$_2$ (над 40 мол %) състави. Рентгенофазовият анализ на термично третираните до 300°С гели показа присъствие предимно на органична аморфна фаза и метален телур. Над тази температура, няколко кристални фази TiTe$_3$O$_8$, TeO$_2$, TiO$_2$ (анатаз) и TiO$_2$ (рутил) са регистрирани. УВ – Вис спектроскопията показа присъствие на две абсорбционни ивици при 230 – 250 нм и 290 – 330 нм, които могат да се отнесат съответно към изолираните TiO$_4$ и TiO$_6$ групи. Нагряването на всички образци над 500°С доведе до повишаването на абсорбционния пик при 330 nm, което може да се свърже с по-пълно протеклите кондензационни процеси. За състави съдържащи до 50 мол % TeO$_2$ бе наблюдавано едно отместване на абсорбционният ръб към по – високите стойности на дължината на вълната, докато при състави съдържащи над 60 мол % TeO$_2$ отместването на абсорбционният ръб е към по – ниските стойности на дължината на вълната.

Optical characterization of glass and glass- crystalline materials in the B_2O_3-Bi_2O_3-La_2O_3 system doped with Eu^{3+} ions

R. S. Iordanova[1], M. K. Milanova[1], L. I. Aleksandrov[1]*, A. Khanna[2], N. Georgiev[3]

[1]*Institute of General and Inorganic Chemistry, Bulgarian Academy of Sciences, G. Bonchev, str. bld. 11, 1113 Sofia, Bulgaria,*
[2] *Department of Physics, Guru Nanak Dev University, Amritsar, Punjab, India*
[3] *Department of Organic Synthesis and Fuels, University of Chemical Technology and Metallurgy, 8 Kl. Ohridski, 1756 Sofia, Bulgaria*

Glass and glass-crystalline materials with nominal composition $55B_2O_3 \cdot 35Bi_2O_3 \cdot 10La_2O_3$ doped with 1 mol% Eu_2O_3 were synthesized by melt quenching method. Different phases were developed, applying several melting temperatures. According to the XRD data, glass-crystalline materials containing $LaBO_3$ as crystalline phase were obtained at 1050 °C and 1100 °C, while X-ray amorphous samples were prepared at 1200°C. Thermal parameters of the obtained glass samples were estimated by DTA analysis. It was found that the thermal stability of the glass drastically increased with the addition of Eu_2O_3 (1 mol%). UV–Vis diffuse reflectance spectrum showed that the quenched glass is transparent in the visible region. $LaBO_3$:Eu^{3+} crystals enhanced red $^5D_0$–$^7F_2$ photoluminescence emission of the glass–crystalline samples as compared with the glass sample. This is due to the incorporation of the active Eu^{3+} ions with low symmetry into the crystal phase.

Keywords: Glass; IR spectra; Luminescence spectra

INTRODUCTION

In the last decades, borate materials have largely demonstrated their potential for the development of new optoelectronics devices. Their interesting properties do not only limit to the crystalline phases but also can be extended to the glass form with different compositions [1]. In particular, remarkable attention has been directed towards complex bismuth-borate based glass systems, containing rare - earth metal oxides (RE) [1-3]. Such glasses have many technological applications as lenses, lasing materials, magneto-optic materials, optical-switching materials and sensors [1-3]. They have to posses, a high thermal stability, excellent surface polishing properties, high refractive index, etc. [1, 4] to be promising materials for use in all-optical devices. It has been reported that the glass structure of bismuth borate glasses can be stabilized by doping with RE oxides. In particular, $Bi_2O_3 \cdot B_2O_3$ glasses doped with suitable amount of La_2O_3 could tighten the glass network structure and improve the microhardness of bismuth-borate glass [2, 5, 6]. In this study, glass and glass-crystalline materials with

nominal composition $55B_2O_3 \cdot 35Bi_2O_3 \cdot 10La_2O_3$ doped with 1 mol% Eu_2O_3 have been prepared by melt quenching method. The influence of Eu^{3+} ions on the structure and optical properties of the $55B_2O_3 \cdot 35Bi_2O_3 \cdot 10La_2O_3$ glass has been also investigated.

EXPERIMENTAL

Reagent grade Bi_2O_3, H_3BO_3, La_2O_3 and Eu_2O_3 were used as starting materials to prepare one sample with nominal composition $55B_2O_3 \cdot 35Bi_2O_3 \cdot 10La_2O_3$ and three samples with the same nominal composition doped with 1 mol% Eu_2O_3. The homogenized batches were melted at the temperature range between 1050-1200 ºC for 30 min in a platinum crucible in air. The melts were quenched by pouring and pressing between two copper plates (cooling rates 10^1–10^2 K/s). The phase formation of the samples was established by x-ray phase analysis. Powder XRD patterns were registered at room temperature with a Bruker D8 Advance diffractometer using Cu-K_α radiation. The data were obtained in the $10 < 2\theta < 60°$ range with a step 0.02 for two different scanning times - of 0.02 seconds for the $55B_2O_3 \cdot 35Bi_2O_3 \cdot 10La_2O_3$ sample and at longer scanning time of 0.1 seconds

*To whom all correspondence should be sent:
E-mail: lubomirivov@gmail.com

for the three Eu_2O_3 doped specimens. Thermal parameters of the glasses were determined using differential thermal analysis (DTA) (Setaram, LabsysEvo 1600). The heating rate was 10K/min in air atmosphere under air flow of 20 mL/min. The IR spectra of the glasses were recorded in the 1600–400 cm^{-1} region, using the KBr pellet technique (Nicolet-320 FTIR spectrometer). The optical spectra of powder samples at room temperature were recorded with a spectrometer (Evolution 300 UV-vis Spectrophotometer) employing the integration sphere diffuse reflectance attachment. The uncertainty in the observed wavelength is about ± 1 nm. The Kubelka–Munk function ($F(R\infty)$) was calculated from the UV–Vis diffuse reflectance spectra. The band gap energy (Eg) was determined by plot $(F(R\infty) h\nu)^{1/n}$, n = 2 versus hν (incident photon energy). The photoluminescence (PL) spectra in the visible region of Eu^{3+} ions for the glass and glass–crystalline samples were recorded with PL spectrometer (Scinco FS-2 with wavelength accuracy 1 nm) at room temperature in which the excitation light of a wavelength λ = 464 nm was used.

RESULTS

Different phases were developed, applying several melting temperatures. According to the XRD data (Fig. 1 a, b, c, d), glass-crystalline materials containing $LaBO_3$ (JCPDS-00-012-0762) as crystalline phase were obtained at 1050 °C and 1100 °C, while x-ray amorphous samples were prepared at 1200°C. Visual observation of the obtained samples supported these experimental results. The two glasses $55B_2O_3 \cdot 35Bi_2O_3 \cdot 10La_2O_3$ and $55B_2O_3 \cdot 35Bi_2O_3 \cdot 10La_2O_3$: Eu^{3+} were dark brown and completely transparent. Glass-crystalline $55B_2O_3 \cdot 35Bi_2O_3 \cdot 10La_2O_3$: Eu^{3+} specimen obtained at 1100 °C was yellow and opaque, while the sample melted at 1050 °C was opaquer probably as a result of its higher crystallinity.

We used the IR spectroscopy in order to check the effect of addition of Eu_2O_3 in $55B_2O_3 \cdot 35Bi_2O_3 \cdot 10La_2O_3$ glass matrix (Fig. 2). As it is seen from the figure, there is no noticeable difference in the spectra of both glasses. They contain absorption peaks characteristic of the BO_3 (1360 cm^{-1}, 1290 cm^{-1}, 1190 cm^{-1} and 695 cm^{-1}); BO_4 (1020 cm^{-1} and 910 cm^{-1}) and BiO_6 (540 cm^{-1} and 480 cm^{-1}) structural groups [6-8]. In order to get more precise information about the europium ions effect on the glass structure, we deconvoluted glass spectra to check the relative population of

boron in different structural units (BO_3 and BO_4). Fig 3 (a, b) shows the deconvolution in Gaussian bands, of the investigated spectra. Each component
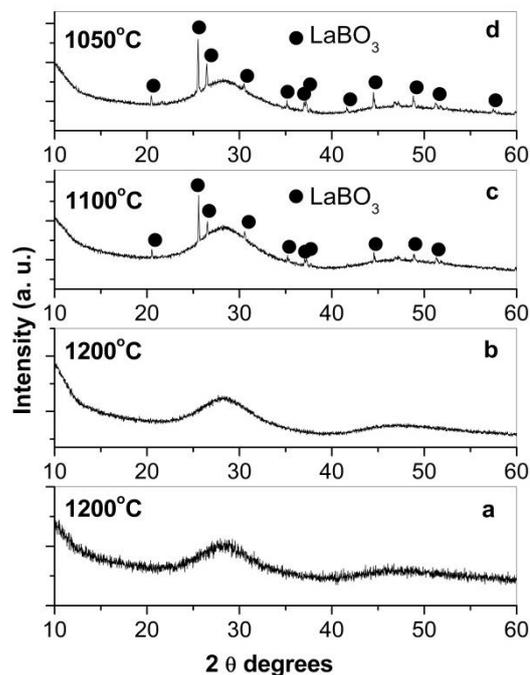

Fig. 1. XRD patterns of $55B_2O_3 \cdot 35Bi_2O_3 \cdot 10La_2O_3$ (a) and $55B_2O_3 \cdot 35Bi_2O_3 \cdot 10La_2O_3$: Eu^{3+} (b-d) glass and glass-crystalline samples obtained by melt quenching at different temperatures.
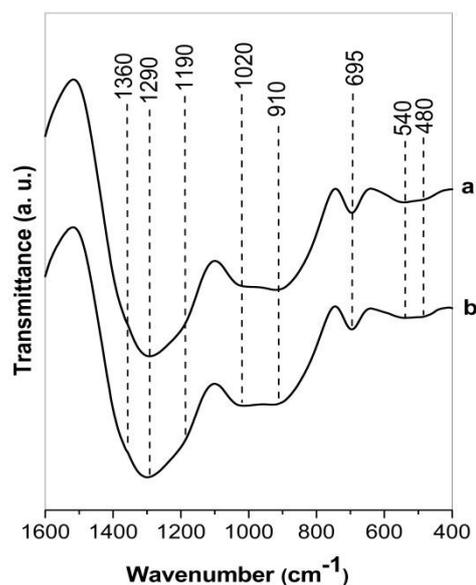
Fig. 2. IR spectra of $55B_2O_3 \cdot 35Bi_2O_3 \cdot 10La_2O_3$ (a) and $55B_2O_3 \cdot 35Bi_2O_3 \cdot 10La_2O_3$: Eu^{3+} (b) glass samples obtained by melt quenching technique.

band is related to some type of vibration in specific structural groups. The concentration of the structural group was considered to be proportional

to the relative area of its component band. The deconvolution parameters (the band centre at C and the relative area A) and the band assignments are given in Table 1. These characteristic parameters are used to calculate the fraction N_4 of BO_4 units in the bismuth-borate matrix. N_4 can be defined as the
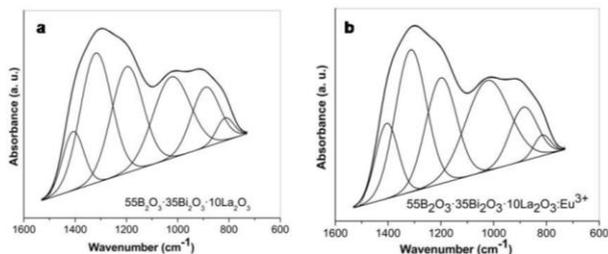

Fig. 3. Deconvoluted IR spectra of:
(a) $55B_2O_3 \cdot 35Bi_2O_3 \cdot 10La_2O_3$ and (b)
$55B_2O_3 \cdot 35Bi_2O_3 \cdot 10La_2O_3 : Eu^{3+}$ glass samples obtained by melt quenching technique.

Table 1. Deconvolution parameters (the band centers C and the relative area A) and the band assignments for the undoped and Eu^{3+} doped $55B_2O_3 \cdot 35Bi_2O_3 \cdot 10La_2O_3$ glass

| Sample	C	A	Assignments	Ref.
$55B_2O_3$ $35Bi_2O_3$ $10La_2O_3$	815	2.8	B-O stretch vibration in BO_4 groups	6-8
	892	12.1	B-O stretch vibration in BO_4 groups	6-8
	1025	21.9	B-O stretch vibration in BO_4 groups	6-8
	1197	24.7	B-O stretch vibration in BO_3 groups	6-8
	1319	29.5	B-O stretch vibration in BO_3 groups	6-8
	1408	9.0	B-O stretch vibration in BO_3 groups	6-8
$55B_2O_3$ $35Bi_2O_3$ $10La_2O$ Eu^{3+}	816	2.2	B-O stretch vibration in BO_4 groups	6-8
	887	9.7	B-O stretch vibration in BO_4 groups	6-8
	1024	26.18	B-O stretch vibration in BO_4 groups	6-8
	1199	21.4	B-O stretch vibration in BO_3 groups	6-8
	1314	29.2	B-O stretch vibration in BO_3 groups	6-8
	1405	11.2	B-O stretch vibration in BO_3 groups	6-8

samples ratio of the concentration of BO_4 units to the concentration of (BO_3+BO_4) units [4, 8]. The calculated N_4 values for the studied compositions are 0.36 and 0.38 for the undoped and Eu^{3+} doped $55B_2O_3 \cdot 35Bi_2O_3 \cdot 10La_2O_3$ glass respectively. The higher N_4 values for the Eu^{3+} doped sample calculated reveals that the presence of europium ions influences the surroundings of the B^{3+} cations favouring the formation of the BO_4 structural units and in this way the glass network became more stable [8].
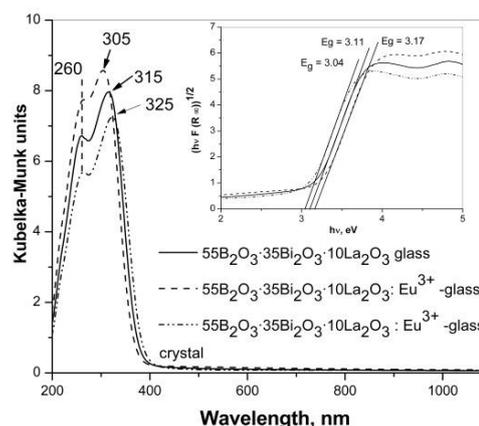
Fig. 4. DR-UV-Vis spectra and the band gap energy E_g (inset) of $55B_2O_3 \cdot 35Bi_2O_3 \cdot 10La_2O_3$ and $55B_2O_3 \cdot 35Bi_2O_3 \cdot 10La_2O_3:Eu^{3+}$ glasses and $55B_2O_3 \cdot 35Bi_2O_3 \cdot 10La_2O_3 : Eu^{3+}$ glass-crystal obtained by melt quenching technique.

The structural modification of the $55B_2O_3 \cdot 35Bi_2O_3 \cdot 10La_2O_3$ glass network, caused by the presence of Eu_2O_3 is also evidenced by DR-UV-vis spectroscopy. Fig. 4 displays the diffuse reflectance spectra of undoped and Eu^{3+} doped $55B_2O_3 \cdot 35Bi_2O_3 \cdot 10La_2O_3$ glasses and $55B_2O_3 \cdot 35Bi_2O_3 \cdot 10La_2O_3: Eu^{3+}$ glass-crystal. In all spectra, two absorption bands at 260 nm and 305-325 nm are observed. In the Eu^{3+} free spectrum these bands are due to $^1S_0 \rightarrow {}^3P_1$ and $^1P_1$ transitions of Bi^{3+} ions [9, 10]. The higher absorption intensity in the spectrum of Eu^{3+} doped glass is a result of the contribution of ligand-to-metal charge-transfer band of Eu^{3+} ions (310-315 nm) [11, 12]. In addition, the band located at 315 nm in the spectrum of Eu^{3+} free glass slightly blue shifts to 305 nm in the presence of Eu_2O_3. The observed spectral differences can be explained in terms of the structural changes that are taking place with the incorporation of the Eu^{3+} ions in the glass network [9, 10]. The shift towards lower wavenumber can be explained with the formation of more symmetrical EuO_6 and BiO_6 units [13]. Optical band gap values (E_g) evaluated from the UV–Vis spectra can also give information about the structural arrangement of the glasses under

investigation. The calculated band gap (E_g) energy values for indirect transition (see the inset in the Fig. 4) are 3.11 eV and 3.17 eV for the undoped and Eu^{3+} doped $55B_2O_3 \cdot 35Bi_2O_3 \cdot 10La_2O_3$ glass respectively. According to the literature in glasses the variation of E_g may be attributed to the network structural changes [14, 15]. It is well known that in metal oxides, creation of non-bonding orbitals with higher energy than bonding ones shifts valence band to higher energy which results to E_g decreasing. However, in our case, E_g value of Eu^{3+} doped glass increases which evidence that Eu_2O_3 improves the connectivity inside the network by decreasing of the non-bridging oxygen species. In the case of glass-crystalline Eu^{3+} doped sample, the band above 300 nm shifts to higher wavenumber – 325 nm and E_g value is lower – 3.04 eV. These spectral features indicate that Eu^{3+} ions are with lower local symmetry.

obtained, Eu^{3+} doped glass has higher glass crystallization temperature T_x and possesses much higher thermal stability (higher ΔT) as compared with the undoped glass. These results suggest that the network structure of $55B_2O_3 \cdot 35Bi_2O_3 \cdot 10La_2O_3$: Eu^{3+} glass is becoming stronger with the introduction of Eu_2O_3.
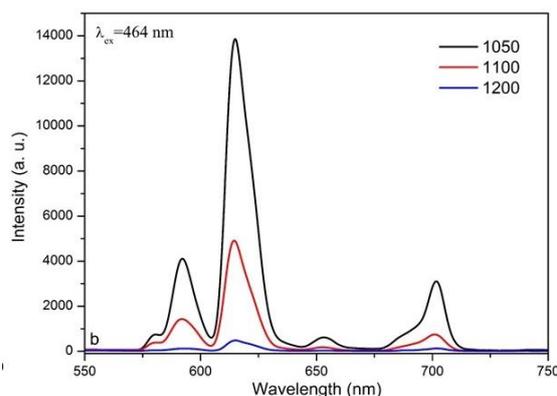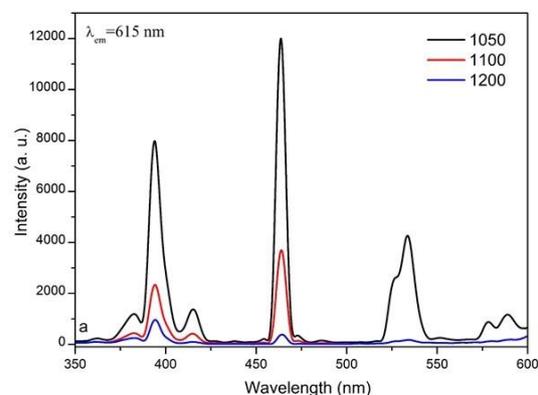
Fig. 6. PL (a) excitation and (b) emission spectra of $55B_2O_3 \cdot 35Bi_2O_3 \cdot 10La_2O_3 : Eu^{3+}$ glass and glass-crystal samples obtained by melt quenching technique at different temperatures.

Fig. 5. DTA curves of $55B_2O_3 \cdot 35Bi_2O_3 \cdot 10La_2O_3$ and $55B_2O_3 \cdot 35Bi_2O_3 \cdot 10La_2O_3 : Eu^{3+}$ glass samples obtained by melt quenching technique.

The formation of more rigid glass structure with the addition of Eu_2O_3 is also confirmed by the DTA data obtained (Fig. 5). For the undoped $55B_2O_3 \cdot 35Bi_2O_3 \cdot 10La_2O_3$ glass, DTA shows a hump, corresponding to the glass transition temperature T_g at 505 °C, followed by one exothermic peak at 530 °C, corresponding to crystallization temperature - T_x and other endothermic event, corresponding to the melting temperature T_m – 650 °C. For the Eu^{3+} doped glass the glass transition temperature T_g is at 457 °C, exothermic peak of crystallization T_x at 590 °C and endothermic peak, corresponding to the melting temperature T_m at 680 °C. The temperature difference $\Delta T = T_x - T_g$, gives a measure of the thermal stability of a glass against crystallization is 25 °C and 133 °C for the undoped and Eu^{3+} doped glass respectively. As it is seen from the DTA data

The PL excitation and emission spectra at room temperature for prepared $55B_2O_3 \cdot 35Bi_2O_3 \cdot 10La_2O_3 : Eu^{3+}$ glass and glass-crystals are shown on Fig. 6 a and b. The monitoring of excitation spectra (Fig. 6a) shown that the intensity of the absorption peak at 464 nm dominates in comparison with the intensity of the absorption at 394 nm. That is why the emission was registered with excitation at 464 nm. The emission spectra (Fig. 6b) excited at λ_{ex}=464 nm consist five peaks assigned to the 4f transitions of Eu^{3+} ions, i.e., $^5D_0 \rightarrow {}^7F_J$ (J=0, 1, 2, 3 and 4). It is seen that the peaks intensity for sample melted at 1050°C dominate as compared to the other samples because of its higher degree of crystallinity. It is well known that the $^5D_0 \rightarrow {}^7F_1$ transition situated around orange light (590 nm) is due to the magnetic dipole transition while

$^5D_0 \rightarrow {}^7F_2$ with red line (615 nm) corresponds to the electric dipole transition which band is dominant in all spectra [16, 17]. The ratio of integrated emission peaks intensity of the $^5D_0 \rightarrow {}^7F_2$ transition to that of the $^5D_0 \rightarrow {}^7F_1$ transition can be connected with the covalent/ionic bonding between Eu^{3+} ions and surrounding ligands. The increasing ratio value is due to the increasing of asymmetry between europium and oxygen ions [17]. For the sample synthesized at 1050 ^{o}C the calculated value is 0.25 while for the glass sample decrease to 0.15. These values indicate that Eu^{3+} ions are with lower local symmetry in the glass crystalline sample and they are in agreement with the DR-UV-vis results.

CONCLUSIONS

Glass and glass crystalline materials with nominal composition $55B_2O_3 \cdot 35Bi_2O_3 \cdot 10La_2O_3$ doped with 1 mol% Eu_2O_3 were synthesized by melt quenching technique and the influence of Eu^{3+} on the structure and optical properties of the glasses was investigated. The IR studies revealed the existence of BO_3, BO_4 and BiO_6 as the main structural units of the amorphous network. Europium ions generate structural changes, favoring the formation of the BO_4 units. The optical absorption studies revealed that the optical band gap energy (E_g) of glasses increases in the presence of Eu^{3+} ions, while Eg of glass crystalline sample decreases. Increase in Eg value evidence the decrease in number of non-bridging oxygen ions in the glass structure. DTA data showed that the introduction of Eu_2O_3 significantly improves thermal stability of $55B_2O_3 \cdot 35Bi_2O_3 \cdot 10La_2O_3$ glass. $LaBO_3$:Eu^{3+} crystals enhanced red $^5D_0 - {}^7F_2$ photoluminescence emission of the glass–crystalline samples as compared to the glass sample.

REFERENCES

1. P. Yasaka, J. Kaewkhao, *2015 4th International Conference on Instrumentation, Communications, Information Technology, and Biomedical Engineering (ICICI-BME),* Bandung, pp. 4, (2015), doi: 10.1109/ICICI-BME.2015.7401304.
2. M.A. Marzouk, *J. Molec. Struct.,* **1019**, 80 (2012).
3. A. Bajaj, A. Khanna, N. K. Kulkarni, S. K. Aggarwal, *J. Am. Ceram. Soc.*, **92**, 1036 (2009).
4. M. Farouk, A. Samir, F. Metawe, M. Elokr, *J. Non- Cryst. Solids*, **371-372**, 14 (2013).
5. Y. Cheng, H. Xiao, W. Guo, *Ceram. Int.*, **34**, 1335 (2008).
6. Y. Cheng, H. Xiao, W. Guo, *Mater. Sci. Eng. A,* **480**, 56 (2008).
7. E. I. Kamitsos, M. A. Karakassides, G. D. Chryssikos, *J. Phys. Chem.*, **91**, 1067 (1987).
8. P. Pascuta, S. Rada, G. Borodi,, M. Bosca, L. Pop, E. Culea, *J. Mol. Struct.*, **924-926**, 214 (2009).
9. A. Sontakke, A. Tarafder, K. Biswas, K. Annapurna, *Phys. B*, **404**, 3525 (2009).
10. C. Kim, H. Park, S. Mho, *Solid State Commun.*, **101,** 109 (1997).
11. M. Gusik, E. Tomaszewicz, S. M. Kaczmarek, J. Cybińska, H. Fuks, *J. Non-Cryst. Sol.*, **356**, 1902 (2010).
12. C. A. Kodaira, H. F. Brito, O. L. Malta, O. A. Serra, *J. Lumin.*, **101**, 11 (2003).
13. E. I. Ross-Medgaarden, I. E. Wachs, *J. Phys. Chem. C*, **11**, 15089 (2007).
14. R. Jose, T. Suzuki, Y. Ohishi, *J. Non-Cryst. Solids*, **352**, 5564 (2006).
15. S. Rani, S. Sanghi, N. Ahlawat, A. Agarwal, *J. Alloys Comp.,* **597**, 110 (2014).
16. Y. Zhou, J. Xu, Z. Zhang, M. You, *J. Alloys Comp.*, **615**, 624 (2014).
17. J. Pisarska, L. Zur, W. A. Pisarsky, *Opt. Fibers Their Aplic.*, **8010**, 80100N1 (2011).

ОПТИЧНО ОХАРАКТЕРИЗИРАНЕ НА ДОТИРАНИ С EU³⁺ ЙОНИ, СТЪКЛА И СТЪКЛОКРИСТАЛНИ МАТЕРИАЛИ В СИСТЕМАТА B_2O_3-BI_2O_3-LA_2O_3

Р. С. Йорданова[1], М. К. Миланова[1], Л. И. Александров[1], А. Канна[2], Н. Георгиев[3]

[1]*Институт по обща и неорганична химия, Българска академия на науките, ул. Г. Бончев, бл. 11, 1113 София, България, *e-mail:lubomirivov@gmail.com*

[2] *Университет Гуру Нанак Деф, Амритсар, Пенджаб, Индия*

[3]*Химикотехнологичен и металургичен университет, ул. Климент Охридски 8, 1756 София, България*

(Резюме)

По метода на преохладена стопилка, са синтезирани стъкла и стъклокристални материали с номинален състав $55B_2O_3 \cdot 35Bi_2O_3 \cdot 10La_2O_3$, дотирани с 1 мол.% Eu_2O_3. В зависимост от приложената температура на топене, са получени различни фази. Според данните от рентгенофазовият анализ, са получени стъклокристални материали, съдържащи $LaBO_3$ като кристална фаза при 1050 °C и 1100 °C, докато при 1200°C е синтезиран рентгено-аморфен образец. Термичните параметри на получените стъкла, са определени чрез диференциално-термичен анализ. Установено е, че термичната стабилност на стъкло, съдържащо Eu_2O_3 драстично нараства. Оптичните спектри, показват, че стъклата са прозрачни във видимата област на спектъра. Установено е, че стъклокристалните образци, съдържащи $LaBO_3$:Eu^{3+} се характеризират с повишена червена емисия $^5D_0-^7F_2$ в сравнение със стъклото. Това може да се обясни с по-ниската локална симетрия на Eu^{3+} йоните в кристалната фаза в сравнение със стъклото.

Optical band gap dependence on the oxalic acid concentration of antimony anodic oxide films

E. Lilov, V. Lilova, S. Nedev*

*Department of Physics, University of Chemical Technology and Metallurgy,
8 Kl. Ohridski blvd, 1756 Sofia, Bulgaria*

A decrease of the optical band gap of thin films of anodized antimony was observed when the concentration of the oxalic acid used as an electrolyte was increased. The thin films of antimony were obtained using vacuum-thermal evaporation on glass substrates. Electrodes were attached to them and the samples were galvanostaticaly anodized at a constant temperature in a standard two-electrode cell in an aqueous solution of oxalic acid at various concentrations. The normal-incident transmittance and reflectance spectra of the samples were measured and used to calculate by different numerical methods the absorption coefficients and the optical band gaps.

Key words: anodized antimony, oxalic acid, optical band gap, Tauc plot

INTRODUCTION

Interest in the thin antimony oxide layers is mainly related to their use in batteries, corrosion protection and the creation of catalysts. The anodizing is a very simple and cheap process used to obtain thin oxide films. Layers of various metals and semiconductors in which a high voltage anodizing can be achieved were investigated over many years. Antimony is such a valve metal, which in anodizing shows interesting features such as the presence of induction periods of time when in galvanostatic mode the voltage remains stable for a long period of time, and then suddenly begins to grow as normal. The study [1] of this phenomenon shows dependence on the electrolyte concentration and has no generally accepted explanation yet. The aim of our experiment is to find if another physical property - the optical band gap depends on the concentration too. Such dependence is interesting from theoretical and practical point of view.

An effect of reducing the width of the band gap of anodically grown ZnO thin films by increasing the concentration of oxalic acid has been observed in [2]. The same phenomena of band gap structure modification of amorphous anodic Al oxide film by Ti-alloying is observed in [3].

EXPERIMENTAL

Anodized antimony films, the objects of this study, were prepared in two stages. First, on borosilicate glass plates, thin layers of antimony were obtained by thermal evaporation in vacuum, situated to get gradually changing thickness. At the second stage a copper wire was attached to the film surface and the samples were placed in a galvanic bath at a constant room temperature. In a galvanostatic mode they were anodized using, at different concentrations, water solutions of oxalic acid as electrolyte. It is not possible to prepare a continuous, unbroken antimony oxide film if the thickness of the metallic antimony layer is constant. In this case cracks appear which can stop the process of anodizing on the parts of the film. The variable thickness of the antimony film provides a possibility for fully and smoothest oxidation of the layer, starting from the end with a smaller thickness and spread to the other end.

Measurements and calculations

X-ray diffraction studies show that the anodized layers have an amorphous structure. The thickness of the film on each sample was measured by interferometric method and used in calculations. All thicknesses are in the range of 200 – 340 nm.

In order to determine the optical band gap the spectrophotometer JASCO V-600 was used and the coefficients of transmission T and reflectance R were measured, illuminating the samples by incident light with different wavelengths, nearly normal to the surface. The optical band gap E_g can be extracted from the dependence of the absorption

* To whom all correspondence should be sent:
E-mail: nedev@uctm.edu

coefficient α on the light energy, which for amorphous materials is [4]:

$$(\alpha E)^{1/2} \approx E - E_g$$

E_g can be found approximating $(\alpha E)^{1/2}$ by straight line in the absorption region (Fig. 1 and Fig. 2).
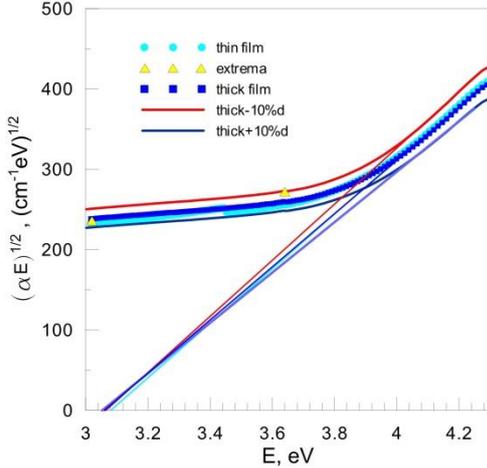
Fig. 1. Tauc plot for 0.01 M oxalic acid concentration. The results shown by circles are calculated from expressions for thin film, the boxes are from formulae for thick film, triangles correspond to results obtained from extrema of *R* and *T*.
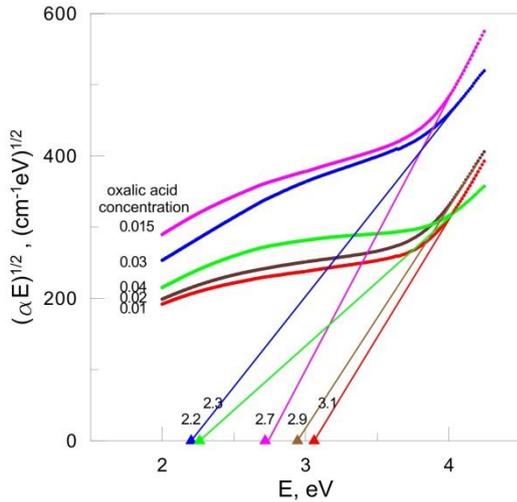
Fig. 2. Tauc plots for all oxalic acid concentrations. The tangent straight lines are used to find the optical energy bands shown at the bottom axis.

According to this method the absorption coefficient *α* have to be calculated from measured transmission coefficient *T* and reflectance coefficient *R*. They depend on the refractive indexes of the film and substrate, their absorption coefficients and the film thickness, according

expressions (1) – (2) given in Appendix. This system of two equations with two unknowns can be solved numerically for each wavelength, but a problem exists due to the periodic functions in Eqns. (1) and (2), which results in many solutions for the refractive index *n*. To select one an additional criterion is needed. We used *n*, calculated from the extreme of *R* and *T* according Eqn. (4) in Appendix and approximated linear in the regions between two extreme. The closest numerical solution is taken and referred in Fig. 1 as thin film.

We are interested of the region above 3.5 eV (Fig. 1), where the effects of interference are suppressed by the absorption. In the case of no coherent interference which happens in thick films, *T* and *R* are given by Eqns. (5) in Appendix. They are simpler then Eqns. (1) – (2) and have this advantage than can be solved explicitly – Eqns. (6) in Appendix. The results obtained, using this method, are referred in Fig. 1 as thick film.

We calculated absorption coefficients for all our samples using both methods. An example for a sample at 0.01M concentration is shown in Fig. 1. Dots denoted by circles are obtained from expressions for thin film Eqns. (1) – (2), the boxes are from Eqns. (6) for thick film and triangles correspond to results calculated from extreme of *R* and *T*. The difference between absorption coefficients obtained by both methods is small and the difference between correspondent optical band gaps does not exceed 0.06 eV for all samples. We calculated *R* and *T* according different models for the refractive index and extinction coefficient, including those in [5], and in all cases we found negligible the difference for the absorption coefficient in the absorption region.

Transmission and reflectance coefficients spectra for each sample are obtained in two separate measurements. It is possible that light rays from the spectrophotometer have been passed through different regions of the sample with different thickness. In order to explore the influence of this effect on the final results we calculated the absorption coefficient under assumption that transmission coefficient has a measured thickness, but the reflectance coefficient has a thickness which differs at ±10%. The Eqns. (6) for thick film were modified and Eqns. (7) obtained were solved numerically as explained in Appendix. The correspondent results for one sample are shown in Fig. 1 by solid lines. The error due to different width is less than 0.02 eV in all cases.

RESULTS

The Tauc plot for samples anodized in oxalic acid with different concentrations is shown in Fig. 2. The absorption coefficients are calculated using Eqns. (6) for thick film. The corresponding concentration is shown at the beginning of each curve. The line tangent to the curve in the region of absorption intercepts the abscissa at the optical band gap E_g. Each point is denoted by triangle in Fig. 2 and the corresponding value for band gap is given.
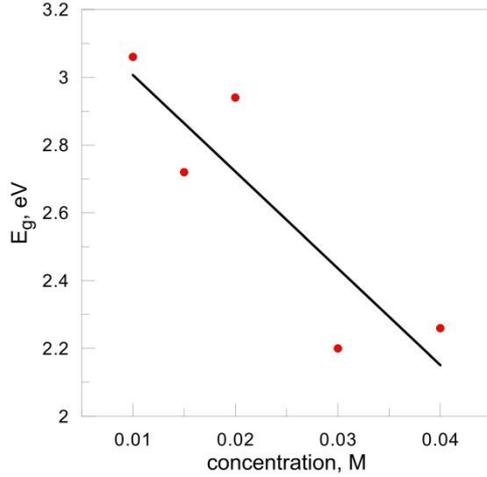
Fig. 3. Optical band gap of anodized antimony films depending on the concentration of the oxalic acid.

Fig. 3 shows the dependence of the optical band gap of anodized antimony thin films on the oxalic acid concentration. The straight line in Fig. 3 is a fit to the data. It is seen the variation of the molar concentration of the electrolyte has a significant effect on the optical band gap of the antimony films obtained in the process of anodic oxidation. The increase of the concentration leads to decrease of the band gap.

Our result corresponds to the reducing of the band gap of anodic oxid film of other metals. Such a decrease of the band gap due to increase of the concentration of oxalic acid has been observed in [2], but for ZnO thin films. This effect is explained there by the structure of the layer, composed of nanocrystals. The observed dependence correlates with the increasing size of the nanocrystals with concentration. Our case is different because the anodized antimony film has an amorphous structure. In [3] is observed the decrease of the band gap energy of Ti-alloyed anodic Al oxide with increasing Ti concentration.

CONCLUSIONS

Thin films of anodized antimony in solution of oxalic acid at various concentrations were obtained.

Their optical band gaps were calculated using very simple methods, based on the measurements of the coefficients of transmission and reflectance. A strong dependence of the optical band gap on the oxalic acid concentration has been observed.

REFERENCES

1. E. Lilov, Ch. Girginov, E. Klein, *Bulgn Chem. Commun.*, **45**, Special Edition A, 94 (2013).
2. P. Basu, E. Bontempti, S. Madji, H. Saha, S. Basu, *J. Mater Sci: Mater Electron*, **20,** 1203 (2009).
3. S. Canulescu, K. Rechendorff, C. Borca, N. Jones, K. Bordo, J. Schou, L. Nielsen, S. Hoffmann and R. Ambat, *App. Phys. Lett.*, **104**, 121910 (2014).
4. O. Stenzel, The physics of Thin Film Optical Spectra, Springer, (2005).
5. R Swanepoel, *J. Phys. E: Sci. Instrum.*, **16**, 1214 (1983).
6. J. Mullerova and J. Mordon, *Acta Phys. Slovaca*, **50**, 477 (2000).

APPENDIX

For a thin film on a thick transparent layer the transmission coefficient T for light normal to the surface is given by [5]:

$$T = \frac{Ax}{B - Cx - Dx^2}$$

$$A = 16s(n^2 + k^2)$$

$$B = [(n+1)^2 + k^2][(n+1)(n+s^2) + k^2]$$

$$C = [(n^2 - 1 + k^2)(n^2 - s^2 + k^2) - 2k^2(s^2 + 1)]2\cos\phi$$
$$- k[2(n^2 - s^2 + k^2) + (s^2 + 1)(n^2 - 1 + k^2)]2\sin\phi$$

$$D = [(n-1)^2 + k^2][(n-1)(n-s^2) + k^2] \qquad (1)$$

where n is the refractive index and k is the extinction coefficient of the film, s is the substrate refractive index and:

$$\phi = 4\pi nd/\lambda, \quad x = exp(-\alpha d), \quad \alpha = 4\pi k/\lambda \quad (2)$$

According to [6] the reflectance R from a thin film on a thick substrate illuminated at nearly normal incident light is given by:

$$R = \frac{A + Bx + Cx^2}{D + Ex + Fx^2}$$

$$A = [(n-1)^2 + k^2][(n+s)^2 + (k+k_s)^2]$$
$$C = [(n+1)^2 + k^2][(n-s)^2 + (k-k_s)^2]$$
$$D = [(n+1)^2 + k^2][(n+s)^2 + (k+k_s)^2]$$
$$F = [(n-1)^2 + k^2][(n-s)^2 + (k-k_s)^2]$$

$A' = (1 - n^2 - k^2)(n^2 - s^2 + k^2 - k_s^2) + 4k(nk_s - sk)$

$B' = 2(1 - n^2 - k^2)(nk_s - sk) - 2k(n^2 - s^2 + k^2 - k_s^2)$

$B = 2[A' \cos\phi + B' \sin\phi]$

$C' = (1 - n^2 - k^2)(n^2 - s^2 + k^2 - k_s^2) - 4k(nk_s - sk)$

$D' = 2(1 - n^2 - k^2)(nk_s - sk) + 2k(n^2 - s^2 + k^2 - k_s^2)$

$E = 2[C' \cos\phi + D' \sin\phi]$ 　　　　(3)

where *n, k, s, x*, α, ϕ have the same meaning and k_s is the substrate extinction.

The condition for extreme of *T* and *R* is:

$2nd = m\lambda$ 　　　　　　　(4)

where *m*=1,2,3… is an integer number in the case of maximum of *T* and minimum of *R*, and a half-integer number 1/2,3/2,5/2… in the case of minimum of *T* and maximum of *R*. It is seen the refractive index can be easily calculated if the thickness *d* is known and the order *m* of at least one extremum is known.

The formulae of transmittance and reflectance from a thick slab given in [4] are:

$$R = R_0 \left(1 + \frac{(1+R)^2 \left(1 + \frac{k^2}{n^2}\right) e^{-2\alpha d}}{1 - R_0^2 e^{-2\alpha d}} \right),$$

$$T = \frac{(1-R_0)^2 e^{-\alpha d}}{1 - R_0^2 e^{-2\alpha d}} \left(1 + \frac{k^2}{n^2}\right)$$

$$R_0 = \frac{(n-1)^2 + k^2}{(n+1)^2 + k^2}$$ 　　　　(5)

In our case $k / n \ll 1$, and Eqns. (5) can be rewritten:

$$R = R_0 \frac{1 + (1 - 2R_0)x^2}{1 - R_0^2 x^2}, \quad T = \frac{(1-R_0)^2 x}{1 - R_0^2 x^2}$$

These equations can be solved explicitly:

$$R_0 = \frac{1 + 2R - R^2 + T^2 - \sqrt{(1 - 2R + R^2 - T^2)^2 + 4T^2}}{2(2 - R)}$$

$$x = \frac{-1 + 2R - R^2 + T^2 + \sqrt{(1 - 2R + R^2 - T^2)^2 + 4T^2}}{2T}$$

　　　　　　　　　(6)

The absorption coefficient is calculated from (2), and after that *k* and *n*:

$$n = \frac{1 + R_0 + \sqrt{4R_0 - k^2(1 - R_0)^2}}{1 - R_0}$$

If *R* and *T* of a sample are measured at different thickness the formulae above must be changed. Let us suppose that *R* is measured at thickness d_1 and *T* at d_2:

$$x_1 = \exp(-\alpha d_1), \qquad x_2 = \exp(-\alpha d_2),$$

$$R = R_0 \frac{1 + (1 - 2R_0)x_1^2}{1 - R_0^2 x_1^2}, \quad T = \frac{(1-R_0)^2 x_2}{1 - R_0^2 x_2^2}$$ 　(7)

These equations can be solved very easily by iteration method. Starting with the values obtained at equal thickness, R_0 from the first equation is found and after that α from the second. The convergence is very fast and 2-3 iterations are enough.

ЗАВИСИМОСТ НА ОПТИЧЕСКАТА ШИРОЧИНА НА ЗАБРАНЕНАТА ЗОНА НА АНОДИРАНИ АНТИМОНОВИ ФИЛМИ ОТ КОНЦЕНТРАЦИЯТА НА ОКСАЛОВАТА КИСЕЛИНА

Е. И. Лилов, В. Д. Лилова, С. Н. Недев

Физически факултет, Химикотехнологичен и металургичен университет,
бул. Климент Охридски, 8, София 1756, България

(Резюме)

Наблюдавано е намаляване на оптическата широчина на забранената зона на тънки слоеве от анодиран антимон, когато концентрацията на оксаловата киселина използвана като електролит се увеличава. Тънките слоеве от антимон бяха получени чрез вакуумно-термично изпарение върху стъкло. Към тях бяха прикрепени електроди и бяха анодирани галваностатично при постоянна температура в стандартна дву-електродна клетка във воден разтвор на оксалова киселина с различни концентрации. Спектрите на преминаване и отражение, перпендикулярно на повърхността на пробите, бяха измерени и използвани за пресмятане чрез различни числени методи на коефициентите на поглъщане и широчините на забранените зони.

Proton exchange technology for optical waveguides in lithium niobate and lithium tantalate – an overview

M. Kuneva*

Institute of Solid State Physics, Bulgarian Academy of Sciences, 72 Tzarigradsko Chaussee Blvd, 1784 Sofia, Bulgaria

Lithium niobate (LN) and lithium tantalate (LT) are nonlinear, birefringent crystals with an important role in optoelectronics. Beside their excellent optical properties, their most prominent feature is the high electro-optical coefficient (r_{33}»30.5 pm/V) which allows the light field to be easily controlled by electric signals. Proton exchange (PE) is a method of obtaining $LiM_{1-x}H_xO_3$ layers (M = Nb, Ta) on $LiMO_3$ substrates. The PE layers have a significantly higher extraordinary refractive index (n_e) than the non-protonated crystal; the change is $\Delta n_e = 0.120$-0.150 for LN and $\Delta n_e = 0.015$-0.020 for LT at wavelength 0.633 μm providing a strong waveguide and polarizing effect.

The present paper aims at summarizing the most significant technological modifications of the method of PE and the most important waveguide structures of $LiM_{1-x}H_xO_3$ for different modulators used in modern optoelectronic devices (navigation and communication systems, biosensors, etc.).

Keywords: proton exchange, optical waveguides, integrated optics

INTRODUCTION

Two of the most widely used ferroelectric materials in integrated optics (IO) are lithium niobate - $LiNbO_3$ (LN) and lithium tantalate - $LiTaO_3$ (LT). This is due to their high electro-optical (EO) coefficients ($r_{33} \approx 30.5$ pm/V) and the possibility to change the refractive index by modifying their composition in regions where waveguiding of light is required. These features, combined with excellent optical properties and suitability for industrial production, make them key materials for photonics.

Proton exchange is a technology with already well-studied advantages and known prospects for the obtaining of optical waveguides in LN and LT, as well as of a wide range of passive elements and active optoelectronic devices.

PROTON EXCHANGE TECHNOLOGY

Proton exchange is an induced - at favorable conditions - diffusion of protons into the surface layer of a crystal substrate, whereby the layer's refractive index becomes higher than that of the substrate. The method is interesting with its simplicity and fastness, combined with the possibility of a strong waveguide effect (a significant change of the refractive index), low diffusion temperature (150-300 °C, of particular importance for LT) and decreased photorefractive susceptibility. Proton exchange increases the extraordinary refractive index (up to 0.15 for LN and 0.02 for LT at 633 nm) and lowers the ordinary refractive index; therefore, depending on the orientation of the substrate, the propagation of only one polarization is sustained (TE for X- and Y-cut samples or TM for Z-cut samples), i.e. PE waveguides guide only light polarized along the optical axis of the crystal. Going by the scheme:

$LiMO_3 + xH^+ \Rightarrow Li_{1-x}H_xMO_3 + xLi^+$ (M=Nb, Ta),

PE modifies the surface layer (several μm in depth) by Li-H ion exchange at a relatively low temperature (160÷250 °C), usually in acidic melts. The diffusion is anisotropic and the value of the diffusion coefficient depends on the substrate crystallographic orientation. This process changes the structure and the composition of the exchanged area. The PE layers show complex phase behavior depending on the hydrogen concentration (the value of x). The value of x determines the concentration limits of the different phases that could form in the waveguide layer (up to 7 in LN and 5 in LT) [1, 2]. The formation of phases depends in a complex way on the crystallographic orientation and the diffusion parameters. Each phase forms a separate sublayer of submicron thickness, and differs from the others by its structural and optical properties. The phases

* To whom all correspondence should be sent:
E-mail: m_kuneva@yahoo.com

also have different lattice parameters. At the interface of two phases, a rapid change of the extraordinary refractive index (Δn_e) and the deformation perpendicular to the surface is observed. Within each phase, Δn_e is proportional to x. The phase composition determines the properties and the quality of the obtained waveguides. Strong protonation considerably worsens the electro-optical properties, causes higher losses and some instability of the parameters over time. These can be avoided by using the methods given below for optimization of proton concentration and optical profiles of the PE layers:

PE – proton exchange [3] – a one-step process which takes place when LN or LT substrate is immersed in an appropriate proton source. PE waveguides usually have step-like optical profile and nearly vanished EO-coefficients [4].

DPE – deep proton exchange [5] – proton exchange for achieving a large change of the refractive index (Δn_e=0.15). Optical profile is almost step-like, better approximated by two rectangular steps (or truncated parabolic profile shape) [6].

ADPE – DPE with subsequent long time and high temperature annealing (two-step process) applied for obtaining deeper (over 20 μm thick) waveguides [5].

VPE – PE in vapors (one-step process) [7, 8]. VPE allows highly homogeneous monophase waveguides with very low propagation losses to be obtained by PE and reverse diffusion within a single chemical reaction [7].

SPE – soft proton exchange in buffered melts (i.e. lithium benzoate added to the benzoic acid) - one-step process for obtaining of waveguides with preserved EO properties [9].

HTPE – high temperature PE (one-step process). Acid with a higher boiling point and lower vapor pressure is used as a proton source [10]. High quality α-phase waveguides could be obtained directly (with no phase transitions) for a short time.

APE – PE with subsequent annealing (two-step process) for obtaining monophase (α) waveguides with restored EO properties after phase transitions from phases of high values of x to the phase of lower value of x [11].

PEAPE – two-step PE with intermittent annealing (three-step process) [12, 13], appropriate for obtaining deep waveguides with high refractive index change in Y-cut LN.

RPE – reverse PE (two-step process) [14] for obtaining buried waveguides with various properties. Takes place when PE-waveguide is immersed in eutectic mixture of $LiNO_3$, KNO_3 and $NaNO_3$.

RAPE – RPE in APE waveguides (three-step process) [15] used to bury the waveguide under the crystal surface, increasing that way the circular symmetry of the optical mode.

Thus a predetermined phase composition that meets particular requirements – a high refractive index, high electro-optical coefficients, low optical losses, stable parameters over time, decreased photorefractive susceptibility, or combinations thereof – can be achieved with an appropriate selection of proton exchange conditions.

APPLICATIONS IN PHOTONICS, OPTOELECTRONICS AND SENSORS

Proton exchange is mainly used for the obtaining of high-quality waveguides for different modulators, switches, multiplexers and Y-splitters as main elements of modern optoelectronic devices for navigation equipment, communication systems, in a number of sensors (detectors of molecules in fluids, biosensors, contamination detectors, temperature sensors, etc.) and many devices for interferometric control. Proton-exchanged LN and LT waveguide devices are favored over Ti-diffused LN ones in cases where high optical powers are to be transmitted and/or single polarization operation is desired. Some examples illustrating the use of the PE technology in modern optoelectronics are given below.

1. Phase modulator

Phase modulation originates from the elecrto-optical properties of LN (LT) when the refractive index changes, causing phase variation of propagating light. Principle schemes of three modifications of the phase modulator are shown in Fig.1. The device consists of a stripe waveguide (2) formed in the crystal substrate (1) and electrode configuration (3) (Fig. 1 a and b). When electric field is applied via electrodes, a phase change ($\Delta\varphi$) takes place in the light travelling along the electrodes (longitude L). The phase shifting is expressed by

$$\Delta\varphi=k\Delta nL \tag{1}$$

where k is a wave factor $k=2\pi/\lambda$ (λ is the light wavelength in vacuum) and Δn is the refractive index change.

As a phase shifter, this modulator is an important component in many EO lightguiding

structures, due to its simplicity, efficiency and high speed, e.g., in different interferometric systems for phase deviation or compensation in the two arms. The EO phase shifters are very popular in fiber optic sensor technology because of the advantage that the phase measurements are not influenced by amplitude variations.
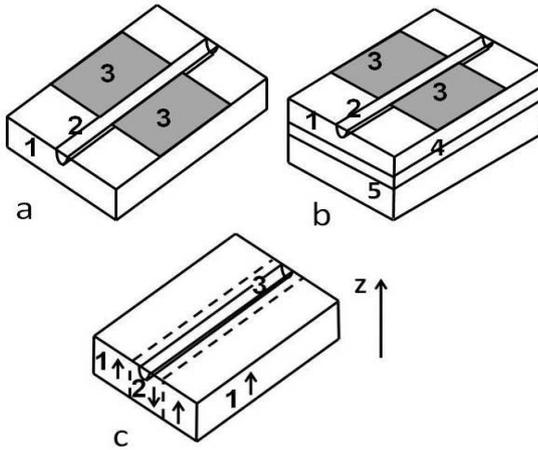
Fig. 1. A principle scheme of a phase shifter (a); PELN on insulator phase modulator (b): 1 – substrate, 2 – PE stripe waveguide, 3- electrodes, 4 – SiO$_2$ layer; schematic representation of a dipole inverted PE element for electric field sensor (c): 1, 2 – DI regions, 3 – PE stripe

An example of the application of combined advanced technologies for obtaining a phase modulator is discussed in [16]. A proton-exchanged stripe waveguide (near cut-off) is formed in the LN on insulator film (Fig. 2b). The lithium niobate on insulator technology (LNOI) is attractive due to the high optical confinement and enhanced lightguiding capability. The structure has a low driving voltage and could be used in high sensitivity sensors.

Another example of a device based on dipole inverted (DI) PELN is an all-optical electric field sensor proposed in [17]. A proton-exchanged stripe waveguide (3) near cut-off is fabricated in the central DI region (2) of a Z-cut LN substrate (Fig. 2c). When external electric field is applied parallel to the z-axis of the substrate, the refractive index in the DI region increases/decreases but that in the surrounding domains (1) decreases/increases causing mismatch of the guided modes between active and passive regions and thus produces a loss after a sufficient propagation length. Electric field intensities up to 20 MV/m could be measured this way.

2. Mach-Zehnder (MZM) modulator/interferometer

The Mach-Zehnder interferometer structure is the most frequently used type of EO amplitude modulator and is a basic structure in a variety of IO devices. As in the classical bulk configuration of the MZ interferometer, light splits into two optical paths with no possibility of interaction. The key point in the interferometric modulators working on the Mach-Zehnder principle from classic optics consists of (in their integrated-optical version) two Y-junctions which perform the function of beam splitting and coupling into the stripe waveguides which represent the interferometer's channels (Fig. 2a). The refractive index (i.e. the propagation velocity) in each arm could be modified by applying electric field, changing that way the interferometric pattern at the output. The performance of the device strongly depends on the electrode configuration and waveguide architecture.
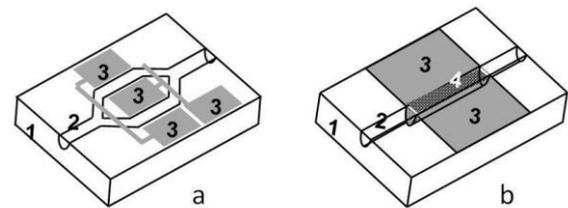
Fig. 2. Principle schemes of MZM: (a) - classical configuration; (b) – single-stripe MZM; 1 – substrate, 2- PE-stripe (supports single mode), 3 – electrodes, 4 – deeper stripe (supports 2 modes)

A fundamentally new, technologically simpler broadband IO modulator - a single-stripe MZM (Fig. 2b) has been designed based on the polarizing action of PELN [18]. The waveguide structure is formed in the LN X-cut wafer (1) and consists of a single-mode channel waveguide (2) whose central region (4) is deeper (produced via double proton exchange), has a higher rate of refractive index change and supports two modes. This new construction uses the simplest electrode configuration consisting of two parallel driving electrodes (3). Upon reaching region (4), light divides into two orthogonal modes which propagate independently, and after voltage is applied to the electrodes, the phase for each optical mode changes in a different way because the overlapping integrals for electric and optic fields are different for each mode. Reaching the end of the two-mode region, these two modes interfere and the light continues propagating as a single mode whose intensity depends on the phase difference between modes in the central region, i.e. on the voltage applied. This construction together with the technology used allows easier control of the geometry and the composition of waveguiding regions as well as

23

further device minimization (long Y-splitter's length being avoided).

CONCLUSIONS

Due to the importance of PELN and PELT for integrated optics, a variety of methods have been developed for fabrication of waveguides in these materials but none of them is universally applicable. Very promising appear to be the combined methods, and the efforts are aimed at the introduction of some technological modifications of the existing methods.

The PE technology has left its laboratory research level and reaches the manufacturing stage. Integrating single components and structures on a common chip allows a great variety of IO devices to be obtained.

The future developments will tend to attract new technologies like photonic crystal technologies and nanotechnologies for solving the problem of input and output coupling with application of IO devices. The achievement of higher data processing speeds and an increased level of integration are also among the current objectives of the development of PELN and PELT based optoelectronics.

REFERENCES

1. Yu. Korkishko, V. A. Fedorov , *Proc. SPIE*, **2700**, 186 (1996).
2. Yu. Korkishko, V. Fedorov, *IEEE J. Select. Top. Quant. El.*, **2**, 187 (1996).
3. J. L. Jackel, C. E. Rice, J. J. Veselka, *Appl. Phys. Lett.*, **41**, 607 (1982).
4. A. Méndez, G. De La Paliza, A. Garsia-Cabanes, J. M. Cabrera, *Appl. Phys. B*, **73**, 485 (2001).
5. M. Okazaki, T. Chichibi, S. Yoshimoto, H. Mizuna, and T. Suhara, *Jap. J. Appl. Phys.*, **54**, 301 (2015).
6. M. Kuneva, S. Tonchev, M. Sendova-Vasileva, D. Dimova-Malinovska, P. Atanasov, *Sensors and Actuators A*, **99**, 154 (2002).
7. M. Kuneva, S. Tonchev, P. Dimitrova, *J. Mat. Sci.:Materials in Electronics*, **14**, 859 (2003).
8. J. Rams, J. M. Cabrera, *J. Opt. Soc. Am. B*, **16**, 401 (1999).
9. K. Wong (1985). *Gec. J. Research*, **3**, 243 (1985).
10. Yu. N. Korkishko, V. A. Fedorov, O. Y. Feoktistova, *J. Lightwave Technol.*, **18**, 562(2000).
11. S. Al-Shukri, A. Dawar, R. De La Rue, A. Nutt., M. Taylor, J. Tobin, *Proc. 7th Top. Meet. On Integrated and guided wave optics* **PD7**, 1 (1984).
12. M. Kuneva, S. Tonchev, M. Pashtrapanska, *Cryst. Res. Technol.*, **32**, 387 (1997).
13. M. Kuneva, S. Tonchev, M. Pashtrapanska, I. Nedkov, *Materials Science in Semiconductor Processing*, **3**, 581 (2001).
14. Yu. N. Korkishko, V .A. Fedorov, T. M. Morozova, F. Caccavale, F. Gonella, F. Segato, *JOSA* A, **15**, 1838 (1998).
15. H. Hui, R. Richen, W. Sohler, Proc. ECIO'08, Eindhoven, The Netherlands, 2008, WeD3.
16. L. Cai, Y. Kang, H. Hu, *Optics Express*, **24**, 4640 (2016).
17. D. Tulli, D. Janner, M. Garcia-Granda, R. Ricken, V. Pruneri, *Appl. Phys. B*, **103**, 399 (2011)
18. S. Tonchev, M. Kuneva, *Proc. SPIE*, **3950**, 246 (2000); BG Patent, No. 63788, Bull. No.12, 29.12.2002.

ТЕХНОЛОГИЯТА ПРОТОНЕН ОБМЕН ЗА ОПТИЧНИ ВЪЛНОВОДИ В LiNbO$_3$ И LiTaO$_3$ – КРАТЪК ОБЗОР

М. Кънева

Институт по физика на твърдото тяло „Акад. Г. Наджаков",бул. Цариградско шосе 72, 1784 София

(Резюме)

Литиевият ниобат (ЛН) и литиевият танталат (ЛТ) са нелинейни, двойно лъчепречупващи кристали, които са от важно значение за оптоелектрониката. Най-забележителното в тях, освен отличните оптични качества, са високите им електрооптични коефициенти (r$_{33}$»30.5 pm/V), които позволяват светлинното поле да бъде лесно управлявано с помощта на електрически сигнали. Протонният обмен е метод за получаване на слоеве от LiM$_{1-x}$H$_x$O$_3$ (M = Nb, Ta) върху подложка от LiMO$_3$. Обменените слоеве имат съществено по-висок показател на пречупване (n$_e$) за необикновения лъч отколкото непротониран кристал (промяната в показателя на пречупване след протониране е Δn$_e$ = 0.120-0.150 за ЛН и Δn$_e$ = 0.015-0.020 за ЛТ при дължина на вълната 0.633 μm). Поради това те проявяват силно вълноводно и поляризиращо действие. Целта на настоящата публикация е обобщение на основните технологични модификации на метода и приложението му за различни модулатори, използвани като основна част на съвременните оптоелектронни устройства (навигационни и комуникационни системи, биодатчици и др.)

Digital image processing: denoising by adaptive median filtering and wavelet transform

P. Sharlandjiev, D. Nazarova and N. Berberova*

Institute for Optical Materials and Technologies "Acad. J. Malinowski", Bulgarian Academy of Sciences, "Acad. G. Bonchev" str. Bl. 109, 1113 Sofia, Bulgaria

Digital image processing is an important area of preservation and representation of cultural and historical objects. Part of it is the task of cleaning images corrupted by noise. Many different methods and approaches have been successfully implemented, but still filtering and denoising techniques are developing and improving intensively. Herein, we report numeric simulations of 2D image filtering. Effects of impulse noise are very efficiently reduced by adaptive median filtering. The situation of additive noise, which itself depends on the intensity of the original image, is more complicated. However, we demonstrate that in this case the use of wavelet transforms in the denoising procedure is very productive and promising..

Keywords: Digital image processing, adaptive median filter, wavelet denoising

INTRODUCTION

One of the principle areas of digital image processing methods is related to an improvement of pictorial information for human interpretation [1]. It includes preservation and representation of cultural and historical objects. Image enhancement and image restoration no doubt are related to denoising images with certain degradation. Many different methods and techniques have been successfully implemented, but still filtering and denoising are developing and improving intensively. That is due to the fact that there is no such thing as the 'best' or the 'ultimate' filter. Restoration techniques are based on mathematical models of image degradation [1]. Thus denoising (a particular case of restoration) uses certain á priori knowledge of the degradation phenomena. It develops a probabilistic model of the noise and by a variety of numeric approaches, then solves the so-called inverse problem i.e. recovers the original.

Herein, we report numeric simulations of 2D image filtering. The original image is assumed to be without noise, and then it is corrupted by certain degradation. In Section 1 we consider the so-called 'impulse noise', which is widespread in many image deteriorations. In this case, we have implemented the adaptive median algorithm [1]. The denoising software is 'friendly' and effective,

so it can be used by non-IT specialists. Section 2 is addressed to image processing specialists. There, the situation of additive noise, which itself depends on the intensity of the original image, is treated. We demonstrate that in this case the use of wavelet transforms [1, 2] in the denoising procedure is very productive and promising.

IMPULSE NOISE: ADAPTIVE MEDIAN FILTERING

Impulse noise is also called shot noise, binary noise or 'salt and pepper' noise. It is easily identified in grayscale images because its appearance has randomly scattered white ('salt') and black ('pepper') dots (pixels) over the image [1]. In color images, the noisy pixels bear no relation to the color of the surrounding pixels. It is known [1, 2, 3] that Median Filtering (MF) is effective and widely used technique for reducing such noise. The main idea of MF is to scan the 2D image with a window (mask) of smaller size, and replace the value of each pixel in the image by the median of the neighboring pixels. A significant drawback of this nonlinear filter is that it does not preserve all details (edges) while removing noise [1, 3, 4]. As a result, the denoised image appears blurred. That is why we implemented the so-called Adaptive Median Filter (AMF). ADF main feature is that the size of the mask is changing during the processing. The filter adapts its behavior on the characteristics of the image in the mask region [1,

* To whom all correspondence should be sent:
E-mail: natali.berberova@gmail.com

4]. So, details are preserved and distortion is reduced. In our implementation there is one additional parameter: the size of the mask. In the modeling, we use another additional parameter: noise density. It gives the number of noise affected pixels (randomly selected over the image).

Fig. 1. Original image.

In Fig. 1 we present the original image that will be corrupted with impulse noise. It is a 19-th century icon and its grayscale image has 988 x 768 pixels. We have affected 7% of pixels with impulse noise. In Fig. 2 a section of the 'degraded' image is shown, so that salt and pepper dots are clearly visible.

Fig. 2. Section of the original image, contaminated with impulse 'salt and pepper' noise.

The AMF used in the denoising procedure has maximum window size of 11 x 11 pixels. The processing is robust and effective. In fact, AFM can smooth other noises that may be not impulsive [1, 4, 5].

In practice, visual control of the AMF denoised images is quite enough. However, for evaluation of the denoising procedure, we apply the Figure of Merit (FM) criterion, defined below in Section 2. The lower FM value, the better - when FM = 0, the denoised image is 'equal' to the original. The FM before the processing of the degraded image gives the starting point of the filtering. In this case FM = 0.036. After AMF processing, FM = 0.002 and we can consider the denoising as very effective. We have compared this result to the 'classical' median filtering, which results in FM = 0.02. Section of the denoised image is shown in Fig. 3.

Fig. 3. Section of the denoised image.

INTENSITY DEPENDENT NOISE: WAVELET TRANSFORM FILTERING

In digital image processing Wavelet Transforms (WT) are successfully used for edge detection, image enhancement and restoration, signal compression, denoising, etc. [1, 6, 7]. WT are often compared to the Fourier transform. WT have the advantage over Fourier transform because they provide insight into both image spatial and frequency characteristics [7, 8]. That is why WT are more efficient in image restoration. However, WT efficiency in denoising depends on the type of disturbance in the image. If we have in the preprocessing activity some information on the type of noise, which is to be expected, we can choose the most appropriate denoising method. If no such information is available, several WT should be explored [1, 7]. For 2D images usually discrete

wavelet transformations are applied and the wavelet is discretely sampled.

In general, the procedure includes several steps: 1) Compute signal WT. 2) Alter the transform coefficients. 3) Compute the inverse transform. 4) Evaluate the result.

In what follows we consider an image model (O) with additive intensity dependent noise. The 'degraded' image (J) can be described by the equation: J = O + N*O, where N is uniformly distributed random noise with zero mean and certain variance V. In the numeric modeling we have chosen the variance to be V = 0.02.
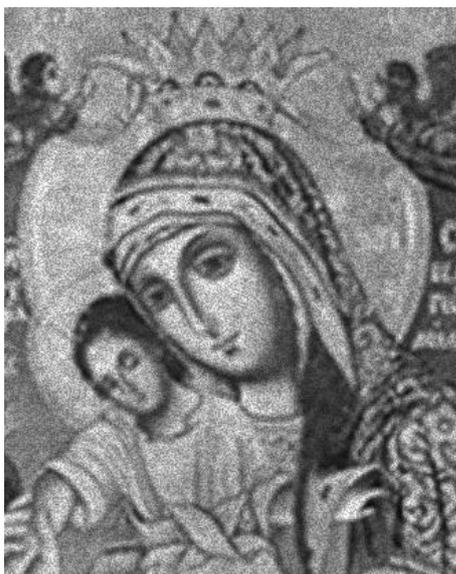
Fig. 4. Section of the original image, contaminated with intensity dependent noise
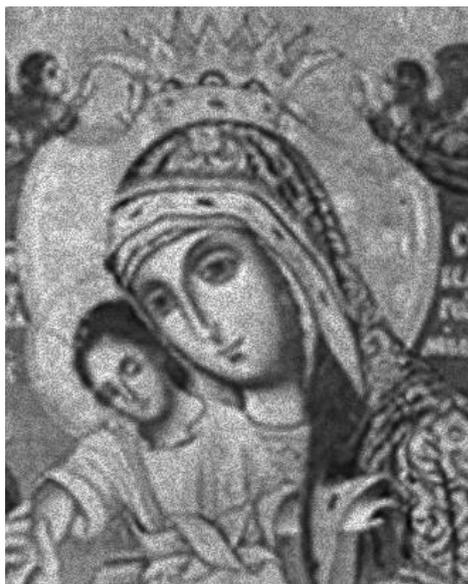
Fig. 5. Section of the denoised image.

In Fig. 4 we present a section of the model (original) image from Fig. 1, contaminated with intensity dependent noise. We have tried to denoise the image J by the adaptive median filtering, but the results were not satisfactory. Much better results were obtained when the denoising was performed with orthonormal wavelet "db4-2" (Daubechies wavelet of order 4, level of decomposition - 2).

In order to evaluate the efficiency of the filtering, we define a Figure of Merit (FM) as the ratio of the Euclidean norm of the difference between the original image and the processed image, to the Euclidean norm the original image. The norm of the difference between the original and the noisy image gives the starting point of the processing. In this case FM = 0.0612.

After the denoising, the FM is equal to 0.0087. This is a 7 fold improvement, even without optimization of the process. We continue the investigations in this field and results will be published elsewhere. Section of the denoised image with "db4-2" wavelet is shown in Fig. 5.

CONCLUSIONS

We have demonstrated that 2D images can be efficiently denoised by the help of adaptive median filtering and wavelet transforms. In the numeric modeling presented here, only the case of additive noise was considered. The impulse noise is cleared by AMF, while intensity dependent noise is better removed by WT. Both filtering approaches are found to be very robust and effective. The correlation between noise and filter characteristics indicates that we need a variety of filtering procedures and that the filtering process should be optimized over several different approaches. We intend to develop a set of diverse filters in order to attack the problem of multiplicative noise, which is of high practical importance.

REFERENCES

1. R.C. Gonzalez, R. E. Woods, Digital Image Processing, Prentice Hall, New Jersey, 2008.
2. G. Arce, Nonlinear Signal Processing: A Statistical Approach. Wiley, New Jersey, 2005.
3. M. Piccardi, IEEE Intern. Conf. on Systems, Man and Cybernetics, 4, 3099-3104 ISBN: 0-7803-8566-7, 2004.
4. H. –L. Eng, K.-K. Ma, *IEEE Trans. Image Proc.*, **10**, 242 (2001).

5. C. Penland, M. Ghil, K. Weickmann, *J. Geophys. Res.,* **96**, 22659 (1991).

6. S. Mallat, A Wavelet Tour of Signal Processing, Academic Press, London, 1999.

7. M. Petrou, C. Petrou, Image Processing: The Fundamentals, John Wiley & Sons, United Kingdom, 2010.

8. A. Akansu, W. A. Serdijn, I. W. Selesnick, *Phys. Comm.*, **3**, 1 (2010).

ОБРАБОТКА НА ЦИФРОВИ ИЗОБРАЖЕНИЯ: ИЗЧИСТВАНЕ НА ШУМА ЧРЕЗ АДАПТИВЕН МЕДИАНЕН ФИЛТЪР И ПО МЕТОДА НА ВЪЛНИЧКИТЕ

П. Шарланджиев, Д. Назърова, Н. Берберова

Институт по оптически материали и технологии "Акад. Й. Малиновски", Българска Академия на науките, ул. "Акад. Г. Бончев", бл. 109, 1113 София, България

(Резюме)

Обработването на цифрови изображения е важна част от съхраняването и предс-тавянето на културни и исторически обекти. Част от задачите са свързани с из-чистването на шума, насложен в изображенията. Много различни методи и под-ходи са успешно прилагани, но техниките за филтриране и изчистване на шума все по–интензивно се развиват и подобряват. В тази статия се докладва числена симулация за филтриране на двумерни изображения. Влиянията на импулсния шум са много ефикасно редуцирани чрез филтриране с адаптивен медианен филтър. При адитивен шум, който зависи от интензитета на оригиналното изображение, ситуацията е по-сложна. Въпреки това, ние показваме, че в този случай използване на трансформацията по метода на вълничките за премахването на шума е с добри резултати и е много обещаващо.

Phase recovery from fringe patterns with global carriers: approach based on Hilbert transform and wavelet de-noising techniques

P. Sharlandjiev*, N. Berberova, D. Nazarova and G. Stoilov[1]

Institute for Optical Materials and Technologies "Acad. J. Malinowski", Bulgarian Academy of Sciences,
"Acad. G. Bonchev" str. Bl. 109, 1113 Sofia, Bulgaria
[1]Institute of Mechanics, Bulgarian Academy of Sciences
„Akad. G. Bonchev" Str., block 4, Sofia PS-1113, Bulgaria,

Fringe pattern analysis is an important task in optical metrology. Fringe patterns can be formed by optical interference, by projection techniques, by overlapping two similar wave structures, etc. Patterns with constant global angular carriers represent straight lines in the field-of-view. The presence of an object under investigation distorts the fringes. Analysis of these distortions is called also phase recovery and it is widely used in many applications of science and engineering, i.e. for retrieval of surface topography of 3D objects. Usually, three steps are discerned: pre-processing (noise reduction, background zeroing), phase retrieval (extraction of the phase distribution), and post-processing (unwrapping, smoothing and 'cleaning').

Herein we present an approach based on a combination of Hilbert transform for phase recovery and different wavelet techniques for de-noising and smoothing. By numeric simulations we show that this technique is effective and robust. Different types of noise are considered: Gaussian additive noise, multiplicative intensity dependent (speckle) noise, high frequency environmental noise, jitter, fringe distortion due to non-sinusoidal modulation (presence of second and third harmonics in the fringes). Each type of noise can be considered separately or all of them – cumulatively.

Keywords: Optical metrology; Fringe projection; Numeric filter techniques

INTRODUCTION

Fringe pattern analysis is an important task in optical metrology. Fringe patterns can be formed by optical interference, by projection techniques, by overlapping two similar wave structures, etc. [1]. Patterns with constant global angular carriers represent straight lines in the field-of-view. The presence of an object under investigation distorts the fringes. Analysis of these distortions is called also phase recovery and it is widely used in many applications of science and engineering, i.e. for retrieval of surface topography of 3D objects [1,2]. Usually, three steps are discerned: pre-processing (noise reduction, background zeroing), phase retrieval (extraction of the phase distribution), and post-processing (unwrapping, smoothing and 'cleaning').

Herein we present an approach based on a combination of Hilbert transform [2] for phase recovery and different wavelet techniques for de-noising and smoothing. Different types of noise are considered: Gaussian additive noise, multiplicative intensity dependent (speckle) noise, high frequency environmental noise, jitter, fringe distortion due to non-sinusoidal modulation (presence of second and third harmonics in the fringes). Each type of noise can be considered separately or all of them - cumulatively.

The effectiveness of the Hilbert transform is compared to that of complex Gabor transform [1], which can be used for phase retrieval, too. Wavelet de-noising is compared to that of windowed Fourier filter [2] and others filters, as well (see below).

In all simulations the phase unwrapping is done by the Itoh approach [3]. The smoothed final result is 'cleared' by an adaptive Wiener filter [1].

PHASE AND NOISE MODELS; FRINGES AND COMPUTATIONAL PROCEDURES

The phase model (pm) in the simulations below is the function "peaks", which is more or less accepted as a standard in surface profile analysis:

* To whom all correspondence should be sent:
E-mail: pete@iomt.bas.bg

$$p = 3 * (1 - x)^2 * exp(-(x)^2 - (y + 1)^2) - $$
$$1/3 * exp(-(x + 1)^2 - (y)^2) - $$
$$10 * (x/5 - x^3 - y^5) * exp(-x^2 - y^2);$$

$$pm(x, y) = 3.5 * p; \qquad 0 \le x, y \le 511;$$

The difference between the absolute maximum and absolute minimum of the phase model is ~50 radians. In Fig. 1 pm(x, y) is shown.
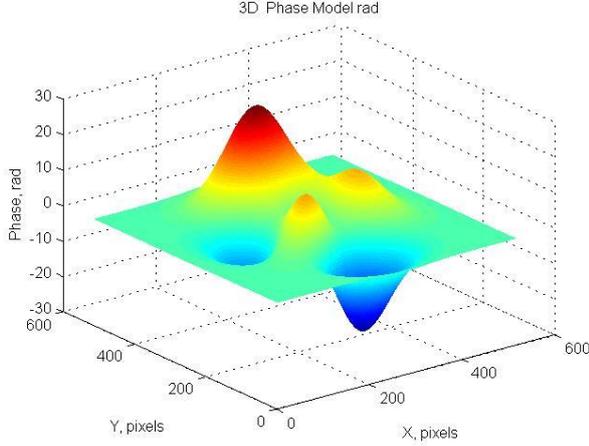
Fig. 1. Phase model function

The reference fringes I0(x, y) are simulated as greyscale images with 8 bits per pixel with background intensity of 0.5 and amplitude modulation of 0.3. A certain and an avoidable degradation of any registered image is due to noise N(x, y). By 'noise' we mean any unwanted component of the image, including jitter, non-sinusoidal waveforms, speckle, etc. In the simulations we consider additive Gaussian or uniform noise; multiplicative noise; fringe deformation and stochastic jitter of CCD rows. Each noise can be considered separately or all of them - cumulatively.

$$I_o = 255 * \{0.5 + 0.3 * cos(w_o * x)\}$$

$$I_o = 255 * \{0.5 + 0.3 * cos(w_o * x + pm)\} + N(x, y)$$

where $w_o = 2 * \pi/T$; T is the fringe period (in pixels). *N(x, y)* is the noise, additive in this case. To treat the case of fringes with constant global carriers, it is considered that fringes lie parallel to Oy axis. In Fig 2. the computer generated fringe pattern, corrupted with cumulative noises (with multiplicative noise) is shown.

The presented approach runs as follows:

1). Pre-process the input pattern. If multiplicative noise is present, make a homomorphic transformation [1]. Smooth the pattern with wavelet techniques. We do it with the 2 level discrete reverse bi-orthogonal wavelet [1, 2].

2). Phase evaluation is fulfilled with 1D Hilbert transformation on row-by-raw basis. First, eliminate the background illumination by averaging, if the intensity is constant. We use also an adapted envelope approach for illumination with Gaussian distribution [2]. The four-quadrant arctangent function supplies the wrapped phase. We unwrap it, following Itoh approach [2, 3].

3). Smooth the estimated phase function by wavelet techniques. We use 4 level symlet wavelet [1] of 4-th order, followed by adapted Wiener filtering [1].
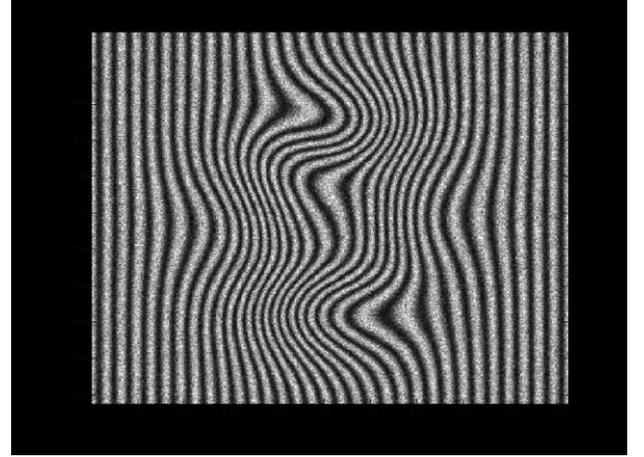
Fig. 2. Computer generated fringe pattern, corrupted with noise.

In order to evaluate the efficiency of the processing, we define a Figure of Merit (FM) as the ratio of the Euclidean norm of the difference between the estimated phase function and the model phase function, to the Euclidean norm the phase model.

RESULTS AND DISCUSSIONS

The specific features of the noise models are as follows:

- Additive noise with Gaussian probability density function (PDF) with zero mean and standard deviation (STD) of +/- 10 intensity gray levels (out of 256)
- Multiplicative noise with Rayleigh PDF mean value of 1 and STD = 0.2732 (maximum for this PDF, which corresponds to two fully developed correlation cells within one pixel of the CCD detector)
- Non-sinusoidal modulation with second harmonic (ratio 2-nd to 1-st harmonic is equal to 0.25) and third harmonic (ratio 3-rd to 1-st harmonic is equal to 0.15)
- Noise due to stochastic high-frequency (environmental) vibrations with uniform PDF and values within +/- $\pi/20$ for each pixel, or

jitter noise for each row of the phase model (same PDF, same value)

The corrupted fringe pattern is processed with our approach. The presented results are for multiplicative noise. The obtained FM is 99.7%.

The difference between the model phase function and the evaluated phase is presented in Fig. 3.
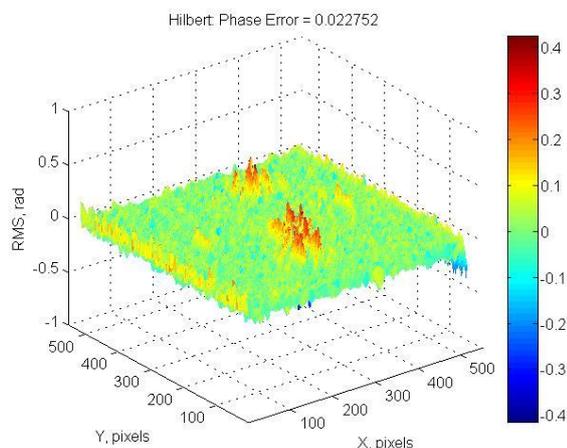
Fig. 3. Difference between model and evaluated phase function.

In Fig. 4 we present the histogram of that difference. The result of de-noising and phase evaluation and unwrapping is very satisfactory.
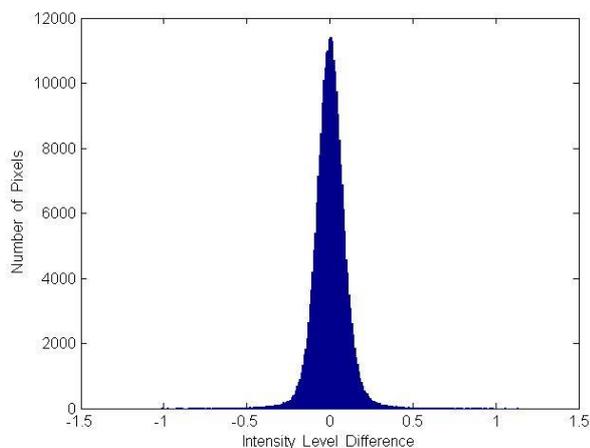
Fig. 4. Histogram of the difference model and evaluated phase function.

Also, we extracted the phase with 1D complex Gabor wavelet and compared it to the Hilbert transform, keeping all the rest of the approach

intact. The results are similar, but somewhat better for Hilbert (FM = 99.7% to 95.7% for Gabor).

We compared and analyzed the performance of different pre-processing algorithms and methods. To name a few: windowed Fourier filters, Frost filter, adaptive weight Wiener filter, anisotropic diffusion method [1, 2, 4]. Their performances were similar, but anisotropic diffusion had the highest figure of merit - FM = 99.8%.

CONCLUSIONS

We presented an approach for phase recovery from data, obtained from experiments in optical interferometry, by projection techniques, etc. The approach is based on a combination of Hilbert transform and different wavelet techniques for de-noising and smoothing. In our numeric simulations, we introduced different types of noise in order to get as close as possible to the physical reality. Our results on patterns with constant global angular carriers show that this approach is effective and robust. It is competitive with other methods, which are more complicated to implement and demand sophisticated software.

We intend to apply this approach for comparative analysis of single frame phase recovery and the well-known multiframe phase shifting algorithms.

REFERENCES

1. R. C. Gonzalez, R. E. Woods, S. L. Eddins, Digital Image Processing Using MATLAB, Second Edition, Gatesmark Publishing, LLC, 2009.
2. Q. Kemao, Windowed Fringe Pattern Analysis, SPIE Press, Washington, 2013.
3. D. Ghigla, M. Pratt, Two-dimensional Phase Unwrapping: Theory, Algorithms and Software, John Wiley & Sons, Inc., New York, 1998.
4. J. Weickert, Anisotropic Diffusion in Image Processing,, B. Teubner, Stuttgart, 1998.

ВЪЗСТАНОВЯВАНЕ НА ФАЗАТА ОТ СТРУКТУРИ С ИВИЦИ: ПОДХОД, БАЗИРАН НА ХИЛБЕРТОВА ТРАНСФОРМАЦИЯ И ОБЕЗШУМЯВАНЕ ЧРЕЗ ВЪЛНИЧКИ

П. Шарланджиев, Н. Берберова, Д. Назърова и Г. Стоилов[1]

*Институт по оптически материали и технологии "Акад. Й. Малиновски", Българска Академия на науките,
ул. "Акад. Г. Бончев", бл. 109, 1113 София, България*
*[1]Институт по механика, Българска академия на науките, ул. "Акад. Г. Бончев", блок 4, София ПС-1113,
България*

(Резюме)

Анализът на структури с ивици е важна задача в оптическата метрология. Ивични структури се формират чрез оптична интерферометрия, проекционни техники, припокриване на подобни вълнови полета и др. Структури с постоянна ъглова честота представляват прави ивици в полето на наблюдение. Изследваният обект деформира ивиците. Анализът на тези изкривявания се нарича извличане на фазата и се използва широко в науката и техниката, напр. за получаване на топографията на 3Д обекти. Този анализ обикновено има 3 етапа: предварителна обработка (намаляване на шума в изображението, нулиране на фона), извличане на фазата (намиране на фазовото разпределение) и крайна обработка на резултатите (разопаковане на фазата, изглаждане, „почистване").

В тази статия представяме подход, базиран на комбинация от преобразование на Хилберт за извличане на фазата и различни техники с вълнички за обезшумяване и сглаждане на данните. Чрез числено моделиране показваме, че тази методология е ефективна и стабилна. Различни видове шум са моделирани и анализирани: гаусов добавъчен, интензитетно зависим мултипликативен (спекъл), джитер, наличие на високи хармонични в ивиците др.

Multiple cycles of recording/reading/erasing birefringence in azopolymers

L. Nedelchev[1,2,*], D. Ivanov[1], G. Mateev[1], B. Blagoeva[1], D. Kostadinova[1],
N. Berberova[1] and D. Nazarova[1]

[1]*Institute for Optical Materials and Technologies "Acad. J. Malinowski", Bulgarian Academy of Sciences,
"Acad. G. Bonchev" str. Bl. 109, 1113 Sofia, Bulgaria*
[2]*University of Telecommunications and Post, Acad. St. Mladenov 1 Str., Sofia 1700, Bulgaria*

In this work we investigate the characteristics of reversible polarization recording in an azopolymer. Polarized light from DPSS laser with wavelength 444 nm is used for recording photoinduced birefringence. Afterwards, two methods for its erasure are used: heating the polymer to certain temperature or illumination with circularly polarized light. Multiple cycles of recording and erasure are successfully realized with both methods, which allows us to compare and outline the advantages of each of them. The photoinduced birefringence is calculated from the Stocks parameters, monitored in real time, during the entire experiment.

Keywords: Azopolymers; Thermal and optical reversibility; Photoinduced birefringence; Polarization recording.

INTRODUCTION

In contrast to conventional optical data storage (CD/DVD/Blu-ray technologies), where recording is in one plane (2D), holographic data storage allows to address the entire volume of the media (3D) and to achieve much higher density of information [1, 2]. Polarization holography makes possible to increase the information density even further by registering also the polarization state of the recording light and realizing polarization multiplexing [3-5].

Since 1984, when Todorov et al. [6] discovered the possibility to inscribe high-efficient polarization holograms in azobenzene-containing materials, these materials are subject of intensive research for numerous application, including holographic data storage [7, 12]. Essential parameters for each data storage media are the stability of the recorded information, as well as its reversibility i.e. the ability of the media to ensure multiple cycles of recording, non-destructive reading and erasure of information.

Here we present a study of the reversibility properties of birefringence in amorphous azo polymer. The value of the photoinduced linear birefringence Δn is defined as the difference between the component of the refractive index perpendicular to the polarization of the recording beam and the component parallel to it – $\Delta n = n_\perp - n_\parallel$. It is known that on illumination with linearly polarized light within the absorbance band of the photochromic azo groups, they undergo cycles of *trans-cis-trans* isomerizations and tend to reorient perpendicularly to the polarization direction of light [3, 6]. As a result, birefringence is induced in the material at a macroscopic level. On the other hand, when the azopolymer film is illuminated with circularly polarized light, no preferential direction exists, so the molecules orientation becomes random again, and the birefringence is erased.

We apply two methods of erasure in this study – optical and thermal. Both methods are compared in terms of speed of erasure and anisotropy values retention during multiple write/read/erase cycles.

EXPERIMENTAL

Materials

The polymer used in this experiment is side-chain amorphous azocopolymer, denoted as P_{1-2}, synthesized earlier in the Institute of Optical Materials and Technologies [13]. The azopolymer chemical structure and spectrum of absorbance are shown in Fig. 1. Its molecular weight is $M_w = 3600$ g/mol and glass transition temperature is $T_g = 102\ °C$ [14].

---

* To whom all correspondence should be sent:
E-mail: lian@iomt.bas.bg

P$_{1-2}$

(a)

(b)
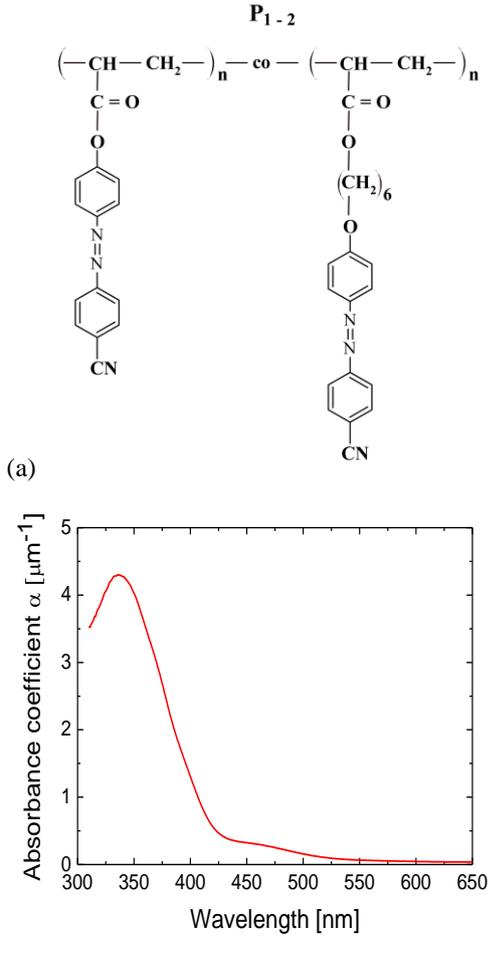
Fig. 1. (a) Chemical structure of the azocopolymer P$_{1-2}$; (b) Spectrum of absorbance of P$_{1-2}$.

Methods of characterization

The preparation of the polymer films includes dissolving of the P$_{1-2}$ copolymer in 1,2-dichloroethane and spin coating the solution at 1500 rpm on glass substrates. As a result, thin homogeneous films are formed. The thickness of the films is measured by a Talystep profilometer (Taylor Hobson) and for the samples used in this work is $d = 700$ nm.

To record and probe the photoinduced birefringence, two diode-pumped solid state lasers (DPSSL) are used: recording laser with $\lambda_{rec} = 444$ nm, power 35 mW, and reading (referred also as probe) laser with $\lambda_{probe} = 635$ nm and power below 2 mW. As it can be seen in Fig. 2, the reading laser beam passes through polarizer, oriented at 45°, while the recording beam passes through vertical polarizer. After passing through the azopolymer sample, the reading beam enters a polarimeter (PAX5710 Polarization Analyzing System, Thorlabs), which monitors the Stokes parameters of light in real time.
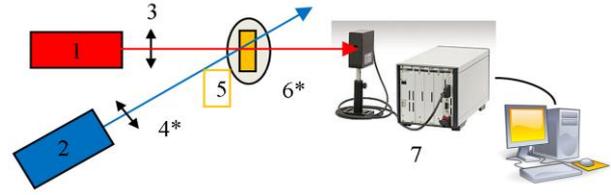
Fig. 2. Experimental setup : 1 – reading laser (635 nm, P < 2mW), 2 – recording laser (444 nm, P = 35 mW), 3 – polarizer oriented at 45°, 4* – vertical polarizer/QWP, 5 – azopolymer sample, 6* – hot stage, 7 – Thorlabs polarimeter. (* denotes an element, which is replaceable, depending on the erasing method used).

In this case the birefringence can be calculated from the expression:

$$\Delta n = \frac{\lambda_{probe}}{2\pi d} \arctan\left(\frac{S_3}{S_2}\right) \qquad (1)$$

where d is the film thickness, and S_2 and S_3 are Stokes parameters [10, 15].

RESULTS AND DISCUSSIONS

Fig. 2 is a representation of the experimental setup for both deleting methods. The reading laser is on throughout the entire experiment. Initially, 60 seconds of background signal is measured, without illumination with the recording laser. During the data processing, these background values are subtracted from the measured data. Then we start the illumination with the recording laser until the photoinduced birefringence reaches saturation – Δn_{max}. Using Eq. (1), the time dependence of the birefringence can be determined.

Optical erasure

During the recording, the light from the laser at 444 nm passes through a vertical polarizer, while for the erasure it is replaced by quarter wave plate (QWP), which converts the linearly polarized light in circularly polarized (CP). CP light with the same wavelength as the recording one, randomizes the orientation of the azochromophores which leads to erasure of the birefringence.

The processes of recording and deleting in the azopolymer film had been repeated 10 times, all in the same place of the sample. The results are shown in Fig. 3. The recording time for each cycle is 4 minutes, then the recording laser is stopped and only the reading beam is on for another 4 minutes to determine the stability on reading. After that, starts the illumination with circularly polarized light at 444 nm for another 4 minutes.

a)

b)
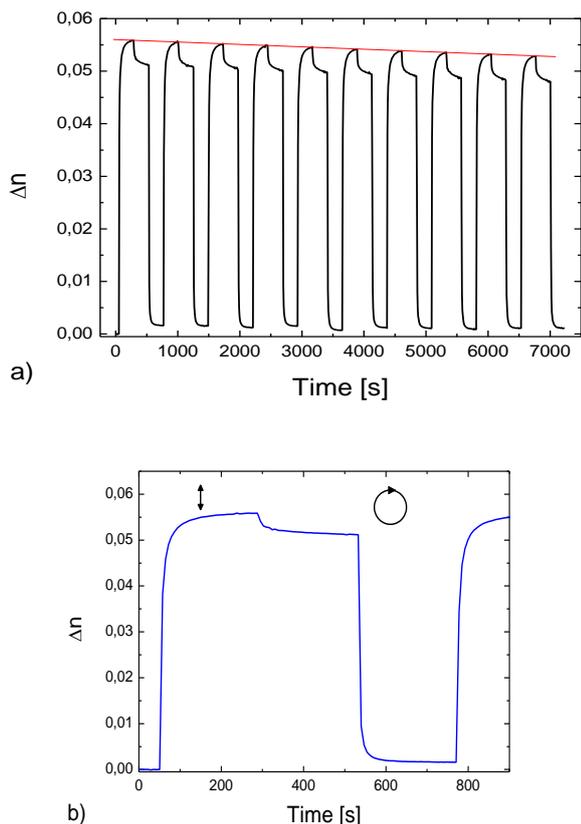
Fig. 3. (a) Ten cycles of inducing and optically deleting linear birefringence; (b) Zoom on the first cycle. The symbols indicate the state of polarization of the laser with $\lambda = 444$ nm.

As can be seen from Fig. 3, this polymer can be successfully used for multiple cycles of recording and deleting of linear birefringence. The response of the polymer to different polarizations is fast and relatively high values of birefringence have been achieved. However, we should note, that after each cycle the maximum value of birefringence is reduced. This phenomena could be explained with the reorientation of part of the chromophores perpendicular to the film surface [9]. Hence, these molecules do not contribute to the formation of birefringence.

Thermal erasure

To study the thermal erasure, the sample was mounted on a hot stage THMS600 (Linkam Scientific), which can maintain or vary sample temperature at a given speed, with high precision. The recording and relaxation time in this experiment were set to 2 minutes. After that time, starts the heating process with rate 10°C/min. The starting temperature for the measurement was 30°C. The heating continues until temperature of 90°C is reached, which leads to erasure of the photoinduced

birefringence, as shown in Fig. 4. Then the temperature is decreased back to 30°C for the next cycle of recording/reading/erasure. It is important to notice, that in this case no decrease of the maximal value of birefringence in the consecutive cycles is observed.

a)

b)
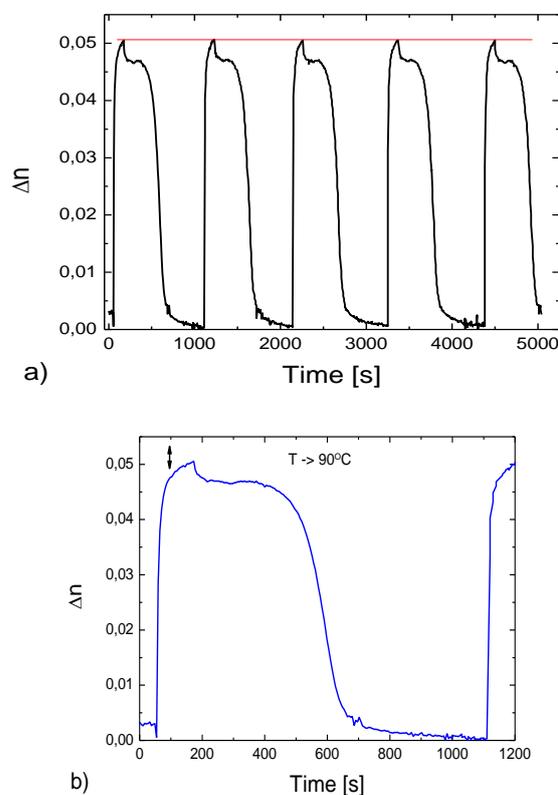
Fig. 4. (a) Five cycles of inducing and thermally deleting linear birefringence; (b) Zoom on the first cycle. The arrow indicates the polarization state of the pump laser.

CONCLUSIONS

We have demonstrated experimentally the possibility for multiple cycles of recording, reading and thermal or optical erasure of photoinduced birefringence in the azocopolymer P_{1-2} synthesized in IOMT. Reversible recording with linearly polarized light and erasure with circularly polarized light at the same wavelength is realized, in contrast to other methods where a separate UV laser is used for the erasure [9]. The processes can be repeated many times only with slight decrease of the amplitude – less than 5% for 10 cycles. A possible reason for this behaviour can be the fact that some molecules reorient perpendicularly to the plane of the circularly polarized light. Being in such position they cannot be addressed by the linearly polarized light in the next recording cycle, which results in decrease of the maximal value of the birefringence (Δn_{max}), as seen in Fig. 3a. This drawback has been

overcome using thermal erasure. By this method the anisotropy can be also easily erased by heating to temperature of around 90°C and the films can be used for recording again. Although the thermal erasure is slower, we have shown that it retains the maximal value of birefringence, as indicated by the red line in Fig. 4a. Therefore, the erasure method can be selected depending on the application, or alternatively, after a given number of cycles using optical erasure, a thermal erasure can be applied in order to restore the birefringence value to its maximal level.

REFERENCES

1. S. Orlov, W. Phillips, E. Bjornson, Y. Takashima, P. Sundaram, L. Hesselink, R. Okas, D. Kwan, R. Snyder, *Appl. Opt.,* **43**, 4902 (2004).
2. K. Curtis, L. Dhar, A. J. Hill, W. L. Wilson, M. R. Ayres, Holographic Data Storage: From Theory to Practical Systems, John Wiley & Sons, New Jersey, 2010.
3. L. Nikolova, P. Ramanujam, Polarization Holography, Cambridge University Press, Cambridge, 2009.
4. L. Nedelchev, D. Ilieva, Tz. Petrova, N. Tomova, V. Dragostinova, L. Nikolova, *Proc. SPIE*, **5830**, 95 (2005).
5. D. Ilieva, L. Nedelchev, Ts. Petrova, N. Tomova, V. Dragostinova, L. Nikolova, *J. Opt. A: Pure Appl. Opt.*, **7**, 35 (2005).
6. T. Todorov, L. Nikolova, N. Tomova, *Appl. Opt.,* **23**, 4309 (1984).
7. A. Natansohn, P. Rochon, J. Gosselin, S. Xie, *Macromolecules*, **25**, 2268 (1992).
8. S. Hvilsted, F. Andruzzi, C. Kulinna, H. W. Siesler, P. S. Ramanujam, *Macromolecules*, **28**, 2172 (1995).
9. N. C. R. Holme, P. S. Ramanujam, S. Hvilsted, *Opt. Lett.*, **21**, 902 (1996).
10. L. Nedelchev, A.S. Matharu, S. Hvilsted, P.S. Ramanujam, *Appl. Opt.,* **42**, 5918 (2003).
11. H. Audorff, K. Kreger, R. Walker, D. Haarer, L. Kador, H.W. Schmidt, *Adv. Polym. Sci.,* **228**, 9 (2010).
12. A. Ryabchun, A. Sobolewska, A. Bobrovsky, V. Shibaev, J. Stumpe, *J. Polymer Sci., Part B: Polym. Phys.,* **52**, 773 (2014).
13. G. Martinez-Ponce, T. Petrova, N. Tomova, V. Dragostinova, T. Todorov, L. Nikolova, *J. Opt. A: Pure Appl. Opt.,* **6**, 324 (2004).
14. L. Nedelchev, D. Nazarova, V. Dragostinova, *J. Photochem. Photobiol. A: Chem.,* **261**, 26 (2013).
15. N. Berberova, D. Nazarova, L. Nedelchev, B. Blagoeva, D. Kostadinova, V. Marinova, E. Stoykova, *J. Phys.: Conf. Series*, **700**, 012032 (2016).

МНОГОКРАТЕН ЗАПИС/ЧЕТЕНЕ/ИЗТРИВАНЕ НА ДВУЛЪЧЕПРЕЧУПВАНЕ В АЗОПОЛИМЕРИ

Л. Неделчев[1,2], Д. Иванов[1], Г. Матеев[1], Б. Благоева[1], Д. Костадинова[1], Н. Берберова[1] и Д. Назърова[1]

[1]*Институт по оптически материали и технологии "Акад. Й. Малиновски", Българска Академия на науките, ул. "Акад. Г. Бончев", бл. 109, 1113 София, България*
[2]*Висше училище по телекомуникации и пощи, ул. «Акад. Ст. Младенов» 1, 1700, София, България*

(Резюме)

Изследван е процесът на многократен обратим поляризационен запис в азополимер. За запис на фотоиндуцирано двулъчепречупване е използвана поляризирана светлина от лазер с дължина на вълната 444 nm. За изтриване на записа са използвани два метода: загряване на полимерния слой или облъчване с кръгово поляризирана светлина. Успешно са реализирани многократни цикли на запис и изтриване и чрез двата метода, което ни позволява да ги сравним и посочим преимуществата на всеки от тях. Фотоиндуцираното двулъчепречупване е изчислено от параметрите на Стокс, които се следят в реално време по време на целия експеримент.

White light viewable silver-halide holograms in design applications

J-S. Park[1], E. Stoykova[1,2,*], H-J. Kang[1]

[1]*Korea Electronics Technology Institute, 8 Floor, 11, World cup buk-ro 54-gil, Mapo-gu, Seoul, Korea*
[2]*Institute for Optical Materials and Technologies "Acad. J. Malinowski", Bulgarian Academy of Sciences, "Acad. G. Bonchev" str. Bl. 109, 1113 Sofia, Bulgaria*

A human-centered design is an important factor for improvement quality of human life all over the world. This work presents application of holography in human-centred design in view of the unique properties holography demonstrates for 3D imaging. Holography enables design solutions with highly positive impact and supports design diversity. The paper shows how holographic art-work can be used for creation of idea-based design. It proposes different types of holograms suitable for environmental and interior design as outdoor holographic installation, artworks from rainbow holograms or cylindrical holograms and presents their real implementation. Potential of the wavefront holographic printing technique in holographic design is also discussed.

Keywords: holography, white light viewable holograms, holographic design

INTRODUCTION

Design is of crucial importance for human society. Holography, as an optical tool with unique properties, is a perspective candidate for human-centered design because it enables solutions with highly positive impact. It has also a potential to support design diversity. The holograms make possible accurate photorealistic 3D imaging with all depth cues provided and thus enrich our perception by expanding information capacity [1]. This intrinsic property of the holograms can be used to produce efficient and well-harmonized environment, to change the interior design and to improve quality of life [2]. Although holographic optical elements are already widely used for labelling products and security purposes, a lot of research and practical implementations are needed before the holograms can steadily step in environmental and interior design. This task requires understanding of 3D space perspectives provided by the hologram.

This paper presents various types of white-light viewable silver-halide holograms created recently by the holographic artist Ray Park (or Joosup Park, the first author of the paper) and discusses perspectives of their usage in holographic design. Potential of the recently developed wavefront holographic printing techniques for production of white-light viewable holograms in holographic design is also addressed.

HOLOGRAPHIC ARTWORKS

In holography, the light scattered from three-dimensional (3D) objects is recorded onto a 2D plate with a photosensitive layer or encoded as a 2D numerical array under coherent illumination. Both real and virtual objects can get holographic representation, and a variety of effects as e.g. directionally dependent motion can be introduced in the encoding process. Reconstruction of 3D images from 2D holograms allows for development of new design components and combinations leading to irreplaceable design solutions. One may argue that this really great advantage is counterbalanced by the necessity to provide special lighting to obtain high quality reconstructions. Nevertheless, plane or curved holographic panels which generate 3D reconstructions of objects always impress the general public. The white-light viewable holograms make possible outdoor installations or indoor decorations by applying inexpensive illumination with a point light source as Sun or light-emitting diodes respectively. Rainbow holograms allow for construction of decorations which change their coloring with the viewer position. Holographic displays are autostereoscopic displays and no special means are required to view the 3D images. Additional attractive feature the holographic artwork has is

* To whom all correspondence should be sent:
E-mail: elena.stoykova@gmail.com

ability to be easily combined with other design solutions. In the following we present several holographic design solutions with the photographs of real holograms produced during the recent years.

Fig. 1. Holographic installation 'Holographic Lighting Design'.

Fig. 2. Holographic lighting with the hologram attached to a glass wall.
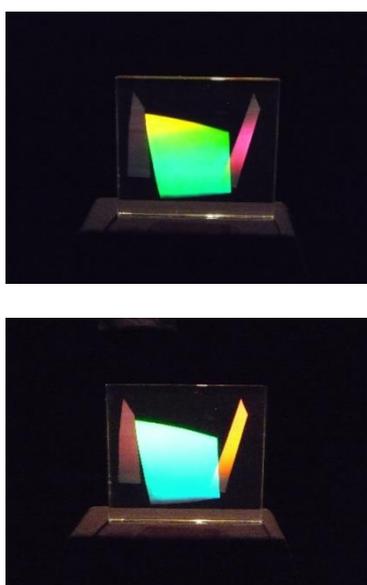
Fig. 3. Rainbow configuration: top view and bottom view.

Holography makes possible design of holographic lighting which can be a part of large

outdoor installation. Fig. 1 shows a large size holographic installation 'Holographic Lighting Design' that has been presented at the Design Cube competition held at Korean Foundation of Design Culture in 2008. The author Ray Park was selected for the 'Designer of December'. The holograms in this design work are attached to a glass pane; they can be installed on a wall or in space. The size of each panel in Fig. 1 is 250 mm by 820 mm. Another holographic lighting design introduced to the Design Cube was exhibited at the outdoor space of the Namsan Tower in Seoul, South Korea (Fig. 2). The size of the hologram was 140 mm by 210 mm. The holograms presented in Fig. 1 and Fig. 2 are analogue transmission type holograms recorded on a silver-halide emulsion VRP-M (produced by Slavich) with a diode pumped solid state laser (DPSS) at a wavelength of 532 nm and laser power of 150 mW. The holograms diffract light coming from a light source and reconstruct incandescent lamps floating in the air; the created impression is of reemitted light.

A basic rainbow hologram configuration design work has been developed by cutting the holographic films used to record rainbow holograms and arranging them as is shown in Fig. 3. The holograms were recorded on the VRP-M emulsion. Their size is 160 mm by 140 mm. The different parts of this composition reflect different colors which vary with the viewing angle. By overlaying the colors, a rainbow hologram design of additive color mixture is formed. Fig. 4 shows such rainbow hologram configuration of size 200 mm by 180 mm. When observed from the front, varying colors can be seen by moving up and down. The additive mixture of red, green and blue colors in the middle creates perception of a white color. Such rainbow hologram design works may be coated on tiles, blocks, furniture, or walls.

Fig. 4. Composition made from rainbow holograms (left) and its magnified view (right).

Impressive design solution is to use a static holographic display which provides a 3D image floating in space. A holographic display design work was manufactured in 2013 by combining projection mapping with a 360 degrees cylindrical hologram. Projection mapping experiences limitations related to projector location and objects shape that hamper 3D observation of objects. A cylindrical hologram is an attractive choice to make all-directional observation available. Fig. 5 represents the cylindrical hologram of the Turtle Ship used by Royal Korean Navy from 15th to 19th century that is combined with projection mapping. The hologram was recorded using a DPSS laser (532 nm) on a silver-halide emulsion U08 (produced by Ultimate). The hologram enables observation of the floating in the air 3D object from all directions. The 2D representation of the Turtle Ship is observed on the floor. One may expect application of this method to the advertisement design.

Fig. 5. Holographic display design by combining a cylindrical hologram of a 3D object with its 2D projection mapping.

HOLOGRAPHIC WAVEFRONT PRINTING

Advances in optical technology open new prospects for holographic design. Nowadays, analogue holography is available practically to anyone and can be applied to the art and design work. However, difficulties are arising when modifying the already complicated optical set-up to capture large scenes on the holographic plate. The holographic printers are successful solution to this problem [3, 4]. They record a white light viewable hologram by partitioning it into 2D array of elemental holograms and forming digital 3D contents for each of them from the information acquired about the 3D object. The numerical data

for each elemental hologram are fed to a spatial-light modulator (SLM) which forms the object beam for recording the hologram on the silver-halide holographic emulsion. The holographic stereogram printer has already proved its capability to print large size horizontal parallax only color holograms and so to be used for 3D advertisement and visual design [4]. The 3D contents are composed as parallax-related images from multi-view incoherent capture of 3D objects. However, the holographic stereogram records only directional and color information, and quality of reconstruction is not equivalent to that from the analogue hologram.
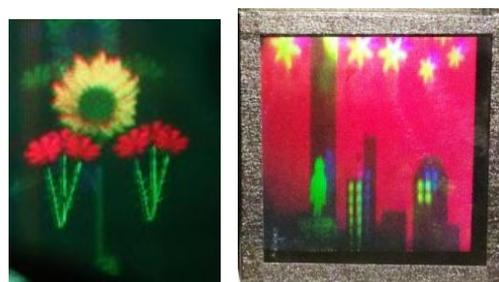
Fig. 6. Reconstruction from the first printed color hologram by the wavefront printer (left); printed hologram "Night of passion", holographic artist Ray Park (right).

Recently, we proposed and built a wavefront holographic printer whose input is a computer-generated hologram (CGH) [5]. The printed hologram is partitioned into a 2D array of elemental holograms. A set of CGHs is generated to make 3D contents for the printer by using accelerated computation of the fringe patterns. The CGHs fed to the amplitude SLM encode the wavefront of light coming from the 3D object and the latter is extracted optically by a spatial filter and a telecentric lens system to impinge the holographic emulsion. This printer allows for manufacture of Denisyuk and transmission type holograms with the same quality of reconstruction as in analogue holography. By using three continuous wave DPSS lasers emitting at 640 nm, 532 nm and 473 nm it is possible to print color holograms. The main advantage of this printing modality is its ability to produce holograms from virtual objects by using their computer graphic models. This creates a lot of opportunities for advertisement or design which rely on 3D imaging. The photographs of reconstructions from two holograms printed by our wavefront printer are shown in Fig. 6. Actually, Fig. 6(a) presents reconstruction from the first color hologram printed this way. The bright saturated colors of the reconstructed image are achieved by

mosaic recording of the primary colors when an elemental hologram gets a single color [5]. The printed output can be used also as a master hologram.

CONCLUSIONS

Unique properties of holographic 3D imaging provided by white-light viewable analogue holograms and recent achievements in computer generation of holograms create rich platform for developing impressive design solutions. The holographically manufactured artworks can be used for outdoor and interior decorations. The main advantage of the outdoor white-light viewable holographic installations is no need of a special light source for their reconstruction. Recently developed holographic wavefront printing makes possible producing of white light viewable reflection holograms from digital contents encoding 3D information about virtual objects. The paper included various original holographic examples to illustrate the potential of holographic artworks based on white-light viewable analogue holography in design applications.

REFERENCES

1. H. Bjelkhagen and D. Brotherton-Ratcliffe, Taylor and Francis, 2013, p 341.
2. V. Sainov V and E. Stoykova, in: Optical Imaging and Metrology: Advanced Technologies, W Osten and N. Reingand (eds.), Wiley-VCH Verlag GmbH&Ko KGaA, 2012, pp 93-117.
3. H. Kang, E. Stoykova, J. Park, S. Hong, Y. Kim, in Holography - Basic Principles and Contemporary Applications, E. Mihaylova (ed.), InTech, 2013, pp.171-201.
4. D. Brotherton-Ratcliffe, S. Zacharovas, R. Bakanas, J. Pileckas, A. Nikolskij, and J. Kuchin, *Opt. Eng.*, **50** (9), 091307 (2011)
5. Y. Kim, E. Stoykova, H. Kang, S. Hong, J. Park, J. Park, and J. Hong, *Opt. Express,* **23**, 172 (2015).

ХОЛОГРАФСКИ ДИЗАЙН С ВЪЗСТАНОВЯВАНИ В БЯЛА СВЕТЛИНА ОТРАЖАТЕЛНИ ХОЛОГРАМИ ВЪРХУ СРЕБЪРНО-ХАЛОГЕНИДНА ЕМУЛСИЯ

Дж. С. Парк[1], Е. Стойкова[1,2], Х. Дж. Канг[1]

[1]*Корейски институт по електронни технологии, 8 етаж, 11, Уорлд-кап бук-ро, 54-джил, Мапо-гу, Сеул, Корея*
[2]*Институт по оптически материали и технологии към Българската Академия на науките, ул.,,Акад. Георги Бончев", бл.109, 1113 София, България*

(Резюме)

Дизайн, ориентиран към човека, е важен фактор за подобряване на качеството на живот по света. Работата представя използването на холографията в ориентиран към човека дизайн предвид уникалните свойства, които демонстрира за тримерно визуализиране. Холографията дава възможност да се осъществят дизайнерски решения с голямо положително въздействие и помага за увеличаване на тяхното разнообразие. Работата представя използването на холографски артистични творби за създаване на идеен дизайн. Тя предлага различни видове холограми, подходящи за вписване в околната среда и за интериорен дизайн като холографски инсталации на открито, художествени творби от дъгови или цилиндрични холограми и представя реалното им изработване. Обсъжда се потенциалът на холографска принтираща техника за случая на принтер на вълновия фронт за целите на дизайна.

Printing of digital holographic content as a color white light viewable silver-halide hologram

H-J. Kang[1], E. Stoykova[1,2]*, Y-M. Kim[1], S-H. Hong[1], J-S. Park[1], J-S. Hong[1]

[1]*Korea Electronics Technology Institute, 8 Floor, 11, World cup buk-ro 54-gil, Mapo-gu, Seoul, Korea*
[2]*Institute for Optical Materials and Technologies "Acad. J. Malinowski", Bulgarian Academy of Sciences, "Acad. G. Bonchev" str. Bl. 109, 1113 Sofia, Bulgaria*

The most advanced 3D imaging technology of digital holography is holographic printing. It combines digital and analogue holography by recording a hologram onto a holographic silver-halide emulsion as a volume reflection hologram from digital contents fed to a spatial light modulator. The hologram is built as a 2D array of successively recorded elemental analogue holograms. In the first developed holographic printing technique multiple perspectives of the 3D scene are incoherently captured and printed as a holographic stereogram to allow the viewer to perceive 3D objects by binocular vision. Recording of only directional data leads to distorted reconstruction from the recorded stereogram. Direct printing of holographic fringes as a thin transmission hologram onto a holographic emulsion without a reference wave provides non-distorted reconstruction but without color selectivity. The paper presents a color holographic wavefront printer which prints a white light viewable hologram on a silver-halide emulsion as a two-dimensional array of elemental holograms. The 3D contents for the printer are formed as a set of computer generated holograms and contain depth, directional and colour information. The input data for each elemental hologram are fed to an amplitude spatial light modulator. The light wavefront coming from a three-dimensional object is extracted by a spatial filter and demagnified before recording. The printed hologram provides highly photorealistic reconstruction similar to an analogue reflection hologram.

Keywords: Holography, holographic printer, 3D imaging, silver-halide emulsion, computer generated holograms.

INTRODUCTION

The most advanced 3D imaging technology of digital holography is holographic printing [1]. It combines digital and analogue holography by recording a hologram onto a holographic emulsion from digital contents fed to a spatial light modulator (SLM). The hologram is built as a 2D array of successively recorded elemental analogue holograms. The first developed printing technique was the holographic stereogram printing [2,3]. In this printer multiple perspectives of the 3D scene are incoherently captured and processed to allow the viewer to perceive 3D objects by binocular vision. These data are recorded as a volume reflection hologram on a silver-halide emulsion. Recording of only directional data leads to distorted reconstruction from the recorded stereogram. Non-distorted 3D reconstruction is provided by a direct fringe printer which records a thin transmission computer generated hologram (CGH) onto a

holographic emulsion without a reference wave [4], and the printed hologram has no color selectivity. The drawbacks of these two printers are avoided by the wavefront printing proposed independently by us [5] and Yoshikawa [6]. In this approach, the SLM displays a CGH which diffracts light to be recorded as a volume reflection hologram. The paper presents design and implementation of a color holographic wavefront printer with demagnification of the object beam which makes possible mosaic delivery of primary colors on a silver-halide emulsion.

GENERATION OF 3D CONTENTS AND OBJECT BEAM EXTRACTION

The essence of the wavefront printing is optical extraction of the light wavefront which carries information about the 3D object from the light diffracted by a SLM which displays a CGH of this object. We proposed a printer, in which the CGHs for the elemental holograms were displayed in succession on amplitude SLM. The CGH

synthesized for this SLM is a 2D real-valued array which encodes four terms:

$$H(\xi,\eta) = O(\xi,\eta)O^*(\xi,\eta) + R(\xi,\eta)R^*(\xi,\eta) + \\ O(\xi,\eta)R^*(\xi,\eta) + R(\xi,\eta)O^*(\xi,\eta) \quad (1)$$

where $O(\xi,\eta) = a_O(\xi,\eta)\exp[i\varphi_O(\xi,\eta)]$ and $R(\xi,\eta) = a_R(\xi,\eta)\exp[i\varphi_R(\xi,\eta)]$ are the complex amplitudes or wavefronts of mutually coherent object and reference beams that digitally interfere in the plane (ξ,η) of the CGH or the SLM respectively; $a_{O,R}(\xi,\eta)$ and $\varphi_{O,R}(\xi,\eta)$ are the amplitude and phases of these wavefronts and "i" is the imaginary unit. The sum of the first two terms forms the zero-order term while the other two terms give the beam coming from the object and the beam converging to the object. In the proposed printing system, the beams encoded in the CGH and diffracted from the SLM focused at separate spots in the back focal plane of a lens which collected the beam diffracted from the SLM when the CGH was calculated in off-axis geometry. Thus the object wavefront was optically extracted by spatial filtering in this plane. The extracted object beam was further demagnified to be recorded onto the holographic silver-halide emulsion as a small size elemental hologram. In view that the object beam corresponded to the light beam scattered from the 3D object, we called our printer a wavefront printer.
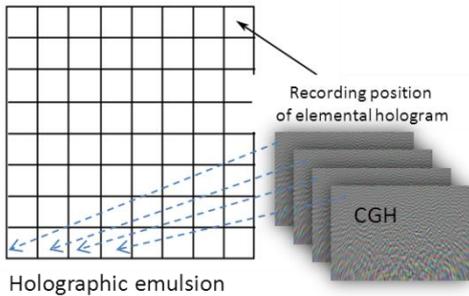
Fig. 1. Printing a volume reflection hologram as a collection of elemental holograms recorded from a set of CGHs.

The hologram printed by the wavefront printer was built as a 2D collection of elemental holograms which are recorded in succession. The 3D contents to be printed consisted of a set of CGHs. Each CGH was calculated according to the position of a given elemental hologram (Fig. 1). The elemental hologram in the wavefront printer is a part of the whole hologram and exhibits all properties of a hologram by encoding color, directional and distance related phase information. Theoretically,

its size is limited by the used active area of the SLM. Substantial decrease of the elemental hologram in our printer design made possible mosaic delivery of exposures at primary colors when each elemental hologram got a single color [7]. Separation of color channels allowed for avoiding the crosstalk and for achieving high diffraction efficiency.
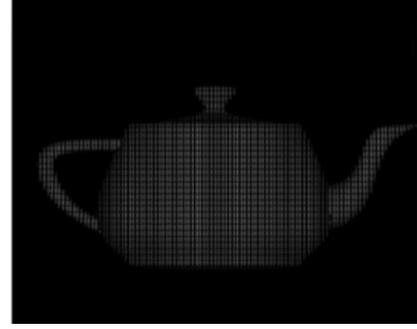
Fig. 2. Point-cloud representation of a 3D object.

We adopted the ray-casting approach to generate the 3D contents by using a point-cloud object representation (Fig. 2). The point cloud method considers the 3D object as a collection of point light sources which emit spherical waves. A set of point clouds with *P* self-emitting points each was extracted for all elemental holograms. The fringe pattern for a given elemental hologram was computed using the corresponding point cloud. For the purpose, we developed content creation software with tools for forming point-clouds of 3D objects and computing of CGHs at RGB wavelengths. Usage of high resolution SLM for displaying CGHs makes computation of 3D contents a complicated task at the chosen small size of the elemental hologram. To accelerate computation we developed a fast phase-added stereogram algorithm [8] that allowed for fast Fourier transform (FFT) implementation. The principle of fast CGH computation is elucidated in Fig. 3. The point "p" in a point cloud with spatial coordinates (x_p, y_p, z_p) is located at the distance $r_p = \left[(\xi - x_p)^2 + (\eta - y_p)^2 + z_p^2 \right]^{1/2}$ from the point (ξ,η) on the hologram plane located at $z = 0$. This point emits three spherical waves at the RGB wavelengths with different amplitudes and initial phases (a_p, ϕ_p). The algorithm partitioned each CGH into $M \times N$ square segments. The segment size is chosen small enough to use a plane wave for description of contribution of a point to the fringe pattern on the segment. The spatial frequencies (u_{mn}^p, v_{mn}^p) of the sinusoidal function for the point "p" and the segment $(m,n), m = 1..M, n = 1..N$ at a

given wavelength are determined with respect to the segment central point. The distance between the point "p" and the central point is r_{mn}^{p}. The initial phase of the sinusoid, Φ_{mn}^{p}, is a crucial parameter for matching the wavefronts of the plane waves diffracted from all segments. The phase Φ_{mn}^{p} contains the phase ϕ_{p} of the wave coming from the point "p" and may include the distance related phase. It is also determined with respect to the central point. Taking in view all object points, the fringe pattern across the segment is approximated as a superposition of 2D complex sinusoids. The fringe pattern in each segment was calculated by FFT of the 2D distribution in the spatial frequency domain of complex amplitudes associated with the points in the point-cloud seen from this CGH. Locations of the complex amplitudes corresponded to spatial frequencies determined with respect to the center of the segment. The segment size should be small to ensure good reconstruction from the phase-added approximation. That's why we applied the FFT with zero-padding for a number of pixels larger than the number of pixels in the segment to decrease the error due to discretization of the spatial frequencies. We used CUDA platform for parallel programming and computing to implement the developed algorithm.
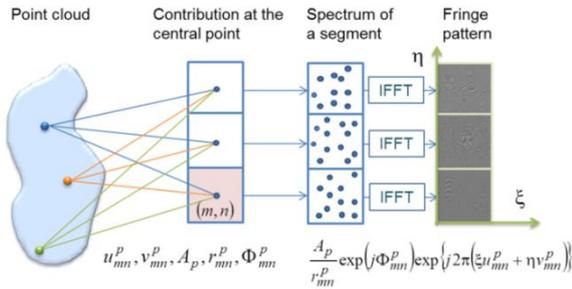
Fig. 3. Schematic of the accelerated computation of fringe patterns for elemental holograms.

RESULTS

The wavefront printer we built is depicted in Fig. 4. Three continuous wave DPSS lasers emitting at 640 nm, 532 nm and 473 nm were used. Each laser exposed a single elemental hologram. The first polarizing beam splitter (PBS$_1$) after the collimating system formed the object and reference beams. The object beam illuminated the amplitude type SLM by means of the PBS$_2$. We used a liquid crystal on silicon projector Sony VPL-HW10 SXRD with 1920×1080 pixels and a pixel interval 7 μm. After diffraction from the SLM, optical filtering and demagnification by the telecentric lens system, the beam impinged the holographic silver-

halide plate. Due to demagnification, the pixel interval at the plane of the hologram was 0.42 μm. We used the silver-halide emulsion Ultimate08 with an average grain size of 8 nm. The plate was moved by a X-Y stage at precision of 1 μm. For uniform intensity distribution at the object beam footprint on the hologram, we used only the central part of the SLM, so the size of the elemental hologram was 380 μm by 380 μm. The shutters controlled the exposure time. A personal computer controlled the wavefront printer operation.
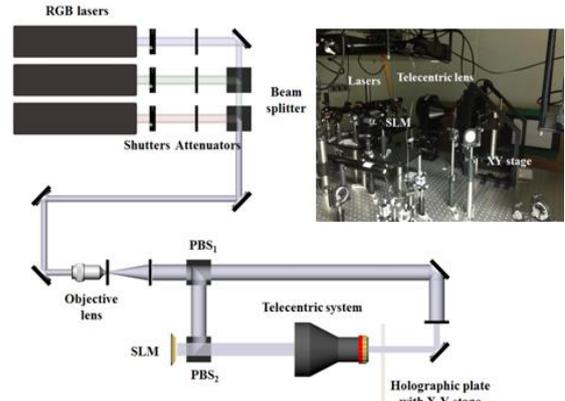
Fig. 4. Optical scheme and photograph of the wavefront printer with demagnification of the object beam.

Fig. 5. Photographs of reconstruction from printed holograms.

We achieved bright 3D reconstruction with a motion parallax at saturated colors from holograms of test objects (Fig. 5). The size of the holograms in the top row and the left hologram in the bottom row is 5 cm by 5 cm. They are built from 131×131 elemental holograms. Thus we proved feasibility of recording analogue color volume holograms from digital contents by applying spatially separated exposures at primary colors to the elemental holograms. The SLM partitioning was applied for enhancement of reconstruction quality at mosaic delivery of exposures for primary colors. We

checked a 3 × 3 partitioning scheme which results in an elemental hologram built as a mosaic of 9 non-overlapping color patches recorded at the RGB wavelengths. Thus we achieved smooth color reproduction without high-end optical components. The reconstruction from a 9 cm by 9 cm hologram of a bunch of flowers that has been printed by this method shows very good quality (Fig. 5). The reconstructions prove that the wavefront printer is a desirable choice for realistic 3D imaging with quality of reconstruction as in analogue holography.

CONCLUSION

In summary, we described a holographic printer for analogue reflection holograms from digital contents. The information about a color 3D object is encoded in a set of computer generated holograms which are printed as a set of color elemental holograms on a silver-halide emulsion. The printed hologram is a full parallax hologram and provides realistic 3D imaging. For accelerated generation of 3D contents for the numerous elemental holograms, a fast phase-added stereogram approach is proposed. High quality of reconstruction from the printed white-light viewable holograms recorded from the computer generated holograms produced with accelerated computation proved the algorithm efficiency.

REFERENCES

1. H. Kang, E. Stoykova, J. Park, S. Hong, Y. Kim, in Holography - Basic Principles and Contemporary Applications, E. Mihaylova (ed.), InTech, 2013, pp.171-201.
2. D. Brotherton-Ratcliffe, S. Zacharovas, R. Bakanas, J. Pileckas, A. Nikolskij, and J. Kuchin, *Opt. Eng.*, **50** (9), 091307 (2011).
3. H. Bjelkhagen and D. Brotherton-Ratcliffe, Taylor and Francis, 2013, p 341.
4. H. Yoshikawa and M. Tachinami, *SPIE Proc.,* **5742** , 259 (2005).
5. Y. Kim, E. Stoykova, H. Kang, S. Hong, J. Park, J. Park, and J. Hong, *Opt. Express,* **23**, 172 (2015).
6. T. Yamaguchi, O. Miyamoto, and H. Yoshikawa, *Opt. Eng.*, **51** (7), 075802 (2012.
7. H. Kang, S. Hong, Y. Kim, E. Stoykova, K. Jung, and K.-H. Seo, *KR Patent* 1014231630000 (2014).
8. H. Kang, E. Stoykova, and H. Yoshikawa, *Appl. Opt.*, **55**, A135 (2016).

ПРИНТИРАНЕ НА ЦИФРОВИ ХОЛОГРАФСКИ ДАННИ КАТО ЦВЕТНА ОТРАЖАТЕЛНА ХОЛОГРАМА ВЪРХУ СРЕБЪРНО-ХАЛОГЕНИДНА ЕМУЛСИЯ

Х. Дж. Канг[1], Е. Стойкова[1,2*], Ю. М. Ким[1], С. Х. Хонг[1], Дж. С. Парк[1], Дж. С. Хонг[1]

[1]*Корейски институт по електронни технологии, 11, Уорлд-кап бук-ро, 54-джил, Мапо-гу, Сеул, Корея*
[2]*Институт по оптически материали и технологии към Българската Академия на науките, ул.,,Акад. Георги Бончев", бл.109, 1113 София, България*

(Резюме)

Най-напредналата технология за триизмерно визуализиране с цифрова холография е холографският принтер. Той обединява цифровата и аналогова холография чрез запис на отражателна холограма върху сребърно-халогенидна емулсия от цифрови данни, подавани към пространствено-светлинен модулатор. Холограмата е масив от последователно записвани елементарни аналогови холограми. Първият разработен холографски принтер се базира върху некохерентен запис на изображения на тримерната сцена от различни ъгли и принтиране на стереограма, които се възприема тримерно посредством бинокулярно зрение. Записът само на посоката и цветовете изкривява възстановенич образ. Директното принтиране на интерференчни ивици като тънка пропускаща холограма върху холографска емулсия без опорен сноп дава неизкривено възстановяване без селективност към цветовете. В статията се представя цветен холографски принтер на вълновия фронт, който принтира възстановявана с бяла светлина холограма като двумерен масив от елементарни холограми върху сребърно-халогенидна емулсия. Тримерните данни за този принтер се формират като съвкупност от компютърно генерирани холограми и съдържат информаци за дълбочината, посоката и цвета. Данните за всяка елементарна холограма се подават на амплитуден пространствено-светлинен модулатор. Вълновичт фронт от тримерния обект се извлича с пространствен филтър и се намалява напречно преди записа. Принтираната холограма предоставя реалистично възстановяване подобно на това от аналогова отражателна холограма.

Improving activity visualization in dynamic speckle testing of paint drying by evaluation of a temporal correlation radius

E. Stoykova[1,2,*], B. Ivanov[1], T. Nikova[1], H-J. Kang[2]

[1]*Institute for Optical Materials and Technologies "Acad. J. Malinowski", Bulgarian Academy of Sciences, "Acad. G. Bonchev" str. Bl. 109, 1113 Sofia, Bulgaria*
[2]*Korea Electronics Technology Institute, 8 Floor, 11, World cup buk-ro 54-gil, Mapo-gu, Seoul, Korea*

We propose an approach for improving visualization of activity map obtained as an output of pointwise dynamic laser speckle analysis. The map reflects the speed of change of the speckle pattern formed on the surface of the tested object and thus provides information about the speed of processes leading to these change. The approach is based on pointwise calculation of the normalized temporal correlation function and further determination of the correlation radius. In case of negative exponential dependence of the correlation function on the time lag between the recorded speckle patterns, the obtained description of activity is quantitative. The proposed visualization enhancement of the activity map has been verified by processing raw data from a paint drying experiment.

Keywords: dynamic speckle, paint drying, pointwise processing, correlation function

INTRODUCTION

Dynamic laser speckle metrology provides a highly sensitive tool for non-destructive testing of paint drying [1]. Evaporation process during the drying leads to microscopic changes of the sample surface that create "boiling" speckle pattern on the sample under coherent illumination. This pattern carries information about the dynamics of the undergoing processes. Dynamic speckle testing includes sequential acquisition of correlated speckle patterns and their pointwise statistical processing [2,3]. The output of the measurement is a two-dimensional map which gives the distribution of a certain statistical parameter chosen to differentiate between the regions of lower or higher activity on the sample surface. The expectations are to obtain a detailed map with a good contrast to ensure high sensitivity, but processing of raw data yields a strongly fluctuating distribution of the parameter estimate that renders difficult visualization of activity. Furthermore, the chosen parameter usually maps non-linearly activity time scales and this makes possible only qualitative evaluation.

In this work we propose to enhance activity visualization by using as a statistical parameter the temporal correlation radius of intensity fluctuations.

As a first task we determined the form of the temporal correlation function of the fluctuations, $R(\tau)$, where τ was the time lag, for the paint drying experiment. We checked the applicability of the widely used exponential model [4], $R(\tau) = \sigma^2 \exp(-\tau/\tau_{corr})$, where σ^2 is the variance and τ_{corr} is the correlation radius, to describe intensity fluctuations in this case. As a second task, we verified quality of the activity map built as a distribution of the ratio between the correlation radius and the time lag and proved the contrast improvement.

PAINT DRYING EXPERIMENT

The experiment with paint drying was carried out with a specially designed circular metal object with two hollow regions of the same depth – a central circular section and an annular region – and two flat annular regions. A transparent polyester paint was used to cover the object to form a flat layer on its surface. Thus the circular and annular hollow regions contained larger quantity of paint than the other two annular regions. As a result, the speed of paint drying was different on the object surface. The object was illuminated with a He-Ne laser, and dynamic speckle patterns were recorded by a CMOS camera with a pixel interval $\Delta = 7$ μm. The camera optical axis was normal to the object

* To whom all correspondence should be sent:
E-mail: elena.stoykova@gmail.com

surface. The set-up was positioned on a vibration-insulated table. The 8-bit encoded speckle patterns were acquired at an interval $\Delta t = 250$ ms. The size of the processed images was $N_x \times N_y = 780 \times 582$ pixels.
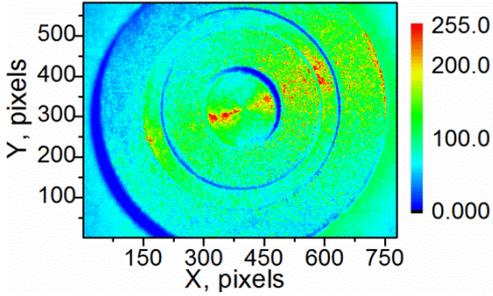
Fig. 1. Speckle pattern formed on the surface of a circular metal object covered with polyester paint; the pattern is presented as a contour map of the recorded intensity.

A typical speckle pattern is shown in Fig. 1 as a contour map. It is seen that the speckle pattern is characterized with non-uniform intensity distribution across the object, most probably due to non-uniform reflectance. The regions of different activity are not recognizable without statistical processing. We processed $N = 128$ images. The acquired raw data allowed for pointwise processing which means that the entries corresponding to a given pixel $(i,k), i = 1,2...N_x, k = 1,2...N_y$ form a temporal sequence of intensity values, $I_{ik,n}, n = 1,2...N$ of length N and enable evaluation of the chosen statistical parameter at this pixel by averaging over the whole sequence. The result of the pointwise processing is a two-dimensional distribution of size $N_x \times N_y$ of the obtained parameter values.

RESULTS

Fig. 2 depicts the two-dimensional (2D) distribution of the variance estimate of intensity fluctuations. The variance estimate at a pixel (i,k) is found from the formula

$$\hat{v}(i,k) = \frac{1}{N}\sum_{n=1}^{N}\left(I_{ik,n} - \bar{I}_{ik}\right)^2; \bar{I}_{ik} = \frac{1}{N}\sum_{n=1}^{N}I_{ik,n} \qquad (1)$$

where $\bar{I}_{ik}$ is the mean intensity at pixel (i,k). Due to the fixed length of the formed temporal sequences, the map of the variance estimate shows different behaviour in the hollow regions and on the

flat surfaces of the test object. Due to non-uniform intensity distribution in the speckle patterns (Fig. 1), the variance distribution reflects incorrectly the developing activity on the object surface as a result of paint evaporation. The variance estimate must have practically the same value in the hollow regions; the same should be true for the flat regions. However, we see substantial variance variation in these regions. We built also the 2D map of the speckle contrast as a ratio of the square root of the variance estimate and the mean value; the map is shown in Fig. 3. The contrast is not very high and its variation across the object does not provide correct description of activity.
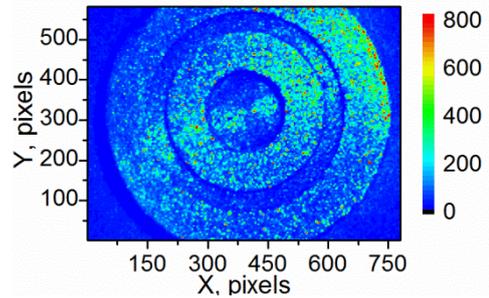
Fig. 2. Contour map of the variance estimate that reveals regions of different activity.
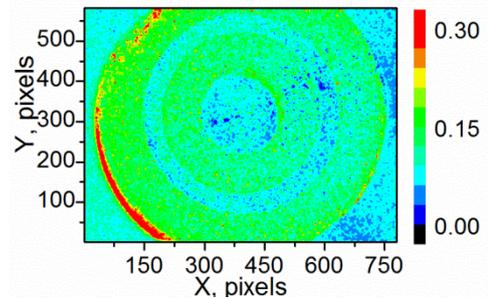
Fig. 3. Contour map of the pointwise contrast estimate.

In case of non-uniform illumination and varying reflectivity across the object surface one should apply normalized processing. Recently we introduced pointwise estimation of the normalized temporal correlation function [5] according the formula

$$\hat{R}_{norm}(i,k,m) = \frac{1}{N-m}\frac{1}{\hat{v}(i,k)}\sum_{n=1}^{N}\left(I_{ik,n} - \bar{I}_{ik}\right)\left(I_{ik,n+m} - \bar{I}_{ik}\right) \qquad (2)$$

where the index "m" corresponds to the time lag $\tau = m\Delta t, m = 1,2..M$ between the compared speckle images. The maximum value of the normalized function is 1. The 2D map of $\hat{R}$ at $m = 5$ is depicted in Fig. 4. The map shows much higher activity in

the leftmost part of the object. Probably this is due to less quantity of paint there. The map reveals the regions of different activity but for this particular time lag the contrast is not satisfactory.
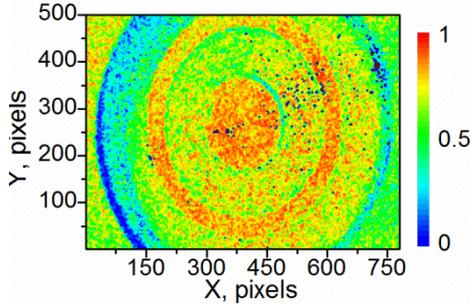

Fig. 4. Contour map of the normalized temporal correlation function at a time lag $\tau = 5\Delta t$.

The temporal correlation function provides information about the time scales of the undergoing activity. The width of this function determined at some level gives the correlation radius of the observed process. The problem is that the correlation function maps non-linearly the dependence on the time lag. This results in decreased contrast of activity visualization based on the normalized correlation function. The results of processing the raw data obtained by us for different objects [6,7] give a negative exponential dependence on the time lag, $R_{norm}(\tau) = \sigma^2 \exp(-\tau/\tau_{corr})$, as a close description to the experimentally estimated curves. To illustrate this statement, we calculated $\hat{R}(i,k,\tau)$ inside the spatial window of 50×50 pixels in the region of constant activity on the object surface starting from the pixel (325,90). The average value of the obtained estimates is shown as a function of the time lag in Fig.5. The correlation radius is determined at level $1/e$. Figure 6 gives the parameter $\Omega(\tau) = -\ln\{\hat{R}_{norm}(\tau)\}$ as a function of the time lag. We see practically linear dependence on τ. This result can be used for improving activity map quality by transforming $\hat{R}_{norm}(\tau)$ to $\Omega(\tau)$. In the case of negative exponential dependence on τ of the normalized correlation function it is possible to build the 2D map of the estimate of the correlation radius across the object:

$$\hat{\tau}_{corr} = \frac{m\Delta t}{\Omega(m\Delta t)} \qquad (3)$$

In principle, it is enough to find $\Omega(\tau)$ for a given time lag. We used Eq.(3) at $m = 5$ and obtained the correlation radius distribution presented in Fig. 7.

The map gives variation of the correlation radius across the object in seconds. Besides the fact that the map in Fig.7 provides better visualization of activity than the map in Fig.4, it also allows for its quantitative evaluation. The value of 6 s obtained from Fig. 5 corresponds well to the mean value in the spatial window of 50 by 50 pixels with its first pixel located at (325,90).
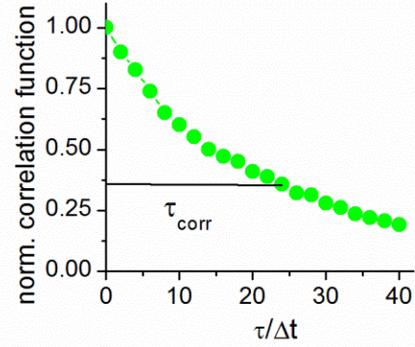
Fig. 5. Normalized temporal correlation function (the abscissa gives the ratio between the time lag and the acquisition interval $\Delta t = 250$ ms).
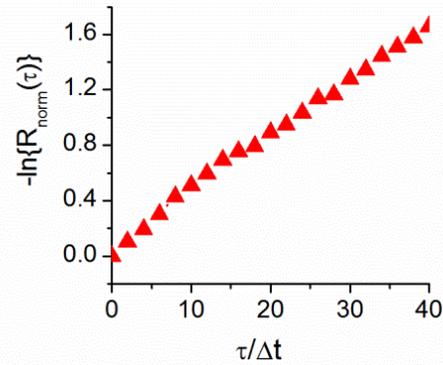
Fig. 6. Linear dependence of the logarithm of the normalized correlation function on the time lag (the abscissa gives the ratio between the time lag and the acquisition interval $\Delta t = 250$ ms).
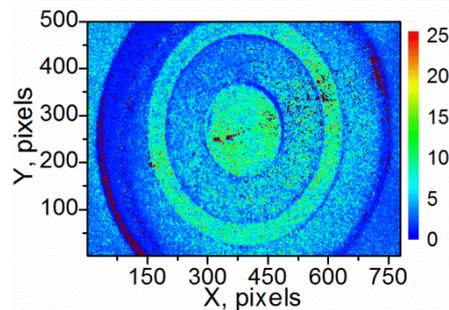
Fig. 7. Contour map of the normalized temporal correlation function at a time lag $\tau = 5\Delta t$; the time scale is given in seconds.

CONCLUSIONS

Based on processing of experimental data, we proposed an approach for enhancing visualization of regions of slower or faster changes on a surface of a diffusely reflecting object that are relied to undergoing processes of physical or biological nature inside it. The approach included pointwise calculation of the normalized temporal correlation function from a recorded sequence of speckle patterns formed on the object surface under laser illumination and determination of the 2D contour map of the correlation radius by accepting a negative exponential model for the correlation function of intensity fluctuations. The approach was verified by processing a paint drying experiment at which the correlation function at a given point corresponded to the accepted model. Then it is possible to describe activity quantitatively. Nevertheless, even when the accepted model for the logarithm of the correlation function is not strictly linear, it is expected to achieve activity map visualization enhancement.

REFERENCES

1. H. Rabal, R. Braga, Dynamic laser speckle and applications, CRC Press, Boca Raton, 2009.
2. A. Saúde, F. de Menezes, P. Freitas, G. Rabelo, and R. Braga, *J. Opt. Soc. Am. A*, **29**, 1648 (2012).
3. E. Stoykova, D. Nazarova, N. Berberova, and A. Gotchev, *Opt. Express*, **23**, 25128 (2015).
A. Federico, G. H. Kaufmann, G. E. Galizzi, H. Rabal, M. Trivi, and R. Arizaga, *Opt. Commun.*, **260**, 493 (2006).
4. E. Stoykova, B. Ivanov, and T. Nikova, *Opt. Lett.*, **39**, 115 (2014).
5. T. Lyubenova, E. Stoykova, E. Nacheva, B. Ivanov, I. Panchev, V. Sainov, SPIE Proc. **8770**, 87700S (2013).).
6. T. Nikova, E. Stoykova, B. Ivanov, *Phys. Scripta,* **T162,** 014044 (2014).

ПОДОБРЯВАНЕ НА ВИЗУАЛИЗИРАНЕТО НА АКТИВНОСТТА ЧРЕЗ ОЦЕНЯВАНЕ НА РАДИУСА НА КОРЕЛАЦИЯ ПРИ ТЕСТВАНЕ НА СЪХНЕНЕ НА БОЯ С ДИНАМИЧЕН СПЕКЪЛ

Е. Стойкова[1,2], Б. Иванов[1], Т. Никова[1], Х. Дж. Канг[2]

1Институт по оптически материали и технологии "Акад. Й. Малиновски", Българска Академия на науките, ул. "Акад. Г. Бончев", бл. 109, 1113 София, България
2Корейски институт по електронни технологии, 8 етаж, 11, Уорлд-кап бук-ро, 54-джил, Мапо-гу, Сеул, Корея

(Резюме)

В работата се предлага подход за подобряване на визуализирането на картата на активността, която се получава като изходен резултат при поточковия динамичен спекъл анализ. Картата показва промяната в спекъл картината, формирана върху повърхността на тествания обект и осигуряваща по този начин информация за скоростта на процесите, предизвикали тази промяна. Подходът се базира върху поточково пресмятане на нормираната времева корелационна функция, последвано от определяне на радиуса на корелация. В случая на отрицателна експоненциална зависимост на корелационната функция от времевия лаг между записаните спекъл картини полученото описание на активността е количествено. Предложеното подобряване на визуализирането на картата на активността е проверено чрез обработка на експериментални данни от експеримент със съхнене на боя.

Monitoring of a drying process in polymer water solutions by dynamic speckle detection

D. Nazarova, E. Stoykova*, L. Nedelchev, B. Ivanov, N. Berberova, N. Malinowski

Institute for Optical Materials and Technologies "Acad. J. Malinowski", Bulgarian Academy of Sciences, "Acad. G. Bonchev" str. Bl. 109, 1113 Sofia, Bulgaria

Observation of speed of processes by dynamic speckle analysis has been applied to different samples of industrial or biological nature. The method allows for indicating regions of lower or higher activity on the sample surface through statistical processing of the speckle patterns formed on this surface under laser illumination. The aim of the paper is to check applicability of dynamic speckle technique for detection of the drying process in polymer water solutions. For the purpose, we recorded several sets of 256 correlated in time speckle patterns of a transparent drop of PAZO water solution on a glass plate illuminated by a He-Ne laser. The sets were separated by intervals of 5 minutes, and the last set was recorded 75 minutes after the start of the experiment. For statistical description of activity on the observed sample we chose evaluation of a temporal structure function. The obtained two-dimensional maps of the structure function at different time lags demonstrated efficiency of dynamic speckle analysis for monitoring of drying processes in polymer water solutions.

Keywords: polymer, drying, dynamic speckle analysis

INTRODUCTION

Non-destructive detection of physical or biological activity through statistical processing of speckle patterns on the surface of diffusely reflecting objects is gaining popularity in optical metrology. Known as dynamic laser speckle analysis, this method is sensitive to microscopic changes of the surface over time and needs simple optical means for implementation [1,2]. This technique has been applied to study blood flow perfusion in human tissues [3], bacterial response [4], plant growing processes [5], seeds viability [6], animal reproduction [7], drying of paints and coatings [8], fruits quality [9] and bread cooling [10]. Advances in two-dimensional (2D) optical sensors and computers make possible development of pointwise algorithms, which rely on acquisition of a temporal sequence of correlated speckle patterns and show activity as a 2D spatial contour map of the estimate of a given statistical measure. The most widely used pointwise estimates are the intensity-based estimates. The map entry at each point for such an estimate is composed from a time sequence of intensity values taken at one and the same pixel in the acquired speckle patterns. By building such activity maps at different moments, one may follow the undergoing processes in time.

The aim of the paper is to check applicability of dynamic speckle technique for detection of the drying process in polymer water solutions. For the purpose, we recorded several sets of 256 correlated in time speckle patterns of a transparent drop of PAZO water solution on a glass plate. Processing was performed by intensity based pointwise algorithms [11]. For statistical description of activity on the observed sample we chose evaluation of a temporal structure function [12].

EXPERIMENTAL

In the present study, we use the azopolymer Poly[1-[4-(3-carboxy-4-hydroxyphenylazo) benzenesulfonamido]-1,2-ethanediyl, sodium salt] or shortly PAZO. The azopolymer is commercially available from Sigma Aldrich. Its chemical structure is shown in Fig. 1. An important advantage of this polymer is that it is water soluble. For our experiments water solution of PAZO with concentration C = 50 mg/ml was used. The average molecular weight of the azopolymer is M_w = 50 000−65 000 g/mol and glass transition temperature is T_g = 95 ± 5°C [13]. The parameters of the photoinduced birefringence (Δn) in thin films of PAZO and PAZO based nanocomposites have

* To whom all correspondence should be sent:
E-mail: elena.stoykova@gmail.com

already been studied by our group [14, 15]. The observed high values of Δn and its very high thermal stability attracted our attention to the process of thin film formation by drying of azopolymer water solution casted on a glass substrate. This was the reason to evaluate the potential of the dynamic speckle technique to study this drying process. To the best of our knowledge, this is the first time to monitor a polymer water solution by dynamic speckle technique.
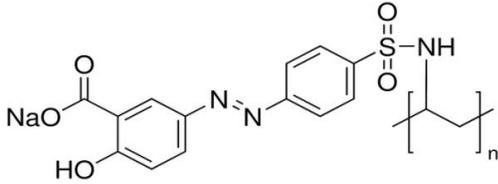
Fig. 1. Chemical structure of the PAZO azopolymer.

For the experiment, a drop of PAZO water solution was deposited on a glass plate. A specific feature of this sample was its transparency at the used wavelength. The plate was placed in a Petri dish. A CMOS camera with a pixel interval $\Delta = 7$ μm was adjusted to focus the sample with its optical axis normal to the glass surface. The set-up was positioned on a vibration-insulated table. We used a He-Ne laser. The camera recorded successively a sequence of $N = 256$ correlated images of size $N_x \times N_y = 500 \times 780$ pixels for time T at a sampling rate $1/\Delta t = N/T$ with the time interval $\Delta t = 250$ ms between the frames. Exposure time was 10 ms. A time sequence of 8-bit encoded intensities $I_{kl,n} \equiv I(k\Delta, l\Delta, n\Delta t), n = 1..N$ was formed at each pixel $(k\Delta, l\Delta), k = 1..N_x, l = 1..N_y$ of the acquired images. This data were used to build a point wise estimate of a given statistical measure over T. One of the captured speckle patterns is shown as a bitmap image in Fig.2. The borders of the drop and the glass plate are clearly seen. We put also a marker on the glass plate. We captured 6 sets of 256 correlated images with time offset from the start of the experiment 0, 5, 10, 15, 20 and 75 minutes.
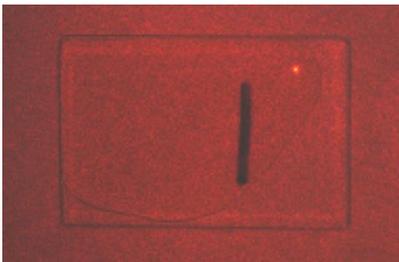
Fig. 2. Speckle pattern of a glass plate with PAZO water solution.

RESULTS AND DISCUSSIONS

In order to choose a proper processing, we calculated the two-dimensional (2D) distributions of the mean value and the variance of intensity fluctuations at each point. The estimates of these two parameters were obtained from the algorithms:

$$\hat{I}_{kl} = \frac{1}{N} \sum_{i=1}^{N} I_{kl,i} \,, \quad \hat{\upsilon}_{kl} = \frac{1}{(N-1)} \sum_{i=1}^{N} \left(I_{kl,i} - \hat{I}_{kl} \right)^2, \quad (1)$$

where averaging was done for the time sequences formed from the captured images. The 2D maps of the average value at time offsets 0 and 75 minutes are shown in Fig.3. The observed distributions are not strictly uniform because of slightly non-uniform intensity distribution within the illuminating laser beam. The same is valid at all time offsets.
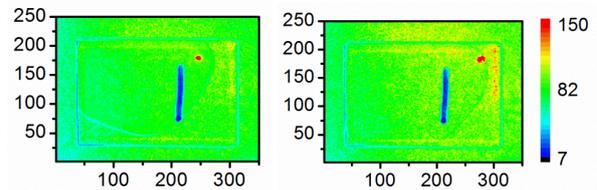
Fig. 3. 2D distribution of the mean value at time offsets 0 minutes (left) and 75 minutes.

Nevertheless, we chose for this first experiment a non-normalized estimate as providing better contrast of the activity map. We applied a temporal structure function. Its estimate at a time lag $\tau = m\Delta t$, where $m \geq 0$ takes integer values, is determined by

$$\hat{S}(k,l,m) = \frac{1}{N-m} \sum_{i=1}^{N-m} \left(I_{kl,i} - I_{kl,i+m} \right)^2 \quad (2)$$

As it can be seen from Eq.(2), the structure function is zero at zero activity and full correlation. It increases with the time lag and theoretically should reach the value of the variance multiplied by 2 when there is no correlation between images. The higher the value of the structure function, the lower is the correlation and the higher is the activity within the sample. The results of applying Eq.(2) to the acquired sets of correlated images are given in Fig.4 which depicts 2D maps of the structure function at time lags $\tau = 10\Delta t$ and $\tau = 50\Delta t$. We processed all sets, but Fig.4 presents only the data corresponding to three time offsets. Several conclusions can be made from the obtained distributions. The most important result is that the dynamic speckle techniques allows for detecting the process of drying. To be sure that the observed result was due to evaporation from the drop surface, we recorded a set of 256 speckle images of a glass plate without the drop.
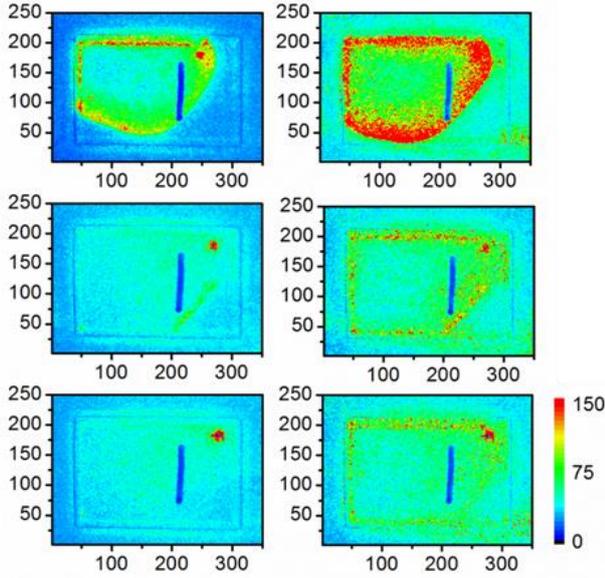
Fig. 4. 2D distribution of the temporal structure function at time offsets 0 minutes (top), 20 minutes (middle) and 75 minutes (bottom); left - $\tau = 10\Delta t$, right - $\tau = 50\Delta t$.

Processing of this set of images confirmed that the activity on the plate surface was the same as for the surrounding Petri dish and the values of the variance of intensity fluctuations in time were much lower. We see the change of the drop in time and much higher activity at its borders. As it should be expected, with increase in time elapsing from the start of the drying process activity within the sample is decreasing. Furthermore, the contrast of the speckle, given by the ratio between the square root of the variance and the average value of intensity fluctuations, is also decreasing. Evaporation of the drop caused also rise of activity around the glass plate. Strong variation of activity within the drop is detected at the beginning of the drying process whereas at larger time offsets activity equalizes within the drop and increases only on the borders.

To evaluate the time scale of the drying process, we found the dependence of the structure function on the time lag for the spatial region around the approximate center of the drop. For the purpose, we averaged the estimate (2) within a spatial window of 30×30 pixels. The size of the window was so chosen as to ensure relatively large number of points corresponding to uniform intensity. Speckle nature of the raw data leads to a very low spatial correlation of the estimate within the window and makes possible to obtain practically smooth curves by averaging over 900 points. The uniform intensity within the window is necessary to guarantee correct average value. The functions evaluated at three different time offsets are depicted

in Fig.5. The fall of the variance is clearly seen at large time lags. For the elapsed 75 minutes it decreases more than two times. To find the time scales we normalized the obtained functions to the variance estimates (1). The result is shown in Fig.6. Judging from the normalized curves activity remains very high within the drop even after 75 minute, so the drying process is not completed yet. Actually, the steepest normalized structure function is observed at time offset 75 minutes due to decrease of the water solution in the drop and faster evaporation. We can determine the correlation radii from the formula $S_{norm}(\tau) = 2[1 - R_{norm}(\tau)]$ relating the normalized structure and correlation functions of intensity fluctuations in time [12]. If we adopt a widely used negative exponential model $R_{norm}(\tau) = \exp(-\tau/\tau_c)$ to approximate $S_{norm}(\tau)$, the correlation radii determined at level $1/e$ from for the offsets 0, 20 and 75 minutes are approximately 2 s, 3 s and 1.25 s respectively.
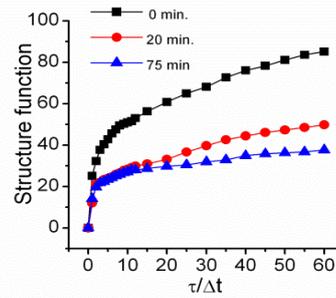
Fig. 5 Structure function of intensity fluctuations in the center of the drop pf PAZO water solution at three time offsets.).
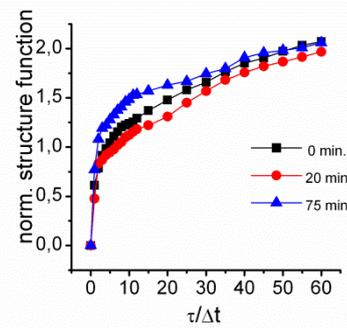
Fig. 6. Normalized structure function of intensity fluctuations in the center of the drop pf PAZO water solution at three time offsets.

CONCLUSIONS

In summary, we proved by experiment that the dynamic speckle analysis could be applied for monitoring of the drying process of polymers water solutions. The method is capable to demonstrate

changes in different size drops of such solutions in time by building 2D maps of a given statistical measure that includes the tested polymer water solution sample. By following time variation of the correlation radius of intensity fluctuations within speckle patterns formed on the sample surface it is possible to determine the time scales of the drying process. Since the aim of this preliminary study was to prove applicability of dynamic speckle analysis for observing the drying process of transparent polymers, we did not record sequences of speckle images till the end of this process, when practically full correlation should be observed.

REFERENCES

1. H. Rabal, R. Braga, Dynamic laser speckle and applications, CRC Press, Boca Raton, 2009.
2. J. Goodman, Statistical Optics, Wiley – Interscience, 2000.
3. V. Rajan, B. Varghese, T. Leeuwen, W. Steenbergen, *Opt. Lett.,* **31**, 468 (2006).
4. S. Murialdo, G. Sendra, L. Passoni, R. Arizaga, J. Gonzalez, H. Rabal, M. Trivi, *J. Biomed. Opt.,* **14**, 064015 (2009).
5. R. Braga, L. Dupuy, M. Pasqual, R. Cardoso, *Eur. Biophys. J.,***38**, 679 (2009).
6. R. Braga, G. Rabelo, L. Granato, E. Santos, J. Machado, R. Arizaga, H. Rabal, M. Trivi, *Biosystems Eng.,* **91**, 465 (2005).
7. R. Macedo, J. Filho, R. Braga, G. Rabelo, *Reprod. Fertil. Dev.,* **22**, 170 (2009).
8. M. Limia, A. Núñez, H. Rabal, M. Trivi, *Appl. Opt.*, **41**, 6745 (2002).
9. C. Mulone, N. Budini, F.Vincitorio, C. Freyre, A. Díaz, A. Rego, *Proc. SPIE* **8785**, 87851X (2013).
10. T. Lyubenova, E. Stoykova, E. Nacheva, B. Ivanov, I. Panchev, V. Sainov, *Proc. SPIE* **8770**, 87700S (2013).
11. E. Stoykova, D. Nazarova, N. Berberova, A. Gotchev, *Opt. Expres,s* **23**, 25128 (2015).
12. E. Stoykova, B. Ivanov, T. Nikova, *Opt. Lett.*, **39**, 115 (2014).
13. Q.Ferreira, P. Ribeiro, O. Oliveira, M.Raposo, *ACS Appl. Mater. Interfaces*, **4**, 1470 (2012).
14. L. Nedelchev, D. Nazarova, G. Mateev, N. Berberova, *Proc. of SPIE,* **9447**, 1I-1-7 (2015).
15. N. Berberova, D. Nazarova, L. Nedelchev, B. Blagoeva, D. Kostadinova, V. Marinova, E. Stoykova, *J. Phys.: Conf. Ser.,* **700**, 012032 (2016).

МОНИТОРИНГ НА ПРОЦЕСА НА СЪХНЕНЕ НА ВОДНИ РАЗТВОРИ ОТ ПОЛИМЕРИ ЧРЕЗ ДЕТЕКТИРАНЕ НА ДИНАМИЧЕН СПЕКЪЛ

Д. Назърова, Е. Стойкова, Л. Неделчев, Б. Иванов, Н. Берберова, Н. Малиновски

Институт по оптически материали и технологии "Акад. Й. Малиновски", Българска Академия на науките, ул. "Акад. Г. Бончев", бл. 109, 1113 София, България

(Резюме)

Наблюдаването на скоростта на протичане на процеси с помощта на динамичен спекъл анализ е прилагано към различни образци от индустриално или биологично естество. Методът позволява да се посочат областите с по-ниска и по-висока активност върху повърхността на образеца чрез статистическа обработка на спекъл картините, формирани върху тази повърхност при осветяване с лазер. Целта на настоящата работа е да се провери приложимостта на техниката на динамичния спекъл за детектиране на процеса на съхнене на водни разтвори на полимери. За осъществяване на проверката са записани няколко серии от 256 корелирани във времето спекъл картини на прозрачна капка на воден разтвор на PAZO полимер върху стъклена подложка, осветена с He-Ne лазер. Сериите бяха разделени с пет минутни интервали, като последната серия е записана 75 минути след капването на капката. Статистическото описание на активността в наблюдавания образец е проведено чрез пресмятане на времева структурна функция. Получените двумерни разпределения на тази функция за различни времеви лагове потвърдиха ефективността на динамичния спекъл анализ за наблюдаване на процеси във водни разтвори на полимери.

Elimination of zero-activity regions in dynamic laser speckle coating drying experiments

E. Stoykova[1,2,*], T. Nikova[1], B. Ivanov[1], Y-M. Kim[2], H-J. Kang[2]

1Institute for Optical Materials and Technologies "Acad. J. Malinowski", Bulgarian Academy of Sciences, "Acad. G. Bonchev" str. Bl. 109, 1113 Sofia, Bulgaria
2Korea Electronics Technology Institute, 8 Floor, 11, World cup buk-ro 54-gil, Mapo-gu, Seoul, Korea

Dynamic laser speckle method is a useful approach for monitoring the speed of processes by statistical processing of speckle patterns formed on the surface of diffusely reflecting object at laser illumination. The most popular algorithms are the intensity-based pointwise algorithms which rely on capture of correlated in time speckle patterns. These algorithms fail at non-uniform illumination and require pointwise normalization to produce correct results. The normalized processing encounters difficulties in detection of non-varying regions on the object surface. The paper proposes usage of a specially designed estimator to eliminate these regions.

Keywords: dynamic speckle, intensity-based algorithms, pointwise processing,

INTRODUCTION

Dynamic laser speckle method enables monitoring of processes by detection of speckle patterns formed on the surface of diffusely reflecting objects at coherent light illumination [1,2]. The speckle patterns reflect the microscopic changes on the object surface and thus provide a very sensitive tool for indicating changes. The method is effective for non-destructive testing of industrial samples as drying of paints or coatings, biomedical applications and food quality assessment [3-5]. Dynamic speckle metrology has been pushed forward by advances in modern optical sensors and computers that make possible pointwise processing and characterization of the monitored process by a two-dimensional (2D) distribution of a given statistical parameter related to its speed. This map is called an activity map and allows for differentiation of regions with slow or fast changes of speckle patterns on the object surface [6]. The main advantage of dynamic speckle technique is the simple experimental means of performing the measurement. The main disadvantage is that the statistical processing is vulnerable to non-uniform illumination or varying reflectivity across the object due to the signal-dependent nature of speckle fluctuations. To overcome this drawback, pointwise normalization is applied to the statistical estimates of activity [7]. Normalization, however, fails in the regions with almost zero activity and gives an erroneous result by indicating activity much greater than the existing really. The goal of this paper is to develop reliable procedure for detecting zero-activity regions by combining normalized and non-normalized processing. Experimental verification of the developed approach is done by processing paint coating drying.

POINTWISE CHARACTERIZATION

Generally speaking, capture of 2D dynamic speckle patterns by a CCD camera allows to build a 2D spatial distribution of some measure which characterizes activity related to different spatial regions of the sample under study for a given time interval. For the purpose, a series of N frames is acquired for the observation time T. Thus, the 8-bit encoded and sampled intensities, $I_{kl,n} = I(k\delta x, l\delta y; n\Delta t), n = 1,2..N$, which correspond to a given pixel $(k\delta x, l\delta y)$ in the recorded N frames, form a time sequence (Fig. 1). Here $(\delta x, \delta y)$ are the sampling intervals along the N_x rows and N_y columns of the captured image and $\Delta t = T/N$ is the time interval between two consecutive images. The estimate of the chosen statistical measure is found at all points $(k\delta x, l\delta y)$, $k = 1,2..N_x, l = 1,2..N_y$, after

* To whom all correspondence should be sent:
E-mail: elena.stoykova@gmail.com

averaging over the formed time sequences. The obtained 2D distribution of the estimate corresponds to T and hence it gives localized in space and not localized in time estimate of sample activity. The time interval T should cover several radii of the temporal correlation function of intensity fluctuations caused by the undergoing activity within the sample to have enough data for a reliable estimate.
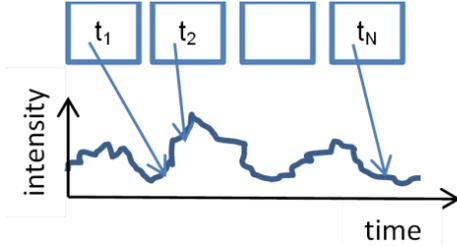
Fig. 1. Capture of a time sequence of 2D speckled patterns

A measure based on evaluation of the temporal structure function (TSF) at $(k\delta x, l\delta y)$, $k = 1,2..N_x, l = 1,2..N_y$ yields localized in time 2D descriptions of activity for time lags $\tau = m\Delta t, m = 1,2..M$ which correspond to the averaging interval T:

$$\hat{S}(k.l.m) = \frac{1}{(N-m)}\sum_{n=0}^{N}\left(I_{kl,n} - I_{kl,n+m}\right)^2 \qquad (1)$$

We can also describe the time fluctuations by using a normalized temporal structure function (NTSF). The estimate of the NTSF for each point $(k\delta x, l\delta y)$ is built as follows:

$$\hat{S}_{norm}(k.l.m) = \frac{1}{(N-m)}\frac{1}{\bar{\upsilon}(k,l)}\sum_{n=0}^{N}\left(I_{kl,n} - I_{kl,n+m}\right)^2 \qquad (2)$$

$$\bar{\upsilon}(k,l) = \frac{1}{N}\sum_{n=1}^{N}\left(I_{kl,n} - \bar{I}_{kl}\right)^2, \quad \bar{I}_{kl} = \frac{1}{N}\sum_{n=1}^{N}I_{kl,n} \qquad (3)$$

where $\bar{\upsilon}(k,l)$ and $\bar{I}_{kl}$ are the estimates of the variance and the mean intensity that are calculated at the spatial point $(k\delta x, l\delta y)$. For a time lag $\tau = m\Delta t$ the estimates $\hat{S}_{norm}(k,l,m)$ and $\hat{S}(k,l,m)$ are given by 2D spatial distributions where the small values of $\hat{S}_{norm}$ or $\hat{S}$ correspond to large correlation and hence indicate lower activity within the sample and vice versa. Theoretically the NTSF varies from 0 to 1.

EXPERIMENTAL

To check the efficiency of correlation-based algorithms to locate different activity regions we performed measurements with the test object in Fig. 2. The surface of the object was covered with concentric grooves of varying depth and width. A coin was placed in the circular hollow region at the centre of the object. The object was covered with a nail polish, whose drying produced a dynamic speckle. The correlation of data in the regions corresponding to the grooves is larger in comparison to those of the flat surface due to the larger quantity of the nail polish there. The same is valid to some extent for the different parts of the coin due to its varying relief. For the experiment, only the lower half of the object was covered with the nail polish. Illumination of the object was done with a He-Ne laser. The acquisition of speckle patterns was made at a rate of $\Delta t = 500$ ms between the frames. The captured images size was 580×780 pixels.

Fig. 2. Test object.
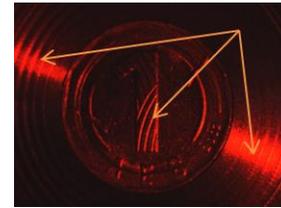
Fig. 3. Image acquired by the CCD camera (the arrows show unusable regions.

We processed 170 speckle patterns with the NTSF and TSF algorithms. An exemplary captured image is shown in Fig. 3. As it is seen, the object surface has non-uniform reflectivity. The arrows indicate the regions of specular reflection for which the recorded intensity everywhere reaches 255 gray levels, and moreover it keeps this value for the whole series. Obviously, information is lost in these regions, and the data in them should be discarded. We excluded the rightmost part of the recorded images due to the large non-informative area and chose to process the data in the region with size

500×500 pixels with a bias of 50 rows and 0 columns. The results obtained for the NTSF are shown in Fig. 4. The light regions correspond to lower correlation and hence to higher activity. Registration of activity is expected for the lower half of the object. The NTSF in the upper part should remain constant. We see that the data in the narrow grooves on center of the coin should be also discarded. The obtained NTSF maps clearly show regions of different activity. We see higher correlation in the region of the concentric grooves as well as on the surface of the coin up to the lag 20Δt; at greater lags there is no correlation between the recorded images. However, the NTSF estimate does not reflect properly the lack of activity in the upper half of the object. Theoretically the NTSF in this region should be close to zero everywhere. The averaged NTSF distribution is uniform indeed, but the mean value of the NTSF in this region is constantly decreasing and is much higher than zero. The inaccuracy of the estimate is due to the short length (170 images) of the series used for calculations. We may conclude that the algorithms with the normalization when applied to short time-series fail to indicate clearly the zero-activity regions. The processing should pick-up automatically and correctly these regions.
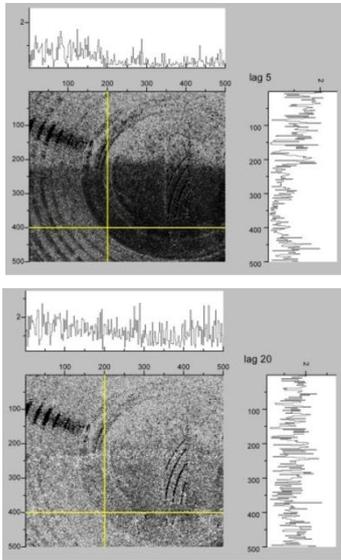
Fig. 4. NTSF at time lags $\tau = 5\Delta t$ and $\tau = 20\Delta t$ (the grey scale varies from 0 to 2.5).

The SF without normalization also clearly separates the upper and the lower object parts (Fig. 5). The mean square of the difference between the intensities is much higher in the lower half of the TSF map. One should take in mind, however, that the value of the mean square rapidly increases with

the reflective property of the object. For example, reflectivity in the grooves region and the coin is higher than on the flat object sections. Dependence of the TSF on the reflectivity across the object renders difficult obtaining information about the activity time scale in different regions of the object. Nevertheless, we could use these function to cut out the zero activity regions
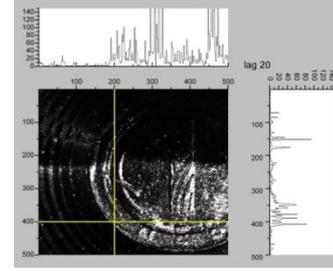
Fig. 5. TSF at a time lag 20□t (the grey scale varies from 0 to 140).

To locate the regions with almost zero activity, we introduce the following estimator:

$$\hat{P}(k,l,m) = \frac{1}{(N-m)} \frac{1}{\hat{M}_{sq}(k,l)} \sum_{n=1}^{N} \left(I_{kl,n} - I_{kl,n+m}\right)^2 \qquad (4)$$

where $\hat{M}_{sq} = \frac{1}{N}\sum_{n}^{N} I_{kl,n}^2$ is the estimate of the mean square. To clarify $\hat{P}(k,l,m)$ let us suppose that the intensity fluctuations have the same mean value and variance across the image and that the variation in time is a stationary process. Therefore, we may write for any point $I(n\Delta t + m\Delta t) = I(n\Delta t) + \delta I(m\Delta t)$, where $\delta I(m\Delta t)$ is the rise of intensity. Then

$$\left\langle \hat{P}(m) \right\rangle \approx \frac{1}{\Im}\left\{2\Im - 2\left[\Im + \left\langle I(n\Delta t)\delta I(n\Delta t)\right\rangle\right]\right\} \qquad (5)$$

where $\Im = \left\langle I^2(n\Delta t)\right\rangle = \left\langle I^2(n\Delta t + m\Delta t)\right\rangle$ is the mean square. It is clearly seen from the above expression that the estimator $\hat{P}(k,l,m)$ is zero when $\delta I(m\Delta t) = 0$. When the intensities $I(n\Delta t)$ and $I(n\Delta t + m\Delta t)$ are not correlated, the estimator becomes

$$\left\langle \hat{P}(m) \right\rangle \approx 2\left[1 - \frac{\bar{I}^2}{\Im}\right] = 2\left[1 - \frac{\bar{I}^2}{\upsilon + \bar{I}^2}\right] = \frac{2}{1 + \left(\sigma_I / \bar{I}\right)^{-2}} \qquad (6)$$

where $\sigma_I = \sqrt{\upsilon}$ is the standard deviation of the fluctuations and υ is their variance. We see that the higher the fluctuations, the higher is the value of $\hat{P}(k,l,m)$. At $\sigma_I = \bar{I}$, which is the case of the fully developed speckle [1], the estimator value is one.

We propose to use the introduced estimator in the following way:

1) to calculate $\hat{P}(k,l,m)$ for a comparatively large time lag which guarantees detection of variations in the recorded speckle pattern;
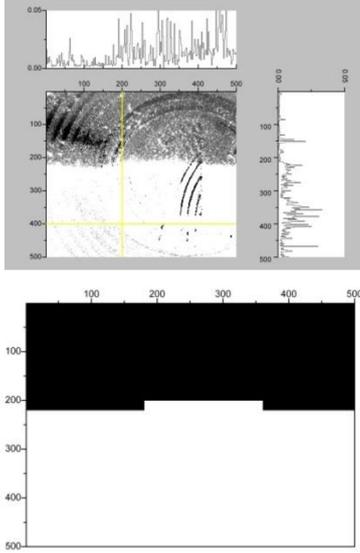
Fig. 6. Distribution of the estimator $\hat{P}(k,l,m)$ at m = 30 (top) and the calculated mask (bottom).
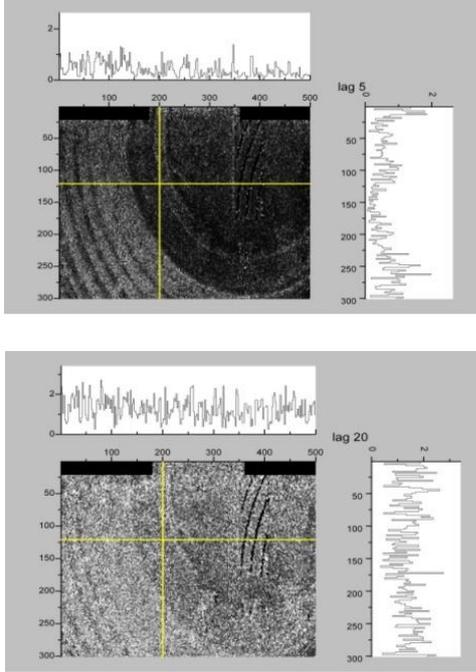
Fig. 7. NTSF at time lags $\tau = 5\Delta t$ and $\tau = 20\Delta t$, multiplied by the mask (the grey scale is from 0 to 2.5).

2) to set a threshold value close to zero, e.g. ε = 0.002, and to create the mask:

$$M(k,l) = \begin{cases} 0 & if \quad \hat{P}(k.l.m) < \varepsilon \\ 1 & if \quad \hat{P}(k.l.m) \geq \varepsilon \end{cases} \tag{7}$$

3) to eliminate the spurious fluctuations in $\hat{P}(k.l.m)$ that may lead to non-connected single points in the mask, the mask is filtered with a sliding window of size 10×10; if the sum of the values in the window exceeds 60, a unity value is attached to all values inside the window;

4) the NTSF distributions are multiplied by the mask to remove the regions of zero activity.

Fig. 6 depicts the distribution of $\hat{P}(k,l,m)$ at m = 30, and the mask derived from it. Fig. 7 shows the distributions of the NTSF multiplied by the mask. We obtain the highest correlation of fluctuations on the surface of the coin. The correlation is higher in the grooves than in the flat object sections. As it should be expected, the correlation disappears first for the thinner grooves. They are undistinguishable from the flat sections at time lags 20 and 40 whereas the thicker grooves are still seen.

CONCLUSIONS

In summary, we developed a dynamic speckle approach based on combined usage of normalized and non-normalized processing for elimination of zero-activity regions from activity maps obtained for the normalized correlation-based algorithms. The problem with erroneous detection of activity in these regions arises from small value of the variance and inaccurate determination of its estimates at short lengths of the temporal sequences formed from the acquired speckle images. Efficiency of the proposed approach was confirmed by processing a test object half coated with a polyester paint. The developed algorithm formed automatically a mask to preserve only regions with non-zero activity.

REFERENCES

1. J. Goodman, Statistical Optics, Wiley – Interscience, 2000.
2. H. Rabal, R. Braga, Dynamic laser speckle and applications, CRC Press, Boca Raton, 2009.
3. B. Zheng, C. Pleass, and C. Ih, *Appl. Opt.*, **33**(2), 231-237 (1994).
4. R. Arizaga, N. Cap, H. Rabal, and M. Trivi, *Opt. Eng.*, **41,** 287 (2002).
5. A. Saúde, F. de Menezes, P. Freitas, G. Rabelo, and R. Braga, *J. Opt. Soc. Am. A*, **29**, 1648 (2012).

6. E. Stoykova, D. Nazarova, N. Berberova, and A. Gotchev, *Opt. Express*, **23**, 25128 (2015).

7. E. Stoykova, B. Ivanov, and T. Nikova, *Opt. Lett.*, **39**, 115 (2014).

ОТСТРАНЯВАНЕ НА ОБЛАСТИТЕ С НУЛЕВА АКТИВНОСТ ПРИ ДИНАМИЧЕН СПЕКЪЛ АНАЛИЗ НА СЪХНЕНЕ НА ПОКРИТИЯ

Е. Стойкова[1,2], Т. Никова[1], Б. Иванов[1], Й.М. Ким[2], Х.Дж. Канг[2]

1Институт по оптически материали и технологии "Акад. Й. Малиновски", Българска Академия на науките, ул. "Акад. Г. Бончев", бл. 109, 1113 София, България
2Корейски институт по електронни технологии, 8 етаж, 11, Уорлд-кап бук-ро, 54-джил, Мапо-гу, Сеул, Корея

(Резюме)

Динамичният спекъл метод е полезен подход за мониторинг на скоростта на протичане на процеси чрез статистическа обработка на спекъл картините, образиващи се върху повърхността на дифузно отразяващи обекти при осветяване с лазер. Най-популярни са интензитетно-базираните алгоритми, които изискват запис на корелирани във времето спекъл изображения. Тези алгоритми не са ефективни при неравномерно осветяване и се налага провеждането на поточково нормиране за постигане на коректни резултати. Обработката с поточково нормиране среща трудности при детектирането на области без промяна върху повърхността на обекта. В статията се предлага използването на специално изградена оценка за отстраняване на тези области.

Surface plasmon and guided modes excitation of cholesteric liquid crystal layer

K. Zhelyazkova[1], M. Petrov[3], B. Katranchev[3], G. Dyankov[2,*]

[1]*Faculty of Physics, Plovdiv University "Paisii Hilendarski", 24 Tzar Assen Str, 4000 Plovdiv, Bulgaria*
[2]*Institute of Optical Materials and Technologies, Bulgarian Academy of Sciences, 109 Acad. G. Bontchev Str., 1113 Sofia, Bulgaria*
[3]*Institute of Solid State Physics, Bulgarian Academy of Sciences, 72 Tzarigradsko shosse Blvd, 1784 Sofia, Bulgaria*

The features of optical excitation of surface plasmon and guided modes in nematic liquid crystal layer (NLCL) are well studied. This problem has never been considered for cholesteric liquid crystal layer (CLCL). There are a lot of open questions, in spite some considerations have been recently performed. The aim of this work is to answer some questions by a theoretical study. A series of guided modes and surface plasmon are excited in CLCL at the condition of attenuated total reflection. The structure we consider has two main differences, compared with the nematic liquid crystal cell: i) the twist angle is a function of layer's thickness; ii) the pitch of the helical structure defines how the wavelength "sees" the refractive index profile of the liquid crystal layer. These special features presume that the critical angles for extraordinary modes are different than that of NLCL. We propose to use "effective critical angle" defined in terms of pitch length. The effective critical angle explains very well the dependence of number of guided modes on tilt angle and on pitch.

Keywords: Surface plasmon, guided mode, chiral anisotropic media

INTRODUCTION

Some early studies have treated the surface plasmon polariton (SPP) behavior at the interface metal layer/nematic liquid crystal (LC). In this context a series of papers of J.R.Sambles has to be acknowledged [1- 9], for example. These studies have been focused not only on SPP features, defined by the adjacent anisotropic medium but on the interaction SPP/guided modes in LC layer. These detailed studies have shown that the coupling SPP/guided mode is very sensitive to the surface director tilt profile near to the metal layer. In all studies nematic LC layer has been used. This is understandable - the nematic LC have been an object of great interest because of their application in LC display - the technology has required a precise knowledge of all LC characteristics.

Recently, the problem has been formulated in opposite direction – is it possible to obtain specific plasmon response by introducing anisotropic dielectric into the plasmon structure [10-14]. Two dimensional rotation of LC on a metal surface was studied in [15] as a first step toward the considering a cholesteric LC. Such kind of analysis was completed in [16] but comprehensive study has yet not been achieved.

Our research [17-19] has focused on the influence of the parameters of chiral anisotropic layer, adjacent to the metal layer, on the plasmon characteristics and on the possibility of controlling plasmon propagation.

Unlike our previous study, this paper is focused on the conditions for guided modes excitation in cholesteric liquid crystal layer and on the interaction plasmon/guided modes. This is the first time to our knowledge that such problem is considered for a chiral anisotropic structure.

THE STRUCTURE

The chosen structure consists in high-index glass prism with a deposed on gold layer, chiral liquid crystal layer, and a low index glass substrate (Fig.1). The prism refractive index must be greater that the highest index inherent to the LC, whereas the lower-index glass substrate must have an index lower than the lowest index inherent to the LC. The LC is uniaxial and specified by permittivities parallel and perpendicular to the director – $\varepsilon_{\parallel}$ and $\varepsilon_{\perp}$, respectively. In such structure there exist a range of incident angle defined by the critical angle of high-index prism and the effective index of the LC and the critical angle of high-index prism and low index substrate. In this range the guided modes

* To whom all correspondence should be sent:
E-mail: gdyankov@iomt.bas.bg

in LC layer are excited because of evanescent optical field.

We suppose $\varepsilon_\parallel > \varepsilon_\perp$ ($\Delta\varepsilon = \varepsilon_\parallel - \varepsilon_\perp$) and the director is defined by tilt θ and twist φ (Fig. 1). The twist in CLCL is a function of thickness $\varphi = f(z)$. The prism and the substrate are homogeneous with the permittivity ε_1 and ε_3, respectively.

$$\beta_1 = \sin^{-1}(\varepsilon_3/\varepsilon_1)^{1/2} \tag{2}$$

$$\beta_3 = \sin^{-1}\left[\frac{\varepsilon_\parallel \varepsilon_\mid}{\{\Delta\varepsilon(\cos(\theta)\cot(\alpha) - \sin(\theta)\sin(\phi))^2 + \varepsilon_\perp(1 + \cot^2(\alpha))\}|_{\min}}\right]\frac{1}{\varepsilon_1} \tag{3}$$
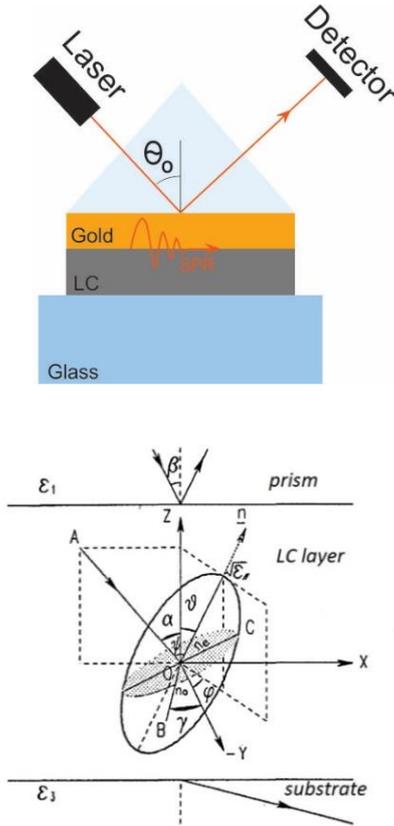
Fig. 1. Configuration of the structure and orientation of the principle axes of the local dielectric tensor ellipsoid defined by Euler angles in some chiral molecular layer.

The first critical angle is defined by the lowest refractive index of the substrate. The second critical angle is defined by the propagation constant of the extraordinary mode. For this mode the refractive index n_e depends on α and φ. While we are interested on the maximum value of the incidence angle, the denominator of (3) has to be minimized for a specific value of α. Thus, the dependence of α is cancel and the critical angle is a function only on tilt and twist.

CRITICAL ANGLE OF CLCL

A point worthy of note is that (3) is in the case of

The incidence angles range over which guided modes are excited is [20]:

$$\beta_1 < \beta < \beta_3 \tag{1}$$

Where β_1 and β_3 are critical angles defined as [20]:

nematic LC. The question now is: how it is possible to extend (3) for chiral structure? We propose an idea to generalize (3) following the physics behind the light propagation in chiral LC. The optical field "seas" the twist structure when the pitch p is longer and compatible to the wavelength of incident light ($\lambda = 632$ nm). That why it is important to model numerically a CLCL with thickness d compatible to the wavelength. For the case $p = d$ (i.e. $\phi \in [0, 2\pi]$) the optical field will follow the twist of LC molecule. Then, the extraordinary mode has some effective refractive index n_e corresponding to the continuously changed φ in the range $0 - 2\pi$. Consequently, (3) has to be changed to reflect this feature. Reasonably, the new form of the denominator in (3) is:

$$\int_0^{2\pi}\{\Delta\varepsilon(\cos(\theta)\cot(\alpha) - \sin(\theta)\sin(\phi))^2 + \varepsilon_\perp(1 + \cot^2(\alpha))\}d\phi \tag{4}$$

then the minimization is provided for (4).

NUMERICAL SIMULATIONS

On the purpose to check our model we simulated guided modes and SPP excitation in nematic and cholesteric LC layer in the structure shown in Fig.1 for different tilt angle as a function of incident angle.

The simulations are based on a theoretical model, obtained by solving Maxwell equations in 4x4 matrix form, for an anisotropic medium [21]. The reflectance of the layered structure for incident p-polarized light, is presented in Fig. 2. For the prism we used permittivity $\varepsilon_1 = 4.84$ and for the substrate $\varepsilon_3 = 2.25$. The gold film is with a thickness $d_{Au} = 50$nm. The permittivity of gold is according [22]. The thickness of LC layer is $d=620$ and the tilt angle is $\theta=70^0$.

The spectra for nematic layer (Fig. 2a) at twist angle $\varphi=\pi$ and $\varphi=2\pi$ are the same because the molecule orientations are identical to the lab

coordinate system.
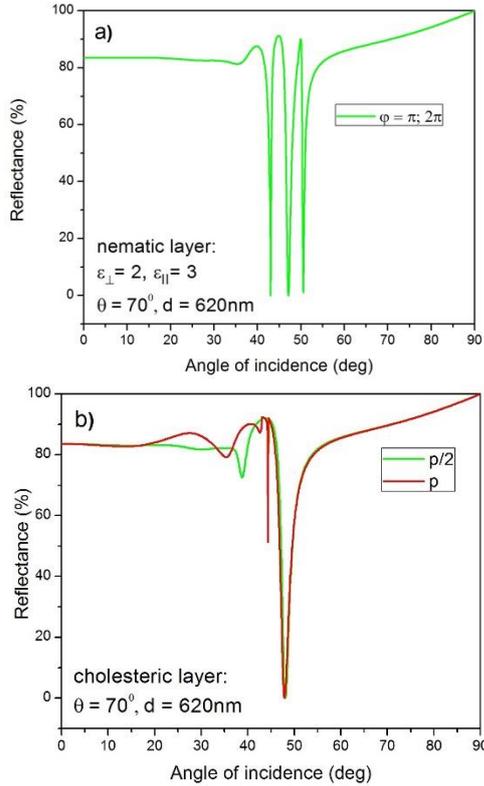
Fig. 2. Reflection spectra of p- polarized light as a function of incident angle for structures with a) nematic and b) cholesteric layer. All other parameters of the structures are identical.

For cholesteric layer (Fig. 3b) calculation are performed for half pitch ($p/2$ - $\phi \in [0, \pi]$) and for one pitch (p - $\phi \in [0, 2\pi]$). The results are compatible with Fig. 2a because the final orientations of molecules are identical. For cholesteric SPP is well observed. The spectra related to the mode excitation are slightly different, in spite the final orientations of molecule are identical, what demonstrate the effect of molecule continuous rotation "seen" by the optical field.

According to our previous results [19] SPP has to be observed in the both structures. It is reasonable to suggest that the guided modes excited in the nematic LC layer mask SPP. Obviously, the conditions for mode excitation in nematic and in cholesteric structures are different. Following the model for the nematic [20] and our model for cholesteric layer expressed by (4), we analyzed the range of incident angle (1). The low limit β_1 is the same for both structures. However, β_2 are different what is shown in Fig.3. The critical angle for nematic structure is close to 52^0 at $\varphi=\pi$ as shown in Fig. 3a. This defines a wide window of incident angles (from 33.8^0 according to (1)) which covers the plasmon resonance angle ($\approx 49^0$). This explains the spectra at Fig. 2a – guided modes are excited and they completely destroy SPP.

Fig. 3. a) Critical angle as a function of twist angle for nematic layer and b) Effective critical angle as a function of twist angle, corresponding to pitch length, for cholesteric layer at different tilt angles.
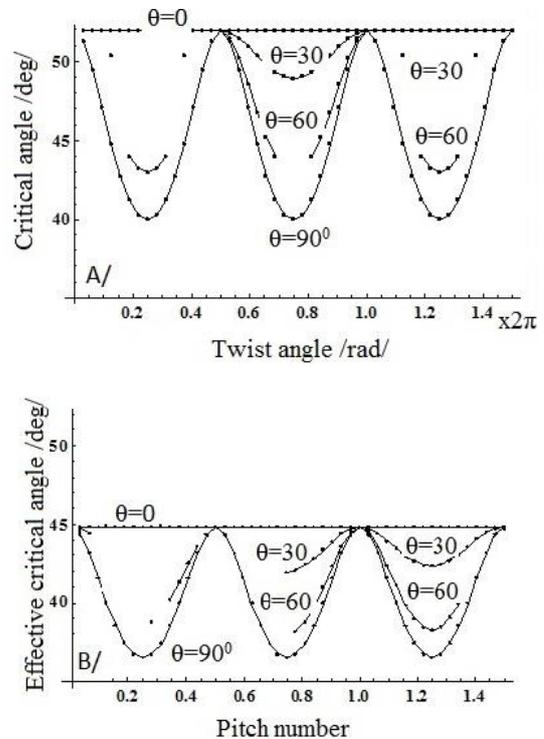
Fig. 4. a) Critical angle as a function of twist angle for different tilt angles for nematic layer; b) Effective critical angles as a function of pitch number for different tilt angles for cholesteric layer.

60

For cholesteric layer (Fig. 3b) the effective critical angle, calculated according (3) with modified denominator (4) does not exists at half pitch *p*/2. Hence, there is not a range of incident angles for which the mode excitation is permitted. That why the effective excitation of SPP is possible as shown in Fig. 2b. Moreover, this result confirms the correctness of our model for cholesteric structure.

Following our model one can expect that at short pitch length the optical field could not be able to follow the chiral stricture. The extraordinary modes will have some average effective n_e and the dependence on twist angle will be blurred. Hence, one can expect that *p* reduction increases the number of critical angles – the chiral structure is not a limiting factor. Indeed, this is the real behavior as illustrated in Fig. 4. Reasonably, the values of critical angles for nematic structure are symmetric against $\varphi=270^0$, as shown in Fig 4a, because the structure is symmetric. For cholesteric LC layer (Fig. 4b) the behavior is absolutely different – the number of effective critical angles increases with pitch number, as expected. It is worthy to note, that the values of effective critical angle for extraordinary modes in chiral structure are lower than the plasmon resonance angle. Hence, the excitation of SPP in CLCL is more effective than in nematic LC. Also, the range of incident angle for which guided mode excitation is permitted, is shorter than in for NLCL.

CONCLUSION

In this paper we study the conditions for guided modes excitation in CLCL and the interaction plasmon/guided modes. For the purpose we introduce a simple but effective extension of the model about guided modes excitation in NLCL. Our model introduces the "effective critical angle" following the physics behind the light propagation in chiral anisotropic medium. The correctness of the model is proved by numerical simulations regarding the mode and SPP excitation in such structures. We show that it is more effective to excite SPP in CLCL. The reported results are for a fixed tilt angle $\theta=70^0$, only. However, our study showed that different guided mode structures and interaction with SPP can be achieved for numerous tilt angles what can be used for exploration of cholesterc liquid-crystal layers parameters.

REFERENCES

1. K. Welford and J. Sambles, *Appl. Phys. Lett.*, **50**, 871 (1987).
2. K. Welford, J. Sambles, and M. Clark, *Liq. Cryst.*, **2**, 91 (1987).
3. S. Elston, J. Sambles, and MClark, *J. Mod. Opt.*, **36**, 1019 (1989).
4. S. Elston and J. Sambles, Jpn. *J. Appl. Phys.*, Part 2 **29**, L641 (1990).
5. F. Yang, L. Ruan, S. Jewell, and J. Sambles, New J. Phys., **9**, 49 (2007).
6. F. Yang, L.. Ruan and J. Sambles, *J. Appl. Phys.* **88**, 6175 (2000).
7. S. Jewell and J. Sambles, *J. Appl. Phys.,* **92,** 19 (2002).
8. S. Jewell and J. Sambles, *Mol. Cryst. Liq. Crys.,* **401,** 181 (2003).
9. F. Yang, L. Ruan, J. Sambles, *Appl. Phys. Lett.*, **92**, 151103 (2008).
10. Z. Jacob and E. Narimanov, *Appl. Phys. Lett.*, **93**, 221109 (2008).
11. X. Wang, P. Wang, J. Chen, Y. Lu, H. Ming, and Q. Zhan, *Appl. Phy Lett.*, **98**, 021113 (2011).
12. Y. Takeichi, Y. Kimoto, M. Fujii, and S. Hayashi, *Phys. Rev. B,* **84**, 085417 (2011).
13. T. Nagaraj and A. A. Krokhin, *Phys. Rev. B,* **81**, 085426 (2010).
14. R. Luo, Y. Gu, X. Li, L. Wang, I. Khoo, Q. Gong, *Appl. Phys. Lett.*, **102**, 011117 (2013).
15. R. Li, C. Cheng, F. Ren, J. Chen, Y. Fan, J. Ding, and H. Wang, *Appl. Phys. Lett.,* **92**, 141115 (2008).
16. Y. Yen, T. Lee, Z. Wu, T. Lin and Y. Hung, *Opt. Express*, **23**, 32377 (2015).
17. G. Dyankov, K. Zhelyazkova, M. Petrov, and B. Katranchev, *Molec. Cryst. Liquid Cryst.,* **632**, 2, (2016).
18. K. Zhelyazkova, M. Petrov, B. Katranchev, and G. Dyankov , *Proc. SPIE* **9447**, 18th International School on Quantum Electronics: Laser Physics and Applications (2015).
19. K. Zhelyazkova, M. Petrov, B. Katranchev, and G. Dyankov, *J. Phys.:Conf. Ser.,* **558,** 012024 (2014).
20. F.Yang and J. Sambles, *JOSA B*, **10**, 858 (1993).
21. D.W.Berreman, *JOSA,* **62**, 502 (1972).
22. P. Johnson and R. Christy, *Phys. Rev. B,* **6**, 4370 (1972).

ВЪЗБУЖДАНЕ НА ПОВЪРХНИНЕН ПЛАЗМОН И НАПРАВЛЯЕМИ МОДИ В СЛОЙ ОТ ХОЛЕСТЕРИЧЕН ТЕЧЕН КРИСТАЛ

К. Желязкова[1], М. Петров[3], Б. Катранчев[3], Г. Дянков[2]

[1]*Физически факултет, Пловдивски университет „П.Хилендарски“, ул. „Цар Асен“ 24, Пловдив*
[2]*Институт по оптични материали и технологии, БАН, ул. „Акад. Г.Бончев“ 108, София*
[3]*Институт по физика на твърдото тяло, БАН, бул. „Цариградско шосе“ 72, София*

(Резюме)

Към момента добре са изучени особеностите на оптичното възбуждане на повърхнинни плазмони и направляеми моди в слой от нематичен течен кристал. Тези особености, обаче, не са изучени за случая на слой от холестеричен течен кристал. Съществуват много проблеми, свързани разпространението на светлина в анизотропна хирална среда, които не са решени, въпреки, че напоследък такива изследвания се провеждат. Целта на тази работа е да се отговори на някои въпроси чрез теоретично изследване. Моделирано е възбуждане на повърхнинен плазмон и направляеми моди в слой от холестиричен кристал при ъгли на падащата светлина, по-големи от ъгъла на пълно вътрешно отражение. Съществуват две съществени различия на структурата, която разглеждаме, от тази с нематичен кристал: 1/ ъгъла на завъртане е функция на дебелина на слоя; 2/ стъпката на хеликса определя до колко светлината с определена дължина на вълната е чувствителна към локалния показател на пречупване на течния кристал. Това предполага, че критичният ъгъл на възбуждане на „необикновените“ моди е различен от същия за нематичен слой. Ние възвеждане понятието „ефективен критичен ъгъл“, дефинирано в термините на дължина на стъпката на хеликса. Този ъгъл описва много добре зависимостта на броя на възбудените моди от ъгъла на наклона на молекулите и от стъпката на хеликса.

Study of thermal expansion in a joint material by optical Hilbert transform method for phase analysis based on orthogonal linear polarization phase shifting

V. D. Madjarova[1]*, H. Kadono[2]

[1]*Institute for Optical Materials and Technologies "Acad. J. Malinowski", Bulgarian Academy of Sciences, "Acad. G. Bonchev" str. Bl. 109, 1113 Sofia, Bulgaria*
[2] *Graduate School of Science and Engineering, Saitama University, 255 Shimo-okubo, Saitama-shi, Saitama-ken, 338-0825, Japan,*

We study thermal expansion in a joint material (ceramic-copper-steel) by optical interferometry with spatial phase shifting. The method for quantitative phase analysis is based on optical Hilbert transform (HT) method. It uses both temporal and spatial interference signal, where HT is carried out optically by separation of orthogonal components of polarized light via Wollaston prism. The phase is obtained from the cosine and sine interference patterns that are recorded simultaneously in one frame. Volume data representing the temporal development of 2D deformation field were obtained. The accuracy of the method was estimated to $\lambda/10$.

Keywords: spatial phase shifting, phase analysis, thermal expansion, joint material

INTRODUCTION

In many structural components ceramic–metal joint materials are used. Such joint materials are subjected to different mechanical stresses due to the difference in thermal expansion coefficients and elastic modules, which can lead to fracture of the material. Therefore the studies of the deformation of the joint materials under thermal loading are of great interest in experimental mechanics. Optical interferometry as a method that provides high spatial and temporal resolution is an ideal one for *in-situ* measurement of dynamic events [1]. To obtain the deformation field, in optical interferometry it is necessary to analyze the phase distribution. Currently there exist numerous methods that mainly include Fourier transform for fringe demodulation, phase shifting and Wavelet transforms [2]. For dynamic event analysis of special interest are the spatial phase shifting methods, because the phase shift is carried out in one frame. Recently, several methods for spatial phase shifting have been proposed [1-11] that can be used for studying both static and dynamic events. Generally they use either diffractive element or a polarizing element to perform the spatial phase shifting, where in one frame two, three or four phase shifted images are recorded. In all these methods, however, some additional technique is required to estimate the bias intensity. Moreover, the unwrapping of the phase is performed in space domain, which is not always a trivial task, especially in speckle metrology and in circularly distributed fringe patterns, for example. In this study we propose a method that combines both time and space domain to obtain the phase distribution and does not require capturing of additional reference images. To obtain the bias intensity we use temporal averaging of the interference signal. The unwrapping of the phase is also performed in time domain, which makes the method entirely automatic and straightforward. The spatial phase shifting is carried out with Wollaston prism where the orthogonal components of polarized light are separated spatially and recorded in one frame. Since in one frame we capture both sine and cosine functions, we call this optical Hilbert transform. We implemented the method for studying temporal development of deformation field in joint material (ceramic-cupper-stainless steel) due to thermal expansion.

EXPERIMENTAL

In the experiment, a Michelson interferometer was constructed with light source SHG-YAG laser at wavelength of 532 nm. The schematic of the setup is shown on Fig. 1. Linearly polarized light from the laser passes through a quarter-wave plate

* To whom all correspondence should be sent:
E-mail: madjarova@iomt.bas.bg

(QWP) and is converted into circularly polarized light. The light beam is equally split into a reference and a sample beams by a non-polarizing beam splitter (NPBS). The circularly polarized light is incident to the sample. A polarizer at +45° with respect to the horizontal direction is introduced in the reference arm that converts the circularly polarized light into linearly polarized one.
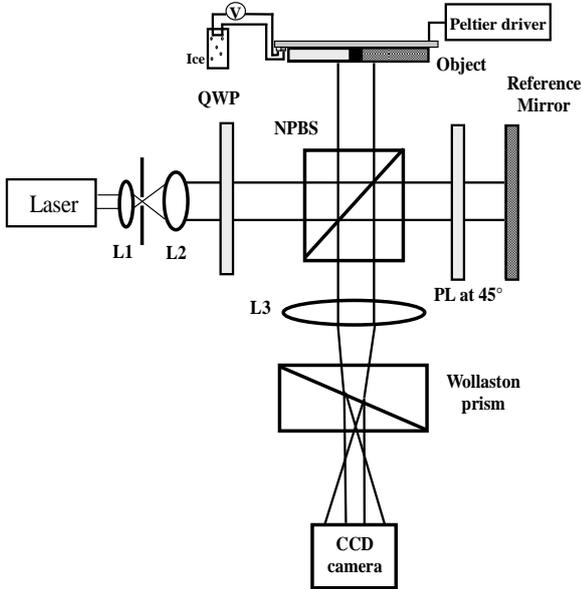
Fig. 1. Michelson type interferometer for spatial phase shifting. L1-L3 lenses; PL – polarizer; NPBS – Non polarizing beam splitter; QWP – quarter wave plate.

The reference and sample beams are recombined at the NPBS where there is a $\pi/2$ phase difference between the horizontal and the vertical component. The two orthogonal components, which represent the sine and cosine interference patterns, are spatially separated by Wollaston prism. They are captured in one single frame with CCD camera (Sony XCL-U1000) with resolution of 1200x1600 pixels and acquisition rate of 15 frames/s. Fig. 2 illustrates one frame of spatially shifted sine and cosine fringe patterns. The imaged part of the specimen is 3 mm by 6 mm.
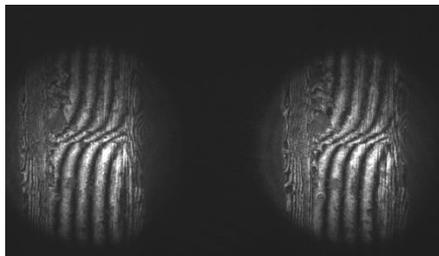
Fig. 2. Spatially shifted patterns, imaged on the CCD camera plane.

The mathematical expressions for interference patter have been previous presented in our work

[12]. They were obtained using Jones matrices formalism. Here we present only the expressions for the sine (Eq. 1) and cosine (Eq. 2) functions, and the estimated phase (Eq. 3):

$$I_{si}(x,y,t) = I_{bias}(x,y) + I_m(x,y)sin\left(\Delta\varphi(x,y,t) - \frac{\pi}{4}\right) \quad (1)$$

$$I_{co}(x,y,t) = I_{bias}(x,y) - I_m(x,y)cos\left(\Delta\varphi(x,y,t) - \frac{\pi}{4}\right) \quad (2)$$

where $I_{bias}(x,y), I_m(x,y)$ and $\Delta\varphi(x,y,t)$ are the bias intensity, modulation intensity and the phase difference between the reference and object fields, respectively. The bias intensity and the modulation intensities in general do not vary considerably in time, especially in short time span, which allows us to obtain them by applying some signal processing method in time domain. In our experiment the sine $I_{si}(x,y,t)$ and cosine $I_{cos}(x,y,t)$ fringe patterns are captured continuously and we can obtain $I_{bias}(x,y)$ by averaging the frames in time over the whole acquisition interval. The obtained $I_{bias}(x,y)$ image is binarized and then used to determine the identical points on each sine and cosine patterns. This procedure is critical to the correct calculation of the phase value. The translation vector of sine image towards cosine is determined by using the autocorrelation function of the binarized image and used to adjust positions of sine and cosine images. After subtracting the bias intensity, translating the sine image to overlap the cosine image, the phase can be obtained as follow:

$$\Delta\varphi(x,y,t) - \pi/4 = tan^{-1}\left(\frac{I_{si}(x,y,t)-I_{bias}(x,y)}{I_{bias}(x,y)-I_{co}(x,y,t)}\right) \quad (3)$$

The phase is then unwrapped in time domain, where each point is unwrapped independently, converted into deformation field and filtered in space domain with median filter to remove the spiky noise. The two-dimensional distribution of the deformation field yielded in this manner can be followed in time, since it is obtained for each point in time.

RESULTS AND DISCUSSIONS

In this experiment we use joint material Ceramic-Copper-Stainless Steel illustrated in Fig. 3.
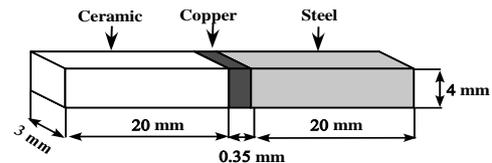
Fig. 3. Schematics of the joint material

The linear thermal expansion coefficients as follows: ceramic (Si_3N_4) - $3 \times 10^{-6}/K$; copper - $17.7 \times 10^{-6}/K$ and stainless steel - $15 \times 10^{-6}/K$.

The joint material was heated from 33 ^{0}C to 51 ^{0}C and then cooled from 60 ^{0}C to 46 ^{0}C using a Peltier device. During the heating frames were captured, until temperature reaches predetermined value. The same was performed when the sample was cooled. The temperature of the Peltier device was monitored with thermocouple. These data were used to stop the acquisition of the frames when no change in the temperature was monitored. Fig. 4 shows the temporal change in the temperature, compared with the temporal change in the deformation at one point. It demonstrates clearly that the deformation growth follows nearly the same slope as the temperature change slope.
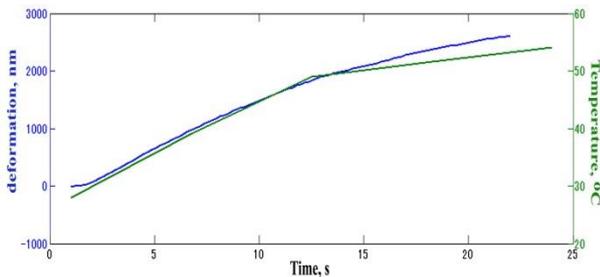
Fig. 4. Comparison between the temperature growth and the deformation growth at given point of the deformation field.

Fig. 5 shows two-dimensional distribution of the deformation field due to temperature change from 33 °C to 51 °C. The step-like change that occurs due to considerable difference in the linear thermal expansion coefficients can clearly be seen. There are several areas with remaining spikes, where the phase was not correctly determined. The incorrect determination of the phase is mainly due to incorrect overlapping of the sine and cosine images and the presence of high level of noise.
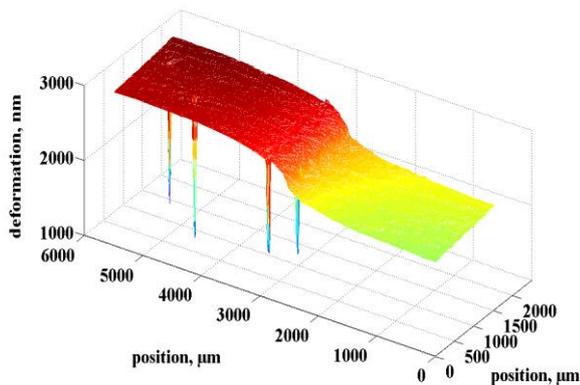
Fig. 5. Two dimensional distribution of the deformation filed due to temperature change from 32 °C to 50 °C.

We examine the difference between the deformation in the steel and in the ceramics.

Theoretically it has to be 864 nm and we estimated it experimentally to be 811 nm. The deviation of $\lambda/10$ from the theoretical value accounts for the imperfection in the polarisation elements, the presence of noise, the expansion of materials along other directions, the uneven surface of Peltier device, and the incorrect superposition of the sine and cosine fringes. The method is especially sensitive to incorrect superposition and can be improved by the improving the autocorrelation algorithm.
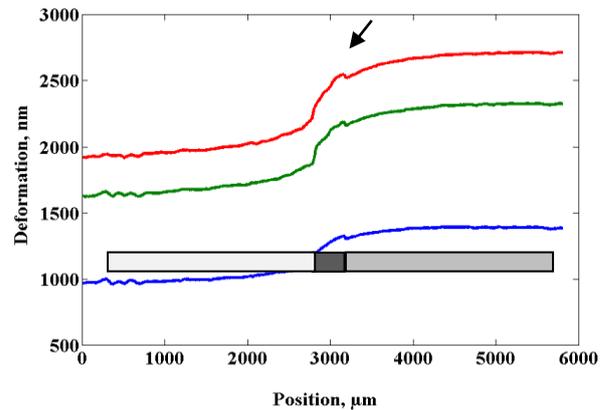
Fig. 6. Cross-sections of deformation at different moments of thermal load at 40 ^{0}C – blue line, 48 ^{0}C – green line and 51 ^{0}C – red line.

In Fig. 6 we demonstrate cross-sections along ceramic-copper-steel at different moments of thermal load (40 ^{0}C, 48 ^{0}C and 51 ^{0}C). The step-like distribution of deformation can clearly be seen. It can be noticed also a slight dent (indicated by arrow in Fig. 6) in the curve corresponding to the joint between the copper and steel and caused by the slight difference in their thermal expansion coefficients.

CONCLUSIONS

In this paper we presented spatial phase shifting method based on the separation of orthogonal components of polarized light via Wollaston prism. The phase analysis method is performed in both space and time domain. The method was applied for studying thermal expansion of joint material. We demonstrated two dimensional step-like distribution of the deformation field that is due to considerable difference in the thermal expansion coefficients of ceramic and steel. The temporal change of deformation for different thermal loads was also demonstrated. The method achieved $\lambda/10$ accuracy that can be improved further by applying a more sophisticated algorithm for superposition of sine and cosine patterns.

REFERENCES

1. R. S. Sirohi, Optical methods of measurement. Wholefield techniques, CRC Press, Boca Raton, 2009.
2. P. Rastogi, E. Hack (eds), Phase estimation in optical interferometry, CRC Press, Boca Raton, 2015.
A. Hettwer, J. Kranz, J. Schwider, Opt. Eng., **39**, 960 (2000).
3. J. A. Ferrari, E. M. Frins, Opt. Comm., **279**, 235 (2007).
4. T. Kiire, S. Nakadate, M. Shibuya, Appl. Opt., **47**, 4787 (2008).
5. N.T. Shacked, M. T. Rinehart, A. Wax, Opt. Lett., **34**, 767 (2009).
6. N.T. Shacked, T. M. Newpher, M. D. Ehlers, A. Wax, Appl. Opt., **49**, 2872 (2010).
7. J. Min, B. Yao, P. Gao, R. Guo, J. Zheng, T. Ye, Appl. Opt., **49**, 6612 (2010).
8. R. Guo, B. Yao, P. Gao, J. Min, J. Han, X. Yu, M. Lei, Sh. Yan, Y. Yang, D. Dan, T. Ye, Appl. Opt., **52**, 3484 (2013).
9. H. Bai, M. Shan, Z. Zhong, L. Guo, Y. Zhang, Appl. Opt., **54**, 9513 (2015).
10. V. H. F. Munoz, N. I. T. Arellano, D. I. S. Garcia, A. M. Garcia, G. R. Zurita, L. G. Lechuga, Appl. Opt., **55**, 4047 (2016).
11. V. D. Madjarova, H. Kadono, N. Kurita, in: Fringe 2009, Springer-Verlag (2009) W. Osten, M. Kujawinska (eds), Springer-Verlag Berlin, 2009, p. 132.

ИЗСЛЕДВАНЕ НА ТЕРМИЧНО РАЗШИРЕНИЕ НА СЪСТАВЕН МАТЕРИАЛ ЧРЕЗ ОПТИЧНА ХИЛБЕРТ ТРАНСФОРМАЦИЯ ЗА АНАЛИЗ НА ФАЗАТА, ОСНОВАНА НА ФАЗОВО ОТМЕСТВАНЕ НА ОРТОГОНАЛНО ЛИНЕЙНО ПОЛЯРИЗИРАНА СВЕТЛИНА

В. Д. Маджарова[1], Х. Кадоно[2]

[1]Институт по оптически материали и технологии "Акад. Й. Малиновски", Българска Академия на науките, ул. "Акад. Г. Бончев", бл. 109, 1113 София, България

Факултет по приложни и технически науки, Университет Саитама,

255 Шимо-окубо, Саитама-ши, Саитама-кен, 338-0825, Япония

(Резюме)

Изследвано е термичното разширение при съставен материал (керамика-мед-стомана) с помощта на оптична интерферометрия с пространствено отместване на фазата. Методът за количествен анализ на фазата се основава на оптична Хилберт трансформация (ХТ). Той използва както времевия, така и пространствения интерференчен сигнал, където ХТ се извършва оптично чрез разделяне в пространството на ортогонално поляризираните компоненти на поляризираната светлина с помощта на призма на Уоластън. Фазата е получена от cosine и sine интерференчни ивици, записани едновременно в един кадър. Получени са обемни данни, които дават времевата промяна на 2D полето на деформация. Точността на определяне на деформацията е оценена на $\lambda/10$.

Characterization of photoinduced periodic microstructures by digital in-line holographic microscopy

I. T. Peruhov and E. M. Mihaylova*

Department of Mathematics, Informatics and Physics, Agricultural University Plovdiv, Bulgaria,

Digital in-line holographic microscopy (DIHM) was used for the first time for visualization and characterization of periodic microstructures in photopolymers. The method provides virtual focusing throughout the depth of the sample from a single hologram and quantitative information about the intensity and phase distribution can be obtained.

A digital in-line holographic microscope, developed at the Agricultural University Plovdiv, was used for characterization of periodic microstructures photoinduced in Bayfol HX200 photopolymer. Intensity and phase images of a photopolymer diffraction grating have been digitally reconstructed. DIHM proves to be an efficient new approach for visualizing periodic microstructures in holographic photopolymers.

Keywords: digital in-line holographic microscopy, photoinduced periodic microstructures, diffraction gratings, photopolymer

INTRODUCTION

Digital in-line holographic microscopy (DIHM) is a relatively new microscopic technique showing distinctive advantages over conventional microscopy. Unlike conventional light microscopy, in-line holographic microscopy proposed by Gabor [1] can give visual information about an object not only in the focal plane. It has the ability to acquire holograms fast and reliably and to extract the amplitude and phase of the optical field simultaneously. As the hologram is recorded digitally one can afterwards apply different image processing methods in order to extract information at will.

In contrast to off-axis setups, the in-line setup is less sensitive to vibrations because it does not involve beam splitters, mirrors or lenses. This imaging technique is also called "lensless imaging" [2, 3, 4], as it involves no lens between the object and the sensor.

Digital in-line microscopy is very suitable for investigating transparent objects. Separate images corresponding to different focal planes can be calculated from the hologram without time consuming mechanical scanning used in conventional microscopy. One can extract both amplitude and phase information by holography. It is possible to reconstruct a 3D image or a stack of 2D images.

Photopolymers are extensively studied advanced materials for holographic recording. The visualization of photoinduced periodic microstructures in photopolymers is necessary for their full characterization [5, 6]. Babeva et al. [5] employed White Light Interferometry (WLI) to visualize the formation of surface relief profile in photopolymerisable systems, when illuminated with a focused beam of light. Trainer et al. [6] used Atomic Force Microscopy (AFM) to scan the photopolymer layers immediately after holographic exposure in order to visualize the surface relief periodical profile.

Both of the methods described above are suitable only for visualization and characterization of the surface profile of periodic microstructures. Another common feature of the WLI profilers and AFM is the necessity of multiple scans, of the surface under investigation, in order to visualize its profile. We suggest an application of digital holographic microscopy as a quick and inexpensive, but very sensitive method to directly observe and characterize the periodic microstructures inscribed in a holographic photopolymer.

We used successfully digital in-line holographic microscopy for the first time to visualize in depth the intensity and phase modulation in volume diffraction gratings (VHGs).

*To whom all correspondence should be sent:
E-mail: emmihaylova@gmail.com

EXPERIMENTAL SET-UP

The DIHM presented in this paper was developed at the Agricultural University of Plovdiv. The light source is a diode laser (Lasiris) with wavelength of 673.2 nm and output of 6.98 mW. The intensity of the illumination, focused onto pinhole is controlled via a polarizer (Fig. 1). The spherical wave emerging from the pinhole illuminates the object. The perturbed by the object and the unperturbed wave interfere and are recorded as a hologram on a CCD sensor and stored in a computer. The monochrome camera WAT-902DM with resolution: 570TVL, effective pixels 768(H) x 494(V) and unit cell size 6.35 μm(H) x 7.4 μm(V) is used in the DIHM set-up.

The intensity and the phase of the object are reconstructed by numerical computer calculations [7].
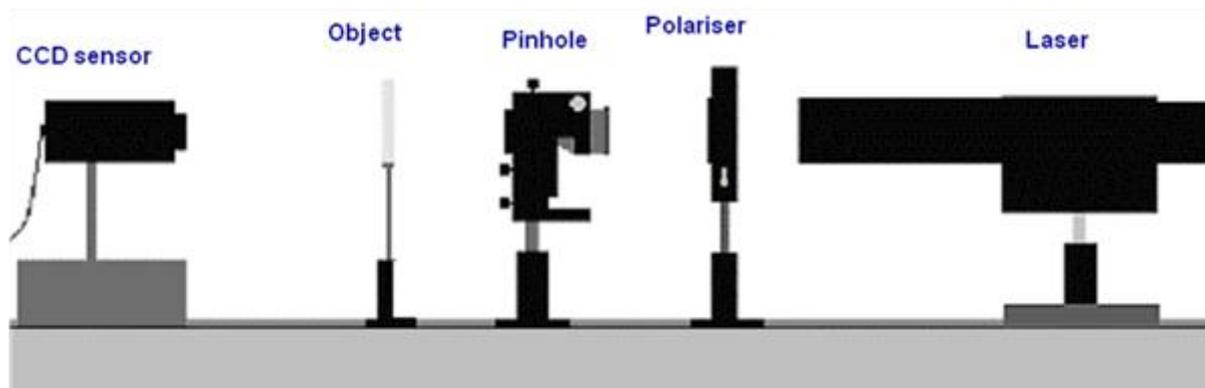
Fig. 1. Optical set-up of the digital in-line holographic microscope.

RESULTS AND DISCUSSIONS

A two-beam holographic optical set-up was used to record un-slanted transmission gratings using a 532 nm diode laser. Diffraction gratings were recorded in Bayfol HX200 photopolymer layers at a spatial frequencies of 100 l/mm. Bayfol HX200 is a light-sensitive, self-developing photopolymer film which can be used to produce phase holograms in the form of volume reflection and volume transmission holograms. Bayfol HX200 can be recorded with appropriate laser light within the visible spectral wavelength range from 440 nm to 671 nm. For hologram formation no further post-treatment is necessary, e.g. neither wet nor thermal treatment. The photopolymer can be used for recording of a variety of types of volume holograms.

Digital in-line holographic microscopy was employed to visualize the microstructure of the diffraction gratings. The diffraction gratings were positioned at a distance of 23.8 cm to the CCD sensor and 3.2 cm to the pinhole of the spatial filter.

Figures 2 – 4 show the experimental results for the visualisation of a diffraction grating by DIHM. Both the reconstructed intensity and the reconstructed phase give reliable information about the spatial frequency of the grating. The structure of the grating was investigated in depth. The reconstruction of the hologram was performed numerically at steps of 2 μm inside the photopolymer layer. It is clearly shown that the digital in-line holographic microscopy can be easily applied for in depth characterization of periodic microstructures photoinduced in holographic photopolymers.
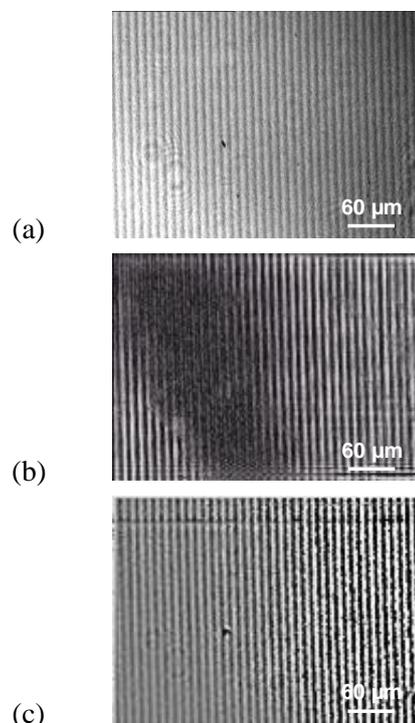
Fig. 2. Images of diffraction grating with spatial frequency of 100 lines/mm recorded in Bayfol HX200 photopolymer: a) a digital hologram; b) reconstructed intensity on the surface of the photopolymer layer; c)

reconstructed phase on the surface of the photopolymer layer.

(a)

(b)

(c)
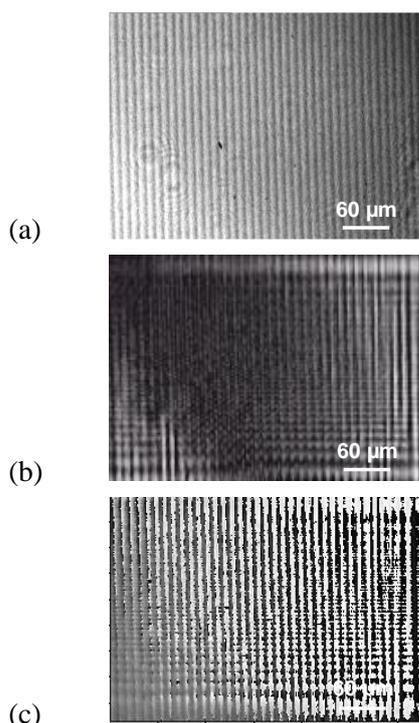
Fig. 3. Images of diffraction grating with spatial frequency of 100 lines/mm recorded in Bayfol HX200 photopolymer: a) a digital hologram; b) reconstructed intensity at 2 μm depth inside the photopolymer layer; c) reconstructed phase at 2 μm depth inside the photopolymer layer.

(a)

(b)

(c)
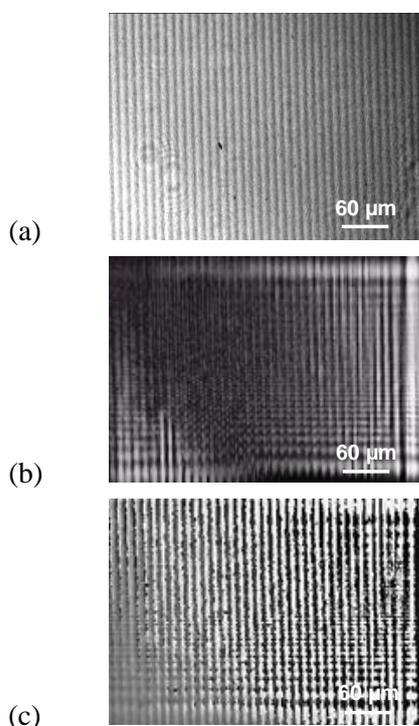
Fig. 4. Images of a diffraction grating with spatial frequency of 100 lines/mm recorded in Bayfol HX Photopolymer: a) a digital hologram; b) reconstructed

intensity at 4 μm depth inside photopolymer layer; c) reconstructed phase at 4 μm depth inside the photopolymer layer.

CONCLUSIONS

Digital in-line holographic microscopy was successfully used for in depth characterization of periodic microstructures photoinduced in Bayfol HX200 photopolymer. It was demonstrated that digital in-line holographic microscopy can be used to visualize photoinduced periodic microstructures, recorded in holographic photopolymers.

Unlike conventional light microscopy, the method of in-line holographic microscopy proposed here provides virtual focusing throughout the depth of the diffraction grating by the use of a single hologram.

Both the reconstructed intensity and the reconstructed phase give reliable information about the spatial frequency of the grating.

It is clearly shown that the digital in-line holographic microscopy can be easily applied for in depth characterization of periodic microstructures photoinduced in holographic photopolymers.

DIHM proved to be an attractive novel tool for in-depth investigation of volume holographic gratings (VHGs), which have been intensively developed for applications such as data storage, optical correlators, optical information encryption, fiber optic communication and spectroscopy.

REFERENCES

1. D. Gabor, *Nature*, **161**, 777 (1948).
2. L. Repetto, E. Piano, and C. Pontiggia, *Optics Letters*, **29**, 1132 (2004).
3. C. P. Allier, G. Hiernard, V. Poher, and J. M. Dinten, *Biomed. Opt. Express,* **1,** 762 (2010).
4. J. R. Fienup, *OSA Technical Digest,* IMD2 (2010).
5. K. Trainer, K. et al., *Conf. Proc. of the Intern. Commission for Optics Topical Meeting on Emerging Trends and Novel Materials in Photonics,* **1288**, 184 (2009).
6. T. Babeva, D. Mackey, I. Naydenova, S. Martin, V. Toal, *Conf. Proc. of the Intern. Commission for Optics Topical meeting on Emerging trends and novel materials inphotonics,* **1288**, 43 (2009).
7. M. Seifi, C. Fournier, L. Denis, HoloRec3D (2012).

ХАРАКТЕРИЗИРАНЕ НА ФОТОИНДУЦИРАНИ ПЕРИОДИЧНИ МИКРОСТРУКТУРИ ЧРЕЗ ЦИФРОВА ЛИНЕЙНА ХОЛОГРАФСКА МИКРОСКОПИЯ

И. Т. Перухов и Е. М. Михайлова

Катедра „Математика, информатика и физика", Аграрен Университет Пловдив, България

(Резюме)

За първи път използваме цифрова линейна холографска микроскопия (ЦЛХМ) за визуализиране и характеризиране на периодични микроструктури във фотополимери. Предложеният метод позволява виртуално фокусиране в дълбочина на образеца от една единствена холограма и получаването на количествена информация за разпределението на интензитета и фазата.

Цифров линеен холографски микроскоп, разработен в Аграрен Университет Пловдив, е използван за характеризиране на периодични микроструктури, фотоиндуцирани във фотополимер Bayfol HX200. Образи на интензитета и фазата на дифракционни решетки са реконструирани числово. Показано е, че ЦЛХМ е ефикасен нов метод за визуализация на фотоиндуцирани периодични микроструктури във фотополимери.

In-depth visualisation of Triglycine-Sulfate's domain structure

I. T. Peruhov and E. M. Mihaylova*

Department of Mathematics, Informatics and Physics
Agricultural University Plovdiv, Bulgaria

The domain structure is an important characteristic of ferroelectrics. One of the most intensively studied ferroelectrics is triglycine sulfate (TGS). Although many methods have been developed for the observation of the domain structure in TGS, it still cannot be visualized routinely.

We suggest a new method for observation of the domains in TGS, in particular digital in-line holographic microscopy. A big advantage of the new method is its ability to extract information about the change of the domain structure in depth from one digital hologram only.

The domain structure of TGS monocrystals doped with Yb was visualized by digital holographic microscopy for the first time.

Keywords: digital in-line holographic microscopy, DIHM, Triglycine sulfate, TGS, domain structure, Yb

INTRODUCTION

Triglycine sulfate $(NH_2CH_2COOH)H_2SO_4$ (TGS) is one of the most intensively investigated ferroelectrics because of its excellent ferroelectric and pyroelectric properties. Single crystals of TGS are considered to be the most suitable material for developing pyroelectric infrared sensors [1-3]. Hoshino et al. [4] described in detail the crystal structure of pure TGS. An extensive list of related references is given by Nakatani [5].

The basic principle of holography was introduced by Gabor [6], who invented the in-line holography. The new principle was used soon afterwards with visible light [7]. Its power has been revealed after discovery of the laser, which delivered much higher contrast in the holograms, and later with the implementation of the CCD camera as a recording device. This type of holography, which uses CCD (or CMOS) camera to record a hologram, is called digital in-line holography.

Digital in-line holographic microscopy (DIHM) is a relatively new microscopic technique showing many advantages over conventional microscopy. Digital holography is a non – destructive, marker – free imaging method offering a full field of view. Unlike conventional light microscopy, in-line holographic microscopy can give visual information about an object not only in the focal plane. From the captured hologram the real image is reconstructed by means of numerical deconvolution. The method provides virtual focusing throughout the depth of the sample from a single hologram as quantitative information about the intensity and the phase distribution.

The advantages of digital holographic microscopy listed above encouraged the authors to investigate its suitability for observation of ferroelectrics domains in TGS.

The present methods to observe the domain structure of ferroelectrics are not easily applied. As a common feature they need preliminary preparations of the object and the observing system and are generally expensive. We suggest an application of digital holographic microscopy as a quick and inexpensive, but very sensitive method to directly observe the ferroelectrics domains and determine their dimensions.

Digital in-line holographic microscopy (DIHM) was used for characterization of domain structure of TGS doped with Yb.

EXPERIMENTAL

A digital in-line holographic microscope (DIHM) was developed at the Agricultural University of Plovdiv. The light source is a diode laser (Lasiris) with wavelength of 673.2nm and

---

*To whom all correspondence should be sent:
E-mail: emmihaylova@gmail.com
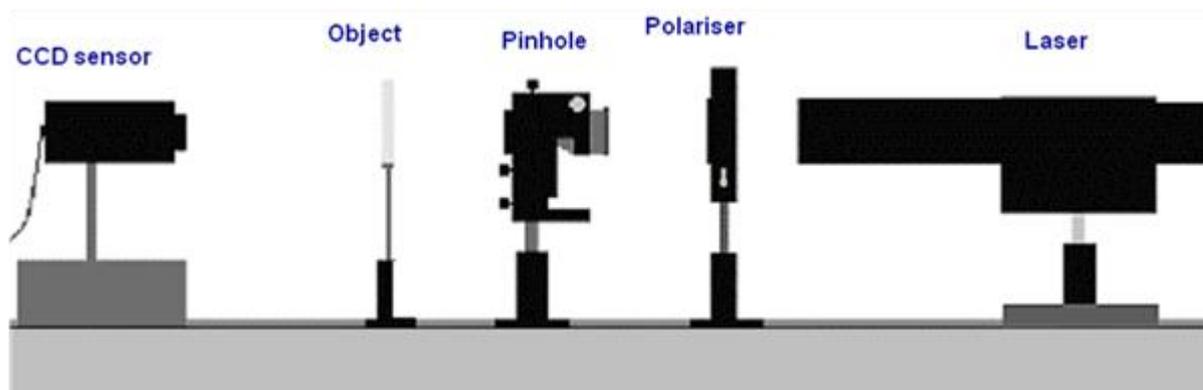
Fig. 1. Optical set-up of the digital in-line holographic microscope

output of 6.98 mW. The intensity of the illumination, focused onto pinhole is controlled via a polarizer (Fig. 1).

The spherical wave emerging from the pinhole illuminates the object. The perturbed by the object and the unperturbed wave interfere and are recorded as a hologram on a CCD sensor and stored in a computer. The intensity and the phase of the object are reconstructed by numerical computer calculations using the back light propagation method of HoloRec3D: A free Matlab toolbox for digital holography [8].

TGS single crystals, doped with Yb, were grown by the dynamical method in the ferroelectric phase [9]. All samples used in these experiments were grown from aqueous solution. The dopant salt was in the form of sulfate. The concentration of $Yb_2(SO_4)_3$ in the solution was 1 % and 4 % for the different monocrystals. The crystals of TGS show a clear cleavage plane perpendicular to its ferroelectric axis.

The samples for the present investigations were plates, cleaved perpendicular to the polar axis [010] from clear regions far from the seeding area. The principal optical axis X coincides with the polar crystal axis. According to the notation of Damen et al. [10] our experiments were performed in the x(yy) geometry.

RESULTS AND DISCUSSIONS

We report four examples of application of the DIHM for TGS's domain structure investigation. The four holograms and their amplitude reconstructions are given in Figs. 2 - 5. Figs. 2 – 3 show results for two different samples of TGS monocrystal, doped with 1% Yb in the solution of growth, while Figs. 4 – 5 show results for two samples of TGS monocrystal, doped with 4% Yb in the solution of growth.
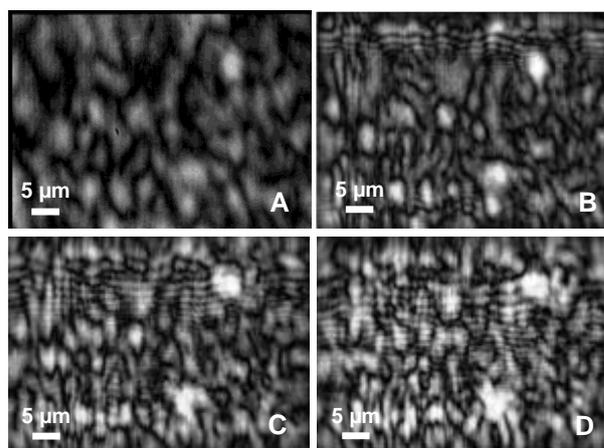
Fig. 2. A – a digital hologram of TGS monocrystal, doped with 1% Yb in the solution of growth; B – reconstruction of the intensity of hologram 2A on the surface of the sample, C - reconstruction of the intensity of the hologram 2A at 1 μm depth inside the TGS sample and D - reconstruction of the intensity of the hologram 2A at 2 μm depth inside the TGS sample.
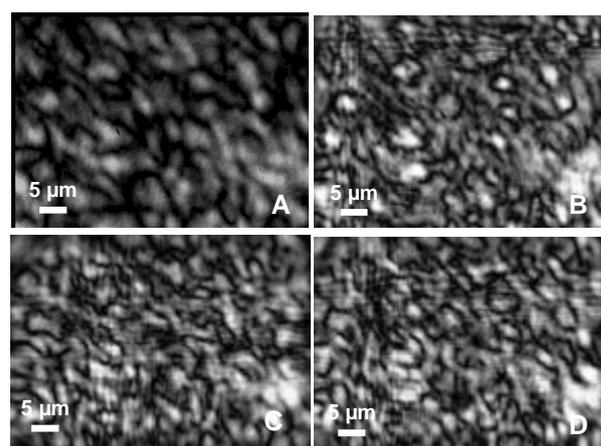
Fig. 3. A – a digital hologram of TGS monocrystal, doped with 1% Yb in the solution of growth; B – reconstruction of the intensity of hologram 3A on the surface of the sample, C - reconstruction of the intensity of the hologram 3A at 1 μm depth inside the TGS sample and D - reconstruction of the intensity of the hologram 3A at 2 μm depth inside the TGS sample.

It is important to note that using samples in the form of plates with thickness of 1 mm, cleaved perpendicular to the polar axis [010] of the monocrystal, we should observe the cross-sections of the domains in the TGS material. It is known that the domains in TGS are parallel to its ferroelectric axis [11].
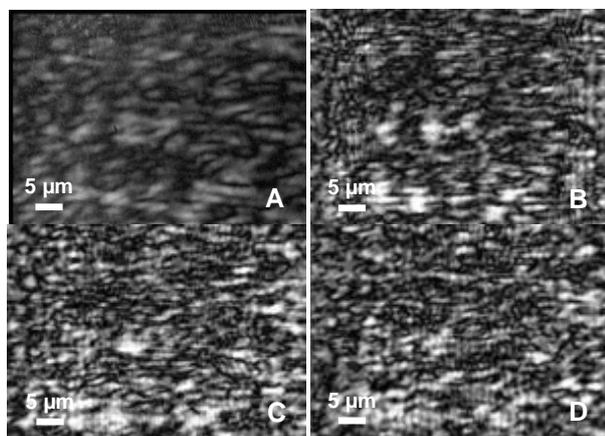
Fig. 4. A – a digital hologram of TGS monocrystal, doped with 4% Yb in the solution of growth; B – reconstruction of the intensity of hologram 4A on the surface of the sample, C - reconstruction of the intensity of the hologram 4A at 1 μm depth inside the TGS sample and D - reconstruction of the intensity of the hologram 4A at 2 μm depth inside the TGS sample.
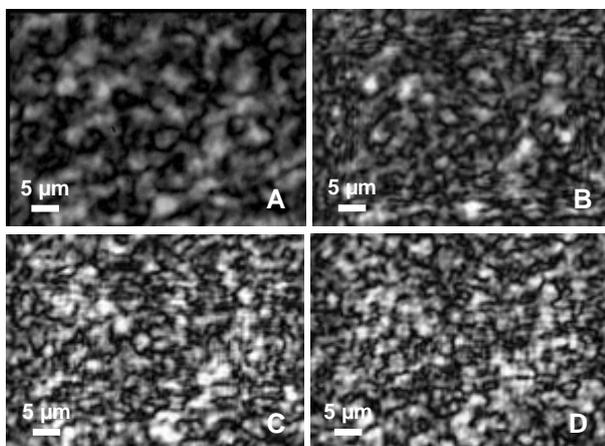
Fig. 5. A – a digital hologram of TGS monocrystal, doped with 4% Yb in the solution of growth; B – reconstruction of the intensity of hologram 5A on the surface of the sample, C - reconstruction of the intensity of the hologram 5A at 1 μm depth inside the TGS sample and D - reconstruction of the intensity of the hologram 5A at 2 μm depth inside the TGS sample.

Figs. 2 – 5 show that the diameters of the single domains (cross sections) in TGS monocrystals doped with Yb vary between 2 μm and 4 μm for the thickness of the cross section and between 3 μm and 7 μm for the length of the cross section. It was established that the domains became thinner and longer with increasing the concentration of the dopant.

CONCLUSIONS

The domain structure of TGS doped with Yb was visualised by digital in-line holographic microscopy for the first time. The DIHM was employed without any preliminary preparation of the triglycine sulfate samples. It was established that the diameters of the single domains (cross sections) in TGS monocrystals doped with Yb vary between 2 μm and 4 μm for the thickness of the cross section and between 3 μm and 7 μm for the length of the cross section. It was established that the size of the domains changes with increasing the concentration of the dopant – they became thinner and longer.

The DIHM was successfully used for observation of the TGS domains in depth. The digital virtual focusing inside the TGS crystals doped with Yb show the same dimensions for the ferroelectric domains as observed on the top surface of the samples.

We conclude that DIHM is a promising novel technique for domain visualisation and can be easily used for structural studies in all transparent ferroelectrics.

REFERENCES

1. F. Schwarz, R. Poole, *Appl. Opt.*, **9**, 1940 (1970).
2. E. H. Putley, in: Semicond. Semimetals, Vol. 5, Academic, New York, 1970, p.259.
3. Y.H. Xu, Ferroelectric and Piezoelectric Materials, Science Press, Beijing, 1978, p.332.
4. S. Hoshino, Y. Okaya, R. Pepinsky, *Phys. Rev.*, **115**, 323 (1959).
5. N. Nakatani, *Ferroelectrics*, **412**, 238 (2011).
6. D. Gabor, *Nature*, **161**, 777 (1948).
7. G. L. Rogers, in: Experiments in diffraction microscopy, Proc. Roy. Soc., Edinburgh, 63A, 1952, p.193.
8. M. Seifi, C. Fournier, L. Denis, HoloRec3D, 2012.
9. J. Novotny, F. Moravec, *J. Cryst. Growth*, **11**, 329 (1971).
10. T. Damen, S. Porto, B. Tell, *Phys. Rev.*, **142**, 570 (1960).
11. E. Mihaylova, PhD Thesis, Plovdiv University, Plovdiv (2000).

ВИЗУАЛИЗАЦИЯ НА ДОМЕННАТА СТРУКТУРА НА ТРИГЛИЦИНСУЛФАТ В ДЪЛБОЧИНА

И. Перухов и Е. Михайлова

Катедра „Математика, информатика и физика", Аграрен Университет Пловдив, България

(Резюме)

Доменната структура е важна характеристика на сегнетоелектриците. Един от най-интензивно изучаваните сегнетоелектрици е триглицинсулфата (ТГС). Въпреки, че много методи са разработени за наблюдаване на доменната структура в ТГС, тя все още не може лесно да бъде визуализирана. Ние предлагаме нов метод за наблюдение на доменната структура в ТГС, по-точно цифрова линейна холографска микроскопия. Голямо предимство на новия метод е възможността да се извлича информация за промяната на доменната структура в дълбочина само от една цифрова холограма. За първи път доменната структура на монокристали от ТГС легирани с Yb е визуализирана с цифрова холографска микроскопия.

Photoinduced birefringence in thin azopolymer films recorded at different temperatures

D. Nazarova[1,*], G. Mateev[1], D. Ivanov[1], B. Blagoeva[1], D. Kostadinova[1], E. Stoykova[1] and L. Nedelchev[1,2]

[1]*Institute for Optical Materials and Technologies "Acad. J. Malinowski", Bulgarian Academy of Sciences, "Acad. G. Bonchev" str. Bl. 109, 1113 Sofia, Bulgaria*
[2]*University of Telecommunications and Post, Acad. St. Mladenov 1 Str., Sofia 1700, Bulgaria*

In this work we investigate the dependence of characteristics of polarization recording and erasure in thin azopolymer films on the starting temperatures of the sample. Polarized light from DPSS laser with wavelength 444 nm is used for recording of photoinduced birefringence. For erasing the records, thermal method is applied. Birefringence is successfully recorded at different starting temperatures from 25 to 100°C. 3D graphics for visualization of the experimental data are presented. Photoinduced birefringence is calculated from real time monitored Stocks parameters during the entire experiment. This investigation allows us to determine the optimal conditions of recording at elevated temperatures in order to achieve shortest response time or maximal birefringence.

Keywords: Azopolymers; Temperature dependence of photoinduced birefringence; Polarization recording.

INTRODUCTION

In the last few decades material science has a huge development, and increasingly expanding borders. Extensive applications and increased demands for different materials are some of the reasons for this development. Some of the most investigated materials for polarization holographic recording are azobenzene containing polymers [1-3]. The main feature that defines the widespread use of these materials is photo-induced optical anisotropy in them. Investigation of the anisotropy in azopolymers is of interest to applications in photonics and optical data storage [4-6], as well as for fundamental research [7, 8]. Many researchers [9-15] observed that the physical properties of azopolymers depend significantly on temperature, especially near the glass-transition temperature (T_g), where the mobility of polymer chains increases. In some cases birefringence is relatively stable below the azopolymer T_g [9] and is erasable by heating the polymer to this temperature. However some studies report that maximum birefringence can be obtained at temperatures above the T_g [11, 13].

This paper presents experimental data obtained from real time monitoring of recording and thermal erasure of birefringence with different starting temperatures of the thin film samples. Dependence of the maximal photoinduced birefringence, response time and relaxation decrease on the recording temperature are presented.

EXPERIMENTAL

Materials

The polymer used is side-chain amorphous azocopolymer, denoted as P_{1-2}, synthesized in the Institute of Optical Materials and Technologies, as described by Martinez-Ponce *et al* [16].
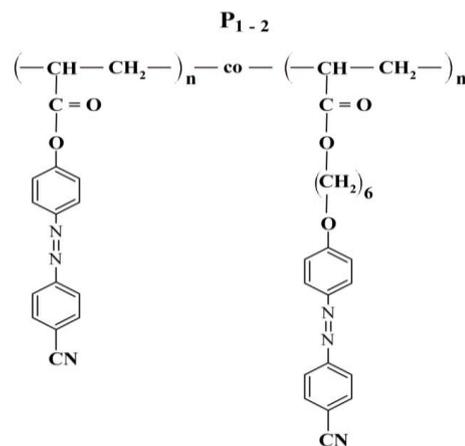
Fig. 1. Chemical structure of azocopolymer P_{1-2}.

---

* To whom all correspondence should be sent:
E-mail: dimana@iomt.bas.bg

Its chemical structure is presented in Fig.1. The molecular weight of P_{1-2} is $M_w = 3600$ g/mol and its glass transition temperature T_g is 102°C.

Methods of characterization

In this work we use thin films of the azocopolymer P_{1-2}. It was dissolved in 1,2-dichloroethane and the solution was spin coated at 1500 rpm on glass substrates making thin homogeneous film. As the thickness of the film is important for the determination of photoinduced birefringence [see Eq. (1)], we used a Talystep profilometer (Taylor Hobson) in order to measure it. The thickness for our samples was 700 nm. The birefringence is determined by recording the Stokes parameters of probe laser beam ($\lambda_{probe} = 635$ nm, power <2 mW) passing through the samples. The measurement is performed by PAX5710 Polarization Analyzing System (Thorlabs) and the birefringence is calculated from the following expression [3,17]:

$$\Delta n = \frac{\lambda_{probe}}{2\pi d}\arctan\left(\frac{S_3}{S_2}\right) \tag{1}$$

where d is the film thickness, and S_2 and S_3 are two of the four Stokes parameters. Vertically polarized light from DPSS laser with $\lambda_{rec} = 444$ nm and power 43 mW was used for recording.

The temperatures of recording are 25, 40, 50, 60, 70, 80, 90 and 100 °C. At first, we evaluate the background for 60 seconds. Then we turn on the recording laser for 300 s, than there are another 300 seconds for relaxation. In these three stages the temperature is constant. Then starts the heating. The control of temperature and subsequent thermal erasure was achieved by mounting the samples on stage THMS600 (Linkam Scientific), which is capable of maintaining a given speed of heating with high precision. We heated the sample with speed of 10 °C/min until reaching 100 °C. From our previous investigations, we know that the temperature for which the birefringence is reduced by 50% ($T_{50\%}$) is approximately 75 °C, and the temperature of complete erasure is 85 °C. For this reason in the last two experiments (at 90 and 100 °C) the films weren't heated because their starting temperature was high enough to erase the birefringence immediately after the end of recording. Also their recording and relaxation time were reduced to 180 and 120 seconds respectively.

RESULTS AND DISCUSSIONS

The experimental curves for starting temperatures 40, 50, 60 and 70 °C are shown on Fig. 2. In these cases the temperature of recording is below $T_{50\%}$.
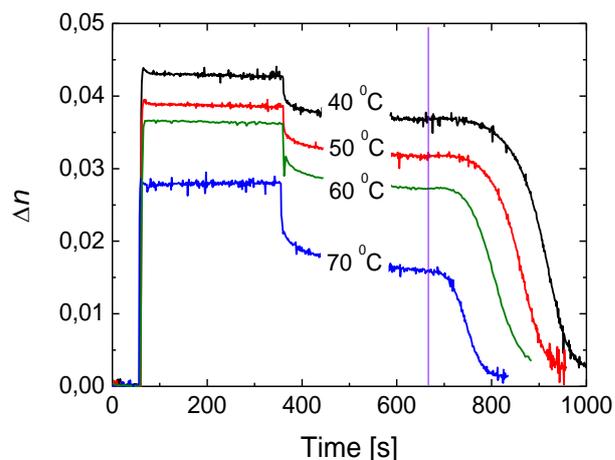
Fig. 2. Birefringence values during recording and thermal erasure. Recording temperatures are: 40°C, 50°C, 60°C, 70°C . The vertical line at 660 seconds indicates the start of temperature increase.

As seen from Fig. 2, the maximal induced birefringence is $\Delta n = 0.045$ at starting temperature 40°C and decreases with increasing the starting temperatures. However, the response time τ, as defined in Ref. 5, decreases as well, which is a desirable effect for many applications. Also we introduce a parameter R [%] as the ratio between the birefringence after 300 s of relaxation and the maximal value of the birefringence for the given recording temperature. It gives us information about the memory of the material and according to our results R decreases too. It is interesting that we observe the same value of $T_{50\%}$ − around 75 °C, though the recording temperature increases. As $T_{50\%}$ is higher than 70 °C, there is still residual anisotropy even for the sample with relaxation at 70 °C.
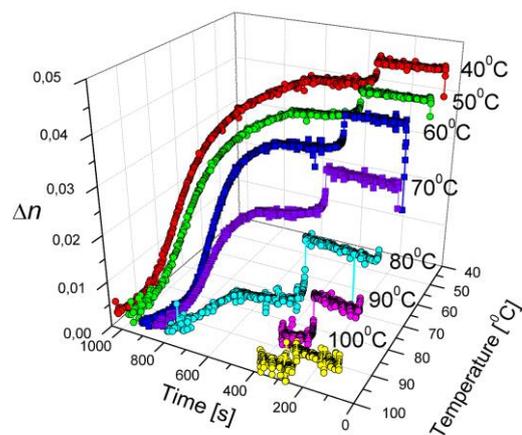
Fig. 3. 3D graph for all starting temperatures.
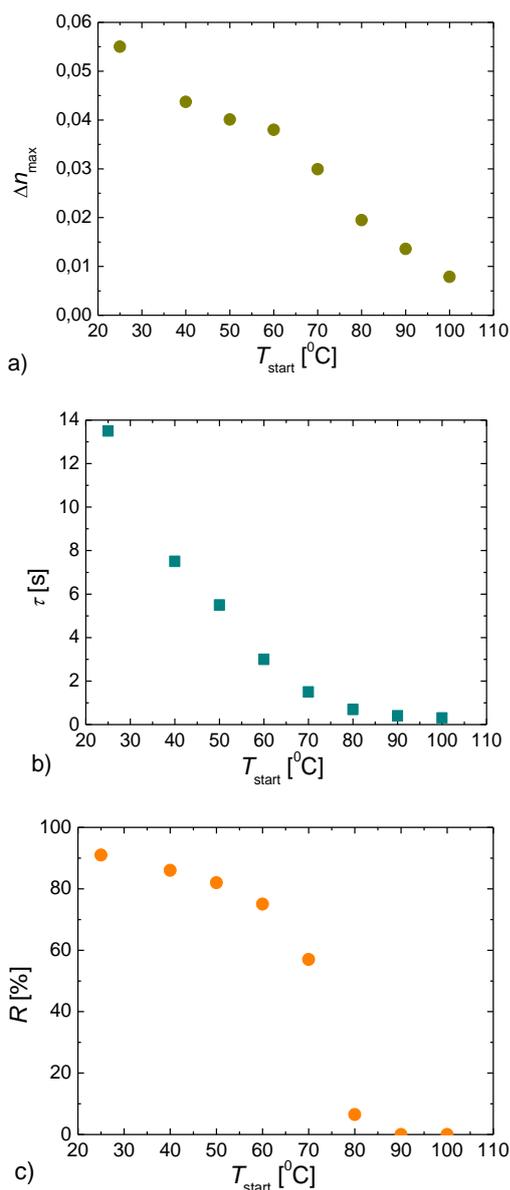
Fig. 4. Recording temperature dependences of (a) the maximal induced birefringence, (b) response time, and (c) parameter R.

In comparison, for higher starting temperatures (80, 90 and 100 °C) no residual birefringence after relaxation is observed. For these experiments we obtain very fast response, less than 1 second. All the results are visualized in a 3D Graph on Fig. 3 and summarized in Fig. 4.

As seen from the graphs, even at higher temperatures we are still able to induce birefringence while we illuminate the film with the recording laser.

The birefringence decrease at higher temperatures, as shown in Fig. 4(a), indicates the possibility to achieve an increase of birefringence at lower temperatures (below 20°C), which will be

subject to our further studies. Fig. 4(b) shows a rapid decrease of the response time. At 60 °C the response is more than 4 times faster, than at room temperature, namely it drops from 13.5 s at 25°C to 3 s at 60 °C. We should also note on Fig. 4(c) the significant decrease at 70 °C of the parameter R, which reflects the memory properties of the material. It is reduced nearly ten times between 70 °C ($R = 57\%$) and 80 °C ($R = 6.5\%$). This temperatures are very close to the temperature of half-erasure $T_{50\%} = 75$ °C.

CONCLUSIONS

In conclusion we can summarize that the parameters of the induced birefringence strongly depend on the temperature. The maximal birefringence and the parameter R decrease when increasing the temperature. On the other hand, the response time τ is reduced at higher temperatures and this gives us the opportunity to choose the optimal combination of parameters for a given application. We should also note, that the temperatures of half- and full erasure ($T_{50\%}$ and T_{erase}) remain the same for all starting temperatures.

REFERENCES

1. T. Todorov, L. Nikolova, N. Tomova, *Appl. Opt.,* **23**, 4309 (1984).
2. S. Xie, A. Natansohn, P. Rochon, *Chem. Mater.,* **5**, 403 (1993).
3. L. Nikolova, P. S. Ramanujam, Polarization Holography, Cambridge University Press, Cambridge (2009).
4. S. Hvilsted, F. Andruzzi, C. Kulinna, H. W. Siesler, P. S. Ramanujam, *Macromolecules* **28**, 2172 (1995).
5. L. Nedelchev, A. S. Matharu, S. Hvilsted, P. S. Ramanujam, *Appl. Opt.,* **42**, 5918 (2003).
6. A. Natansohn, P. Rochon, *Chem. Rev.,* **102**, 4139 (2002).
7. L. Nikolova, L. Nedelchev, T. Todorov, Tz. Petrova, N. Tomova, V. Dragostinova, P.S. Ramanujam, S. Hvilsted, *Appl. Phys. Lett.,* **77**, 657 (2000).
8. P. S. Ramanujam, O. B. Jensen, P. Tidemand-Lichtenberg, *Opt. Express,* **21**, 1812 (2013).
9. Q. Ferreira, P. A. Ribeiro, O. N. Jr. Oliveira, M. Raposo, *ACS Appl. Mater. Interfaces* **4**, 1470 (2012).
10. P. Rochon, J. Gosselin, A. Natansohn, S. Xie, *Proc. SPIE* **1774**, 181 (1992).
11. N. C. R. Holme, P. S. Ramanujam, S. Hvilsted, *Appl. Opt.,* **35**, 4622 (1996).

12. V. P. Shibaev, S. G. Kostromin, S. A. Ivanov, *Polym. Sci., Ser. A Ser.B* **39**, 36 (1997).
13. I. Zebger, M. Rutloh, U. Hoffmann, J. Stumpe, H. W. Siesler, S. Hvilsted, *J. Phys. Chem. A,* **106**, 3454 (2002).
14. J. Minabe, K. Kawano, Y. Nishikata, *Appl. Opt.,* **41**, 700 (2002).
15. M. Ivanov, D. Ilieva, G. Minchev, Ts. Petrova, V. Dragostinova, T. Todorov, L. Nikolova, *Appl. Phys. Lett.,* **86**, 181902 (2005).
16. G. Martinez-Ponce, T. Petrova, N. Tomova, V. Dragostinova, T. Todorov, L. Nikolova, *J. Opt. A: Pure Appl. Opt.*, **6**, 324 (2004).
17. N. Berberova, D. Nazarova, L. Nedelchev, B. Blagoeva, D. Kostadinova, V. Marinova, E. Stoykova, *J. Phys.: Conf. Series* **700**, 012032 (2016).

ФОТОИНДУЦИРАНО ДВУЛЪЧЕПРЕЧУПВАНЕ В ТЪНКИ АЗОПОЛИМЕРНИ СЛОЕВЕ ЗАПИСАНИ ПРИ РАЗЛИЧНИ ТЕМПЕРАТУРИ

Д. Назърова[1], Г. Матеев[1], Д. Иванов[1], Б. Благоева[1], Д. Костадинова[1], Е. Стойкова[1] и Л. Неделчев[1,2]

[1]*Институт по оптически материали и технологии "Акад. Й. Малиновски", Българска Академия на науките, ул. "Акад. Г. Бончев", бл. 109, 1113 София, България*
[2]*Висше училище по телекомуникации и пощи, ул. «Акад. Ст. Младенов» 1, 1700, София, България*

(Резюме)

В тази работа са изследвани характеристиките на поляризационен запис и изтриване в тънък азополимерен слой в зависимостт от различните стартови температури на образеца. За записа на фотоиндуцираното двулъчепречупване е използван лазер с дължина на вълната 444 nm. Изтриването на записите става чрез загряване на образеца. Успешно е реализиран запис на двулъчепречупване при различни температури от 25 до 100°C. Представена е тримерна (3D) графика за визуализация на експерименталните данни. Фотоиндуцираното двулъчепречупване е изчислено на базата на параметрите на Стокс, регистрирани в реално време през целия експеримент. Това изследване ни позволява да определим оптималните условия за запис при по-високи температури с цел да постигнем най-кратко време на отклик или максимално двулъчепречупване.

Two-wavelength lasers based on pumping by laser Gaussian-beam as instrumentation for materials and chemical products analysis

M. Deneva*

"QOE" Scientific Laboratory, R&D Dept., Technical University of Sofia and "OELE" Dept., TU-Branch Plovdiv, BG

We have developed, as a tool for differential-absorption spectroscopy and two-photon study of materials and chemical products composition, effective lasers with two or more independently tunable wavelengths. Our solution is based on the idea to combine a standard laser Gaussian beam longitudinal pumping of lasers, especially of dye lasers, with patented by us multi-coaxial-channels laser geometry. The Gaussian beam, due to its unique intensity distribution in the cross section, creates in the pumped laser active medium high pumping in the axial part and low pumping in the periphery. These two parts are optically separated and each generates in its own spectrally selective resonator. Beside the competition-less generation at two independently controlled wavelengths, other specific and essential advantages of the proposal are: i) both emissions – at the weeker line, generated in the amplified curve wings, and at the stronger line - arround the maximum of amplification, are produced with equalized energy without loss of pump energy for the equalisation and simultaneously ii) the two emissions are produced and emitted naturally in coaxial beams using entire laser medium volume. We report general modelling and detailed theoretical analysis of such a laser action on the basis of Rhodamine Dye in ethanol, pumped by Gaussian beam of Nd:YAG laser (0.53 μm). We succesifully tested the new solution with its advantages. We applied the two-wavelength laser light as a tool in differential absorption spectroscopy (DAS) to detect the presence and to measure concentration of Nd^{3+}-ions in a material under investigation.

Keywords: tool for DAS, two-wavelength lasers, dye lasers, Gaussian beam pumping, two-coaxial channel laser geometry, DAS chemical composition study.

INTRODUCTION

Today various specialized laser instrumentation has become a perspective tool for studying composition of materials and chemical products. Widespread application is the Differential-Absorption Spectroscopy (DAS) for local and remote use, the last especially for study of gas components in the atmosphere [1, 2]. The DAS method is based on comparison of the passed or diffused light power at two laser wavelengths - one of them coinciding with a specific line of absorption and the other – with non-absorption parts of the spectrum. The development of this technique is closely related to development of specific lasers that produce emission at two (or more) independently tunable lines, i.e. the so called two-wavelength lasers. Such lasers find wide application also in general spectroscopy, in non-linear optics, in bio-medical investigations and treatments [3-5]. More detailed review of the two-wavelength lasers and their applications is given in the recent papers [6-8].

The aim of this work is to report a new and highly efficient two-wavelength laser. This includes the proposed principle, detailed theoretical description, test implementation and experiment to prove the potential of such a laser to find the presence and concentration of given atomic particles in a mixed substance. We employ a new idea to combine the standard longitudinal pumping of wideband amplification laser medium (in the work - laser dye) with a Gaussian laser beam and our coaxial multi-channel laser geometry [9, 6]. The Gaussian beam, due to its peculiar intensity distribution in the cross section, creates in the pumped cylindrical laser active medium high pumping (and high amplification) in the axial part and low pumping (low amplification) in the periphery. We can separate optically these two parts to generate in two different spectrally selective resonators. If in the high amplification axial part we generate at wavelength with low emission cross-section and at the periphery part – at wavelength with high cross-section and choose convenient diameters of the two volumes, we can generate the two lines with equal energy without

* To whom all correspondence should be sent:
E-mail: mar.deneva@abv.bg

introduction of any corrected additional losses in the channels. The two generations are without competition and are produced and emitted naturally in coaxial beams using entire laser medium volume. These advantages are unique for the proposal. Still more, the longitudinal pumping has as general advantages, in comparison with the transversal pumping, use of low concentration and a big diameter pumped region of the active medium, which lead to better homogeneity and lower divergence. In the work, firstly we described the proposed laser scheme, secondly we modeled and provided detailed theoretical and numerical analysis of the action of such new laser solution. We made succesiful tests of the new solution to show its advantages. As an application, we used the produced two-wavelength laser light as a tool in DAS and found the presence of the searched Nd^{3+}-ions and measured their concentration in a sample under investigation.

PRINCIPLE AND THEORETICAL ANALYSIS

Schematic of the proposed longitudinally pumped with a Gaussian beam two-wavelength coaxial-architecture laser is shown in Fig.1. The principle is described on the example of Rhodamine Dye in ethanol (concentration 2x10-4 mol/l), longitudinally pumped by Gaussian beam distribution, second harmonic (0.53 μm) of Nd:YAG laser (pump energy of ~25 mJ; pulse length of ~ 30 ns). The dye solution filled a cylindrical cell (noted as Dye AM – Active Medium) with length l and diameter d (5 mm and 6 mm, respectively). The input pump beam passes through lens with suitable focal length (0.6 cm) to form a spot at the input of the AM with a diameter of the pumped part of ~ 6 mm that contains ~ 99 % of the incident beam power P_{tot} (i.e. 1.6 times higher than the Gaussian radius of 3.75 mm on the AM input). The Rayleigh length is essentially larger than the length l of the cell, which permits to accept parallel propagation of the Gaussian beam in the AM. After the lens, a multichroic mirror M_{ref} tilted at ~30° is placed (reflectivity R ~0.9 for 0.54-0.6 μm, and ~ 0.1 for 0.53 μm). The laser output mirror M_{out} is also multichroic (R ~ 0.7 for 0.54 - 0.6 μm and ~ 0.1 for 0.53 μm). At the opposite end of the AM, a near-plane multichroic mirror M_{pb} with radius of curvature few meters (R ~ 0.1 for 0.54-0.6 μm and ~ 0.8 for 0.53 μm) is suitably adjusted The generation at the two wavelengths (scheme in Fig.1) is produced in two coaxially disposed and optically separated parts of the AM. A spectrally-selective resonator with length

L (~ 5 cm) was formed for each part. The separation (hatched differently in Fig.1) is obtained using a dividing rectangular prism (DP), declined at a small angle (~5°) with respect to the cell axis to avoid the back Fresnel's reflection. The prism has a 0.3 cm diameter bored hole with length of 0.4 cm. In the hole a very thin (~0.1 mm wall) metal tube with 2 cm length is introduced, that assures very good separation of both channels as we have shown in our previous work [6]. The resonator for generation in the internal part (internal channel, generation at λ_i), built of M_{out} and M_i and the active volume, is separated by the tube through the prism. The spectral selection is done by the Interference Wedge IW_i [10] with thickness of 6 μm, reflectivity of the layers ~0.9 and apex angle of 5.10^{-5} rad that assures tunable selection in the amplification range of the generated dye and with linewidth ~ 0.3 nm. The external part (external channel, λ_e) generates in the resonator formed by M_{out}, internal reflection by the prism DP and selector combination of 1200 l/mm Diffraction Grating DG_e and the plane mirror M_e providing tunable selection with linewidth of ~ 1 nm in the gain region of the AM. We will use below the given already parameters of the laser construction.
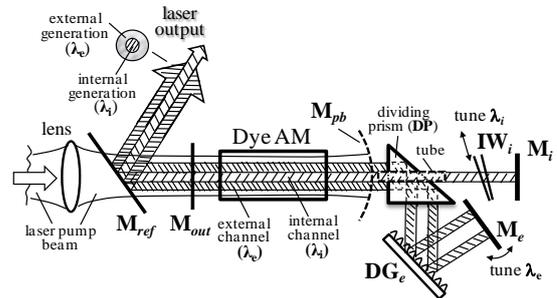
Fig. 1. Optical scheme of the laser with channels dividing prism DP with a hole.

THEORETICAL MODELLING

Theoretical analysis aims to obtain the conditions – especially AM separation in combination with the wavelength shift, for which simultaneous generation is possible with near equal output energies. We will consider the important, however difficult case, when one line is near the maximum of the amplification gain, and the second - shifted far from the maximum. In the common volume for lasers with homogeneously broadened amplification (our case), due to the so-called "wavelength competition" effect [11, 12], the generation of the weaker line is completely suppressed by the stronger one.

Firstly, in the theoretical analysis, we have calculated the pumped power distribution in the AM. For the used Rh6G dye concentration from the measurement, we have evaluated the non-saturated absorption coefficient for the pump 0.53 μm light to be ~ 12 cm⁻¹. The approach applied by us is schematically clarified in Fig.2. AM is divided radially into rings and longitudinally - in slices. The cross section of the cell is divided at 7 rings with equal increasing radii for each sequent by Δr (see Fig.2b). Along the axis Z of the crystal the division is at 5 slices each with equal length Δ*l*=*l*/5. We have Δ*l* =0.1 cm and Δr = 0.042 cm.
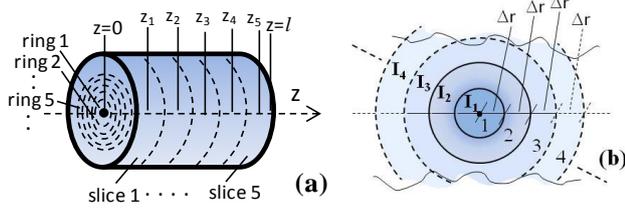
Fig. 2. Schematic dye cell division: **(a)** longitudinally in slices and **(b)** radially in rings

The Gaussian pumping (radius 3.75 mm) is with 25 mJ in ~30 ns pump pulse. The input beam is centered on the AM axis. Let's first consider the distribution of the pumping for each cylinder formed by border lines parallel to the axis of the dye cell and closed by the pair of rings at the front and rear sections of the dye cell (partial cylinders). The maximal intensity I_0 in the center of the beam at the entry plane of the dye cell was calculated on the base of well-known relation:

$$I_0 = \frac{2P^{\max}}{\pi \cdot \omega^2} \tag{1}$$

where $P^{\max}$ is the maximal pump power in the pulse and ω is the Gaussian radius of the pump beam. The intensity for each partial cylinder is calculated at the middle of the ring radius ($r_i = (2 \cdot i - 1) \cdot (\Delta r/2)$, $r = 1, 2 \ldots 6$) and is assumed to be homogeneous for the ring. The points on the graphics in Fig.3 present the values for the corresponding rings.

The distribution of the pump power for each ring and starting pump intensity are presented in Fig.3(b). In the calculations for propagation along the Z axis, we have used the Bouger's law, taken into account the effect of absorption saturation. We have evaluated the change of the pump intensity correspondingly for each ring, slice by slice – forward and backward after reflecting by the mirror M_{pb}. For each slice we sum forward and backward values, accepting that for any ring of the slice the

intensity is constant, equal to this one at the half length of the slice. We assume a total input in the crystal pump power $P_{tot} \approx 25$ mJ / 30 ns at Gaussian beam intensity distribution.
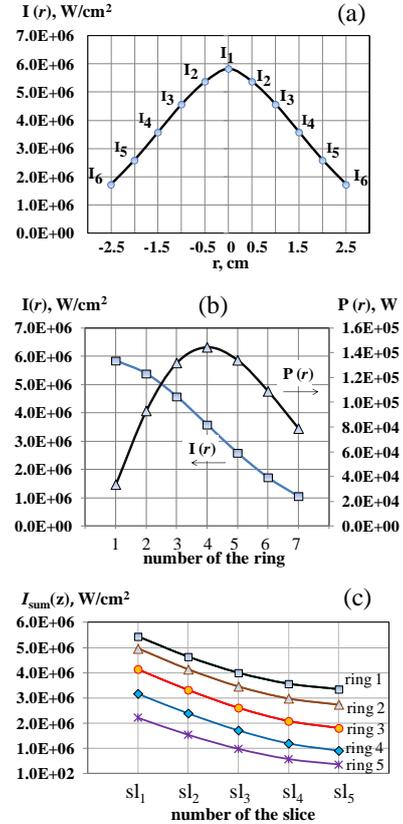
Fig.3. **(a)** Calculated distribution of the pump intensity (I_i) in the cross section; **(b)** The pumping power P(r) corresponding to each ring; **(c)** The result pump intensity for the first five rings (the axis X shows the number of the slice sl$_i$, i=1,2..5).

In Fig. 2(a) z_i (i = 1, 2, …5) corresponds to the middle of the slice length, where the result intensity is calculated. The values of the obtained intensity $I_{r,zi}$ for the first five rings, after summing the forward and backward values, calculated slice by slice are presented in Fig.3(c). The calculated plots in this figure show for each partial cylinder, with acceptable accuracy, the sum pump power (and energy) to be uniform both in slices and in the cross section – i.e. in the corresponding ring. This uniformity determines the fact that we can accept homogeneity of the pumping with different energy density for the partial cylinders. The change in the intensities from the first to the last slice for the corresponding cylinder is of the order of a few percents and practically could be taken as constant for each ring. On this base, we can calculate the generation for each partial cylinder applying the set of rate differential equations [11] adapted for the

case, presented in the next point. The considerable difference in the pump power for the cell parts around the axis and in the peripheral areas makes possible generation at weaker lines (with smaller values of the emission cross-section) comparable to that at the stronger lines, when they are generated in peripheral part of the dye cell. We show this possibility for the wavelength 594 nm, generated in near axial part and the wavelength 558 nm generated in the peripheral part of the cell.

ANALYSIS OF THE LASER GENERATION

Taking the approximately constant value of the pump energy into slices along the axis of the crystal – i.e. possibility to assume homogeneity of excitation (with different energy density for the corresponding ring), we apply the adapted set of differential rate equations [11] for the analysis. The adapted system that describes our case at assumed parameters is:

$$\frac{dN_2}{dt} = R_p^{(e,i)}(t) - B^{(e,i)} \cdot q^{(e,i)} \cdot N_2 - \frac{N_2}{\tau}$$

$$\frac{dq^{(e,i)}}{dt} = Va^{(e,i)} \cdot B^{(e,i)} \cdot q^{(e,i)} \cdot N - \frac{q^{(e,i)}}{\tau_c^{(e,i)}} \qquad (2)$$

with $P_{out}^{(e,i)}(t) = \left(\gamma_{out}^{(e,i)} \cdot c / 2L' \right) \cdot h\nu^{(e,i)} \cdot q^{(e,i)}(t)$ (3)

Here $B^{(e,i)} = \sigma_{21}^{(e,i)} \cdot l \cdot c / V_a^{(e,i)} \cdot L'$ s^{-1};

$\sigma_{21}^{(e)} = 2 \times 10^{-16}$ cm^2; $\sigma_{21}^{(i)} = 1.14 \times 10^{-16}$ cm^2 – emission cross-section of the Dye laser medium for $\lambda_e = 558$ nm and $\lambda_i = 594$ nm [11], l – dye cell length; c = 3×10^{10} cm/s is the light velocity; $L' = 6.7$ cm is the optical length of the resonator. The lifetime of the upper laser level is $\tau = 3$ ns. The term in (3) $h\nu^{(e,i)} \sim 3.3 \times 10^{-19}$ J is the energy of the generated photons for the corresponding wavelength. The dumping time of the photon in the resonator is $\tau_c^{(e,i)} = L'/c \cdot \gamma^{(e,i)}$, where $\gamma^{(e,i)}$ describes the losses in the respective resonator following Ref. [11] accounting the corresponding considered ring (partial cylinder). The calculations are for the laser and pumping parameters, given already. The total number of active Rh6G molecules cm^3 used in the calculations is 1.2×10^{17} cm^{-3} (2×10^{-4} mol/l Rh6G). The pump rate $R_p^{(e,i)}(t) = P_p^{(e,i)}(t) / \left(h \cdot \nu^{(e,i)} \right) \cdot V_a^{(e,i)}$ is defined on the base of the part of the optical pumping power that corresponds to the considered ring and wavelength. According our data, the obtained pump power for each ring can be determined from Fig.3. The pump power is a function of the area and the intensity in the ring.

$R_p^{(e,i)}$ is related to the temporal shape of pump energy in combination with the laser pump pulse shape. The Q-switched laser pump pulse can be well approximated by a trapezoid shape with a rise time of 10 ns, near-plateau part of 10 ns and fall time of 30 ns. $V_a^{(e,i)}$ is the active volume of the considered ring for the generation of the corresponding wavelength. In the calculations we have taken the geometrical data for each ring derived from the description of the laser cell separation given above.

The system (2-3) is solved using the Runge-Kutta method independently for the generation in each considered coaxial part – for each cylinder, with initial conditions N = 0 and $q^{(e,i)} = 1$. Solution of the system gives the temporal shapes of the laser outputs and their integration [11] is the output energy. For the used parameters, generation in six rings in total is obtained – in the first three rings the 594 nm wavelength is generated, and for the next three rings generation for the 558 nm wavelength is produced. Typical plots for generation at 594 nm (rings 1+2+3) and at 558 nm (rings 4+5+6) are presented in (Fig.4a). The plot modulation at 558 nm we relate to the small number of the rings, however this fact does not change essentially the real temporal shape of the laser emission at this wavelength, as shows the experimental results. The output energy for the wavelengths for the corresponding partial cylinder is plotted in Fig.4(b). The calculations show also that both generations are temporally superimposed with some difference of the starting of each generation of order of 5 ns.
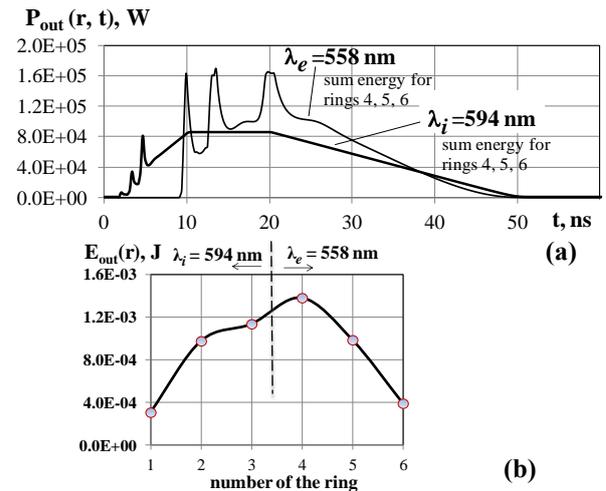
Fig. 4. (a) Temporal generation at $\lambda_e = 558$ nm (1+2+3 rings) and at $\lambda_i = 594$ nm (4+5+6 ring), respectively; **(b)** Calculated output energy in rings 1, 2, 3 (at $\lambda_i = 594$ nm) and in rings 4, 5, 6 (at $\lambda_e = 558$ nm).

The total output energy produced at 594 nm is ~ 2.5 mJ and at 558 nm ~ 2.8 mJ. Thus it is really possible to obtain practically equal energetic characteristics of both generations. For generation in a single common volume, the lasing at 558 nm suppresses the lasing at 594 nm.

THE EXPERIMENTAL TEST

The analysis in the previous section, besides showing the feasibility of our proposal with its advantages, confirms that the chosen parameters are well suitable for such laser realization. We have realized the laboratory prototype of the laser with elements and pumping parameters close to those in the previous section. To realize the DAS testing experiment, the two wavelengths are tuned to be at 561 nm (λ_e) and 579.6 nm (λ_i), with energy ratio ~ 1:0.6. The sum output at these two wavelengths (for our non-completely optimized test laser), was ~ 1.6 mJ that easily can be decreased using filters. The tuning in the range of ~ 6 nm conserves the two generations with acceptable equality of ~ 1:0.6 at the optimum (our case) to 1:0.3 at the ends. Both generations are emitted in coaxial beams, each with similar cross-section distribution to the spot of two-coaxial beam emission of a solid-state laser, shown in our work [6]. The internal beam has a circular ~3 mm diameter spot and the external - a ring one.
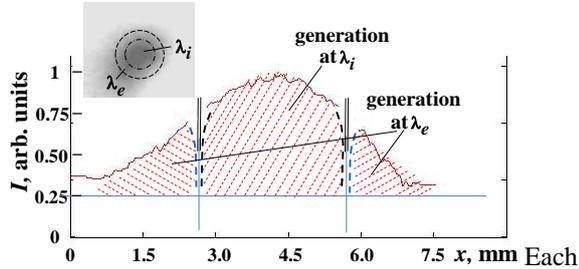
Fig. 5. The curve of spatial distribution of the two-wavelength laser output and the actual photograph –in the inset.
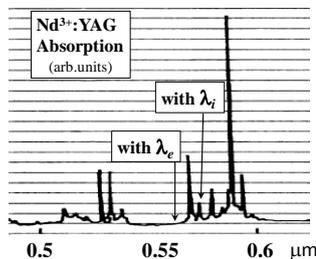
Fig. 6. The parts of the absorption spectrum of Nd^{3+}-ions in the YAG crystal and the wavelengths of the illuminating laser beams [13].

Each beam can be presented as superposition of few transversal modes [6], for internal – TEM_{00} +

TEM_{01*} and for the external – of two cylindrical modes of type TEM_{04}, turned radially with respect to each other at $\pi/8$ (each mode has maximums in the minimum-holes of the other). The external boundary of the internal spot and the internal boundary of ring-spot of the external beam, at some distance (of ~ 1.5 m) from the laser output, merge due to diffraction. The spots of the two-wavelength generation are shown in Fig.5.

We demonstrate the two-wavelength DAS spectroscopy method, using the two-wavelength laser for evaluation of Nd^{3+}-ions concentration in Nd^{3+}:YAG crystal. The part of the absorption spectrum of Nd^{3+}-ions is shown in Fig.6 [13]. The wavelength at λ_e coincides with the absorption minimum (practically zero) at 561 nm and the other - λ_i - with the absorption line (with $\sigma_{ab}=0.54 \times 10^{-20}$ cm^{-1} [11]). When the light at these two wavelengths passes through the crystal sample with length ξ, decreasing of intensity at each wavelength is different. We can write for our case for the decreased power of the incident intensities $I_0^{e,i}$ (W/cm^2), that is adjusted to be less than 25 kW/cm^2 (saturation intensity for Nd^{3+}), for non-saturated transmission $I_{pas}^i = I_0^i \cdot e^{-\left(\sigma_{ab}^i \cdot N \cdot \xi + \alpha \cdot \xi\right)}$ at λ_i,

$I_{pas}^e = I_0^e \cdot e^{-(\alpha \cdot \xi)}$ at λ_e. Here α, in cm^{-1}, is the coefficient of light decreasing due to different reasons, common for both wavelengths – reflection at the sample input and output surfaces, scattering, non-spectral selective absorption of impurities. After some simple calculation, we have:

$$N = -\left(\sigma_{ab}^i\right)^{-1} \xi^{-1} \cdot \ln\left[\left(I_{pas}^i / I_0^i\right) \cdot \left(I_{pas}^e / I_0^e\right)^{-1}\right] \qquad (4)$$

In our case, from the easily measured ratios $\left(I_{pas}^i / I_0^i\right)=0.042$ and $\left(I_{pas}^e / I_0^e\right)=0.64$, at $\sigma_{ab}^i=$ 0.52x10^{-20} cm^2 [13] and ξ =8 cm, the concentration of Nd^{3+}-ions is 6.4x10^{19} cm^{-3}.

CONCLUSION

In the work we have shown – theory and the experimental test - the possibility to use the specific light intensity pump beam distribution in the Gaussian beam in combination with special coaxial geometry to obtain a new two-wavelength laser. This laser, beside the absence of non-desired wavelength-competition effect [12, 14], assures laser emission simultaneously at tunable weak and strong lines with practically equal energies without loss of pump energy for the equalisation. The two emissions are produced and emitted naturally in coaxial beams using the entire rod volume. Such

lasers can be considered as an effective tool in differential absorption spectroscopy in chemical analysis. Confirming experimental test, using the two-wavelength light to detect the presence and concentration of Nd^{3+}-ions in mixed substance, is also given.

REFERENCES

1. W. Demtröder, Laser spectroscopy: basic concept and instrumentation, 3th ed., Springer, (2003).
2. V. Vaicikauskas, Z. Kuprionis, M. Kaucikas, V. Svedas, V. Kabelka, *Proc. of SPIE*, **6214**, 62140E (2006).
3. M. L. Rico, J. L. Valdes, J. Martinez-pastor, J. Capmany, *Optics Communs.,* **282**, 1619 (2009).
4. L. Zhao, J. Su, X. Hu, X. Lv, Z. Xie, G. Zhao, P. Xu, S. Zhu, *Opt. Express*, **18**, 13331 (2010).
5. B. Devaux, F. Roux, Acta Neurochirurgia, the Eur. J. Neurosurgery, **138**, 1135 (1996) and the literature cited there in.
6. M. Deneva, M. Nenchev, E. Wintner, S. Topcu, *Opt. Quant. Electron.,* **47**, 3253 (2015).
7. A. Sato, Sh. Okubo, K. Asai, Sh. Ishii, K. Mizutani, N. Sugimoto, *Appl. Opt*., **54**, 3032 (2015).
8. Y. G. Bassov, *Sov. J. Appl. Spectr.* (ed. USA), **49**, 6 (1989).
9. M. N. Nenchev, *BG patent* IIR 25954 (1978).
10. E. Stoykova, M. Nenchev, *JOSA*, **27**, 58 (2010),
11. O. Svelto, Principles of lasers, 5th ed. Springer Science+Business Media, LLC 2010 (2010).
12. Y. Louyer, J. Wallerand, M. Himbert, M. Deneva, M. Nenchev, *Appl. Opt*., 42 (27), 5463 (2003).
13. W. Koechner, Solid-State Laser Engineering, 6 revised and updated edition, Springer, Berlin (2005).
14. M. Deneva, P. Uzunova, M. Nenchev, *Opt. Quant. Electron.*, **39**, 193 (2007).

ДВУВЪЛНОВИ ЛАЗЕРИ, БАЗИРАНИ НА ЛАЗЕРНО ВЪЗБУЖДАНЕ С ГАУСОВ СНОП КАТО ИНСТРУМЕНТАРИУМ ЗА АНАЛИЗ НА МАТЕРИАЛИ И ХИМИЧЕСКИ ПРОДУКТИ

М. Денева

Лаборатория „Квантова и оптоелектроника", НИС, Технически университет София и Катедра „Оптоелектронна и лазерна техника" – ТУ-Ф-л Пловдив;

(Резюме)

В работата ние предлагаме нов атрактивен двувълнов лазер, отнасящ се към важните инструменти за спектрален анализ на състава на материали и химически продукти с техниката на диференциално-абсорбционна спектроскопия (ДАС) и дву-фотонно третиране. Нашето решение се основава на нова идея да се комбинира надлъжно възбуждане на лазер, особено багрилен лазер, чрез стандартен Гаусов лазерен сноп с нашата патентована мулти-коаксиална геометрия на каналите в лазера. Гаусовият сноп, поради специфичното разпределение на интензитета в напречно сечение, създава във лазерната активна среда високо възбуждане в аксиалната й част и ниско възбуждане в нейната периферия. В нашето решение, тези две части оптически са разделени коаксиално и всяка генерира в свой собствен спектрално – селективен резонатор. Освен генерация на две независимо управляеми дължини на вълната без конкуренция, други специфични предимства на предложението са: 1). двете генерации – на слабата линия, генерирана в краищата на спектралната крива на усилване, и на силната линия – около максимума на спектрално усилване на средата, се произвеждат с приблизително еднаква (изходна) енергия без загуба на възбуждаща енергия за изравняването им, и едновременно; 2). двете генерации се произвеждат и генерират естествено в коаксиални снопове, използвайки целия лазерен обем на средата. Ние представяме обобщено моделиране и детайлен теоретичен анализ на действие на този нов лазер, с използването на числено обсъждане на родаминово багрило в етанол, възбуждано от Гаусов сноп от Nd:YAG лазер (0.53 μm) и успешно сме тествали новото решение с неговите предимства. Като приложение, използвайки двувълновата лазерна светлина като инструмент в ДАС, ние показваме присъствието на Nd^{3+}-йони и измерихме концентрацията им в изучаван материал.

Xerox treated tracing paper as suitable and accessible material for development of new laser beam–profiler technique

V. Kazakov, M. Deneva*, M. Nenchev, N. Kaymakanova

"QOE" Scientific Laboratory, R&D Dept., Technical University of Sofia and OELE Dept., TU-Branch Plovdiv, BG

On the base of systematic investigation, we have introduced as suitable and accessible material for the laser beam profile study appropriately treated tracing paper by standard Xerox type copy machine. As we show, the whitening of this material by laser illumination in combination with appropriate computer analysis can be a base for development of very competitive non-electronic technique for complex laser spot energetic profile study. Such whitening of the accidentally taken, non-defined, blacked materials and without any quantitative treatment, is used previously in the literature and in the laboratory practice only for visual illustrative marking (including also successfully - for the interesting cases) of laser spot. We have taken into account that the discussed registration presents, as a potential, some essential advantages in competition with the modern electronic beam-profilers - the registration is in very wide spectral range (from UV to IR - e.g. 0.3 - 3 μm and longer), cannot be disturbed by the electromagnetic noise and such spot visualization is extremely cheap and accessible. Via a complex investigation, we have developed a suitable technique of noted above type for real laboratory and practical laser spot study applications. As first important point in this development, we have found suitable, reproducible and widely accessible materials for spot registration that, in defined range of illumination (sufficiently large), offer possibility by using a standard computer treatment to obtain a good quantitative spot energetic parameters determination. The noted advantages of such type technique are shown in the work.

Keywords: material for laser beam profile study; new non-electronic technique for energetically laser spot study; registration in very large spectral range; non-disturbance by the electromagnetic noise.

INTRODUCTION

The work presents a systematic study of a treated by standard Xerox type copy machine tracing paper as a suitable and accessible material for laser beam profile evaluation. We show that this material combined with computer processing can be a base for development of very competitive apparatus of non-electronic Thermo-Paper Registration Approach (TePRA) for laser spot profile study. The principle of the TePRA is the whitening within the laser beam illuminated area of the black thermo-sensitive material. This registration is used in the literature and in the laboratory practice only for visual illustration of the laser spot marking [1] on the randomly chosen sensitive materials and without any quantitative processing. However, looking in details, the TePRA registration presents as a potential some essential advantages in competition with the electronic beam-profilers [2]. Firstly, as we have shown also in our experiments including two-wavelength lasers [3], a correct registration is not spectrally sensitive in a very wide range, for example - from UV to IR (e.g. 0.3 - 3 μm and longer). Secondly, this registration cannot be disturbed by electromagnetic noises and in addition such spot registration is extremely cheap and accessible. The adaptation of such laser spot marking as suitable technique for real laboratory and practical applications needs essential development. Important issues must be solved as i) to find suitable, reproducible and widely accessible materials for spot marking, ii) to determine the range of variation of the illuminating light intensity for correct and usable response of the materials and iii) to develop convenient procedure combined with standard computer processing of the marked spot. This is the aim of the present work.

EXPERIMENTAL

There are many blackened paper-materials, on which a laser beam makes a spot within the illuminated area. As laser beam sources we used pulsed Nd:YAG and Nd:Glass lasers. The laser output energy in most of the experiments was equal

* To whom all correspondence should be sent:
E-mail: mar.deneva@abv.bg

to the energy of the beam, illuminating the studied material, except the case where a fine plate filtes was used. The energy was measured with FIELDMAX energy meter, Coherent, USA and the pulse duration - with a 250 MHz storage oscilloscope. The study was performed at different laser parameters, generally for the energy between 0.3 J to 10 J and pulse length from 100 μs to 3000 μs. This was obtained by the Nd:YAG free mode of operation with spectrally and energetically controlled output, variable from 0.3 J to 1.8 J, repetition rate – single pulse to 1 Hz, and pulse length of 150 μs to 350 μs; with tuned lines – at 1.06 μm and at 1.32 - 1.36 μm. The second Nd:Glass laser in free lasing mode of operation produced output energy up to 10 J at 1.06 μm with pulse length from 2500 μs to 3000 μs. Also, we have investigated the laser beam in a short pulse, produced by passively Q-switched operation of the Nd:YAG laser with pulse length of 1 μs and energy of 0.4 J to 0.9 J at the line 1.06 μm. The lasers operated in a multimode regime.

Following the aim of the work, we performed a sequence of related experiments.

We started with testing of different blackened papers - conventional paper and blackened Xerox copy paper, and observed a common effect. If such paper is illuminated on the blackened side, the produced white spot has "mustaches" and black traces within the spot (Fig. 1a,b). We explain this unfavorable fact with action of the light pressure on the formed cloud of vaporized (generally – ablated) micro-particles. The pressure returns back part of the particles to the spots area. Adhering of the heated ablated micro-particle also contribute to the noted undesired effect.

a)   b)   c)
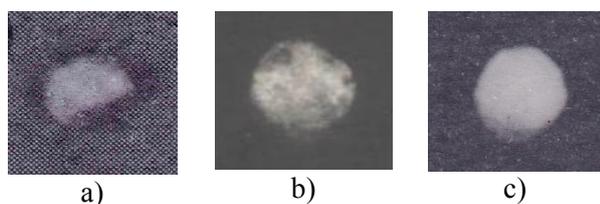
Fig. 1. Whitened by laser illumination materials: (a) Usual black paper; (b) Xerox blackened tracing paper, illuminated on the blackened side and (c) - illuminated on the non-blackened side

Typical example of the described spot type is shown in Fig. 1: (a) is in usual black paper; (b) is made on the blackened side of Xerox- blackened tracing-paper (one passing, copy of the black paper) and (c) – at its opposite side.

Thus, the suitable material must be transparent, or partially transparent with a black layer on the one side and the illumination must be done at the non- blackened side. We have tested different paper and plastic materials of this type. Our attention was focused on paper-materials, which can be well defined and easily accessible for a large number of users. In summary, we found that most suitable for application is the tracing paper, blackened at one side by Xerox type copy machine. We have used the widespread tracing paper A4 92 gr/m^2 from Sihl Digital Imaging Company (the light transmission measured with a bulb lamp of pure tracing sheet gives ≈ 55 %). Note that we have compared the blackening, in a manner described below, for several different type Xerox-machines: Konica Minolta Dialfa Di 5510 – used basically in the work, also as testing - Sharp-MX-3500; Toshiba 2500c with standard toner powder (such as Toner Cartridge 360 for use in Konica digital copier, India). We did not observe noticeable difference of the blackened tracing-paper behavior. The same, not critical difference was observed using spot tracing with different scanners - BENQ S2W 3300u, CANON LIDE 25, Canon Pixma MX320. Our test of scanning spots from the tracing paper gives correct results when at the back side is placed white sheet (non-black or coloured one). The illumination of the blackened tracing paper by free-lasing beams with the described above parameters, made good white spot on the impact area, as a typical one, shown in Fig. 1(c). Under other conditions – Q-switching operation, noted above, the formed spot has white-brown color. Firstly, we tested the simplest procedure – to use transmission through the white spots under illumination with a low-power (~mW) homogeneous laser light (spot by spot) to determine the incident spot energy distribution. However, we found non-acceptable difference of typically ~ 40% and more. The tracing, point by point, along the diameter of the white spots, of transmission with a system composed from diaphragm-receiver-oscilloscope - also gave non-acceptable results. We explain this fact with appearance of white products due to the burning of the black layer and remaining products of the black layer, which combination leads to non-proportionality to the transmitted incident light intensity. The actual photograph of the part of whitened by the laser illumination spot (on the border with non-treated part black side) of the sheet is shown in Fig. 2. The formation of the layer of white burning products can be seen. Important for the purpose of the work is that at large energy

density range from ≈ 0.5 J/cm^2 to ≈ 4 J/cm^2 the whitening is proportional to the illuminating energy density.
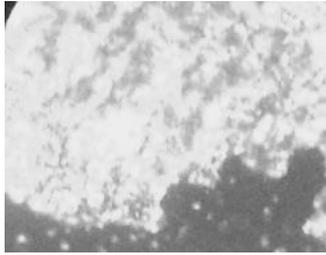
Fig. 2. Actual photograph of the part of whitened paper within the laser illuminated spot.

From series of measurements, we obtained that the whitening is proportional to the light energy density in a wide range. To describe the whitening we introduced the function $W_w(x,y)$ whose value in a given small area (dxdy) around the point (x,y) is proportional to the illuminating energy density $W_E(x,y)$ in the considered area. The coefficient of proportionality is denoted as k_1. This schematically is shown in Fig. 3.
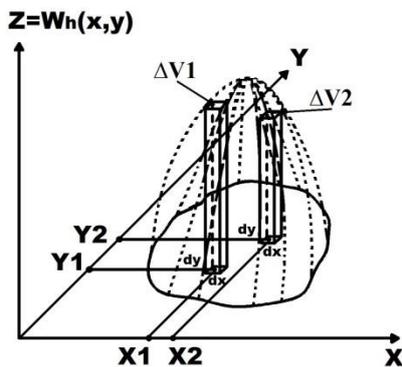
Fig. 3. To the analysis of the relation beam illumination energy - volume of the spatial figure within the whitening boundaries.

After the integration, we obtain:

$$V = \int\limits_x \int\limits_y k_1 \cdot w_E(x, y)\,dxdy = k_1 \cdot E_{jb} \qquad (1)$$

Here V is the volume below the given surface by the function $k_1 \cdot W_E(x,y)$, E_{jb} is the illuminating beam energy and k_1 is accepted to be constant. Thus, if the whitening is proportional to the energy density, the energy in the incident spot is proportional to the volume under the laser spot whitening envelope surface. This gives us good and easy approach to determine the energy density distribution in the marked laser spot (Fig. 4a) by taking the 2D trace (the radial distribution-Fig. 4b) and 3D volume envelope surface (the distribution in

the spot plane – Fig. 4c), built by computer scanning of the whitening. The description can be done in relative units or knowing one of the values of $W_w(x_1,y_1)$ preliminary obtained at a given point x_1,y_1, to know the absolute value of energy density distribution in the different point (x,y). The correctness of the description can be verified taking as measure the ratio R of computed volume V versus illuminating pulse energy E or V/E = R. If R is equal for the group of spots on the blackened tracing paper with different energies, R can be considered as a proof for correctness of using the envelope surface (3D) and diametric lines (2D) for description of energy density distribution by the computer graphs. The correctness of whitening – computer processed energy density-description is in good agreement with the electronic technique of the type point by point (ITBRO) by moving a diaphragm within the spot on the paper and receiver-oscilloscope registration [3]. The cross-section lines of the volume envelope–2D image give the energy distribution in the spot cross-section, where the line is traced. If the 3D image has radial symmetry (at good laser adjustment) the tracing in the cross section across the peak gives the energy intensity distribution along the spot diameter (Fig. 3c).

a)   b)   c)
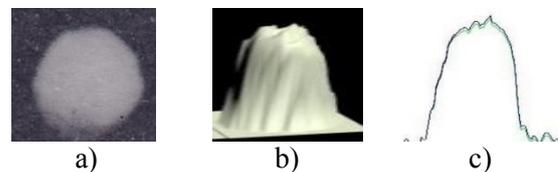
Fig. 4. **(a)** The spot on the tracing black paper and the computer image from the computer processed spot: **(b)** - the volume envelope (3D) and **(c)**-along the diameter.

Important issue is how the blackness of the tracing-paper impacts the whitening and the limits of linear whitening versus illuminating energy density. For this purpose, we prepared series of Xerox- blackened tracing paper by most common and widely accessible procedure.

The first three type sheets – the series A were produced by: one time blackening, noted as 1x, two times - 2x and three times - 3x, at "maximum" blackening regime of the machine and completely open shutter (day light illumination). For the considered corresponding series we added the notation of the series – A1x, A2x, A3x respectively. Second series (B sheets) was blackened in the same manner, but for operation regime "normal". Also, we prepared the tracing-paper sheets, blackened by one time copy (C1x) and two times copy (C2x) of

black paper at "normal" operation (with closed shutter). The corresponding measurements of the transparency, as characterization of the paper, gave for the transmissions: A1x – (10 ± 1)%; for A2x- (1 ± 0.1)% and A3x ≈ 0.1%; for B1x - (7 ± 2)%, and for the sheet C1x - (7 ± 1.5)% and C2x - (4.4 ± 1)%. The observed fluctuations are related to transmission variation from place to place at the sheet, being practically negligible for A3x. In Fig. 5 are given the microscope photographs of pure parts of the sheets A (1x, 2x and 3x), illuminated underneath with the microscope bulb-lamp; the shown spots are with ~ 1 mm diameter. In the same figure, 2D and 3D images, corresponding to marking spots computer processing for the sheets A1x and A3x, are also shown. The pulsation of A3x is negligible in comparison with the case when A1x is used, where incompletely uniform blackening and many transparent points are presented.

This was one of the reasons to prefer application of A3x (or A2x - low pulsation as for A1x).
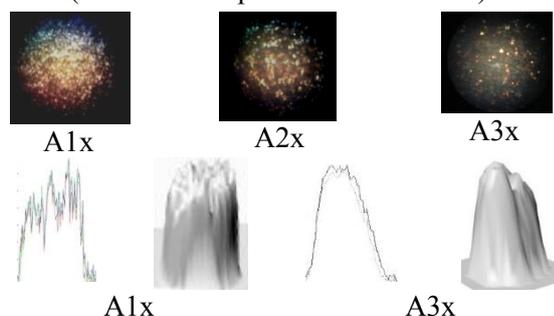
Fig. 5. The microscope photographs of the non laser light marked parts of the sheets with microscope bulb-lamp illumination in transmission –top; he bottom images correspond to marked spots 2D and 3D processing for the sheets A1x and A3x.

Important for the purpose of the work is that at large energy density range from ≈ 0.5 J/cm^2 to ≈ 4 J/cm^2 the whitening is proportional to the illuminating energy density. Given limits are for the sheet A3x, however they are not essentially different for the other samples, noted above. We have found these limits by studying the whitening in the spots, formed by the laser beam at different distances from the laser output, exploiting the beam spot divergence, or the spots enlarging by the lens, an example of the experiment that is given in Fig. 6. We studied correctness of registration thoroughly for the noted series of papers – prepared in very reproducible and widespread accessible manner. Thus we prepared the samples of stacked with each other pieces of the sheets A1x, A2x and A3x (Fig. 7a) and we formed the white spots with diameters varying between 6 and 7 mm and for energy density that is in range of 0.5 J/cm^2 and 4 J/cm^2 (Nd:YAG

laser, multimode, near bell-like shape of energy density distribution by combina-
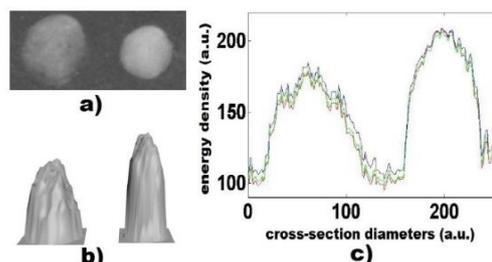
Fig. 6. Example - the enlargement of the spot of whitening with a distance for energy density dependence study.

tion of $TEM_{00} + TEM_{01}^{*}$ modes at 1.06 μm and 1.36 μm, and pulse length ~ 200 μs). As a quantitative measure of the suitability of the corresponding sheet to give correct energy density, we took, as stated above, the range of illuminating density that conserved the value of K_1 constant, given by the ratio $V/E = R$, where V is the computed volume and E is the illuminating energy. The plot of the parts of investigated sheets A1x–A3x with registered spots is shown in Fig. 7(a). In Fig. 7(b) are given the line of blackness for corresponding sheets. The spots on the sheet A3x in increased scale and their 2D and 3D computer processing images are given in Fig. 7(c)-7(e).
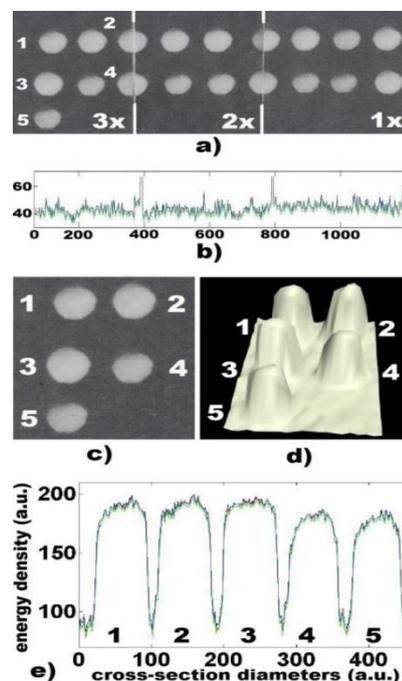
Fig. 7. (a) The plot of the parts of sheets under investigation A1x–A3x with registered spots; **(b)** the line of blackness for the different sheets; **(c)** the spots on the sheet A3x in increased scale and their **(d)** 2D and **(e)** 3D computer processing obtained images.

Processing of each sheet will be detailed on example of A3x, for which best results are obtained. After computer processing of the shown five (1,2,3,4,5) spots and with known energy that formed each of them, we obtained the average $R_{av} = (\sum V_i / E_i) / N$ where sum is for i=1-5, V_i and R_i are the volume and the energy of the spots numbered i and N=5: R_{av}=(0.63/0.53 + 1.038/0.86 + 0.977/0.75 + 0.888/0.78 + 0.595/0.51) / 5 = 1.2. We defined the deviation (or error) ΔR_i for each spot as $\Delta R_i = (R_i - R_{av})$ and the relative average deviation for the considered group spots of A3x sheets was ΔR_{av} = (|-0.01| + 0.01 + 0.1 + |-0.06| + |-0.04|)/ (5.Rav) = 0.036 ≈ 4%. We calculated also the relative maximal deviation $\Delta R_{max} = (R_{max} - R_{min})/ \{(R_{max} + R_{min}) / 2\}$, where R_{max} and R_{min} are maximal and minimal deviation from R_{av}, respectively for the group, in practice a single case. For A3x we obtained $\Delta R_{max} = (0.1 + |-0.06|) / \{(1.3 + 1.14) / 2\} = 0.13 = 13\%$. Note that if we exclude the exceptional case of deviation for the spots, in our consideration, ΔR_{av} is ≈ 2 % with ΔR_{max} ≈ 6 %. In the same manner we have treated the noted other cases. The results are given in Table 1. The case B is very close to the case A2x - A3x and case C2x is better for the C type blackening. The investigations show that more suitable for the aim of spot registration is the tracing paper A3x (some illustration – Table 1).

Table 1. The experimental results confirming the correctness of the spots treatment (details in the text)

Sheet	ΔR_{av} (a.u.)J^{-1}	ΔR_{av} %	ΔR_{max} % (single case)	ΔR^{wec}_{max} %
A1x	1,1	6 %	24%	18%
A2x	1.3	5,8 %	18%	16%
A3x	1.2	3,6 %	13%	5,8%
C2x		4,3%	13,7%	-

Important experiment was to study the dependence on the illuminating wavelength. Using our laser, we obtained for the two wavelengths – 1.06 μm and 1.36 μm [3] no change of K_1. This is the case for all considered in the work blackened tracing papers. The example for the paper type A3x is shown in Fig.8; (spots at 1.06 μm and 1.36 μm for 1.1 J and 0.5 J illuminating energy and pulses duration 250 μs respectively). This can be expected for general reasons (thermal and ablation effect). The present results concern the investigation of the illumination with pulse length in the range 100 – 3000 μs. This is very common case of laser use – e.g. solid-state lasers in regime of free generation.

The effect of bleaching arises from combination of material burning and ablation processes. The two effects are evident – the burning from the microscope photographs with shown typical case in Fig. 2. The ablation is evident in the experiments by formation
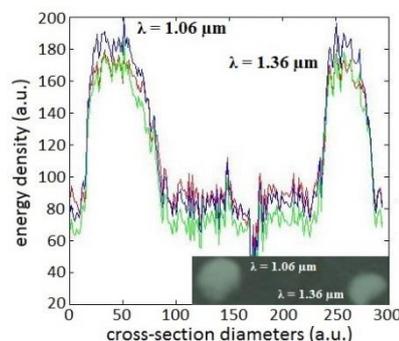
Fig. 8. The 2D computer processing graphs of two spots -at 1.06 and 1.36 μm. The spots (in the inset) are marked on the blackened tracing paper A3x type

of cloud after the shots of the laser pulse. It can be noted that, for cw light illumination, the effects on the studied material are quite different and not suitable for the discussed treatment.

SUMARISING THE EXPERIMENTAL RESULTS AND DISCUSSION

Summarizing the experimental results gives:
In summary, Xerox treated tracing paper in combination with standard computer treatment can be a base of development of advantageous techniques for laser beam profile registration:
- this material has been selected experimentally among a number of potential materials as most suitable; this study gives optimal conditions how to prepare and use the samples;
– applicability is shown for correct registration in a large energy density and pulse lengths range of the illuminated beam (0.3- 4 J/cm^2 ; 100-3000 us), that is typical for the widely used laser -Nd:YAG, ND:Glass; Ruby, Ho:YAG, Er:YAG; the typical error is within the limits of 4-5 %, with maximal value for a single case of ~ 13 % (for the shown in the work optimal treatment tracing paper, as it is shown in Table 1);
- the experiments confirm the expected no dependence on the wavelength of the laser beam under investigation;
- no noticeable dependence on the prepared samples when using different standard and widely accessible Xerox-type machine and tracing papers;
In addition, the prepared simples are very cheap and accessible.

CONCLUSION

We presented in the work original technique for laser beam-profiling and found a very suitable material for its application. The technique is competitive with the electronic beam-profiler with the proposed and positively characterized by us material for registration – the simplest suitably Xerox-blackened tracing paper. As additional advantage the technique is non-wavelength sensible, also cannot be disturbed by electromagnetic noise.

We have shown its real and correct applicability as a beam profiler for the laser pulses that is typical for the widely used lasers, such as Nd:YAG, generating at different wavelengths, including the case of two-wavelength operation [3], Nd:Glass, the Yb:YAG, Ho:YAG, Er:YAG, flash lamp pumped Dye, semiconductors etc. Except more important possibility for energy distribution, the shown dependence additionally gives also the approach to determine the laser beam energy using comparison of the calculated spot volume with this of a given etalon spot on the same paper.

REFERENCES

1. R. Ifflander, Solid-State Lasers for Materials Processing, Springer-Verlag, Berlin, Heidelberg, New York, series in Optical Sciences, 2001.
2. Carlos B. Roundy, Spiricon, Inc., http://aries.ucsd.edu/LMI/TUTORIALS/profile-tutorial.pdf, Beam Profile Measurements and the literature therein.
3. M. Deneva, M. Nenchev, E. Wintner, S. Topcu, *Opt. Quant. Electron*., **47**, 3253 (2015), and the literature therein.

КСЕРОКС ТРЕТИРАН ПАУС КАТО ПОДХОДЯЩ И ДОСТЪПЕН МАТЕРИАЛ ЗА РАЗВИТИЕ НА НОВА ТЕХНИКА ЗА РЕГИСТРАЦИЯ НА ПРОФИЛА НА СЕЧЕНИЕ НА ЛАЗЕРЕН СНОП

В. Казаков, М. Денева, М. Ненчев, Н. Каймаканова

Лаборатория „Квантова и оптоелектроника", НИС, Технически университет София и Катедра „Оптоелектронна и лазерна техника" – ТУ-Ф-л Пловдив

(Резюме)

На базата на систематично изследване, ние въвеждаме като подходящ и достъпен материал за изследване на профила на лазерния сноп подходящо обработена хартия от стандартна ксерокс копирна машина. Както показваме, побеляването на този материал при осветяване с лазер в комбинация с подходяща компютърна обработка може да бъде база за развитие на много конкурентна нееклектронна техника за комплексно изследване на енергетичния профил на лазерното петно. Такова побеляване на случайно избран, недефиниран, почернен материал и без някаква количествена обработка, е използвано и преди в литературата и в лабораторната практика, но само за визуално илюстративно маркиране на лазерното петно (също и успешно за илюстрация на интересни случаи). Ние взехме под внимание, че обсъжданото регистриране представя, като потенциал, някои съществени предимства в конкуренция с модерния електронен регистратор на профила на снопа. Разработваната от нас техника е използваема в много широк спектрален диапазон (от УВ до ИЧ – напр. 0.3 - 3 µm и повече), не се влияе от електромагнитните шумове и е изключително евтина и достъпна. Чрез комплексно изследване, ние разработихме конкурентна техника от отбелязания по-горе вид за реални приложения в лабораторни и практически изследвания на лазерното петно. Като първа важна точка в това развитие, е намерения подходящ, възпроизводим и широко достъпен материал за регистрация на петното, който в определен, достатъчно широк диапазон на параметри на лазерното лъчение предлага възможност чрез използване на стандартна компютърна обработка да се получи добро количествено определяне на енергетичните параметри на петното. Отбелязаните предимства на такъв тип техника са показани в работата.

Modeling the penetration of laser radiation in enamel-dentin tissue

H. Kisov, G. Dyankov

Institute for Optical Materials and Technologies "Acad. J. Malinowski", Bulgarian Academy of Sciences, "Acad. G. Bonchev" str. Bl. 109, 1113 Sofia, Bulgaria

A model for numerical calculation of laser radiation penetration in enamel-dental tissue has been developed. For these numerical computations a phase function suitable for the specific case is used and statistical methods for modeling the behavior of photons in the turbid media are implemented. By means of this model, we can get an idea of the proportion of radiation that passes and that is dissipated inside the tissue. Similar calculations are convenient to guide us in the use of certain techniques for laser impact on the dental tissues.

Keywords: Penetration laser radiation, enamel-dental tissue, Monte-Carlo simulation

INTRODUCTION

The penetration of laser radiation in dental tissues is a very important process related with the interaction of this radiation with tissues and respectively its impact on their structure and properties. Understanding the light propagation in teeth is important for therapeutic laser applications [1, 2] or diagnostics. For the treatment of hard tooth tissue, the parameters of laser radiation should be precisely controlled. The exposure of the pulp to laser radiation depends on the penetration of this radiation through the enamel and dentin. Upon irradiation with laser radiation a fraction of the energy is absorbed in the enamel and dentin, which in turn leads to increase in their temperature. The evaluation of this thermal effect is an important procedure.

In this article we consider a model of passing series of photons with the same parameters in enamel-dentin structure. The estimates based on this model are made of the portion of photons absorbed into the enamel and dentin respectively (in percentage).By varying the parameters such as wavelength, anisotropic factor and thickness of the layers enamel and dentin we can estimate the absorption in the respective layers in these set parameters.

MODELING

The enamel is the hardest substance of the human body [3]. It is made ofapproximately 95% (by weight) hydroxyapatite, 4% water, and 1% organic matter. Hydroxyapatite is a mineralized compound with the chemical formula $Ca_{10}(PO_4)6(OH)_2$. Its substructure consists of tiny crystallites which form so called enamel prisms with diameters ranging from 4 μm to 6μm. This forms the inorganic apatite-like tooth surface [4]. The crystallattice itself is intruded by several impurities, especially Cl^-, F^-, Na^+, $K^+$and Mg^{2+}. The crystals are approximately 15 to 40 nm in the diameter and can be as long as 20 μm. Prisms are surrounded by a protein/lipid/water matrix.

The dentin, on the other hand, is much softer. Dentin can be described as a conglomerate of several compartments. Only 70% of its volumeconsists of hydroxyapatite, whereas 20% is organic matter − mainly collagen fibers − and 10% is water. The internal structure of dentin is characterizedby small tubuli which measure up to a few millimeters in length, and between100nm and 3 μm in diameter. These tubuli are essential for the growth of the tooth. It contains long tubules surrounded by the peritubular dentin. Between the tubules with their peritubular dentin lays intertubular dentin.

Intertubular dentin, in its turn, is divided into collagen fibrils and interfibrillar compartments. Except for the tubules all compartments contain mineral crystals of hydroxyapatite, which are needle shaped with an ~ 5 nm thickness and an ~ 20 nm length. The tubules have the diameter of 1 to 5 μm, and its density is 15 000–75 000 tubules per mm^2 [4]. They are uniformly oriented from the

*To whom all correspondence should be sent:
E-mail: hristokisov@iomt.bas.bg

enamel-dentin junction to the pulp, and so in a small sample they lay more or less parallel (Fig. 1).
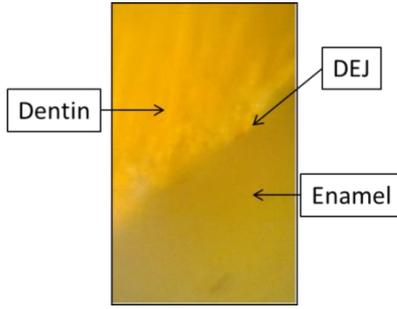
Fig. 1. Optical microscope picture of tooth structure - enamel, dentin and DEJ (dentin-enamel junction).

In stochastic models of photon transport through tissue, individual photon paths are simulated by considering the probability of absorption and scattering interactions. One of the most commonly used stochastic models is the Monte Carlo method.

The term Monte Carlo (MC) method (stochastic) refers to numerical simulations based on random sampling from appropriate probability distributions. Light is considered as a stream of particles (photons) that are injected into the medium, and move in straight lines through tissue between successive interactions. The advantages of the Monte Carlo method include simple implementation, the ability to handle any complex geometry and inhomogeneity, as well as the possibility to incorporate time-dependency. It is even possible to model wave phenomena such as polarization and interference. The main disadvantage is the inherently high computational cost.

Fig. 2 presents a simple model of enamel-dentin structure. There are denoted three layers of enamel, DEJ (dentin-enamel junction) [5, 6] and dentin through which passes the laser radiation.
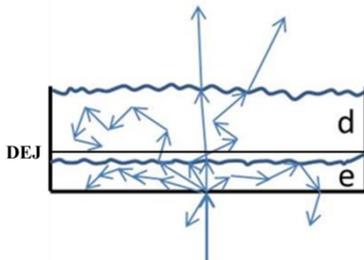
Fig. 2. Model of enamel-dentin structure representing the three successive layers – enamel, DEJ and dentin.

This radiation is represented as series of photons which sequentially enter perpendicularly to the surface of the enamel (the first layer) after which each of these photons undergoes reflection or multiple scattering in the structure with the result that the photon is reflected, absorbed or passes. We

model these processes with Monte Carlo [7, 8, 9] simulation and Henyey-Greenstein (HG) phase function [10], since this phase function is a good approximation of the light scattering in the turbid tissue. In our model, we consider the penetration of the laser radiation with a wavelength of 1,064μm in dental tissue. This laser radiation is directed along the normal to the surface of the tooth sample, and has the shape of a Gaussian pulse. For the intensity of this impulse we can write:

$$I = I_{max} \cdot e^{-2\frac{r^2}{\omega^2}} \tag{1}$$

where $r = \sqrt{x^2 + y^2}$, and ω is the width of the laser beam. In our case we have chosen r=0.1 mm and ω=1 mm.

The first assumption in our model is that for each particular step the number of photons in the pulse is proportional to the intensity. Thus at some initial value for the number of photons, the intensity value is close to the maximum and we can get values for the number of photons at other levels of intensity, using approximation for a given distribution. So with every step we take certain volume of the spatial distribution of energy in the pulse, which corresponds to the number of photons, entering through the surface of the tissue. It is clear that in this case, at each step the area through which the photons enter increases. In the model, this is done using Monte-Carlo simulation for each step.

Next assumption in our model is that the anisotropy factor **g** of DEJ is not a constant, but is a function of the coordinate **z**, i.e. it is a function of the depth of penetration of laser radiation. In this way we consider it appropriate to introduce a function in the form:

$$g(z) = (Ag_1 + Bg_2 \frac{1}{e^{\beta(z-z_0)}}) \tag{2}$$

where g_1 and g_2 are anisotropic factors for enamel and dentin respectively and **g(z)** is the anisotropy factor in junction. Coefficients A and B show which anisotropy dominates from the respective border. Here **z** denotes the current coordinate and z_0 corresponds to the coordinate at DEJ depth. Coefficient β indicates how deep the change of anisotropy in DEJ is.

If we assume also that the A=B=1/2 and coefficient β≈1 (in order to ensure almost complete anisotropy of DEJ in close proximity to the dentin), we can write:

$$g(z) = \frac{1}{2}\left(g_1 + \frac{g_2}{e^{(z-z_0)}}\right) \tag{3}$$

Also the coefficients of the scattering are a function of the wavelength [11]. These functions are introduced by their polynomial approximations. The parameters which are required to trace a

photon path through some arbitrary random medium are the local absorption coefficient μ_a, scattering coefficient μ_s, and scattering phase function. Scattering in tissue is characterized by the Henyey-Greenstein phase function:

$$p(\theta) = \frac{1}{4\pi}\frac{1-g_{1,2}^2}{\left(1+g_{1,2}^2-2g\cos\theta\right)^{3/2}} \qquad (4)$$

where g is the mean cosine of the scattering anisotropy angle θ. This coefficient g is called factor of anisotropy and is expressed as follows:

$$g = \int_0^\pi p(\theta)\cos\theta\,2\pi\sin\theta d\theta \qquad (5)$$

The assumption of random distribution of scatters in a medium, leads to normalization

$$\int_0^\pi p(\theta)\,2\pi\sin\theta d\theta = 1 \qquad (6)$$

Photons are emitted by a source and travel in straight lines until theyare scattered. The probability for a photon to be scattered after a distance $d\tau$ is defined by

$$p(\tau)d\tau = e^{-\mu_s\tau}d\tau \qquad (7)$$

Hence the cumulative probability of being scattered after travelling a distance τ is

$$\int_0^\tau e^{-\mu_s\tau'}d\tau' = 1 - e^{-\mu_s\tau} = \rho_1 \qquad (8)$$

where $\rho_1 \in$ [0...1] is a random number. Thus the distance between scattering events is given by

$$\tau = -\frac{1}{\mu_s}ln(\rho_1) \qquad (9)$$

The azimuthally and polar scattering angles, θ and ψ, relative to the previous direction of motion are given by

$$\psi = 2\pi\rho_2 \qquad (10)$$

$$\int_0^\theta p(\theta')\,d\theta' = \rho_3 \qquad (11)$$

where ρ_2 and $\rho_3 \in$ [0...1] are uniformly distributed random numbers.

Absorption can be taken into account either by terminating an absorbed photon's path or by introducing a weighting scheme. Thereby the photon's weight $W \in$ [0...1] is reducedbetween successive scattering events according to

$$W = W'e^{-\mu_a\tau}, \qquad (12)$$

where W is the weight before the interaction, and τ is the distance travelled since the lastscattering event. Photon paths are terminated when either the weight becomes negligible (by a predetermined value) the photon leaves the boundary or region of interest, or hits the detector. In the latter event the detection count rate is increased by the remaining photon weight W.

The possibility of internal reflection occurs when the photon is propagated across the boundary into the region with a different index of refraction. The probability that the photon will be internally reflected is determined by the Fresnel reflection coefficient $R(\theta_i)$

$$R(\theta_i) = \frac{1}{2}\left[\frac{sin^2(\theta_i-\theta_t)}{sin^2(\theta_i+\theta_t)} + \frac{tan^2(\theta_i-\theta_t)}{tan^2(\theta_i+\theta_t)}\right] \qquad (13)$$

Where $\theta_i = cos^{-1}\mu_z$ is the angle of incidence on the boundary and the angle of transmission θ_t is given by Snell's law

$$n_i\sin\theta_i = n_t\sin\theta_t \qquad (14)$$

where n_i and n_t are the indices of refraction of the medium from which the photon incident and transmits, respectively. The random number ρ_2 uniformly distributed between zero and unit is used to decide whether the photon is reflected or transmitted. If $\rho_2 < R(\theta_i)$ the photon is internally reflected, otherwise the photon exits the tissue and the event is recorded as backscattered light or transmitted light (when it exits the bottom). If the photon is internally reflected, then the position and direction of the photon is adjusted accordingly. For a slab geometry, infinite in the x and y directions with a thickness τ in the z-direction, the internally reflected photon position (x'', y'', z') is obtained by changing only the z-component of the photon coordinates

$$\left(x'', y'', z''\right) = \left(x, y, -z\right) \text{if } z < 0$$

$$\left(x'', y'', z''\right) = \left(x, y, 2\tau - z\right) \text{if } z < \tau \qquad (15)$$

The new photon direction (μ_x', μ_y', μ_z') is

$$\left(\mu_x', \mu_y', \mu_z'\right) = \left(\mu_x', \mu_y', -\mu_z'\right) \qquad (16)$$

and both μ_x and μ_y remain unchanged.

A normalized phase function describes the probability for density function for the azimuth and longitudinal angles for a photon when it is scattered. If the phase function has no azimuth dependence, then the azimuth angle $\psi$is uniformly distributed between 0 and 2π, and may be generated by multiplying a pseudo-random number ρ_2 uniformly distributed over the interval zero to one by 2π ($\psi = 2\pi\rho_2$). The deflection angle θ for an isotropic distribution is given by

$$\cos\theta = 2\rho_2 - 1 \qquad (17)$$

If a photon is scattered at an angle (θ, ψ) from the direction (μ_x, μ_y, μ_z) in which it is travelling, then the new direction (μ_x', μ_y', μ_z') is specified by

$$\mu_x' = \frac{\sin\theta}{\sqrt{1-\mu_z^2}}\left(\mu_x\mu_z\cos\psi - \mu_y\sin\psi\right) + \mu_x\cos\theta \qquad (18)$$

$$\mu_y' = \frac{\sin\theta}{\sqrt{1-\mu_z^2}}\left(\mu_y\mu_z\cos\psi + \mu_x\sin\psi\right) + \mu_y\cos\theta \qquad (19)$$

$$\mu_z' = -\sin\theta\cos\psi\sqrt{1-\mu_z^2} + \mu_z\cos\theta. \qquad (20)$$

RESULTS AND DISCUSSIONS

We performed numerical method Monte Carlo using a computer program designed for the specific case. Into the computer program we used the following coefficients, as shown in Table 1 [4,5]. The results of numerical calculation are presented in Table 2.

Table 1. Specific coefficients of enamel and dentin tissues

Coefficients	Enamel	Dentin
μ_a	<1,cm^{-1}	4, cm^{-1}
$\mu_s(\lambda)$	18, cm^{-1}	205, cm^{-1}
$g_{1,2}$	0,93	0,96
Thickness	1, mm	3, mm
$n_{e,d}$	1,63	1,54
Weight	10^{-4}	
λ	1064nm	

In Table 2 are presented coefficients for absorption in enamel (Abs1) and dentin (Abs2) respectively as well as reflectance (Ref) and transition (Tr) coefficients for this biological structure. These results were obtained by computer simulation program created by us in Matlab software package by implementation thirty numbers of calculations with a total number of 10^6 photons.

Table 2. Results of numerical calculation

Abs1	Abs 2	Ref	Tr
23%	66%	24%	0,34%

Computer calculations are shown graphically in Figs 3 - 4 for one case of photons penetrating in tooth tissue.

(a)

(b)
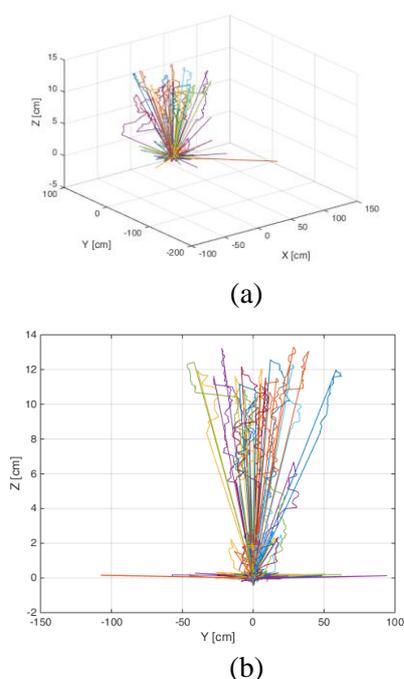
Fig. 3. (a) 3D view and (b) 2D (Y, Z axis) view of path of the penetrating photons.

Our calculations show that the assumptions made in the model are selected appropriately and the obtained results come close to the experimental results [12, 13]. For the transition of radiation through the dentine at [12] we have obtained experimentally 4% with a wavelength of 1064 nm, laser beam diameter 1 mm and incident energy of 10mJ. The thickness of the test slice is 1 mm. For this case we have a thickness of 3 mm, i.e. if is valid the Beer-Bouguer-Lambert law then we must have approximately 20 times greater attenuation of radiation. This means that in this case the photons will have a transition to the amount of 0.2 %. Computer calculations show value of 0.34 %.
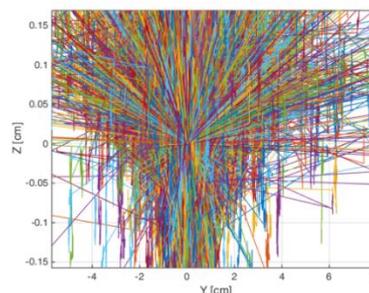
Fig. 4. Enlarged view of the photons path (Y, Zaxis).

CONCLUSIONS

Use and development of numerical methods, in particular methods based on Monte Carlo simulations are an essential part of the whole scientific study of penetration of laser radiation in turbid tissues. Monte Carlo modeling has been used for applying the technique to light dosimetry in tissue by receiving quantitative estimates of absorbed and transited radiation through various components of the tissue, which is very complex and difficult experimental process.

REFERENCES

1. A. Chan, A. Punnia-Moorthy, P. Armati, *Laser Therapy,* **23**, 4, 255 (2014).
2. M. De Magalhães, E. Matson, W. De Rossi, J. Alves, *Photomedicine and Laser Surgery*, **22**, 527(2004).
3. M. H. Niemz, Laser – Tissue Interaction, Springer, Berlin Heidelberg, 2007.
4. A. Kienle, F. K. Forster, R. Diebolder and R. Hibst, *Phys. Med. Biol.*, **48**, 2, N7 (2003).
5. S. Marshall, M.Balooch, S.Habelitz, G.Balooch, R. Gallagher, G. Marshall, *J. Eur. Cer. Soc.*, **23**, 2897(2003).
6. R. Gallagher, S. Demos, M. Balooch, G. Marshall, Jr., S. Marshall, in: Wiley Periodicals, 2002, p. 372.

7. C. Zhu and Q. Liu, *J. Biomed. Opt.*, **18**, 050902 (2013).

8. L. Wang, S. Jacques, L. Zheng, *Computer methods and programs in biomedicine*, **47**, 131 (1995).

9. E. Stoykova, O. Sabotinov, *Pros. SPIE*, **5449**, 474 (2004).

10. L. Henyey, J. Greenstein, "Diffuse radiation in the galaxy", *Astrophys. J.*, **93**, 70 (1941).

11. D. Fried, R. Glena, J. Featherstone, and W. Seka, *Appl. Opt.*, **34**, 7, 1278 (1995).

12. P. Uzunova, S. Rabadgiiska, T. Uzunov, H. Kisov, N. Kaimakanova, M. Deneva, E. Dinkov, M. Nenchev, *Proc. SPIE*, **8770**, 87701A (2013).

13. L. J. Miserendino and R. M. Pick (eds.), Laser in Dentistry, Quintessence Publ. Co, Inc, Chicago, 1995, p.300.

Моделиране на проникването на лазерно лъчение в емайл-дентинна тъкан

Хр. Кисов, Г. Дянков

Институт по оптически материали и технологии "Акад. Й. Малиновски", Българска Академия на науките, ул. "Акад. Г. Бончев", бл. 109, 1113 София, България

(Резюме)

В настоящата работа е развит модел за числено пресмятане на проникването на лазерно лъчение в емайл-дентин биологична тъкан. За численото пресмятане е използвана фазова функция, подходяща за дадения случай, както и статистически методи за моделиране на поведението на фотоните в мътна тъкан. От получените чрез този модел резултати можем да добием представа за преминалото лъчение и за лъчението, погълнато от тъканта. Подобни пресмятания ни помагат за подбора на определени техники за лазерно въздействие върху зъбна тъкан.

Terbium doped and europium doped NaAlSiO$_4$ nano glass-ceramics for LED application

I. Koseva*, P. Tzvetkov, P. Ivanov[1], A. Yordanova, V. Nikolov

Institute of General and Inorganic Chemistry, Bulgarian Academy of Sciences, 1113 Sofia, Bulgaria
[1]Institute of Optical Materials and Technologies, Bulgarian Academy of Sciences, 1113 Sofia, Bulgaria

Terbium doped and europium doped homogeneous glasses from the system Na$_2$O-Al$_2$O$_3$-SiO$_2$-NaBO$_2$ are prepared. Glass-ceramics are obtained after thermal treatment of the parent glass at different temperatures and time. The crystallizing phases, the degree of crystallinity and the particle size are determined. The main crystallizing phase after thermal treatment is NaAlSiO$_4$. X-ray analyses show the presence of Na$_2$SiO$_3$ as the second phase. The crystallinity degree after 24h thermal treatment at 650°C of the glass-ceramic samples is about 90%. The particle size for NaAlSiO$_4$ is between 50 and 60 nm, and for Na$_2$SiO$_3$ - between 30 and 70 nm. Emission and excitation spectra of the glass-ceramics show the characteristic peaks of Tb^{3+} and Eu^{3+}. The main emission peak of Tb^{3+} is $^5D_4 \rightarrow {}^7F_5$ transition at 549 nm, corresponding to green color. The Tb^{3+} excitation spectrum shows the strongest peak located at 379 nm. The main emission peak of Eu^{3+} is $^5D_0 \rightarrow {}^7F_2$ transition at 612 nm, corresponding to orange-red color. The Eu^{3+} excitation spectrum shows the strongest peak located at 393 nm.

Keywords: Silicate phosphor, Nano glass-ceramic, Rare-earth ions, X-ray, Photoluminescence

INTRODUCTION

Light emitting diodes (LED) are of special interest as they are environmental friendly and efficient energy saving devices [1, 2]. The commercial white LEDs (WLEDs) can be realized by combining a blue chip with yellow phosphor or by combining of blue, green and red (RGB) emitting tricolor multiphased phosphors [1, 3]. Therefore, it is important to investigate novel blue, red and green phosphors which show high emission intensities.

The luminescence behavior of the rare earth activated phosphors depends strongly on the composition of the host, concentration of the activator and methods of preparation [3]. Silicates are one of the most suitable materials because of their high chemical and mechanical stability and various crystal structures [2]. In addition, silicate glasses and glass-ceramics doped by rare earth ions are among the most commonly used materials for optical fibers, wave guides for opto-electronic communication and color display devices. Many investigations are published on Eu^{2+} and Mn^{2+} doped (Ba,Sr)3MgSi$_2$O$_8$ [4], Ce^{3+} and Tb^{3+} doped BaLu$_2$Si$_3$O$_{10}$ [5], Eu^{2+} doped Ba$_2$Zn$_3$Si$_3$O$_{11}$ [6], Ce^{3+} and Eu^{2+} doped Ca$_3$Si$_2$O$_7$

[7], Ce^{3+} and Mn^{2+} doped Ca$_3$Sc$_2$Si$_3$O$_{12}$ [8], Li$_2$SiO$_3$ doped by Er^{3+}, Eu^{3+}, Dy^{3+}, Sm^{3+}, Tb^{3+}, Ce^{3+} [9, 10], Eu^{2+} doped NaAlSiO$_4$ [11], Ce^{3+} and Mn^{2+} doped NaAlSiO$_4$ [12], Fe^{3+} doped NaAlSiO$_4$ [13], Eu^{2+} doped NaAlSiO$_4$ [14], Tb^{3+} doped NaAlSiO$_4$ [15], Dy^{3+} doped NaAlSiO$_4$ [16]. These compounds are synthesized by conventional solid state method or by sol-gel method. Compared with these phosphors and glasses, rare earth doped glass-ceramics are a good alternative because of the low cost preparation process, simple manufacturing procedure, free from halo effect. Mechanical, thermal, electrical and optical properties of the material could be improved by controlled heat treatment of the parent glass [17-19].

NaAlSiO$_4$ compound is with nepheline like structure.

The crystal structure of this compound is hexagonal with space group P63. It consists of AlO$_4$ and SiO$_4$ tetrahedra, connected with oxygen bridges. Charge compensation is achieved by incorporation of sodium cations in the cavities of the structure [20, 21]. At room temperature the nepheline compound also exists in different polymorphic modifications, depending on the method of preparation [22, 23]. These modifications transform themselves to hexagonal at 160 – 200°C [24].

*To whom all correspondence should be sent:
E-mail: ikosseva@svr.igic.bas.bg

NaAlSiO₄ glass-ceramics are investigated for optical and telecommunication systems applications, [19, 25], for medical applications [26, 27], for ceramic hot plates and microwave ovens [28]. The structure of NaAlSiO₄ allows doping by Rare Earth ions.

Tb^{3+} and Eu^{3+} doped phosphor materials have a strong excitation band in the near UV region. Tb^{3+} ion shows green emission due to $^5D_4 \rightarrow ^7F_5$ transition. The increase of Tb^{3+} concentration leads to decrease of emission intensity from $^5D_3$, which is due to cross relaxation between $^5D_3 \rightarrow ^7F_J$ and $^7F_J \rightarrow ^5D_4$ Eu^{3+} ion shows orange-red emission corresponding to $^5D_0 \rightarrow ^7F_1$ or $^5D_0 \rightarrow ^7F_2$ transitions [3, 10, 15].

In this paper we report our efforts to obtain Tb^{3+} and Eu^{3+} doped NaAlSiO₄ nano glass-ceramics for LED applications. To our knowledge this kind of investigations are not published to this moment.

EXPERIMENTAL

Na₂CO₃ (p.a.), Al₂O₃ (p.a.), SiO₂ (p.a.), H₃BO₃ (p.a.), Tb₄O₇ (p.a.) and Eu₂O₃ (p.a.) were used as row materials. Glass synthesis were carried out in a resistive furnace with Kantal heating wire permitted maximum working temperature of 1200 ºC and in a chamber furnace with MoSi₂ heating elements permitted maximum working temperature of 1550 ºC. The temperature was controlled with Pt/Pt–10%Rh thermocouple and Eurotherm controller. Glasses were melted in platinum crucibles. First the mixture was heated at 700 ºC for decomposition of the sodium carbonate and boric acid. Then the melt was heated at 1400 ºC during 4h for homogenization and obtained glass were cooled to the room temperature by quick removing from the furnace. Finally the glasses were thermally treated for establishing of the crystallizing phases. The structural characterization was carried out by powder X-ray diffraction using a Bruker D8 Advance powder diffractometer with Cu Ka radiation and SolX detector. X-ray diffractograms were recorded at room temperature. Data were collected in the 2θ range from 10 to 80º with a step 0.04º and 1 s step−1 counting time. X-ray diffractograms were identified using the Diffractplus EVA program. The mean crystallite size were calculated from the integral breadth of all peaks using Scherrer equation and the TOPAS 3 program 3 – General profile and structure analysis software for powder diffraction data, 2005, Bruker AXS, Karlsruhe, Germany. The area of the amorphous phase was

determined by using a straight line for description of the background and single line for fitting the amorphous component. The emission and excitation spectra where measured on Horiba Fluorolog 3-22 TCS spectrophotometer equipped with a 450 W Xenon Lamp as the excitation source. All spectra were measured at room temperature.

RESULTS AND DISCUSSION

Our previous investigations show, that the glasses from the system Na₂O-Al₂O₃-SiO₂-B₂O₃ are suitable for preparation of the glass-ceramics containing NaAlSiO₄ phase. For these investigations NaAlSiO₄-NaBO₂ = 66:34 component ratio was chosen and the concentration of the dopants was 0.25, 0.33 and 0.5 at% for Tb^{3+} or 0.1 at% for Eu^{3+} related to NaAlSiO₄. The experiments show that the maximal terbium concentration is 0.5 at.% and the maximal europium concentration is 0.1 at.%, at which the homogeneous glasses can be prepared in the described conditions.

The glasses were thermally treated at 650ºC during 2, 5 and 24 h for determination of the crystallizing phases, crystal part and mean particle size of the nano-crystals. These regimes were chosen on the base of our previous investigations. The result after thermal treatment at lower temperatures is a large glass part and small peaks of NaAlSiO₄. Thermal treatment of the glasses at 650ºC more than 5h leads to crystallization of NaAlSiO₄ and Na₂SiO₃ in both terbium and europium doped glasses. XRD patterns of the terbium doped glass treated at 650ºC during 24h is shown in Fig. 1.
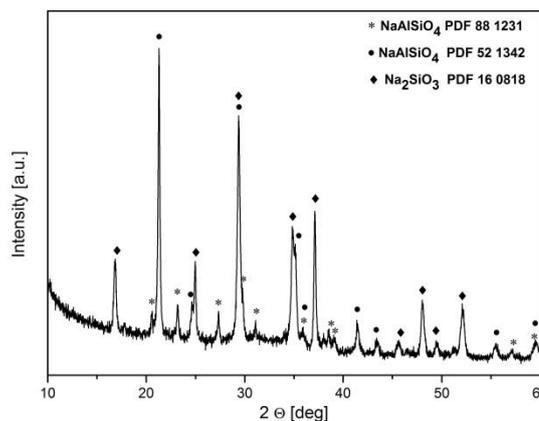
Fig. 1. XRD patterns of the terbium doped glass ceramic treated at 650ºC during 24h.

Crystal part of the samples doped by 0.5 at.% Tb^{3+} or 0.1 at.% Eu^{3+} treated at 650ºC with different duration and the ratio between two crystallizing phases $NaAlSiO_4$ and Na_2SiO_3 are presented in Table 1. As can be seen from the table, terbium makes the crystallization process more difficult in thermal treatment during 5h. So the crystallinity degree of terbium-doped glass-ceramic is 54%, while the degree of crystallinity of europium-doped glass-ceramic is 78%. The crystallinity degree after 24h thermal treatment is about 90%. XRD patterns of the samples treated at 650ºC for 5 and 24h, presented in Fig. 2, show the same tendency. The intensity of the peaks is in a good collation with the crystallinity degree.

Table 1. Crystal part of the samples doped by 0.5 at.% Tb^{3+} and 0.1 at.% Eu^{3+} treated at 650ºC with different duration [%] and ratio between two crystallizing phases $NaAlSiO_4$ and $Na_2SiO_3.$

Sample Time[h]	Tb:NaAlSiO₄	Eu:NaAlSiO₄
2	glass	
5	54% 68:32	78% 69:31
24	88% 71:29	90% 70:30
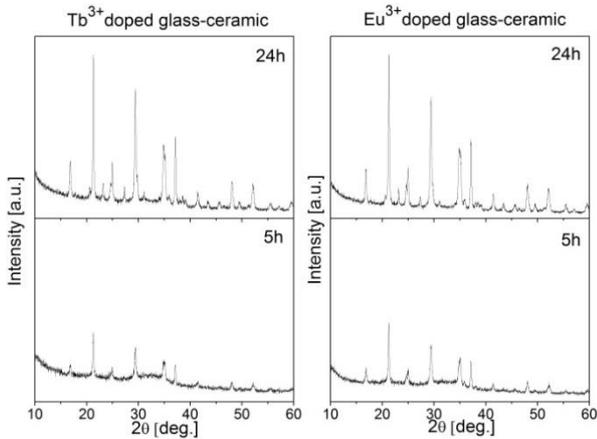
Fig. 2. XRD patterns of the samples doped by 0.5 at.% Tb and 0.1 at.% Eu treated at 650ºC during 5 and 24h.

The ratio between the two crystallizing phases $NaAlSiO_4$ and Na_2SiO_3 is 70:30 and does not depends on the dopants and thermal treatment time. The mean particle size for $NaAlSiO_4$ nanocrystals is between 50 and 60 nm and weak depend on the dopants and thermal treatment time. The particle size of Na_2SiO_3 nanocrystals is between 30 and 70 nm.

Emission and excitation spectra of 0.5 at.% Tb^{3+} doped sample and 0.1 at.% Eu doped sample treated at 650ºC during 24h are presented in Fig.

3. The Tb^{3+}:NaAlSiO₄ glass-ceramic excitation spectrum covers the range from 300 to 500 nm. The sample shows characteristic transitions of Tb^{3+}: $^7F_6 \to ^5H_7$ transition for 317 nm, $^7F_6 \to ^5D_2$ transition for 350 nm, $^7F_6 \to ^5L_{10}$ transition for 357 nm, $^7F_6 \to ^5D_3$ transition for 379 nm, and the $^7F_6 \to ^5D_4$ transition for 482 nm. These lines are attributed to the f–f transitions of Tb^{3+}. The strongest peak is located at 379 nm corresponding to the $^7F_6 \to ^5D_3$ transition.
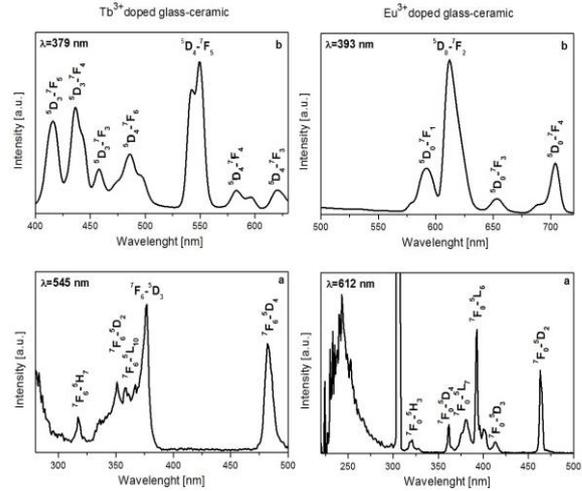
Fig. 3. Excitation (a) and emission (b) spectra of the 0.5 at.% Tb doped glass-ceramic sample and 0.1 at.% Eu doped glass-ceramic sample treated at 650ºC during 24h. CIE 1931 coordinates for Tb^{3+} doped sample x=0.23, y=0.27. CIE 1931 coordinates for Eu^{3+} doped sample x=0.45, y=0.29.

The main emission peak of Tb^{3+}:NaAlSiO₄ glass-ceramic is $^5D_4 \to ^7F_5$ transitions at 549 nm, corresponding to green color. Other transitions from $^5D_3 \to ^7F_5$, $^5D_3 \to ^7F_4$, $^5D_4 \to ^7F_6$, $^5D_4 \to ^7F_4$ and $^5D_4 \to ^7F_3$ are located at 415, 436, 458, 485, 583 and 620 nm [3, 29].

The Eu^{3+}:NaAlSiO₄ glass-ceramic excitation spectrum covers the range from 300 to 500 nm. The sample shows characteristic transitions of Eu^{3+}: $^7F_0 \to ^5H_3$ transition for 320 nm, $^7F_0 \to ^5D_4$ transition for 361 nm, $^7F_0 \to ^5L_7$ transition for 380 nm, $^7F_0 \to ^5L_6$ transition for 393 nm, $^7F_0 \to ^5D_3$ transition for 413 nm, and $^7F_0 \to ^5D_2$ transition for 463 nm. These lines are attributed to the f–f transitions of Eu^{3+}. The strongest peak is located at 393 nm corresponding to the $^7F_0 \to ^5L_6$ transition. The band around 250 nm is due to the charge transfer Eu^{3+}-O^{2-}.

The main emission peak of Eu^{3+}:NaAlSiO₄ glass-ceramic is $^5D_0 \to ^7F_2$ transitions at 612 nm, corresponding to orange-red color. Other

transitions from $^5D_0 \rightarrow ^7F_1$, $^5D_0 \rightarrow ^7F_3$ and $^5D_0 \rightarrow ^7F_4$ are located at 592, 653 and 704 nm. The red emission at 612 nm is an electric dipole transition and displays the highest intensity. The orange emission at 592 nm is allowed magnetic dipole transition. The second emission intensity is lower, which indicates that Eu^{3+} ions occupy sites without an inversion center [3, 30, 31].

Comparison of the samples with different concentrations of terbium ion is shown in Fig. 4. It is seen that the Tb^{3+} emission is the most intense at a concentration of 0.5 at% in the investigated concentration range.
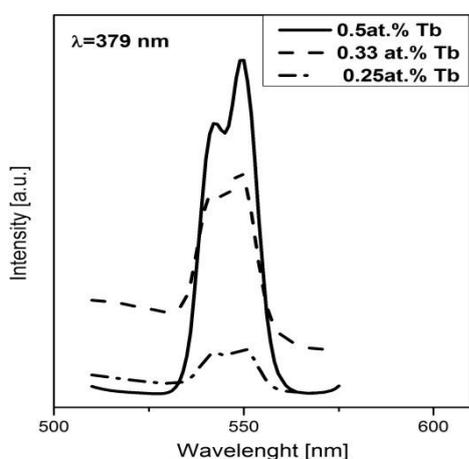
Fig. 4. The emission spectra of samples with different terbium ion concentration.

Comparison of the spectrum of Tb^{3+}:NaAlSiO₄ glass-ceramic with those of the sol-gel prepared Tb^{3+}:NaAlSiO₄ powder [15] show difference in the range 400-530 nm. The peaks in the first spectrum are more intensive and clearer. This may be due to the additional emission from some part of the glass and Na_2SiO_3 as the second phase. The spectrum of Eu^{3+}:NaAlSiO₄ glass-ceramic is very similar to the spectrum published for Eu^{3+} doped NaAlSiO₄-NaY₉Si₆O₂₆ glass-ceramic [31].

CONCLUSION

Terbium doped and europium doped homogeneous glasses from the system Na_2O-Al_2O_3-SiO_2-$NaBO_2$ are prepared with the highest concentration of the dopants 0.5 at% for Tb^{3+} and 0.1 mol% for Eu^{3+}. Glass-ceramics are obtained after thermal treatment of the parent glass at different treatment time. The main crystallizing phase after thermal treatment at 650 ℃ with different duration is NaAlSiO₄ and some presence of Na_2SiO_3 as a second phase is detected. The ratio between these two phases is 70:30. The crystallinity degree of the glass-ceramic samples could reach up to 90%. The particle size for the two crystallizing phases is between 30 and 70 nm. Emission and excitation spectra of the glass-ceramics show the characteristic peaks of Tb^{3+} and Eu^{3+}.

The obtained results show that as prepared terbium doped NaAlSiO₄ glass-ceramics could be used as a green phosphor. Europium doped NaAlSiO₄ glass-ceramics could be used as an orange-red phosphor. It would be interesting to find a suitable terbium and europium concentration into the glass-ceramics, giving the mix between these two colors.

REFERENCES

1. C. Lin, R. Liu, *J. Phys. Chem. Lett.,* **2**, 1268 (2011).
2. M. Shur, A. Zukauskas, *Proc. IEEE,* **93**, 1691 (2005).
3. W. Yen, S. Shionoya, H. Yamamoto, Phosphor Handbook, CRC Press, Boca Raton, 1998.
4. Q. Lu, J. Li, D. Wang, *Curr. Appl. Phys.,* **13**, 1506 (2013).
5. K. Li, S. Liang, H. Lian, M. Shang, B. Xing, J. Lin, *J. Mat. Chem. C*, (2016) (in press).
6. D. Wei, Y. Huang, S. Kim, Y. Yu, H. Seo, *Mater. Lett.,* **99**, 122 (2013).
7. L. Wenzhen, G. Ning, J. Yongchao, Z. Qi, Y. Hongpeng, *Opt. Mater.,* **35**, 1013 (2013).
8. Y. Liu, X. Zhang, Z. Hao, Y. Luo, X. Wang, L. Ma, J. Zhang, *J. Lumin.,* **133**, 21 (2013).
9. I. Sabikoglu, M.Ayvacıklı, A.Bergeron, A.Ege, N.Can, *J. Lumin.,* **132**, 1597 (2012).
10. Y. Naik, M. Mohapatra, N. Dahale, T. Seshagiri, V. Natarajan, S. Godbole, *J. Lumin.,* **129**, 1225 (2009).
11. D. Jo, Y. Luo, K. Senthil, K. Toda, B. Kim, T. Masaki, D. Yoon, *Opt. Mater.*, **34**, 696 (2012).
12. J. Zhou, T. Wang, X. Yu, D. Zhou, J.i Qiu, *Mat. Res. Bull.,* **73**, 1 (2016).
13. M. Nayak, T.R.N. Kutty, *Mater. Chem. Phys.,* **57**, 138 (1998).
14. G. Yuzhu, Y. Xibin, L. Jie, Y. Xuyong, *J. Rare Earth,* **28**, 34 (2010).
15. J. Dhoble, B. Kore, A. Yerpude, R. Kohale, P. Yawalkar, N. Dhoble, *Optik,* **126**, 1527 (2015).
16. A. Kumar, S. Dhoble, D. Peshwe, J. Bhatt, *J. Alloy. Compd.,* **609**, 100 (2014).
17. P. Babu, K. Jang, S. Rao, L. Shi, C. Jayashankar, V. Lavin, H. Seo, *Opt.Express,* **19**, 1836 (2011).
18. R. Krsmanovic, S. Bals, G. Bertoni, G. Tendeloo, *Opt. Mater.,* **30**, 1183 (2008).
19. D. Chen, W. Xiang, X. Liang, J. Zhong, H. Yu, M. Ding, H. Lu, Z. Ji, *J. Eur. Ceram. Soc.,* **35**, 859 (2015).

20. T. Hahn, M.J. Buerger, *Z. Kristallographie*, **106**, 308 (1955).
21. K. Tait, E. Sokolova, F. C. Hawthorne, *Can. Mineral.*, **41**, 61 (2003).
22. C. Henderson, J. Roux, *Contrib. Mineral. Petr.*, **61**, 279 (1977).
23. C. Henderson, A. Thompson, *Am. Mineral.*, **65**, 970 (1980).
24. H. Schneider, O. Flörke, R. Stoeck, *Z. Kristallographie*, **209**, 113 (1994).
25. M. Hirose, T. Kobayashi, K. Maeda, *Reports Res. Lab. Asahi Glass Co., Ltd.,* **55** (2005).
26. E. Hamzawya, E. El-Meliegy, *Mat. Chem. Phys.,* **112**, 432 (2008).
27. M. Wang, N. Wu, M. Hon, *Mat. Chem. Phys.,* **37**, 370 (1994).
28. J. Mac Dowell, *J. Am. Ceram. Soc.,* **58**, 258 (1975).
29. G. Blaase, B. C. Grabmeier, Luminescent materials, Springer (1994).
30. S. Lu, J. Zhang, *J. Lumin.,* **122**, 500 (2007).
31. R. Bagga, V. Achanta, A. Goel, J. Ferreira, N. P. Singh, D. Singh, V. Contini, M. Falconieri, G. Sharma, *Opt. Mater.,* **36**, 198 (2013).

ДОТИРАНА С ТЕРБИЙ И ЕВРОПИЙ НАНОРАЗМЕРНА СТЪКЛОКЕРАМИКА СЪДЪРЖАЩА NaAlSiO₄ ЗА ПРИЛОЖЕНИЕ КАТО ЛУМИНЕСЦЕНТЕН МАТЕРИАЛ

Йв. Косева, П. Цветков, П. Иванов[1], Ан. Йорданова, В. Николов

Институт по обща и неорганична химия, Българска академия на науките, 1113 София, България

[1]*Институт по оптични материали и технологии, Българска академия на науките, 1113 София, България*

(Резюме)

Синтезирани са дотирани с тербий и европий хомогенни стъкла от системата Na₂O-Al₂O₃-SiO₂-NaBO₂. Стъклокерамиката е получена след термично третиране на тези стъкла при различни температури с различна продължителност. Определени са кристализиращите фази, степента на кристалност и размера на частиците в стъклокерамиката. Основната кристализираща фаза след термично третиране е NaAlSiO₄. Рентгеновите анализи показват наличието на Na₂SiO₃ като втора кристализираща фаза. Степента на кристалност на стъклокерамиката след термично третиране при 650°C в продължение на 24 часа е около 90%. Размерът на частиците на NaAlSiO₄ е между 50 и 60 nm, а на Na₂SiO₃ – между 30 и 70 nm. Спектрите на емисия и възбуждане на стъклокерамиката показват характерните за йоните Tb³⁺ и Eu³⁺ пикове. Основният емисионен пик за Tb³⁺ се дължи на прехода $^5D_4 \rightarrow ^7F_5$ и е локализиран при 549 nm, отговарящ на зелен цвят. Спектърът на възбуждане показва най-интензивен пик при 379 nm. Основният емисионен пик за Eu³⁺ се дължи на прехода $^5D_0 \rightarrow ^7F_2$ и е локализиран при 612 nm, отговарящ на оранжево-червен цвят. Спектърът на възбуждане показва най-интензивен пик при 393 nm.

Preparation of chromium doped glass-ceramics containing NaAlSiO₄ and Na₃B₃O₆ phases

I. Koseva*, P. Tzvetkov, A. Yordanova, M. Marychev[1], V. Nikolov, O. Dimitrov[2]

Institute of General and Inorganic Chemistry, Bulgarian Academy of Sciences, 1113 Sofia, Bulgaria.
[1]N.I. Lobachevsky State University of Nizhni Novgorod, Nizhni Novgorod 603950, Russia
[2]Institute of Electrochemistry and Energy Systems, Bulgarian Academy of Sciences, 1113 Sofia, Bulgaria

Pure and chromium doped homogeneous glasses from the systems $Na_2O-Al_2O_3-SiO_2$ and $Na_2O-Al_2O_3-SiO_2-B_2O_3$ are prepared. Transparent glass-ceramics are obtained after thermal treatment of the parent glass at different temperatures and time. The crystallizing phases, the degree of crystallinity and the particle size are determined. Absorption and emission spectra are presented for the glass-ceramic sample with crystallizing phases $NaAlSiO_4$ and $Na_3B_3O_6$. The spectra show co-existing emission of the Cr^{3+} and Cr^{4+} ions and are discussed in the terms of Cr^{3+} and Cr^{4+} ions.

Keywords: $NaAlSiO_4$, chromium doped glass-ceramics, X-ray diffraction, absorption and emission spectra

INTRODUCTION

Tunable lasers are widely used in medicine and engineering. They allow customizing the laser radiation wavelength depending on the specific application. Especially attractive are lasers operating in the near infrared range (1.1 - 1.6 μm), important for optical communications, remote sensing and biomedical applications (as called eye-safe wavelength range). Suitable active ion emitting in this range is Cr^{4+} being in tetrahedral position. Therefore, a proper for Cr^{4+} doped laser matrix is particularly important. Obtaining of single crystals from many silicates, germinates and garnets is connected with different technological problems [1-10]. In recent years more researchers are interested in obtaining of glass-ceramics substituting the relevant single crystals. Chromium doped glass-ceramics obtaining is published for different compounds - $Cr^{4+}:Mg_2SiO_4$ [11], $Cr^{4+}:Ca_2GeO_4$ [12], $Cr^{4+}:LiGaSiO_4$ [13, 14], $Cr^{4+}:Li_2ZnSiO_4$ [15], $Cr^{4+}:Li_4SiO_4$ [16], $Cr^{4+}:YAG$ [17]. Most of these glass-ceramics are connected with too high glass melt and homogenization temperatures.

In this paper the investigation of Cr^{4+} doped glass-ceramics from the systems $Na_2O-Al_2O_3-SiO_2$ and $Na_2O-Al_2O_3-SiO_2-B_2O_3$ glasses is reported. Crystallizing from these glasses compound $NaAlSiO_4$ is with nepheline like structure. The crystal structure is hexagonal with space group $P6_3$. It consists of AlO_4 and SiO_4 tetrahedra, connected with oxygen bridges [18, 19]. Nepheline compound exists at room temperature also in different polymorphic modifications, depending on the method of preparation [20-22]. Non-doped nepheline glass-ceramics were investigated for optical and telecommunication systems applications [23], for medical applications [24, 25], for ceramic hot plates and microwave ovens [26].

The presence only of AlO_4 and SiO_4 tetraherda in the nepheline structure is favorable for doping of the matrix with chromium ion in 4+ state of oxidation. To our knowledge this kind of investigations are not published to this moment.

EXPERIMENTAL

Na_2CO_3 (p.a), Al_2O_3 (p.a), SiO_2 (p.a.), H_3BO_3 (p.a.) and Cr_2O_3 (p.a.) was used as row materials. Glass synthesis were carried out in a resistive furnace with Kantal heating wire permitted maximum working temperature of 1200^oC and in a chamber furnace with $MoSi_2$ heating elements permitted maximum working temperature of 1550^oC. The temperature was controlled using a Pt/Pt–10%Rh thermocouple connected to a Eurotherm controller. Glasses of the desired compositions were melted in platinum crucibles. First the mixture was heated at 700^oC for decomposition of the carbonates and boric acid and then the powder was heated at the proper

* To whom all correspondence should be sent:
E-mail: ikosseva@svr.igic.bas.bg

temperature for homogenization. As obtained glass were cooled to the room temperature by quick removing from the furnace. Some of the glasses were quenched by pouring onto a steel plate and pressing with another steel plate. The prepared glasses were thermally treated for phase nucleation into the glass. Structural characterization was carried out by powder X-ray diffraction (XRD) using a Bruker D8 Advance powder diffractometer with Cu Kα radiation and SolX detector. X-ray diffractograms were recorded at room temperature. X-ray diffractograms were identified using the Diffractplus EVA program. The mean crystallite size was calculated from the integral breadth of all peaks (Pawley fit) using Scherrer equation and the TOPAS 3 program.3 – General profile and structure analysis software for powder diffraction data, 2005, Bruker AXS, Karlsruhe, Germany. The area of the amorphous phase was determined by using a straight line for description of the background and single line for fitting the amorphous component. The particle morphology were determined using a Transmission electron microscopy JEOL model JEM 200 CX accomplished with EM-ASID3D scanning attachment, working in secondary electrons regime. Specimens were covered with carbon-gold film. The particle size distribution was determined by the micrographs using Lince v2.4 – Linear Intercept program. The UV–Vis spectra were taken with a Thermo Evolution 300 UV-Vis Spectrophotometer equipped with a Praying Mantis device. The emission spectra where measured with 813.4 nm excitation by laser diode ATC-C1000-100-TMF-808-10. InGaAs ID-441-C was as detector in near infrared. The emissions from a black body specimen at determined temperature were utilized for standardization of the data. All spectra were established at room temperature.

RESULTS AND DISCUSSION

Two series of glasses were synthesized:

1. Glasses from the system $Na_2O.Al_2O_3.2SiO_2$-$Na_2O.SiO_2$ with different ratio between the two phases. The ratio is conforming to the phase diagram Na_2O-Al_2O_3-SiO_2 [27, 28]. The glasses are with eutectic composition between $Na_2O.Al_2O_3.2SiO_2$-$Na_2O.SiO_2$ at 915ºC or on the isotherms at 768 and 900ºC in the field of nepheline crystallization;

2. Glasses from the system $NaAlSiO_4$-$NaBO_2$. It was expected that $NaBO_2$ decrease the melting and homogenization temperature of the glass and by increasing of the viscosity to suppress the glass crystallization during its cooling.

The obtained glasses were thermally treated at different temperatures and with different duration. The content of the glasses, the homogenization temperatures, the homogenization time, the thermal treatment temperatures, the thermal treatment time and the crystallizing phases obtained after thermal treatment are listed in Table 1.

As can be seen from the table, for the glasses numbered from 1 to 4 higher temperature for homogenization is required, but the process time is shorter. In the opposite, the glasses containing B_2O_3 numbered from 5 to 7, homogenized at significant lower temperature (200ºC lower). At this lower temperature the evaporation of B_2O_3 is absent. Of course, the homogenization time in this case is longer. In all investigated glasses under the described conditions of thermal treatment except the desire phase another phases are observed. In the glasses 1, 2 and 4 this phase is Na_2SiO_3 (Fig. 1). In the borate glasses the second phase depends on the content of the chromium oxide. In non-doped glass crystallizes $NaBO_2$ (Fig. 2a). In the glasses doped by 5 at.% Cr, a part of Cr_2O_3 crystallizes as a second phase (Fig. 2b). The quantity of the Cr_2O_3 decreases with increasing of the treatment time. **IN** the glasses doped by 2 at.% Cr, $Na_3B_3O_6$ crystallizes as a second phase (Fig. 2c). We choose to investigate more detailed glasses with composition 7. This glass could be obtained at lower temperature. In addition, the desired phase $NaAlSiO_4$ mainly crystallize after thermal treatment and non-desired Cr_2O_3 do not crystallize. X-ray patterns of the received glass-ceramic samples treated at different temperatures and time using the glass composition 7 are presented on Fig 3. The results for crystal part of some samples, calculated from the X-ray patterns, the glass transparency evaluated microscopically and the particle size, calculated according to Sheerer equation are given in Table 2.

As can be seen, the crystallinity part and the transparency are in good agreement. Glass treated at 540ºC for 4 h is 58% crystallized and transparent. Glasses treated at 560ºC for 2 and 4 h are 28 and 73% crystallized respectively and transparent. Glasses treated at 560ºC for 8 h and at 580ºC for 4 h are 100% crystallized and opaque. So, the time treatment has a greater influence in the beginning of the crystallization. After treatment more than 4 hours the crystallization rate decreases. The opposite effect is observed in the temperature dependence – as the temperature is higher, the greater part of the glass crystallizes, but the process speed is lower up to 560ºC.
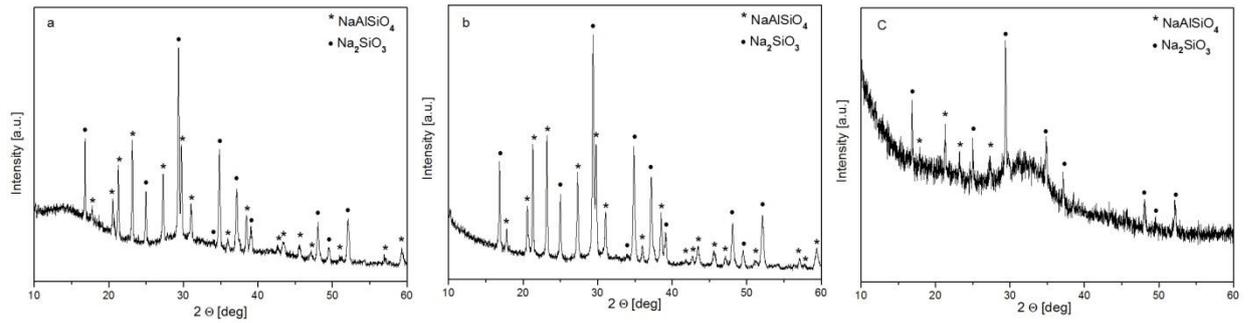
Fig. 1. XRD patterns of the glass-ceramics obtained from the glass compositions numbered 1, 2 and 4 treated at 700ºC 24h (a), 600ºC 24h (b) and 600ºC 16h (c) respectively.

Table 1. Glass composition, thermal treatment temperatures, thermal treatment time and crystallizing phases obtained after thermal treatment.

	Glass composition [wt%]	Homogenization temperature [°C]	Duration [h]	Thermal treatment temperature [°C]	Duration [h]	Crystalized phases after thermal treatment
1.	$Na_2O.Al_2O_3.2SiO_2$-$Na_2O.SiO_2$ = 47:53 2 at% Cr Eutectic at 915°C	1300°C	3	700°C 700°C	1 24	glass $NaAlSiO_4$ Na_2SiO_3
2.	$Na_2O.Al_2O_3.2SiO_2$-$Na_2O.SiO_2$ = 47:53 5 at% Cr Eutectic at 915°C	1300°C	3	600°C 600°C	16 24	$NaAlSiO_4$ Na_2SiO_3 $NaAlSiO_4$ Na_2SiO_3
3.	$Na_2O:Al_2O_3:2SiO_2$ = 30:11.5:58.5 Isotherm at 768°C	No homogenization	6			
4.	$Na_2O:Al_2O_3:2SiO_2$ = 37:13:50 5 at% Cr Isotherm 900°C	1300°C	3	600°C	16	$NaAlSiO_4$ Na_2SiO_3
5.	$NaAlSiO_4$-$NaBO_2$ = 63:37	1100°C	24	550°C	16	$NaAlSiO_4$ $NaBO_2$
6.	$NaAlSiO_4$-$NaBO_2$ = 66:34 5 at% Cr	1100°C	24	500°C 520°C 550°C	24 16 4 12 16	glass glass $NaAlSiO_4$ Cr_2O_3
7.	$NaAlSiO_4$-$NaBO_2$ = 66:34 2 at%	1100°C	24	540°C 560°C 580°C	4 8 12 16 2 4 8 12 1 2 4 8	$NaAlSiO_4$ $Na_3B_3O_6$ $NaAlSiO_4$ $Na_3B_3O_6$ $NaAlSiO_4$ $Na_3B_3O_6$

Fig. 2. XRD patterns of the glass-ceramic obtained from glass composition numbered from 5 to 7. (a) – composition 5 treated at 550°C 16h; (b) - composition 6 treated at 550°C 12h; (c) composition 7 treated at 580°C 8h.
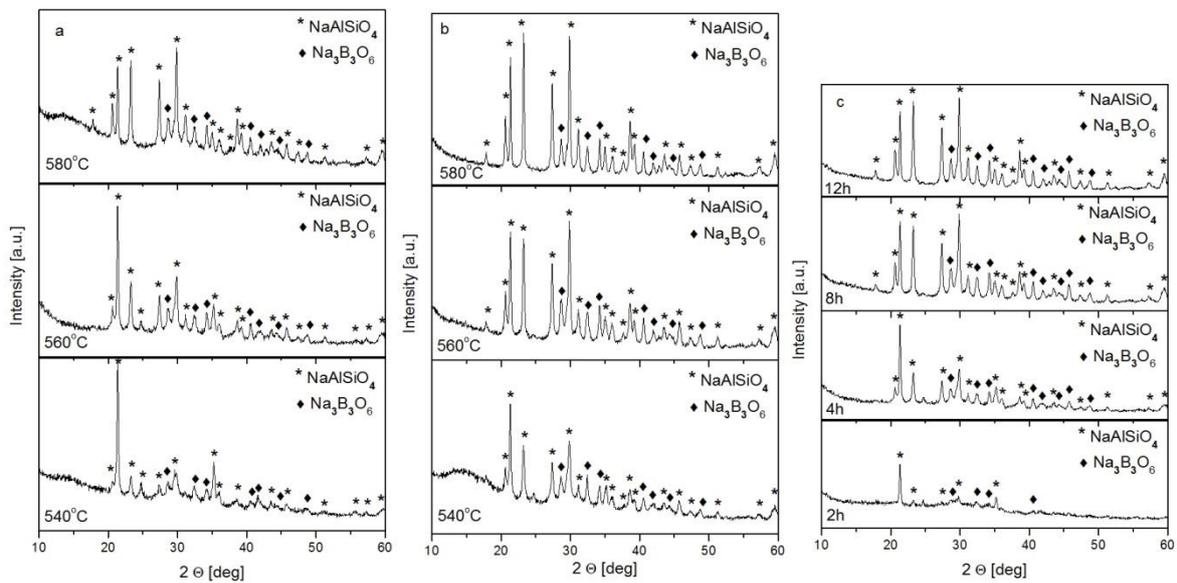
Fig. 3. XRD patterns of the glass-ceramic obtained from the glass with composition numbered 7 treated at (a) 540, 560 and 580°C during 4h; (b) 540, 560 and 580°C during 8h; (c) 560°C during 2, 4, 8 and 12h.

Table 2. Crystallinity part into the parent glass [%], transparency and particle size [nm] of the thermal treated samples:

Time °C	1	2	4	8	12	16
540			58% Transparent 45 nm	Translucent 28 nm	Opaque 34 nm	Opaque 36 nm
560		28% Transparent 30 nm	73% Transparent 35 nm	100% Opaque 35 nm	Opaque 40 nm	
580	Transparent 41 nm	Translucent 35 nm	100% Opaque 36 nm	Opaque 50 nm		

The particle size is in the range 30-50 nm and weak depends on the temperature and the time treatment. This results show that after the beginning of the crystallization, the increasing of the time treatment or increasing the temperature leads not to expanding of the seeds, but to arising of the new particles.

SEM micrographs of the different part of the glass-ceramic treated at 560°C during 4 hours are presented on Fig. 4 a, b, c. The particles are located predominantly on the surface of the sample. They

are relatively regular distributed between 5 and 45 nm and with an average size of 25 nm. The particle distribution is presented on Fig. 4d.
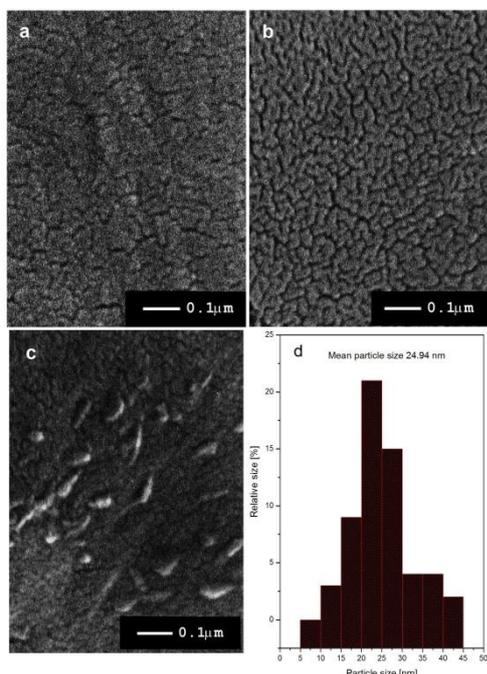
Fig. 4. SEM micrographs of the glass and different part of the glass-ceramic treated at 560ºC during 4 hours: (a) – glass, (b) – center of the glass-ceramic, (c) – edge of the glass-ceramic and (d) - particle distribution and average particle size of the same glass-ceramic.

Absorption spectra of the glass and glass-ceramic samples (Fig. 5a) show similar chromium ions absorption bands belonging. The absorption spectra consist of strong absorption bands between 520 and 760 nm and the weak band near infrared absorption between 800 and 1100 nm. According to the literature [12, 29], in the region 520-800 nm the strong band is $^4A_2 \rightarrow {}^4T_2$ transition of the Cr^{3+} ion. Maximum in our glass and glass-ceramic is observed at 625 nm. Multiplet bands at 650 nm may be caused to the of $^3A_2 \rightarrow {}^3T_1$ transition of Cr^{4+}. The $^3A_2 \rightarrow {}^3T_1$ absorption band of the tetrahedral Cr^{4+} centers overlap with the $^4A_2 \rightarrow {}^4T_2$ absorption band of octahedral Cr^{3+} centers. Another band from 800 to 1100 nm is due to $^3A_2 \rightarrow {}^3T_2$ transition of Cr^{4+}. There is more intense absorbance in the glass-ceramic sample compared with the initial glass. So, absorption spectra show the different oxidation state of chromium ions (Cr^{3+} and Cr^{4+}).

The emission spectra (Fig. 5b) overlap from 1000 to 1500 nm. There is a strong peak at 1067 nm and a weak and wide one at 1340 nm. The emission spectra shows different oxidation states of the chromium ions in the glass-ceramic samples. In accordance to the absorption spectra the first emission peak could be attributed to $^4T_2 \rightarrow {}^4A_2$ of Cr^{3+} ions and second peak is attributed to $^3T_2 \rightarrow {}^3A_2$ of Cr^{4+} in tetrahedral occupation. Such summarized emission spectra is expected [12, 30], taking into account the existence of three matrix (residual glass, $NaAlSiO_4$ and $Na_3B_3O_6$), where the chromium ion could be incorporated.
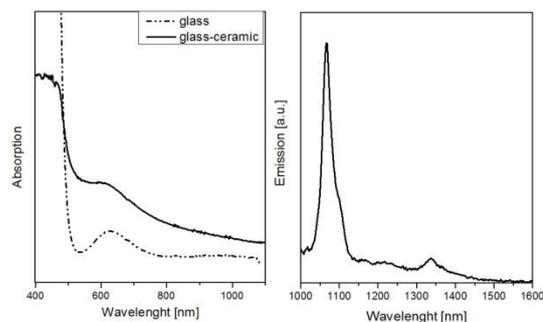
Fig. 5. Absorption and emission spectra of the glass-ceramic samples obtained from the glass with composition numbered 7 treated at 580ºC for 1 hour.

CONCLUSION

Pure and chromium doped homogeneous glasses from the systems Na_2O-Al_2O_3-SiO_2 and Na_2O-Al_2O_3-SiO_2-$NaBO_2$ are prepared. Transparent glass-ceramics are obtained after thermal treatment of the parent glass at different temperatures and time. The crystallizing phases, the degree of crystallinity and the particle size are determined. In all thermal regimes $NaAlSiO_4$ appears. Except $NaAlSiO_4$, different phases crystallize depending on the glass-composition and treatment conditions. The glass-ceramics are transparent to the crystallization degree of about 75%. The mean particle size is about 25 nm and weak depends on the thermal treatment time and the thermal treatment temperature. Absorption and emission spectra of the sample with crystallizing phases $NaAlSiO_4$ and $Na_3B_3O_6$ doped by 2 at% Cr show co-existing of the Cr^{3+} and Cr^{4+} ions and are discussed in the terms of Cr^{3+} and Cr^{4+} ions.

REFERENCES

1. V. Petričević, S. Gayen, R. Alfano, K. Yamagishi, H. Anzai, Y. Yamaguchi, *Appl. Phys. Lett.*, **52**, 1040 (1988).
2. H. R. Verdun, L. M. Thomas, D. M. Andrauskas, T. McCollum, A. Pinto, *Appl. Phys. Lett.*, **53**, 2593 (1988).
3. L. Yang, V. Petricevic, R. R. Alfano, in: Novel laser sources and applications: Proc. workshop, Nov.12-13, 1993, San Jose, California, *USA, 1993*, p. 103.

4. R. Alfano, A. Bykov, V. Petricevic, US Patent 7,440,480 (2008).

5. A. Bykov, V. Petricevic, J. Steiner, Di Yao, L. Isaacs, M. Kokta, R. Alfano, J. Cryst. Growth, 211, 295 (2000).

6. K. Soubbotin, E. Zharikov, L. Iskhakova and S. V. Lavrishchev, *Crystallogr. Rep.,* **46**, 1030 (2001).

7. K. Subbotin, L. Iskhakova, E. Zharikov, S. Lavrishchev, *Crystallogr. Rep.,* **53**, 1107 (2008).

8. C. Anino; J. Thery, D. Vivien, in Tunable Solid State Lasers, Intern. Soc. Optics and Photonics, 1997, p. 38.

9. A. Sugimoto, Y. Nobe, K. Yamagishi, *J. Cryst. Growth* **140,** 349 (1994).

10. M. Jazi, M. D. Baghi, M. Hajimahmodzadeh, M. Soltanolkotabi, *Optics & Laser Technol.,* **44,** 522 (2012).

11. A. Ulyashenko, N. Nikonorov, A. Przhevuskii, *B. Russ. Acad. Sci.: Physics*, **71**, 159 (2007).

12. M. Sharonov, A. Bykov, T. Myint, V. Petricevic, R. Alfano, *Opt. Commun.*, **275**, 123 (2007).

13. K. Subbotin, V. Smirnov, E.. Zharikov, L. Iskhakova, V. Senin, V. Voronov, I.. Shcherbakov, *Opt. Mater.,* **32**, 896 (2010).

14. K. Subbotin, S. Arakelian, V. Voronov, V. Senin, M. Gerke, V. Smirnov, D. Nikolaev, E. Zharikov, I. Shcherbakov, *J. Cryst. Growth*, **328**, 95 (2011).

15. Y. Zhuang, Y. Teng, J. Luo, B. Zhu, Y. Chi, E. Wu, H. Zeng, J. Qiu, *Appl. Phys. Lett.,* **95**, 111913 (2009).

16. D. Deng, S. Xu, H. Ju, S. Zhao, H. Wang, C. Li, *Chem. Phys. Lett.,* **486,** 126 (2010).

17. J. Dong, K. Ueda, A. Shirakawa, H. Yagi, T. Yanagitani, A. A. Kaminskii, *Opt. Express,* **15**, 14516 (2007).

18. T. Hahn, M. Buerger, *Z. Kristallogr.*, **106**, 308 (1955).

19. K. Tait, E. Sokolova, F. Hawthorne, *The Can. Mineral.*, **41**, 61 (2003).

20. C.M.B. Henderson, J. Roux, *Contrib. Mineral. Petr.*, 61, 279 (1977).

21. C. Henderson, A. Thompson, *Am. Mineral.*, **65**, 970 (1980).

22. H. Schneider, O. Flörke, R. Stoeck, *Z. Kristallogr.*, **209**, 113 (1994).

23. M. Hirose, T. Kobayashi, K. Maeda, *Reports Res. Lab. Asahi Glass Co., Ltd.,* **55** (2005).

24. E. Hamzawya, E. El-Meliegy, *Mater. Chem. Phys.*, **112**, 432 (2008).

25. M. Wang, N. Wu, M. Hon, *Mater. Chem. Phys.,* **37**, 370 (1994).

26. J. Mac Dowell, *J. Am. Ceram. Soc.* **58**, 258 (1975).

27. E. Levin, *Phase Diagrams for Ceramists*, Columbus, Ohio: American Ceramic Society, (1956), p. 96.

28. G. Kostorz, H. Herman. *Phase diagrams in advanced Ceramics*. Ed. Allen M. Alper, Elsevier, 1995.

29. C. Jousseaume, D. Vivien, A. Kahn-Harari, B.Z. Malkin, *Opt. Mater.,* **24**, 143 (2003).

30. S. Morimoto, *J. Ceram. Soc. Jpn.,* **112**, 486 (2004).

ПОЛУЧАВАНЕ НА ДОТИРАНА С ХРОМ СТЪКЛОКЕРАМИКА СЪДЪРЖАЩА NaAlSiO$_4$ И Na$_3$B$_3$O$_6$

Йв. Косева, П. Цветков, Ан. Йорданова, М. Маричев[1], В. Николов, О. Димитров[2]

Институт по обща и неорганична химия, Българска академия на науките, 1113 София, България
[1]Нижни Новгородски университет „Н.И. Лобачевски", Нижни новгород 603950, Русия
[2]Институт по електрохимия и енергийни системи, Българска академия на науките, 1113 София, България

(Резюме)

Синтезирани са чисти и дотирани с хром хомогенни стъкла от системите Na$_2$O-Al$_2$O$_3$-SiO$_2$ и Na$_2$O-Al$_2$O$_3$-SiO$_2$-B$_2$O$_3$. Прозрачни стъклокерамики са получени след термично третиране на стъклата при различни температури и с различна продължителност. Определени са кристализиращите фази, степента на кристализация и размерът на частиците. Представени са спектри на абсорбция и емисия за стъклокерамични образци с кристализиращи фази NaAlSiO$_4$ и Na$_3$B$_3$O$_6$. Спектрите показват едновременното присъствие на йони Cr^{3+} и Cr^{4+} и са обсъдени от гледна точка на енергетичните нива на йоните Cr^{3+} и Cr^{4+}.

3D profilometry of the fracture line in endodontically treated premolars, restored with metal posts

E. Karteva[1,*], N. Manchorova[1], T. Babeva[2], D. Pashkouleva[3], S. Vladimirov[1]

[1]*Department of Operative Dentistry and Endodontics, Faculty of Dental Medicine,*
Medical University – Plovdiv, Bulgaria
[2]*Institute of Optical Materials and Technologies, Bulgarian Academy of Sciences, Bulgaria*
[3]*Institute of Mechanics, Bulgarian Academy of Sciences, Bulgaria*

Endodontically treated teeth tend to be more fragile and susceptible to fracture than vital ones. There are numerous techniques used for their restoration, but the assessment of the survival rates is limited because of the difficulties in diagnostics. The aim of our study was to investigate the application of 3D profilometry for the visualization of cracks and vertical root fractures in endodontically treated teeth. Eighteen extracted premolars, restored with prefabricated metal posts and composite resin, were used. They were divided into 3 groups according to the extent of lost coronary hard dental tissues. After thermocycling, they were tested in a standard mechanical test machine until fracture. The fracture lines were visualized using 3D Profilometry. The results showed deeper, wider cracks with a vertical direction towards the apex of the roots in the groups with extensive tissue loss. In conclusion, 3D profilometry proved to be a quick, easy and highly informative method for assessing vertical root fractures.

Keywords: profilometry, fracture resistance, premolars, vertical root fractures, cracks.

INTRODUCTION

Endodontic treatment is usually associated with a reduction in the fracture resistance and the resilience of the treated teeth [1]. This leads to an increased number of vertical root fractures (VRF), extraction of the tooth and subsequent prosthodontic treatment [2]. The reduced mechanical properties of endodontically treated teeth (ETT) could arise from a variety of factors: changes in the moisture content of dentin with aging and loss of pulp tissue [3], disintegration of the organic matrix [4], the extent of tooth structure reduction, as well as the restorative procedures used. The different treatment options include: size, diameter, length and material of the cemented post, the presence of a ferrule and the cementation of an appropriate crown [5].

The influences of these factors have been extensively studied. Nevertheless, the options for the assessment and visualization of the cracks and fractures of ETT, remain limited. In many cases, the VRF are not diagnosed until after the extraction of the tooth in question. The prevalence of fractures reported in clinical practice varies between 8.8 – 10.9 % [6, 7]. Still, the real percentage is believed to be much higher, the reason being the difficulties in diagnosing and assessing them.

3D profilometry is a fast, accessible and highly informative contemporary method for the measurement of a surface's profile. It provides both qualitative and quantitative information of the examined object's roughness and topography. One of the main advantages of profilometry is that there is no need for any preliminary sample preparation and there is no contact with the sample's surface. Therefore, the objects involved in the study cannot be damaged in any way.

The highly detailed information, provided by the method, is ideal for registering the subtle changes that can occur in hard dental tissues. In dentistry, it has been mainly used for the evaluation of enamel surfaces after treatment with different abrasive techniques [8]. Another possible application is for the assessment of the qualities of new dental materials, such as orthodontic wires that can lessen biofilm adaptation, reduce friction and improve corrosion resistance [9].

There is no available information in the literature about the use of 3D profilometry in the studying of vertical root fractures. Therefore, the aim of our experiment was to explore the potential

* To whom all correspondence should be sent:
E-mail: katya.kk@gmail.com

of this technique in assessing the depth, width and topography of cracks that occur in ETT.

MATERIALS AND METHODS

Eighteen human, single root premolars, free of cracks and defects were extracted for orthodontic or periodontal reasons. They were stored in 0.2% thymol solution for no longer than three months. The bucco-lingual and mesio-distal widths of the crowns were measured and only teeth of similar sizes were selected for the experiment. They were divided in 3 groups (n=6): teeth with a prepared endodontic cavity only (E), teeth prepared with a mesio-occlusal cavity (MO) and teeth prepared with a messio-occlusal-distal cavity (MOD). All of the samples were restored with rigid, passive stainless steel prefabricated posts and composite resin.

The teeth were then thermocycled for 5000 cycles between 5±5°C and 55±5°C (LTC 100, LAM Technologies, Italy). Subsequently, their roots were embedded in self-curing resin to a level 2 mm apical to the cementoenamel junction (CEJ) using a modified technique, proposed by Soares et al. [10]. The periodontal ligament was simulated using a polyether-based impression material (Impregum Garant L Duo Soft, 3M ESPE).
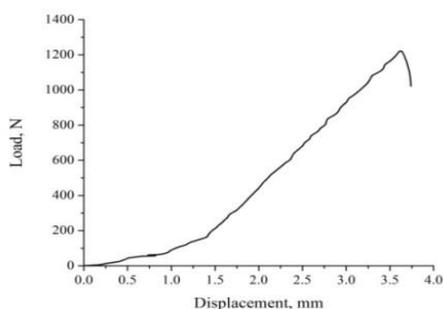
Fig. 1. Typical load-strain diagram of premolars, restored with metal posts.

The specimens were loaded in compression along the axis of the tooth until failure in an universal testing machine Fu1000e at a cross-head speed 4mm/min. For each groups, a diagram of the load at initial fracture was recorded (Fig. 1). Afterward, the mean failure loads were calculated. One-way analysis of variance (ANOVA) was applied to determine statistically significant differences. The significance level was established at a P value < 0.05. They were then examined under

magnification for fracture lines determination. One representative tooth of each group was selected for examination with 3D profilometry. The profilometer used was Zeta-20 (Zeta Instruments) with vertical resolution <1 mm, field of view between 0.006 mm^2 and 15 mm^2 and magnification of 5x, 20x, 50x and 100x. The examined region of the tooth was the coronal 1/3 of the root for all the specimens. At each Z position, the profiler records the XY location and the precise Z height of the pixels and this information is used to create a true color 3D image and a 2D composite image.

RESULTS AND DISCUSSION

The summarized results of the width and depth of the examined cracks are presented in Table 1.

Table 1. Width and depth of the cracks for each of the representative teeth (E – endodontic cavity, MO – mesio-oclusal cavity, MOD – mesio-occlusal-distal cavity).

Group	Width (μm)	Depth (μm)
E	3.2 – 6.5	4 – 7.8
MO	25 – 28	14 – 31. 7
MOD	96.7 – 107.6	68.4 – 148.6

A 3D image of the surface topography for each representative tooth is presented in Fig. 2 – Fig. 4.
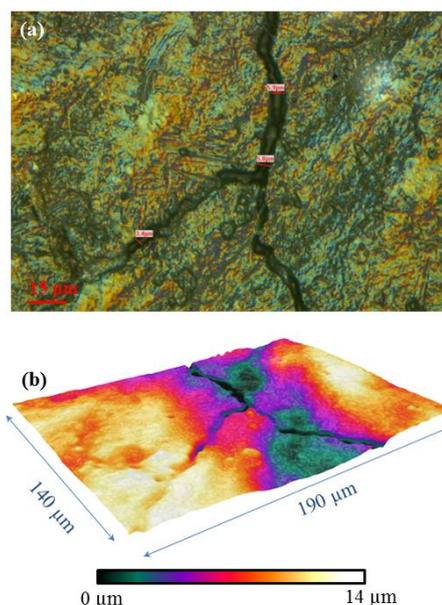
Fig. 2. Topography of the representative sample from group E (50x magnification).

In endodontics, 3D profilometry has been mainly used for the assessment of dentin's roughness, after treatment with different

medicaments. Yassen et al. investigated the effect of various endodontic regeneration protocols (NaOCl, CaOH, EDTA and antibiotic paste) on dentin [11]. The surface roughness was characterized using optical profilometry and the results showed a significant increase in the groups treated with a combination of NaOCl and EDTA. A different approach was successfully attempted by Larimer et al. [12]. Instead of using profilometry on hard dental surfaces, they attempted to measure the biofilm thickness from initial colonization to maturity.
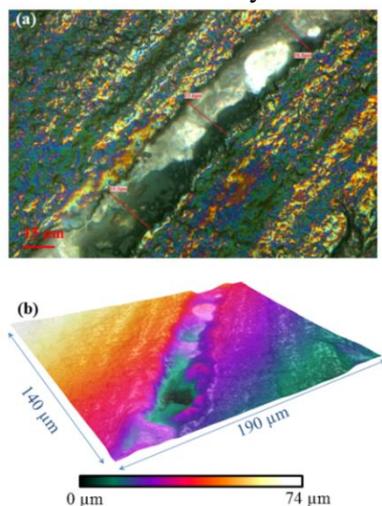
Fig. 3. Topography of the representative sample from group MO (50x magnification).
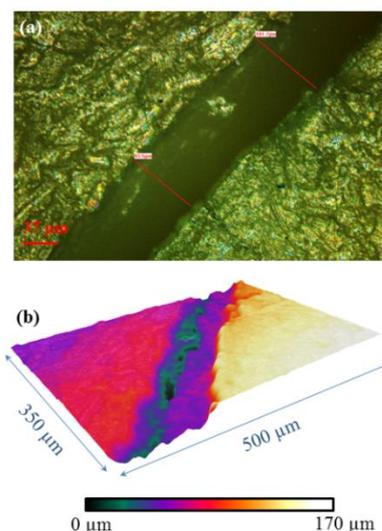
Fig. 4. Topography of the representative sample from group MOD (20x magnification).

The evidence, presented in the literature, shows that profilometry can successfully be used not only in the general field of dentistry, but also in endodontics. This is confirmed by our results.

The traditional method for assessment of vertical root fractures is the use of a stereomicroscope [13, 14]. Another way for achieving a better visualization is through the use of different dying techniques [15]. These methods, like profilometry, provide a quick and easy way of investigating cracks, without the need of any sample preparation. They, however, rely only on the subjective visual assessment of the operator, in order to determine the severity of the cracks/vertical root fractures. In contrast, the method of profilometry can provide quantitative information about their depth and width.

In our study, there is a clear tendency in the formation of wider and deeper cracks on the surface of the teeth with the increase in dental tissue loss (Table 1). This is in agreement with the information that is available in the literature. Teeth with extensive cavity preparations and loss of dentin (because of caries, fracture and endodontic treatment) tend to be more fragile and show higher rates of catastrophic vertical root fractures. According to Reeh et al., endodontic treatment alone decreases the fracture resistance of premolars with 5%, but when combined with a mesio-occlusal or mesio-occluso-distal preparation, the percentage rises to 20% and 63%, respectively [16].

The obtained 3D images of the surface topography are also highly informative. The image of tooth in the group with endodontic cavity only (Fig. 2) shows a network of narrow cracks that span vertically towards the apex, as well as horizontally. In contrast, the images of the teeth in the groups with MO and MOD cavities (Fig. 3 and Fig. 4) show one wide, deep crack that extends towards the apical region. Therefore, in teeth without extensive loss of dentin, the formation of the cracks tends to be in a more horizontal direction, which in turn can result in a more favourable outcome. Teeth with cracks that do not extend beyond the coronal 1/3 of the root can be restored with a combination of surgical or orthodontic methods. On the other side, the deep, vertical fracture lines observed in the teeth with extensive loss of dentin (groups MO and MOD), are less likely to be restorable. In most cases, the only choice of treatment remains the extraction of the tooth, in combination with prosthodontic or implant dental treatment.

CONCLUSIONS

In conclusion, the method of 3D profilometry

proved to be applicable in the study of vertical root fractures in ETT. The obtained information showed highly-detailed topographic images, as well as quantitative data on their widths and depths. The results between the examined groups can be easily compared and showed more severe cracks in teeth with considerable dentin loss. The comprehensive examination of the surfaces proved that optical profilometry is a method with great potential in the field of dental medicine. It could successfully be used in vivo for the surface assessment of hard dental tissues, as well as various dental materials, after exposure to the oral environment.

REFERENCES

1. E. Hansen, E. Asmussen, N. Christiansen, *Dent. Traumatol.*, **6**, 49 (1990).
2. P. Lagouvardos, P. Sourai, G. Douvitsas, *Oper. Dent.*, **14**, 28 (1989).
3. T. J. Huang, H. Schilder, J. Endod., 18, 209 (1992).
4. J. L. Gutmann, *J. Prosthet. Dent.*, **67**, 458 (1992).
5. A. Samran, S. El Bahra, M. Kern, *The Acad. of Dent. Mater.*, **29**, 1280 (2013).
6. Y. Zadik, V. Sandler, R. Bechor, R. Salehrabi, *Oral Surg Oral Med. Oral Pathol. Oral Radiol. Endod.*, **106**, 31 (2008).
7. Z. Fuss, J. Lustig, A. Tamse, *Int. Endod. J.*, **32**, 283 (1999).
8. A. B. Borges L. F. Santos, M. G. Auqusto, D. Bonfiette, A. T. Hara, C. R. Torres, *J. Dent.*, **49**, 54 (2016).
9. M. Krishnan, S. Seema, B. Tiwari, H. S. Sharma, S. Londhe, V. Arora, *Armed Forces Med. J. India.*, **71**, S340 (2015).
10. P. V. Soares, P.C. Santos-Filho, L. R. Martins, C. J. Soares, *J. Prosthet. Dent.*, **99**, 30(2008).
11. G. H. Yassen, A. H. A. Sabrah, G. J. Eckert, J. A., *J. Endod.*, Elsevier Ltd., 1 (2015).
12. C. Larimer, J. D. Suter, G. Bonheyo, R. S. Addleman, *J Biophotonics*, **9**, 656 (2016).
13. C. J. Soares, F. R. Santana, N. R. Silva, J. C. Preira, C. A., *J. Endod.*, **33**, 603 (2007).
14. C. J. Soares, P. V. Soares, P. C. de Freitas Santos-Filho, C. G. Castro, D. Maqalhaes, A. Verslhaes, *J. Endod.*, **34**, 1015 (2008).
15. F. P. Nothdurft, E. Seidel, F. Gebhart, M. Naumann, P. J. Motter, P. R. Pospiech, *J. Dent.*, **36**, 444 (2008).
16. E. S. Reeh, H. H. Messer, W. H. Douglas, *J. Endod.*, **15**, 512 (1989).

3D ПРОФИЛОМЕТРИЯ НА ЕНДОДОНТСКИ ЛЕКУВАНИ ПРЕМОЛАРИ, ВЪЗСТАНОВЕНИ С МЕТАЛНИ ЩИФТОВЕ

Е. Къртева[1], Н. Манчорова[1], Цв. Бабева[2], Д. Пашкулева[3], С. Владимиров[1]

[1] *Катедра по Оперативно зъболечение и ендодонтия, Факултет по дентална медицина, Медицински университет – Пловдив, България*

[2] *Инстиут по Оптични материали и технологии, Българска Академия на Науките, София, България*

[3] *Институт по механика, Българска Академия на Науките, София, България*

(Резюме)

Ендодонтски лекуваните зъби (ЕЛЗ) са по-крехки и податливи на фрактури от виталните. Съществува разнообразие от техники и материали за тяхното възстановяване, но възможностите за оценка на преживяемостта на лекуваните зъби са ограничени. Основни причини за това са трудностите в диагностиката, пред които се изправя всеки лекар по дентална медицина. Целта на нашето изследване е да се оценят възможностите на 3D профилометрията за визуализация на пукнатините и вертикалните коренови фрактури, които настъпват при ЕЛЗ. В изследването са включени 18 екстрахирани премолара, възстановени с фабрични метални щифтове и композитен материал. Образците са разпределени в 3 групи, според степента на загуба на коронарни твърди зъбни тъкани (ТЗТ). След термоциклиране, те са подложени на тест за фрактурна издръжливост в стандартна изпитателна машина, до настъпването на фрактура. Фрактурните линии са визуализирани с помощта на 3D профилометрия. Резултатите за групите с екстензивна загуба на ТЗТ показват наличието на пукнатини с голяма ширина и дълбочина, които се разпространяват във вертикална посока към апекса на зъба. В заключение, 3D профилометрията е бърз, достъпен и високо информативен метод, който успешно може да се прилага за оценка на вертикални коренови фрактури при ЕЛЗ.

Enhancement of the photocatalytic ability of alumina by mechanochemical activation and silver doping

K. Zaharieva[1]*, K. Milenova[1], S. Dimova[2], M. Todorova[3], S. Vassilev[4], I. Stambolova[5], V. Blaskov[5]

[1]*Institute of Catalysis, Bulgarian Academy of Sciences, Acad. G. Bonchev St., bl. 11, 1113 Sofia, Bulgaria*
[2]*Institute of Polymers, Bulgarian Academy of Sciences, "Acad. G. Bonchev" St., Bl.103A, 1113 Sofia, Bulgaria*
[3]*University of Chemical Technology and Metallurgy, 8 Kl.Ohridski, 1756 Sofia, Bulgaria*
[4]*Institute of Electrochemistry and Energy Systems, BAS, "Acad. G. Bonchev" St., Bl. 10, 1113, Sofia, Bulgaria*
[5]*Institute of General and Inorganic Chemistry, Bulgarian Academy of Sciences, Acad. G. Bonchev St., Bl. 11, 1113 Sofia, Bulgaria*

In the present paper the photocatalytic ability of commercial alumina, 5 wt% Ag supported Al_2O_3 synthesized by impregnation and the respective mechanochemically activated (MCA) materials was investigated for degradation of aqueous solutions of Malachite Green (MG) and Reactive Black 5 (RB5) dyes as model contaminants under UV light. The Powder X-ray diffraction analysis and FT-IR spectroscopy were used to establish the phase composition and structure of the prepared samples. The photocatalytic tests determined that the presence of Ag dopant and especially the mechanochemical treatment lead to lower degree of crystallinity, decreasing the mean crystallite size and enhancement of the photocatalytic activity of the investigated materials. The degrees of degradation of the two tested dyes decrease as follows: Ag-Al_2O_3, MCA, RB5 (99%) > Ag-Al_2O_3, MCA, MG (98%) > Al_2O_3, MCA, MG (92%) > Al_2O_3, MCA, RB5 (91%) > Ag-Al_2O_3, RB5 (72%) > Ag-Al_2O_3, MG (67%) > Al_2O_3, MG (47%) > Al_2O_3, RB5 (41%).

Keywords: mechanochemical activation, dopant, photocatalytic efficiency, Malachite Green, Reactive Black 5.

INTRODUCTION

Mechanical treatment leading to enhancement of the reactivity of solids has been known in the ceramics industry, as a method for generating various defects and new surfaces [1]. Aluminium oxide (Al_2O_3), also known as alumina, has several thermodynamically stable transitional phases as gamma alumina (γ-Al_2O_3), delta alumina (δ-Al_2O_3), kappa alumina (κ-Al_2O_3), theta alumina (θ-Al_2O_3) and alpha alumina (α-Al_2O_3). The γ-Al_2O_3 (activated alumina) has been widely used as a catalyst supports, catalysts, dehydrators and adsorbents due to its good porosity, large specific surface area, acid-base and adsorbability characteristics [2]. Heterogeneous and homogeneous photocatalyses have played an important role in many photochemical conversion processes, and have been extensively investigated over the last two decades [3]. Li Hua et al. treated Methyl Orange, Direct Brown and Direct Green azo dyes by catalytic wet air oxidation using CuO/γ-Al_2O_3 composite catalysts synthesized by consecutive impregnation [4]. Lung-Chuan Chen et al. established that incorporating of Ag in TiO$_2$/γ-Al_2O_3 significantly increased the rate of photo decolorization of Methyl Orange [5]. Yan Liu et al. revealed that Acid Orange 52, Acid Orange 7 and Reactive Black 5 azo dyes can be efficiently degraded with Fe_2O_3/γ-Al_2O_3 and Fe_2O_3–CeO_2/γ-Al_2O_3 catalysts in a catalytic wet peroxide oxidation under standard atmospheric conditions [6]. Sung-Chul Kim et al. proved the high activities of Pd–Pt/Al_2O_3 bimetallic catalysts toward the wet oxidation of the reactive dyes in the presence of 1% H_2 together with excess oxygen [7].

The goal of the present study is a comparative investigation of the photocatalytic efficiency of commercial alumina and Ag supported Al_2O_3 photocatalytic materials prepared by impregnation for degradation of aqueous solutions of Malachite Green and Reactive Black 5 dyes as model

*To whom all correspondence should be sent:
E-mail: zaharieva@ic.bas.bg

pollutants. The influence of mechanochemical treatment on the photocatalytic properties of Al_2O_3 and Ag supported Al_2O_3 samples was also studied.

EXPERIMENTAL

For the preparation of Ag-Al_2O_3 photocatalyst, commercial γ-Al_2O_3 (Valerus Co.) was used. The alumina powder was impregnated with aqueous solutions of $AgNO_3$ under heating and stirring in accordance to achieve 5 wt% silver.

One part of the commercial alumina and Ag supported Al_2O_3 samples were mechanochemically activated using a high-energy planetary ball mill model PM 100 (Retsch, Germany). The mechanochemical activation (MCA) was performed in an agate milling container of 80 ml volume at milling speed 390 rpm for milling time interval of 20 minutes using air atmosphere. The weight ratio between the balls to sample was 13:1.

The Powder X-ray diffraction analysis (PXRD) and FT-IR spectroscopy were used for physicochemical characterization of the samples. The PXRD spectra of the samples were collected using Philips PW 1050 with CuK$_\alpha$-radiation. The phases were determined using the JCPDS database. FT-IR spectroscopy was carried out on a Fourier infrared spectrometer Bruker-Vector 22. The obtained materials using KBr tablets were studied in the 400-4000 cm^{-1} range.

The photocatalytic activity of the samples (0.15g catalyst in 150 ml water solution of the dye) was investigated in a semi-batch photocatalytic reactor under constant stirring, at room temperature, for the oxidative degradation of Malachite Green (5 ppm) or Reactive Black 5 (20 ppm) dyes. The first half an hour of the tests was carried out in the dark, without illumination in order to obtain adsorption-desorption equilibrium. After that UV illumination (power 18 W, λmax = 365 nm) was switching on for period of 2 hours. The photocatalytic degradation was evaluated by taking aliquote of the solution after centrifugation and measuring the adsorbance by means of UV-1600PC Spectrophotometer (wavelength range from 200 to 800 nm). The degree of the model dye degradation was calculated using the dependence (Co-C/Co) x100, where Co and C were initial concentration before turning on the illumination and residual concentration of the dye solution after illumination for selected time interval.

RESULTS AND DISCUSSION

The Powder X-ray diffraction patterns of the
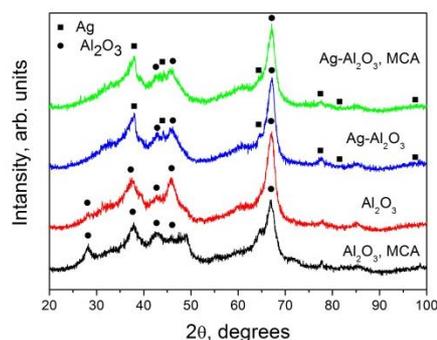
Fig. 1. PXRD patterns of the investigated materials.
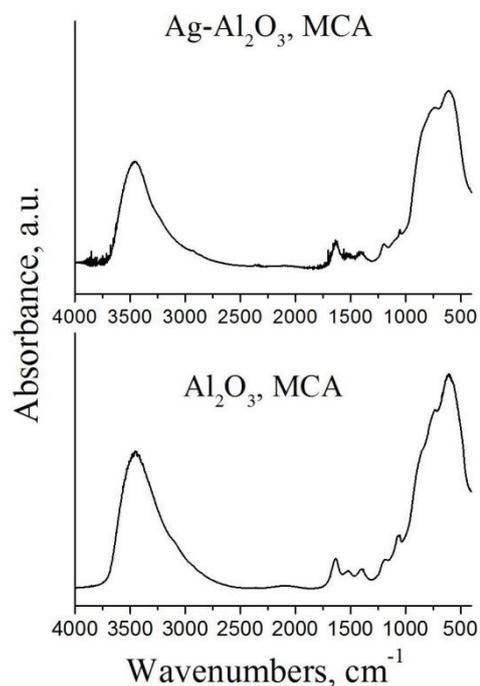
Fig. 2. FT-IR spectra of the studied samples.

commercial alumina, Ag supported Al_2O_3 and respective mechanochemically treated materials are presented in Fig 1. The presence of only one γ-Al_2O_3 phase (PDF-49-0134; 29-1486) was registered in the spectra of the commercial Al_2O_3 and mechanochemically activated alumina samples. The γ-Al_2O_3 (PDF-49-0134) and the additional silver crystallographic phase (PDF-04-0783) were established for Ag supported Al_2O_3 and the mechanochemically treated Ag supported alumina materials. The lower degree of crystallinity was determined for mechanochemically treated samples. The calculated mean crystallite size of Al_2O_3 using PowderCell 2.4 program [8] are 16, 14, 15 and 14 nm for commercial Al_2O_3, Al_2O_3, MCA, Ag supported Al_2O_3 and Ag supported Al_2O_3, MCA. The results established that the presence of silver dopant or mechanochemical activation lead to decreasing of the average crystallite size of Al_2O_3.
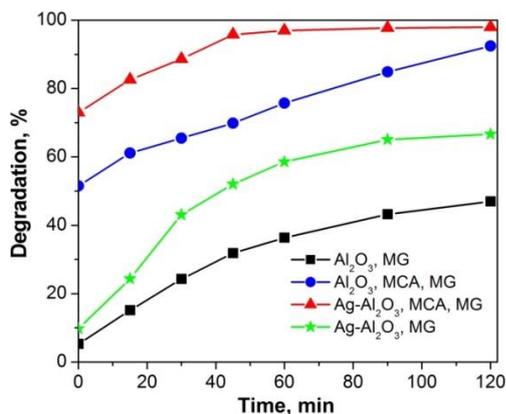
Fig. 3. Degree of degradation of MG dye as a function of the time of UV illumination.
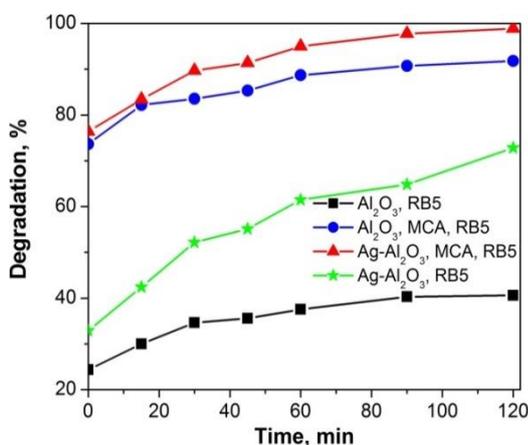
Fig. 4. Degree of degradation of RB5 dye as a function of the time of UV illumination.

FT-IR spectra of mechanochemically treated commercial alumina and Ag supported Al_2O_3 samples are displayed in Fig. 2. The absorption bands at around 3450 and 3472 cm^{-1} could be due to the presence of -OH species, showing the presence of Al-OH bond in the samples. The band at around 1636 cm^{-1} corresponds to the H-O-H angle bending vibration of weakly bound molecular water [9]. The peaks at around 609 and 611 cm^{-1} were attributed to Al–O stretching mode [9-11]. The absorption band at around 1400 cm^{-1} could be attributed to the presence of carbon-hydrogen (CH_3), - carbon (C-C) and -oxygen (C=O) deformations. The peaks at around 1518; 1187-1189 and 1050-1065 cm^{-1} may be due to the presence of others impurities in the investigated samples [9]. The results obtained by FT-IR spectroscopy are in agreement with the PXRD analysis.

Figs. 3 and 4 present the degree of degradation of MG and RB5 dyes as a function of the time of illumination under UV light. After the mechanochemical activation of Ag/Al_2O_3 photocatalyst, the degradation degree of RB5 dye reached 99% and of MG dye 98%, while Al_2O_3, MCA photocatalyst showed 92% and 91% for RB5 and MG dyes accordingly. The photocatalytic activity for the degradation of MG and RB5 dyes on Ag supported Al_2O_3 samples was 72 and 67%. The commercial alumina samples exhibited lower photocatalytic efficiency for degradation of the MG and RB5 dyes: 47% and 41% respectively. The comparison data of apparent rate constants of all investigated catalysts for both dyes was exhibited in Fig. 5. The presented apparent rate constants were calculated using linear dependence $-\ln(C/C_0) = k.t$. The photocatalytic efficiency of the investigated samples for degradation of MG dye (based on rate
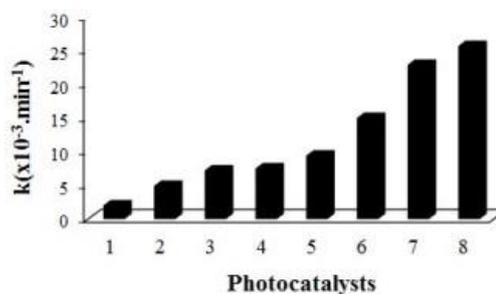
Fig. 5. Comparison data of apparent rate constants of: **1**-Al_2O_3, RB5; **2**-Al_2O_3, MG; **3**-Ag-Al_2O_3, RB5; **4**-Ag-Al_2O_3, MG; **5**-Al_2O_3, MCA, RB5; **6**-Al_2O_3, MCA, MG; **7**- Ag-Al_2O_3, MCA, MG; **8**- Ag-Al_2O_3, MCA, RB5 photocatalysts in degradation of RB5 and MG dyes.

constants) is: Ag-Al_2O_3, MCA (22.8×10^{-3} min^{-1})> Al_2O_3, MCA (14.9×10^{-3} min^{-1}) > Ag-Al_2O_3 (7.4×10^{-3} min^{-1})> Al_2O_3 (4.8×10^{-3} min^{-1}). The RB5 photodegradation decreases in the following order: Ag-Al_2O_3, MCA (25.6×10^{-3} min^{-1})> Al_2O_3, MCA (9.3×10^{-3} min^{-1}) > Ag-Al_2O_3 (7.1×10^{-3} min^{-1})> Al_2O_3 (1.9×10^{-3} min^{-1}).The highest rate constant belongs to Ag-Al_2O_3, MCA. We can conclude that the silver doping influenced catalytic activity to some extent, whereas mechanochemical activation increased it significantly. It is well-known that the mechanical energy obtained during milling can have effects such as generating new interfaces and crystal defects, changes in particle size and amorphization [12]. In our study the mechanochemically treated samples possess lower degree of crystallinity and decreased average crystallite size which leads to higher photocatalytic activity. Similar effects have been established for mechanochemically activated Ag/ZnO particles [13].

CONCLUSIONS

The obtained photocatalytic results show that both the silver doping and mechanochemical activation of Al_2O_3 lead to enhancement in the photocatalytic properties of the investigated materials in the oxidative degradation of aqueous solutions of MG and RB5 dyes under UV light. The mechanochemical activation improves significantly the photocatalytic efficiency of the studied samples. The mechanochemically activated Ag supported Al_2O_3 shows the highest photocatalytic activity for the oxidative degradation of the model pollutants, compared to the other tested materials.

REFERENCES

1. J. Temuujin, *Himiya v interesah ustojchivogo razvitiya (*in Russian), **9**, 589 (2001).
2. J. Xu, Ab. Ibrahim, X. Hu, Y. Hong, Y. Su, H. Wang, J. Li, *Microporous and Mesoporous Mater.*, **231**, 1 (2016).
3. J Choi, J. Ban, S. Choung, J. Kim, H. Abimanyu, K. Yoo, *J. Sol-Gel. Sci. Technol.*, **44**, 21 (2007).
4. L. Hua, H. Ma, L. Zhang, *Chemosphere*, **90**, 143 (2013).
5. L.-C. Chen, F.-R. Tsai, C.-M. Huang, *J. Photochem. Photobiol. A: Chemistry*, **170**, 7 (2005).
6. Y. Liu, D. Sun, *J. Hazard. Mater.*, **143**, 448 (2007).
7. S.-C. Kim, H.-H. Park, D.-K. Lee, *Catal. Today*, **87**, 51 (2003).
8. W. Kraus, G. Nolze, Powder Cell for Windows, Federal Institute for Materials Research and Testing, Berlin, Germany, (2000).
9. J. Gangwar, B. Gupta, S. Tripathi, A. Srivastava, *Nanoscale*, **7,** 13313 (2015).
10. M. Tafreshi, Z. Khanghah, *Materials Science* (Medžiagotyra), **21** (1), 28 (2015).
11. C. Mo, Z. Yuan, L. Zhang, C. Xie, *Nanostruct. Mater.*, **2**, 47 (1993).
12. K. Ralphs, Ch. Hardacre, S.-L. James, *Chem. Soc. Rev.*, DOI: 10.1039/c3cs60066a (2013).
13. K. Milenova, K. Zaharieva, A. Eliyas, I. Stambolova, V. Blaskov, O. Dimitrov, L. Dimitrov, Z. Cherkezova-Zheleva, S. Rakovsky, *Tribological Journal BULTRIB*, **5**, 255 (2015).

ПОВИШАВАНЕ НА ФОТОКАТАЛИТИЧНАТА СПОСОБНОСТ НА АЛУМИНИЕВ ОКСИД ЧРЕЗ МЕХАНОХИМИЧНА АКТИВАЦИЯ И ДОТИРАНЕ СЪС СРЕБРО

К. Л. Захариева[1*], К. И. Миленова[1], С. С. Димова[2], М. В. Тодорова[3], С. В. Василев[4], И. Д. Стамболова[5], В. Н. Блъсков[5]

[1]*Институт по катализ, Българска академия на науките, ул. „Акад. Г. Бончев“, бл. 11, 1113 София, България*
[2]*Институт по полимери, Българска академия на науките, ул. „Акад. Г. Бончев“, бл. 103А, 1113 София, България*
[3]*Химикотехнологичен и металургичен университет, бул. Кл.Охридски 8, 1756 София, България*
[4]*Институт по електрохимия и енергийни системи, Българска академия на науките, ул. „Акад. Г. Бончев“, бл. 10, 1113 София, България*
[5]*Институт по обща и неорганична химия, Българска академия на науките, ул. „Акад. Г. Бончев“, бл. 11, 1113 София, България*

(Резюме)

В настоящата статия е изследвана фотокаталитичната способност на търговски алуминиев оксид, дотиран с 5 тегловни % сребро Al_2O_3 синтезиран чрез импрегниране и съответните механохимично активираните (МХА) материали бяха изследвани за разграждането на водни разтвори на Малахитово Зелено (МЗ) и Реактивно Черно 5 (РЧ5) багрила като моделни замърсители под действието на УВ светлина. Рентгенофазов анализ и инфрачервена спектроскопия с фурие трансформация бяха използвани за установяване на фазовия състав и структурата на получените проби. Фотокаталитичните тестове определиха, че присъствието на Ag като допант и особено механохимичната обработка водят до по-ниска степен на кристалност, намаляване на средния размер на кристалитите и повишаване на фотокаталитичната активност на изследваните материали. Степента на разграждане на двете тествани багрила намалява както следва: Ag-Al_2O_3, МХА, РЧ5 (99%) > Ag-Al_2O_3, МХА, МЗ (98%) > Al_2O_3, МХА, МЗ (92%) > Al_2O_3, МХА, РЧ5 (91%) > Ag-Al_2O_3, РЧ5 (72%) > Ag-Al_2O_3, МЗ (67%) > Al_2O_3, МЗ (47%) > Al_2O_3, РЧ5 (41%).

Effect of preparation procedure on the formation of nanosized mesoporous TiO_2-CeO_2 catalysts for ethyl acetate total oxidation and methanol decomposition

A. Mileva[1]*, G. Issa[1], J. Henych[2], V. Štengl[2], D. Kovacheva[3], T. Tsoncheva[1]

[1]*Institute of Organic Chemistry with Centre of Phytochemistry, BAS, Bulgaria,*
[2]*Materials Chemistry Department, Institute of Inorganic Chemistry AS CR*
[3]*Institute of General and Inorganic Chemistry, BAS, Bulgaria*

Two series TiO_2–CeO_2 samples were synthesized using homogeneous precipitation with urea and template-assisted hydrothermal procedures. The samples were characterized by nitrogen physisorption, XRD, UV–Vis, Raman and TPR techniques. The catalytic properties of the obtained materials were studied in oxidation of ethyl acetate and methanol decomposition. The effect of preparation procedure on the phase composition, texture, structure and redox properties was discussed in close relation with the possibilities for fine tuning of their catalytic activity.

Keywords: Ti-Ce oxides, ethyl acetate total oxidation, methanol decomposition.

INTRODUCTION

Recently, the design and synthesis of nanostructured titanium oxide with high surface area, high thermal stability, and crystalline framework have attracted considerable interest because of their superior electrical, mechanical, optical and catalytic properties combined with non-toxicity and cost effectiveness [1]. Nowadays, titania is widely used in preparation of optical devices, pigment, bio-materials, gas sensors, electrodes, solar cells, catalysts for degradation of various pollutants [1, 2]. Different preparation techniques have been developed for effective control of titania properties for various applications [1, 2] and among them, doping with ceria have attracted particular attention due to its excellent redox chemistry and oxygen storage capacity [3]. The aim of present study is the preparation of series of nanostructured TiO_2–CeO_2 oxide materials two using homogeneous precipitation with urea and template-assisted hydrothermal synthesis. The obtained materials were characterized by nitrogen physisorption, XRD, Raman, UV–Vis and TPR. The catalytic properties were studied in methanol decomposition (MD) and total oxidation of ethyl acetate (EA) with an environmental potential as alternative clean and efficient fuel [4] and elimination of organic pollutants in air [5], respectively.

EXPERIMENTAL

Mono and bi-component titania and ceria materials were synthesized by hydrothermal procedure using CTAB as a structure directed template (HT) and homogeneous precipitation with urea technique (U) as was described in [4] and [6], respectively. The samples were denoted as xTiyCe M, where x/y was the metal mol ratio and M was the preparation method used. The textural characteristics were collected from nitrogen adsorption-desorption isotherms measured at 77 K using a Coulter SA3100 instrument. Powder X-ray diffraction patterns were collected on a Bruker D8 Advance diffractometer with Cu Kα radiation using a LynxEye detector. Mean crystallite size were determined with the Topas-4.2 software package using the fundamental parameters peak shape description including appropriate corrections for the instrumental broadening and diffractometer geometry. The UV–Vis spectra were recorded on a Jasco V-650 UV-Vis spectrophotometer. Raman spectra were collected on a DXR Raman microscope using a 780 nm laser. The TPR/TG analyses were performed on a Setaram TG92 instrument in a flow of 50 vol% H_2 in Ar. Catalytic oxidation of EA was performed in a flow type reactor with a mixture of EA in air. Gas chromatographic analyses were done on a HP 5890 apparatus using carbon-based calibration. MD was carried out in a fixed bed flow reactor and Ar as a carrier gas. On-line gas chromatographic analyses

* To whom all correspondence should be sent:
E-mail: aleksandra_bunalova@abv.bg

were performed on HP apparatus equipped with flame ionization and thermo-conductivity detectors, on a PLOT Q column, using an absolute calibration method and a carbon based material balance.

RESULTS AND DISCUSSION

In Fig. 1a are presented nitrogen physisorption isotherms for the samples obtained by various techniques and the corresponding data are listed in Table 1. According to IUPAC classification the isotherms are of IV type, typical of materials with mesoporous structure. The observed differences in the shape of hysteresis loop indicate predominantly presence of cylindrical pores for TiO_2 HT and TiCe HT, cage-like pores for TiO_2 U and TiCe U and slit-like pores for CeO_2 HT and CeO_2 U.
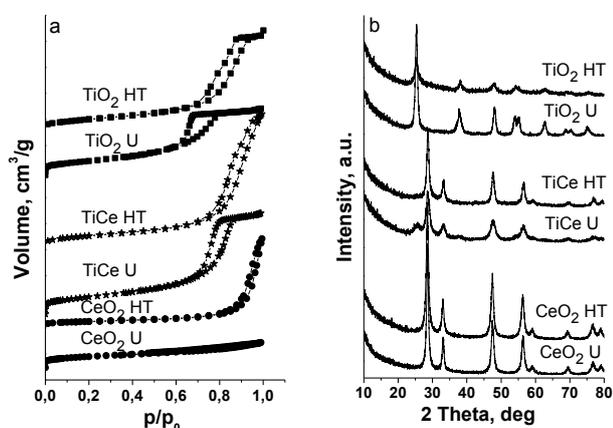
Fig. 1. Nitrogen physisorption isotherms (a) and XRD patterns (b) of TiCe materials.

As compared to the hydrothermally obtained materials, the urea samples possess lower porous volume (Table 1.) and higher specific surface area. Besides, an increase in the surface area and pore volume is also observed for both bi-component

volume is also observed for both bi-component samples. Thus, the development of the mesoporous structure strongly depends on the preparation procedure and the initial phase composition. It is predominantly directed by the organic template used during the hydrothermal procedure and by the interparticles interaction for the urea assisted one and the effects are better pronounced for the binary oxides.

Fig. 1b shows the XRD patterns of titania and ceria materials. The diffraction peaks in the pattern of TiO_2 HT and TiO_2 U are indexed to anatase phase of TiO_2 [2] with average crystallite size of about 17 nm and 13 nm, respectively. The diffraction features for both CeO_2 materials are typical of cubic fluorite-like structure of cerianite [3] with average crystallite size of 10-13 nm. Ceria with average crystallite size of 12 nm is only registered phase for TiCe H, while a mixture of anatase and ceria with average crystallite size of 5 and 7 nm, respectively, is found for TiCe U. The observed decrease of unit cell parameters for the ceria components in binary materials (5.403Å for TiCe-HT and 5.401Å for TiCe-U) as compared to pure CeO_2 samples (5.416 Å for CeO_2-HT and 5.414 Å for CeO_2-U) does not exclude partial substitution of Ce^{4+} ions by smaller Ti^{4+} ions.

In Fig. 2 are presented Raman spectra of TiCe materials, obtained by various procedures. The Raman shifts at 143 cm^{-1} (E_{1g}), 195 cm^{-1} (E_{2g}), 396 cm^{-1} (B_{1g}), 514 cm^{-1} (A_{1g}) and 637 cm^{-1} (E_{3g}) in the spectra of both TiO_2 samples demonstrate presence of pure anatase phase [7]. Only one Raman-active E_{2g} mode, centered at about 463 cm^{-1}, which is typical of cubic structure, is detected for both ceria materials [3].

Table 1. Nitrogen physisorption data of TiCe materials.

Sample	BET m^{2}g^{-1}	V_t cm^{3}g^{-1}	$T_{50\%}$, K	$T_{30\%}$, K	SA, EA mol.m^{-2}	SA, MD mol.m^{-2}
TiO_2 HT	85	0.29	660	662	0.29	0.37
TiO_2 U	97	0.19	651	630	0.23	0.54
TiCe HT	99	0.45	586	685	0.60	0.37
TiCe U	117	0.30	574	661	0.65	0.53
CeO_2 HT	46	0.26	560	730	1.74	0.43
CeO_2 U	76	0.07	535	604	1.09	0.60

*BET-surface areas; V_t -pore volume; *$T_{50\%}$- temperatures for 50% conversion of ethyl acetate (EA); $T_{30\%}$- temperatures for 30% conversion of methanol decomposition (MD); *SA-specific catalytic activity
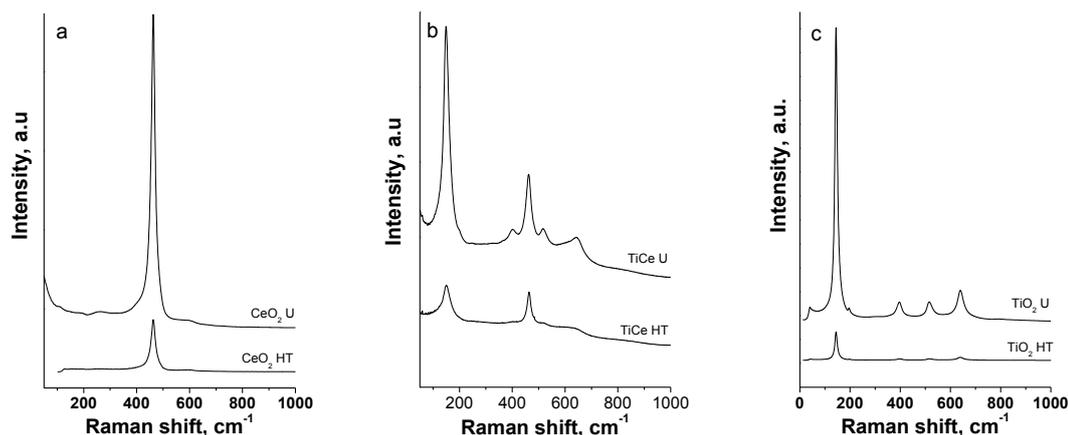
Fig. 2. Raman spectra of CeO₂ (a), TiCe (b) and TiO₂ (c) materials.
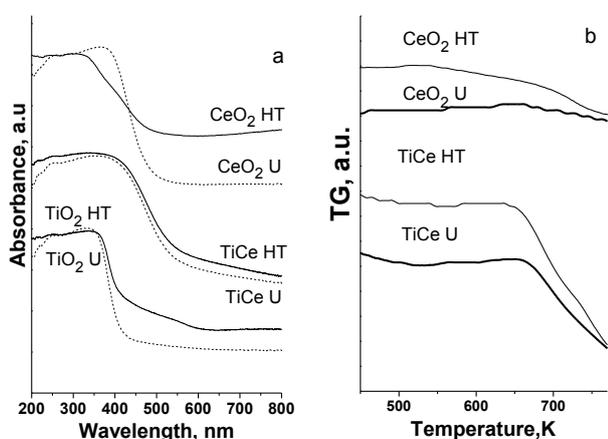
Fig 3. UV-Vis spectra (a), TPR–TG profiles (b) of TiCe materials.

The Raman spectra of binary oxides reveal that they represent a mixture of ceria and anatase phases, the latter being in higher amount for the urea obtained sample, in consistent with the XRD data. The observed slight blue shift of the Raman E_{1g} mode to 150 cm^{-1} could be an indication for the changes in the environment of titanium ions in anatase lattice. The significant decrease in the intensity of the Raman peaks for the binary materials as well as the slight blue shift of the main E_{1g} mode of anatase could be due to the improved metal oxide dispersion, which is in accordance with the XRD data (Fig. 1b). In Fig. 3a are compared UV–Vis spectra of the samples obtained by hydrothermal and urea procedures. The strong absorption feature in the spectra of both TiO₂ samples at 350 nm, which is typical of anatase [2], which is also in consistent with the Raman and XRD data. The spectra of pure CeO₂ samples display absorption in the 300-500 nm range corresponding to $Ce^{4+} \leftarrow O^{2-}$ charge transfer, which

is typical of pure ceria phase. The shift in the main absorption edges for both individual oxides indicates higher dispersion for the hydrothermally obtained materials. The red shift of the curves for the bi-component TiCe materials could be due to the formation of new energy level within the band gap of TiO₂ and/or presence of highly dispersed ceria. Substitution of Ti ions in ceria lattice is not excluded as well.

TPR-TG profiles of hydrothermally and urea obtained TiCe samples are compared in the 450–770 K region (Fig. 3b). The observed weight loss for CeO₂ HT (0.18 mg) and CeO₂ U (0.08 mg) corresponds to the reduction of Ce^{4+} to Ce^{3+} and it is about 10 and 4 %, respectively. The reduction effects for the TiCe-HT (0.55 mg) and TiCe-U (0.38 mg) are larger in comparison with the pure CeO₂ samples and they are also detected at lower temperature. In accordance with the other physicochemical measurements, this indicates increased mobility of lattice oxygen which could be due to the improved dispersion and distortion of ceria lattice during the titanium incorporation. The reduction behaviour for all materials is not in a simple relation to their specific surface area. Thus, the facile reduction for the hydrothermal samples is probably related to their higher dispersion, well developed mesoporous structure and homogeneous phase composition.

In Fig. 4 are presented temperature dependencies of total oxidation of EA on various materials. Beside CO₂, which is the most important product of EA oxidation, (Fig. 4b), ethanol (EtOH), acetaldehyde (AA), acetic acid (AcAc) and ethene are also registered as by-products. For both series of samples the ethylacetate oxidation is initiated above 500 K and 80–100% conversion is achieved at 650 K. Among all materials, both pure mono-

117

component ceria compounds exhibit lowest T_{50} (Table 1) which indicates their high catalytic activity. Besides, on these materials high selectivity to EtOH is observed. The lowest catalytic activity combined with high selectivity to AA, EtOH and ethene is registered for both TiO_2 samples. The binary materials possess intermediate catalytic activity as compared to the individual oxides and here high selectivity to ethanol is also observed. A common feature is the higher activity for all urea obtained materials as compared to their hydrothermally prepared analogues. In order to ignore the impact of the differences in the specific surface area of the samples, the specific catalytic activity as conversion per unit BET was calculated (Table 1.). Surprisingly, here urea samples exhibit lower or similar SA to the HT analogues indicating that the observed catalytic behaviour is strongly related to the improved surface area during the urea synthesis.
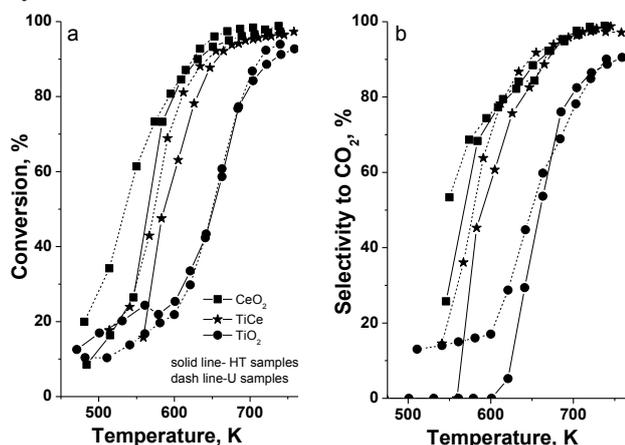
Fig. 4. Ethyl acetate conversion (a) and selectivity to CO_2 (b) of TiCe materials.

It was well established that for many oxide systems, the total oxidation of EA is a step-wise process including hydrolysis to EtOH and AcAc and their further oxidation *via* Mars van Krevelen mechanism [5]. The improvement of the selectivity to CO_2 for the binary materials and for all urea obtained ones clearly indicates the dominant effect of the surface redox over the acid-base properties for these materials, which is obviously regulated both by the preparation method and the substitution of ceria with Ti.

The temperature dependencies of methanol conversion and CO selectivity for titania and ceria samples are presented in Fig. 5. Besides CO, which is the most important product from the decomposition, CO_2, CH_4, dimethyl ether (DME) and C_2-C_3 hydrocarbons are registered as by-

products. All materials exhibit activity above 500-550 K. The temperatures at which 30% conversion is achieved (Table 1.) demonstrate high catalytic activity combined with 90% selectivity to CO due to the formation of CO_2 for CeO_2 U. Just the opposite, the HT obtained analogue possesses extremely low catalytic activity and about 50% selectivity to CO due to the formation of CH_4.
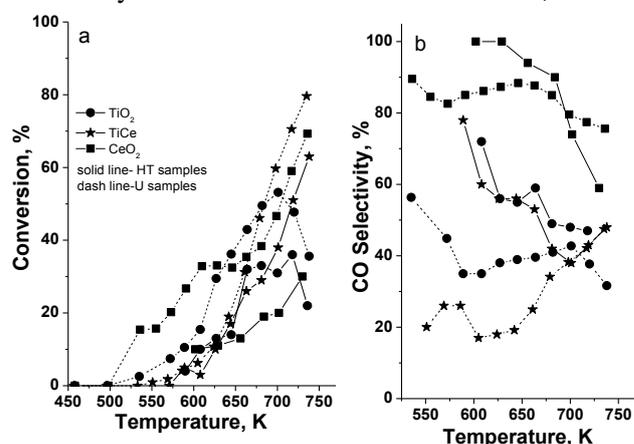
Fig. 5. Methanol conversion (a) and selectivity to CO (b) of TiCe materials.

The main by-products during the methanol decomposition on both TiO_2 materials are DME (about 50%) and hydrocarbons (about 17% for TiO_2 HT) which clearly indicates existence of high acidic function. Here, well pronounced trend to deactivation with the temperature increase for both materials is detected, which could be due to the deposition of non-desorbable products. Both binary materials demonstrate improved catalytic activity and stability at higher temperatures as compared to the individual oxides. Their relatively low selectivity to CO is due to the contribution of methane (about 30%) and DME (30-40%) as by-products. All urea materials exhibit higher catalytic activity as compared to their HT analogues. The higher values of the specific activity for the urea samples (Table 1.) strongly evidences that their higher catalytic activity is not in simple relation with the improved specific surface area.

Thus the variations in the SA values (Table 1.) as well as the differences in the selectivity for both catalytic processes urge the authors to assume more complex effect than the expected one from the differences in the specific surface area. The XRD, Raman, UV-Vis and TPR analyses demonstrate higher dispersion for the hydrothermally obtained materials, which can also influence the degree of substitution of Ti in ceria lattice for binary materials. This can affect the generation of oxygen

vacancies and cerium and titanium ions in lower oxidative state [1]. As a result changes in the surface acidic-base and redox properties and the related with them catalytic behaviour of the solids is expected (Figs. 4, 5). The complexity of this process needs more detail analysis with appropriate techniques and further investigation is in progress.

CONCLUSION

By using homogeneous precipitation with urea and template-assisted hydrothermal procedures, nanosized titania-ceria materials with high specific surface area and pore volume were successfully prepared. The strong interaction between CeO_2 and TiO_2 as well as the crystallization of particles in the nanoscale improve the redox properties of the TiO_2–CeO_2 mixed oxides. The control of the catalytic activity and selectivity requires fine tuning of the phase composition, texture, structure, morphology and surface properties which could be tuned by the preparation method used. The hydrothermal method provides the formation of more homogeneous, better dispersed materials with higher mesopore volume, but their lower specific surface area provides lower catalytic activity in ethyl acetate oxidation and methanol decomposition as compared to the urea synthesized materials.

REFERENCES

1. S. Yuesong, Z. Dahai, Y. Bo, N. Songbo, Z. Shemin, J. Rare Earths, **30,** 431 (2012).
2. M. Altomare, M. V. Dozzi, G. L. Chiarello, A. Paola, L. Palmisano, E. Selli, *Catal. Today,* **252**, 184 (2015).
3. J. Ding, J. Lin, J. Q. Xiao, Y. Zhang, Q. Zhong, S. Zhang, L. J. Guo, M. H. Fan, J. Alloys Comp., **665,** 411 (2016).
4. T. S. Tsoncheva, I. G. Genova, M. D. Dimitrov, E. Sarcadi-Priboczki, A. M. Venezia, D. G. Kovacheva, N. Scotti, V. dal Santo, *Appl. Catal. B,* **165**, 599 (2015).
5. P. O. Larsson, A. Andersson, *Appl. Catal. B,* **24**, 175 (2000).
6. J. A. Subrt, V. A. Stengl, S. Bakardjieva, L. J. Szatmary, Powder Technol., **169**, 33 (2006).
7. K. C. Silva, P. Corio, J. J. Santos, Vibrational Spectroscopy, **86**, 103 (2016).

ВЛИЯНИЕ НА МЕТОДА НА ПОЛУЧАВАНЕ ВЪРХУ ФОРМИРАНЕТО НА НАНОРАЗМЕРНИ МЕЗОПОРЕСТИ TIO₂-CEO₂ КАТАЛИЗАТОРИ ЗА ПЪЛНО ОКИСЛЕНИЕ НА ЕТИЛАЦЕТАТ И РАЗПАДАНЕ НА МЕТАНОЛ

А. Милева[1], Г. Исса[1], И. Хених[2], В. Щенгъл[2], Д. Ковачева[3], Т. Цочева[1]

[1]Институт по Органична химия с Център по Фитохимия, БАН, България
[2]Институт по неорганична химия, Чехия
[3]Институт по обща и неорганична химия, БАН

(Резюме)

TiO_2–CeO_2 материали са синтезирани чрез хомогенно утаяване с уреа и хидротермален синтез в присъствието на органичен темплейт. Образците бяха характеризирани чрез физична адсобция на азот, XRD, UV-Vis и Раман спектроскопии, както и TPR. Каталитичните свойства на получените материали бяха изследвани в окисление на етилацетат и разпадане на метанол. Беше изследвано влиянието на метода на получаване върху фазовия състав, текстурата, структурата и окислително-редукционните свойства на образците в тясна връзка с възможностите за фина настройка на тяхната каталитична активност.

Capture of carbon dioxide by mesoporous carbon-silica composites

N. Stoeva*, I. Spassova, D. Kovacheva, G. Atanasova, M. Khristova

*Institute of General and Inorganic Chemistry, Bulgarian Academy of Sciences,
1113 Sofia, Bulgaria.*

Mesostructured silica-carbon composites were synthesized by soft template approach and were characterized by TG, XRD, low temperature N_2- adsorption, TEM, XPS. The CO_2 adsorption capacities were investigated and the heats of adsorption were determined. The CO_2 capture from flue gas was tested. The carbon-containing materials exhibit better performance as sorbents for carbon dioxide than the single silica. For the silica–carbon composites improved CO_2 capture with increasing the carbon content is observed. The capacity of the silica-carbon materials for CO_2 capture from flue has is related to the value of the average pore diameter of the composites and their micropore volume.

Keywords: silica-carbon composites; mesoporous adsorbents; CO_2 capture;

INTRODUCTION

Fossil fuels as non-renewable resources are the major source of energy. Their burning produces billions tons of CO_2 and thus leads to severely adverse impacts on the environment, like air pollution and global warming. Therefore, the development of efficient low-cost way for reduction of CO_2 emission becomes important to control it. Currently, a variety of methods, such as membrane separation, cryogenic distillation, chemical absorption and adsorption, have been proposed for CO_2 purification from the flue gases [1]. Adsorption is considered as one of the most promising technologies for commercial and industrial application because of the low energy requirement, cost advantage, and ease of applicability over a relatively wide range of temperatures and pressures [2]. However, the success of this approach is dependent on the development of effective adsorbent with high CO_2 selectivity and adsorption capacity. During the past few years, extensive experimental and theoretical investigations were carried out with the purpose of developing novel porous materials for adsorption of CO_2 including zeolites, MOFs, mesoporous silicas and carbons [3-6]. Mesoporous materials are attractive for adsorption of gases due to the high specific surface area and relatively controllable porosity, moreover the rate of diffusion of CO_2 inside the pores of such adsorbents is ~ three orders

higher than with the liquid phase absorption. Carbon adsorbents are widely used for CO_2 capture due to their accessibility, low cost and low sensitivity to moisture. For the stabilization of mesoporous carbons siliceous materials could be used, as silica could serve as template material for the synthesis. Studies on mesoporous sorbents have shown that not only the pore volumes determine the sorption activity, but the pore sizes also [7]. These parameters can be adjusted during the synthesis of silica-carbon composites varying the ratio between silica and carbon.

Because of its relevance to practical applications, we found it compelling to synthesize mesostructured silica-carbon nanocomposites with various silica:carbon ratio in order to tune the texture parameters of the materials, to characterize them and to investigate the adsorption of CO_2 and the CO_2 capture from flue gas at higher than ambient temperature.

EXPERIMENTAL

Mesostructured silica-carbon composites with a various Si:C ratio were prepared by co-assembly [8] of resol, silica oligomers from TEOS, and triblock copolymer Pluronic F127 via the EISA method. The thermal treatment was performed in two steps- at 350^oC for 2h and at 900^oC for 3 h. Single mesostructured silica and carbon samples were prepared by the same approach for comparison. Silica was treated at 550^oC in air in order to remove the remaining carbon. Samples are denoted as MS (mesoporous silica), MSC1, MSC3,

*To whom all correspondence should be sent:
E-mail: n.stoeva@svr.igic.bas.bg

MSC5, MSC7 (with 10 % to 70% carbon) and MC (mesoporous carbon).

Physicochemical parameters of the composites were determined by TGA, XRD, N_2-physisorption, TEM and XPS analyses. The TG analyses were carried out on LABSYSEvo, SETARAM (France) at atmospheric pressure in air in 25-1000°C and dynamic mode. Powder XRD patterns were collected on Bruker D8 Advance diffractometer with Cu Kα radiation and LynxEye detector. Low-angle part of the patterns was collected from 0.3 to 8° 2θ using the knife-edge anti-scatter screen attachment of the primary beam. The texture characteristics were determined in a Quantachrome Instruments NOVA 1200e (USA). Pore size distributions were calculated by DFT method [9]. The TEM investigations were performed on a JEOL JEM-2100. The XPS measurements were made on ESCALAB-Mk II (VG Scientific) electron spectrometer with a Al Kα$_{1,2}$ radiation (hν = 1486.6 eV).

The adsorption isotherms and kinetics of CO_2 were measured using a static volumetric Quantachrome NOVA 1200e instrument. Isotherms were obtained at two temperatures (0°C and 30°C) for the purpose of determining heats of adsorption. The CO_2 capture experiments were performed using an integrated quartz micro-reactor and mass-spectrometer system (CATLAB, Hiden Analytical, UK). The CO_2 capture tests were performed at 45°C, with a concentration of 3000 ppm CO_2 in Ar, volume rate of 10 ml/min. The CO_2 uptake was calculated after integration of the curves and according to the exact weight of the sample.

RESULTS AND DISCUSSION

The framework compositions were established by TGA. TG curves (not presented) show a significant weight loss for all samples in the temperature range from 500 to 1000°C, the range depending on the carbon content. The template is removed at about 350°C and the weight loss in 500-

900°C can be attributed to carbon. The obtained silica and carbon content is presented in Table 1 as SiO_2 and C.

XRD patterns of the samples are presented in Fig. 1. Wide angle pattern comprise of weak diffraction shoulder at 22.5° 2θ due to the presence of amorphous silica (and or carbon) and a broad peak at 43.5°C 2θ, the intensity of the second one increases with the increase of carbon content (Fig. 1A), revealing formation of amorphous carbon in the composites. Low-angle diffraction patterns show two or three resolved diffraction peaks, indicating the well regularity of their structures in the long-range (Fig. 1B). The first intense diffraction peak can be indexed as (100). Because of the low intensity of the other two weak peaks in the diffractograms, (110) and (200) reflections are presented as inset with higher magnification. These peaks reveal a 2D-hexagonal symmetry (space group *p6mm*). The corresponding unit cell parameters a_0, calculated by the formula $a_0=2d_{(100)}/\sqrt{3}$ are listed in Table 1. The unit cell parameter varies for the different compositions, single materials having the lowest values (Table 1).
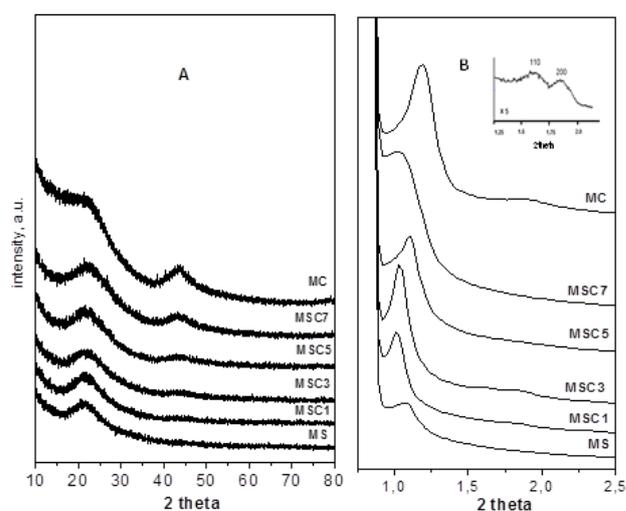
Fig. 1. Wide-angle (A) and low-angle (B) XRD patterns of the investigated samples.

Table 1. Physicochemical and texture parameters of the synthesized samples.

Sample	a_0 nm ±0.1	SiO_2 (wt.%) ±1	C (wt.%) ±1	S m^2/g	S_{mi} m^2/g	S_{ext} m^2/g	V_t* cm^3/g	V_{mi}** cm^3/g	V_{mes} cm^3/g	D_{DFT} nm
MS	11.4	100	0	152	9	143	0.22	0.00	0.22	5.7
MSC1	12.1	84	16	206	19	187	0.29	0.01	0.28	4.8
MSC3	12.2	70	30	339	69	270	0.43	0.03	0.40	5.0
MSC5	11.2	53	47	387	49	338	0.53	0.02	0.51	5.1
MSC7	12.2	30	70	500	197	303	0.45	0.09	0.37	5.9
MC	10.3	0	100	588	223	365	0.36	0.10	0.27	4.5

*Total pore volume at p/po ~ 0.99. **Evaluated by the t-plot method.

The errors of the determination of the texture parameters vary from 0.2 to 2% depending on the pressure and C-constant of the sample

The texture parameters of the materials are summarized in Table 1. With the increase of the carbon content specific surface areas and micropore volumes enlarge gradually, the total pore volume passes through maximum. Nitrogen adsorption-desorption isotherms (not presented) of all samples are of IV type with a distinct capillary condensation step occurring at p/p_0 of 0.5–0.7. The pore distributions are narrow that is characteristic for the mesostructured materials. MS has the narrowest distribution and the addition of carbon leads to gradual broadening of the distributions due to the mesostructure framework shrinkage. Additional structural characterization is revealed by TEM images, as shown in Fig. 2. The images show large domains of highly ordered stripe-like well-ordered materials with arrays of mesopores with 1D channels. The pore width could be estimated from the images as varying from 5 nm to 7 nm, confirming the results from N_2 physisorption. However, more detailed explanation could be done after HRTEM investigations.

The corresponding surface composition of C, O and Si in all samples derived from the respective photoelectron peak area is presented in Table 2. Irrespective of the C and Si content (Table 1) in all cases the C content on the surface is higher than in the bulk. Hence, carbon in the composites is situated mostly on the external surface along the pores.

The adsorption isotherms of CO_2 at 0^oC and 30^oC and pressure up to 100 kPa are given in Fig. 3. All isotherms have reversibility without hysteresis, indicating that the adsorbed gas molecules can be completely removed during the desorption. The isotherms have modest curvatures that suggest good regenerability of the adsorbent. Adsorption capacity is one of the major properties of the adsorbent. The CO_2 uptake capacities at 100 kPa and at 0^oC and 30^oC are 4.0 and 2.9 mmol/g, respectively for MC. These values decrease gradually with increasing the silica content. The results are in a good agreement with the values obtained in [13].

Fig. 2. Bright field TEM micrographs for the synthesized mesostructured materials.
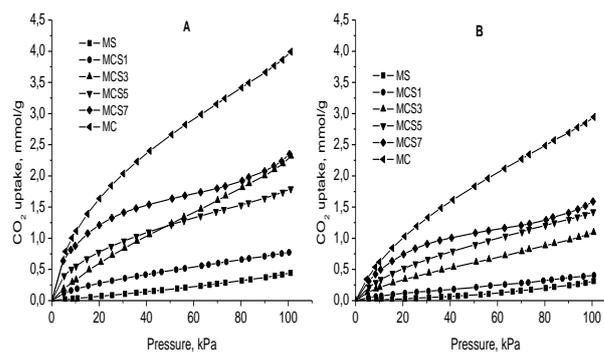
Fig. 3. CO_2 adsorption isotherms at: A – 0 ºC and B – 30 ºC for various mesoporous silica-carbon composites.
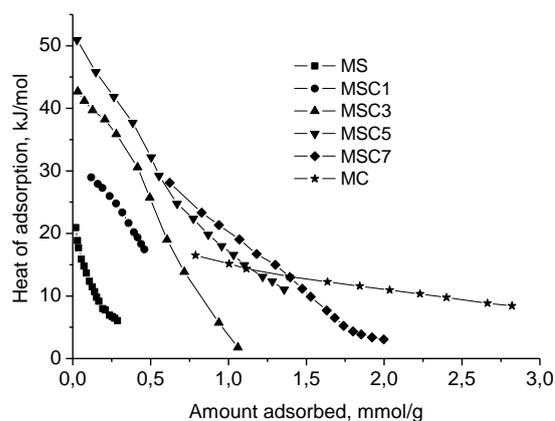
Fig. 4. Heats of adsorption for CO_2.

Table 2. Surface composition

Sample	C [at.%]	O [at.%]	Si [at.%]
MS	6.7	56.3	37.0
MSC1	27.7	46.4	25.9
MSC3	42.0	35.4	22.6
MSC5	56.4	29.5	14.1
MSC7	80.8	13.4	5.8
MC	94.9	5.1	-

The heat of adsorption is always taken into account to estimate the temperature change of the adsorption process. On other hand, it is an indicator for the regenerability of the adsorbent and for the surface energetic heterogeneity of the material. The heats of adsorption (Fig. 4) decrease as the surface coverage increases within the experimental range, which can be attributed to decrease in the interaction between the adsorbate molecules and the surface with increasing loading. This indicates the heterogeneity of the surface for the adsorption of CO_2. The limiting heats of adsorption at zero loading are calculated. Single MC and MS have lower values than mixed silica-carbon composites, however small change is observed with MC with increasing the surface coverage. At loadings greater than a monolayer the composites MSC5, MSC7, MC have larger adsorption heats than others.

The prepared silica-carbon composites as well as silica and carbon analogues were tested for CO_2 capture from flue gas in order to find whether these materials are suitable for purification.

Fig. 5 shows the CO_2 capture curves. Here, C_0 is the initial concentration of carbon dioxide and C is the concentration of CO_2 after time t.
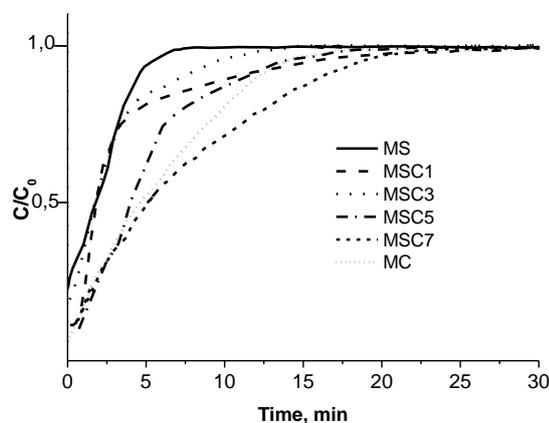
Fig. 5. CO_2 capture curves (0.3 vol% CO_2, 10 ml/min, 45°C).

The CO_2 captures are found to be: MS- 3.2 µmol/g, MSC1- 3.5 µmol/g, MSC3- 4.3 µmol/g, MSC5- 5.9 µmol/g, MSC7- 9.7 µmol/g, MC-8.6 µmol/g. One could notice that the captured CO_2 quantity increases with increasing the carbon content in the composites. However, the pure carbon mesostructured MC presents less capacity than MSC7, showing the difference of the energetic state of the surface of the silica-carbon samples and the pure carbon. Apparently, the mixed samples ensure beneficial surface for the interaction with

CO_2. This is in a good agreement with the heats of adsorption, presented in Fig. 4.

In generally, it is considered that large pore volume [14], large pore size [15], and good pore interconnection [16] is beneficial for the CO_2 capture capacity of sorbents. However, it was found that the values of the surface area and pore volume have little influence on the CO_2 capture performance of carbons [7]. Sevilla and Fuertes [17] have found that the CO_2 capture capacity seems to depend on the presence of narrow micropores rather than on the surface area or pore volumes. This is in a good agreement with our results, as the materials we found as the best samples have larger micropore volumes. Additionally, these materials are with large pore sizes, facilitating the mass transfer that is beneficial for CO_2 adsorption.

CONCLUSIONS

The synthesized ordered mesoporous silica-carbon composites have high specific surface areas, uniform mesopore-size distribution, and large mesoporous volume. The CO_2 adsorption capture results indicate that the mixed materials exhibit better performance as sorbents for CO_2 than the single silica. The capacity of the best materials is related to the large average pore sizes and to the micropore volumes. Silica-carbon composites could be a good base for further chemical modification in order to improve the sorption capacity.

REFERENCES

1. K.M.K.Yu, I. Curcic, J. Gabriel, S.C.E. Tsang, *Chem. Sus. Chem.*, **1**, 893 (2008).
2. IEA Greenhouse Gas R&D Programme, CO_2 Capture and Storage, 2006.
3. G.-P. Hao, W.-C. Li, and A.-H. Lu, *J. Mater. Chem.*, **21**, 6447 (2011).
4. A. R. Millward and O. M. Yaghi, *J. Am. Chem. Soc.*, **127**, 17998 (2005).
5. D. Zhao, Y. Wan, W. Zhou, Ordered Mesoporous Materials, Wiley-VCH, Weinheim, 2012.
6. S. Himeno, T. Komatsu, S. Fujita, *Adsorption*, **11**, 899 (2005).
7. L. Wang, M. Yao, X. Hu, G. Hu, J. Lu, M. Luo, M. Fan, *Appl. Surf. Sci.*, **324**, 286 (2015).
8. R. Liu, Y. Shi, Y. Wan, Y. Meng, F. Zhang, D. Gu, Z. Chen, B. Tu, D. Zhao, *J. Am. Chem. Soc.*, **128**, 11652 (2006).

9. A. Neimark, P. Ravikovitch, *Micropor. Mesopor. Mater.*, **44/45**, 697 (2001).
10. S. Gregg, K. Sing, Adsorption, Surface Area and Porosity, Second ed., Academic Press, London, 1982.
11. D. Chen, Z. Li, Y. Wan, X. Tu, Y. Shi, Z. Chen, W. Shen, C. Yu, B. Tu, D. Zhao, *J. Mater. Chem.*, **16**, 1511 (2006).
12. R. Ryoo, Ch. Ko, M. Kruk, V. Antochshuk, M. Jaroniec, *J. Phys. Chem. B*, **104**, 11465 (2000).
13. V. Saini, M. Andrade, M. Pinto, A. Carvalho, J. Pires, *Sep. Purif. Technol.*, **75**, 366 (2010).
14. X. Feng, G. Hu, X. Hu, G. Xie, Y. Xie, J. Lu, M. Luo, *Ind. Eng. Chem. Res.*, **52**, 4221 (2013).
15. X. Yan, L. Zhang, Y. Zhang, K. Qiao, Z. Yan, S. Komarneni, *Chem. Eng. J.*, **168**, 918 (2011).
16. C. Chen, S.-T. Yang, W.-S. Ahn, R. Ryoo, *Chem. Commun.*, 3627 (2009).
17. M. Sevilla, A. Fuertes, *J. Coll. Interface Sci.*, **366**, 147 (2012).

УЛАВЯНЕ НА ВЪГЛЕРОДЕН ДИОКСИД ВЪРХУ МЕЗОПОРЕСТИ СИЛИКАТНО-ВЪГЛЕРОДНИ КОМПОЗИТИ

Н. Стоева, Ив. Спасова, Д. Ковачева, Г. Атанасова, М. Христова

Институт по обща и неорганична химия, Българска академия на науките, 1113 София, България.

(Резюме)

Мезоструктурирани силикатно-въглеродни композити са синтезирани чрез мек темплейтен подход и са охарактеризирани посредством TG, XRD, азотна физисорбция. TEM, XPS. Изследвани са адсорбционните капацитети спрямо CO_2 и са определени топлините на адсорбция. Тествано е улавянето на CO_2 от газов поток. Композитите, съдържащи въглерод показват по-добри резултати като сорбенти за CO_2 от чист SiO_2. За силикатно-въглеродни композити се наблюдава подобрено улавяне на CO_2 с увеличаване съдържанието на въглерод. Капацитетът на силикатно-въглеродни композити за улавяне на CO_2 от газов поток се свързва със средния диаметър на порите и с обема на микропорите .

Influence of the presence/absence of bulky surfactant during the preparation of nanostructured ceria-zirconia materials on their catalytic performance in ethyl acetate total oxidation

R. Ivanova[1]*, M. Dimitrov[1], D. Kovacheva[2], T. Tsoncheva[1]

[1]Institute of Organic Chemistry with Centre of Phytochemistry, BAS, Sofia, Bulgaria
[2]Institute of General and Inorganic Chemistry, BAS, 1113 Sofia, Bulgaria

Novel nanostructured ceria-zirconia materials were synthesized in the presence or absence of bulky cetyltrimethylammonium bromide (CTAB) surfactant using an original approach combining the utilization of urea as a precipitator followed by hydrothermal treatment. The obtained materials were characterized by X-ray diffraction, nitrogen physisorption, UV-Vis spectroscopy, temperature-programmed reduction (TPR) with hydrogen and their potential application in catalysis was studied in ethyl acetate total oxidation as a model reaction for elimination of volatile organic compounds. The results show that the presence of the bulky CTAB molecules not only does not improve notably the textural characteristics of the obtained nanomaterials but limits Ce-Zr interactions in case of mixed oxide samples and thus provides a negative effect on their catalytic performance in the studied reaction. With increasing the amount of Zr in the mixed oxide samples both Ce-Zr interactions and textural mesoporosity are enhanced and this has beneficial effect on the catalytic activity in the total oxidation of ethyl acetate.

Keywords: CeO_2-ZrO_2 nanocomposites, precipitation with urea, CTAB, ethyl acetate total oxidation

INTRODUCTION

Ceria based systems are extensively investigated and have wide applications in materials science as they are able to easily form oxygen vacancies releasing surface and lattice oxygen [1 and references therein]. To enhance the redox properties and thermal stability of pure ceria, zirconia is often mixed as an additive to form solid solutions [2]. Actually, CeO_2-ZrO_2 system is one of the most studied mixed metal oxides in the literature due to its important role in the operation of automotive catalysts [3]. $Ce_xZr_{1-x}O_2$ mixed oxides are recognised to exhibit high resistance to thermal sintering and high oxygen mobility, which improves their catalytic behaviour in some reactions, such as volatile organic compounds (VOCs) combustion [4]. In our previous study highest catalytic activity in ethyl acetate combustion was demonstrated for the binary materials, where a complete integration of both metal oxides into one mixed oxide phase is realized [5]. Here, for the first time, a series of nanosized ceria-zirconia mixed oxides were prepared by co-precipitation of the corresponding metal chlorides with urea in the presence/absence of CTAB, followed by a hydrothermal treatment step at 373 K. We chose urea as precipitator instead of ammonia for better control of the processes of metal salt hydrolysis and metal oxide condensation. The obtained materials were characterized by X-ray diffraction, nitrogen physisorption, UV-Vis spectroscopy, temperature-programmed reduction (TPR) with hydrogen and their potential application in catalysis was tested in ethyl acetate combustion as a model reaction for total oxidation of volatile organic compounds. Particular attention was paid to the influence of both precipitator and template on the textural and structural properties of the obtained nanocomposites and their role in the studied reaction.

EXPERIMENTAL

Materials

Mono- and bi-component oxide samples were synthesized using precipitation technique in the presence/absence of template followed by hydrothermal treatment step according to a procedure reported by Tsoncheva et al. [6]. Here, the difference is the use of urea as a precipitator instead of ammonia and the further overnight

* To whom all correspondence should be sent:
E-mail: radostinaiv@abv.bg

stirring of the solution under reflux conditions at 85 °C before the following hydrothermal treatment. The obtained mixed oxide samples are designated as follows: xCeyZr(a,T) where x/y represents the mol ratio between Ce and Zr, a indicates the organic template if used and T is the temperature of hydrothermal treatment.

Methods of characterization

Powder X-ray diffraction patterns were collected on Bruker D8 Advance diffractometer equipped with Cu Kα radiation and LynxEye detector. The size of the crystalline domains in the samples was determined using Topas 4.2 software with Rietveld quantification refinement. Nitrogen sorption measurements were recorded on a Quantachrome NOVA 1200e instrument at 77 K. The UV–Vis spectra were recorded on a Jasco V-650 UV-Vis spectrophotometer equipped with a diffuse reflectance unit. The TPR/TG (temperature-programmed reduction/ thermogravimetric) analyses were performed in a Setaram TG92 instrument. The catalytic experiments were performed in a flow type reactor (0.030 g of catalyst) with a mixture of ethyl acetate (1.21 mol %) in air with WHSV – 335 h^{-1}. Gas chromatographic (GC) analyses were carried out on HP5850 apparatus using carbon-based calibration. The samples were pretreated in Ar at 423 K for 1 h and then the temperature was raised with a rate of 2 K/min in the range of 423–773 K.

RESULTS AND DISCUSSION

Some physicochemical characteristics of the obtained samples are presented in Table 1.

X-ray diffraction technique (XRD) has been used for determination of samples crystallinity and phase composition (Fig. 1).

Table 1. Texture and structure characteristics of the obtained materials.

Sample	S_{BET}, m^2/g	V_{total}, cc/g	S_{micro}, m^2/g	V_{micro}, cc/g	Space Group	Unit cell, Å	Crystallite size, nm
CeO$_2$(CTAB, 373)	70.7	0.10	64.0	0.026	Fm-3m	5.4150(7)	12
CeO$_2$(no, 373)	71.9	0.06	59.0	0.024	Fm-3m	5.4146(6)	13
7Ce3Zr(CTAB, 373)	67.4	0.09	26.5	0.01	Fm-3m	5.4128(8)	14
					P4$_2$/nmc	a=3.616(1) c=5.204(4)	12
7Ce3Zr(no, 373)	90.1	0.10	46.2	0.02	Fm-3m	5.4139(9)	13
					P4$_2$/nm	a=3.616(1) c=5.191(3)	14
5Ce5Zr(CTAB, 373)	67.3	0.10	17.6	0.008	Fm-3m	5.4118(8)	13
					P4$_2$/nm	a=3.618(1) c=5.208(3)	13
5Ce5Zr(no, 373)	55.2	0.10	20.1	0.009	Fm-3m	5.4139(9)	11
					P4$_2$/nm	a=3.616(1) c=5.194(2)	17
3Ce7Zr(CTAB, 373)	66.8	0.12	1.3	0.0004	Fm-3m	5.4138(9)	13
					P4$_2$/nm	a=3.617(1) c=5.206(2)	13
3Ce7Zr(no, 373)	80.4	0.11	5.2	0.003	Fm-3m	5.414(1)	11
					P4$_2$/nm	a=3.620(1) c=5.210(2)	13
ZrO$_2$(CTAB, 373)	59.3	0.11	-	-	P2$_1$/c	a=5.150(5) b=5.202(5) c=5.303(4) β=98.85(2)	13
					P4$_2$/nmc	a=3.592(5) c=5.19(1)	10
ZrO$_2$(no, 373)	44.3	0.09	-	-	P2$_1$/c	a=5.16(1) b=5.20(2) c=5.31(1) β=98.68(5)	11
					P4$_2$/nmc	a=3.608(5) c=5.173(9)	13

Pure ceria as well as all cerium-containing samples show well defined reflections of cubic fluorite-like structure with crystallite sizes of about 11-14 nm (Fig. 1, Table 1). Both monoclinic (P2$_1$/c)

and tetragonal ($P4_2/nmc$) phases are registered in case of pure zirconia samples (Fig. 1, Table 1.).
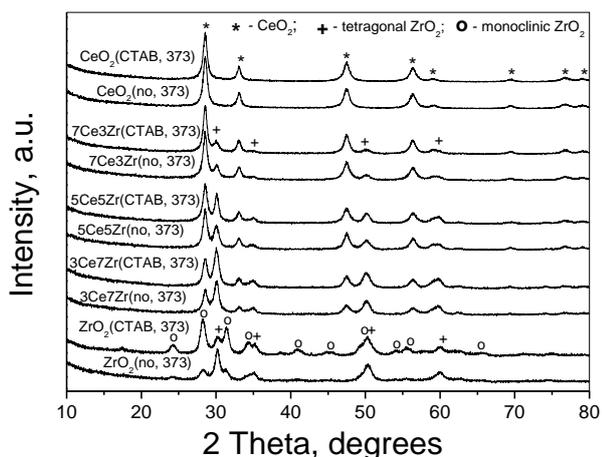
Fig. 1. XRD patterns of the studied samples.

Here, the absence of CTAB template molecules during the synthesis of ZrO_2(no, 373) sample seems to provoke the formation of tetragonal phase in a higher extent at the expense of monoclinic one (Fig. 1, Table 1). In case of mixed oxide samples, the intensity of ceria reflections decreases with zirconium content increase, but the ceria phase seems to remain unchanged as its unit cell parameter is almost not influenced by zirconium addition (Fig.1, Table 1). For these materials zirconia phase with tetragonal symmetry was also detected (Table 1). Its unit cell parameters are slightly expanded in comparison with the corresponding ZrO_2 individual oxides. This indicates partial introduction of cerium within the zirconia phase, the effect being more pronounced with the zirconium content increase.
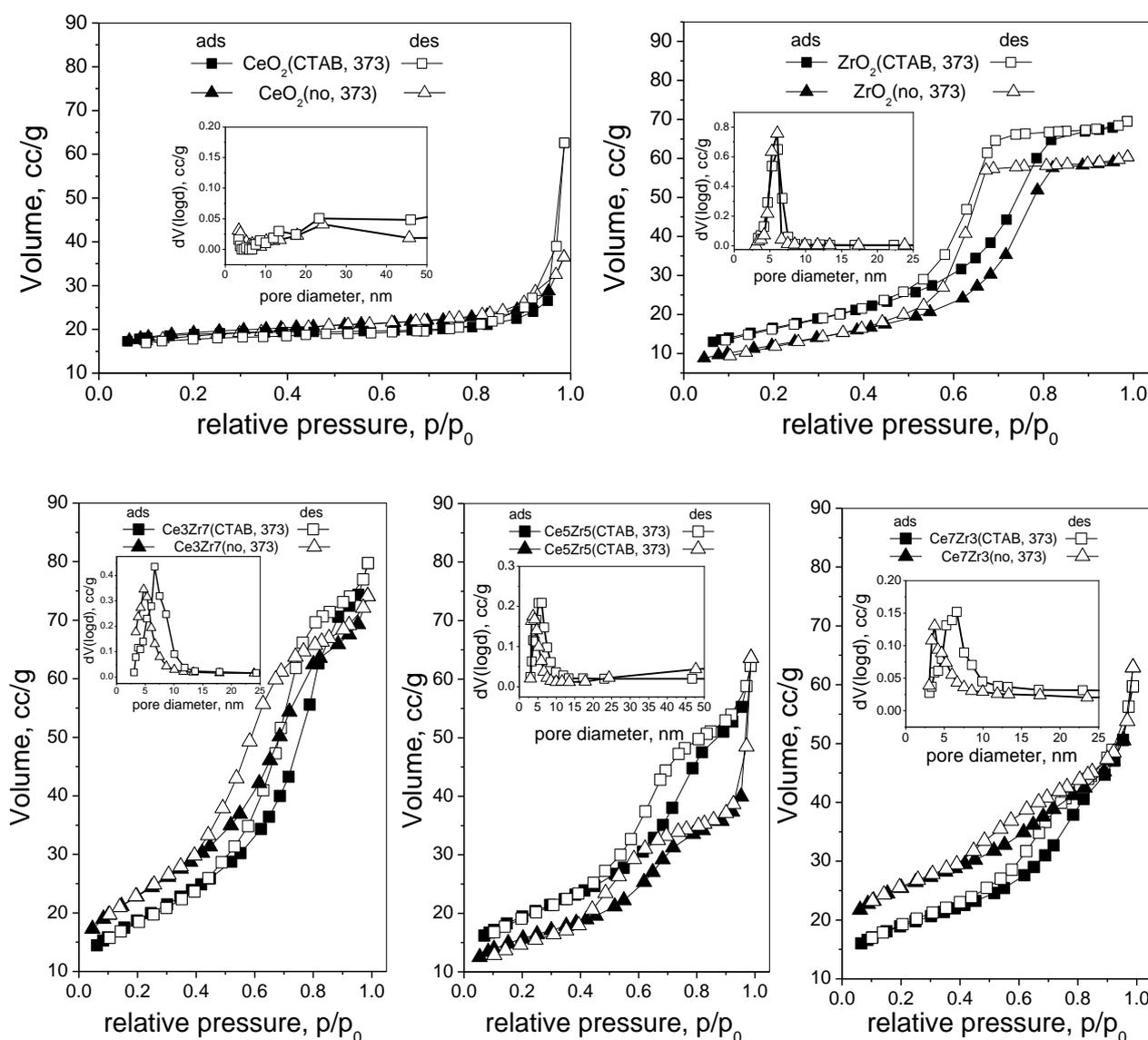
Fig. 2. Nitrogen physisorption isotherms with pore size distributions as insets for the studied pure and mixed metal oxide samples.

Nitrogen physisorption measurements were conducted in order to elucidate the textural properties of the studied samples (Fig. 2, Table 1). All isotherms are of type IV that is characteristic of mesoporous materials with the exception of pure ceria samples, which isotherms are combination of types I and IV with predominant presence of micropores (Fig. 2, Table 1). At the same time, both pure zirconia samples are exclusively mesoporous, characterized with steep adsorption step within 0.6-0.8 relative pressure and H1 type hysteresis due to narrow pore size distribution (Fig. 2, Table 1). In case of mixed oxide samples the shape of their isotherms is in-between those of the pure metal oxides with mesoporosity increasing with Zr content and with comparable textural characteristics for the analogous samples, however, smaller pore sizes and narrower pore size distributions are found for the samples obtained without CTAB (Table 1).

Uv-Vis analysis has been used to obtain information for the coordination and oxidative state of metal ions. The spectra of both ZrO_2 samples show two absorption bands at around 215 and 230 nm, as expected for monoclinic ZrO_2 [7]. The second broad feature in their spectra positioned at around 320 nm reveals the co-existence of tetragonal ZrO_2 [7] and it is larger for ZrO_2(no, 373). For pure ceria (Fig. 3), the strong absorption with maximum at about 350-360 nm is ascribed to $O^{2-} \rightarrow Ce^{4+}$ charge transfer (CT) transitions, while that one at about 250 nm – to $O^{2-} \rightarrow Ce^{3+}$ CT transitions [8]. In case of all mixed oxides samples these bands are preserved, however, the latter one is slightly red-shifted and the former – blue-shifted, which together with the slightly increased overall absorption above 500 nm could be ascribed to the appearance of additional defects due to incorporation of Ce within zirconia lattice.

Additional information for the redox properties of the studied materials was obtained by temperature-programmed reduction (TPR) with hydrogen (Fig. 4). No significant TG effect is observed for both ZrO_2 samples, indicating negligible reduction transformations under studied conditions. The reduction degree of both pure ceria samples is about 14 %. The reduction of all mixed oxide samples obtained without CTAB template is facilitated as the start of the reduction is shifted to lower temperatures compared to pure ceria samples and/or the reduction degree is significantly increased, especially with Zr content above 30 mol % (Fig. 4). We could ascribe the observed effects to the partial introduction of cerium within the zirconia phase and the presence of smaller ceria crystallites within these samples (Table 1).
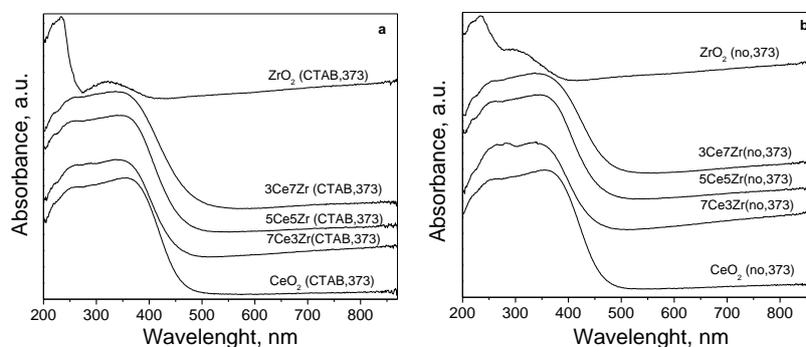
Fig. 3. UV-Vis spectra for the samples prepared with CTAB template (a) and without (b)
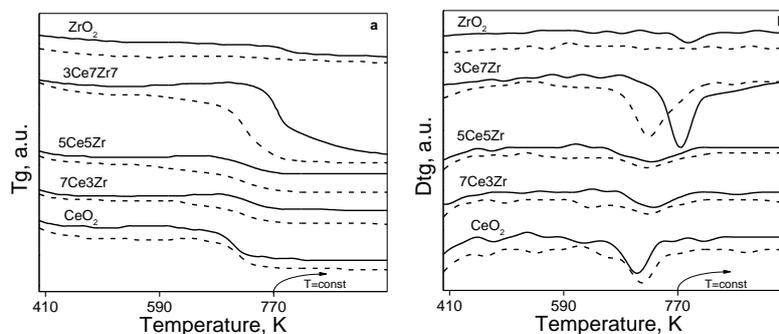
Fig 4. TG (a) and DTG (b) data for the samples prepared with CTAB template (solid line) and without (dash line).
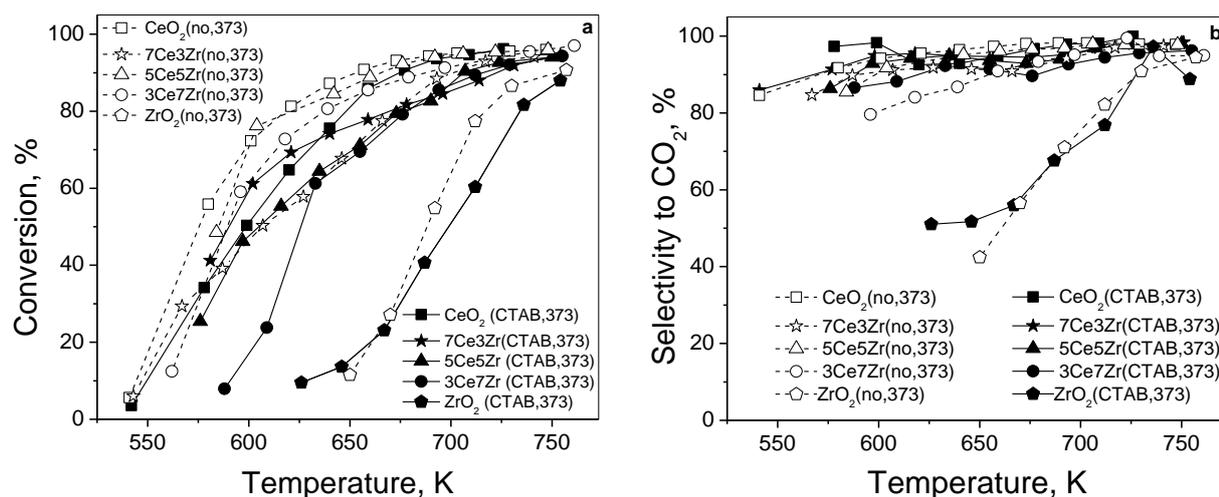
Fig. 5. Temperature dependency of ethyl acetate total oxidation for the studied samples.

The catalytic properties of the samples were studied in temperature-programmed regime within the range of 423–773 K (Fig. 5). Pure zirconia samples show catalytic activity just above 625-650 K with relatively low selectivity to CO_2 due to their significant acidic function and relatively low redox ability. At the same time, both pure ceria materials display steeply increasing conversion activity above 550 K combined with enhanced selectivity to total oxidation that could be assigned to their superior redox properties. All mixed oxide samples show improved catalytic activity, taking into consideration their cerium content, as well as very high selectivity to CO_2, and we assign this to their overall enhanced redox properties in comparison with pure ceria samples due to cerium substitution within zirconia lattice. The latter seems to be favoured by the absence of template during the synthesis (especially for the samples with Zr content above 30 mol %) and this is probably provoked by the improved intimate contact between the metal oxide particles.

CONCLUSION

By using an original synthetic approach we have prepared highly active and selective in total oxidation of ethyl acetate nanostructured ceria-zirconia materials comprised of nanosized particles arranged in a micro-mesoporous structure. The use of urea only as both precipitator and template gives optimal textural and structural characteristics of the obtained mixed oxides, especially for the samples

with Zr content above 30 mol %, while the additional presence of bulky CTAB molecules during synthesis seems to limit Ce-Zr interactions and thus has a negative effect on their catalytic performance. Further investigations with time-on-stream catalytic experiments are in progress.

REFERENCES

1. S. McIntosh, R. J. Gorte, *Chem. Rev.,* **104**, 4845 (2004).
2. S. Arai, S. Muto, J. Murai, T. Sasaki, Y. Ukyo, K. Kuroda, H. Saka, *Mater. Trans.*, **45**, 2951 (2004).
3. M. Boaro, M. Vicario, C. Leitenburg, G. Dolcetti, A. Trovarelli, *Catal. Today*, **77**, 407 (2003).
4. M. V. Ganduglia-Pirovano, A. Hofmann, J. Sauer, *Surf. Sci. Rep.*, **62**, 219 (2007).
5. M. D. Dimitrov, R. N. Ivanova, V. Štengl, J. Henych, D. G. Kovacheva, T. S. Tsoncheva, *Bulg. Chem. Commun.,* **47**, 323 (2015).
6. T. Tsoncheva, R. Ivanova, J. Henych, M. Dimitrov, M. Kormunda, D. Kovacheva, N. Scotti, V. Dal Santo, V. Štengl, *Appl. Catal., A*, **502,** 418 (2015).
7. S. Damyanova, B. Pawelec, K. Arishtirova, M.V. Martinez Huerta, J.L.G. Fierro, *Appl. Catal., A*, **337**, 86 (2008).
8. A. Kambolis, H. Matralis, A. Trovarelli, Ch. Papadopoulou, *Appl. Catal., A*, **377**, 16 (2010).

ВЛИЯНИЕ НА ПРИСЪСТВИЕТО/ОТСЪСТВИЕТО НА ОБЕМНО ПОВЪРХНОСТНО АКТИВНО ВЕЩЕСТВО ПРИ ПОЛУЧАВАНЕТО НА НАНОСТРУКТУРИРАНИ CeO_2-ZrO_2 МАТЕРИАЛИ ВЪРХУ ТЕХНИТЕ КАТАЛИТИЧНИ ОТНАСЯНИЯ В РЕАКЦИЯТА НА ПЪЛНО ОКИСЛЕНИЕ НА ЕТИЛАЦЕТАТ

Р. Иванова[1], М. Димитров[1], Д. Ковачева[2], Т. Цончева[1]

[1]Институт по органична химия с Център по фитохимия, БАН, 1113 София, България
[2]Институт по обща и неорганична химия, БАН, 1113 София, България

(Резюме)

Бяха синтезирани нови наноструктурирани материали в присъствие или отсъствие на цетилтриметиламониев бромид (СТАВ), като беше използван оригинален подход, включващ използването на уреа като утаител с последваща хидротермална обработка. Получените материали бяха характеризирани с помощта на прахова рентгенова дифракция, физична адсорбция на азот, UV-Vis спектроскопия, температурно-програмирана редукция с водород, а тяхното потенциално приложение в катализа беше изследвано в изгаряне на етилацетат, като моделна реакция за елиминиране на летливи органични съединения. Резултатите показват, че присъствието на СТАВ не само не подобрява значително текстурните характеристики на получените материали, но има негативен ефект върху техните каталитични свойства като ограничава взаимодействието Ce-Zr. С увеличаване на съдържанието на Zr в смесените образци се подобряват мезопористостта и взаимодействието Ce-Zr, което има благоприятен ефект върху каталитичната активност на образците в пълно окисление на етилацетат.

Physicochemical characterization of chia (*Salvia hispanica*) seed oil from Argentina

G. Uzunova[1], Kr. Nikolova[2]*, M.Perifanova[1], G. Gentscheva[3], M. Marudova[4], G. Antova[4]

[1]*University of Food Technologies, blv. Meritza 26, Bulgaria, Plovdiv, 4002*
[2]*Medical University, blv. Marin Drinov 54, Bulgaria, Varna, 9002*
[3]*Institute of General and Inorganic Chemistry, BAS, Acad. G. Bonchev Str., Bulgaria, Sofia, 1113*
[4]*Plovdiv University, 24 Tzar Assen Str., Bulgaria, Plovdiv,4000*

The physicochemical characteristics of chia oil from Argentina, which is one of the most efficient omega-3 (n-3) sources for enriching foods, have been studied. The results from analysis show that the chia oil has a relative density of 0.9288, refractive index 1.4810 and yellow color component that dominates over the red one. Its acidity index is 1.68 mg KOH/g, its saponification index is 197.9 mg KOH/g, iodine index is 208.3 g I_2/ 100g and the peroxide index is 1.95 meq O_2/kg. The fluorescence spectra for excitation wavelength 350 nm contain 3 peaks at about 472 nm, 503 nm and 670 nm, which are attributed to pigments, vitamins and oxidation products. Besides, the spectra in visible and UV range are used for determination of chlorophyll content, content of β-carotene, oxidation products and oxidant stability. Phase transition is observed at -36.9 °C. The content of some essential, non essential and toxic elements in the solution obtained after microwave-assisted (MW) digestion of the examined oil were determined by Inductively Coupled Plasma Mass Spectrometry (ICP-MS). This method could be useful for quality control of the oil when used in food industry, medicine and cosmetics

Keywords: UV and visible spectroscopy, fluorescence, mineral contents, color characteristic

INTRODUCTION

Chia (*Salvia hispanica* L.) seed oil is an interesting source of polyunsaturated fatty acids (PUFA). It contains the highest proportion of α-linolenic acid (*60%) of any known vegetable sources [1]. This fatty acid (FA) belongs to the n-3 family which is essential for the normal growth and development of the human body and plays an important role in the prevention and treatment of coronary artery disease, hypertension, diabetes, arthritis, other inflammatory and autoimmune disorders, and cancer [2]. Further, chia oil is used as a base for face and body paintings. The activation energy of chia seed oil, calculated from the extrapolated temperature of the start of oxidation (T_e), was similar to that reported for pure α-linolenic acid (62–70 kJ/mol) [3], the main fatty acid presented in chia seed oil, and lower than the activation energy for corn oil (104.3 kJ/mol) [4]. The physicochemical characteristics and fatty acid composition of chia oils were investigated by Velasco Vargas, Alvarez-Chavez, Bushway [5-7].

However, no information was found about the mineral content and optical properties as fluorescence spectra and absorption spectra in UV region, which are connected with the presence of pigments and oxidative products. Obviously, further knowledge on chia seed oil properties is needed, which may lead to different uses in the food industry or medical, pharmaceutical and other non-food industrial applications. Based on that, the main objectives of this work are to study mineral content, some important physicochemical and quality characteristics of *Salvia hispanica* seed oil from Argentinahe .

EXPERIMENTAL

Chia (*Salvia hispanica*, L.) seeds were obtained in Argentina and the oil was extracted in a Bulgarian factory. The samples were poured into a 10-mm thick dish. The color parameters in two colorimetric systems XYZ and SIE Lab have been measured by Lovibond PFX 880 (UK). The refractive index of the oil was measured using an Abbe refractometer (Carl Zeiss, Germany) at 20°C.

The thermal characteristics of the chia oil samples were investigated in the temperature range of - 60°C to 20°C by differential scanning

* To whom all correspondence should be sent:
E-mail: kr.nikolova@abv.bg

calorimeter DSC 204 F1 Phoenix (NETZSCH, Germany), equipped with intracooler. The DSC apparatus was calibrated with indium standart. In order to avoid condensation of water, argon gas was used to purge the furnace chamber at 20 ml min^{-1}. The samples (5-10 mg) were weighed into 40 μl aluminum standard crucible and hermetically sealed with aluminum standard lead. An empty aluminum crucible was used as a reference.

Iodine and saponified values and free fatty acid content were determined according to AOCS recommended practices Cd 1c-85, Ca 6a-40 and Ca 5a-40, respectively [8]. Oil oxidative stability was evaluated by the Rancimat (Mod 679, Metrohm) method, using 3 g of oil sample warmed at 100°C with air flow of 20 L h^{-1}.

Determination of dynamic and kinematic viscosity was obtained by using degrees *Engler*. They are presented as ratio of the time of flow of 200 ml of the investigated oil to the time of flow of 200 ml of distilled water at the same temperature (usually 20°C, but sometimes 50°C or 100°C).

Samples of about 0.3 g were weighed in Teflon vessels of microwave digestion system, then 8 ml 67% HNO_3 (supra pure) and 2 ml 30% H_2O_2 (supra pure) were added and samples were left to stay overnight. Microwave digestion was performed as follows: 15 min to reach 220°C and 20 min left to stay at this temperature. After cooling the samples were transferred in 100 ml volumetric flask and diluted up to the mark with deionized water. A blank sample was passed through the whole analytical procedure. Inductively coupled plasma-mass spectrometer "X SERIES 2"– Thermo Scientific was used for the determination of elements.

The sources used to measure the fluorescence spectra are 250 nm, 300 nm, 350 nm, 400 nm and 450 nm light emitting diodes (LEDs). A fiber optic spectrometer (AvaSpec-2038, Avantes) with sensitivity in the 200-1100 nm range and a resolution of about 8 nm was used to measure the fluorescence spectra. The oil samples were placed in a 10 mm x 10 mm cuvette and irradiated by LEDs.

RESULTS

In the present study various techniques have been used for the characterization of chia (*Salvia hispanica*) seed oil from Argentina. The obtained main values for some physical and chemical characteristics are given in Table 1.

As seen, the relative density of Argentinian chia oil is greater than sunflower and soybean oils, but its value is very close to the relative density of Mexican chia oil 0.9241 [9]. According to Alvarado and Aguilera [10], the relative density is high to higher unsaturation's content in the fatty acids. The refractive index is greater than the values measured by the other author for Mexican chia oil 1.4761 and for Argentinian chia oil 1.4768 [12]. The Iodine value registered here (208.3 gI_2/100 g oil) showed the unsaturation grade of chia's oil, and that this parameter is proportional to the number of double bonds in the fatty acid chains.The Iodine index in chia oil could be compared only with the Iodine value in linseed oil (187 gI_2/100 g oil) [13]. The acidity value is similar to chia oil obtained by pressing seed from Guatemalan seeds with 1.64 mg KOH/g oil [12]. The oxidative stability of foods is dependent on the composition, concentrations and activity of reaction substrates and antioxidants. In order to minimize the use of food additives, the oxidative stability can be potentially improved by preserving or enhancing the endogenous oxidation control systems of foods [14]. The accelerated stability test showed that chia oils have a low oxidative stability of 2.4 h. In spite of the presence of antioxidant compounds, the high content of poly unsaturated fatty acids makes chia seed oil very instable. In this respect, some innovative technologies to protect from oxidation of this oil are needed.

Table 1 Physical and chemical properties of chia oils.

Physical and Chemical Properties	Argentinian chia oil
Peroxide value (meqO_2/kg oil)	1.95
Acidity value (mg KOH/g oil)	1.68
Saponification value (mg KOH/g oil)	197.9
Iodine value (g I_2/100 g oil)	208.3
Relative density	0.9288
Refractive index	1.4810
Oxidative stability (h)	2.4
Dynamic viscosity (Pa.s)	4.25. 10^{-2}

The color characteristics in two color systems XYZ and SIELab are shown in Table 2. On the base of transmission spectra in the visible region the pigments chlorophyll and β-carotene are determined. It is evident that color coordinates **x** and **y** are almost equals. Parameter *a** assumed a negative but low value, similar to data reported for β-carotene [15]. Besides, the chia seed oil samples showed positive values of parameter *b**, which is characteristic of yellow colors. Obviously, this oil is very rich of pigments.

There are data for fatty acid composition of chia oil in the literature, but the optical and especially

fluorescence properties are not investigated. That's why in the present study the fluorescence spectra in the UV and visible region are recorded. The excitation – emission matrices are presented on the Fig 1.

Table 2 Color parameters of chia oils.

Color parameters	Argentinian chia oil
X	73.20
Y	79.81
Z	26.20
x	0.4085
y	0.4454
L	91,55
a	-10.03
b	64.31
Chlorophyll	22.08 ppm
β - carotene	0.156 ppm
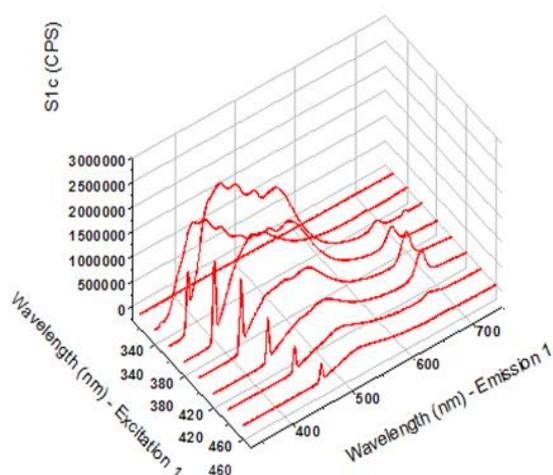
Fig. 1. Excitation-emission matrix for chia oil.

The fluorescence peaks give the connection between the optical and chemical properties of the sample and afford on the opportunity for its quality investigation. The good ratio between the intensities of emission and excitation is observed for excitation wavelength 350 nm. The distinct fluorescence peak is observed at about 440 nm, which is connected with phenol antioxidants. Among the primary oxidation products are hydroperoxides which further degrade to secondary products: aldehydes, alcohols, hydrocarbons and ketones [16]. It's important to notice that the known products formed during oxidation of vitamin E group are all non-fluorescent [17]. Changing in the content of tocopherols and phenols is also detected at about 503 nm. The fluorescence properties of the pigments are very similar and that's way signals in the wide wavelength range 600 - 720 nm are detected [17]. There is presence of the chlorophyll

group in the studied sample and the band at 670 nm is attributed to it. The fluorescence maxima at 472 nm can be explained with the presence of β-carotene.

The extent of oxidation of chia oil has been estimated by the obtaining of absorption peaks in the UV region. The UV spectrum is presented on the Fig. 2.
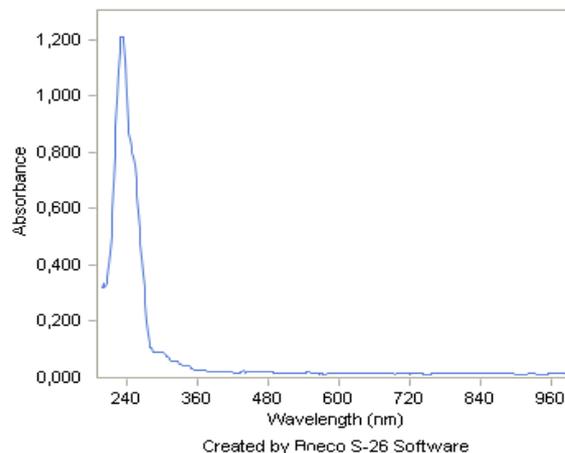
Fig. 2. UV spectrum for chia oil

The degree of oxidation of the studied sample is estimated through indirect determination of primary oxidation products (peroxides) of absorption of conjugated diene structures which are formed from linoleate units using UV spectroscopy at 232 nm and from the absorption of conjugate triene structures at 268 nm. The chia oil has a high content of polyunsaturated fatty acids (80%) and according to the obtained values of absorbance at 232 nm is oxidized. The absence of an absorption peak around 270 nm, however, proves the absence of by-products of the oxidation of carbonyl character. These results show that the oil of chia can be used for food purposes, but not recommended to be subjected to the heat treatment.

Further, the transmittance of the oil in the visible region has been investigated. It is seen that the oil strongly absorbs in the short wavelength of the spectrum from 400 nm to 500 nm. The transmittance is over to 90% of light flux from 550 nm to the end of the visible region.

Trace elements Fe, Cu, Ni and Mn [18] increased the rate of oxidation of the oil by the formation of free radicals of fatty acids and hydroperoxides. As mineral composition, chia oil is low in elements like all other oils (Ca=37.6 $\mu g\ g^{-1}$; K=6.78 $\mu g\ g^{-1}$; Mg=3.67 $\mu g\ g^{-1}$; Zn=2.35 $\mu g\ g^{-1}$; Cr=0.19 $\mu g\ g^{-1}$; Mn= 0.23 $\mu g\ g^{-1}$; Fe=2.32 $\mu g\ g^{-1}$; Co, Cu and Se<0.01 $\mu g\ g^{-1}$). There are no toxic elements (Ni=0.03 $\mu g\ g^{-1}$; Pb=0.06 $\mu g\ g^{-1}$; As, Cd, Tl and Hg<0.01 $\mu g\ g^{-1}$) and it can be used in food,

medical and cosmetics industry. It is possible that concentrations of some elements are influenced by the manufacturing process and equipment.

Fig. 3 shows the DSC thermogram of chia oils stydied. The maximum of the largest peak takes place at around -32 °C, the maximum of the second largest peak is at around -10 °C.
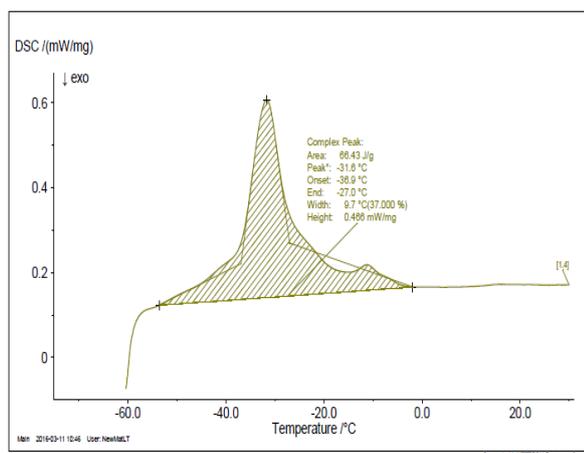
Fig. 3. DSC thermogram for chia oil

The relatively low melting temperatures could be related to the chia oil fatty acid composition - high amount of poly unsaturated triacylglycerols, like α-linolenic acid and linoleic acid [19]. As a consequence, the chia oil may be stored in a refrigerator, as it is not expected to partially crystallize (like other oils, such as olive oil). This ensures better storage conditions since the oxidative stability is low due to its high unsaturation.

CONCLUSION

Because of the increasing popularity of chia oil as a very important source of n-3 and n-6 fatty acids, this study presents a view of the characteristics of chia oil and the obtained parameters that could be used as a starting point to define quality standards since there are little specifications available for this nontraditional vegetable oil.

The chia oil has a high content of polyunsaturated fatty acids (80%) and according to the obtained values of absorbance at 232 nm it can serve as an evaluation of the degree of oxidation. The absence of an absorption peak at around 270 nm suggests that this oil can be used for food purposes, but it is not recommended to be used after heat treatment. The experimental results from fluorescence spectra show that the oil is reach of tocopherols and phenols (emission fluorescence peak at about 503 nm), chlorophyll group (λ_{em}= 670

nm), β-carotene (fluorescence maxima at 472 nm).

The absence of toxic elements shows that the product can be used in food, medical and cosmetics industry. An important problem is to improve the oxidative stability of the chia oil from Argentina, which could be resolved by the addition of natural antioxidants such as phenolic components.

REFERENCES

1. R. Ayerza, W. Coates, *Ind. Crops Prod.*, **34**, 1366 (2011).
2. A. Simopoulos, *J. Am. Coll. Nutr.*, **21**, 495 (2002).
3. G. Litwinienko, *J. Therm. Anal. Calorim.*, **165**, 639 (2001).
4. G. Litwinienko, T. Kasprzycka-Guttman, M. Jarosz-Jarszewska, *J. Therm. Anal.*, **45**, 741 (1995).
5. L. Alvarez-Chavez, M.. Valdivia-Lopez, M. Aburto-Juarez, A. Tecante, *J. Food Prop.*, **11**, 687 (2008).
6. A. Bushway, P. Belyea, R. Bushway, *J. Food Sci.*, **46**, 1349 (1981).
7. I. Vargas, A. Tecante, M. Lopez, Proceeding of the IV Encuentro nacional de Biotecnologia IPN, Santa, Cruz, Tlaxcala, Mexico (2004).
8. AOCS Official methods and recommended practices of the AOCS, 5th edn. AOCS Press, Champaign, 1998.
9. M. Segura-Campos, N. Ciau-Solís, G. Rosado-Rubio, L. Chel-Guerrero, D. Betancur-Ancona, *Agricult. Sci.*, 5, 220 (2014).
10. J. Alvarado, J.Aguilera., Métodos para medir propiedades físicas en industrias de alimentos. Ed. Acribia, Zaragoza, España, 2001.
11. V. Ixtaina, M. Martínez, V. Sportono, C. Mateo, D. Maestri, B. Diehl, S. Nolasco, and M. Tomas, *J. Food Comp. Anal.*, **24**, 166 (2011).
12. R. Patil, A. Nawab, *Int. J. Food Prop.*, **9**, 227 (2006).
13. E. Decker, *Trends Food Sci. Technol.*, **9**, 241 (1998).
14. A. Meléndez-Martínez, J. Britton, I. Vicario, F. Heredia, *Food Chem.*, **101**, 1145 (2006).
15. K. Poulli, N. Chantzos, G. Mousdis, C. Georgiou, *J. Agric. Food Chem.*, **57**, 8194 (2009).
16. E. Sikorska, I. Khmelinskii, M. Sikorski, "Olive Oil - Constituents, Quality, Health Properties and Bioconversions", Chapter 4 "Analysis of Olive Oils by Fluorescence Spectroscopy: Methods and Applications", InTech, 2012.
17. E. Sikorska, T. Górecki, I. Khmelinskii, M. Sikorski, J. Koził, *Food Chem.*, **89**, 217 (2005).
18. I. Karadjova, G. Zachariadis, G. Boskou and J. Stratis, *J. Anal. Atom. Spectrom.*,, **13**, 201 (1998).
19. M. Grompone, B. Irigaray, D. Rodríguez, S. Maidana, N. Sammán, *J. Food Sci. Eng.*, **5**, 49 (2015).

ФИЗИКОХИМИЧНИ ХАРАКТЕРИСТИКИ НА ЧИА (SALVIA HISPANICA) МАСЛО ОТ АРЖЕНТИНА

Г. Узунова, Кр. Николова[2], М. Перифанова[1], Г. Генчева[3], М. Марудова[4], Г. Антова[4]

[1]Университет по хранителни технологии, бул. Марца 26, България, Пловдив, 4002
[2]Медицински университет, бул. Марин Дринов 54, България, Варна, 9002
[3]Институт по обща и неорганична химия, БАН, ул. Акад. Г. Бончев, България, София, 1113
[4]Пловдивски университет, ул. Цар Асен 24, България, Пловдив, 4000

(Резюме)

Изследвани са физикохимичните характеристики на масло от чиа /Аржентина/, което е един от най-ефективните омега-3 (N-3) източниците за добавка към храни. Резултатите показват, че маслото от чиа има относителна плътност - 0.9288, показател на пречупване - 1.4810 и жълта цветова компонента, която доминира над червената. Както и киселинно число: 1.68 mg KOH/g; индекс на осапуняване: 197.9 mg KOH/g; йодно число: 208.3 g I_2/100g, пероксидно число: 1.95 meq O_2/kg. Флуоресцентните спектри, получени при възбуждане с дължина на вълната 350 nm имат 3 пика: около 472 nm, 503 nm и 670 nm, които се дължат на пигменти, витамини и продукти на окисление. Освен това, спектри във видимата и UV област са използвани за определяне на съдържанието на хлорофил, β-каротин, продукти на окисление и оксидантна стабилност. Наблюдаван е фазов преход при -36.9ºC. Концентрацията на някой основни, есенциални и токсичните елементи в пробите са определени чрез ICP-MS, след микровълново разлагане на маслото. Този метод може да бъде полезен за контрол на качеството на маслото, когато се използва в хранително-вкусовата промишленост, медицината и козметиката

Mechanism of bacterial co-aggregation between *Bacillus subtilis* and *Escherichia coli* K-12 strains

I. Ganchev*, S. Mihailova

The Stephan Angeloff Institute of Microbiology, Bulgarian Academy of Sciences
1113 Sofia, "Acad. Bonchev" str., bl. 26

This work aims at exploring the co-aggregation of Bacillus subtilis 170 and Bacillus subtilis 168 with Escherichia coli K-12 strains. The influence of different physical and chemical factors involved in this features was investigated. Co-aggregation was found to be dependent on various factors: pH, temperature. Treatment with trypsin, proteinase K and chelating agents such as EDTA (ethylene diamine tetra acetic acid), heat treatment was found to inhibit co-aggregation. Among the different kind of sugars, the co-inoculation of Bacillus subtilis 170 and Bacillus subtilis 168 with Escherichia coli K-12 strains inhibited in a higher degree in the presence of N-acetyl glucosamine as compared to the other monosaccharides. Therefore, co-aggregation between tested strains was mediated by the lectin – polysaccharide interactions.

Keywords: *Bacillus subtilis* 170, *Bacillus subtilis* 168, *Escherichia coli* K-12, co-aggregation, biofilms

INTRODUCTION

Microorganisms are found in a wide range of diverse ecosystems as highly structured, multispecies communities termed biofilms [1, 2, 3, 4, 5]. Actually, biofilms can develop on a wide range of surfaces of food industry plants: stainless steel surfaces of open or closed pieces of equipment, floor, belts, rubber seal and so on [6].

Co-aggregation is an integral process in the formation of mixed biofilms and is therefore ecologically important [7, 8, 9] is characterized as an intra- or inter-species interaction of bacteria [1, 2, 10]. It differs from autoaggregation, which is defined as the adherence of bacteria belonging to the same strain [11, 12].

Physical interactions between co-aggregating bacteria facilitate metabolic interactions, such as oxygen protection, cell–cell communication and genetic exchange between cells [13, 14, 15]. The co-aggregation interaction is a highly specific process mediated by the recognition of complementary lectin — carbohydrate molecules between the aggregating partners [13, 14, 15, 12, 9], specific host-like patterns within the hexa- and heptasaccharide repeating units of different receptor polysaccharides [16].

Many studies have described the mechanisms of oral biofilm formation [16]. Co-aggregation also occurs between members of the urogenital flora and between strains of Lactobacillus from chicken crops [17, 18], as well as on human enteropathogens [19], uropathogens and chronic periodontitis [20]. In addition, co-aggregation has also been shown to occur between bacteria derived from aquatic ecosystems [19, 21] and rhizosphere [22].

This article is a thorough study of impact of environmental factors on the degree of co-aggregation between of *B. subtilis* 168 and *B. subtilis* 170 strains at their interaction with of *E. coli* K-12 strains.

MATERIALS AND METHODS

Bacterial strains. This study used of *Bacillus subtilis*168, *Bacillus subtilis* 170 strains, *Escherichia coli* W1655, *Escherichia coli* 406, *Escherichia coli* 420, *Escherichia coli* 446 K-12 strains, deposited in the collection of National Bank of Industrial Microorganisms and Cell Cultures, Sofia, Bulgaria, and *E. coli* 1655 K-12 strain from the collection of Institute of Molecular Biotechnology, Jena, Germany. All strains were inoculated into 9.00 ml of a liquid culture medium (LB broth) and incubated at 37 ° C for a period of 18 hours before the beginning of each determination.

---

*To whom all correspondence should be sent:
E-mail: ivotg@abv.bg

Co-aggregation assay. 1.00 ml aliquots of B. subtilis and E.coli K-12 overnight cultures were mixed together in 10,00 ml co-aggregate buffer (0,01 mM CaCl$_2$, 0,01 mM MgCl$_2$, 0,15 M NaCl) and vortexed for 10 s. The mixture was incubated in a rotary shaker for three min and left undisturbed for 4 h. Then co-aggregation assay was investigated according to methods described from Rathi et co-workers [21].

Effect of proteinase, trypsin and heat treatment, pH and temperature, chelating agent EDTA and sugars on the co-aggregation. All experiments were investigated according to methods described by Rathi et co-workers [21].

Scanning electron microscope assays. Bacterial co-aggregates were prepared according to method described by Phuong et co-workers [19]. Observations were performed on a scanning electron microscope.

Confocal laser scanning microscope assays. Bacterial co-aggregates were staining with Live Bacterial Gram Stain Kit according to instructions of the manufacturing company Biotum.

Statistical analysis. To investigate differences in co-aggregation between various *B. subtilis* strains and *E.coli* K-12, a one-way ANOVA and a Student's t -test was performed for the comparison between strains. The level of significance for all statistical tests was set at P < 0.05.

RESULTS AND DUSCUSSION

Bacteria in multispecies biofilms are able to make physical contact each other [23]. Specific direct interactions are known as co-aggregation [24]. This process underlies formation of biofilms of different microbial species [1, 2] and is influenced by features of the cell surface, environmental factors and the presence of specific compounds, inhibitors of co-aggregation.

In the present investigation of *Bacillus subtilis* 170, and *Bacillus subtilis* 168, and *Escherichia coli* K-12 have been tested for co-aggregation capability as reported in Table 1. The combination of *Bacillus subtilis* 170 with *Escherichia coli* K-12 1655 and *Bacillus subtilis* 168 with *Escherichia coli* K-12 1655 resulted in the highest co-aggregation percentage (77,01 ± 0,63% and 79,21 ± 0,72%).

Reports regarding the co-aggregation between *B.subtilis* 170, *B.subtilis* 168, and *E.coli* K-12 strains were scarce. The scanning electron micrograph of co-aggregates (Fig. 1 and Fig. 2) shows intermingled cells of *B.subtilis* 170, and *B.subtilis* 168 (long rods with surface protrusion), and *E.coli* K-12 (smaller smooth-surfaced rods).

Table 1. Co-aggregation of *B.subtilis* 170 with *E.coli* K-12 strains.

№	Strains	Autoaggregation index, %	Co-aggregation index, % with	
			B.subtilis 170	*B.subtilis* 168
1.	*Bacillus subtilis* 170	54,32±0,58	-	-
2.	*Bacillus subtilis* 168	52,85±0,26	-	-
3.	*Escherichia coli* 1655	53,94±0,95	77,01 ± 0,63	79,21 ± 0,72
4.	*Escherichia coli* 406	44,52±0,06	76,10 ± 0,00	79,08 ± 0,23
5.	*Escherichia coli* 446	44,95±0,73	77,02 ± 0,08	78,50 ± 0,42
6.	*Escherichia coli* 420	43,97±0,21	73,57 ± 0,11	78,06 ± 0,61
7.	*Escherichia coli* W3110	41,53±0,51	71,04 ± 0,60	78,86 ± 0,21
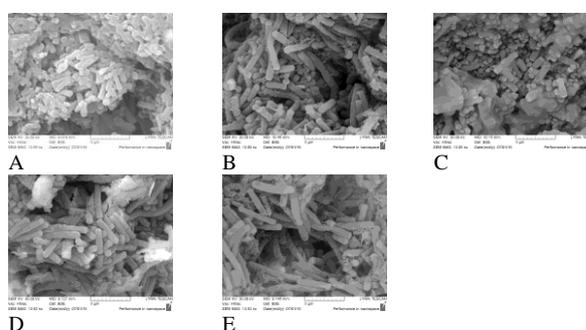
Fig. 1. SEM micrographs of the co-aggregates formed between Bacillus subtilis 170 strain and their co-aggregating partners: (A) Escherichia coli K-12 406 ; (B) Escherichia coli K-12 420; (C) Escherichia coli K-12 446; (D) Escherichia coli K-12 1655; (E) Escherichia coli K-12 W 3110.
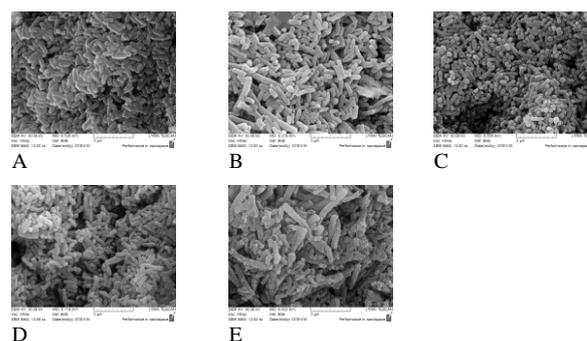
Fig. 2. SEM micrographs of the co-aggregates formed between Bacillus subtilis 168 strain and their co-aggregating partners: (A) Escherichia coli K-12 406 ; (B) Escherichia coli K-12 420; (C) Escherichia coli K-12 446; (D) Escherichia coli K-12 1655; (E) Escherichia coli K-12 W 3110.

The co-aggregation of *B. subtilis* 170 and *B. subtilis* 168 with *E. coli* K-12 strains at different pH levels is presented in graphical form inFig. 3 and Fig. 4. Co-aggregation percentage is higher at

lower and higher pH levels namely 5,0 and 8,0 irrespective of strains. However at a neutral pH of 7,0 the results show a slight decrease in the co-aggregation percentage for all tested pair strains.
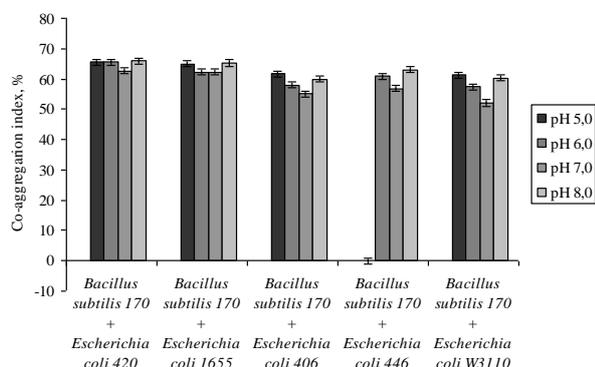
Fig. 3. Effect of different levels of pH on co-aggregation of *Bacillus subtilis* 170 with *Escherichia coli* K-12 strains
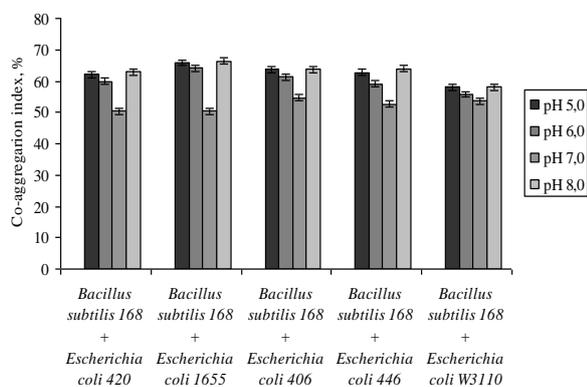
Fig. 4. Effect of different levels of pH on co-aggregation of *Bacillus subtilis* 168 with *Escherichia coli* K-12 strains

Rathi et co-workers [21], Burdman et co-workers [25, 26] reported that *Azospirillum* strain FAJ0204, *P. fluorescens* and *B. subtilis* strains displayed an increase in aggregation at a lower pH level. At acidic pH, negative ionized groups can be neutralized by protonation thus diminishing the strength of the repulsive forces between bacteria and leading to increased aggregation. After a decline in co-aggregation at pH 7.0, the increase observed in pH 8,0.

The effect of different temperature on the co-aggregation was studied. The increasing level of growth temperature showed an increase in co-aggregation percentage up to 35–40 °C, and beyond 40 °C was observed a reduction in co-aggregation index (Fig. 5 and Fig. 6). Burdman co-workers [26] reported the positive effect of growth temperature on co-aggregation of *A. brasilense* cells. A similar trend was also observed in *Azospirillum*, when co-aggregated with other PGPR strains.

In order to determine the nature of surface components, involved in cell–cell interaction leading to aggregation, the bacterial strains were treated with a variety of potential disaggregating reagents such as Tween, EDTA, Triton, protease, trypsin, and heat treatment.
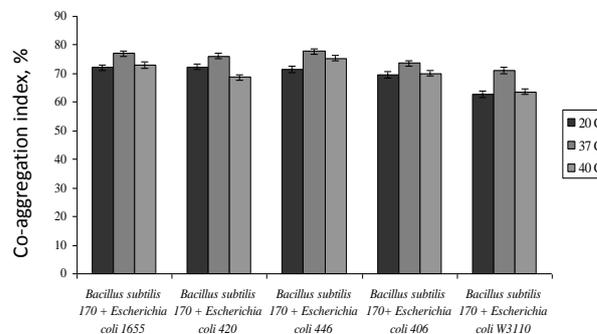
Fig. 5. Effect of different levels of temperature on co-aggregation of *Bacillus subtilis* 170 with *Escherichia coli* K-12 strains.
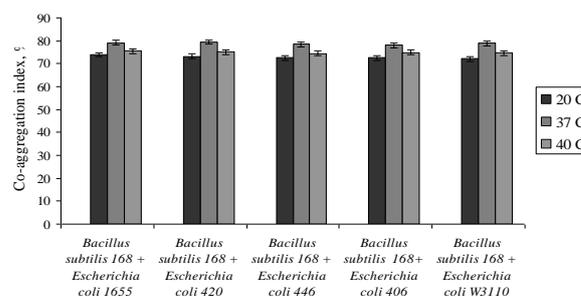
Fig. 6. Effect of different levels of temperature on co-aggregation of *Bacillus subtilis* 168 with *Escherichia coli* K-12 strains.

Table 2. Effect of EDTA, Tween и Triton on the co-aggregation of *B.subtilis* 170 with *E.coli* K-12 strains

№	Strains	Co-aggregation index, %			
		Control	EDTA	Tween	Triton
1.	*Bacillus subtilis* 170 + *Escherichia coli* 1655	77,01 ± 0,63	69,55 ± 0,75	57,05 ± 0,42	58,88 ± 0,21
2.	*Bacillus subtilis* 170 + *Escherichia coli* 420	76,10 ± 0,00	62,37 ± 0,42	59,06 ± 0,21	58,94 ± 0,42
3.	*Bacillus subtilis* 170 + *Escherichia coli* 446	77,82 ± 0,08	65,76 ± 0,13	55,76 ± 0,17	56,30 ± 0,39
4.	*Bacillus subtilis* 170+ *Escherichia coli* 406	73,57 ± 0,11	64,98± 0,27	59,49 ± 0,91	61,89 ± 0,33
5.	*Bacillus subtilis* 170 + *Escherichia coli* W3110	71,04 ± 0,60	58,92 ± 0,71	56,19 ± 0,23	57,20 ± 0,21

Table 3. Effect of EDTA, Tween и Triton on the co-aggregation of *B.subtilis* 168 with *E.coli* K-12 strains

№	Strains	Co-aggregation index, %			
		Control	EDTA	Tween	Triton
1.	*Bacillus subtilis* 168 + *Escherichia coli* 1655	79,21 ± 0,72	70,68 ± 0,28	55,84 ± 0,87	62,06 ± 0,49
2.	*Bacillus subtilis* 168 + *Escherichia coli* 420	79,48 ± 0,23	70,18 ± 0,32	55,76 ± 0,49	63,46 ± 0,48
3.	*Bacillus subtilis* 168 + *Escherichia coli* 446	78,50 ± 0,42	69,62 ± 0,43	61,03 ± 0,79	64,35 ± 0,50
4.	*Bacillus subtilis* 168+ *Escherichia coli* 406	78,06 ± 0,61	70,53± 0,30	60,11 ± 0,41	64,87 ± 0,36
5.	*Bacillus subtilis* 168 + *Escherichia coli* W3110	78,86 ± 0,21	71,33 ± 0,41	58,81 ± 0,40	66,42 ± 0,95

Results of Table 2 and 3 shows that with the greatest inhibitory activity against co-aggregation process differs Tween, the index of inhibition of co-aggregation process ranges from 19,12% to 28,35% at *B. subtilis* 170 and *E. coli* K-12 strains, while at the pair of *B. subtilis* 168 and *E. coli* K-12 strain its value varies in the range of 22,26% to 29,84%. The lower degree of reduction of co-aggregation between investigated strains is under effect of Triton, followed by EDTA.

The highest resistance to thermal impact at 80 ° C for 15 min. were featured pairs of *B.subtilis* 170 and *E.coli* K-12 1655, and *B.subtilis* 168 and *E.coli* K-12 1655 strains, followed by pairs of *B.subtilis* 170 and *E.coli* K-12 406, *B.subtilis* 168 and *E.coli* K-12 406 (Tables 4 and 5). In the base of thermal tolerance of flocs, formed by strains of *B. subtilis* and *E. coli* species is most likely standing increase of intracellular content of poly-β-butyrate [24, 11]. The reduction of value of the index of co-aggregation between tasted pair strains of the *B. subtilis* and *E. coli* species in the present study was more pronounced under the influence of the cells with proteinase K compared to trypsin (Table 4 and Table 5). Addition of proteinase K enzyme reduced the co-aggregation percentage from 72,45 to 62,69 % of *B. subtilis* 170 and *E. coli* K-12 strains, from 72,45 to 62,69 % at *B. subtilis* 168 and *E. coli* K-12 strains, as seen in Table 5. There results are in conformity with the earlier findings of Burdmanet and co-workers [26] which indicated significant reduction in the aggregation inducing *Azospirillum* cells on protease treatment. These results suggest

that adhesive proteins are at least partially responsible for the aggregation-inducing activity.

Table 4. Co-aggregation index between *B. subtilis* 170 and *E. coli* K-12 strains after heat treatment at 80 °C, treatment with Trypsin and Proteinase K

Strains	Co-aggregation index, %			
	Control	Heat treatment	Trypsin	Proteinase K
B.subtilis 170+*E.coli* K-12 420	70,55±0,13	68,21±0,23	72,37±0,68	64,26±0,48
B.subtilis 170+*E.coli* K-12 1655	74,30±0,93	73,90±0,55	68,49±0,71	69,17±0,25
B.subtilis 170+*E.coli* K-12 446	70,55±0,12	70,38±0,41	70,33±0,15	68,47±0,33
B.subtilis 170+*E.coli* K-12 406	73,99±0,18	70,36±0,02	65,16±0,34	62,69±0,24
B.subtilis 170+*E.coli* K-12 W3110	70,92±0,18	69,38±0,46	67,98±0,64	63,17±0,44

Table 5. Co-aggregation index between *B. subtilis* 168 and *E. coli* K-12 strains after heat treatment at 80 °C, treatment with Trypsin and Proteinase K

Strains	Co-aggregation index, %			
	Control	Heat treatment	Trypsin	Proteinase K
B.subtilis 168+*E.coli* K-12 420	73,99±0,18	71,19±0,65	71,32±0,15	62,69±0,39
B.subtilis 168+*E.coli* K-12 1655	74,30±0,90	72,85±0,80	70,92±0,09	58,78±0,81
B.subtilis 168+*E.coli* K-12 446	70,55±0,13	68,66±0,45	71,57±0,45	69,36±0,52
B.subtilis 168+*E.coli* K-12 406	72,53±0,50	71,24±0,37	63,40±0,66	59,11±0,97
B.subtilis 168+*E.coli* K-12 W3110	70,92±0,88	70,55±0,32	68,56±0,47	63,55±0,55

The presence of methyl mannoside did not affect significantly on the co-aggregation capability of *B. subtilis* 170 and *E. coli* K-12 and *B. subtilis* 168 and *E. coli* K-12. However, the presence of N-acetyl galactosamine and N-acetyl glucosamine

significantly (p<0,05) inhibited the co-aggregation of *B. subtilis* 170 and *E. coli* K-12, *B. subtilis* 168 and *E. coli* K-12 (Table 6 and Table 7). Therefore

Table 6. Co-aggregation index between *B. subtilis* 170 and *E. coli* K-12 strains in the presence of N-acetylgalactosamine, N- acetylglucosamine and methylmanoside.

Strains	Co-aggregation index, %			
	Control	N-acetylgalactosamine	N-acetylglucosamine	Methylmannoside
B.subtilis 170+*E.coli* K-12 420	70,55 ±0,13	67,28±0,21	68,03±0,21	65,49± 0,77
B.subtilis 170+*E.coli* K-12 1655	74,30 ±0,93	64,63±0,90	65,39±0,51	66,01± 0,84
B.subtilis 170+*E.coli* K-12 446	70,55 ±0,12	67,28±0,21	68,03±0,21	65,49± 0,77
B.subtilis 170+*E.coli* K-12 406	73,99 ±0,18	66,89±0,36	72,28±0,38	67,85± 0,46
B.subtilis 170+*E.coli* K-12 W3110	70,92 ±0,18	65,79±0,60	68,48±0,92	59,79± 0,86

Table 7. Co-aggregation index between *B. subtilis* 168 and *E. coli* K-12 strains in the presence of N-acetylgalactosamine,N- acetylglucosamine and methylmannoside

Strains	Co-aggregation index, %			
	Control	N-acetylgalactosamine	N-acetylglucosamine	Methylmannoside
B.subtilis 168+*E.coli* K-12 420	73,99 ±0,18	66,89±0,36	65,40±0,66	71,88±0,71
B.subtilis 168+*E.coli* K-12 1655	74,30 ±0,90	64,63±0,90	66,42±0,16	72,31±0,37
B.subtilis 168+*E.coli* K-12 446	70,55 ±0,13	68,59±0,63	65,93±0,96	69,01±0,14
B.subtilis 168+*E.coli* K-12 406	72,53 ±0,50	66,52±0,91	68,86±0,45	70,95±0,86
B.subtilis 168+*E.coli* K-12 W3110	70,92 ±0,88	57,92±0,23	62,84±0,22	68,63±0,13

co-aggregation between tested strains was mediated by the lectin – polysaccharide interactions. This conclusion correlates with Ebisu and co-workers [27] on the formation of co-aggregates of *Eikenella corrodens* 1073 strain at his association with *Actinomyces viscosus* ATCC 19246, *A. viscosus* T14AV, *Streptococcus sanguis* 34 and*S.*

sanguis ST160R strains. The protein adhesin was associated with *E. coli* K-12 strains, the complementary galactosamine- like sugar receptor was associated with *B. subtilis* 170 strain and *B. subtilis* 168 strain.
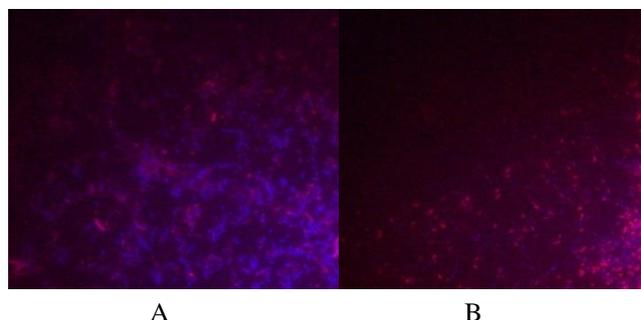
Fig. 7. Confocal laser scanning micrographs of the coaggregates formed between (A) *Bacillus subtilis* 170 (red) and *Escherichia coli* K-12 1655 (blue) , (B) *Bacillus subtilis* 168 (red) and *Escherichia coli* K-12 1655 (blue)

By using confocal laser scanning microscopy are illustrated intercellular contacts in formed co-aggregates. The obtained results indicate that during a process of co-aggregation bacterial cells of *B. subtilis* 170 and *E. coli* K-12 strains, *B. subtilis* 168 and *E. coli* K-12 strains are viable (Fig. 7). In the study of Bradshaw et co-workers [24] it is concluded that the formation of flocs of bacterial cells ensure their protection against reactive oxygen species among the obligate and facultative anaerobe species.

CONCLUSIONS

The values of temperature and pH have an impact on the degree of co-aggregation between the *B. subtilis* 170 and *E. coli* K-12, *B. subtilis* 168 and *E. coli* K-12 strains, the maximum value of the index of co-aggregation is achieved in the alkaline (pH 8.0) and acidic (pH 5.0) medium and at a temperature of 37 ° C.

The high degree of inhibition of co-aggregation between strains of *B. subtilis* 170 and *E. coli* K-12 species at treatment of cells with Tween, Triton, and N-acetylglucosamine give grounds to assume that in the base of the process stands lectin-polysaccharide interactions.

REFERENCES

1. A. Rickard, P. Gilbert, N. High, P. Kolenbrander, P. Handley, *Trend. Microbiol.*, **11,** 94 (2003).
2. P. Rickard, N. Gilbert, P. High, P. Kolenbrander, Handley, *Trend. Microbiol.*, **11,** 2 (2003).

3. F. Mizan, I. Jahid, S. Ha, *Food Microbiol.*, **49**, 41 (2015).
4. T. Faille, G. Bénézech, Y. Midelet-Bourdin, M. Lequette, G. Clarisse, A Ronse,. C. Ronse, R. Slomianny, *Food Microbiol.*, **40**, 64 (2014).
5. L. Simoes, M. Simoes, M. Vieira, *Appl. Environ. Microbiol.*, **74**, 1259 (2008).
6. S. Srey, I. Jahid, S. Ha, *Food Control*, **31**, 572 (2013).
7. P. Bogino , M. Oliva , F. Sorroche , W. Giordano, *Int. J. Mol. Sci.*, **14**, 15838 (2013).
8. Y. Sano, K. Shibayama, K. Tanaka, R. Ito, S. Shintani, M. Yakushiji, K. Ishihara, *Anaerobe*, **30**, 45 (2014).
9. P. Zilm, A. Rogers. *Anaerobe*, **13**, 146 (2007).
10. P. Liu, W. Shi, W. Zhu, J. Smith, S. Hsieh, R. Gallo, C. Huang, *Vaccine*, **28**, 3496 (2010).
11. E. Samet, S. Sowinski, Y. Okon, *FEMS Microbiol. Lett*., **237**, 195 (2004).
12. S. Shen, L. Samaranayake, H. -K. Yip, *Archives of Oral Biology*, **50**, 23 (2005).
13. N. Shimotahira, Y. Oogai, M. Kawada-Matsuo, S. Yamada, K. Fukutsuji, K. Nagano, F. Yoshimura, K. Noguchi, H. Komatsuzawaa, *Infection and Immunity*, **81**, 1198 (2012).
14. R. Kolenbrander, D. Andersen, P. Blehert, J. Egland, R. Foster, R. Palmer, *Microbiol. Molec. Biol. Rev.*, **66**, 486 (2002).
15. C. Buswell, Y. Herlihy, P. Marsh, C. Keevil, S. Leach, *J. Appl. Microbiol.*, **83**, 477(1997).
16. Y. Yoshida, J. Yang, K. Nagano, F. Yoshimura, J. Cisar, *J. Oral Biosci.*, **56**, 125 (2014).
17. A. Nivoliez, P. Veisseire, E. Alaterre, C. Dausset, F. Baptiste, O. Camarès, M.Paquet-Gachinat, M. Bonnet, C. Forestier, S. Bornes, *Appl. Microbiol. Biotechnol.*, **99**, 399 (2015).
18. V. Morya, W. Choi, E. Kim, *Appl. Microbiol. Biotechnol.*, **98**, 1389 (2014).
19. K. Phuong , K. Kakii, T. Nikata, *Journal of Biosci. Bioeng.*, **107**, 394 (2009).
20. T. Sato, F. Nakazawa, *J. Microbiol., Immunol. Infect.*, **47**, 182 (2014).
21. N. Rathi, S. Singh, J. Osbone, S. Babu, *Biocatal. Agricult. Biotechnol.*, **4**, 304 (2015).
22. S. Adav, D. Lee, J. Lai, *Appl. Microbiol. Biotechnol.*, **79**, 657 (2008).
23. E. Giaouris, E. Heir, M. Hébraud, N. Chorianopoulos, S. Langsrud, T. Møretrø, O. Habimana, M. Desvaux, S. Renier, G. Nychas, *Meat Sci.*, **97**, 298 (2014).
24. D. Bradshaw, P. Marsh, G. Watson, C. Allison, *Infect.Immun.*, **66**, 4729 (1998).
25. S. Burdman, E. Jurkevitch, B. Schwartsburd, Y. Okon, *Microbiology.*, **145**, 1145 (1999).
26. S. Burdman, E. Jurketvitch, B. Schwartsburd, M. Hampel, Y. Okon*, Microbiology*, **144**, 1000 (1998).
27. S. Ebisu, H. Nakae, H. Okada, *Adv. Dent. Res.*, **2**, 323 (1988).

МЕХАНИЗЪМ НА КОАГРЕГАЦИЯ МЕЖДУ ЩАМОВЕ BACILLUS SUBTILIS AND ESCHERICHIA COLI K-12

Ив. Ганчев, Сн. Михайлова

Институт по микробиология „Стефан Ангелов", БАН
1113 София, ул. „Акад. Бончев", бл. 26

(Резюме)

Целта на проучването е да се изследва коагреацията между щамове Bacillus subtilis и Escherichia coli K-12. Проучено е влиянието на отделните физични и химични фактори. Коагрегацията се повлиява от pH и температурата на средата. Въздействието с трипсин, протеиназа К, етилендиаминотетраоцетна киселина, както и термичното въздействие води до инхибиране на процеса на коагрегация. N-ацетилглюкозаминът в най-голяма степен инхибира процеса на коагрегация между щамове *Bacillus subtilis* 170 и *Escherichia coli* K-12, *Bacillus subtilis* 168 и *Escherichia coli* K-12. Следователно, в основата на процеса стоят лектин-полизахаридни взаимодествия.

Characterization of gold nanoparticles synthesized on the surface of organanoclay

V. A. Angelov*, E. H. Ivanov, R. K. Kotsilkova

Institute of Mechanics, Bulgarian Academy of Sciences Acad. G. Bonchev St., bl. 4, 1113 Sofia, Bulgaria

This article studies two methods for synthesis of gold nanoparticles over organoclay – wet impregnation with UV treatment and wet chemical method (using sodium citrate as reducing agent). The study is focused on the determination of the size of gold nanoparticles synthesized with the two methods using TEM and XRD analysis with the corresponding computer software. The methods show a good match in the determined size of gold nanoparticles. The TEM analysis of the sample prepared with the wet chemical method showed better control over the size of the gold nanoparticles.

Keywords: Synthesis, gold nanoparticles, organoclay, TEM, XRD, software application

INTRODUCTION

The interest in the synthesis of metal nanoparticles has been growing because of their unique electronic, optical, thermal and catalytic properties and promising applications in interdisciplinary fields [1]. Various wet chemical methods have been used for synthesis of gold nanoparticles, the most common involve reduction of chloroauric acid ($H[AuCl_4]$) solution using a reducing agent. Two widely used reducing agents: sodium citrate and sodium borohydride are postulated by Turkevich method and Brust method, respectively. Another method for synthesis of gold nanoparticles is wet impregnation, well known in the development of heterogeneous catalysts. It comprises of adding the gold nanoparticles precursor ($H[AuCl_4]$) onto support component (organoclay).

The decoration of gold nanoparticles on layered silicates has been also reported in the scientific literature by Zhang *et al.* [2]. They suggest a simple wet chemical method to synthesize clay-APTES-Au nanocomposites. APTES (3-aminopropyltriethoxy-silane) acts as the linkage. The silane terminal of APTES formed bonds with the clay surface, while the other $-NH_2$ terminal bonds to gold nanoparticles.

Boev *et al.* [3] describe the preparation of hybrid organic-inorganic nanocomposites containing uniform distributions of metal nanoparticles prepared by mixing a preformed nanoparticle colloid with the precursors of ureasil, prior to the sol-gel transition.

Tamoto *et al.* [4] describe new methods to prepare gold nanoparticle/silica nanohelix hybrid nanostructures which form a 3D network in the aqueous phase. Nanometric silica helices and tubules obtained by sol-gel polycondensation on organic templates of self-assembled amphiphilic molecules were further funcionalized with (3-aminopropyl)-triethoxysilane (APTES) or (3-mercaptopropyl)-triethoxysilane (MPTES).

EXPERIMENTAL

Materials

Clay Cloisite 30B (Southern Clay Products, Inc.), organically modified with methyltallow bis-2-hydroxyethyl quaternary ammonium chloride (MT2EtOH), was used as a substrate for gold nanoparticle synthesis. Tetrachloroaurate trihydrate ($HAuCl4 \cdot 3H2O$) from Sigma-Aldrich was the precursor for the synthesis of gold nanoparticles. Trisoduim citrate dihydrate ($Na3C6H5O7.2H2O$) from Merck was used as a reducing agent for the synthesis of gold nanoparticles.

Synthesis methods

Impregnation Method in Water (IM wt)

A variation of the wet impregnation method for "decoration" of clay with gold nanoparticles is proposed using water solutions of $HAuCl_4$ as a precursor. Quaternary alkylammonium MT2EtOH, as the organoclay intercalate was used to attach the gold nanoparticles onto organoclay and as a

* To whom all correspondence should be sent:
E-mail: v.angelov@imbm.bas.bg

reducing agent. Solution of $HAuCl_4$ in distilled water was prepared with concentration: 1.73 wt % (3.35 g, 0.00017 mol $HAuCl_4$). After that HAuCl4 water solution was mixed with 1.71 g clay for 30 min. The resulting mixture was further dried in an oven at 80 °C for 8 h then irradiated for several hours using UV light until the color of the treated clay turned to dark gray. Thus, both the organoclay modifier and the UV treatment produced a subsequent reduction of the gold cations to neutral gold atoms forming the gold nanoparticles on the clay platelets. The result of this synthesis was clay decorated with 1.92 wt% of gold nanoparticles with average size ranged from 5 to 150 nm, as described in details in our previous work [14].

Citrate Method (Cit)

The Turkevich method [5] was applied for the synthesis of gold nanoparticles using trisodium citrate as a chemical reducing agent. 10 mL of 2.05 wt % HAuCl4 solution were added to 60 mL of boiling distilled water, and the mixture was heated at 100 °C, and then 5 mL of 18.06 wt % sodium citrate were added. The citrate was selected with the appropriate concentration in order to get the following mole ratio: $[Au^{3+}]/[citrate]$ = 0.0006 mol/0.0035 mol = 0.17. After the citrate was added to the gold salt solution, the mixture was stirred for 5−10 min. The color of the mixture started to change first to blue and then to dark red. After the last color change, the heating was stopped and the mixture was left to cool to room temperature. The size of the gold nanoparticles synthesized using the above $[Au^{3+}]/[citrate]$ mole ratio was between 10 nm and 30 nm. Further on, a suspension of 1 g of clay in 30 mL of isopropanol was prepared by ultrasonic treatment for 15 min at 250 W and then poured into the water solution containing the gold nanoparticles. The clay/gold suspension was again submitted to an ultrasonic treatment for 15 min and then left for 1 day to let the gold nanoparticles further grow on the surface of the clay platelets. The mixture was then filtrated and the gold nanoparticles decorated clay (AuNPs/clay) was dried in oven for 16 h at 80 °C. Synthesis protocol is described in details in Ref. [6].

Characterization methods

Transmission electron microscope JEOL JEM 2100 was used for characterization of the morphology of the samples. Powder samples were deposited on the standard TEM grids. High magnification TEM has been provided with magnification 40 000 times, 50 000 times and 200 000 times.

The X-ray diffractograms were obtained by using Bruker D8 Advance diffractometer with Cu Kα radiation (λ= 0,15418 nm) and LynxEye detector.

RESULTS AND DISCUSSIONS

TEM characterization of gold nanoparticles

Fig. 1 shows the TEM images of synthesized gold nanoparticles using wet impregnation method on the surface of organoclay before and after the UV treatment of the powder.
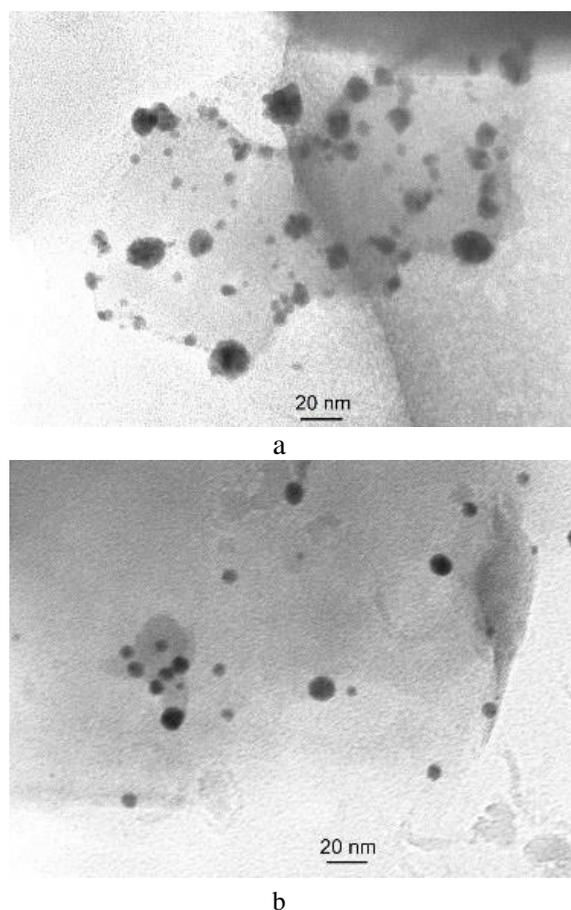
Fig. 1. TEM images with 200 000 times magnification of a sample obtained using wet impregnation method: a) before; b) after UV treatment

The size and the shape of the gold nanoparticles shown in the TEM images can be further analyzed using PEBBLES software - a user-friendly software which implements an accurate, unbiased, reproducible, and fast method to measure the morphological parameters of a population of nanoparticles (NPs) from TEM micrographs. In this software, the morphological parameters of the projected NP shape are obtained by fitting intensity

models to the TEM micrograph [7]. The success of each fitting procedure is characterized by a fitting score (GoF). GoF summarize the discrepancy between the observed values and the values expected under the intensity model in question. Lower GoF values means that the intensity model better fits to the observed nanoparticle's morphological parameters.

Using Pebbles software, the gold nanoparticles shown in Fig. 1a) are analyzed and most of them can't be fitted by the standard intensity models with an acceptable fitting score (GoF < 1000) suggesting that the process of formation is still in progress. In Fig. 1b) all of the shown gold nanoparticles are clearly shaped and can be fitted into the standard intensity model of spheres with acceptable fitting score suggesting that the process of formation is significantly advanced compared to the fresh synthesized sample due to the process of photoreduction caused by the UV treatment [8].
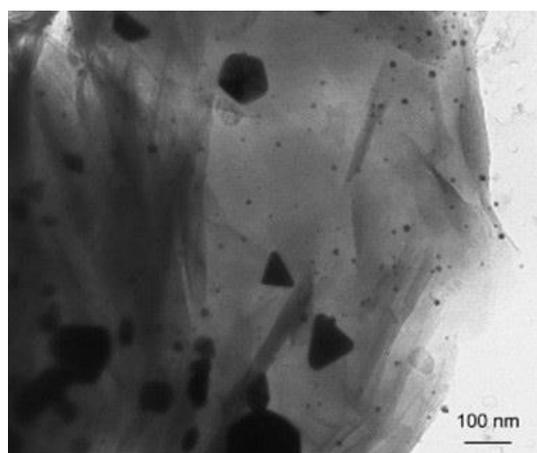
a
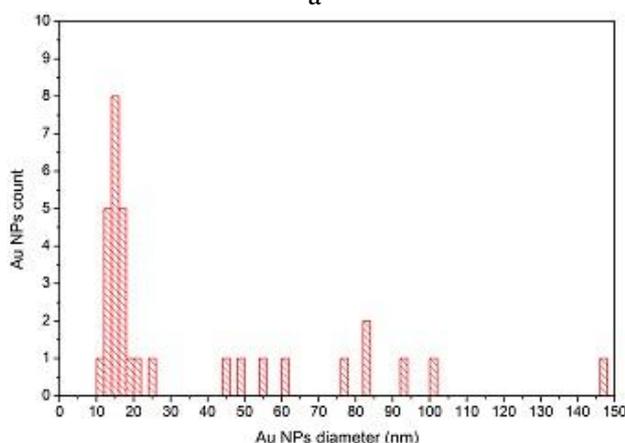
b

Fig. 2. a) TEM image with 50 000 times magnification of the sample after UV treatment; b) Histogram showing size distribution of 32 gold nanoparticles observed in Fig. 2a.

Fig. 2a shows TEM image of the sample shown in Fig. 1b), but with a smaller magnification of 50 000 times. Fig. 2b shows a high variation of the size of the nanoparticles, especially in the interval 40 nm to 150 nm. The observed nanoparticles have various shapes, mostly spherical, but also with ellipsoid, cylindrical, triangular or pentagonal basis. The agglomeration effect can be contributed to the UV treatment that induces further aggregation of gold nanoparticles [9].

The size variation can be improved by using a wet chemical method (citrate method) shown in Fig. 3.
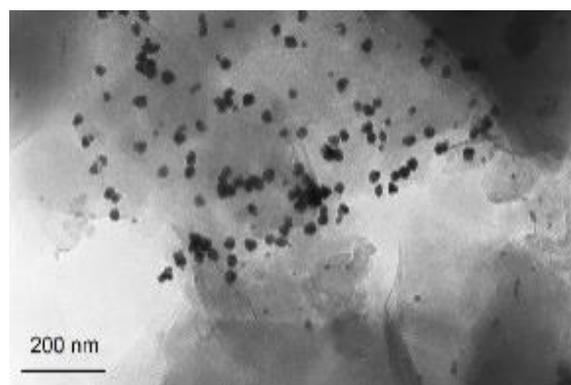
a
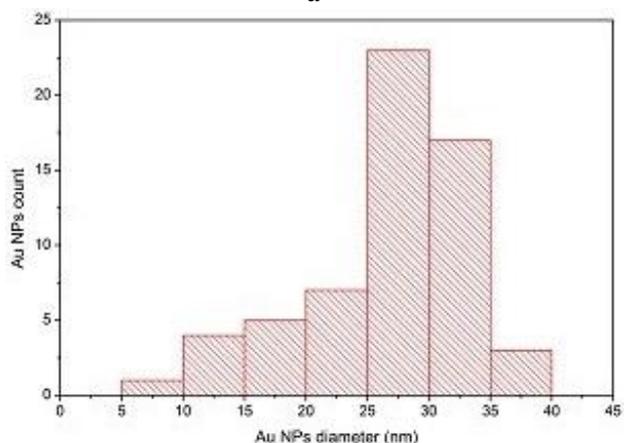
b

Fig. 3. a)FTEM image with 40 000 times magnification of the sample synthesized using citrate method; b) Histogram showing size distribution of 60 gold nanoparticles observed in Fig. 3a.

Almost all of the particles are with similar size, but the variance in the shape of the gold nanoparticles is still high. The particles sizes are normally distributed with mean value around 28 nm, fitting into the size range defined by the preparation protocol.

Table 1 illustrates a comparison between the results of the statistical analysis of the TEM images of the two studied methods illustrating that the

citrate method provides better control over the size the synthesized gold nanoparticles compared to the

wet impregnation method with UV treatment.

Table 1. Statistical analysis of gold nanoparticle sizes showing a comparison between the two methods.

Method	Statistical analysis of gold nanoparticle sizes (nm)				
	Mean	Standard Deviation	Minimum	Median	Maximum
Wet impregnation with UV treatment	35.63	34.31	10.30	16.86	146.69
Wet chemical (using sodium citrate as reducing agent)	26.78	6.50	10.00	28.69	35.38

Table 2. Results from FIT software analysis of XRD diffractogram shown in Fig. 4.

k	λ (nm)	β (rad)	2θ (deg)	θ (deg)	L (nm)
0.94	0.15418	0.292 ± 0.0049	38.218	19.109	30.01

XRD characterization of gold nanoparticles
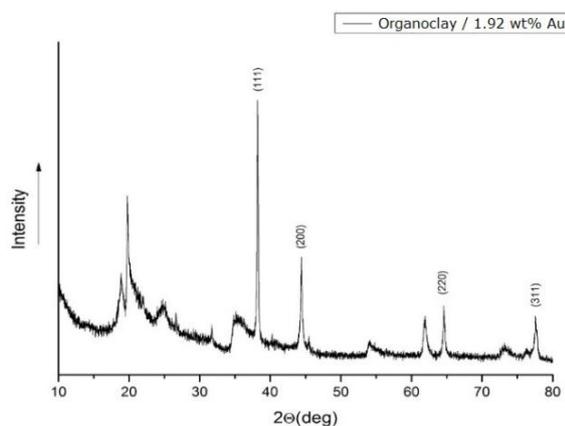
Fig. 4. XRD diffractogram of the sample synthesized using wet impregnation after UV treatment.

Fig. 4 shows the XRD diffractogram of gold nanoparticles synthesized over organoclay using the wet impregnation method after UV treatment. This XRD diffractogram is further analyzed to determine the mean size of the gold nanoparticles in the sample. The crystalline phases are identified using the Joint Committee on Powder Diffraction Standards (JCPDS) files. The mean particle size (L) of gold nanoparticles is calculated based on the line broadening reflections, using the Scherer equation [10]:

$$L = \frac{k\,\lambda}{\beta\,cos\theta}$$

where: β is full width at half maximum of the highest phase in radians; λ is the X-ray wavelength; θ is the Bragg angle; *k* is a dimensionless shape factor.

The calculations are done using FIT software – an interactive software for decomposition and profile analysis of X-ray diffractograms [11]. FIT software uses full width at half maximum method for determination of the peak width and the shape of the observed gold nanoparticles is mostly spherical, therefore k = 0.94 is appropriate value for this case [10].

Table 2 shows the results of the analysis of XRD diffractogram. The mean size of the nanoparticles is calculated to be around 30 nm. This value is relatively close to the mean values calculated from the TEM image analysis.

CONCLUSION

In the present study gold nanoparticles over organoclay were prepared with two different methods – wet impregnation with UV treatment and wet chemical method (using sodium citrate as reducing agent). The gold nanoparticles were characterized using TEM at different stages of the preparation process – before and after the UV treatment. The results of this comparison

demonstrate that the UV treatment influence the formation process of gold nanoparticles. Citrate method showed better control over the size of the Au nanoparticles. XRD analysis was also performed and it provides similar results as TEM analysis.

REFERENCES

1. M. C. Daniel, D. Astruc, *Chem. Rev.,* **104**, 293 (2004).
2. R. Zhang, M. Hummelgard, H. Olin, *Langmuir,* **26**, 5823 (2010).
3. V. Boev, J. Perez-Juste, I. Pastoriza-Santos, C. J. R. Silva, M. J. M. Gomes, Liz- L. M. Marzan, *Langmuir,* **20**, 10268 (2004).
4. R. Tamoto, S. Lecomte, S. Si, S. Moldovan, O. Ersen, M. H. Delville, R. Oda, *J. Phys. Chem. C,* **116**, 23143 (2012).
5. V. Angelov, H. Velichkova, E. Ivanov, R. Kotsilkova, M. H. Delville, M. Cangiotti, A. Fattori, M. F. Ottaviani, *Langmuir,* **30**, 13411 (2014).
6. J. Turkevich, P. C. Stevenson, J. Hillier, *Discuss. Farad. Soc.,* **11**, 55 (1951).
7. S. Mondini, A. M. Ferretti, A. Puglisi, A. Ponti, *Nanoscale,* **4**, 5356 (2012).
8. K. Torigoe, K. Esumi, *Langmuir,* **8**, 59 (1992).
9. S. Yang, Y. Wang, Q. Wang, R. Zhang, B. Ding, *Colloids and Surfaces A: Physicochem. Eng. Aspects*, **301**, 174 (2007).
10. P. Scherrer, *Nachr. Ges. Wiss. Göttingen* **26,** 98 (1918).
11. V. Petkov, N. Bakaltchev, *J. Appl. Crystallogr.,* **23**, 138 (1990).

ХАРАКТЕРИЗИРАНЕ НА ЗЛАТНИ НАНОЧАСТИЦИ СИНТЕЗИРАНИ ВЪРХУ ПОВЪРХНОСТТА НА ОРГАНОГЛИНА

В. А. Ангелов, Е. Х. Иванов, Р. К. Коцилкова

Институт по Механика, Българска Академия на Науките

ул. „акад. Г. Бончев“, бл. 4, 1113 София, България

(Резюме)

Статията описва два метода за синтез на златни наночастици върху повърхността на органоглина – мокро импрегниране с последващо УВ облъчване и мокър химичен метод (т. нар. цитратен метод, при който се използва натриев цитрат, като редуциращ агент). Фокусирана е, върху определянето на размера на златните наночастици получени по тези два метода чрез използване на ТЕМ и РФА анализ със съответните компютърни програми. Методите показват добро съвпадение на получените резултати в размера на наночастиците, чрез различните компютърни програми. ТЕМ анализът на образеца, получен чрез цитратен метод показва, че по този метод имаме по-добър контрол върху размера на получените златни наночастици.

Study of quasi-monophase Y-type hexaferrite Ba$_{0.5}$Sr$_{1.5}$Zn$_2$Al$_{0.08}$Fe$_{11.92}$O$_{22}$ powders

B. V. Georgieva[1]*, T. I. Koutzarova[1], S. M. Kolev[1], Ch. G. Ghelev[1], B. Vertruyen[2], R. Closset[2], R. Cloots[2] and A. Zaleski[3]

[1]*Institute of Electronics, Bulgarian Academy of Sciences, 72 Tsarigradsko Chaussee, 1784 Sofia, Bulgaria*
[2]*Inorganic Materials Chemistry, Chemistry Department B6, University of Liege, Sart Tilman, B-4000 Liege, Belgium*
[3]*Institute of Low Temperature and Structure Research, Polish Academy of Sciences, ul. Okólna 2, 50422 Wroclaw, Poland*

Y-type hexaferrite Ba$_{0.5}$Sr$_{1.5}$Zn$_2$Al$_{0.08}$Fe$_{11.92}$O$_{22}$ powder was synthesized by ultrasonic co-precipitation. The XRD spectrum showed the presence of small amount of a second spinel phase of ZnFe$_2$O$_4$. The powder exhibited a triple hysteresis loop at room temperature corresponding to the presence of an intermediate magnetic phase between ferromagnetic and proper-screw spin. Magnetic phase transitions in the temperature range of 4.2 K - 300 K were also observed connected to the different spin structure.

Keywords: Y-type hexaferrites, ultrasonic co-precipitation, magnetic phase

INTRODUCTION

Multiferroics are a class of multifunctional materials in which at least two of the ferroic order parameters, including ferroelectricity, ferromagnetism, and ferroelasticity, exist simultaneously. In some multiferroics, where ferroelectricity and ferromagnetism co-exist, one can control the magnetic phase by applying an external electric field, as well as to influence the electric phase by applying an external magnetic field (magneto-electric effect). From the viewpoint of applying multiferroics to multifunctional devices, it is important to be able to control the electric polarization, or the dielectric constant, by means of weak magnetic fields at temperatures close to room temperature. In recent years, there has been increasing interest in M-, Y- and Z-type hexaferrites, because some of them are multiferroic materials at room temperature and have large magneto-electric effect, which is associated with the presence of spinoidal and spiral magnetic structures [1, 2]. The magneto-electric effect in the Y-type hexagonal ferrite Ba$_{1.5}$Sr$_{0.5}$Zn$_2$Fe$_{12}$O$_{22}$ at room temperature in a low magnetic field of 0.1 T was reported for the first time by Kimura et al. [3]. Chun et al. [4] reported a large magnetoelectric effect in Ba$_{0.5}$Sr$_{1.5}$Zn$_2$Al$_{0.08}$Fe$_{11.92}$O$_{22}$, which occurred at a much lower magnetic field.

The prospects of applications as a multiferroic material prompted extensive studies of the structural, magnetic and ferroelectric properties of single crystals of Y-type hexaferrites [5-8]. However, the properties of powder Y-type hexaferrites have not been sufficiently explored. One of the reasons is that preparing a single-phase sample is very difficult, as is the case with most complex hexaferrites. The process of synthesizing Y-type hexaferrites always involves the presence of various accompanying magnetic oxides, the main cause of this is being the fact that the temperature interval for Y-phase synthesis is very narrow. Typically, the Y-type hexaferrite phase synthesis begins at 900 ^{o}C and ends at 1200 ^{o}C. R. Pullar [9] provided a detailed study on the processes of hexaferrites synthesis. In brief, at the beginning, the preparation of Ba$_{0.5}$Sr$_{1.5}$Zn$_2$Al$_{0.08}$Fe$_{11.92}$O$_{22}$ is accompanied by the presence of another type of hexaferrite, namely, M-type barium hexaferrite and of small amounts of second phases of barium ferrite, strontium ferrite and zinc ferrite. A Z-type hexaferrite appears at temperatures above 1200 ^{o}C. The type of the second phases present depends to a large extent on the type of the Me^{2+} cations and the preparation technique. On the other hand, the most common method for fabrication of these materials is the ceramic method, which requires multiple annealing and sintering steps.

Here we present a single-step annealing process for the synthesis of Ba$_{0.5}$Sr$_{1.5}$Zn$_2$Al$_{0.08}$Fe$_{11.92}$O$_{22}$

* To whom all correspondence should be sent:
E-mail: b.georgiewa@abv.bg

powders by ultrasonic co-precipitation. A study on the powders' structural and magnetic properties is also presented.

EXPERIMENTAL

The Ba$_{0.5}$Sr$_{1.5}$Zn$_2$Al$_{0.08}$Fe$_{11.92}$O$_{22}$ powder was prepared by ultrasonic co-precipitation. Stoichiometric amounts of the corresponding metal nitrates were dissolved in deionized water and, after homogenization, the co-precipitation process was initiated by adding NaOH at pH = 12. High-power ultrasound stirring was applied to assist this process, which, as it is known, enhances the reaction rate, the mass transport and the thermal effects. Ultrasound with amplitude 40% was applied for 15 min, pulse on: 2 s, pulse off: 2 s, by an ultrasonic processor (Sonics, 750 W). The precipitate was separated in a centrifuge, dried and milled. The precursor was calcined at 1170°C for 7 h to obtain the Ba$_{0.5}$Sr$_{1.5}$Zn$_2$Al$_{0.08}$Fe$_{11.92}$O$_{22}$ powder.

The Ba$_{0.5}$Sr$_{1.5}$Zn$_2$Al$_{0.08}$Fe$_{11.92}$O$_{22}$ powder was characterized using X-ray diffraction analysis with Cu-K$_\alpha$ radiation and scanning electron microscopy (Philips ESEM XL30 FEG). The magnetic measurements were carried out at room temperature using a PPMS (Quantum Design) at a maximum magnetic field of 50 kOe. The *ac* magnetization was performed on an Oxford Design susceptometer in an *ac* magnetic field with amplitude 10 Oe and frequency 1 kHz. The sample was first cooled down to 4 K without magnetic field and the *ac* magnetization was measured at increasing temperature up to 300 K.

RESULTS AND DISCUSSIONS

The XRD spectra of the powder showed the characteristic peaks corresponding to the Y-type hexaferrite structure (Ba$_{0.5}$Sr$_{1.5}$Zn$_2$Al$_{0.08}$Fe$_{11.92}$O$_{22}$) as a main phase and to some ZnFe$_2$O$_4$ as a second phase (Fig. 1). Unlike preparation of BaFe$_{12}$O$_{19}$, the Ba$_{0.5}$Sr$_{1.5}$Zn$_2$Al$_{0.08}$Fe$_{11.92}$O$_{22}$ cannot be directly obtained due to the complexity of its structure, which imposes progressive transformation through intermediate ferrites before achieving the final structure required. This is the main reason why the second phase of ZnFe$_2$O$_4$ with a spinel structure is present.

A SEM image of the Ba$_{0.5}$Sr$_{1.5}$Zn$_2$Al$_{0.08}$Fe$_{11.92}$O$_{22}$ sample is presented in Fig. 2. The powder consists almost entirely of large hexaferrite-phase particles with a size of about 1 nm and an almost perfect hexagonal shape. We assume that the small

particles with a size of less than 200 nm and an irregular shape are of ZnFe$_2$O$_4$.
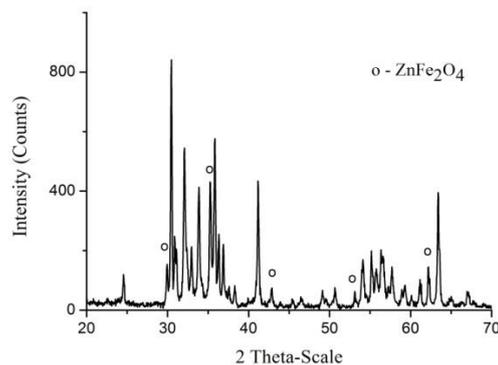
Fig. 1 XRD spectrum of Ba$_{0.5}$Sr$_{1.5}$Zn$_2$Al$_{0.08}$Fe$_{11.92}$O$_{22}$ powder.
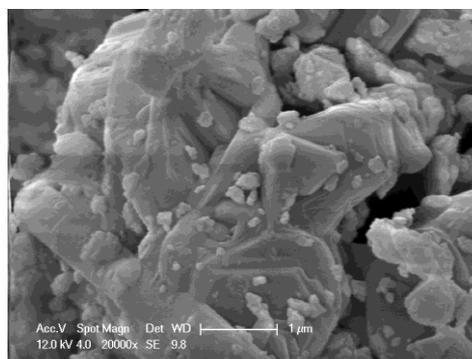
Fig. 2. SEM image of Ba$_{0.5}$Sr$_{1.5}$Zn$_2$Al$_{0.08}$Fe$_{11.92}$O$_{22}$ powder.

The hysteresis loops of the powder at room temperature and at 4.2 K are shown in Fig. 3. The Ba$_{0.5}$Sr$_{1.5}$Zn$_2$Al$_{0.08}$Fe$_{11.92}$O$_{22}$ sample shows a triple loop at room temperature, which is different from typical ferromagnetic materials. This observation of a triple hysteresis loop in low magnetic fields ranging from 1 to −1 kOe indicates that there are two kinds of ferrimagnetic phases (states) with different magnetization values with *H* between 50 and −50 kOe. The magnetization loop exhibits a small hysteresis at 4.2 K typical for a conical spin phase. The absence of a triple loop at 4.2 K means that the hysteresis observed at 300 K is due to the presence of two kinds of ferrimagnetic states in the Ba$_{0.5}$Sr$_{1.5}$Zn$_2$Al$_{0.08}$Fe$_{11.92}$O$_{22}$ phase. Khanduri et al. [10] had also observed a similar hysteresis loop in Ba$_{2-x}$Sr$_x$Mg$_2$Fe$_{12}$O$_{22}$ when *x* was greater than 1. In our case, the triple hysteresis loop is due to an intermediate phase between the proper screw spin phase and the collinear ferrimagnetic one at room temperature.

All Y-type hexaferrites have planar anisotropy at room temperature, i.e. they have an easy axis of

magnetization lying in a plane normal to the *c*-axis direction. This is the main reason for the low coercivity field of Ba$_{0.5}$Sr$_{1.5}$Zn$_2$Al$_{0.08}$Fe$_{11.92}$O$_{22}$.
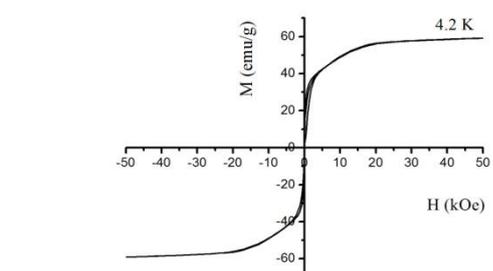
a)
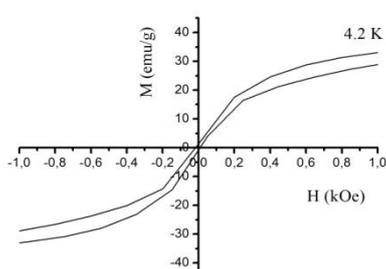
b)
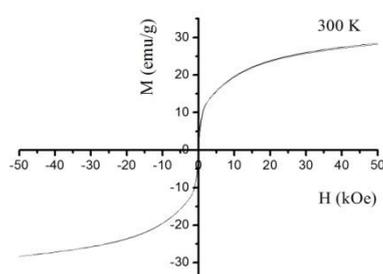
c)
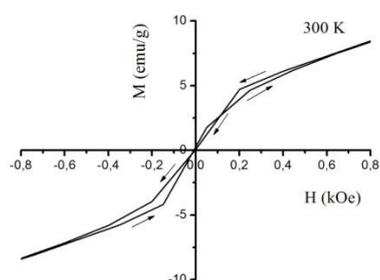
d)

Fig. 3. Magnetization measurements of Ba$_{0.5}$Sr$_{1.5}$Zn$_2$Al$_{0.08}$Fe$_{11.92}$O$_{22}$ powder at 4.2 K (a) and 300 K (c); (b) and (d) - expanded view of the hysteresis loops in the low magnetic field range at 4.2 K and 300 K, respectively.
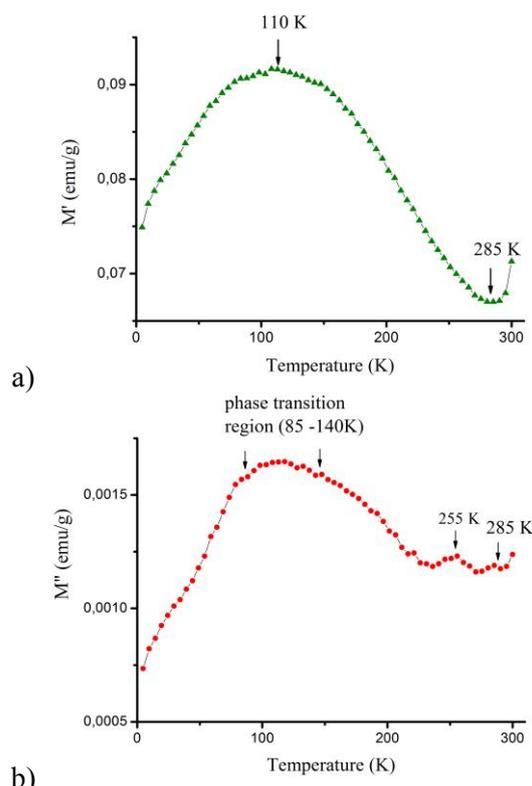
a)

b)

Fig. 4. Temperature dependence of the *ac* differential magnetization of Ba$_{0.5}$Sr$_{1.5}$Zn$_2$Al$_{0.08}$Fe$_{11.92}$O$_{22}$ in an *ac* magnetic field with amplitude 10 Oe and frequency 1 kHz: a) *M'*(*T*) – the real part of the differential magnetization; b) *M''*(*T*) – the imaginary part of the differential magnetization.

The magnetic phase transitions were investigated in an *ac* magnetic field. The phase transition temperatures were determined by following the variation of the powder's *ac* differential magnetization as the temperature was raised in an *ac* magnetic field with frequency 1 kHz and amplitude 10 Oe (Fig. 4). The minimum in *M'* at 285 K and maximum in *M''* at the same temperature corresponds to the collinear ferromagnetic to a proper-screw spin phase transition. This phase transition being near 300 K confirms our suggestion that the triple hysteresis loop in Fig. 3 (c, d) is due to the presence of an intermediate magnetic phase between the ferromagnetic and the proper-screw spin. This transition determines the multiferroic properties of Ba$_{0.5}$Sr$_{1.5}$Zn$_2$Al$_{0.08}$Fe$_{11.92}$O$_{22}$. The small maximum in *M''* at 255 K is associated with the magnetic order changes from a screw spin to a longitudinal conical spin phase, while the large maximum between 85 K and 140 K is associated with the alternating longitudinal conical phase.

CONCLUSIONS

$Ba_{0.5}Sr_{1.5}Zn_2Al_{0.08}Fe_{11.92}O_{22}$ powder was synthesized by ultrasonic co-precipitation followed by a single-step sintering at $1170^{o}C$. We observed several magnetic phase transitions in the temperature range from 4.2 K to 300 K. The magnetic phase transition from collinear ferromagnetic ordering to proper-screw spin one allows us to assume that $Ba_{0.5}Sr_{1.5}Zn_2Al_{0.08}Fe_{11.92}O_{22}$ is a multiferroic below 285 K. Future studies of the electrical polarization is necessary to confirm the magneto-electric effect in $Ba_{0.5}Sr_{1.5}Zn_2Al_{0.08}Fe_{11.92}O_{22}$ near room temperature.

REFERENCES

1. S.-W. Cheong, M. Mostovoy, *Nat. Mater.*, **6**, 13 (2007).
2. M. Gich, I. Fina, A. Morelli, F. Sánchez, M. Alexe, J. Gàzquez, J. Fontcuberta, A. Roig, *Adv. Mater.*, **26**, 4645 (2014).
3. T. Kimura, G. Lawes, A. Ramirez, *Phys. Rev. Lett.*, **94**, 137201 (2005).
4. S. Chun, Y. Chai, Y. Oh, D. Jaiswal-Nagar, S. Ham, I. Kim, B. Lee, D. Nam, K. Ko, J. Park, J. Chung, K. Kim, *Phys. Rev. Lett.*, **104** 037204 (2010).
5. K. Taniguchi, N. Abe, S. Ohtani, H. Umetsu, T. Arima, *Appl. Phys. Express*, **1**, 031301 (2008).
6. S. Shen, Y. Chai, Y. Sun, *Sci. Rep.*, **5**, 8254 (2015).
7. S. Ishiwata, Y. Taguchi, H. Murakawa, Y. Onose, Y. Tokura, *Science*, **319**, 1643 (2008).
8. S. Ishiwata, Y. Taguchi, Y. Tokunaga, H. Murakawa, Y. Onose, Y.Tokura, *Phys. Rev.* B, **79**, 180408R (2009).
9. R. C. Pullar, *Prog. Mater. Sci.*, **57**, 1191 (2012).
10. H. Khanduri, M. Chandra Dimri, H. Kooskora, I. Heinmaa, G. Viola, H. Ning, M. J. Reece, J. Krustok, R. Stern, *J. Appl. Phys.*, **112**, 073903, (2012).

ИЗСЛЕДВАНЕ НА ПРАХОВИ ПРОБИ ОТ КВАЗИ-МОНОФАЗЕН Y-ТИП ХЕКСАФЕРИТ
$Ba_{0.5}Sr_{1.5}Zn_2Al_{0.08}Fe_{11.92}O_{22}$

Б. Георгиева[1], Т. Куцарова[1], С. Колев[1], Ч. Гелев[1], Б. Вертрюйен[2], Р. Клосе[2], Р. Клутс[2] и А. Залески[3]

[1]*Институт по електроника, Българска академия на науките,
бул. „Цариградско шосе" 72, 1784 Sofia, Bulgaria*
[2]*Неорганична химия, Химически департамент, Университет гр. Лиеж,
Сарт Тилман, Б-4000 Лиеж, Белгия*
[3]*Институт за ниски температури и структурни изследвания, Полска академия на науките,
ул. Околна 2, 50422 Вроцлав, Полша*

(Резюме)

Синтезиран е Y-тип хексаферит $Ba_{0.5}Sr_{1.5}Zn_2Al_{0.08}Fe_{11.92}O_{22}$ чрез ултразвуково сътаяване. Рентгенофазовият анализ на получения материал показва присъствието на основна фаза от $Ba_{0.5}Sr_{1.5}Zn_2Al_{0.08}Fe_{11.92}O_{22}$ и малко количество $ZnFe_2O_4$ като втора фаза. Пробата проявява т. нар. тройна хистерезисна крива при стайна температура, отговаряща на съществуването на междинна магнитна фаза между феромагнитното и спираловидно подреждане на магнитните моменти. Наблюдавани са и магнитни фазови преходи в температурния интервал 4.2 K - 300 K, които са свързани с преход от една в друга магнитна структура.

Effect of annealing temperature on the structural and magnetic properties of barium hexaferrite powders prepared by a modified co-precipitation technique

P. Peneva[1]*, T. Koutzarova[1], S. Kolev[1], Ch. Ghelev[1], B. Vertruyen[2], R. Closset[2], C. Henrist[2], R. Cloots[2] and A. Zaleski[3]

[1]Institute of Electronics, Bulgarian Academy of Sciences, 72 Tzarigradsko Chaussee, 1784 Sofia, Bulgaria
[2]Structural Inorganic Chemistry, Chemistry Department B6, University of Liege, Sart Tilman, B-4000 Liege, Belgium
[3]Institute of Low Temperature and Structure Research, Polish Academy of Sciences, 50422 Wroclaw, Poland

We report studies on the influence of the temperature of a high-temperature treatment on the microstructural and magnetic properties of nanosized single-domain $BaFe_{12}O_{19}$ powders synthesized by the modified co-precipitation method. The average particle size decreased from 90 nm to 25 nm as the synthesis temperature was decreased from 900 °C to 800 °C; also, they did not exhibit the well-defined hexagonal shape that is characteristic for the hexaferrites. The value of the saturation magnetization M_s measured was very high, namely, 61.24 emu/g. The coercivity H_c of the powders ranged from 44 Oe to 103 Oe, which indicated that the particles were in a near-superparamagnetic state.

Keywords: hexaferrites, co-precipitation, magnetic properties, superparamagnetic.

INTRODUCTION

Barium hexaferrite ($BaFe_{12}O_{19}$) particles are widely used as permanent magnets, in microwave components and devices, such as circulators and absorbers, as well as a magnetic recording material, due to their unique characteristics, such as a high coercivity, a modest magnetic moment, a low or positive temperature coefficient of coercivity and an excellent chemical stability against environmental corrosion [1, 2]. The magnetic properties of powders of magnetic oxides are fundamentally related not only to their chemical composition, but also to the powders' particle size, crystal structure and morphology, which can vary depending on the preparation route. Conventional techniques for preparation of magnetic nano-particles include co-precipitation [3 ,4], microemulsion [5, 6], sol–gel auto-combustion processing [7, 8], mechano-chemical treatment [9], hydrothermal decomposition [10, 11], spark-plasma processing [12], aerosol pyrolysis [13], glass-ceramic route [14]. However, the particles prepared by these methods have a size of more than 100 nm. One of the reasons is that the hexaferrites are produced at high temperatures (above 1000°C), which leads to an uncontrolled growth of the particles and worsening of their size and shape

homogeneity. It is, therefore, very important to find methods to reduce the synthesis temperature for preparation of single-domain nanosized hexaferrite particles with a size below 100 nm and with a high degree of homogeneity which concerns their size and shape. The most widely used method for synthesis of $BaFe_{12}O_{19}$ is co-precipitation; we present here a modified co-precipitation method − ultrasonically assisted co-precipitation, to produce single-domain nanosized powders of barium hexaferrite. When the solution is subjected to high-power ultrasound, bubbles are formed, grow, and implosively collapse. The collapse of bubbles caused by cavitation produces intense local heating and high pressures, with very short lifetimes. It also produces hot spots with effective temperatures of about 5000 K, pressures of 1000 atm, and heating and cooling rates above 10^{10} Ks^{-1} [15, 16]. This acoustic cavitation generates chemical reactions, in our case co-precipitation. We studied the influence of the high temperature treatment on the structural and magnetic properties.

EXPERIMENTAL

The $BaFe_{12}O_{19}$ powders were synthesized by modified co-precipitation induced by applying a high-power ultrasound wave (ultrasonically assisted co-precipitation). $Ba(NO_3)_2$ and $Fe(NO_3)_3$ were dissolved in deionized water in a molar ratio of Ba to Fe 1:10 due to the weak solubility of barium

*To whom all correspondence should be sent:
E-mail: petya_venelinova_peneva@abv.bg

hydroxide in water ($10^{-3.6}$ at 25 °C) [17, 18, 19]. The co-precipitation was caused by adding NaOH at pH = 11.5. High-power ultrasound (Sonics ultrasonic processor 750 W) was applied to assist this process, which, as it is known, enhances the reaction rate, the mass transport and the thermal effects. The ultrasound wave with amplitude 40% was applied for 15 min, pulse on: 2 s, pulse off: 2 s. The precipitate was separated in a centrifuge, dried and milled. The precursor obtained was synthesized at 800 °C (YLT1C), 850°C (YLT1B) and 900 °C (YLT1A) for 4 h.

The $BaFe_{12}O_{19}$ powders were characterized using X-ray diffraction analysis with Cu-K$_\alpha$ radiation and scanning electron microscopy (Philips ESEM XL30 FEG). The magnetic measurements were carried out at room temperature using a PPMS (Quantum Design) at a maximum magnetic field of 50 kOe. The magnetic measurements were conducted on a disoriented random assembly of particles.

RESULTS AND DISCUSSION

The XRD spectra of the samples exhibited the characteristic peaks corresponding to the $BaFe_{12}O_{19}$ structure only (Fig. 1).
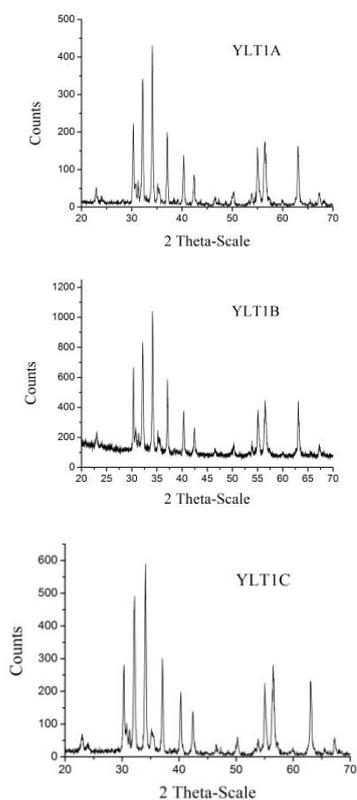
Fig. 1. XRD spectra of $BaFe_{12}O_{19}$ powders: (a) - YLT1A, (b) - YLT1B, (c) - YLT1C.

Scanning electron microscopy (SEM) was used to examine the grain size and morphology (Fig. 2). The average particle sizes of samples YLT1A, YLT1B and YLT1C were 90 nm, 66 nm and 25 nm, respectively (Table 1). The critical diameter for single-domain barium hexaferrite particles is about 460 nm [20], so that the particles were single domain in all powder samples. The particles were agglomerated due to the strong attractive magnetic force and high surface energy of the nanoparticles. The aggregation was strongest for sample YLT1C annealed at 800 °C with the smallest particle size. They did not exhibit the well-formed hexagonal shape that is characteristic for the hexaferrites, but rather an irregular shape between a sphere and a hexagonal platelet, similar to that obtained by single microemulsion technique [5] for particles with a size of less than 150 nm. The particles of sample YLT1C had a shape closer to the spherical. The process of forming the platelet shape typical for the $BaFe_{12}O_{19}$ hexagonal structure has not been completed due to the small particle size.
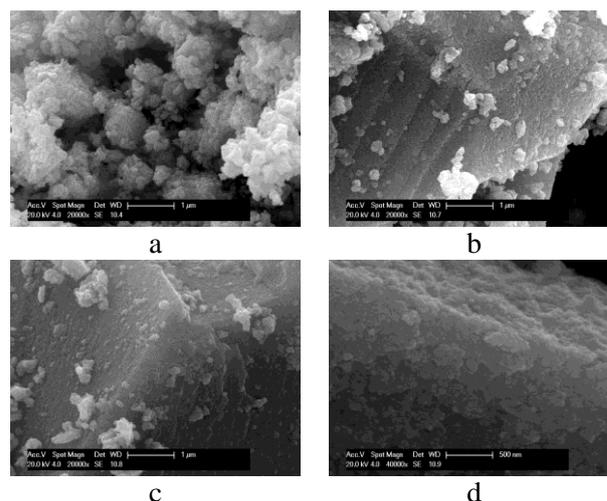
Fig. 2. SEM images of $BaFe_{12}O_{19}$ powders: (a) - YLT1A, (b) - YLT1B, (c, d) - YLT1C.

The hysteresis loops of the powders YLT1A, YLT1B and YLT1C at room temperature at a maximum applied field of 50 kOe are shown in Fig. 3 (a, c, e), respectively. Figs. 3 (b, d, f) show the hysteresis loops at low magnetic field. The magnetic parameters, namely, magnetization at magnetic field of 50 kOe (M_{max}), the remanent magnetization (M_r) and coercivity field (H_c) obtained from the hysteretic curves are given in Table 1. All samples did not reach the saturation magnetization despite the high magnetic field of 50 kOe. The maximum value for M_{max} of 61.24 emu/g at room temperature was measured for

Table 1. Properties of barium hexaferrite powders. *T* - high temperature synthesis, *D* - average particle size, M_s - saturation magnetization at 50 kOe (300 K), M_r - remanent magnetization (300K), H_c - coercivity field (300K).

Sample	T, °C	D, nm	M_{max}, emu/g	M_r, emu/g	H_c, Oe
YLT1A	900	90	61.24	7.54	44.06
YLT1B	850	66	50.85	8.68	59.06
YLT1C	800	25	48.97	11.17	103.17
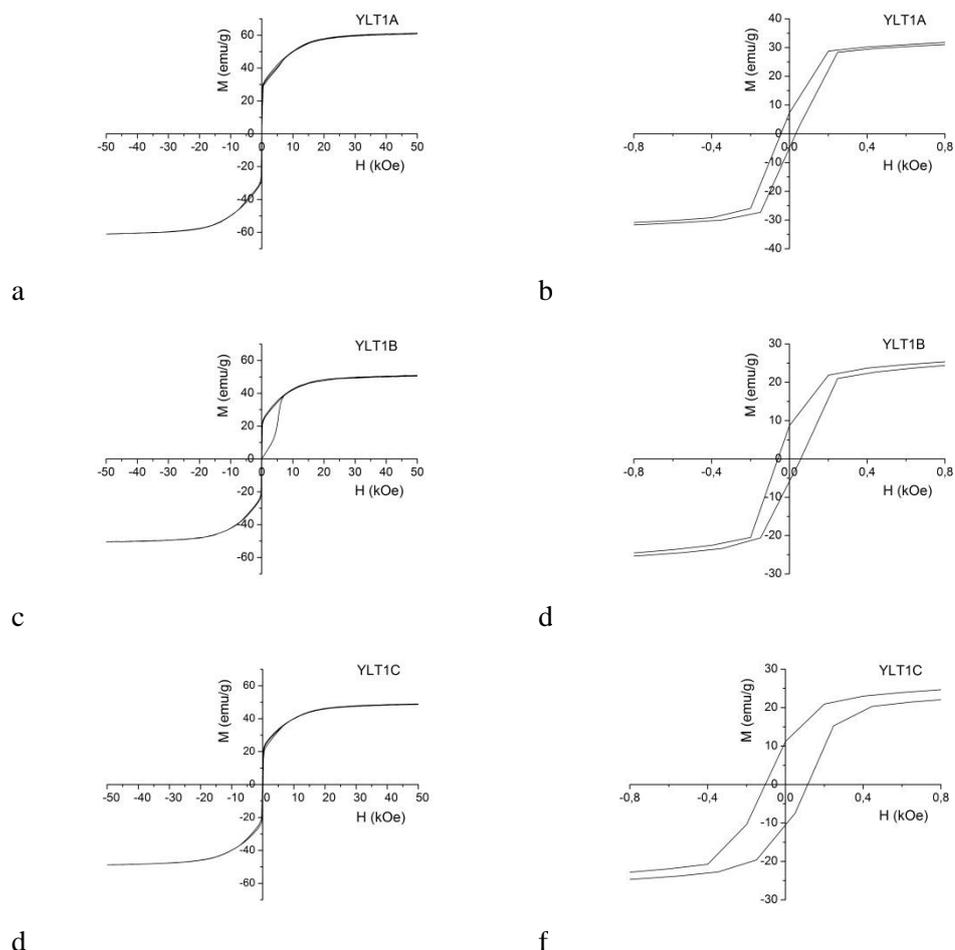
Fig.3. Hysteresis loops of (a, b) YLT1A, (c, d) YLT1B and (e, f) YLT1C samples.

sample YLT1A, which had the largest average particle size compared to the other samples. This value is very high, so that it can be expected that the saturation magnetization will be close to the theoretical values calculated for single crystal particles of barium hexaferrite, i.e. 72 emu/g, as reported by Shirk and Buessem [21].

The hysteresis loops for all samples were very narrow, which is not typical for hard magnetic materials like $BaFe_{12}O_{19}$. The coercivity H_c of powders was in the range 44 Oe − 103 Oe, which indicated that the particles were in a near-superparamagnetic state. For example, the coercivity of single crystal $BaFe_{12}O_{19}$ is 6.7 kOe

[22, 23]. In the case of single-domain particles, the coercivity depends strongly on the particle size and shape, the degree of crystallinity, the magnetocrystalline anisotropy, the shape anisotropy etc. This lower value of coercivity is mainly due to the small particle size. It is interesting to note that H_c for the sample with the smallest particle size had the highest value − 103 Oe. This is probably due to the fact that despite the small size of the particles they are highly agglomerated as shown in Fig. 2c. This leads to pinning of the magnetic field at the boundaries of the particles in the agglomerates in a way similar to the domain-wall pinning in polydomain particles and, therefore, to increasing

the value of the coercive field of the sample compared to the field necessary in the case of a separate small particle.

CONCLUSION

An ultrasonically assisted co-precipitation technique for the synthesis of uniform barium hexaferrite particles was presented allowing one to obtain single-domain $BaFe_{12}O_{19}$ with particle size below 100 nm. The powders consist of particles with an irregular shape between spherical and plate-hexagonal. The particles with the average size of 25 nm have a quasi-spherical shape. The magnetization values of the powders at a magnetic field of 5 T may be attributed to the small particle sizes. The hysteresis loops for all samples are very narrow, which indicates that the particles are in a near-superparamagnetic state.

REFERENCES

1. R. C. Pullar, *Prog. Mater. Sci.*, **57**, 1191 (2012).
2. I. Zavislyak, M. Popov, E. Solovyova, S. Solopan, A. Belous, *Mater. Sci. Eng. B*, **197**, 36 (2015).
3. R. Alam, M. Moradi, M. Rostami, H. Nikmanesh, R. Moayedi, Y. Bai, *J. Magn. Magn. Mater.*, **381**, 1 (2015).
4. M. Rashad, M. Radwan, M. Hessien, *J. Alloy Compd.*, **453**, 304 (2008).
5. T. Koutzarova, S. Kolev, Ch. Ghelev, I. Nedkov, B. Vertruyen, R. Cloots, C. Henrist, A. Zaleski, *J. Alloy Compd.*, **579**, 174 (2013).
6. N. Panchal, R. Jotania, *J. Inter. Acad. Phys. Sci.*, **16**, 189 (2012).
7. S. Galvão, A. Lima⸴ S. de Medeiros, J. Soares, C. Paskocimas, *Mater. Lett.*, **115**, 38 (2014).
8. G. Liu, R. Fan, K. Yan, X. Wang, K. Sun, C. Cheng, Q. Hou, *Mater. Sci. Forum*, **815**, 141 (2015).
9. M. Shafie, M. Hashim, I. Ismail, S. Kanagesan, M. Fadzidah, I. Idza, A. Hajalilou, R. Sabbaghizadeh, *Mater. Sci.: Mater. Electron.*, **25**, 3787 (2014).
10. A. Hilczer, B. Andrzejewski, E. Markiewicz, K. Kowalska, A. Pietraszko, *Phase Transit.*, **87**, 938 (2014).
11. C.-Y. Xu, L.-Sh. Fu, X. Cai, X.-Y. Sun, L. Zhen, *Ceram. Inter.*, **40**, 8593 (2014).
12. W. Zhao, Q. Zhang, X. Tang, H. Cheng, P. Zhai, *J. Appl. Phys.*, **99**, 08E909 (2006).
13. O. Usovich, L. Trusov, P. Kazin, Y. Tretyakov, *Inorg. Mater.*, **46**, 1137 (2010).
14. P. Kazin, L. Trusov, S. Kushnir, N. Yaroshinskaya, N. Petrov, M. Jansen, *J. Phys.: Conf. Series*, **200**, 072048 (2010).
15. K. Suslick, Y. Didenko, M. Fang, T. Hyeon, K. Kolbeck, W. McNamara III, M. Mdleleni, M. Wong, *Phil. Trans. R. Soc. Lond. A*, **357**, 335 (1999).
16. J. Bang, K. S. Suslick, *Adv. Mater.*, **22**, 1039 (2010).
17. S. R. Janasi, D. Rodrigues, M. Emura, F. Landgraf, *phys. stat. sol. (a)*, **185**, 479 (2001).
18. P. Xu, X. Han, H. Zhao, Z. Liang, *Mater. Lett.*, **62**, 1305 (2008).
19. D.-H. Chen, Y.-Y. Chen, *J. Colloid Interface Sci.*, **235**, 9 (2001).
20. L. Rezlescu, E. Rezlescu, P. Popa and N. Rezlescu, *J. Magn. Magn. Mater.*, **193**, 288 (1997).
21. B. Shirk, W. Buessem, *J. Appl. Phys.*, **40**, 1294 (1969).
22. B. D. Cullity, in: Introduction to Magnetic Materials, M. Cohen (ed.), Addison-Wesley Publishing, Reading, MA, USA, 1972.
23. J. Smit, H. P. J. Wijn, in: Ferrites; Phillips Technical Library, Eindhoven, The Netherlands, 1959.

ВЛИЯНИЕ НА ТЕМПЕРАТУРАТА НА СИНТЕЗ ВЪРХУ СТРУКТУРНИТЕ И МАГНИТНИТЕ СВОЙСТВА НА БАРИЕВ ХЕКСАФЕРИТ ПОЛУЧЕН ЧРЕЗ МОДИФИЦИРАН ПРОЦЕС НА СЪУТАЯВАНЕ

П. В. Пенева[1], Т. И. Куцарова[1], С. М. Колев[1], Ч. Г. Гелев[1], В. Вертруен[2], Р. Клозет[2], С. Ненрист[2], Р. Клоотс[2] and А. Залески[3]

[1]*Институт по електроника, Българска академия на науките, бул. "Цариградско шосе" №72, София-1784, България*
[2]*Structural Inorganic Chemistry, Chemistry Department B6, University of Liege, Sart Tilman, B-4000 Liege, Belgium*
[3]*Institute of Low Temperature and Structure Research, Polish Academy of Sciences, 50422 Wroclaw, Poland*

(Резюме)

В настоящата статия се разглежда влиянието на температурата на синтез върху структурните и магнитните свойства на наноразмерен монодоменен $BaFe_{12}O_{19}$ получен чрез модифициран метод на съутаяване - ултразвуково съутаяване. Средният размер на получените частици намалява от 90 до 25 нм с понижаване на температурата на синтез от 900 ^{o}C до 800 °C. Поради малкия си размер, частиците не са с добре изградена хексагонална форма, която е характерна за хексаферитите. Получените стройности на намагнитеността на насищане са много високи (61.24 emu/g). В зависимост от температурата на синтез, полето на коерцитивност H_c е в интервала 44 Oe - 103 Oe, което е индикатор, че частиците се намират в състояние близко до суперпарамагнитно поведение.

Films of recycled polyethylene terephthalate,obtained by electrospraying, for paper and textile impregnation

R. R. Angelov, B. C. Georgieva, D. B. Karashanova*

Institute of Optical Materials and Technologies "Acad. J. Malinowski",
Bulgarian Academy of Sciences, Acad. G. Bonchev Str., Bl. 109, 1113 Sofia, Bulgaria

The possibility of applying the electrospray method for recycling the polyethylene terephthalate (PET) waste has been studied. Besides, the successful deposition of PET films on paper and textile materials with purpose to obtain waterproof coatings has been demonstrated. The surface morphology of uncoated and coated materials has been observed by Scanning electron microscopy (SEM).The results from a comparative study of water permeability of non-impregnated and impregnated with PET both kinds of materials show that theimpregnatedones do not absorb water droplets. Thus, the potential of electrospraying as an effective method for PET wasterecycling and possible production of protective clothing and impervious paper has been revealed.

Keywords: recycled PET, electrospraying, paper and textile impregnation

INTRODUCTION

Environmental pollution can be defined as an introduction of contaminants in the Nature, which is one of the global problems of contemporary society[1]. Anthropogenic activity of producing resistant organic materials is a major factor in the contamination. For example, 15 million tons of plastics have been produced in 2013 only in EU, which is 19% of the European waste stream [2]. Not surprisingly, Earth protectionand the "Idea of green life and technology" are the main topicsof many international events and high-level meetings, where it has been resolved that the plasticsare among the substantial environmental pollutants. That is why the reducing the plastic waste is announced as a major aim of the Member States during the Conference of the Parties(COP21) to the United Nations Framework Convention on Climate Change (UFNCCC), held in Paris.

Polyethylene terephthalate (PET) is one of the most used plastics for food and liquid packaging and other applications. PET is no degradable material, chemically resistant to the environmental conditions. Only around 22.5% of used PET bottles have been recycled in 2013 [2], thus defined PET as a significant waste of the human activity. Hence, the development of effective methods for PET recycling along with finding its new applications is of great importance for the ecology.

Potential methods for PET recycling are electrospinning and electrospraying, which are often considered as 'sister' technologies [3]. At present, the electrospinning is a popular technique for production of fibers [4-6] while the obtaining of PET waterproof coatings by electrospraying is unconventional and low studied recycling process yet. Generally, the electrospraying is a electrohydrodynamic process where a polymer solution is sprayed by the application of high potential electric field in order to obtain liquid droplet [3]. The construction and working principle of the apparatus are described in our previous paper [7]. Design of experimental set-up is shown in Fig.1. The apparatus could work in two regimes - electrospinning and electrospraying. The realization of one or another process is determined by solvents and solutions properties as well as the experimental conditions [3, 8-11] (Fig.2). The electrostatic potential, working distance, orifice diameter, speed of solution pumping, etc., influence PET morphology and define the production of fibers or films.

It has been shown [4, 9, 10] that for the electrospinning process PET could be dissolved in solvents like trifluoroacetic acid (TFA) [12] or tetrahydrofuran (THF) [13]. The concentration of PET in the solution has to be below5 g/cm^3, as reported in [12, 13]. Two-component chemical systems consisting of TFA and dichloromethane

*To whom all correspondence should be sent:
E-mail: dkarashanova@yahoo.com

(DCM) in different ratios, as follows: 7:3 [4] and 1:1 [9, 14] have also been used. Mixture of trichloroacetic acid (TCA) and DCM in 1:1 volume ratio could also dissolve PET [15]. The concentration of PET in the solution should be between 10 and 20 g/cm^3 [4, 8, 9, 15].
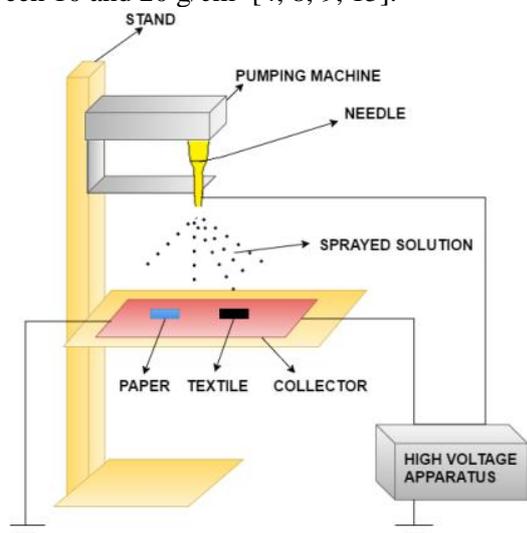
Fig. 1. Design of electrospinning/electrospraying apparatus.
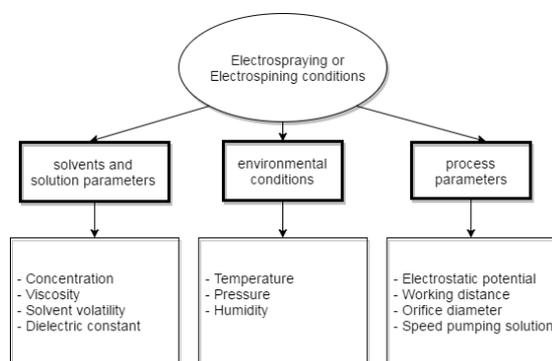
Fig. 2. The electrospraying or electrospinning conditions.

In our experiments we have chosen two-component chemical system consisting of TCA and DCM in 1:1 volume ratio. Up to now, TCA has not been used for electrospraying process to recycle PET waste; regardless it possesses similar to TFA solvent volatility. Moreover, it is environmentally less aggressive, with lower viscosity than TFA, which is favorable for electrospraying process. The lower price of TCA has also been a factor for our purpose.

The aim of the present work is to study the potentiality of electrospraying process for PET waste recycling, using TCA and DCM as solvents,

and deposition of thin films on textile and paper surfaces with a view of possible production of waterproof clothing and impervious paper.

EXPERIMENTAL

Reagents and Materials

The PET waste material was collected from used mineral water bottles (Gorna Bania, Devin, Bankia). Trichloroacetic acid (TCA - ACS, 99% Sigma-Aldrich Chemie GmbH Germany) and dichloromethane (DCM, - ACS, 100% Valerus Ltd Bulgaria) were used as solvents. All chemical materials were utilized as received. Syringes and medical needles (with diameter 0.6mm) were used in the electrospraying process. The sharp end of the needles was preliminarily cut off for homogenization of the electric field. Small paper (blue copy-paper) and textile (black jeans) pieces (2x2 cm^2) have been prepared from relevant materials.

Preparation of polymer solution for electrospraying

All waste bottles were cleaned with pure ethanol, prior to be dried. After that the bottles were cut to small pieces, each of them about 1x1cm^2. 20 wt. % PET solution has been prepared by dissolution of the waste in a mixture of TCA/DCM in 1:1 ratio (vol. %). Then the solutionwas homogenized by magnetic stirrer for 10 min at room temperature.

Electrospraying process

A successful synthesis of PET electrosprayed films was done under electric field strength: E=1 kV/cm (20 kV applied voltage at 20 cm distance between collector and needle). The pumping speed of the solution was fixed at 0.013 cm^3/ min. Paper and textile pieces were positioned on the Al collector of apparatus before starting the process, which was held at environmental conditions.

Characterization of impregnated PET films

The surface morphology of textile and paper pieces, non- impregnated and impregnated with electrosprayed PET films, was observed by digitalized scanning electron microscope (SEM Philips 515)at accelerating voltage 25 kV. The samples were metallized with gold coating films before SEM analysis.

Water permeability was studied by observation of the shape and size of the droplets, pipetted on the non- impregnated and impregnated materials and whether they passed or not through the samples.

For qualitative evaluation a universal wetting indicator, which gives a visible change of the color, was put under the paper and textile (non- and impregnated). The behavior of water droplets on the PET films was recorded by optical digital camera (Olympus TG-610).

RESULTS AND DISCUSSION

Surface morphology of non-impregnated and impregnated textile and paper

SEM micrographs of untreated textile and paper samples are presented in Fig. 3a and Fig. 4a, respectively, while the surface morphology of PET films, deposited on textile and paper is shown in Fig. 3b and Fig. 4b. The typical fibrous morphology of textile and paper is well seen. Usually, when the materials are hydrophilic, this type of microstructure defines high water permeability, due to the presence of voids between the fibers. The surfaces of impregnated textile (Fig.3b) and paper (Fig.4b) look smoother, because the deposited polymer films have evenly encased the fibers of the both types of materials, despite their complicated texture. This is an important prerequisite for reducing of water permeability of textile and paper. A comparison of the morphology between uncovered and impregnated materials allows concluding that the electrospraying process has been successfully applied at the experimental conditions chosen and the surface of textile and paper samples have been evenly coated by the recycled PET films.

a

b
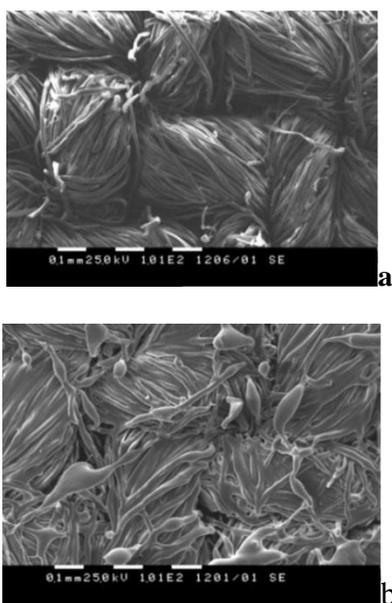
Fig.3. SEM micrographs of the surface morphology of non-impregnated (a) and PET impregnated textile (b).

a

b
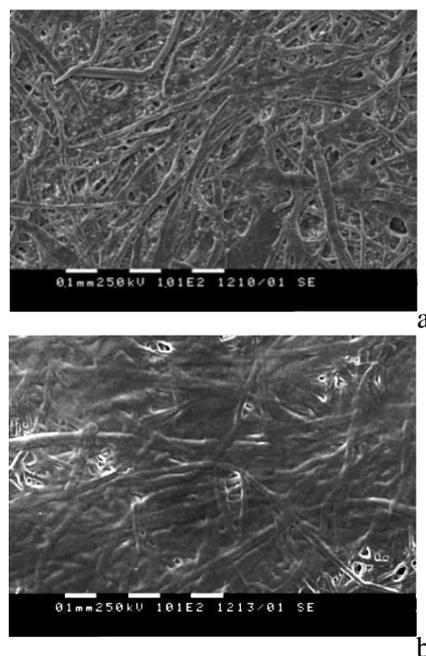
Fig. 4. SEM micrographs of the surface morphology of non-impregnated (a) and PET impregnated paper (b).

Water resistance of non-impregnated and impregnated materials

The results of water resistance study of non-impregnated (a, b, c) and impregnated (d, e, f) textile (Figs. 5, 6) and paper (Figs.7, 8) are presented on Figs. 5 - 8. Two types of pictures – in front (Fig.5, 7) and top view (Fig.6, 8) of the samples, have been taken for better illustration of the droplet behavior on the surface of the materials. Selected images: at the beginning (0 s – a, d), in the middle (5 s – b, e) and at the end (10 s – c, f) of the study are included in the figures. It is clearly demonstrated that the water drop spread (Fig.5, 6 a, b, c) on the textile surface, its shape and size changed and the drop completely disappeared in 10 s. In the same time a change in the color intensity

a

b

c

d

e

f
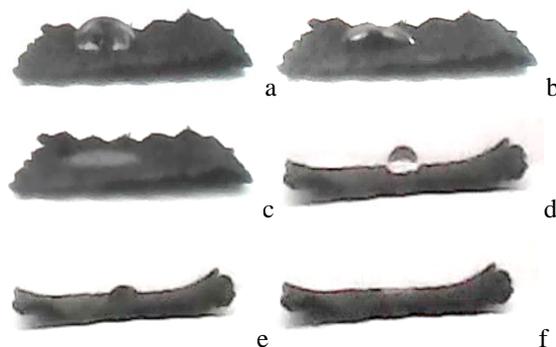
Fig. 5. Digital images of the front view of non-impregnated textile (a-c); PET impregnated textile (d-f); at the beginning of testing (a, d); in the middle (b, e); at the end(c, f).
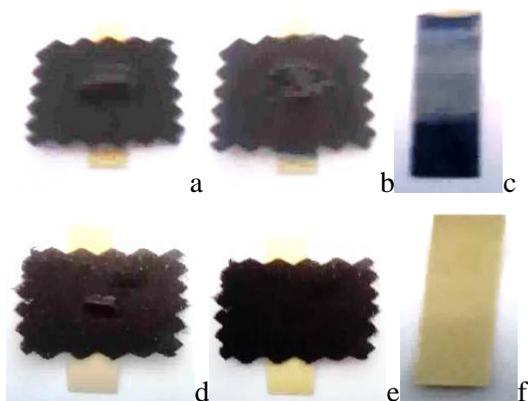
Fig. 6. Digital images of the top view of: non-impregnated textile (a-c); PET impregnated textile (d-f); at the beginning of testing (a, d); at the end(b, e); yellow indicator (c, f).
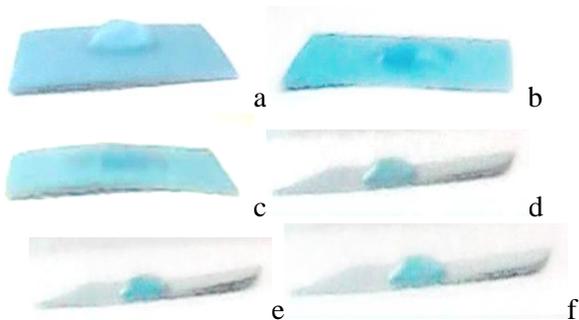
Fig. 7. Digital images of the front view of: non-impregnated paper (a-c); PET impregnated paper (d-f); at the beginning of testing (a, d); in the middle(b, e); at the end (c, f).
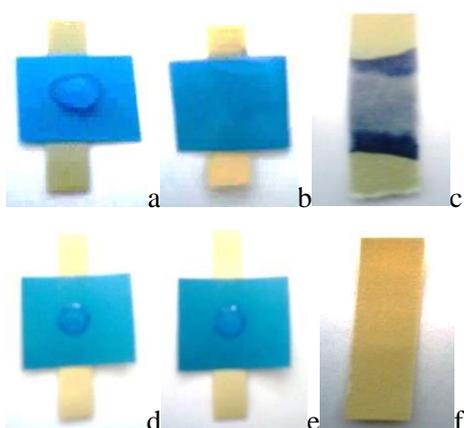
Fig. 8. Digital images of the top view of: non-impregnated textile (a-c), PET impregnated textile (d-f); at the beginning of testing (a, d);at the end (b, e); yellow indicator (c, f).

of the indicator was detected (Fig. 6c), which is a proof that the textile absorbs and leaks the water. Similarly, the drop on the surface of impregnated textile (Fig.5, 6d, e, f) changed its shape and size,

but the color of indicator, disposed under the impregnated textile remained unchanged (Fig. 6f). All of this proves that the PET films have evenly covered the textile surface, thus assuring its waterproof property.

The water permeability survey of the non-impregnated (Fig.7, 8a, b, c) and the impregnated paper is illustrated in the corresponding figures (Fig. 7, 8d, e, f). The water drop spreads on the surface of untreated paper analogically to its behavior on the surface of non-impregnated textile. The indicator under the paper changes its color (Fig.8c), because of the water absorption as it was established in the case of non-impregnated textile. On the surface of impregnated paper the water drop retains its shape and size till the end of the observation (Fig.7, 8d, e, f). Besides, no change of the color intensity of the indicator was registered (Fig.8f). Obviously, this is due to the lack of water absorption in the impregnated waterproof paper.

CONCLUSION

The results of the present study demonstrate the potential of the electrospray process as a promising method for recycling of polyethylene terephthalate (PET), which is one of the most significant wastes of the human activity. For the first time, a two-component chemical system, consisting of TCA and DCM in 1:1 volume ratio, was successfully applied as a solvent in the electrospray deposition of films from PET waste. The selected solvents and PET concentration in the solution provide the required viscosity and electrical conductivity for realizing the electrospraying process. By optimizing the spray process parameters (electric field strength 1 kV/cm and pumping speed –0.013 cm^3/min) thin PET films were successfully deposited on textile and paper samples. The estimation of the water permeability performed show that the impregnated with PET both kinds of materials do not absorb water droplets. Thus, the results obtained demonstrate the prospects for application of recycled PET films in the production of waterproof materials.

REFERENCES

1. J. Trujillo-Reyes, J. Videa, J. Torresdey, *J. Hazard. Mater.*, **280**, 487 (2014).
2. http://ec.europa.eu/eurostat/statistics-explained/index.php/Packaging_waste_statistics.
3. J. Bhushani, C. Anandharamakrishnan, *Tren. Food Sci. Tech.*, **38**, 21 (2014).

4. I. Strain,Q. Wu, A. Pourrahimi, M. Hedenqvist, R. Olsson, R. Andersson, *J. Mater. Chem.* A, **3**, 1632 (2015).

5. D. Hu, X. Li, L. Li, Ch. Yang, *Separation and Purification Tech.*, **149**, 65 (2015).

6. N. Zander, M. Gillan, D. Sweetser, *Materials*, **9**, 247 (2016).

7. M. Dimitrova, E. Krumov, D. Karashanova, *Bulg. Chem. Com.,* **45**, 94 (2013).

8. F. Ahmed, B. Lalia, R. Hashaikeh, *Desalination*, **356**, 15 (2015).

9. Z. -M. Huang, Y. -Z. Zhang, M. Kotaki, S. Ramakrishna, *Compos. Sci. Tech.*, **63**, 2223 (2003).

10. J. Yao, C. Bastiaansen, T. Peijs, http://www. mdpi. com/journal/fibers.

11. C. Feng, K.C. Khulbe, T. Matsuura, S. Tabe, A.F. Ismail, *Separat. Purificat. Tech.*, **102**, 118 (2013).

12. Z. Ma, M.Kotaki, Th. Yong, W. He, S. Ramakrishna, *Biomaterials*, **26**, 2527, (2005).

13. A. Kulkarni, P.A. Mahanwar, *World J. Eng.*, **7**, 454 (2010).

14. M.Khil, H. Kim, M. Kim, S. Park, D.-R. Lee, *Polymer*, **45**, 295 (2004).

15. K. H. Hong, T. J. Kang, *Appl. Polym. Sci.*, **100**, 167 (2006).

ФИЛМИ ОТ РЕЦИКЛИРАНПОЛИЕТИЛЕНТЕРАФТАЛАТ, ОТЛОЖЕНИ ВЪРХУ ХАРТИЯ И ТЕКСТИЛ ЧРЕЗ ЕЛЕКТРОРАЗПРЪСКВАНЕ

Р. Р. Ангелов, Б. Ч. Георгиева, Д. Б. Карашанова

Институт по оптически материали и технологии „акад. Йордан Малиновски“,
Българска академия на науките, ул.„акад. Г. Бончев“ бл.109, 1113 София, България

(Резюме)

Изследвани са възможностите за приложение на метода на електроразпръскване за рециклиране на отпадъчен полиетилен терефталат (ПЕТ) (бутилки, опаковки за храни и др.). Демонстрирано е също така успешното отлагане на ПЕТ филми върху хартия и текстил с цел получаване на водоустойчиви материали. Повърхността на покритите и непокрити хартия и текстил е охарактеризирана чрез сканираща електронна микроскопия (СЕМ). Сравнителното изследване на водната пропускливост на покрити и непокрити повърхности показа, че покритите с ПЕТ материали не пропускат водните капки. На тази основа е заключено, че процесът на електроразпръскване има потенциал като обещаващ метод за рециклиране на отпадъчен ПЕТ, чийто продукт може да се използва за производството на защитни облекла и непропусклива хартия.

Mechanochemical synthesis and properties of ZnS/TiO₂ composites

N. Kostova[1]*, E. Dutkova[2]

[1]*Institute of Catalysis, Bulgarian Academy of Sciences, 1113 Sofia, Bulgaria*
[2]*Institute of Geotechnics, Slovak Academy of Sciences, 04001 Košice, Slovakia*

ZnS/TiO₂ composites have been prepared by simple solid-state mechanochemical route. One sample was prepared in a planetary ball mill by dry milling of TiO₂ P 25 Degussa with mechanochemically synthesized ZnS (cubic sphalerite phase, JCPDS 00-05-0566) in advance. Another sample has been obtained by the wet mechanochemical synthesis from zinc acetate and sodium sulfide in the presence of TiO₂ P 25 Degussa. The phase and structural transformation were studied by XRD analysis. It was established that the dry milling of mixture of TiO₂ P 25 and ZnS induced phase transformation of anatase in TiO₂ P 25 to rutile. Anatase phase was identified in diffraction pattern of the mechanochemically synthesized sample by wet route. Diffuse reflectance spectroscopy was applied in order to evaluate the band gap energy of the synthesized samples. The properties of the prepared ZnS/TiO₂ samples in photocatalytic decoloration of Methyl Orange (MO) dye as model decontaminant in aqueous solution were examined. For determination of the emission behavior of the mechanochemically synthesized ZnS/TiO₂ composites, the room temperature photoluminescence (PL) spectra were recorded by exciting the samples with excitation wavelength of 325 nm. The multiple emission peaks were observed. The lower PL intensity of the mechanochemically synthesized ZnS/TiO₂ sample by dry route indicates a lower recombination rate of photo-excited electrons and holes.

Keywords: mechanochemistry, photocatalysis, titania, ZnS, Methyl Orange

INTRODUCTION

Various semiconductor materials such as TiO₂, ZnO, CdS or ZnS have been employed to study photocatalytic reduction of pollutant in water [1]. TiO₂ has been proved to be efficient photocatalyst due to its optical and electronic properties, chemical stability, non-toxicity and low cost [2]. However, in many cases, the photocatalytic activity of TiO₂ is not enough to make it applicable for industrial purposes [3]. ZnS is the direct-transition semiconductor with the widest energy band gap among the groups of II-VI semiconductor materials. ZnS based composite materials have been developed in order to extend the utilization of ZnS [4]. In last two decades a variety of methods have been used for ZnS synthesis such as hydrothermal method [5], sol-gel method [6], solvothermal method [7] and mechanochemical synthesis [8]. High-energy milling has been widely applied for the synthesis of nanocrystalline materials [9, 10]. Takacs et al. [11] have investigated mechanochemical formation of Zn, Cd and Sn chalcogenides from a mixture of metals and sulfur powders. Mechanochemical reactions are characterized by repeated welding and fracture of reacting particles during ball-powder collisions, which continually regenerate reacting interfaces. The mechanochemical synthesis for preparation of composites has significant potential for large scale production due to high efficiency and low cost process [9].

In recent years ZnS nanocrystals have been studied due to their interesting properties having potential as photocatalysts in environmental contaminant elimination [12]. Nanoscale ZnS coupled TiO₂ photocatalysts have been investigated due to potential applications such as purification of wastewater [13].

In the present work, the mechanochemically synthesized ZnS/TiO₂ composites were tested and their photocatalytic activities were compared with data, previously obtained with the traditionally used reference photocatalyst TiO₂ Degussa P25. Methyl Orange dye was selected as a model reactant for photodegradation. The aim of the present paper was to investigate the influence of the synthesis conditions for the preparation of ZnS/TiO₂ composites by monitoring their optical and photocatalytic properties.

*To whom all correspondence should be sent:
E-mail: nkostova@ic.bas.bg

EXPERIMENTAL

The ZnS/TiO$_2$ composites were synthesized from zinc acetate $(CH_3COO)_2Zn.2H_2O$ (98 %, ITES, Slovakia), sodium sulfide $Na_2S.9H_2O$ (98%, Aldrich, Germany) and TiO$_2$ Degussa P25.

The mechanochemical synthesis of the samples was realized in a Pulverisette 6 planetary ball mill (Fritsch, Germany) under the following conditions: the ball mill was charged with 50 balls of diameter 10 mm having weight of 360 grams, made of tungsten carbide. The rate of rotation of the planetary carrier was 500 rpm. The milling was performed conducted in inert atmosphere of argon at the room temperature.

Pure zinc sulfide was mechanochemically prepared and was described in our study [14].

The first composite sample was denoted as ZnS/TiO$_2$-1 and it was synthesized by milling in a planetary ball mill using the pure zinc sulfide, prepared beforehand and the commercially available TiO$_2$ P25 Degussa at a ratio 1:4. The milling time was 30 minutes.

The second mechanochemically synthesized composite sample labeled ZnS/TiO$_2$-2 was prepared by milling a mixture of zinc acetate, sodium sulfide and TiO$_2$ P25 Degussa. The synthesis was carried out in the planetary ball mill in inert atmosphere under the same conditions as are described above.

The X-ray diffraction (XRD) patterns were recorded on a D8 Advance diffractometer (Brucker, Germany) using CuKα radiation.

The values of specific surface areas (S$_A$) were obtained by the low-temperature nitrogen adsorption method using a Gemini 2360 sorption apparatus (Micromeritics, USA).

The diffuse reflectance UV–vis spectra for evaluation of photophysical properties were recorded in the diffuse reflectance mode (R) and transformed to absorption spectra through the Kubelka-Munk function [15]. A Thermo Evolution 300 UV-vis Spectrophotometer, equipped with a Praying Mantis device with Spectralon as the reference was used.

The photoluminescence (PL) spectra at room temperature were acquired at right angle on a photon counting spectrofluorometer PC1 (ISS) with a photoexcitation wavelength of 325 nm. A 300 W xenon lamp was used as the excitation source. For measuring the PL intensity, the powders were suspended in absolute ethanol.

The photocatalytic activity of the samples in the reaction of Methyl Orange decoloration was measured under UV-C monochromatic illumination (TUV lamp λ=254 nm) and under visible light illumination.

The photocatalytic experiments were carried out in a semi-batch photoreactor equipped with a magnetic stirrer, similarly as in the case of our previous work [16]. The suspension was prepared by adding ZnS/TiO$_2$ sample (100 mg) to 100 mL of Methyl Orange (MO) solution with a concentration 1.10^{-5} M. The suspension was magnetically stirred in the dark for 30 min to ensure an adsorption-desorption equilibrium. Then the suspension was irradiated by Philips TUV lamp (4 W). UV-C monochromatic radiation is λ=254 nm. All experiments were performed at constant stirring rate 400 rpm at room temperature. The concentration of MO during the photocatalytic reaction was determined by monitoring the changes of the main absorbance peak at λ=463 nm.

RESULTS AND DISCUSSION

The XRD measurements were carried out to study the phase composition of the obtained samples. The XRD patterns of ZnS/TiO$_2$ composites, synthesized by mechanochemical route, are given in Fig. 1. The patterns of the commercial product TiO$_2$ P25 Degussa and mechanochemically synthesized ZnS are also given for comparison. The X-ray diffraction pattern of TiO$_2$ P 25 Degussa shows that it is composed of crystallites of anatase and rutile at a ratio 75:25. Some diffraction lines are observable in the XRD pattern of the ZnS, synthesized by us, which indicate the cubic sphalerite structure (JCPDS 00-05-0566). All diffraction peaks are broadened because of fine size of crystals [17] as well as due to structural disorder introduced into zinc sulfide by milling procedure [9]. The crystallite size of ZnS determined from the Scherrer formula from the major peak centered at $2\Theta=28.8^{o}$ was estimated to be about 3.9 nm.
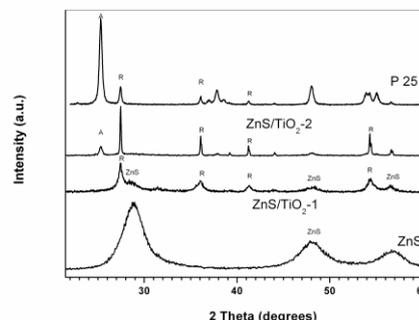
Fig. 1. XRD patterns of initial TiO$_2$ P25 Degussa and mechanochemically synthesized samples ZnS, ZnS/TiO$_2$-1 and ZnS/TiO$_2$-2.

Valuable changes were noticed in the XRD pattern of the sample ZnS/TiO$_2$-1 prepared in a planetary ball mill by dry milling of TiO$_2$ P 25 Degussa with mechanochemically synthesized ZnS. The substantial decrease in the intensity of the peaks at 2θ=27.5^o, 36°, 41° and 54.1^o related to the rutile was observed (Fig. 2). No characteristic lines of anatase phase were registered in the XRD pattern of this composite sample. It follows from that phase transformation of anatase into rutile occurred in this case. A significant broadening was observed for all registered diffraction lines. A considerable decrease in the size of the crystallites was observed in this sample. Some lines characteristic of the ZnS were also present. The rutile was the prevailing phase in the ZnS/TiO$_2$-1 sample.

a

b
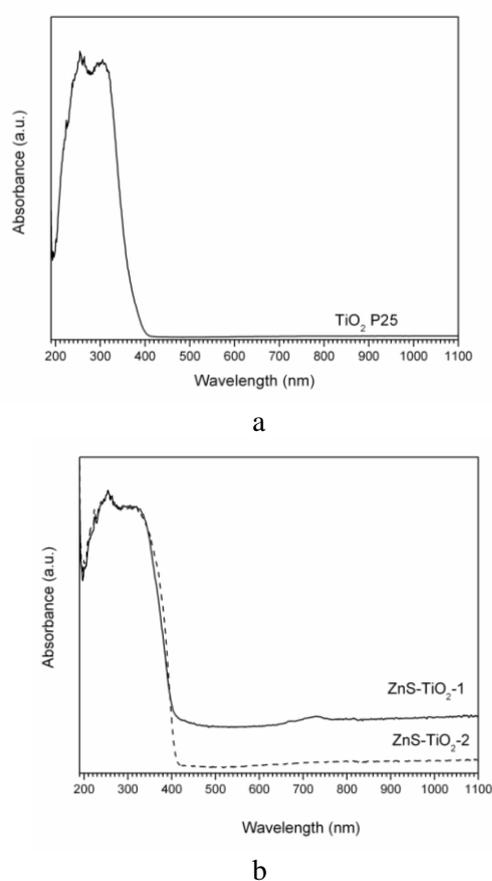
Fig. 2. UV-vis absorbance spectrum of: a) TiO$_2$ P25 Degussa; b) mechanochemically synthesized ZnS/TiO$_2$ composites.

All the lines characteristic of TiO$_2$ P 25 were present in the diffraction pattern of the sample ZnS/TiO$_2$-2, which was prepared by wet mechanochemical synthesis of ZnS from zinc acetate and sodium sulfide on the surface of TiO$_2$ P 25. Partial transformation of the anatase into rutile was registered in this case. The specific surface area of the sample ZnS/TiO$_2$-1 was measured to be

36 m^{2}g^{-1}. The sample ZnS/TiO$_2$-2 had specific surface area 48 m^{2}g^{-1} near to that of initial TiO$_2$ P25 (50 m^{2}g^{-1}). The sample ZnS/TiO$_2$-1 represents a less crystalline material, in comparison with the sample ZnS/TiO$_2$-2 (Fig. 1). The wide diffraction lines of the mechanochemically synthesized ZnS clearly prove the nano-sized nature of the sample [18]. The impact of the energy during the milling process is manifested in the form of phase transformation [19].

The diffuse-reflectance spectra (DRS) in the ultra-violet and in the visible range were recorded aiming at the investigation of the optical properties of the mechanochemically prepared ZnS/TiO$_2$ composites. The TiO$_2$ P25 Degussa has a wide absorption band in the range from 200 to 380 nm (Fig. 2a). For the mechanochemically synthesized ZnS/TiO$_2$ composites, an absorption edge is red shifted and the absorption tail is extended to 420 nm as shown in Fig. 2b.
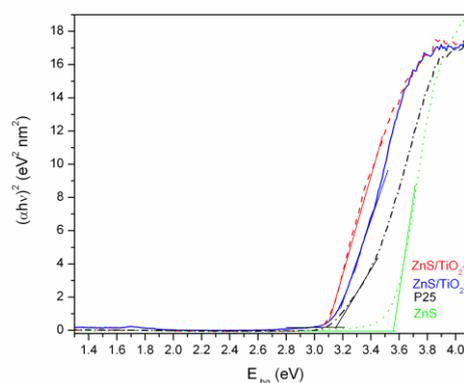
Fig. 3. Band gap energy E$_{bg}$ of TiO$_2$ P25 Degussa, and mechanochemically synthesized ZnS, ZnS/TiO$_2$-1 and ZnS/TiO$_2$-2 samples.

The method of UV-vis diffuse reflectance spectroscopy was employed to estimate the band gap energies of the prepared ZnS/TiO$_2$ composites. The minimum wavelength is required to promote an electrons depended upon the band gap energy E$_{bg}$ of the samples and it is given by relationship E$_{bg}$=1240/λ, where λ is the wavelength in nanometers [20]. The band gap values were calculated using the UV-vis spectra from the following equation: $\alpha(h\nu) = A(h\nu - E_{bg})^{1/2}$, where α is the absorption coefficient and hν is the photon energy. The band gap energy is calculated by extrapolating a straight line to the abscissa axis. The value of hν extrapolated to α=0 gives an absorption energy, which corresponds to a band gap energy. The initial TiO$_2$ P 25 Degussa has E$_{bg}$=3.20 eV. The preliminary mechanochemically

163

synthesized ZnS has a wider energy band gap E_{bg}=3.57 eV (Fig. 3). The estimated E_{bg} value was 3.13 eV for ZnS/TiO$_2$ -1 sample and 3.08 eV for the ZnS/TiO$_2$-2 composite sample. These results suggest the possibility of application of these ZnS/TiO$_2$ composite materials as photocatalysts on degradation process with lower energetic requirements than TiO$_2$.

a

b
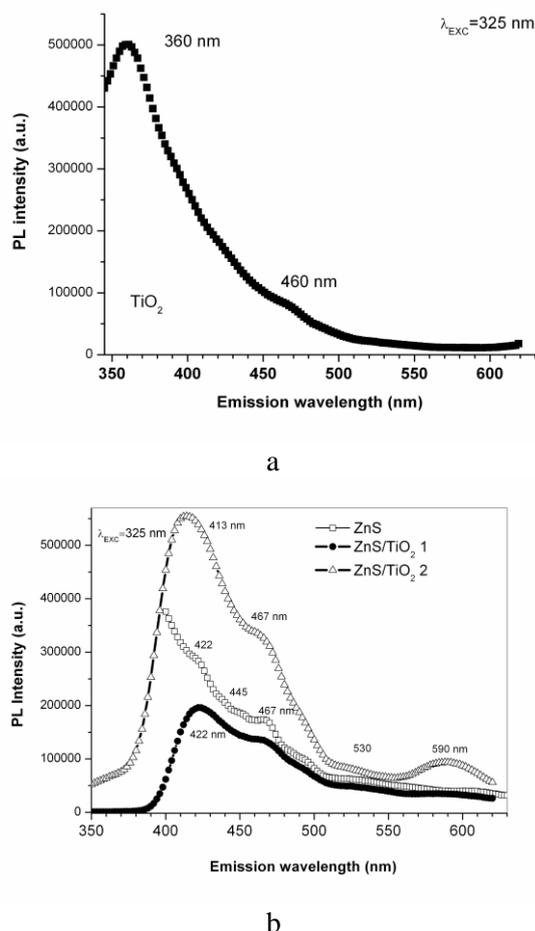
Fig. 4. Photoluminescence spectrum of: a) TiO$_2$ P25 Degussa; b) mechanochemically synthesized samples ZnS, ZnS/TiO$_2$-1 and ZnS/TiO$_2$-2.

The photoluminescence (PL) spectra of the mechanochemically synthesized ZnS, ZnS/TiO$_2$-1 and ZnS/TiO$_2$-2 samples were recorded in order to observe their emission behavior. All samples were photoexcited at wavelength 325 nm at room temperature. The PL spectrum of the initial TiO$_2$ P 25 Degussa is represented in Fig. 4a. The emission intensive peak in the spectrum of TiO$_2$ P 25 Degussa with a maximum in the near ultraviolet region at about 360 nm (Fig. 4a) can be ascribed to emission of a photon having energy equal or slightly higher than the band gap width of the anatase phase of TiO$_2$ and it gives evidence for a direct recombination of a photoexcited electron and

a positively charged hole [21, 22]. As can be seen from Fig. 4b, the cubic ZnS phase is luminescence active. There are emission peaks at 422, 465, 496 and 590 nm. These emission peaks were also registered in the PL spectra of the mechanochemically prepared ZnS/TiO$_2$ composites. Wang et al. [23] reported the multiple defects related emission of ZnS. The emission intensity is decreased in the PL spectrum of ZnS/TiO$_2$-1 composite. The broad emission spectra of ZnS/TiO$_2$ composites are mainly located in the blue region. With its maximum intensity centered at 422 nm, which could be ascribed to the sulfur vacancy and defects in the ZnS microcrystals [28]. The blue shift of the first PL band from 422 to 413 nm in the PL spectrum of ZnS/TiO$_2$-2 composite was registered. The PL intensity of ZnS/TiO$_2$-2 is higher than ZnS/TiO$_2$-1. This is related to the presence of anatase phase in ZnS/TiO$_2$-2 sample provided with XRD (see Fig. 1). The emission peak observed at 465 nm could be associated with an interstitial zinc lattice defect. The emission peak at 496 nm is from the sulfur vacancy related emission [25]. The green PL emission peak at 590 nm can be associated with elemental sulfur species [26]. The photolumine-scence emission is the result of two effects: part of the illuminating photons energy goes for non-radiative transition (transition between two energy levels of vibration of the modes of the crystal lattice). The other part is emitted as a result of recombination of photoexcited electrons and holes (photons of lower energy).

The photocatalytic activities of the mechanochemically synthesized ZnS/TiO$_2$ composites were evaluated by the degradation of representative industrial dye Methyl Orange (MO) in aqueous solution under UV irradiation. All experiments were performed under nature pH condition and room temperature. For comparison, the activities of ZnS and TiO$_2$ P25 Degussa were also investigated under the same conditions. The temporal changes in the concentration of MO were monitored by examining the variation in maximal absorption in UV-vis at 464 nm. In region, where Lamber-Beer law ($A=\varepsilon * c * l$) is significant the concentration of MO dye is proportional to absorbance, where A is the absorbance, c is the concentration of absorbing compound MO, l is the length of absorbing layer and ε is the molar absorbing coefficient. Fig. 5 shows the photocatalytic efficiencies (C/C_o) in presence of mechanochemically prepared ZnS and ZnS/TiO$_2$ composite materials. The C_o is the initial concentration after achieve absorption/desorption

equilibrium. On the basis of blank experiment, the self-photolysis of MO could be neglected (Fig. 5-curve 5). TiO$_2$ P25 Degussa was taken as reference for comparison purpose and in this case the MO degradation was about 70 % after 60 min. The photodegradation performance of MO can be ranked by decreasing order of activity as follows: ZnS/TiO$_2$-2 > ZnS/TiO$_2$-1 > TiO$_2$>ZnS.
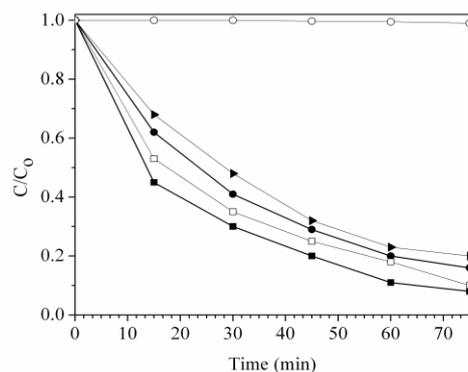
Fig. 5. Photodegradation effect of MO as a function of irradiation time of commercial TiO$_2$ P25 Degussa (●), and mechanochemically synthesized samples ZnS (►), ZnS/TiO$_2$-1(□), ZnS/TiO$_2$-2 (■) and blank experiment (○).

In addition, after the degradation, reaction is completed; the ZnS/TiO$_2$-1 composite photocatalyst was separated centrifugally from the dye solution. Without further treatment, the recycled ZnS/TiO$_2$-1 composite was used to degrade the dye solution for the second time. The degradation rate remains almost unchanged, which shows that the ZnS/TiO$_2$-1 composite photocatalyst has also good repeatability.

CONCLUSIONS

The present paper represents a detailed study of the structural, optical and photocatalytic properties of mechanochemically synthesized ZnS/TiO$_2$ composite materials. The XRD analysis of the ZnS/TiO$_2$-1 sample, prepared by dry milling in a planetary ball mill shows that in this case almost the full phase transition of anatase into rutile is occurred. However, the phase composition of TiO$_2$ P25 during the wet mechanochemical synthesis of the ZnS/TiO$_2$-2 composite sample is preserved. The specific surface area of this sample is close to the initial TiO$_2$ P25. DRS study reveals that all the mechanochemically synthesized samples show strong absorbance in the visible light region. The evaluated band gap values of the samples are 3.3, 3.57, 3.13 and 3.06 eV for TiO$_2$ P25, ZnS,

ZnS/TiO$_2$-1 and for ZnS/TiO$_2$-2, respectively. The enhanced photocatalytic activity of decoloration of MO in aqueous solutions of the synthesized composite materials in the visible range of the spectrum is owing to the efficient separation of photoexcited electrons and holes – the charge carriers between the ZnS and the TiO$_2$ attached phases.

REFERENCES

1. A. Fujishima, T. N. Rao, D.A. Tryk, *J. Photochem. Photobiol. C. Photochem. Rev.*, **1**, 1 (2000).
2. M. Hoffmannn, S. Martin, W. Choi, D. Bahnemann, *Chem. Rev.*, **95,** 69 (1995).
3. H. Tada, A. Hattori, Y. Tokihisa, K. Imai, N. Tohge, S. Ito, *J. Phys. Chem.* B, **104,** 4585 (2000).
4. S. Ummartyotin, Y. Infahsaeng, *Renewable and Sustainable Energy Rev.,* **55**, 17 (2016).
5. N. Jothi, A. Joshi, R. Vijay, A. Muthuvivayaagam, P. Sagayaraj, *Mater. Chem. Phys.*, **138**, 186 (2013).
6. I. Bu, *J. Lumines.*, **134**, 423 (2013).
7. Y. Choi, S. Lee, S. Kim, Y. Kim, D. Cho, M. Khan, Y. Sohn, *J. Alloy. Comp.*, **675**, 46 (2016).
8. P. Baláž, E. Boldižárová, E. Godočíková, J. Briančin, *Mat. Lett.,* **57**, 1585 (2003).
9. P. Baláž, M. Achimovičová, M. Baláž, P. Billik, Z. Cherkezova-Zheleva, J.M. Craido, F. Delogu, E. Dutková, E. Gaffet, F.J. Gotor, R. Kumar, I. Mitov, T. Rojac, M. Senna, A. Streletskii, K. Wieczorek-Ciurowa, *Chem. Soc. Rev.*, **42**, 7571 (2013).
10. C. Xu, S. De, A. Balu, M. Ojeda, R. Luque, *Chem. Commun.*, **51**, 6698 (2015).
11. L. Takacs, M. Susol, *J. Solid State Chem.*, **121**, 394 (1996).
12. A. Roy, G. De, *J. Photochem. Photobiol.* A Chemistry, **157,** 87 (2003).
13. N. Uzar, S. Okur, M.C. Aricom, *Sensor. Actuator. Phys.*, **167**, 188 (2011).
14. P. Balaz, M. Balaz, E. Dutkova, A. Zorkovska, J. Kovac, P. Hronec, J. Kovac Jr, M. Caplovicova, J. Mojzis, G. Mojzisova, A. Eliyas, N.G. Kostova, *Mater. Sci. Eng. C,* **58**, 1016 (2016).
15. Z. Orel, M. Gunde, B. Orel, *Prog. Org. Coat.,* **30**, 59 (1997).
16. N.G. Kostova, M. Achimovičová, A. Eliyas, N. Velinov, P. Baláž, *Nanosci. and Nanotechnol.*, **12**, 52 (2012).
17. J. Niu, W. Xu, H. Shen, S. Li, H. Wang, L. Li, *Bull. Kor. Chem. Soc*., **33**, 393 (2012).

18. V. Sepelak, A. Duvel, M. Wilkeming, K.D., Becker, P. Heitjans, *Chem. Soc. Rev.*, **42**, 7507 (2013).

19. I. Lin, S. Nadiv, *Mater. Sci. Eng.*, **39**, 93 (1979).

20. K. Reddy, S. Panorama, A. Reddy, *Mater. Chem. Phys.*, **78**, 239 (2002).

21. S. Liu, X-J. Zhao, Q. Zhao, X. He, J. Feng, *J. Electron Spectrosc. Relat. Phenom.*, **148**, 158 (2005).

22. D. Dastan, P. Loundhe, N. Chaure, *J. Mater. Sci.-Mater. Electr.*, **25**, 3473 (2014).

23. X. Wang, J. Shi, Z. Feng , M.Li, C. Li, *Phys. Chem. Chem. Phys.*, **13**, 4715 (2011).

24. P. Hu, Y. Liu, L. Fu, L. Cao, D. Zhu, *J. Phys. Chem. B*, **108**, 936-938 (2009).

25. A. Kole, C. Tiwary, P. Kumbhakar, *J. Mater. Chem.*, C **2**, 4338 (2014).

26. A. Ye, X. Fang, G.Li, L. Zhang, *Appl. Phys. Lett.*, **85** 035 (2004).

МЕХАНОХИМИЧЕН СИНТЕЗ И СВОЙСТВА НА ZnS/TiO₂ КОМПОЗИТИ

Н. Г. Костова[1], Е. Дуткова[2]

[1] *Институт по катализ, Българска академия на науките, 1113 София, България*
[2] *Институт по геотехника, Словашка Академия на науките, 04001 Кошице, Словакия*

(Резюме)

ZnS/TiO₂ композити бяха получени чрез твърдотелен механохимичен подход. Един ZnS/TiO₂ композитен материал беше получен в планетарна топкова мелница чрез сухо смилане на TiO₂ P 25 Degussa с предварително механохимично синтезиран ZnS с кубична структура от сфалеритав тип JCPDS 00-05-0566. Друг образец беше получен чрез мокър механохимичен синтез от цинков ацетат и натриев сулфид в присъствие на TiO₂ P 25 Degussa. Фазата и структурните промени бяха изследвани с помощта на РФА. Беше установено, че сухото смилане на смес от TiO₂ P 25 and ZnS индуцира пълно преобразуване на анатаза, присъстващ в TiO₂ P 25 Degussa, в рутил. Анатаз беше идентифициран в дифрактограмата на механохимично синтезирания образец чрез мокър метод. Дифузноотражателна спектроскопия беше приложена за определяне на енергията на забранената зона на механохимичносинтезираните образци. Фотокаталитичните свойства на получените ZnS/TiO₂ образци бяха изследвани във фотокаталитичното обезцветяване на багрило метил оранж като моделен замърсител във воден разтвор. За определяне на емисионното поведение на механохимично синтезираните ZnS/TiO₂ композитни материали бяха записани техните фотолуминесцентни спектри при стайна температура след възбуждане на образците с възбуждаща дължина на вълната 325 нм. Бяха наблюдавани сложни емисионни пикове. По-ниският интензитет на ивиците в спектра на образеца синтезиран чрез сухо механично стриване свидетелства за по-ниска скорост на рекомбиниране на фотовъзбудените електрони и дупки.

Influence of PEO, PDMAA and corresponding di- and triblock copolymers on the optical properties of niobia thin films

R. Georgiev[1], L. Todorova[2], D. Christova[2], B. Georgieva[1], M. Vasileva[1] and T. Babeva[1]*

[1]*Institute of Optical Materials and Technologies "Acad. J. Malinowski", Bulgarian Academy of Sciences, Acad. G. Bonchev Str., Bl. 109, 1113 Sofia, Bulgaria*
[2]*Institute of Polymers, Bulgarian Academy of Sciences, Acad. G. Bonchev Str., Bl. 103-A, 1113 Sofia, Bulgaria*

The present study aims at investigation of the influence of poly(ethylene oxide) (PEO), poly(N,N-dimethylacrylamide) (PDMAA) and corresponding block copolymers (PEO-*b*-PDMAA and PDMAA-*b*-PEO-*b*-PDMAA) on the formation of porosity in thin Nb_2O_5 films using evaporation induced self-assembly (EISA) method. The addition of copolymer solution to Nb sol provoked phase separation and after appropriate annealing a system of pores was generated in the spin-on thin film. The annealing regimes providing complete removal of the polymer from the pores were optimized through Thermogravimetric Analysis (TGA). The morphology and structure of the films were studied by Transmission Electron Microscopy (TEM) and Selected Area Electron Diffraction (SAED). The optical parameters of the films, along with their thicknesses were determined from reflectance spectra and nonlinear curve fitting. The influence of copolymer structure and composition on the optical properties of thin Nb_2O_5 films was established and the tuning of refractive index in wide range was demonstrated.

Keywords: Nb_2O_5 films, spin-coating, sol-gel, optical properties, porosity.

INTRODUCTION

The creation of materials with tailored texture is regarded as a key step toward innovative technologies. Recently, advanced inorganic thin films and especially those with controlled porosity attract increasing attention because of the important roles they play in sorption, catalysis, photoconversion, sensors, and photonic and electronic microdevices. One of the approaches towards fine tunable mesoporous, crystalline inorganic materials relays on the use of block copolymer mesostructures as templates [1].

Amphiphilic copolymers which are composed of thermodynamically incompatible blocks (mostly including polystyrene, polybutadiene, or poly(propylene oxide) as hydrophobic blocks, and poly(ethylene oxide) or poly(vinyl pyridine) as hydrophilic blocks) provide possibilities for continuous tuning of the self-assembly characteristics by adjusting molecular weight, copolymer composition and architecture, or solvent composition [2]. This enables good control over the self-organized superstructures and the length scales and suppose introduction of specific functions as

well. Block copolymer self-assembly has been proven as a powerful platform for structuring morphology and tuning size and porosity of various functional inorganic materials on the nanometer scale [3, 4]. Templating by using variety of amphiphilic diblock or triblock architectures has been widely applied in the synthesis of amorphous silica mesostructures, mesoporous metal oxides and crystalline films [1 - 8].

We have already demonstrated that using different amphiphilic tri-block copolymers (PE6100, PE6800, PE10100, Pluronic, BASF) and varying the molar ratio of polymer and $NbCl_5$ used for preparing the Nb sol it is possible to obtain thin Nb_2O_5 films with tailored pore structure and controlled optical and sensing properties [9, 10]. An improvement of sensing properties of mesoporous films is demonstrated as compared to the films prepared without template [9, 10].

In this work, we report for the first time the utilization of double hydrophilic block copolymers in the formation of porous Nb_2O_5 thin films when applying the evaporation induced self-assembly (EISA) method. Diblock and triblock copolymers comprising poly(N,N-dimethylacrylamide) (PDMAA) and poly(ethylene oxide) (PEO) blocks were synthesized and used as hydrophilic templates in the EISA. The influence of the composition and

concentration of the organic templates on the optical properties of the films have been studied and the tuning of refractive index in a wide range has been demonstrated.

EXPERIMENTAL DETAILS

Niobium oxide thin films were prepared by the methods of evaporation induced self-assembly and spin coating (30 seconds at 3000 rpm) using a mixture of Nb sol and four organic templates (PDMAA, PEO, PEO-*b*-PDMAA and PDMAA-*b*-PEO-*b*-PDMAA) dissolved in water in different concentrations (0.5%, 1.5 % and 5%) thus obtaining ratios of polymers to $NbCl_5$ equal to 0, 0.07, 0.14, 0.23. Niobium sol was prepared by a sonocatalytic method using 0.400 g $NbCl_5$ (99%, Aldrich) as a precursor, 8.3 ml ethanol (98%, Sigma-Aldrich), and 0.17 ml distilled water [11]. The synthesis of used copolymers was carried out as follows [12]: double hydrophilic di- and triblock copolymers were synthesized by means of redox polymerization of DMAA (Sigma-Aldrich, Germany) in deionized water when using polyethylene glycol methyl ether (PEG-ME; 2000 g/mol; Fluka, Switzerland) or respectively polyethylene glycol (PEG; 2000 g/mol; Fluka, Switzerland)) as initiating moiety. PDMAA was synthesized by aqueous free radical polymerization of DMAA initiated by 4,4-azobis (4-cyanovaleric acid) (ABCVA). The obtained polymers were purified by dialysis against water and finally isolated by freeze-drying. The composition of the prepared copolymers was analyzed by Nuclear Magnetic Resonance (NMR): PEO_{45}-*b*-$PDMAA_{37}$, Mn = 5700 g/mol and $PDMAA_{28}$-*b*-PEO_{45}-*b*-$PDMAA_{28}$, Mn = 7500 g/mol, respectively.

The surface morphology and structure of the films were studied by Transmission Electron Microscopy (TEM) using HRTEM JEOL JEM 2100 (Japan) microscope.

Refractive index (*n*), extinction coefficient (*k*) and thickness (*d*) of the films were determined from reflectance spectra (*R*) of the films measured at normal incidence of light by UV-VIS-NIR spectrophotometer Cary 05E (Varian, Australia) using nonlinear curve fitting method [11]. The experimental errors for *R*, *n, k* and *d* are 0.3%, 0.005, 0.003 and 2 nm respectively.

Thermogravimetric analysis was performed using TGA-4000 Perkin Elmer analyzer supplied with PYRIS software. The samples were heated from r.t. to 600 °C at a heating rate of 10 °C/min in inert atmosphere (argon).

RESULTS AND DISCUSSIONS

Typical TEM images of Nb_2O_5 obtained using different organic templates and fixed ratio of 0.23:1 of polymer to $NbCl_5$ are shown in Fig. 1 along with an example of Selected Area Electron Diffraction pattern of the films as an inset. It is seen that the pores in the films are with similar sizes although these formed by addition of di-block copolymer are slightly bigger as compared to the others. The structure of all films at annealing temperature of 320 °C is amorphous.
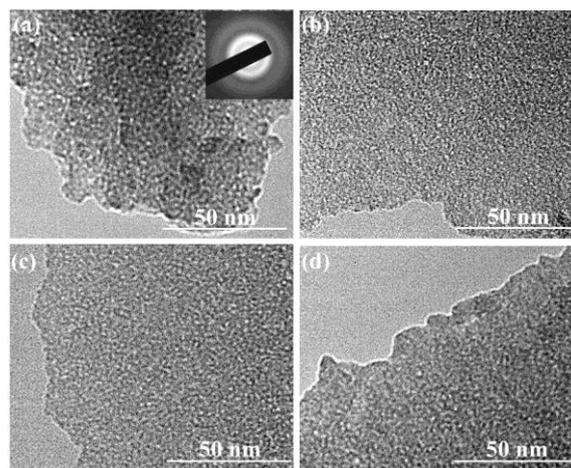
Fig. 1. TEM pictures of Nb_2O_5 thin films prepared using 5 wt % PDMAA-*b*-PEO (a), PDMAA-*b*-PEO-*b*-PDMAA (b), PDMAA (c) and PEO (d) as organic template (ratio polymer to $NbCl_5$ equals to 0.23) and annealed at 320 °C for 30 min. The inset shows Selected Area Electron Diffraction pattern.
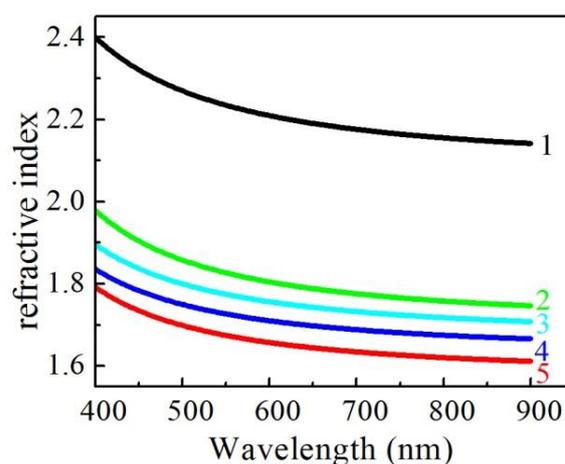
Fig. 2. Refractive index as a function of wavelength for Nb_2O_5 thin films deposited without organic template (curve 1) and with addition of PDMAA (curve 2), PDMAA-*b*-PEO-*b*-PDMAA (curve 3), PDMAA-*b*-PEO (curve 4) and PEO (curve 5) with ratio of template to $NbCl_5$ equals to 0.23. All films were annealed at 320 °C for 30 min.

Effective refractive indices (n) of Nb_2O_5 films prepared with organic templates (5 wt. %) are compared with the values for dense film (without template) in Fig. 2. Addition of polymers leads to a decrease in n depending on the type of the template: the strongest reduction is obtained for PEO, where n at wavelength of 600 nm changes from 2.21 for dense film to 1.65, and the smallest reduction is for PDMAA (n=1.81). The values for copolymers are in between: 1.71 and 1.76 for di and triblock copolymers, respectively.

Thermogravimetric Analysis (TGA) showed that the process of weight loss for PEO starts at a temperature around 200 °C and the polymer has lost more than 95 % of its initial weight at temperature of 320 °C [13]. However, for PDMAA the thermal decomposition starts at a temperature around 400 °C and ends around 500 °C where the polymer has lost its entire weight [14]. If we consider that all films have similar porosity (see Fig. 1) and comprise two phases (dense Nb_2O_5 and air or polymer) it can be expected the Nb_2O_5 films prepared using PEO as template to have the lowest effective refractive index because at 320 °C PEO has been completely burnt and the films consist of air with n=1 as a second phase. However, the rest of the films contain polymer with higher refractive index (n = 1.43, 1.463 and 1.485 for PDMAA, di- and triblock copolymers, respectively [15]) as a second phase, because these templates have not been thermally decomposed at the temperature of 320 °C. Using Brugemann effective medium approximation [16] and assuming that PEO has been fully decomposed we calculate that the free volume fraction in the films prepared with PEO as a template is 45 % (Table 1). The values are close to those previously obtained for mesoporous Nb_2O_5 films prepared using Pluronic template [9, 10].

Table 1. Calculated pore volume fractions in Nb_2O_5 films prepared using different organic templates and annealed for 30 min at 320 oC according to Brugemann EMA [16] and assuming pores filled with air or polymer.

Template type	Pore volume fraction (%)	
	Air	Polymer
PEO	45	n.a
PDMAA	32	50
diblock	39	65
triblock	36	61

The values calculated for the rest of the films, assuming two phases – dense Nb_2O_5 and polymer, are also presented in Table 1. In the case of using PDMAA as a template, the value of pore volume fraction (50 %) is similar to this for PEO template,

but for both copolymers it is substantially greater (more than 60 %). Because TEM pictures do not show significant difference in porosity of the films we may speculate that the pores of Nb_2O_5 films prepared with copolymers as templates are filled with a mixed phase of polymer and air, due to the partially decomposed polymer. Thus their pore volume fractions vary between the values for pores filled with air and pores filled with polymer (Table 1).

To study further the decomposition of polymer inside the pores a mixture of Nb sol and PEO-*b*-PDMAA copolymer (5 wt.%) is prepared and thermogravimetric (TGA) curves are measured. The TGA curves along with derivative TGA curves of pure Nb sol and sol blended with PEO-*b*-PDMAA polymer are presented in Fig. 3. It is seen that the two samples degrade in two main stages. The temperatures of maximum degradation in the first stage are similar for the two samples, 122 °C and 118 °C for pure and blended Nb sol (Fig. 3(b)).
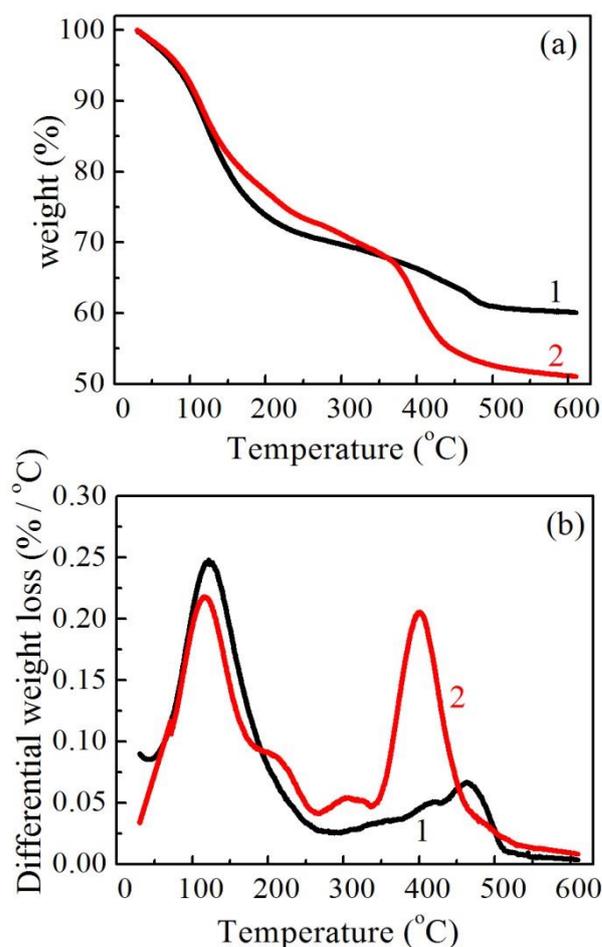
Fig. 3. Thermo gravimetric (TGA) (a) and differential TGA curves (b) for niobium sol (curve 1) and Nb sol blended with PEO-*b*-PDMAA polymer (curve 2) (5 wt%, volume ratio sol : polymer = 5:1).

The weight loss is apparently associated with evaporation of adsorbed water and solvents. However, there is a considerable difference between the samples behavior during the second stage. It is seen from Fig. 3 that the polymer degradation starts around 340 °C and the process ends after reaching 550 °C with temperature of the maximum degradation of 400 °C. For pure Nb sol there is a weak weight loss around 460 °C that may be due to the decomposition of some residual organic species. Knowing i) the mass ratio of polymer and $NbCl_5$ in the blended sample, ii) its initial weight and iii) the weight loss of pure sol it is possible to calculate the expected final weight of the blended sample in the assumption of complete mass loss of the polymer and to compare it with the measured one. The obtained difference is 3.10^{-5} g that is within the framework of measuring accuracy. Therefore we may assume that the high temperature annealing of the films would lead to complete thermal decomposition of polymer in the pores thus leading to decrease of refractive index of the films.
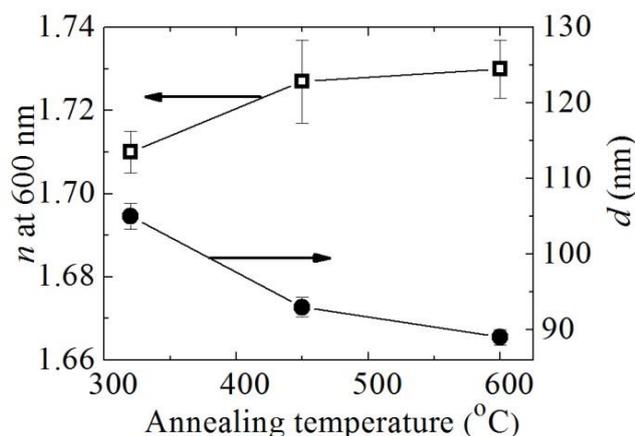
Fig. 4. Refractive index (*n*) at wavelength of 600 nm and thickness (*d*) of Nb_2O_5 films prepared with PEO-*b*-PDMAA template as a function of postdeposition annealing temperature

The temperature dependences of refractive index and thickness of Nb_2O_5 films prepared with PEO-*b*-PDMAA copolymer as a template are presented in Fig. 4. Refractive index slightly increases with temperature (the change is 1.1%), while the thickness decreases with 15 %. Almost the same reduction of *d* (10 %) is obtained for the triblock copolymer, while the increase in *n* is stronger – almost 10 % (Table 2). When PEO is used as a template there is no change of *n* and *d* of Nb_2O_5 films with annealing temperature, while for Nb_2O_5 films with PDMMA template a slight decrease in *n*

accompanied with small reduction in *d* (5 %) are observed (Table 2).

Table 2. Refractive index and thickness of Nb_2O_5 films prepared using the denoted polymers as templates and annealed for 30 min at temperature of 320 °C and 600 °C.

Template type	*n* at 600 nm		*d* (nm)	
	320°C	600°C	320°C	600°C
PEO	1.64	1.64	87	89
PDMAA	1.77	1.75	94	89
diblock	1.71	1.73	105	89
triblock	1.76	1.93	97	84

With increasing the annealing temperature two competing processes take place and the overall film behavior is due to the balance between them. The first one is the densification of the pure Nb_2O_5 matrix that leads to an increase in *n* [11]. The typical changes in the temperature range 300 – 600 °C are 2-3 % in *n* and 7-8 % in *d* [11]. In the porous film this processes is further facilitated due to the thin pore walls and more free volume as compared to dense Nb_2O_5 films. The second process is the thermal decomposition of polymers in the films pores connected with the reduction of effective refractive index. The results presented in Table 2 and Fig. 4 show that when diblock and triblock copolymers are used as templates the first process is prevailing and net increase in *n* with temperature is observed mostly pronounced for the triblock copolymer where the thickness reduction is significant. On the contrary, in the case of PDMAA the second process is predominant and a decrease of *n* is detected although a slight decrease of film thickness occurs. For Nb_2O_5 films prepared with PEO as a template a balance between the two processes is achieved and the net change of *n* is almost zero.
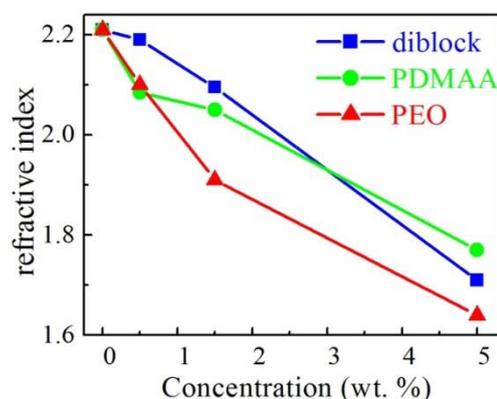
Fig. 5. Template concentration dependence of refractive index of porous Nb_2O_5 films prepared with denoted polymers as templates and annealed at 320 °C for 30 min.

By measuring the reflectance change prior to and after vapors exposure we may conclude that the refractive index of all films does not change under the influence of vapors of various organic solvents (acetone, ethanol, methanol, etc.) and humidity as well. This means that the porosity is predominantly of closed type, i.e. there is no a connectivity between the pores.

The dependence of refractive index of porous Nb_2O_5 films prepared with studied polymers as a function of their concentration is presented in Fig. 5. As the polymer concentration increases, the effective refractive index decreases mostly pronounced when using PEO as a template. At annealing temperature of 320 ºC PEO decomposes leaving empty pores in the film, while for PDMAA and PEO-*b*-PDMAA the temperature is not sufficiently high in order complete thermal decomposition to take place.

CONCLUSIONS

The successful fabrication of Nb_2O_5 thin films with tunable refractive index using simple methods of sol-gel and evaporation induced self-assembly is demonstrated. Double hydrophilic block copolymers (PEO-*b*-PDMAA and PDMAA-*b*-PEO-*b*-PDMAA) and hydrophilic homopolymers (PEO and PDMAA) used as organic templates induce closed porosity proven by reflectance measurements of films prior to and after exposure to different probe molecules. Fine tuning of refractive index can be accomplished through post deposition annealing at various temperatures. Depending on the organic template used an increase or decrease of *n* can be achieved. By varying the concentration of organic template a variation of refractive index in a wide range can be obtained. In the case of using PEO-*b*-PDMAA copolymer as a template almost linear decrease of *n* from 2.21 to 1.71 is observed. The stability of the films when exposed to external stimuli is assigned to the formation of closed porosity. Tunable refractive index attained by the simple methods of post deposition annealing or variation of template concentration opens new opportunities for

applications of Nb_2O_5 thin films in optics and photonics.

REFERENCES

1. B. Smarsly, M. Antonietti, *Eur. J. Inorg. Chem.*, **2006**, 1111 (2006).
2. Y. Li, B. Bastakoti, Y, Yamauchi, *Appl. Mater.*, **4**, 040703 (2016).
3. M. Orilall, U. Wiesner, *Chem. Soc. Rev.*, **40**, 520 (2011).
4. S. Robbins, P. Beaucage, H. Sai, K. Tan, J. Werner, J. Sethna, F. DiSalvo, S. Gruner, R. Van Dover, U. Wiesner, *Sci. Adv.*, **2**, e1501119 (2016).
5. G. Soler-Illia, E. Crepaldi, D. Grosso, C. Sanchez, *Curr. Opin. Colloid Interface Sci.*, **8**, 109 (2003).
6. E. Rivera-Muñoz, R. Huirache-Acuña, *Int. J. Mol. Sci.*, **11**, 3069 (2010).
7. L. Ruiz-Valdepenas, M. Velez, F. Valdes-Bango, L. Alvarez-Prado, F. Garcia-Alonso, J. Martin, E. Navarro, J. Alameda, J. Vicent, *J. Appl. Phys.*, **115**, 213901 (2014).
8. J. Lee, M. Orilall, S. Warren, M. Kamperman, F. Disalvo, U. Wiesner, *Nat. Mater.*, **7**, 222 (2008).
9. R. Georgiev, B. Georgieva, M. Vasileva, P. Ivanov and T. Babeva, *Adv. Cond. Matter. Phys.*, **2015**, 403196 (2015).
10. R. Georgiev, K. Lazarova, B. Georgieva, M. Vasileva and T. Babeva, *Nanosci. & Nanotechnol.*, **16** (2016).
11. K. Lazarova, M. Vasileva, G. Marinov and T. Babeva, *Opt. Laser Technol.*, **58**, 114 (2014).
12. L. Todorova, Ch. Novakov, D. Christova, *Nanosci. & Nanotechnol.*, **16** (2016).
13. K. Fiorini, Field Application Report, Perkin-Elmer Inc, 2005.
14. S. Bennour, F. Louzri, *Advances in Chemistry*, **2014**, Article ID 147398, (2014).
15. K. Lazarova, L. Todorova, D. Christova, M. Vasileva, R. Georgiev, V. Madjarova and T. Babeva, *J. Phys.: Conf. Ser.*, in press.
16. D. Bruggeman, *Ann. Phys.* **24**, 636 (1935).

ВЛИЯНИЕ НА PEO, PDMAA И СЪОТВЕТНИТЕ ДИ- И ТРИБЛОКОВИ СЪПОЛИМЕРИ ВЪРХУ ОПТИЧНИТЕ СВОЙСТВА НА ТЪНКИ СЛОЕВЕ ОТ Nb_2O_5

Р. Георгиев[1], Л. Тодорова[2], Д. Христова[2], Б. Георгиева[1],
М. Василева[1] и Цв. Бабева[1]

[1]*Институт по оптически материали и технологии ''Акад. Й. Малиновски'', Българска академия на науките, ул. "Акад. Г. Бончев", блок 109, 1113, София, България*
[2]*Институт по полимери, Българска академия на науките, ул. "Акад. Г. Бончев", блок 103-А, 1113 София, България*

(Резюме)

Целта на представеното изследване е изучаване на влиянието на полиетиленоксид (ПЕО), поли(N.N-диметилакриламид) (ПДМАА) и съответните блокови съполимери (ПЕО-*б*-ПДМАА и ПДМАА-*б*-ПЕО-*б*-ПДМАА) върху формирането на пори в тънки слоеве от Nb_2O_5. Добавянето на полимерния разтвор към Nb зол провокира фазово разделяне и след подходяща термична обработка на слоевете се създава система от пори. Използваните режими на нагряване, осигуряващи пълно изгаряне на полимера в порите, са оптимизирани чрез термогравиметричен анализ. Морфологията и структурата на филмите е изучена чрез ТЕМ и електронна дифракция от избрана област. Оптичните параметри на слоевете и техните дебелини са определени от измервания на спектрите на отражение и нелинейно минимизиране на разликите между измерените и изчислените стойности. Установено е влиянието на структурата и състава на използваните съполимери върху оптичните свойства на тънки Nb_2O_5 и е демонстрирана възможността за вариране на показателя на пречупване в широки граници.

Optical characterization of antirelaxation coatings for photonics applications

S. Tsvetkov[1]*, S. Gateva[1], K. Nasyrov[2], S. Gozzini[3], E. Mariotti[4], S. Cartaleva[1]

[1]*Institute of Electronics, Bulgarian Academy of Sciences,*
72 Tzarigradsko Chaussee, 1784 Sofia, Bulgaria
[2]*Institute of Automation and Electrometry SB RAS, Novosibirsk, Russia*
[3]*Istituto Nazionale di Ottica del CNR – UOS Pisa, Via Moruzzi 1, 56124 Pisa, Italy*
[4]*DSFTA, Università di Siena, Via Roma 56, 53100 Siena, Italy*

Optical characterization of antirelaxation coatings with regard to their applications in coherent spectroscopy and LIAD experiments is presented. A simple method, based on the recording of the fluorescence intensity of the Rb alkali atoms during resonant light pulse irradiation is used for comparison of the antirelaxation properties of the coatings. The LIAD yield and dynamics are measured by registration of the 780 nm Rb line transmission. The comparison of the parameters of PDMS coatings prepared with two different solutions in ether (PDMS 2% and PDMS 5%) shows that when illuminating with such LED intensity at which the LIAD efficiency is equal in the two cells, the light induced Rb vapor density changes are about an order of magnitude slower in the PDMS 2% cell, and the antirelaxation properties of the two cells are equal.

INTRODUCTION

Antirelaxation coatings (ARC) are organic films (as, for example, paraffin, PDMS, OTS, SC-77 etc.) used in optical cells containing alkali metal vapor, which reduce the depolarization of alkali atoms after collisions with the cell's walls [1]. The long-lived ground state polarization is a basis for development of atomic clocks, magnetometers, quantum memory, slow light experiments, and precision measurements of fundamental symmetries. The antirelaxation properties of the coatings are characterized by the number of collisions of a single atom with the walls without spin randomization. A simple method for ARC characterization was proposed in [2], which comprises recording of the time dependence of the fluorescence intensity of alkali atoms during exposure of the cell to resonant radiation pulses.

Light-induced atomic desorption (LIAD) is a non-thermal process in which atoms are desorbed from the walls (coated or uncoated) of a vapor cell under illumination. It is applied mostly for realization of optical atomic dispensers in cases when high atomic densities at low temperature and/or small dimensions are needed – for example,

for loading atomic devices such as atomic magnetometers, atomic clocks, magneto-optical traps and their miniaturization [3,4 and references therein]. However, as desorption depends on the atom-surface interaction, it can be applied for optical characterization and manipulation of alkali metal nanoparticles [5], too. For the first time LIAD was reported in polydimethylsiloxane (PDMS) coated cell with Na vapor [6]. Since then LIAD in PDMS coated cells has been observed with Rb, Cs, K and radioactive Fr alkali atoms as well.

Polydimethylsiloxane $CH_3[Si(CH_3)_2O]_nSi(CH_3)_3$ is a polymer, which includes inorganic and organic parts, the backbone consists of silicon and oxygen atoms, where each silicon has attached two organic groups to it. PDMS is viscoelastic and has a good stability after dehydration. The glass transition temperature is 144 K and the melting temperature is 232 K. In our experiments it is close to the room temperature. Although the structure of PDMS is suitable for alkali metal atoms adsorption, it causes problems such as bubble formation and sample evaporation [7].

The AFM measurement of coatings prepared with different concentrations of PDMS in ether showed that the surface roughness increases from 20 nm to 50 nm as the PDMS concentration is

raised from 2% to 5%, and the thickness of the PDMS film increases with the concentration [8]. The X-ray photoelectron spectroscopy investigations of the glass surface condition of alkali metal vapor cell have shown that Rb atoms diffuse into the Pyrex glass [9].

In this work we report on methods for optical characterization of ARC from point of view of their application in coherent spectroscopy and LIAD experiments. The yield of LIAD and its dynamics, and the number of atom-wall collisions without spin randomization in two PDMS coated cells prepared with 2% (cell PDMS2) and 5% (cell PDMS5) concentration of PDMS in ether are compared.

EXPERIMENTAL

LIAD and its dynamics are characterized by the vapor density and its changes in time $n(t)$. For an optical medium, the change of the Rb density due to the LIAD effect is measured by the absorption coefficient κ_ω of Rb vapor. According to the Beer's law the transmission is

$$T_\omega = I/I_0 = \exp(-\kappa_\omega L) = \exp(-\sigma_\omega N L), \quad (1)$$

where I_0 is the 780 nm laser power entering the vapor sample; I, the transmitted power; κ_ω, the frequency dependent absorption coefficient; σ_ω, the non-saturated, frequency dependent absorption cross-section; N, the atomic density and L, the cell length.
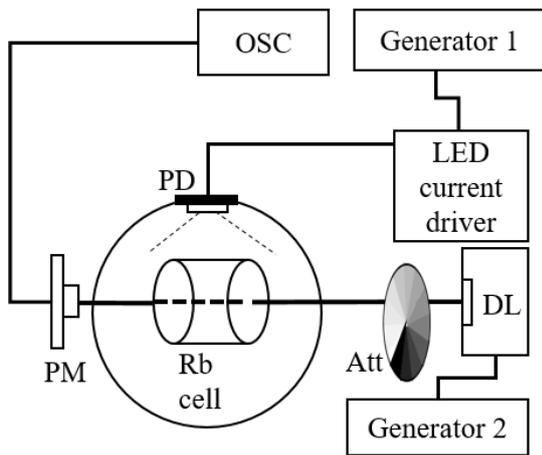
Fig. 1. Experimental setup for LIAD characterization. (DL – 780 nm diode laser; PM – powermeter; PD – photodiode; Att - attenuator; OSC – oscilloscope).

The experimental setup for LIAD and its dynamics characterization is given in Fig. 1. It is described in details in [10, 11]. A 780 nm free running diode laser (DL) is used for measuring the absorption coefficient of the D2 Rb resonance line. The D2 absorption line has 4 Doppler broadened sets of hfs transitions, related to the ground state F_g=1 and F_g=2 of the 87 a.m.u. isotope and F_g=2 and F_g=3 of the 85 a.m.u. isotope of the natural mixture. All LIAD measurements refer to the ^{85}Rb F_g=2 set of lines. A special sphere with diffusion reflectance inner surface is used to improve the efficiency of the blue light illumination from a 460 nm light emitting diode (LED) [11, 12].

All measurements are performed at temperature of 25°C. In order to minimize the optical pumping and deduce the corresponding absorption features, the transmission spectra are measured at relatively low 780 nm light intensity (around 3-4 μW).

The PDMS2 and PDMS5 cells are with radius R_c=1.3 cm and lengths 6.0 cm and 4.7 cm respectively. This results in only 5% difference of the surface to volume ratio S/V and the LIAD yield for the two cells.

The dynamics of desorption and adsorption in different coated cells are compared following the model proposed in [3]. The time constants are determined by fitting the experimental data for the time evolution of the atomic density in the volume of the cell $n(t)$ with the following equation:

$$n(t) = \begin{cases} n_0 + N_\tau \left(1 - e^{-(t-t_0)/\tau_1}\right) e^{-(t-t_0)/\tau_2}, t_0 \leq t \leq t_{off} \\ n_0 + \left[n_{off} - n_0\right] e^{-(t-t_{off})/\tau_3}, \quad t > t_{off} \end{cases}$$

(2)

where t_0 and t_{off} are the times when the desorption light is switched on and off; n_0, the density before illumination; $n_{off} = n(t_{off})$; τ_1, characterizes the exponential density growth after the cell is illuminated; τ_2, the density decrease when the illuminating light is still on; τ_3, the density decrease when the light is off; $\Delta n = n_{max} - n_0$ and $N_\tau = \Delta n(1 + \tau_1/\tau_2)(1 + \tau_2/\tau_1)^{\tau_1/\tau_2}$.

As the LIAD density increase depends on the time of illumination, all measurements are performed with equal time intervals, more specifically by 75 sec during which the cell is illuminated, followed by 75 sec without illumination.

A simple model for characterization of antirelaxation coating of optical cells is proposed in [2]. The method is based on the registration of the temporal dependence of the fluorescence intensity from irradiated alkali atoms by pulsed light at resonance. It was found that in order to find the number of atom-wall collisions without spin randomization N, it is enough to have the value of the fluorescence decay rate β and the ratio between

the intensities of the fluorescence at the beginning I_i and at the end of the decay I_f and the characteristic time between atom collisions with the cell's walls $\tau_c = R_c/2v_T = 27$ μs, where v_T is the atom's thermal velocity

$$1/N = \beta \tau_c I_f/I_i \qquad (3)$$
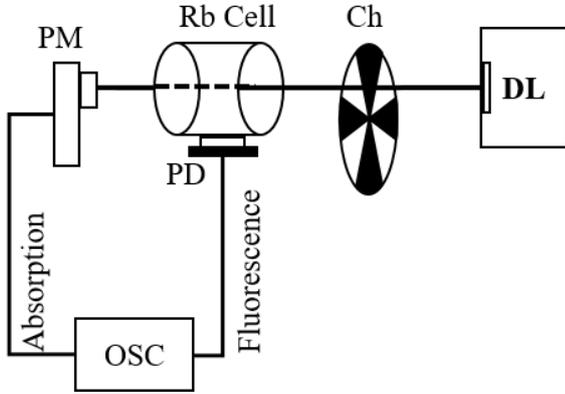
Fig. 2. Experimental setup for ARC characterization. (DL – diode laser; PM – powermeter; PD – photodiode;Ch - chopper; OSC – oscilloscope)

In Fig. 2 the experimental setup for ARC characterization is given. The absorption and the fluorescence of the 780 nm diode laser light, interrupted by a chopper at 5 Hz, are detected by a powermeter (PM) and a photodiode (PD). The measurements are performed on the the ^{85}Rb $F_g=3$ set of hfs lines at 40 μW 780 nm diode laser power.

RESULTS AND DISCUSSION

In Fig. 3 the dynamics of desorption and adsorption in PDMS2 and PDMS5 cells when the blue light is switched on and off are compared. The measurements are at low intensity (0.7 mW/cm^2) where the heating from the LED is negligible. The LIAD yield depends on the LED intensity. At low LED intensities (less than 2.5 mW/cm^2) the LIAD yield in the PDMS2 and PDMS5 cells is almost equal, while at intensities higher than 2.5 mW/cm^2, the yield is higher in the PDMS2 cell [12].

The shape of the transmitted light response is quite different for the two cells and in PDMS5 cell the changes in the Rb vapor density are about an order faster than in PDMS2 cell. The dynamic response in PDMS2 cell is like in the "weak desorbing light regime", when the light induces negligible change in the Rb atom density near the coating surface. The dynamic response in PDMS5 cell is like at the "high desorbing light intensity"

regime, when all atoms in the region close to the surface are desorbed into the cell volume [13,14].
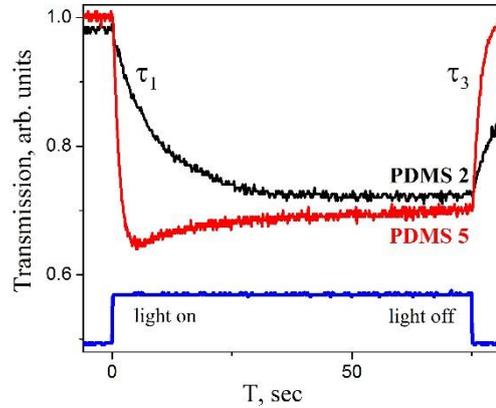
Fig. 3. Comparison of LIAD dynamics in PDMS2 and PDMS5 cells: the measured normalized transmission at 0.7 mW/cm^2 LED intensity.

An explanation of the difference in the adsorption and desorption rates (Fig. 3) in PDMS2 and PDMS5 could be the different probability for alkali atoms to find adsorption sites in substrates with different volume density and surface morphology.

Comparing the dynamics of different cells the influence of the stem has to be considered, too. Difference of one order was measured with open and closed stem in Rb paraffin coated cell [3]. In our case, the comparison of the PDMS2 and PDMS5 cells shows that there is more metal in the PDMS5 cell stem, which can influence the dynamics of the processes.
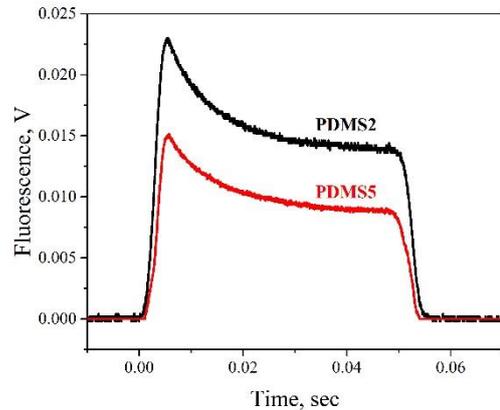
Fig. 4. Experimental fluorescence decay of Rb atoms in the PDMS2 (black) and PDMS5 (red) coated cells, when irradiated by 50 ms square 780 nm laser light pulse.

In Fig. 4 the experimental fluorescence decay of Rb atoms in the PDMS2 (black) and PDMS5 (red)

coated cells, when irradiated by 50 ms square 780 nm laser light pulse are compared. The ratios $I_f/I_i=0.6$, $\tau_c=27\mu s$, and the fluorescence decay rates are equal for the two cells as it is seen from Fig. 4. Following Eq. 3 the number of atom-wall collisions without randomization of the atom spin in PDMS2 and PDMS5 cells (Fig. 4) differ of the order of 3.5%, which is less than the experimental error: 1602(72) in PDMS5 and 1657(266) in PDMS2 cell.

CONCLUSIONS

The comparison of the absorption in two ARC cells, prepared with different solutions of PDMS in ether, from point of view of their application in LIAD experiments, have shown that in PDMS2 the desorption and adsorption rates are about an order lower than in PDMS5, which can be explained by the different morphology of the surface, thickness of the coating, and volume density.

The application of the simple method for optical characterization of ARC for coherent application by registration of the temporal dependence of the intensity of the fluorescence from irradiated alkali atoms by pulsed light at resonance [2] has shown that the number of the atom-wall collisions without a spin depolarization is comparable in the two PDMS cells.

The performed investigation and the results are interesting for the better understanding of light-atom-surface interactions, for development of new optical elements for application in photonics, LIAD-loaded atomic devices and their miniaturization, and new methods for surface and coating diagnostics and monitoring.

REFERENCES

1. M. Bouchiat, J. Brossel, *Phys. Rev.*, **147**, 41 (1966).
2. K. Nasyrov, V. Entin, N. Nikolov, N. Petrov, S. Cartaleva, Proc. *SPIE*, **9447**, 944704 (2015).
3. T. Karaulanov, M. Graf, D. English, S. Rochester, Y. Rosen, K. Tsigutkin, D. Budker, E. Alexandrov, M. Balabas, D. Kimball, F. Narducci, S. Pustelny, V. Yashchuk, *Phys. Rev. A*, **79**, 012902 (2009).
4. L. Torralbo-Campo, G. Bruce, G. Smirne, D. Cassettari, *Nature: Sci. Rep.*, **5**, 14729 (2015).
5. A. Burchianti, A. Bogi, C. Marinelli, C. Maibohm, E. Mariotti, S. Sanguinetti, L. Moi, *Eur. Phys. J. D*, **49**, 201 (2008).
6. A. Gozzini, F. Mango, J. Xu, G. Alzetta, F. Maccarone, R. Bernheim, *Il Nuovo Cimento*, **15D**, 709 (1993).
7. Y. Shin, K. Cho, S. Lim, S. Chung, S.-J. Park, C. Chung, D.-C. Han, J. Chang, *J. Micromech. Microeng.*, **13**, 768 (2003).
8. J. Brewer, A. Burchianti, C. Marinelli, E. Mariotti, L. Moi, K. Rubahn, H.-G. Rubahn, *Appl. Surf. Sci.*, **228**, 40 (2004).
9. R. Kumagai, A. Hatakeyama, *Appl. Phys. B*, **122**, 186 (2016).
10. S. Gateva, M. Taslakov, V. Sarova, E. Mariotti, S. Cartaleva, *Proc. SPIE*, **8770**, 87700O (2013).
11. M. Taslakov, S. Tsvetkov, S. Gateva, *J. Phys.: Conf. Ser.*, **514**(1), 012028 (2014).
12. S. Tsvetkov, S. Gateva, M. Taslakov, E. Mariotti, S. Cartaleva, *J. Phys.: Conf. Ser.*, **514**, 012030 (2014).
13. S. Atutov, V. Biancalana, P. Bicchi, C. Marinelli, E. Mariotti, M. Meucci, A. Nagel, K. Nasyrov, S. Rachini, L. Moi, *Phys. Rev. A*, **60** (6) 4693 (1999).
14. S. Gozzini, A. Lucchesini, *Eur. Phys. J. D*, **28**, 157 (2004).

ОПТИЧНО ХАРАКТЕРИЗИРАНЕ НА АНТИРЕЛАКСАЦИОННИ ПОКРИТИЯ ЗА ПРИЛОЖЕНИЯ ВЪВ ФОТОНИКАТА

С. Цветков[1], С. Гатева[1], К. Назиров[2], С. Гоццини[3], Е. Мариотти[4], С. Карталева[1]

[1]*Институт по електроника, БАН, бул. Цариградско шосе 72, София, България*
[2]*Институт по физика на полупроводниците, СО РАН, Новосибирск, Русия*
[3]*Национален институт по оптика, Виа Моруци 1, 56124 Пиза, Италия*
[4]*Университет на Сиена, Виа Рома 56, 53100 Сиена, Италия*

(Резюме)

Представени са изследвания за оптично характеризиране на антирелаксационни покрития от гледна точка на приложението им в кохерентната спектроскопия и за светлинно индуцирана десорбция на атоми (СИАД). За анализ на антирелаксационните свойства на покритията е използван прост метод, при който се регистрира интензитетът на флуоресценцията на Rb атоми при облъчване с резонансна светлина. Скоростта и ефективността на СИАД са измерени чрез регистриране на преминалата светлина на линията на Rb 780 нм. Сравняването на параметрите на PDMS покритията направени с два различни разтвора в етер (PDMS 2% и PDMS 5%) показва, че при интензитет на облъчване, при който ефективността на СИАД е равна, процесите на адсорбция и десорбция в PDMS 2% клетката са приблизително 1 порядък по-бавни, а антирелаксационните свойства са еднакви в двете клетки.

Dark resonances in potassium vapor for absolute measurement of magnetic fields

A. Krasteva[1]*, S. Gateva[1], A. Sargsyan[2], D. Sarkisyan[2], S. Cartaleva[1]

[1]*Institute of Electronics - BAS, 72 Tzarigradsko Chaussee Blvd., 1784 Sofia, Bulgaria*
[2]*Institute for Physical Research, NAS of Armenia, Ashtarak-2, 0203 Armenia*

In this communication, we present a new approach for development of optical magnetometer based on the D_2 line of potassium (K), where the hyperfine transitions are strongly overlapped. Magnetically unshielded, 8-mm-long cell (containing K + 30Torr Ne) is introduced, in order to reduce the gradients influence of laboratory magnetic field B_{lab} to spectral width of Dark Resonances (DRs), which are used for magnetic field (MF) measurement. K vapor is irradiated by the light of frequency-modulated distributed feedback DFB diode laser that results in formation of narrow resonances with reduced absorption, i.e. DRs. Dark Resonance (DR) spectrum is shown as a function of frequency ν. Depending on the value of measured MF, different modulation frequencies f_m can be used. The spectral transition overlapping results in very good signal, non-critical to laser frequency shifts that is not the case with other alkali. The proposed approach can be used for MF measurement produced by different sources, for example of archaeological origin. Moreover, the principle of MF measurement allows development of self-calibrated optical magnetometer with potential for calibrating various commercially available magnetometers that need frequent calibrations.

Keywords: dark resonance, potassium vapor, magnetic field

INTRODUCTION

When an atomic system is prepared in a coherent superposition state, extremely narrow Dark Resonance [1,2] and related Electromagnetically Induced Transparency (EIT) [3] resonance can be observed where the atomic coherence cancels, or reduces, light absorption. The continuously expanding interest in the topic is due not only to the fascinating physics involving quantum coherence but also to the fact that there are many potential applications with relevance both in development of new techniques and devices, and in new scientific approaches to fundamental studies, such as slowing of light [4], quantum information storage [5], frequency standards [6], and precise magnetometers [7].

Resonances based on Dark State phenomenon have been studied mainly in Rb and Cs vapors, due to the availability of conventional diode lasers matching their resonance lines. Different approaches have been utilized for DR observation: most frequently two ground-state levels of alkali atoms are coupled to a common exited level by means of two coherent light fields, provided by laser frequency modulation in the GHz range. For practical applications it is advantageous to reduce the modulation frequency down to the kHz range, coherently coupling Zeeman sub-levels within single ground-state hyperfine (hf) level [8]. In such approach, however, the optical pumping to the ground-state hf level non-interacting with the laser field causes strong losses in the formation of the dark resonance. The hf optical pumping is particularly efficient when using noble-gas-buffered or anti-relaxation coated cells filled with alkali atoms. However, buffered and coated cells introduce real advantage and are used very often because they provide long-living ground-state coherence.

In this work we report experimental observation of sub-natural-width DR on the D_2 line of K vapor, demonstrating its application for development of simple experimental approach for magnetic field measurement based on the self-calibration of magnetic field value. The method is tested by laboratory magnetic field measurement. Potassium D_1 and D_2 lines provide the possibility to overcome the problem with the hf optical pumping because in this case the ground-level frequency difference (of 461.8MHz) is much less than the Doppler width of optical transition (about 800MHz). Thus, the overlapping of the Doppler profiles of the transitions, starting from both ground-state hf levels

* To whom all correspondence should be sent:
E-mail: anna0kr0stz@gmail.com

can provide the re-population of the resonantly exited by the light ground hf level [9], hence to enhance significantly the efficiency of the DR preparation.

EXPERIMENTAL SETUP AND METHOD FOR MAGNETIC FIELD MEASUREMENT

First the experimental setup shown in Fig.1 is briefly described. The frequency ν of the radiation of a mono-mode distributed feedback diode laser (λ=766.7nm, 2MHz bandwidth) is modulated at constant frequency f_m by means of a signal generator that modulates the diode laser current. The laser frequency modulation transforms the single-frequency laser field into a multi-frequency output, with frequency separation between the adjacent components equal to the modulation frequency f_m. There is a complete optical coherence between the components of the multi-frequency light. The laser beam is circularly polarized by a quarter-wave (λ/4) plate and directed to an optical cell containing K vapor, buffered by 30 Torr of Ne.
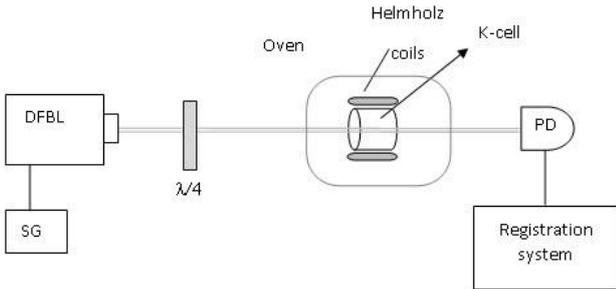
Fig. 1. Experimental set-up diagram: DFBL - distributed feedback laser, SG – signal generator, λ/4 - quarter-wave plate, PD - Photo-Detector.

In our experiment, 8-mm-long optical cell is introduced, in order to reduce the gradients influence of laboratory MF $\mathbf{B}_{lab}$ to spectral width of DRs, as the measurements are performed in magnetically unshielded environment. A pair of Helmholtz coils is situated around the K-cells in a way to produce magnetic field $\mathbf{B}_{coil}$ orthogonal to the laser beam propagating direction. The applied magnetic field $\mathbf{B}_{coil}$ is continuously varied in two opposite directions crossing the $\mathbf{B}_{coil} = 0$ value. A photo-detector (PD) is used for registering the signal of the transmitted thought the K cell laser light.

The laser modulation frequency f_m is kept constant but the magnetic field value is swept in a large interval around $\mathbf{B}_{coil} = 0$. If in laboratory MF $\mathbf{B}_{lab}$ K atoms are irradiated by the light modulated at

constant frequency and their absorption is registered versus an orthogonal to the laser beam summary MF $\mathbf{B} = \mathbf{B}_{lab} + \mathbf{B}_{coil}$, several sub-natural-width dark resonances will be observed: (i) at $\mathbf{B} = 0$ (Hanle resonance), (ii) at MF determined by the laser modulation frequency ($\pm1^{st}$ resonances) and (iii) at its harmonics ($\pm2^{nd}$, $\pm3^{rd}$, … resonances). Generally, two types of DRs are observed. The first type is the DR centered at $\mathbf{B} = 0$, where the Zeeman sublevels belonging to single hyperfine ground levels are degenerate, i.e. of the same energy. The resonance, centered at zero MF is related to the well-known Hanle resonance, which is obtained without any modulation of the light but only scanning the magnetic field around $\mathbf{B} = 0$ value.

Enhancing magnetic field, first two resonances occur on either side of the MF scan, centered at the field values creating Larmour precession of the magnetic moments with frequency ν_L that is equal to laser modulation frequency, i.e. $\nu_L = f_m$. With the MF scanned in the two opposite directions, the side resonances appear at positions symmetrical to B = 0. In this way, the known laser modulation frequency, provided by the SG can be used as a precise measure of the magnetic field value.

RESULTS AND DISCUSSION

Spectroscopy of K is different from those of Rb and Cs, due to the small spacing of its ground-state hyperfine energy levels. In particular, the ground-state hyperfine splitting in K is much less than the Doppler width of hyperfine transition profiles, and hence only summary absorption profile can be seen on each of the D_1 and D_2 lines of K. The energy levels and hyperfine transitions involved in the D_2 line ($\lambda = 766.7$ nm) of K are shown in Fig. 2a. It can be seen that the Doppler profiles of the two groups of hyperfine transitions starting from the ground levels F = 1 and F = 2 suffer strong overlapping due to the 800MHz Doppler width of each F $\rightarrow$ F' hyperfine transition presented in Fig.2a. From the other hand, such overlapping is advantageous for performing coherent spectroscopy based on excitation of ground-state hyperfine levels, providing the repopulation of the resonantly excited ground hyperfine level [9]. It should be stressed that both groups of hyperfine transitions, each starting from single ground state (F = 1 or F = 2) level are completely overlapped. Due to this fact, the formation of the DR is discussed only for the F = 2 $\rightarrow$ F' = 2 hyperfine transition. Fig. 2b illustrates the formation of 4 three-level Λ systems, based on Zeeman sub-levels of the F = 2 hyperfine level.

Starting from the left to the right, the first Λ system shows simultaneous excitations of two ground Zeeman sub-levels (F = 2, m_F = -2 and F = 2, m_F = -1) to a common exited Zeeman sub-level (F' = 2, $m_{F'}$ = -1). The two radiations forming the Λ system should be properly polarized to allow transitions to the level F' = 2, $m_{F'}$ = -1 of the excited state. In the example reported in Fig. 2b, the first radiation is of σ type, while the second one is π polarized light. It is easily to see that in the same way the following 3 pairs of Zeeman sub-levels of the ground state with $\Delta m = \pm 1$ can be connected by Λ systems to respective excited Zeeman sub-levels. Note that all four pairs of ground state levels contribute to formation of single DR, due to the equal energy difference between the two ground Zeeman sub-
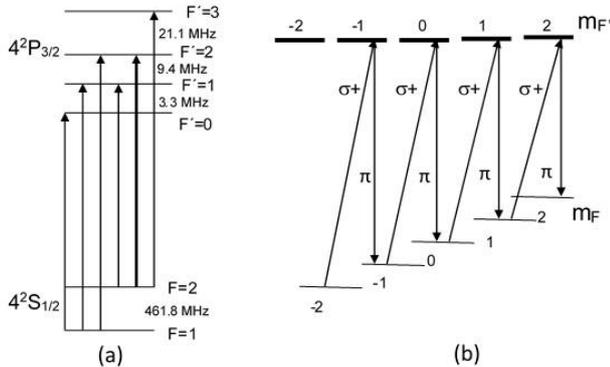
Fig. 2. (a) Energy level diagram of the $4^2S_{1/2} \rightarrow 4^2P_{3/2}$ transitions (D_2 line) of ^{39}K. (b) Simplified energy level diagram. Zeeman splitting of the F = 2 level is only shown because the F' = 2 level splitting is much less than its spectral width.

levels. The two optical frequency fields needed for the simultaneous excitation of the Zeeman sub-levels are produced by means of modulating the current of the diode laser at the frequency difference between the two optical transitions. Optical sidebands of the emission line of the diode are produced with a constant phase relationship between all components. The matching of the energy distance between Zeeman sublevels and the optical frequencies differences is obtained by changing the Zeeman splitting applying the above discussed scanned MF. If a wide scanning of the magnetic field is performed, several Dark Resonances can be observed.

In Fig. 3 the experimentally measured DR spectrum is shown, where the laser light frequency is tuned to the D_2 line absorption profile and it is modulated at the fixed frequency f_m = 200 kHz. The transmitted power is measured with a photodiode and the signal is recorded by a digital oscilloscope.

Scanning MF around **B** = 0, whenever the splitting of Zeeman sub-levels of the ground state matches the frequency difference of a pair of the components of laser spectrum, a Λ chain is created (see fig.2b) and a narrow DR is observed. In Fig. 3, besides the signal at B = 0 (0th dip), two pairs of DR dips in the absorption signal appear. They can be related to the sidebands with frequency separations of modulation frequency f_m and $2f_m$ that exist in the spectrum of the diode laser. It is worth noting that the nth DR is not in simple correspondence with the nth sideband, e.g. the 2nd DR is due to the presence of the 0th and 2nd sidebands, but it may originate also due to the presence of 1st and -1st ones. The highest order of the DR gives information about the most distant pair of sidebands, having a suitably high power.
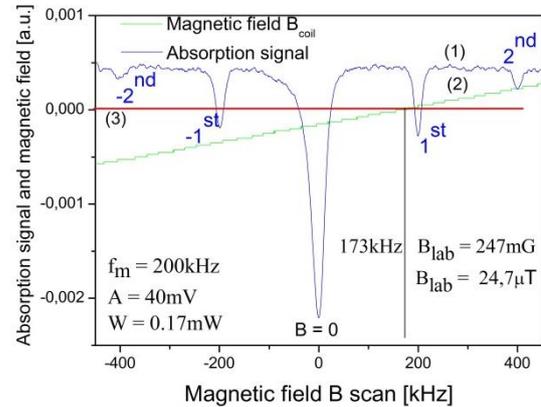
Fig. 3. Dark resonances in K vapor absorption measured as a function of magnetic field B, scanned around B = 0. The measured stray magnetic field in laboratory is: B_{lab} = 24.7μT.

It should be pointed out that very good signal-to-noise, narrow dark resonances are observed for modulation frequency much smaller than the width of the laser line. Hence, the spectral profiles of the two fields producing the dark state are strongly overlapped. In the case of coherent population trapping at Zeeman sublevels of different ground-state hyperfine levels, the modulation frequency is in the GHz region that is several orders of magnitude larger than the laser line width. In Fig. 3, the DR spectrum is shown as a function of frequency ν. In our experiment the DR spectrum is measured as a function of magnetic field B_{coil}, which is not calibrated preliminary. In our case, the absolute calibration of the coil can be done using the presented in Fig. 3 DR spectrum. Measuring the zero point of the coil current (see curve 2, Fig. 3) and using the related to D_2 line equation ν[kHz]=7B[μT] [10] that is determined from the Zeeman splitting of ground levels, the absolute

value of MF B can be deduced. In order to determine the B_{lab} magnetic field (that is the final goal in this work), only the $B_{coil} = 0$ point at $\nu = 173kHz$ has to be used, i.e. the crossing point of line 3 with line 2 (Fig.3). This results in a measured value of $B_{lab} = 24.7\mu T$. Depending on the value of the measured MF, different frequencies f_m can be used.

In order to test the proposed approach for measurement of absolute value of MF without magnetic shielding of the optical cell, several different modulation frequencies of diode laser current are used in the experiment under the same laboratory environment. In Fig. 4, the DR spectrum is shown for $f_m = 100kHz$, $W = 0.2mW$ and the same amplitude of modulation. It can be seen that here the measured $B_{lab} = 24.8\mu T$, which is in agreement with the result shown in Fig. 3. The magnetic field measurements, based on the new approach are also supported by an independent measurement using different magnetometer.
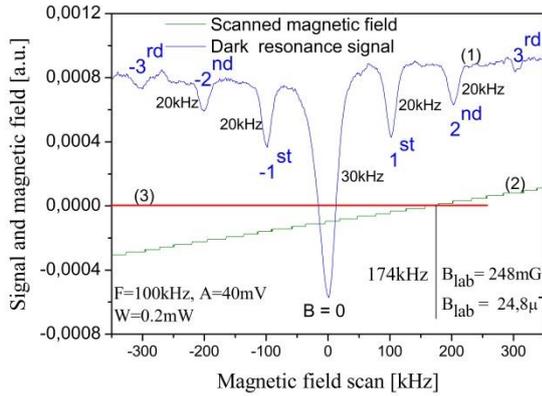
Fig.4. DR spectrum: $B_{lab} = 24.8\mu T$.

Comparing Fig. 3 and Fig. 4, one can conclude that in case of lower modulation frequency, two more DRs ($\pm$ 3rd) are observed, due to more effective modulation of the laser current. It can be seen that the spectral width of observed DRs is well below the natural width (6.2 MHz) of optical transitions, on the first resonance line in K. The DR width is mainly determined by the spectral width of the ground-state energy levels. Mainly, the strong DR narrowing is a result of two factors. The first one is the protection against spin relaxation collision with the cell-walls, provided by the used buffer gas in the optical cell. At the same time, the overlapping of the Doppler broadened profiles of the hyperfine levels in K causes a great reduction of the optical pumping, producing great performance and strong signal/noise improvement for both types of DRs. This is not the case when using other

alkalis, where the poor or absent overlapping of the hyperfine optical transitions causes a more efficient optical pumping, which depletes the populations available for the DR preparation.
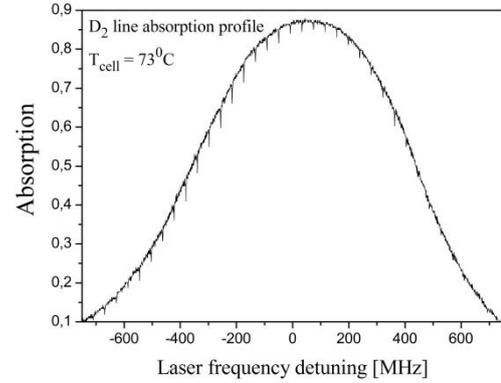
Fig. 5. Double scan: laser frequency slow detuning across the D_2 line and magnetic field faster modulation around B = 0.

Another advantage of K also results from the optical transition profiles overlapping. A double scan of the laser frequency, that is performed by a slow scan of the laser current and faster variations of MF around **B** = 0 allows measurement of the DR contrast over the entire D_2 line profile. In this case no kHz modulation is applied to the current. A double scan applied for the absorption profile measurement of D_2 line with Hanle type resonances is shown in Fig.5. It can be seen that the DRs are registered in very large region of the absorption profile. Hence, due to the strong overlapping of D_2 line hyperfine transitions there is no need of precise fixing of laser current, in order to observe a DR with good amplitude. This is not the case of DR observed in Cs buffered by noble gas, where the narrow resonance exists in a narrow region on the slope of absorption profile.

CONCLUSION

The presented experimental study show important advantages of using K-atoms, for DR-based methodology applied to absolute MF measurement. At the same time, the significant reduction of the optical cell longitudinal dimension and the overlapping of the Doppler broadened profiles of the hyperfine transitions cause a great reduction of the optical pumping, producing efficiency improvements both in the Λ and in the Hanle configurations and relatively narrow DR, less influenced by the laboratory MF gradients. The proposed approach can be used for the measurement of magnetic fields that are produced from different sources. Moreover, the principle of

MF measurement allows development of self-calibrated optical magnetometer with potential for calibration various portable magnetometers that are commercially available but need regular calibration for absolute magnetic field measurements.

REFERENCES

1. G. Alzetta, A. Gozzini, L. Moi, and G. Orriols, *Nuovo Cimento* **36**, 5-20 (1976).
2. E. Arimondo, G. Orriols, *Lett. Nuovo Cimento*, **17**, 333 (1976); E.Arimondo, *Prog.Opt.* , **35**, 257 (1996).
3. L. Hau, S. Harris, Z. Dutton, C. Behroozi, *Nature,* (London) **397**, 594 (1999).
4. A. Zibrov, M. Lukin, M. O. Scully, *Phys.Rev.Lett.,* **83**, 4049 (1999).
5. A. Zibrov, A. Matsko, O. Kocharovskaya, Y. Rostovtsev, G. Welch, M. O. Scully, *Phys.Rev.Lett.,* **88**, 103601 (2002).
6. S. Knappe, V. Shah, P. D. D. Schwindt, L. Hollberg, J. Kitching, L.-A. Liew, et al., *Appl. Phys. Lett.,* **85,** 1460 (2004)
7. D. Budker and M. Romalis, *Nature Physics,* **3,** 227 (2007).
8. Ch. Andreeva, G. Bevilacqua, V. Biancalana, S. Cartaleva, Y. Dancheva, T. Karaulanov, C. Marinelli, E. Mariotti and L. Moi, *Appl. Phys. B*, **76**, 667 (2003).
9. K. Nasyrov, S. Gozzini, A. Lucchesini, C. Marinelli, S. Gateva, S. Cartaleva, and L. Marmugi, *Phys. Rev. A*, Vol.92, 043803, (2015).
10. S. Gozzini, S. Cartaleva, D. Slavov, L. Marmugia, A. Lucchesini, *Proc. SPIE* , **7027**, 70270K (2008).

ТЪМНИ РЕЗОНАНСИ В ПАРИ НА КАЛИЯ ЗА АБСОЛЮТНО ИЗМЕРВАНЕ НА МАГНИТНИ ПОЛЕТА

А. Кръстева[1]*, С. Гатева[1], А. Саргсиан[2], Д. Саркисиан[2], С. Карталева[1]

[1]*Институт по електроника, Българска академия на науките, бул. „Цариградско шосе" 72, 1784 София, България*

[2]*Институт по Физика, Национална академия на науките на Армения, 0203 Ащарак-2, Армения*

(Резюме)

В това съобщение представяме нов подход за развитие на оптичен магнитометър базиран на D_2 линията на калия (K), където срвъх фините преходи са силно препокрити. Магнитно неекранирана 8-мм клетка съдържаща K и 30Torr Ne е използвана с цел да се намали влиянието на градиентите на лабораторното магнитно поле B_{lab} върху спектралната ширина на тъмните резонанси, които са използвани за измерването на магнитното поле. Парите на K са облъчени със светлината на честотно моделиран диоден лазер с разпределена обратна връзка, което води до формораното на тесни резонанси на намалено поглъщане, тоест тъмни резонанси. Спектъра на тъмните резонанси е изследван като функция на честотата ν. Взависимост от стойността на магнитното поле, различни честоти на модулация f_m могат да бъдат използвани. Препокриването на спектралните преходи води до много добър сигнал, некритичен от отместването на лазерната честота, какъвто не е случая при другите алкални пари. Предложения подход може да бъде използван за измерване на магнитно поле предизвикано от различни източници. Освен това, принципа на магнитното измерване позволява развитие на самокалибриращ оптичен магнитометър с потенциал за калибриране на различни налични в търговската мрежа магнитометри.

Characterization of titanium–niobium orthodontic archwires used in orthodontic treatment

I. Ilievska[1]*, D. Karashanova[2], V. Petrunov[3], A. Zaleski[4], M. Drozd[4], V. Mikli[5], A. K. Stoyanova-Ivanova[1]

[1]*Institute of Solid State Physics, Bulgarian Academy of Sciences, 72 Tzarigradsko Chaussee Blvd., 1784 Sofia,Bulgaria*
[2]*Institute of Optical Materials and Technologies, Bulgarian Academy of Sciences, Acad. Georgy Bonchev St., bl. 109, 1113 Sofia, Bulgaria*
[3]*Faculty of Dental Medicine, Medical University Sofia,St. GeorgiSofiiski Blvd., 1431 Sofia, Bulgaria*
[4]*Institute of Low Temperature and Structure Research, Polish Academy of Sciences, ul.Okolna 2, 50-422 Wroclaw, Poland*
[5]*Centre for Materials Research, Tallinn University of Technology, Ehitajate 5, Tallinn 19086, Estonia*

The titanium-niobium (TiNb) alloys are known as superconducting materials and they are used for the production of superconducting wires. They are also widely applied in the medicine, for the needs of orthopaedic reconstructive surgery, implantology etc. due to their properties, as high biocompatibility and high corrosion resistance. Recently, this material has been incorporated in orthodontic braces as finishing archwire during the process of orthodontic treatment. On the market exist different types of archwires, developed by many producers, which obey specifications necessary to apply them during orthodontic patient treatment. But properties of these archwires are deteriorating with time. To apply them properly it is needed to find the reasons of such deterioration and the methods to register it. We try to gather such knowledge – this time for some archwires produced by the ORMCO Company – TiNb ones.

The analyses were carried out by the independent techniques: X-ray diffraction analysis (XRD), Scanning Electronic Microscopy (SEM), Energy Dispersive Spectroscopy (EDX) and Differential Scanning Calorimetry (DSC) and Physical Property Measurement System (PPMS). The composition of the wires was established to be: 57,15wt% Ti and 42,85wt% Nb. The low temperature magnetic studies revealed that the material possessed superconducting properties with transition to zero resistant state at about 10K and above this superconducting transition temperature, the material was paramagnetic. From DSC results it has been concluded that there was no thermal transition of the alloy in the temperature range from -50°C to +50°C. The received knowledge will allow to estimation of the safe TiNb archwires application in orthodontic treatment.

Keywords: TiNb, orthodontic archwires, XRD, SEM, DSC

INTRODUCTION

Titanium – Niobium alloys are well known as cryogenic materials [1], exhibiting superconductivity they are used in superconductor production [2-3]. Due to this property they find an application in magnets for nuclear magnetic resonance imaging systems [4]. This alloy is composed of two of the five elements (Nb, Ta, Ti, Zr and Pt) which do not cause tissue reactions [5-6], it has excellent corrosion resistance and biocompatibility [7]. This is the reason for its wide use in medicine as a substituting material in reconstructive orthopedic surgery and implants.

Due to their low elasticity modulus titanium alloys are beneficial for distributing the stresses between bones and implants [8]. With addition of Nb elastic modulus is further reduced and corrosion resistance is improved [9].

Orthodontic archwires, as a material placed in the oral cavity, in addition to good mechanical properties must also be biocompatible. A number of cases of allergic reactions to orthodontic materials are known and are caused primarily by the release of Ni ions [10-11]. In these cases use of an alloy which does not contain nickel is recommended [12-13]. During the aligment phase of treatment composite arches [14] may be used or ion-impacted Ni-Ti arches in which an amorphous surface layer is formed, inhibiting corrosion and release of Ni ions [15]. After the aligment phase of treatment

---

* To whom all correspondence should be sent:
E-mail: ivannyilievska@gmail.com

TMA arches containing Ti and Mo [16] are most commonly used. As an alternative to this non nickel-containing alloy an innovative Ti-Nb alloy arch is proposed [17] for this there is little available data. This archwire possesses extremely high corrosion resistance thanks to a surface layer of Nb_2O_5, inhibiting the action of fluoride ions responsible for quick corrosion in the oral cavity [18]. In light of its mechanical properties [19] and high friction coefficient [20] it is suitable for the finishing stages of orthodontic treatment, in which bracket sliding is not needed and applying finishing bends is necessary.

The aim of this study is to make characterization of the microstructure, chemical composition and investigation of magnetic properties of two types, as-received TiNb wires, produced by the ORMCO Company. The received knowledge will allow to estimation of the safe TiNb archwires application in orthodontic treatment.

MATERIALS AND METHODS

TiNb orthodontic archwires produced by ORMCO Company, CA, USA, with two different cross sections – 0.019x0.025 inches^2 (0.48 x 0.63 mm^2) and 0.017x0.025 inches^2 (0.43 x 0.63 mm^2) were investigated. Cut wire pieces of both type as-received TiNb archwires were studied with different techniques, as X-ray Powder Diffraction (XRD), Scanning Electron Microscope (SEM), Energy-Dispersive X-ray microanalysis (EDX), Differential Scanning Calorimeter (DSC) and Physical Property Measurement System (PPMS).

To determinate the structure of the material it is used X-ray Powder Diffractometer X'Pert Pro, with low-temperature nitrogen blower attachment Oxford Cryosystem and high-temperature closed attachment HTK 1200 from Anton Paar. The SEM tests were performed using Philips 515 Scanning Electron Microscope with accelerating voltage 0.2 to 30 kV. The composition of the archwires was obtained by EDX method using Bruker Esprit 1.8 system. Minimum acceptable accelerating voltage of 20 kV was applied. Quantification of the EDX results was performed by interactive PB-ZAF standardless method. The DSC analyses were performed using a differential scanning calorimeter Perkin - Elmer – 8000 with TGA attachment model PE-TGA4000. Before introducing the sample in the DSC apparatus for each individual test a calibration with indium was made. The temperature range of DSC is from - 170°C to +600°C. The samples were scanned from -50°C to +50°C and back to -50°C with 20°C per minute. The magnetic properties of

the samples were tested with PPMS from Quantum Design, Inc. which conducts research in the temperature range 1.9K-400K in a magnetic field up to 9T.

RESULTS AND DISCUSSIONS

Fig. 1 displays the diffraction pattern of TiNb (0.019x0.025 inches^2) archwire. The registered diffractions picks demonstrate presence of Ti and Nb, corresponding with the results reported by Mi-Kyung Ha et all. [21]*, whose indicate that TiNb alloys are more sensitive to the Nb content.
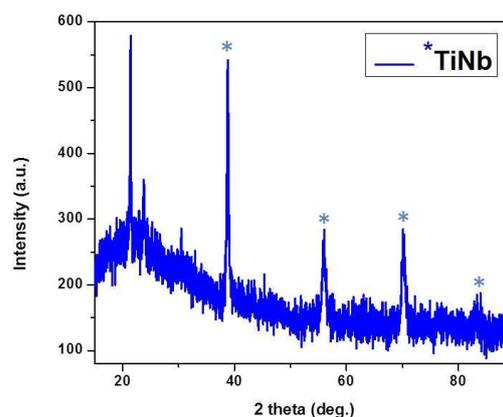
Fig. 1. XRD pattern on TiNb archwire 0.019x0.025inches^2
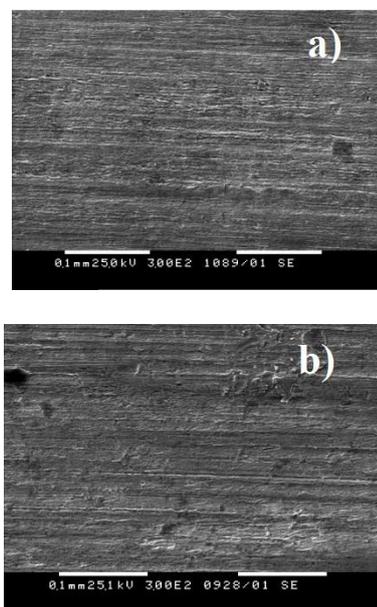
Fig. 2. SEM images of as-received archwire 0.017x0.025 inches^2 (a) and 0.019x0.025 inches^2 (b)

Report about the change in the surface morphology of the archwires with both dimensions is obtained by SEM. The SEM micrographs of two types as-produced TiNb archwire are presented in

Fig. 2a for 0.017x0.025 inches^2 and Fig. 2b for 0.019x0.025 inches^2. Typical surface morphology of wires produced of metal alloys by extrusion is clearly seen. Some defects on the surface, predominantly in the case of 0.019 x 0.025 inches^2 archwire are detected. They might be very deteriorating for applied archwires, as existing micro-cracking and voids might deepen during patient curing and to worse mechanical properties of the archwires (elasticity and shape memory).

For further information of the composition of the surface topography is used EDX. This method allows quantitative identification of the chemical composition by elements. For higher certainty EDX was done in 4 parts of each investigated piece of the both as-received TiNb archwires (0.019 x 0.025 inches^2; 0.017 x 0.025 inches^2). The analysis confirms that the main components of the archwires are only Ti and Nb (Table 1. and Table 2.).

Table 1. Elements content in as-received TiNb archwire (0.019 x 0.025 inches^2).

Spectrum	1	2	3	4
Elements	Wt%	Wt%	Wt%	Wt%
Titanium	57,15	57,52	57,05	57,11
Niobium	42,85	42,48	42,95	42,89
Total	100,00	100,00	100,00	100,00

Table 2. Elements content in as-received TiNb archwire (0.017 x 0.025 inches^2)

Spectrum	1	2	3	4
Elements	Wt%	Wt%	Wt%	Wt%
Titanium	57,26	57,21	57,87	57,57
Niobium	42,74	42,79	42,13	42,43
Total	100,00	100,00	100,00	100,00

There is no presence of additional elements as chromium, cobalt, copper, which are registered on the other popular archwires as NiTi and CuNiTi [22 - 25]. In the orthodontic archwire with the (0.019 x 0.025 inches^2) dimension, has average value of the elemental composition with approximately Ti 57.20 wt. % and Nb 42.79 wt. % . Respectlivity, for the (0.017 x 0.025 inches^2) archwire, Ti 57.47 wt. % nd Nb 42.52 wt. % .

In orthodontics different archwires are used, in some of them (for example heat-activated) the temperature changes lead to changes in the mechanical properties of the archwires. These archwires at body temperature have an austenitic structure and possess high elasticity and shape memory. With cooling of the archwires out of the patient's mouth with cryogenic spray to -50 ^{o}C, the

structure of the material changes to martensitic and the material becomes flexible, easily deformable and adaptable. After placing it in the mouth at 37 ^{o}C, the archwire gradually warms up and changes the structure into austenitic again. That is why it is useful to investigate the thermal behavior of TiNb archwires, which are a new material applied in orthodontics. In this study DSC method is used to verify if there is a transition temperature for the austenitic, martensitic, and rhombohedral (R) structure phases in representative as-received TiNb archwires. For DSC analyses very small samples were prepared and a special test cell is able to cool and heat slowly the sample with a very precise rate. During the cooling or heating process, the cell indicates whether the sample is either giving off more heat or absorbing more heat in exothermic or endothermic reactions, respectively [26]. On Figure 5 are shown DSC curves, which demonstrate that there is no thermal transition on the both 0.019 x 0.025 inches^2 (Fig. 3a) and 0.017 x 0.025 inches^2 (Fig. 3b) archwires, measured in the temperature range from -50 ^{o}C to +50 ^{o}C.
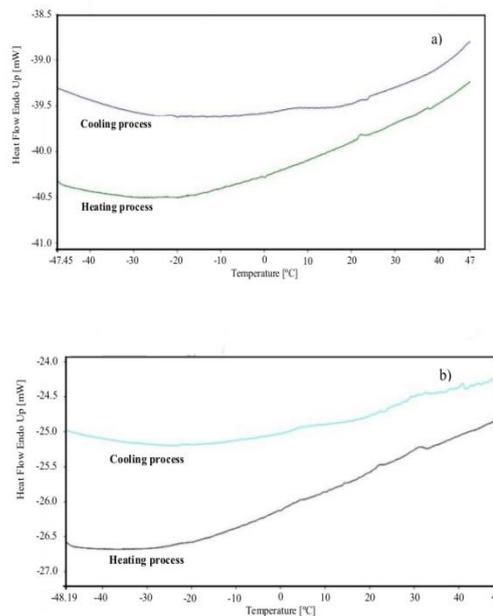
Fig. 3. DSC analysis on as-received TiNb archwires 0.017x0.025 inches^2 (a) and 0.019x 0.025 inches^2 (b)

It is known that the metals Ti and Nb become superconducting at sufficiently low temperatures. Solid solution of Ti and Nb, which can be obtained for the whole range of compositions, is also superconducting and its properties depends mainly on composition, structure and heat-treatment, respectively. Allowing α−titanium precipitate in the volume of TiNb solution leads to obtaining of superconducting material with very high current

density values. This material is used for wire production necessary for superconducting magnets [27]. In order to obtain more information about archwire, made from TiNb alloy, used in orthodontic medicine we studied also their magnetic properties at low temperatures. The results shown on Fig. 4 demonstrate that at about 10K real part of susceptibility changes abruptly from small negative value to strong diamagnetic one, proving that material is superconducting.
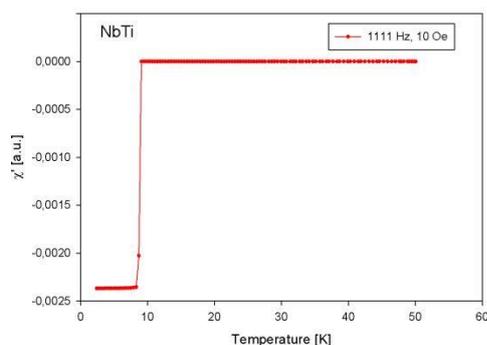
Fig. 4. Temperature dependence of the magnetic susceptibility of TiNb archwire (0.019 x 0.025 inches^2)

Although the material is superconducting it can carry very limited current, what can be seen from Fig. 5, where magnetic hysteresis measured at 2K is presented.
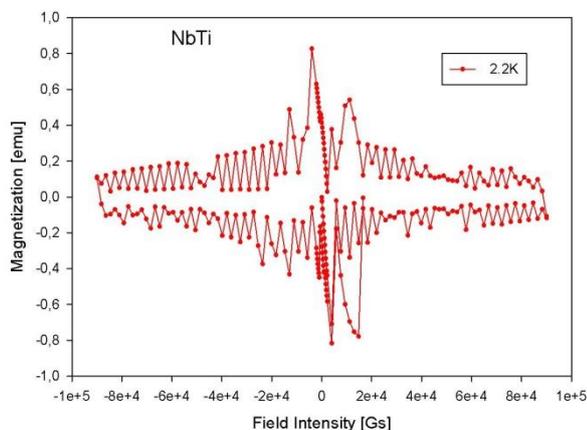
Fig. 5. Magnetic measurements on TiNb archwire (0.019 x 0.025 inches^2).

Above superconducting transition 10 K, the material is weakly paramagnetic. Future measurements will be made near room temperature where very precise DC magnetization measurements are needed.

These results for as-received TiNb archwires from ORMCO Company, will help the orthodonts to apply them successfully for patients treatment.

CONCLUSIONS

The manufacturers are experimenting with the elements of the alloys in order to establish and to improve the properties of the titanium archwires. That's why it is important to obtain the first profile of the elements and structure of TiNb archwires used for orthodontic appliances. Our results showed that the 0.019 x 0.025 inches^2 archwire has elemental composition, approximately Ti 57.20 wt % and Nb 42.79 wt%. Respectlivity, for the (0.017 x 0.025 inches^2) archwire, Ti 57.47 wt% and Nb 42.52 wt%. The DSC results made in the temperature range from -50^{0}C to +50^{0}C, showed that this archwire has no thermal transition. The magnetic properties of the archwires showed that this alloy is superconductor at 10K, and above superconducting transition the material is paramagnetic. The received knowledge will allow to estimation of the safe TiNb archwires application, as well as during the treatment.

REFERENCES

1. E. D. Marquardt, R. Radebaugh, (Proc. 11th Int. Cryo. Conf., Keystone, Colorado, 2000), R.G. Ross, Jr. (ed.), Kluwer Acad./Plenum Publ., New York, 2001, p. 681.
2. https://cds.cern.ch/record/796105/files/CERN-2004-006.pdf.pdf.
3. http://web.ornl.gov/info/reports/1976/3445600237081.pdf.
4. D. Cardwell, D. Gineley, Technology & Engineering, Handbook of Supercon. Mater. Vol 1, CRC Press, 2003.
5. K. Wang, *Mat. Sci. and Eng.,* **213**, 134 (1996).
6. M. Niinomi, *Sci. Technol. Adv. Mater.*, **4**, 445 (2003).
7. Y. Li, Ch. Yang, H. Zhao, Sh. Qu, X. Li, Yu. Li, *Materials*, 7, 1709, (2014).
8. M. Niinomi, *Mater. Sci. Forum.*, **193**, 539 (2007).
9. M. Abdel-Hady, H. Fuwa, K. Hinoshita, H. Kimura, Y. Shinzato, M. Morinaga, *Scr. Mater.,* **57**, 1000 (2007).
10. J. Noble, *Brit. Dent. J.*, **204**, 297 (2008).
11. O. Kolokitha, E. Chatzistavrou, *Angle Orthod.*, **79**, 186 (2009).

12. A. Chitharanjan, *J. Orthod. Sci.,* **4**, 83 (2012).

13. S. Maheshwari, S. Verma, S. Dhiman, *J. Dent. Mater. and Tehnol.*, **4,** 111 (2015).

14. V. Naik, K. Mavani, *Ind. J Den. Adv.*, **4**, 259 (2015).

15. H. Kim, J. Johnson, *Angle Orthod.,* **69,** 39 (1999).

16. C. Burstone, A. Goldberg, *Am. J. Orthod.*, **77**, 121 (1980).

17. R. Kusy, *Angle Orthod.*, **72,** 501 (2002).

18. H. Huang, C. Wang, S. Chiu, J. Wang, Y. Liaw, T. Lee, F. Chen, *Chin. Dent. J.,* **24,** 134, (2005).

19. M. Dalstra, G. Denes, B. Melsen, *Clin. Orthod. Res.,* **3**, 6 (2000).

20. R. Vijayalakshmi, K. Nagachandran, P. Kummi, P Jayakumar, *Ind. J. Dent. Res.*, **20,** 448 (2009).

21. M. Han, J. Kim, M. Hwang, H. Song and Y.J. Park, *Materials,* **8**, 5986 (2015).

22. V. Petrov, S. Terzieva, V. Tumbalev, V. Mikli, L. Andreeva, A. Stoyanova-Ivanova, *Bul. Chem. Commun.*, **47**, 54 (2015).

23. T. Chaturvedi, *The Orthod. Cyber J.*, January (2008), online: www.orthocj.com.

24. R. Kusy, *Angle Orthod.,* **67**, 197 (1997).

25. O. Prymak, A. Klocke, B. Kahl-Nieke, M. Epple, *Mat. Sci. and Eng.,* **378**, 110 (2004).

26. D. Fernandes, R. Peres, A. Mendes, C. Elias, *ISRN Dent.,* **2011**, 132408 (2011).

27. http://spectrum.ieee.org/biomedical/imaging/ superconductivitys-first-century.

ОХАРАКТЕРИЗИРАНЕ НА ТИТАН- НИОБИЕВИ ОРТОДОНТСКИ ДЪГИ ИЗПОЛЗВАНИ ПРИ ОРТОДОНТСКО ЛЕЧЕНИЕ

И. Илиевска[1], Д. Карашанова[2], В. Петров[3], А. Залески[4], М. Дрозд[4], В. Микли[5], А. К. Стоянова-Иванова[1]

[1]*Институт по физика на твърдото тяло „Акад. Георги Наджаков", Българска Академия на Науките, Бул. „Цариградско шосе" 72, 1784 София, България*

[2]*Институт по оптични материали и технологии, Българска Академия на Науките, бул. Акад. Георги Бончев, бл.109, 1113, София, България*

[3]*Факултет по дентална медицина, Медицински Университет , София, Бул. „Св.Св. Георги Софийски" 1,1431 София, България*

[4]*Институт по ниски температури и структурни изследвания, Полска Академия на Науките, ул. Околна 2, 50-422, Вроцлав, Полша*

[5]*Център за изследване на материали към Талински Технологичен Университет – Талин, Ехитиате 5, 19086 Талин, Естония*

(Резюме)

Титан-ниобиевите (TiNb) сплави са известни като свръхпроводими материали и се използват за производството на свръхпроводими кабели. Поради техните свойства като висока биосъвместимост и висока устойчивост на корозия, те намират широко приложение в медицината, за нуждите на ортопедично-реконструктивната хирургия, имплантологията и др. Напоследък, този материал се използва за изработването на ортодонтска дъга, използвана в последния етап на ортодонтското лечение.

На пазара се предлагат различни видове ортодонтски дъги, от различни производители, които се подчиняват на спецификации, необходими, за тяхното прилагане по време на ортодонтското лечение. Но свойствата на тези дъги могат да се променят по време на лечението и за правилното им прилагане е необходимо да се намерят методи, чрез които тези свойства да бъдат проследявани. Целта на това изследване е да се получат данни за структурата, химичния състав и физичните свойства на TiNb ортодонтска дъга, произведена от фирмата ORMCO.

Optical properties of ZnO thin films deposited by the method of electrospray

G. Marinov[1,2], M. Vasileva[1], V. Strijkova[1], N. Malinowski[1] and T. Babeva[1]*

[1]*Institute of Optical Materials and Technologies ''Acad. J. Malinowski'', Bulgarian Academy of Sciences, Acad. G. Bonchev str., bl. 109, 1113 Sofia, Bulgaria*
[2] *TACK Laboratory, 2 Ivan Peev Marusha str., Pravetz, Bulgaria*

ZnO films with thicknesses in the range 60-220 nm were prepared by electrospray method on silicon substrates at temperature of 200 °C using electrostatic set-up with vertical configuration and preliminarily optimized sol-gel recipe including zinc acetate dehydrate as a precursor and ethanol as a solvent. The thin films were subjected to high temperature (550 °C) post annealing. The deposition voltage and distance between the emitter and collector were varied in the range 9.5 – 13.5 kV and 4 – 7 cm, respectively. The surface topography and roughness were measured by Atomic Force Microscope (AFM) and optical profiler. Optical constants and thickness of the films were calculated from reflectance spectra using nonlinear curve fitting. Photoluminescence spectra were measured at room temperature at excitation wavelength of 335 nm. The influence of deposition parameters and post annealing on surface morphology, optical properties and photoluminescence of thin ZnO films was discussed.

Keywords: ZnO films, electrospray, sol-gel, optical properties.

INTRODUCTION

ZnO is a wide band semiconductor with large exciton binding energy. Due to its transparency in UV and NIR ranges, electro and elasto-optical properties, low resistivity, biocompatibility, low cost and long-term stability, ZnO is an attractive material for utilization in various modern devices such as biosensors [1], optical gas sensors [2], piezoelectric sensors [3], optoelectronics [4], transducers and resonators [5], integrated optical devices [6], etc. ZnO thin films are interesting transparent conducting oxides and are regarded as an alternative material to the widely used ITO for optically transparent electrodes in flat panel displays [7] or solar cells [8].

Different physical and chemical methods of ZnO films deposition have already been implemented: rf sputtering [9], pulsed laser deposition [2], plasma enhanced chemical vapor deposition [10], spray pyrolysis [11], sol–gel process [12], molecular beam epitaxy [13], atomic layer deposition [14], electrospray [15], etc.

However, in order to realize high-performance ZnO based devices, it will be a real advantage to grow high quality ZnO thin films with controllable parameters using easy and low cost methods. Sol-gel process emerges as a convenient, efficient and inexpensive technique for thin film preparation, enabling tailored properties and easy doping option at molecular level [12]. Besides, it could be successfully combined with electrospray method for film deposition having advantages of simple setup, low cost and easy control of morphology and stoichiometry. Tailored structural and optical parameters could be achieved simply by variation of applied voltage and substrate temperature [15, 16]. However, for effective technological applications of ZnO films, the impact of different preparation conditions on the film properties have to be thoroughly investigated and mutual relationships to be revealed.

In this paper we combine the advantages of both sol-gel and electrospray methods in order to deposit high quality ZnO thin films with controllable properties. The influence of deposition parameters and post annealing on surface morphology, optical properties and photoluminescence of thin ZnO films is discussed.

EXPERIMENTAL DETAILS

The sol-gel method was used for preparation of solution for electrospray. 0.115 g of zinc acetate dehydrate was dissolved in 0.5 ml H_2O and 3.5 ml ethanol and stirred at room temperature for 2 hours. Two drops of acetic acid were added as

* To whom all correspondence should be sent:
E-mail: babeva@iomt.bas.bg

stabilizers. Prior to the deposition the solution was aged for 24 h at room temperature. All chemicals (Sigma Aldrich) were of analytical reagent grades and used without further purification.

The deposition of thin film was performed using an electrostatic set-up with vertical configuration equipped with home-made heater capable of maintaining the substrate temperature up to 300 °C in controllable manner (Fig. 1).
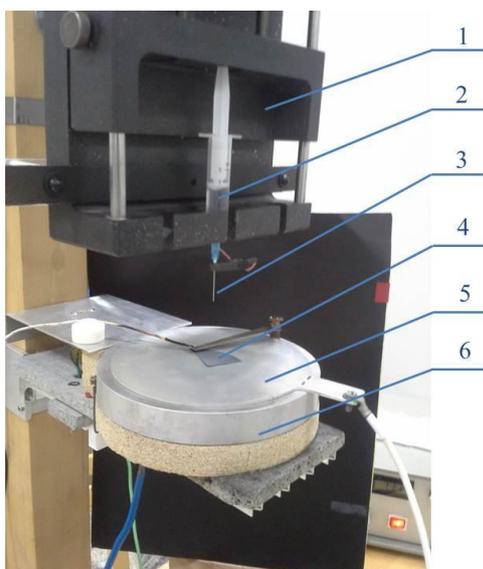
Fig. 1. Vertically configured electrospraying set-up consisting of syringe pump (1), 5 ml syringe with Zn sol (2), emitter (3), substrate (4), collector (5) and heater (6).

The emitter of the electrospraying set-up was a 5 ml syringe with stainless steel needle of inner diameter of 0.3 mm and length of 32 mm and the collector is the stainless steel-duralumin plate put on the heater and grounded in a save way. The distance between the emitter and collector was 4 cm and 7 cm and a high voltage of 9.5 kV and 11 kV in the first case and 12.5 and 13.5 kV in the second one was applied via a DC power supply (Applied Kilovolts, UK). For all films the substrate temperature is kept at 200 °C. Fig. 1 shows a picture of the electrospray set-up.

The surface morphology and roughness of the films were characterized by Atomic Force Microscopy (MFP-3D, Asylum Research, Oxford Instruments), while the dispersion of the droplets over the substrate and the variation of their size with deposition conditions were examined by crossed-polarizer optical profilometry (Zeta-20, Zeta Instruments).

The refractive index (n) and extinction coefficient (k) along with the thickness (d) of the films were determined from reflectance spectra of the films measured at normal light incidence by UV-VIS-NIR spectrophotometer Cary 05E (Varian, Australia) using non-linear curve fitting method [17]. The experimental errors for n, k and d were 0.005, 0.003 and 2 nm, respectively.

The photoluminescence spectra of the films were taken at room temperature at excitation wavelength of 335 nm using spectrofluorometer FluoroLog3-22 (Horiba JobinYvon).

RESULTS AND DISCUSSIONS

The typical surface morphology of the electrosprayed ZnO films is illustrated in Fig. 2 by AFM images of the as-deposited ZnO films. All films are crack-free and have similar surface morphology comprising spherical grains that are tightly packed and distributed uniformly over the entire film surface. For all films the size of the grains is similar varying in the range 50 – 500 nm and no effect of post-annealing on the grains size is observed (Fig. 3). The thickness of the films deposited at 4 cm is 220 nm, while those at 7 cm are 60 nm thick.
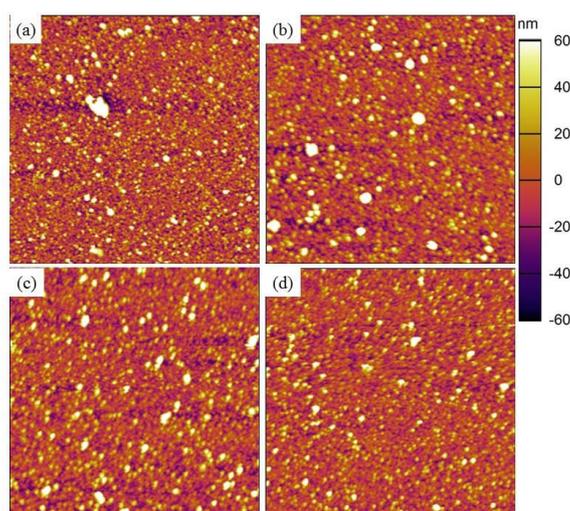
Fig. 2. AFM pictures (10 μm x 10 μm) of the surface of ZnO films deposited on Si-substrate by the electrospray method at applied voltage of 9.5 kV (a), 11 kV (b), 12.5 kV (c) and 13.5 kV (d) and an emitter-to-collector distance of 4 cm (a, b) and 7 cm (c, d).

After annealing a weak smoothing of the surface takes place for films deposited at a distance of 4 cm (Fig. 4 (a)), while a slight roughening is observed for these at 7 cm (Fig. 4 (b)). The typical rms roughness values of 16 – 19 nm are obtained for the films that are consistent with those measured for spin- and dip-coated films [18, 19]. The weak smoothing with distance illustrated in Fig. 3 could be due to a smaller

thickness of the films obtained at a distance of 7 cm.
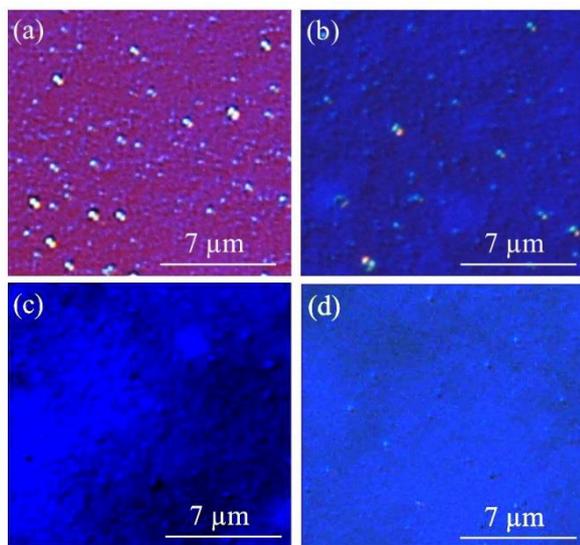
Fig. 3. Optical microscopic images of electrosprayed ZnO using applied voltage of 9.5 kV (a,b) and 13.5 kV (c,d), emitter-to-collector distance of 4 cm (a,b) and 7 cm (c,d) before (a, c) and after annealing at 550 °C (b,d).
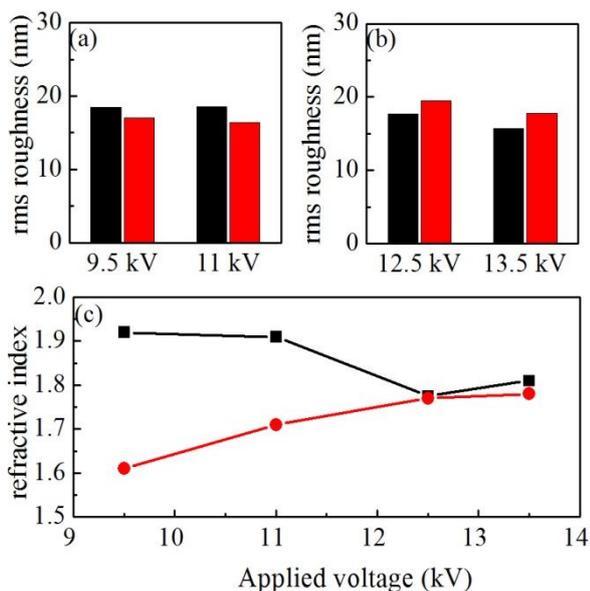
Fig. 4. Surface roughness (rms) in [nm] of ZnO films deposited at emitter-to-collector distance of 4 cm (a) and 7 cm (b) and refractive index at wavelength of 600 nm as a function of applied voltage (c) for as-deposited (black color) and annealed films (red color).

As the distance between the emitter and collector increases from 4 cm to 7 cm a reduction in deposition rate from 5 nm.min^{-1} to 3 nm.min^{-1} is observed which is due to the enlargement of the covered surface area. The increase of applied voltage at fixed distance leads also to a weak

decrease of deposition rate. Besides, a strong lateral thickness gradient is detected for deposition distance of 4 cm unaffected by the applied voltage, while the area of uniform film thickness expands considerably when the deposition is carried out at a distance of 7 cm.

The calculated values of refractive index (n) of the films as functions of applied voltage are presented in Fig. 4 (c). The curves for as-deposited and annealed films show opposite trends: a decrease in n is observed for as-deposited films while after annealing n for the films increases with voltage reaching steady-state at applied voltage greater than 12.5 kV. For all films the post-deposition annealing leads to the reduction of n mostly pronounced for the films deposited at a distance of 4 cm. As shown in [20] the decomposition of zinc acetate occurs for temperature greater than 400 °C. Considering that during the electrospray the substrates are kept at 200 °C it may be expected the as-deposited films to have nonstoichiometric composition due to the residual non-reacted zinc acetate as opposite to the annealed one wherein the thermal decomposition of zinc acetate should be completed. Thus, the difference in chemical composition could be the reason for the change in refractive index after annealing. It is possible the process of organic decomposition to be favored in the case of thinner films (deposited at a distance of 7 cm). As a result it may happen the zinc acetate residual in them to be less as compared to thicker films (deposited at a distance of 4 cm) and their refractive index before annealing to be closer to n for the annealed ones (Fig. 4(c)).
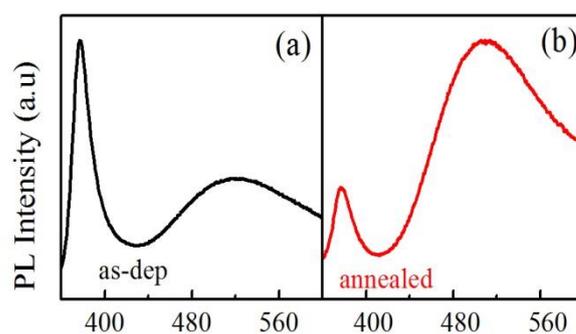
Fig. 5. Room temperature photoluminescence spectra of as-deposited (a) and annealed (b) ZnO films taken at excitation wavelength of 335 nm.

The photoluminescence spectra at room temperature and excitation wavelength of 335 nm of as-deposited and annealed ZnO films are presented in Fig. 5. A narrow UV emission peak

and a broad green emission peak with different relative intensities are observed in both cases. The first one, centered at 377 nm (3.29 eV) is ascribed to the inter-band radiation recombination of photo-generated electrons and holes [21-23]. Usually the light emitted due to the free exciton recombination has an energy equal to or slightly greater than the optical band gap, that for the case of sol-gel ZnO films is in the range 3.20 – 3.30 eV [21, 22]. The broad green emission, centered at 520 nm (2.38 eV) for the as-deposited films and at 510 nm (2.43 eV) for the annealed ones, with energy smaller than the band gap should correspond to the transition between band edges and the local levels in the band gap. The last are formed by some defects in ZnO [24], for example zinc and oxygen vacancies, interstitial zinc, interstitial oxygen, etc. [23, 25]. According to Yu et. al. [26] the stronger green emission relative to UV emission in the case of annealed films suggests that there is a great fraction of oxygen vacancies in the films. They may originate from oxygen deficiency due to the high temperature annealing of films in ambient atmosphere. Further experiments are required for clarification of the exact reason.

CONCLUSIONS

The successful application of electrospray method with vertical set-up for deposition of ZnO thin films is demonstrated. The applied voltage is varied between 9.5 kV and 13.5 kV, while the emitter-to-collector distance is fixed at 4 cm and 7 cm. The deposition parameters and annealing do not influence substantially the surface topography of the films, while after annealing a weak smoothing is observed for films deposited at 4 cm and roughening – for films at 7 cm. In order to obtain broad area of uniform thickness the deposition should be carried out at a higher distance and lower applied voltage. Further, the refractive index increases as the applied voltage increases. The denser ZnO films are obtained at the highest applied voltage (1.78 at wavelength of 600 nm). A narrow UV emission peak and a broad green emission peak with different relative intensities are observed for as deposited and annealed ZnO films assigned to the free exciton recombination and oxygen vacancies, respectively.

REFERENCES

1. A. Ansari, M. Khan, M. Alhoshan, S. Alrokayan, M. Alsalhi, *J. Semicond.*, **33**, 42002-1 (2012).
2. A. Dikovska, P. Atanasov, S. Tonchev, J. Ferreira, L. Escoubas, *Sens. Actuators A: Phys.*, **140**, 19 2007.
3. M. Arnold, P. Avouris, Z. Pan, Z. Wang, *J. Phys. Chem. B*, **107**, 659 (2003).
4. H. Sun, Q. Zhang, J. Wu, *Nanotechnology*, **17**, 2271 (2006).
5. C. Klingshirn, *Chem. Phys. Chem*, **8**, 782 (2007).
6. R. Heideman, P. Lambeck, J. Gardeniers, *Opt. Mat.*, **4**, 741 (1995).
7. T. Hirao, M. Furuta, H. Furuta, T. Matsuda, T. Hiramatsu, H. Hokari, M. Yoshida, H. Ishii, M. Kakegawa, *J. Soc. Inf. Display*, **15**, 17 (2007).
8. K. Kushiya, M. Ohshita, I. Hara, Y. Tanaka, B. Sang, Y. Nagoya, M. Tachiyuki, O. Yamase, *En. Mat. Sol. Cells*, **75**, 171 (2003).
9. M.-S. Wu, W.-C. Shih, W.-H. Tsai, *J. Phys. D. Appl. Phys.*, **31**, 943 (1998).
10. S. Kitova, G. Danev, *J. Phys.: Conf. Ser.*, **223**, ID 012022 (2010).
11. O. Dimitrov, D. Nesheva,V. Blaskov, I. Stambolova, S. Vassilev, Z. Levi ,V. Tonchev, *Mater. Chem. Phys.*, **148**, 712 (2014).
12. L. Znaidi, *Mat. Sci. Eng. B*, **174**, 18 (2010).
13. K. Nakamura, T. Shoji, K. Hee-Bog, *Jpn. J. Appl. Phys. Lett*. **39**, 534 (2000).
14. B. Blagoev, D. Z. Dimitrov, V. Mehandzhiev, D. Kovacheva, P. Terziyska, J. Pavlic, K Lovchinov, E. Mateev, J. Leclercq, P. Sveshtarov, *J. Phys.: Conf. Ser.*, **700**, ID 012040, (2016).
15. A. Hosseinmardi, N. Shojaee , M. Keyanpour-Rad, T. Ebadzadeh, *Ceram. Int.*, **38**, 1975 (2012).
16. K.-S. Hwang, J.-H. Jeong, Y.-S. Jeon, K.-O. Jeon, B.-H. Kim, *Ceram. Int*., **33**, 505 (2007).
17. K. Lazarova, M. Vasileva, G. Marinov and T. Babeva, *Opt. Laser Technol.*, **58**, 114 (2014).
18. B. Shivaraj, H. Murthy, M. Krishna, B. Satyanarayana, *Procedia Mater. Sci.,* **10**, 292 (2015).
19. S. Singh, P. Chakrabarti, *Superlattices and Microstruct.*, **64**, 283 (2013).
20 Y. Ding, P. Zhang, Y. Jiang, F. Xu, J. Chen, H. Zheng, *Solid State Phenom.*, **155**, 151 (2009).
21. F. Ghodsi, H. Absalan, *Acta Phys. Pol. A*, **118**, 659 (2010).
22. Z. Khan, M. Khan, M. Zulfequar, M. Shahid Khan, *Mat. Sci. Appl.*, **2**, 340 (2011).
23. Y.-S. Kim, W.-P. Tai, S.-J. Shu, *Thin Solid Films*, **491**, 153 (2005).
24. B. Lin, Z. Fu, Y. Jia, G. Liao, *J. Electrochem. Soc.*, **148**, G110 (2001).

25. K. Vanheusden, W. Warren, C. Seager, D. Tallant, J. Voigt, B. Gnade, *J. Appl. Phys.* 79, 7983 (1996).

26. K. Yu, Y. Zhang, L. Luo, W. Wang, Z. Zhu, J. Wang, Y. Cui, H. Ma, W. Lu, *Appl. Phys. A*, **79**, 443 (2004).

ОПТИЧНИ СВОЙСТВА НА ТЪНКИ ФИЛМИ ОТ ZnO, ПОЛУЧЕНИ ЧРЕЗ ЕЛЕКТРО-СПРЕЙ

Г. Маринов[1,2], М. Василева[1], В. Стрижкова[1], Н. Малиновски[1] и Цв. Бабева[1]

[1]*Институт по оптически материали и технологии ''Акад. Й. Малиновски'', Българска Академия на Науките, ул. "Акад. Г. Бончев", блок 109, 1113, София, България*
[2] *ТАСК Лаборатория, ул. "Иван Пеев Маруша" №2, Правец, България*

(Резюме)

Изследвани са тънки слоеве от ZnO с дебелини в диапазона 60-220 нм, получени чрез метода на вертикален електро-спрей върху подложки от кристален силиций при температура на подложката 200 ºC. Съставът на използвания зол, състоящ се от цинков ацетат дехидрат като прекурсор и етанол като разтворител, е предварително оптимизиран. След отлагане филмите са загряти на 550 ºC за 2 часа. Подаваното напрежение и разстоянието между емитера и колектора са варирани в диапазона 9.5 – 13.5 kV и 4 – 7 cm, съответно. Топографията и грапавостта на повърхността са измерени чрез AFM и оптичен профиломер. Оптичните константи и дебелината на филмите са изчислени от спектрите на отражение чрез нелинейно минимизиране. Измерена е фотолуминесценцията при стайна температура. Дискутирано е влиянието на параметрите на отлагане и загряването след отлагане върху повърхностната морфология, оптичните свойства и фотолуминесценцията на тънки слоеве от ZnO.

Properties of ALD Aluminum-doped ZnO as transparent conductive oxide

N. Bozhinov[1], B. Blagoev[2], V. Marinova[1], T. Babeva[1], E. Goovaerts[3], D. Dimitrov[1, 2]*

[1]*Institute of Optical Materials and Technologies, Bulgarian Academy of Science Acad. G. Bonchev Str. 109, Sofia, Bulgaria*
[2]*Institute of Solid State Physics, Bulgarian Academy of Science, 72 Tzarigradsko Chaussee Blvd., Sofia, Bulgaria*
[3]*Experimental Condensed Matter Physics, Department of Physics, University of Antwerpen, Universiteitsplein, B-2610, Antwerpen, Belgium*

Thin films of aluminum- doped ZnO are prepared by Atomic Layer Deposition (ALD). The properties of these films toward application as transparent conductive oxides are studied. It is obtained that doped films possess high optical transmittance (>85%) in the visible and near-infrared spectral ranges. A resistivity as low as 3×10^{-3} Ω.cm depending of the Al content in the doped film is measured. The observed high conductivity and high transparency fulfil the requirements for transparent conductors.

Keywords: ALD, doped ZnO, transparent conductive oxide, thin films

INTRODUCTION

Transparent conducting oxides (TCOs) are considered key materials for a range of applications in electronic screens and displays, LEDs and solar cells. These applications take advantage of the unique characteristics of TCOs, which include high electrical conductivity, transparency in the visible range and good chemical and thermal stability. TCOs usually are based on simple oxides as In_2O_3, SnO_2, Ga_2O_3 and ZnO – which are intrinsically or extrinsically doped in order to provide electrical properties similar to those of metals, and high transparency. Tin-doped indium oxide (ITO) is currently the most popular TCO, but concerns for the cost and supply of indium have resulted in increasing efforts to find alternatives. The most promising candidate for the replacement of ITO is aluminum-doped zinc oxide (AZO) which have low resistivity of the order of 10^{-4} Ω.cm, high transparency, and inexpensive non-toxic source materials [1].

The doping is a process in which impurities are intentionally introduced, in order to modulate the electrical properties and thus establish electrical conductivity as a result of free carriers. The process of extrinsic doping involves the addition of metal ions with different valences to the crystal lattice structures of the simple oxides in order to form these free carriers. For intrinsically doped TCOs, the electrons originate from intrinsic defects, or interstitial metal cations. In both cases, these structural imperfections give rise to the increased carrier concentrations and consequently electrical conductivity. Typical point defects observed in intrinsically doped ZnO are oxygen vacancies and Zn^{2+} in an interstitial while in AZO it is Al^{3+} occupying a Zn^{2+} site in the ZnO lattice [2].

Aluminum- doped ZnO thin films can be deposited by several techniques such as sol–gel, chemical spray, thermal evaporation, pulsed laser deposition, DC and RF magnetron sputtering. In our research ALD was used as method for preparation of AZO films with qualities appropriate for application as transparent conductive oxides.

EXPERIMENTAL

TCOs are deposited as thin films for a wide variety of applications demanding electrical conductivity and optical transparency. The desired qualities of a good TCO: transparency, conductivity, and surface texture, depend on the growth technique and the growth parameters. Atomic layer deposition (ALD) is a growth technique which has recently become very popular since it provides uniform and conformal coverage and control of the thin film by atomic layer precision. ALD is a self-limited deposition method that is characterized by alternating exposure of the growing film to chemical precursors, resulting in

* To whom all correspondence should be sent:
E-mail: *ddimitrov@iomt.bas.bg*

the sequential deposition of mono layers over the exposed sample surface. The self-limiting nature of the vapor-solid reactions ensures pinhole free coatings with a precise thickness controlled at the atomic scale and superb conformality onto large scale substrates with complex topologies. The main features which make the ALD distinctive technique for deposition of thin films are shown at Fig. 1. Although the growth rate of the ALD system is relatively low, the uniformity, conformality and the compactness of the film cross-section achieved from the ALD technique are superior to those from other techniques [3].
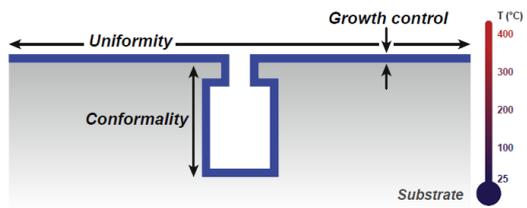
Fig. 1. ALD method features: precise growth and thickness control, high conformality/step coverage, good uniformity on large substrates, low substrate temperatures [4].

The AZO films were grown on two different substrates: p-type single crystal Si (100) and fused silica using Beneq TFS-200 ALD system. The substrates temperature during deposition was 200 °C. Diethylzinc (DEZ, $Zn(C_2H_5)_2$), trimethyl-aluminum (TMA, $Al(CH_3)_3$), and deionized water (H_2O) are used as Zn, Al and oxidant precursor, respectively. Nitrogen was used as a carrier and purge gas. The general reaction sequence for ZnO ALD involves separate DEZ and H_2O exposures, and Al_2O_3 ALD utilizes separate TMA and H_2O exposures. Since H_2O is adsorbed on most surfaces, a formation of Si–O–H hydroxyl group on the Si substrate is expected. The growth sequence can be understood from the following surface reactions on a hydroxylated Si substrate.

$$Zn(C_2H_5)_2 + Si\text{-}O\text{-}H = Si\text{-}O\text{-}Zn(C_2H_5) + C_2H_6 \quad (1)$$

$$Si\text{-}O\text{-}Zn(C_2H_5) + H_2O = Si\text{-}O\text{-}Zn\text{-}O\text{-}H + C_2H_6 \quad (2)$$

$$Si\text{-}O\text{-}Zn\text{-}O\text{-}H + Al(CH_3)_3 = Si\text{-}O\text{-}Zn\text{-}O\text{-}Al(CH_3)_2 + CH_4 \quad (3)$$

$$Si\text{-}O\text{-}Zn\text{-}O\text{-}Al(CH_3)_2 + 2H_2O = Si\text{-}O\text{-}Zn\text{-}O\text{-}Al\text{-}(O\text{-}H)_2 + 2CH_4 \quad (4)$$
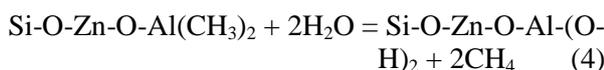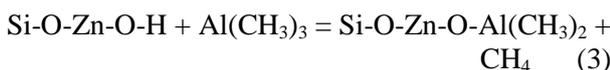
AZO films with targeted thickness were deposited using several supercycles. Usually n monolayers (cycles) of ZnO plus one monolayer (cycle) of Al_2O_3 represent one supercycle as shown in Fig. 2.
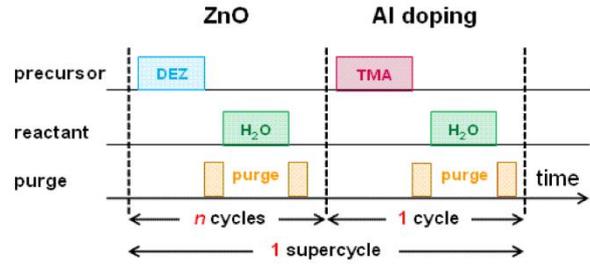
Fig. 2. Super cycle for Al doped ZnO ALD.

Transmittance spectra of samples deposited on fused silica substrate were measured in spectral range covering UV, VIS and NIR using a spectrophotometer. The sheet resistance was obtained by the standard four-probe technique on Veeco EPP-100 apparatus at room temperature and the resistivity was calculated using the thickness data from ellipsometric measurements. Atomic Force Microscopy (AFM) and Scanning Electron Microscopy (SEM) were used for study the morphology of the films with average thickness of 180 nm.

RESULTS AND DISCUSSION

The prepared AZO films were polycrystalline and predominantly *c*-axis oriented perpendicular to the substrate surface, as evidenced by x-ray diffraction analyses [5]. Al doping affects the crystallographic orientation of the grains in the ZnO film, causing the preferred orientation of the films to shift to the (100) direction.
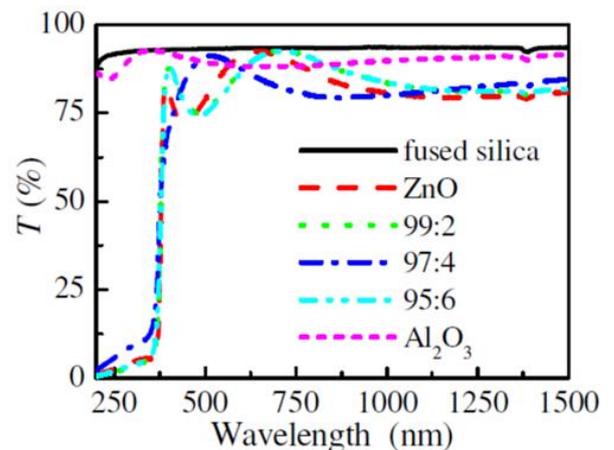
Fig. 3. Transmittance spectra of Al_2O_3, ZnO and samples with compositions ZnO: Al_2O_3 (cycles ratio shown)

Fig. 3 presents transmittance spectra of samples deposited on fused silica substrate. The substrate's spectrum is also shown for comparison. It is seen that all samples containing ZnO are transparent for

wavelength higher than 370 nm and absorbs light with smaller wavelength, while the transparent window of Al_2O_3 extends towards UV range. The position of fundamental absorption edge is almost the same for all samples containing ZnO but more detailed analysis is needed including calculation of optical band gap thus accounting for slightly different thicknesses of the samples. The transmittance in the visible region normalized to that of the substrate oscillated between 90% and 100% due to constructive and destructive interference.
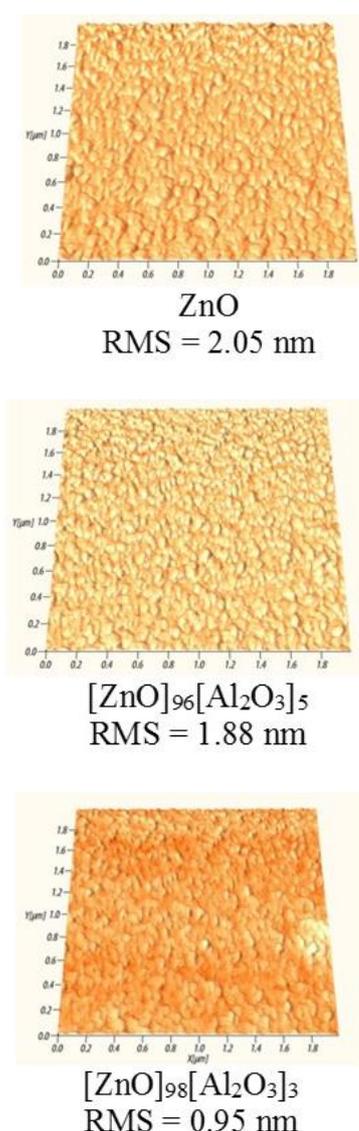
Fig. 4. AFM of ZnO and Al-doped ZnO (AZO).

AZO films are more transparent in the infrared (IR) than ITO films. IR transmission is very important because increasing the long-wavelength response is an approach to increase the efficiency of some solar devices [6]. Thus, AZO films are an appropriate replacements for ITO films in applications such as transparent electrodes for solar cells, flat panel displays, LCD electrodes, touch panel transparent contacts and IR windows [7].

The surface morphology of the thin films was studied by AFM and SEM as shown in Figs. 4 and 5, respectively. The as-grown films are relatively smooth with uniform distribution of grains which are around 60 to 100 nm long and 10–20 nm wide. Another important requirement for TCO electrodes in electronic devices is the formation of tailored interfaces with the active electronic material, which is normally a typical semiconductor [8]. As it shown on the SEM cross-sectional view, the interface between the AZO and Si substrate is very smooth. The incorporation of Al_2O_3 layers into ZnO significantly reduces the surface roughness of the film (from RMS= 2.05 nm to RMS = 0.95 nm, see Fig.4), and by varying the amount of Al_2O_3 layers it is possible to tune the ZnO films' roughness for gas sensor applications [9].
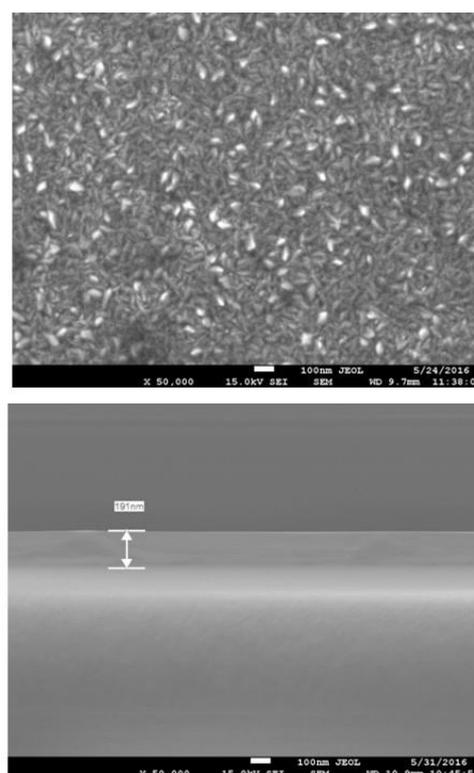
Fig. 5. SEM plan view and cross-section of AZO film showing polycrystalline morphology and smooth interface between the film and Si wafer substrate

The obtainable electrical properties of doped ZnO films are strongly dependent on the deposition methods and conditions. Vacuum evaporation of AZO is difficult to achieve because the vapor pressure of Al_2O_3 is too low in comparison with that of ZnO. AZO films with a resistivity of the

order of 10^{-5} Ω cm have been obtained by PLD, but preparing films on large substrates with a high deposition rate is very difficult to achieve. The deposition of AZO films on large area substrates by dc magnetron sputtering using an oxide target is particularly difficult because the resistivity follows a spatial distribution corresponding to the target erosion area pattern created on the substrate surface [10].

Table 1. Volume percentage of Al_2O_3 layer content, thickness and resistivity of AZO films

$[ZnO]_n[Al_2O_3]_m$	Al_2O_3 layer content, %	Thickness, nm	Resistivity, Ω.cm
ZnO	-	160	7.6×10^{-3}
$[ZnO]_{100}[Al_2O_3]_1$	0.55	196	4.2×10^{-3}
$[ZnO]_{99}[Al_2O_3]_2$	1.11	189	3.3×10^{-3}
$[ZnO]_{98}[Al_2O_3]_3$	1.67	186	3.9×10^{-3}
$[ZnO]_{97}[Al_2O_3]_4$	2.24	183	4.2×10^{-3}

Aluminum doping purpose is the lowering of resistivity as low as possible, and several studies report resistivity values in the 10^{-4} Ω.cm range. The optimal Al doping amount for minimizing resistivity varies from study to study, but is generally reported to be in the 2%–5% range. At higher Al contents the resistivity increases again as the solubility limit of Al into ZnO is exceeded, which is thought to lead either to the formation of separate Al_2O_3 phases or the spinel phase $ZnAl_2O_4$ [11]. The results of our measurements are presented on Table 1. Resistivity values of~$3x10^{-3}$ Ωcm have been reached and the values could still be further optimized. The resistivity is mostly determined by the Zn/Al ratio in the film [12], however the process temperature has also an effect.

CONCLUSIONS

Al-doped ZnO films were grown using thermal mode ALD with DEZ/H_2O precursors for ZnO and Al_2O_3 ALD with TMA /H_2O. The composition of the doped films was controlled by adjusting the relative number of ZnO ALD and Al_2O_3 ALD reaction cycles in the pulse sequence. Films with physical characteristics that could be tuned over the full range of values defined by pure ZnO and Al_2O_3

were grown. A variety of film properties was investigated with Al content including the film optical transmittance, surface roughness, crystallinity, and resistivity. Optical transparency higher than 85% and resistivity up to $3x10^{-3}$ Ωcm were measured. The obtained results show that AZO films are appropriate materials for functionality as transparent conductive oxide.

REFERENCES

1. T. Minami, *Semicond. Sci. Technol.*, **20**, S35 (2005).
2. N. Neves, *Ceramic Applications,* **3**, 62 (2015).
3. T. Dhakal, A. S. Nandur, R. Christian, P. Vasekar, S. Desu, C. Westgate, D. I. Koukis, D.,J. Arenas, D.,B. Tanner, *Sol. Energy,* **86**, 1306 (2012).
4. H. M. Knoops, S. Potts, A. Bol, W. Kessels, in: Atomic layer deposition, Handbook of crystal growth: thin films and epitaxy (second edition), T. Kuech (Ed.), Elsevier, 2014, p. 1101.
5. B. Blagoev, D. Dimitrov, V. Mehandzhiev, D. Kovacheva, P. Terziyska, J. Pavlic, K. Lovchinov, E. Mateev, J. Leclercq, P. Sveshtarov, *J. Phys.: Conf. Ser.*, **700**, 012040 (2016).
6. M. Berginski, J. Hupkes, M. Schulte, G. Schope, H. Stiebig, B. Rech, M. Wuttig, *J. Appl. Phys.* **101**, 074903 (2007).
7. S. Park, T. Ikegami, K. Ebihara, *Jpn. J. Appl. Phys.*, **45**, 8453 (2006).
8. K. Ellmer, *Nat. Photon.,* **6**, 809 (2012).
9. J. W. Elam, Z. A. Sechrist, S. M. George, *Thin Solid Films,* **414**, 43 (2002).
10. T. Minami, H. Sato, H. Imamoto, S. Takata, *Jpn. J. Appl. Phys.* **31**, L257 (1992).
11. T. Tynell and M. Karppinen, *Semicond. Sci. Technol.* **29**, 043001 (2014).
12. J. W. Elam, D. Routkevitch, S. M. George, *J. Electrochem. Soc.*, **150**, G339 (2003).

СВОЙСТВА НА ПОСЛОЙНО АТОМНО ОТЛОЖЕН ЛЕГИРАН С АЛУМИНИЙ ZnO КАТО ПРОЗРАЧЕН ПРОВОДЯЩ ОКСИД

Н. Божинов[1], Б. Благоев[2], В. Маринова[1], Цв. Бабева[1], Е. Гуваертц[3], Д. Димитров[1,2]

[1] *Институт за оптични материали и технологии, Ул. Акад. Г. Бончев 109, София, България*
[2] *Институт по физика на твърдото тяло, бул. Цариградско шосе 72, София, България*
[3] *Експериментална физика на кондензираната материя, Катедра Физика, Университет на Антверпен, Университетплейн 1, В-2610, Антверпен, Белгия*

(Резюме)

Чрез метода на последователно отлагане на атомни слоеве са получени тънки слоеве от ZnO легиран с алуминий. Изследвани са свойствата на тези слоеве за приложение като прозрачни проводими оксиди. Установено е, че легираните слоеве притежават висока оптична пропускливост (>85%) във видимата и близката инфрачервена области на спектъра. Измерени са ниски съпротивления до 3×10^{-3} Ω.cm, зависещи от съдържанието на Al в легираните слоеве. Получените висока проводимост и оптична транспарентност изпълняват условията за приложение на легираните с алуминий ZnO слоеве като прозрачни проводници.

High quality ITO thin films for application as conductive transparent electrodes

S. Kitova*, V. Mankov, D. Dimov, V. Strijkova and N. Malinowski

Institute of Optical Materials and Technologies "Acad. J .Malinowski",
Bulgarian Academy of Sciences, Acad. G. Bonchev Str., Bl.109, 1113 Sofia, Bulgaria

A detailed study of structural, electrical and optical properties of ITO films, obtained under various deposition conditions by RF sputtering in pure Ar gas atmosphere, has been performed. The relationship between sheet resistance and optical transmittance of the films studied was followed through the variation of sputtering voltage, substrate temperature and film thickness. The figure of merit of these films, which is a measure of their quality as transparent conductive electrode, was evaluated. It is established that the deposition of ITO films at higher sputtering voltages leads to a considerably lower sheet resistance, better optical transparency and lower roughness of the films. The investigation of the film microstructure by X-ray diffraction (XRD) analysis showed that the prepared ITO films are polycrystalline with preferred (111) orientation. The AFM study performed revealed the formation of smooth films at higher V_s, with nanosized grains and uniformally distributed electrical current. Besides, smooth uniform ITO films with low resistance of 8 Ω/sq and average transmittance above 82% in the visible range 400-800nm were obtained on glass substrates without additional annealing of films. Thus, the possibilities of producing high quality ITO films by the RF sputtering method used at the established optimal experimental conditons have been demonstrated.

INTRODUCTION

Indium tin oxide (ITO) is one of the most widely used transparent conducting oxides due to its excellent combination of high optical transmission, high electrical conductivity and good chemical stability [1]. Nowadays thin films from ITO are widely used as transparent electrodes in such advanced applications as photovoltaic cells [2, 3] organic light emitting diodes (OLEDs) [4] and flat panel displays (PDPs) [5, 6]. However, due to the complexity of starting ITO materials the thin film properties are strongly dependent on the deposition processes. So far various deposition methods such as RF and DC sputtering, thermal evaporation, chemical vapour deposition, sol–gel method, spray pyrolysis, etc. have been applied for achieving a suitable compromise between low electrical resistivity and high transmittance of the films in the visible spectral range [1-2, 7]. Among them, DC and RF sputtering are the most attractive techniques because of their high deposition rate, good reproducibility and possibility of using available large area commercially sputtering systems [8-11]. Many research groups have studied the effects of the deposition conditions, such as substrate temperature, RF/DC power, oxygen-to-argon ratio, deposition pressure, substrate-to-target distance and bias voltage on the properties of ITO films [10-13]. However, most of the reports in this area were devoted to reactive sputtering and relatively little papers reported on sputtering in pure Ar gas without oxygen mixing [14-16]. Depending on the sputtering system and plasma discharge mode used, an essential difference of optimum sputtering conditions (discharge power, pressure, oxygen concentration, etc.) was observed, as well as a difference in the crystalline structure and morphology of the formed layers [9].

In the present paper the results of a systematic investigation of the structural, electrical and optical properties of the ITO films as a function of the sputtering voltage, substrate temperature and film thickness are presented. The purpose of our study was to obtain ITO films with both high transmittance and low sheet resistance applying RF sputtering of ITO target with RF power supply at 2 MHz in pure Ar gas atmosphere. In order to simplify the growth process we did not introduce oxygen gas during the film deposition.

EXPERIMENTAL

The ITO films were prepared by a commercial

---

* To whom all correspondence should be sent:
E-mail: skitova@iomt.bas.bg

sputtering system HZM-4 with RF power supply at 2.5 MHz and diode electrode configuration. A 20 cm diameter sintered ceramic target with 99.9% purity, containing 90 wt.% of In_2O_3 and 10 wt.% of SnO_2 (supplied by Leadmat Advanced Material Co. Ltd.) was used for the deposition of the films. The system was first pumped down to a base pressure of 1.3×10^{-6} mbar. ITO sputtering was carried out in a pure Ar atmosphere without oxygen at a constant pressure of 7×10^{-3} mbar. The argon gas flow was controlled by MKS mass flow controller. A pre-sputtering of ITO target for 15 min was necessary for preparing homogeneous films with reproducible properties. The sputtering voltage employed during deposition was varied from 800 V to 1400 V which corresponds to sputtering power density from 0.5 Wcm^{-2} to 2.45 Wcm^{-2}. The target to substrate distance was kept constant at 6 cm. The film thickness was varied by adjustment of the deposition time. The film thickness was measured by thin film analyzer (F20, Filmetrics) with accuracy of ± 5nm. The temperature of the substrate was measured by a K-type thermocouple attached directly to the substrate surface and was controlled with 1% measurement accuracy.

ITO films were deposited on polished Corning glass substrates, preliminary ultrasonically cleaned in isopropyl alcohol and de-ionized water baths.

The structural properties of the films were analyzed by X-ray diffraction using a Philips (PW 1710) apparatus with Cu-Kα radiation separated by a graphite focusing monochromator. The intensity and full width at half maximum (FWHM) of an (hkl) plane were determined by profile fitting procedure, using an Gaussian or pseudo Voigt peak shape after baseline correction and Kα2 stripping procedure. Scherer's equation was used to estimate the average crystallite size. This estimate has excluded the effects of peak broadening due to the instrument used and any effect of residual stresses in the ITO films.

The surface morphology of the films was studied by an atomic force microscope (AFM, MFP-3D, Asylum Research, Oxford Instruments). The grain size was determined by Gwyddion mask segmentation function applied to a preprocessed image [17]. The function is based on the classical Vincent algorithm for watershed in digital spaces. The mean size was calculated by averaging the equivalent square size of one grain [17].

The transmittance (*T*) of the samples were measured at normal light incidence in the spectral range λ = 400-800 nm by a Cary 5E spectro-photometer with an accuracy of ±0.5%.

The sheet resistance of the films was determined by four-point probe method. The set-up consisting of Keithley 220 Programmable Current Source and Agilent 3458A multimeter was controlled by a Labview program.

RESULTS

It has been well established that the electrical properties of ITO films depend both on film thickness and deposition parameters such as applied sputtering power, substrate deposition temperature, etc. [1, 2]. The sputtering power is a product of sputtering voltage (V_s) and sputtering current (I_s). We have found that more expressed dependences are obtained using V_s instead of power, most probably due to observed little instabilities in I_s at constant sputtering pressure.
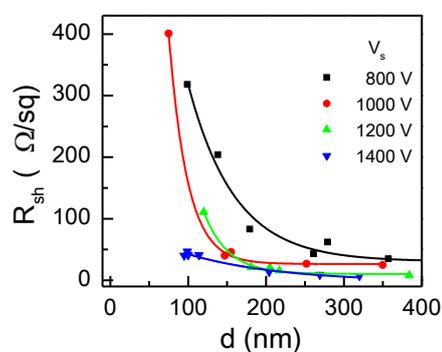
Fig. 1. Sheet resistance of ITO films as a function of the thickness of the films deposited at various sputtering voltages.

Fig.1 shows the influence of sputtering voltage V_s at constant sputtering pressure of 7×10^{-3} mbar on the sheet resistance (R_{sh}) of ITO films with different thickness (d). It can be seen that the R_{sh} decreases considerably with the increase of V_s from 800 V to 1400 V and film thickness from 80 nm to 400 nm, which is in good accordance with the literature data [11]. As seen, the films with thickness 300 nm, deposited at V_s of 1300 – 1400 V have minimum sheet resistance of 8 Ω/sq. Simultaneously, a dramatic rise of R_{sh} is observed for films thinner than 100 nm, which were deposited at V_s lower than 1200 V.

The results from numerous investigations performed have shown that the deposition of ITO without heating the substrate results in the formation of amorphous films with high resistance. are [1, 3]. On the contrary, crystalline ITO films with low resistivity were obtained by raising substrate temperature during deposition or by post annealing of the films at temperatures above 250 °C

[2, 3, 16]. It should be noted here that the results presented in Fig. 1 were obtained without additional heating of the glass substrates during sputtering or after deposition. Nonetheless, we have found that the surface of the substrate is heated during the deposition process in which the sputtered particles condense on the substrate surface and give up energy. Most probably, the substrate heating arises not only from the condensation energy of the depositing adatoms, but also from the high kinetic energy of the depositing particles, particularly at low pressures where the particles have not been thermalized. The substrate heating can also arise from plasma effects such as radiant heat of the target and the bombardment by high energy secondary electrons or energetic neutral [18]. Fig.2 shows the change of the substrate temperature (T_s) with deposition time at different sputtering voltages. For comparision the time for depositing 300 nm thick ITO film at 1200 V was 9.3 min and 8.5 min at 1400 V. It is seen from Fig. 2 that for these deposition times the substrate temperature rised up to 480 ^{o}C at 1200 V and respectively to 620 ^{o}C at 1400 V without need for additional substrate heating. On the one hand this temperature effect is favourable for preparing crystalline films with low resistivity. On the other hand it limits the range of usable voltage up to 1200 V- 1300 V and the deposition time at those voltages up to 10 min.
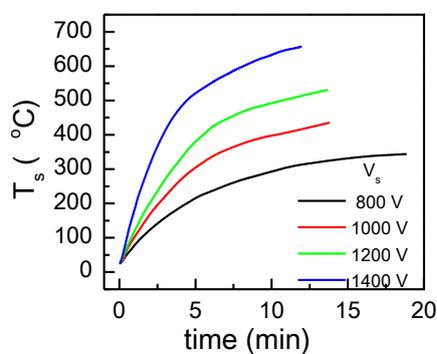
Fig. 2. Variation of the substrate temperature T_s with the deposition time at indicated sputtering voltages.

The X-ray diffraction patterns of ITO films, deposited on different sputtering voltages, are given in Fig. 3. The XRD data show that the deposited films have the cubic bixbyite structure of In_2O_3. Besides, the spectra of all films exhibit an intense (222) peak of In_2O_3, indicating a preferred orientation in the (111) direction, which takes place when T_s increases over 300 ^{o}C (see Fig. 2). This result is consistent with data of other authors, who have obtained the same (222) prominent peak [19, 20]. Furthermore, the (400) peak indicating the coexistence of the (111) and (100) textures, is

observed only in the spectra of films, deposited at 800 V. As seen from the figure, the crystallinity of the ITO films increases with rising sputtering voltage, most probably due the the elevated substrate temperature. No systematic change in orientation was observed with variation of film thickness in the range $50 \leq d \leq 350$ nm. Applying the Scherrer formula, it was found that the crystallite size range from 10 to 20 nm. Fig. 4 presents crystallite size determined by half peak width of the (222) peak as a function of the sputtering voltage. It is seen that the size decreases with increasing V_s up to 1300V.
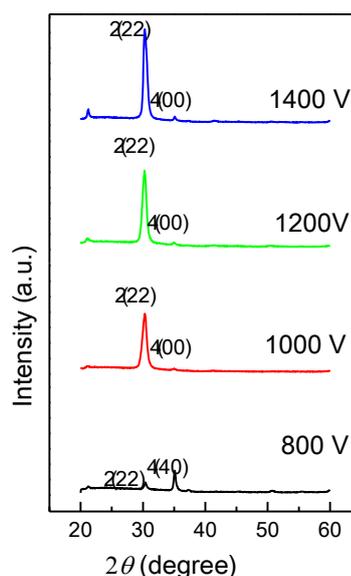
Fig. 3. X-ray diffraction patterns of 180 nm thick ITO films, deposited at indicated sputtering voltage.
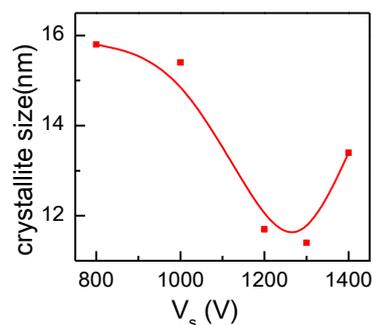
Fig. 4. Crystalite size of 180 nm thick ITO films as a function of sputtering voltage.

In the literature a low resistivity of ITO films was found to be related to a big grain size, which is attributed to less scatting at grain boundaries [3, 21]. Obviously, the established by us decrease of R_{sh} with V_s could not be explained only on the base of the better crystallinity and larger grain size.

The results obtained by AFM study showed that apart from the grain size, the surface of the films

had a significant impact on the sheet resistance values. Figs. 5 presents 3D topography and current map AFM images of 180 nm thick films deposited at different sputtering voltage. The corresponding height and current section across line on the images are shown in Fig. 6. The surfaces of ITO films seem to be formed by small nanosized grains with current uniformly distributed in the grains of films deposited at higher V_s. However, the presence of areas with big peaks and valleys, where the current has very low value was detected on films deposited at low V_s.

Vs = 800 V

Vs = 1000V

Vs = 1200V
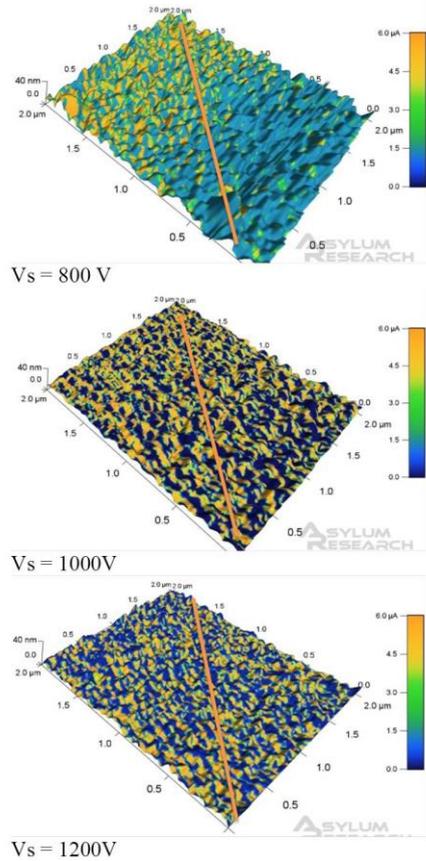
Fig. 5. 3D AFM images (contact mode) of the 180 nm thick ITO films deposited at indicated V_s. The topography is shown in z-scale of 40 nm, while the colour is the measured current, overlaid on the surface. A bias of +100 mV was applied to the sample surface during measurements.

It is known that in quantitative analyses on AFM images the surgface roughness is most commonly described by amplitude parameters including the average deviation R_a, root mean square (R_{RMS}) and the standard deviation R_q. These parametes have units of length with higher values indicating greater height variation. R_{RMS} and R_q are more sensitive than R_a to occasional hight and lows. Fig. 7 shows the standard deviation R_q of surface roughness as a function of the thickness of ITO films deposited at

V_s=800 V

V_s = 1000V

V_s = 1200V
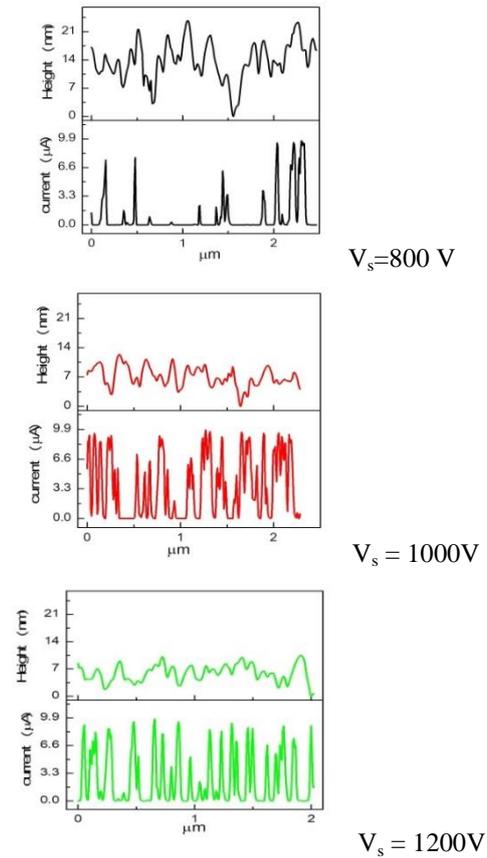
Fig. 6. Height and current section acrros the line shown in Fig. 5
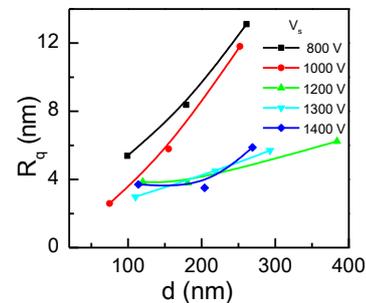
Fig. 7. Standard deviation R_q of surface roughness as a function of the thickness of ITO films, deposited at indicated V_s.

different V_s. It can be seen that the height roughness decreases with increasing the sputtering voltage and hence the deposition power. The ITO thin films, deposited at Vs up to 1000 V have larger clusters and further become rougher with increasing their thicknesses, while the R_q of films deposited at high V_s (1200 V- 1400 V) changes slightly with the thickness. As known, the average energy of adatoms is considered to be determined by the kinetic energy of the sputtered atoms, controlled by sputtering voltage just before arriving at the substrate. Simultaneously, the substrate heating imparts a thermal energy to the heated atoms thus

enhancing the adatom mobility. Consequently, more uniform ITO films with small roughness are deposited at high voltages.

Fig.8 shows the lateral grain size obtained from surface profiles. As a whole, the values derived are larger than the values for crystallite sizes obtained by XRD (see Fig. 4). Most probably this stemps from the fact that the Scherer's equation used is only an approximation, which did not include any effect of residual stresses in the films along with the effects of peak broadening due to the instrument used. However, in accordancane with the XRD results the same tendency of the grain size reduction with the increase of sputtering voltage was obtained. On the contrary, at a given V_s the grain sizes became larger in films with increased thicknesses.
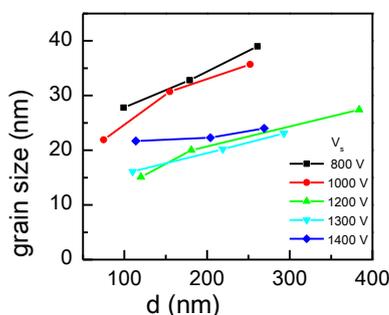
Fig. 8. Grain size, calculated by AFM images as a function of the thickness of ITO films deposited at indicated V_s.
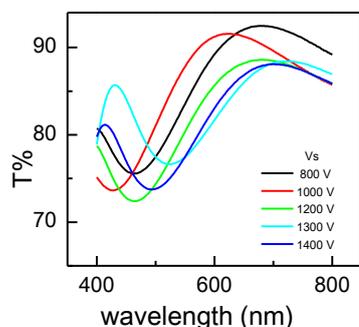
Fig. 9. Transmittance spectra of 180 nm thick ITO films, deposited at indicated V_s.

The resistivity of intrinsic n-type of ITO films strongly depends on the oxygen vacancy amount, Sn dopant and microstructure [1, 22]. It has been supposed that the carrier density is determined mainly by oxygen vacancies while the carrier mobility by the grain size, respectively [22]. On the basis of this assumption we can suppose that the existence of a minimum resistance of films deposited at high sputtering voltage is determined mainly by enhanced oxygen vacancies and hence, the increased carrier density in films, obtained in

atmosphere of oxygen deficiency. At a given V_s further drop in R_{sh} with the film thickness most probably is due to the larger grain sizes that leads to the enhanced electron mobilities in the films.

The optical properties of ITO thin films along with the resistivity are known to depend strongly on the growth techniques, deposition parameters and microstructure. Fig. 9 illustrates the transmittance spectra of 180 nm thick ITO films, deposited on glass substrates at different sputtering voltages. It is seen that the films prepared at higher V_s have lower transmittance, but as a whole the average transmittance (T_a) is above 82 % in the spectral range 450–800 nm. Since T and R_{sh} are inversely related in order to determine the best trade-off between electrical and optical properties, a figure of merit $\phi = T_a^{10}/R_{sh}$ as suggested by Haake for transparent conductive layers, was calculated [23].
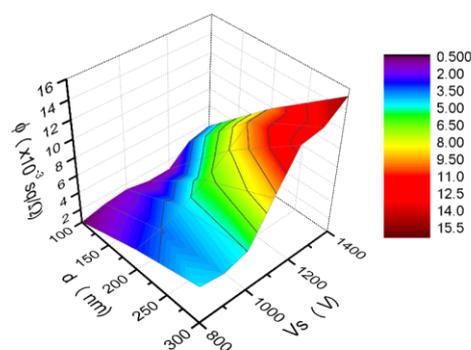
Fig.10. Figure of merit as a function of the film thickness and the sputtering voltage.

The variation of the calculated figure of merit with sputtering voltage and film thickness is presented in Fig. 10. It is evident that the highest value of ϕ (15.5 x10^{-3}sq/Ω) is obtained for 300 nm thick ITO films deposited at sputtering voltage of 1300 V.

CONCLUSION

The present work represents a systemathic investigation of electrical, structural and optical properties of ITO thin films, prepared by RF sputtering in pure Ar atmosphere, aimed at assessing their potentiality as transparent conductive electrodes. A big difference in sheet resistance R_{sh} of ITO films, obtained at different sputtering voltages V_s has been observed. It is established that samples deposited at high sputtering voltage have much lower sheet resistance. Besides, further drop in R_{sh} of the films has been measured whith increasing their thickness. Simultaneously, the analysis of XRD spectra show that the crystallinity of the ITO films increases with

increased sputtering voltage. Strong (222) peak and preferred orientation in the (111) direction was detected for low resistance samples, obtained at high V_s. Furthermore, the surface of the films appeared to have a significant impact on the sheet resistance values. The results from AFM study revealed the formation of smooth films at higher V_s, with nanosized grains and uniformly distributed electrical current. The presence of areas with high roughness, where the current has very low value has been detected in films deposited at low V_s.

Summarizing the above, it is worth to highlight the most important results of the study, which demonstrate the possibilities of preparing high quality ITO films by RF sputtering deposition at high V_s of 1300 V with thickness of 300 nm, the lowest sheet resistance of 8 Ω/sq and the highest figure of merit 15.5 x10^{-3}sq/Ω, without of necessity of additional annealing of films.

REFERENCES

1. F. Zhu in: Optical Properties of Condensed Mater and Application, J. Singh (ed), John Wiley&Sons, Ltd, 2006, ch 12.2, p. 266.
2. A. Ghhedari, E. Soleimani, M. Mansorhoseini, S. Mohajerzadeh, N. Madani, W. Shams-Kolahi, *Material Res. Bul.*, **40**, 1303 (2005).
3. V. Dao, H. Choi, J. Heo, H. Park, K. Yoon, Y. Lee, Y. Kim, N. Lakshminarayan, J. Yi, *Curr. Appl. Phys.*, **10,** S506 (2010).
4. W. Tang, S. VanSlyke, *Appl. Phys. Lett.*, **51,** 913 (1987).
5. Y. Ko, J. Kim, H. Joung, Sh. Ahn, K. Jang, Y. Lee and J, Yi, *J. Ceram. Proc. Res.*, **14**, 183 (2013).
6. S. Park, J. Han, W. Kim, M. Kwak, *Thin Solid Films*, **397**, 49 (2001).
7. H. Kim, N. Kim, J. Myung, *J. Mater. Sci.*, **40**, 4991 (2005).
8. O. Park, J. Lee, J. Kim, S. Cho, Y. Cho, *Thin Solid Films*, **474,** 127 (2005).
9. F. Kurdesau, G. Khripunov, A. Cunha, M. Kaelin, A. Tiwari, *J. Non-Cryst. Sol.*, **352**, 1466 (2006).
10. C. Kumar and A. Mansingh, *J. Appl. Phys.*, **65**, 1270 (1989);
11. A. Mansingh and C. Kumar, *Thin Solid Films*, **167**, L11 (1988).
12. V. Reddy, K. Das, A. Dhar, S. Ray, *Semicond. Sci. Technol.*, **21**, 1747 (2006).
13. L. Zhao, Z. Zhou, H. Peng, R. Cui, *Appl. Surf. Sci.*, **252**, 385 (2005).
14. S.Sathiaraj, *Microelectronics J.*, **39,** 1444 (2008).
15. F. Akkad, A. Punnoose, G. Prabu, *Appl. Phys. A*, **71**, 157 (2000).
16. O. Tuna, Y. Selamet, G. Aygun and L. Ozyuzer, *J. Phys. D: Appl. Phys.*, **43**, 055402 (7pp) (2010).
17. http://gwyddion.net/; An SPM data visualization and analysis tool Gwyddion 2.45.
18. Handbook of Physical Vapor Deposition (PVD) Processing, D. M. Mattox (ed), Noyes Publications, 1998, ch.6, p.365.
19. D. Raoufi, A. Kiasatpour, H. Fallah, A.n Rozatian, *Applied Surface Science*, **253**, 9085 (2007).
20. H. Kobayashi, T. Ishida, K. Nakamura, Y. Nakato, H. Tsubomura, *J. Appl. Phys.,* **72,** 5288 (1992).
21. D. Mergel and Z. Qiao, *J. Appl. Phys.*, **95**, 5608 (2004).
22. S. Park, J. Han, W. Kim, M. Kwak, *Thin Solid Films*, **397**, 49 (2001).
23. G. Haake, *Appl.Phys.*, **47**, 4076 (1976).

ТЪНКИ ITO ФИЛМИ КАТО ПРОВОДИМИ ПРОЗРАЧНИ ЕЛЕКТРОДИ

Сн. Китова, В. Манков, Д. Димов, В. Стрижкова и Н.Малиновски

Институт по оптически материали и технологии "Акад. Й. Малиновски",
Българска Академия на науките,ул. "Акад. Г. Бончев", бл. 109, 1113 София, България

(Резюме)

В работата са представени резултатите от подробно изследване на структурни, електрически и оптични свойства на индиево-калаени (ITO) филми с различна дебелина. Филмите са отложени при различни условия на RF разпрашване на ITO таргет в чиста атмосфера от Ar газ в отсъствие на кислород. Изследвана е зависимостта на листовото съпротивление (R_{sh}) и оптичната пропускливост (T) на получените ITO филми от приложеното напрежение на разпрашване, температура на подложката и дебелина на филма. Направена е оценка за качеството на отложените филми като прозрачни проводящи електроди. Резултатите от проведеният рентгеноструктурен анализ (XRD) показват, че получените ITO тънки слоеве притежават поликристална струйтура с предпочитана (111) ориентация. Установено е, че филмите, отложени при по-високи напрежения на разпрашване са с по-ниска грапавост, значително по-ниско листово съпротивление и по-висока оптична пропускливост. Гладки и равномерни филми с ниско R_{sh} = 8 Ω/sq и средна пропускливост над 82% във видимия диапазон 400-800 nm са получени при отлагането на ITO върху стъклени подложки без тяхното допълнително отгряване.

Application and spectral characterization of vapour deposited 4-aminoazobenzene dyes nanosized films

D. Dimov[1]*, L. Nedelchev[1], D. Nazarova[1], D. Ivanov[1], G. Mateev[1], E. Bubev[2], A. Georgiev[2], D. Yancheva[3], I. Zhivkov[1,4], M. Machkova[2]

[1]*Institute of Optical Materials and Technologies, 1113 Sofia, 109 "Acad. G. Bonchev" Blvd., Bulgarian Academy of Science, Bulgaria*

[2]*Department of Organic and Physical Chemistry, 1756 Sofia, 8 "St. Kliment Ohridski" Blvd, University of Chemical Technology and Metallurgy, Bulgaria*

[3]*Laboratory of Structural Organic Analysis, Sofia 1113, 9 "Acad. G. Bonchev" Blvd., Institute of Organic Chemistry with Centre of Phytochemistry, Bulgarian Academy of Science, Bulgaria*

[4]*Materials Research Centre, Faculty of Chemistry, Purkyňova 118, Brno, Brno University of Technology, Czech Republic*

In this paper two types of 4-aminoazobenzene derivatives were vapour deposited and investigated as nanosized films. The films were characterized by UV-VIS spectroscopy. Birefringence was induced in the films by pump lasers with wavelengths of 355 nm and 444 nm within the absorbance band of the azo chromophores used. Laser light at 635 nm was used to probe the photoinduced birefringence. The recording dynamics and temperature dependence of birefringence have been presented. It was found that 4-aminoazobenzene derivative nanosized films have good photoanisotropic properties for optoelectronic device application.

Keywords: Vapour deposition, 4-aminoazobenzene derivatives, Azo dyes, Thin films, Photoinduced birefringence.

INTRODUCTION

Azobenzene dyes undergo *trans→cis* photoisomerization by laser irradiation with an appropriate wavelength. The reverse *cis→trans* isomerization can be driven by light or occurs thermally in the dark. Azobenzene's photochromatic properties make it an ideal component of numerous molecular devices and functional materials [1]. According to the spectral properties, nature and position of the substituents in the aromatic rings azobenzene derivatives can be classified (by Rau) [2] as: (i) azobenzene derivatives (ABn); (ii) aminoazobenzene derivatives (aAB); (iii) pseudostilbenes (pSB). The pseudostilbenes "push-pull" azo dyes are good chromophores for photoinduced birefringence with blue or green laser pump. The photoinduced birefringence is due to reorientation of azobenzene molecules perpendicular to the polarization of the recording light [3]. It is defined as $\Delta n = n_\perp - n_\parallel$, where $n_\perp$ is the component of the refractive index perpendicular to the polarization of the recording beam, and $n_\parallel$ is the component parallel to it. Therefore the illumination in UV-VIS region where the $\pi \to \pi^*$ absorbs is an efficient process for photoinduced orientation [4]. The substituents influence isomerization of azobenzenes by steric and electronic effects. The presence of electron withdrawing (EW) groups like –COOH, -CHO, -CN, -NO$_2$ decrease the energy of the electron transitions, where the $\pi \to \pi^*$ and $n \to \pi^*$ bands are well separated. The electron donating (ED) substituents lead to unsymmetrical electron distribution (push-pull) and effectively conjugation with lower resonance energy compared to the unsubstituted azobenzenes [1, 4]. Smart surface design on photoisomerizable materials has attracted much attention because of potential applications as optical photoswitches, reversible information storage, organic solar cells, bioengineering devices, nonlinear optic materials, polyelectrolyte multilayers, liquid crystals and other photoactive and photomechanical devices [5, 6]. Therefore in this paper we have investigated two "push-pull" azobenzenes dyes (Azo-a and Azo-d) for optical data storage by photoinduced birefringence with

* To whom all correspondence should be sent:
E-mail: dean@iomt.bas.bg

laser pump at λ = 355 and 444 nm as vapour deposited nanosized films. The electron transitions spectra were calculated by TD-DFT/ B3LYP functional combined with the standard 6-31+G(d,p) basis set in vacuo in order to predict the excitation energies and comparison with experimental results.

EXPERIMENTAL

Vapour deposition of nanosized films

The thin films of azo dyes were prepared by evaporation from Knudsen type vessels on quartz substrates. The temperature of evaporation was kept between 45-60°C. Temperature of substrate was 15°C, controlled by thermal regulator with Peltier element. Sample thickness was 230 nm for Azo-a and 70 nm for Azo-d. They are measured by high-precision Talystep profilometer with 10 nm accuracy. Samples were evaporated on substrates of glass and melted quartz.

Spectral characterization

The UV-VIS spectra were recorded on a Cary 5E (Varian) spectrophotometer in the 250 - 800 nm range as nanosized films on quartz substrates.

Birefringence measurement

The birefringence (Δn) was determined by measuring the Stokes parameters of probe laser beam (λ_{probe} = 635 nm, power <2 mW) passing through the samples. The measurement was performed by PAX5710 Polarimeter (Thorlabs) and Δn is calculated from the Eq. 1 [7, 8]:

$$\Delta n = \frac{\lambda_{probe}}{2\pi d}\arctan\left(\frac{S_3}{S_2}\right) \qquad (1)$$

where *d* is the film thickness, and S_2 and S_3 are two of the four Stokes parameters. Birefringence is induced independently by two diode pumped solid state (DPSS) lasers: (i) an UV laser with wavelength λ_{rec1} = 355 nm and power 20 mW, and (ii) a visible blue laser with λ_{rec2} = 444 nm and power 35 mW. The thermal erasure was studied using heating stage THMS600 (Linkam Scientific) with temperature stability <0.1°C. Rate of heating was set to 1°C/min.

Quantum chemical calculations

The optimization of molecular geometry and excitation states of the studied molecules were performed by GAUSSIAN 09W software package using Time-Dependent Density-Functional Theory TD-DFT/ B3LYP functional combined with the standard 6-31+G(d,p) basis set in vacuo [9].

RESULTS AND DISCUSSION

Fig. 1 presents calculated and experimental electronic (UV-VIS) spectra of vapour deposited nanosized films of Azo-a and Azo-d. The electron transitions π→π* (S_0→S_2) λ_{max} = 376 and 328 nm and n→π* (S_0→S_1) λ_{max} = 461 nm bands of Azo-a is separated due to the unsymmetrical electron distributions (push-pull) of two EW -NO$_2$ groups at positions 2' and 4', while in the spectra of Azo-d they are overlapped in a broad peak at λ_{max} = 351 nm because of properties of the ED groups: -CH$_3$ (+I effect) at position 2' and -Br (–I and +M effects) at position 4'. The calculated spectrum of Azo-a is in a good agreement with experimentally obtained from nanosized film data, while for Azo-d the experimental λ_{max} was shifted 57 nm higher in the energy scale compared to the computed spectrum. Quantum mechanics determines the properties of nanomaterials with one dimension in the range 1 to 100 nm, and calculation methods to deal with nanomaterials are being developed. When one or more dimensions of a material fall below 100 nm, especially below 20 nm, dramatic changes in the optical, electronic, chemical, and other properties from those of the bulk material can occur. The reason is behavior of the materials close to the properties of single molecule in vacuo.
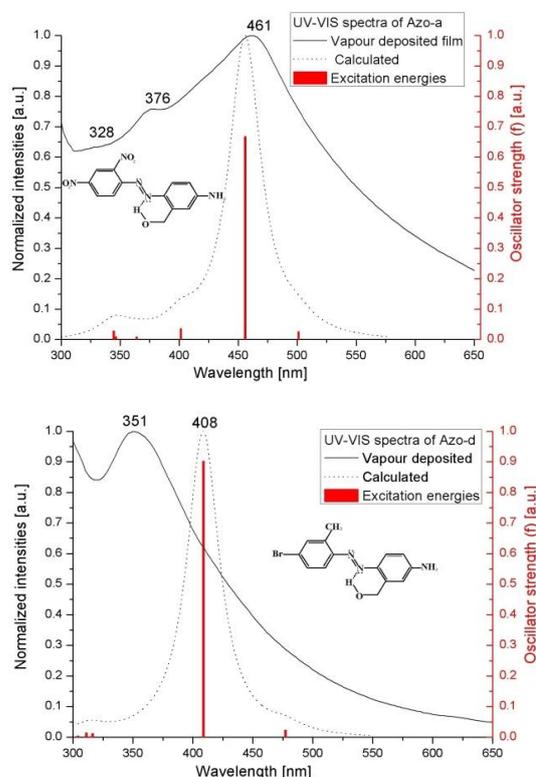
Fig. 1. UV-VIS spectra of Azo-a and Azo-d as vapour deposited nanosized films and theoretically calculated by TD-DFT/ B3LYP 6-31+G(d,p) level of theory in vacuo.

The UV-VIS spectra of azo dyes have determined the futher investigation of photoinduced birefringence with laser pump at λ = 355 and 444 nm for potential application in optical storage devices or diffractive optical elements with unique polarization properties [7]. Fig. 2 presents the data from the birefringence measurement of Azo-d. During the first 60 sec only the probe beam is on allowing to determine the measurement baseline. Then the recording laser is started and increase of the birefringence is observed. Its maximal value is $\Delta n_{max} = 0,006$ for $\lambda_{rec1} = 355$ nm, and $\Delta n_{max} = 0,01$ for $\lambda_{rec2} = 444$ nm. After 300 sec from the beginning of experiment the recording laser is stopped. There is an initial decrease of the birefringence, but then it reaches a stable state with more than 70% of the anisotropy retained in the film. This indicates good stability and possibility to use these azo dyes for various applications.

The temperature dependence of the birefringence is shown in Fig. 3. The values plotted are normalized to the birefringence value measured for the starting temperature of 26°C.

(a)

(b)
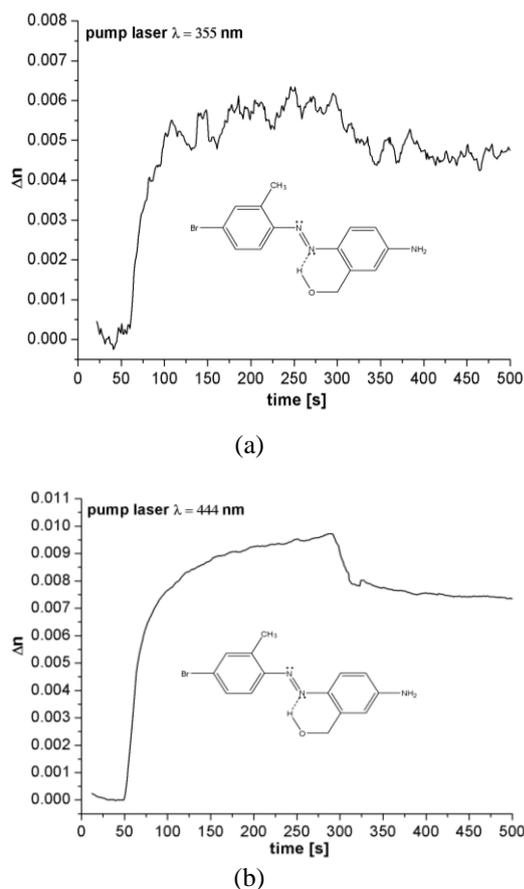
Fig. 2. Time dependence of the photoinduced birefringence Δn in Azo-d in case of recording with pump lasers with wavelengths: (a) 355 nm, and (b) 444 nm, respectively.
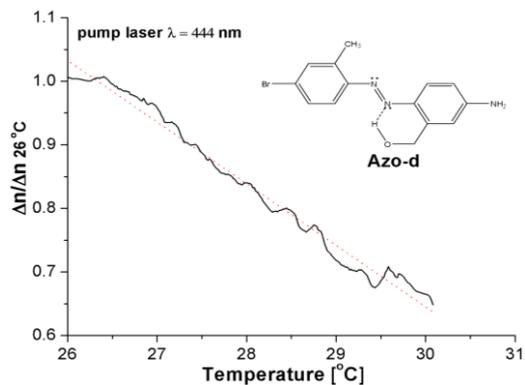
Fig. 3. Temperature dependence of the birefringence in Azo-d. Birefringence is recorded on illumination at 444 nm

CONCLUSIONS

Two "push-pull" azo dyes (Azo-a and Azo-d) were vapour deposited as nanosized thin films. The experimental UV-VIS spectra were compared with the theoretically calculated ones. It was found that the calculated spectrum of Azo-a is in a good agreement with the experimentally measured data, while for Azo-d the experimental λ_{max} value was shifted 57 nm higher in the energy scale compared to the computed spectrum. When the layer is less than 100 nm thick the properties of the film are more close to the properties of single molecule. The observed 57 nm shifting most probably is a result of the impact of Br atom and the interaction of molecules with each other. Vapour deposited nanosized film of Azo-d was investigated by optical birefringence for a potential application as optical storage material. It has been found after pump laser wavelengths at λ = 444 nm and 355 nm the stable state with more than 70% of the anisotropy is retained in the film.

REFERENCES

1. H. Bandara and S.Burdette, *Chem. Soc. Rev*., **41,** 1809 (2012).
2. H. Rau, in: Photoreactive Organic Thin Films*,* (eds.) Zhao, Y. & Ikeda, T. Elsevier Sci. Ltd, 2002, p. 3-48.
3. T. Todorov, L. Nikolova, N. Tomova, *Appl. Opt.*, **23**, 4309 (1984).

4. A. Natansohn, P. Rochon, *Chem. Rev.,* **102,** 4139 (2002).

5. K. Yager and C. Barrett, Azobenzene Polymers For Photonic Applications, (eds.) Yue Zhao and Tomiki Ikeda, Book chapter in Smart Light-Responsive Materials, John Wiley & Sons Inc., 2009, p. 1-27.

6. L. Zhan, J. Cole, *Appl. Mater. & Interfaces,* **6,** 3742 (2014).

7. L. Nedelchev, A. Matharu, S. Hvilsted, P. S. Ramanujam, *Appl. Opt., 42*, 5918 (2003).

8. L. Nikolova, P. S. Ramanujam, Polarization Holography, Cambridge Univ. Press, Cambridge, 2009.

9. M. Frisch, G. Trucks, H. Schlegel, G. Scuseria, M. Robb, J. Cheeseman, G. Scalmani, V. Barone, B. Mennucci, G. Petersson, H. Nakatsuji, M. Caricato, X. Li, H. Hratchian, A. Izmaylov, J. Bloino, G. Zheng, J. Sonnenberg, M. Hada, M. Ehara, K. Toyota, R. Fukuda, J. Hasegawa, M. Ishida, T. Nakajima, Y. Honda, O. Kitao, H. Nakai, T. Vreven, J. Montgomery, J. Peralta, F. Ogliaro, M. Bearpark, J. Heyd, E. Brothers, K. Kudin, V. Staroverov, R. Kobayashi, J. Normand, K. Raghavachari, A. Rendell, J. Burant, S. Iyengar, J. Tomasi, M. Cossi, N. Rega, J. Millam, M. Klene, J. Knox, J. Cross, V. Bakken, C. Adamo, J. Jaramillo, R. Gomperts, R. Stratmann, O. Yazyev, A. Austin, R. Cammi, C. Pomelli, J. Ochterski, R. Martin, K. Morokuma, V. Zakrzewski, G. Voth, P. Salvador, J. Dannenberg, S. Dapprich, A. Daniels, O. Farkas, J. Foresman, J. Ortiz, J. Cioslowski, and D. Fox, Gaussian, Inc., Wallingford CT, 2009.

ПРИЛОЖЕНИЕ И СПЕКТРАЛНО ХАРАКТЕРИЗИРАНЕ НА ОТЛОЖЕНИ 4-АМИНОАЗОБЕНЗЕН БАГРИЛА В НАНОРАЗМЕРНИ ФИЛМИ

Д. Димов[1], Л. Неделчев[1], Д. Назърова[1], Д. Иванов[1], Г. Матеев[1], Е. Бубев[2], А. Георгиев[2], Д. Янчева[3], И. Живков[1,4], М. Мачкова[2]

[1]*Институт по оптични материали и технологии, София 1113, 109 "Акад. Г. Бончев", Българска академия на науките, България*

[2] *Катедра Органична химия и физикохимия, 1756 София, бул "Свети Климент Охридски" 8, Химикотехнологичен и металургичен университет, България*

[3] *Лаборатория по конструктивно органичен анализ, София 1113, 9 "Акад. Г. Бончев", Институт по органична химия с Център по фитохимия, Българска академия на науките, България*

[4] *Изследователски център по материалознание, Химически факултет, ул.Пуркинова 118, Бърно, Бърно технологичен университет, Чехия*

(Резюме)

В статията са изследвани два вида вакуумно отложени 4-аминоазобензенови производни като наноразмерни филми. Филмите са изследвани с UV-VIS спектроскопия. Оптично индуцираното двулъчепречупване е изследвано чрез пробен лазер с дължина на вълната 635 нм. Изследването е направено чрез възбуждане с напомпващи лазери с дължини на вълните 355 нм и 444 нм от абсорбционните спектри на азобагрилата. Изследвани са зависимостите от времето и температурата на двулъчепречупването на азохромофорите. Установено е, че 4-аминоазобензеновите производни като наноразмерни филми притежават добри фотоанизотропни свойства за приложение в оптоелектронни устройства.

Bright green Phosphorescent Organic Light-Emitting Diode with doped Hole Transporting Layer

P. Ivanov*, P. Petrova, R. Tomova

Institute of Optical Materials and Technologies "Acad. J. Malinowski",
Bulgarian Academy of Sciences, Acad. G. Bonchev str. bl. 109, 1113 Sofia,Bulgaria

The application of green phosphorescent complex Tris[2-phenylpyridinato-C^2,*N*]iridium(III) - Ir(ppy)$_3$ as a dopant in the hole transporting layer (HTL) of Organic light emitting diode (OLED) structure: HTL/ElL/ETL has been studied. We have found that devices containing from 4 wt.% - 6 wt.% Ir(ppy)$_3$ emit pure green light with CIE (x;y) chromaticity coordinates 0.2969; 0.4860 - 0.3184; 04905 very close to these of the ideal green color 0.3; 0.6, which is recommended at the displays manufacturing.

INTRODUCTION

Since Baldo et al. reported the first example of electrophosphorescence at room temperature, phosphorescent materials have attracted much attention due to their high external quantum efficiencies in organic light emitting diodes (OLEDs) [1, 2]. Extensive investigations of phosphorescent materials have focused on d^6 and d^8 heavy metal complexes such as Os(II) [3], Ir(III) [4, 5] and Pt(II) [6]. OLEDs based on those phosphorescent materials can significantly improve electroluminescent performances because both singlet and triplet excitons can be harvested for light emission by strong spin-orbit coupling. The internal quantum efficiency of phosphorescent emitters can theoretically approach 100%, and the external quantum efficiency can approach 20% [7, 8, 9]. Due to their strong spin-orbit coupling, these complexes can burrow intensity from the singlet metal-to-ligand-charge-transfer (^{1}MLCT) state and emit effectively from their triplet ^{3}MLCT states. Among all phosphorescent complexes these based on iridium recently are the subject of intensive studying, because Ir atom owns intense phosphorescence at room temperature, stable and accessible oxidation and reduction states and quasi-octahedral geometry, permitting introducing of specific ligands in a controlled manner [1, 10, 11].

Tris[2-phenylpyridinato-C^2,*N*]iridium(III)

(Ir(ppy)$_3$) is one of the most important materials for phosphorescent OLED as its emission color at λ_{max} = 514 nm matches well to the Commission Internationale d'Eclairage coordinates (CIE(x/y)) for green color (0.3;0.6), that makes it very suitable for use in the production of full color displays [12-15]. The high efficiency devices with Ir(ppy)$_3$ doped with electroluminescent layer is based on (i) the high cross-section for formation of electron-hole pairs (singlet and triplet excitons) on Ir(ppy)$_3$ in matrix materials, (ii) a fast intersystem crossing from the excited singlet to the emitting triplet states, and (iii) on the high emission quantum yield of about 40% of the triplet sub-states at ambient temperature [11]. Usually as a host matrix for Ir(ppy)$_3$ guest are preferred materials with wide band gap: small molecule compounds as 4,4′-N,N′-Dicarbazolylbiphenyl (CBP) [16-19]; 4,4',4"-tri(N-carbazolyl) triphenylamine (TCTA) [20]used in multilayered OLEDs obtained by thermal evaporation, and Poly(9-vinylcarbazole) (PVK) in monolayer electrophosphorescent polymer light-emitting diodes (PLED) produced by spin coating or spin casting. PVK is one of the widely used polymers because in addition to its large HOMO–LUMO separation, owns relatively high value of the lowest triplet state T^1 (about 2.5 eV) preventing back crossing of the triplet exciton from the phosphor to the host triplet state [21-23]. The main advantage of using a polymer matrix as a host material in comparison with such based on small molecule compound is the easy manner of control

---

* To whom all correspondence should be sent:
E-mail: ivanov.petar@mail.bg

of the dopant concentration. That is why, in recent years high-performance devices fabricated by employing Ir(ppy)₃ incorporated in conjugated and non-conjugated polymer hosts were reported [12, 24] although PLEDs are less efficient than small molecule type devices.

In this paper we present the results obtained for OLED structure with Ir(ppy)₃ doped composite hole transporting layer (HTL) of PVK:TPD in effort to obtain appropriate for display application device emitting pure and stable green light with CIE coordinates close to these of the ideal green color (0.3**;**0.6).

EXPERIMENTAL

OLED fabrication

We investigated the multilayered OLED structure of ITO/doped-HTL/ElL/ETL/M, where ITO was a transparent anode of In₂O₃:SnO₂, M - a metallic Al cathode, HTL -N,N′-Bis(3-

methylphenyl)-N,N′-diphenylbenzidine (TPD) involved in poly(N-vinylcarbazole) (PVK) matrix, ElL - electroluminescent layer of Bis(8-hydroxy-2-methylquinoline)-(4-phenylphenoxy)aluminum (BAlq) and ETL - electron-transporting layer of Bis[2-(2-benzothiazoly)phenolato]zinc (Zn(bt)₂). Devices with area of 1cm² were prepared on commercial polyethylene terephtalate (PET) substrates coated with ITO (40 Ω/sq). The layer (30 nm) of PVK:TPD (10%(relatively to PVK) + Ir(ppy)₃ composite films were prepared by spin-coating from 0.75% PVK solution in dichloroethane at 2000 rpm. Other organic layers BAlq (40nm) and Zn(bt)₂ (35nm), and the Al cathode (100nm) were deposited by thermal evaporation in vacuum better than 10^{-4} Pa at rates 2-5 Å/s, without interrupting the vacuum. The layers thicknesses were controlled in situ with quartz crystal microbalance sensor, positioned near the PET/ITO substrate.
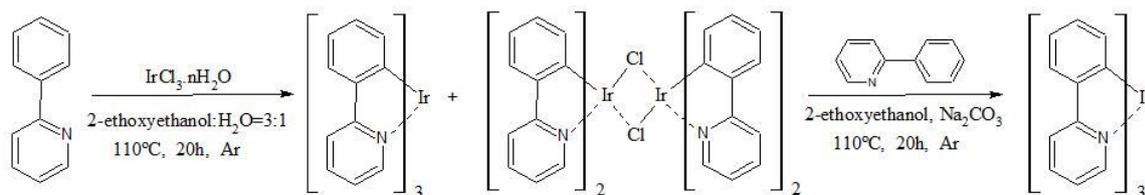
Fig. 1. Scheme of the synthesis of Ir(ppy)₃ complex.

All materials were purchased from Sigma-Aldrich Co. LLC., except Ir(ppy)₃ complex, which was synthesized by us according to procedure developed by King et al. [25] (Fig. 1). 2-Phenylpyridine(1) (2.2 equiv), and iridium trichloride hydrate (1 equiv) dissolved in 2-ethoxyethanol: water = 3:1 were stirred for 20 h at 110 °C under argon atmosphere. After that, the cooled to the room temperature reaction mixture was filtrated. The obtained greenish precipitate was washed with ethanol and hexane several times, and dried at room temperature.

Instruments and measurements

The photoluminescence emission (Pl) spectra of PVK and TPD, electroluminescent emission (El) spectra of OLEDs, and CIE (x;y) chromaticity coordinates of emitted light were obtained by Ocean Optics HR2000+ spectrometer. The excitation (Exc) and Pl spectra of Ir(ppy)₃ complexes were recorded on a Jobin–Yvon–Horiba Fluorolog III spectrofluorometer. The current-

voltage (I-V) curves were measured by programmable with Labview power supply. The electroluminescence (EL) was determined in DC (direct current) mode and the light output was detected using a calibrated Hamamatsu silicon photodiode S2281-01. The current efficiency (η_EL) was calculated by equation (1) and used for quantifying the properties of the OLEDs.

$$\eta_{EL} = EL/I \qquad (1)$$

where EL is the electroluminescence (in cd/m²), I is the current density (in A/m²).

All measurements of OLED structures were performed at room temperature and under ambient conditions, without any encapsulation.

RESULTS AND DISCUSSION

Excitation and photoluminescence

The excitation spectrum, taken at λ_emiss = 536 nm, and photoluminescence emission spectrum, taken (at λ_excit = 400 nm) of Ir(ppy)₃ in CH₂Cl₂ solution are shown in Fig. 2. It is seen that in Exc

spectrum of Ir(ppy)$_3$ there are two excitation bands. The first is centered at region below 300 nm and contains bands for electronic transitions, which lead to excitations in ligands themselves, most probably due to transition to lowest singlet ligand centered (^{1}LC) excited state. The second band is very broad, piked at 372 nm and is connected to singlet and triplet metal to ligand charge transfer (^{1}MLCT, ^{3}MLCT). Effective spin-orbit coupling (SOC) in this complex relax the spin forbiddance and mix the singlet and triplet states making the band for resonant transition $^1S_0 \rightarrow ^3$MLCT detectable in Exc spectrum (around 480 nm).
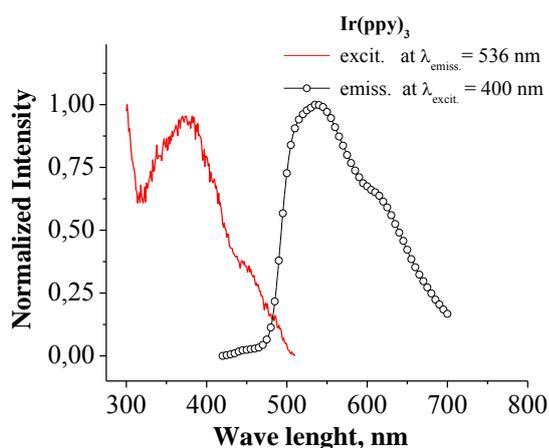
Fig. 2. Excitation (at $\lambda_{emiss.}$ = 536 nm) and photoluminescence emission (at $\lambda_{excit.}$ = 536 nm) spectra of Ir(ppy)$_3$ CH$_2$Cl$_2$ solution.
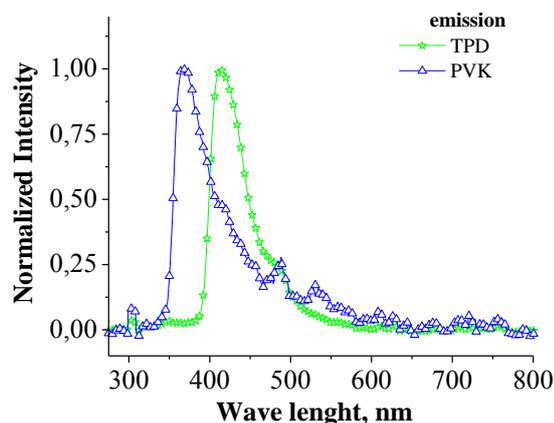
Fig. 3. Photoluminescence emission spectra of PVK and TPD in CH$_2$Cl$_2$ solution taken under excitation with tungsten halogen white light sources (LS-1, Ocean Optics Inc.).

The Pl spectra of PVK and TPD in CH$_2$Cl$_2$ solution taken under excitation with tungsten halogen white light sources (LS-1, Ocean Optics Inc.) are presented in Fig. 3. As can be seen PVK and TPD emit a blue light with peaks at 367 and 415 nm respectively and exhibit good spectral

overlapping with MLCT excitation bands of Ir(ppy)$_3$ ranged from 360 nm to 480 nm, which is a good prerequisite for the efficient Förster or Dexter energy transfer from the host (PVK:TPD) to the Ir(ppy)$_3$ guest.

The Pl emission spectrum of Ir(ppy)$_3$ in non-degassed CH$_2$Cl$_2$ at room temperature obtained under excitation at 400 nm exhibited strong green phosphorescence with maximum emission peak at 533 nm and shoulder at 608 nm.

Electroluminescence

In Fig. 4 are shown the normalized El spectra of investigated device HTL:Ir(ppy)$_3$(x)/ BAlq(40 nm) /Zn(bt)$_2$(35nm) at different doping concentration x (wt.%) and referent devices HTL/Zn(bt)$_2$(75nm) and HTL/BAlq(75nm). For comparison the El spectrum of OLED structure HTL/Alq$_3$(75), widely used for its pure green fluorescent emission, is also presented. As might be seen device with ElL of BAlq emits at 496 nm, and these with Zn(bt)$_2$ and Alq$_3$ relatively at 533nm and 528 nm. The shape of El spectrum of OLED with consequent evaporated layers of BAlq(40)/Zn(bt)$_2$(35nm) was just the same as that of OLED with BAlq. In our opinion, as the HOMO level (5,05 eV) of Zn(bt)$_2$ is much lower than HOMO level (5,90 eV) of BAlq, the Zn(bt)$_2$ cannot stop the holes and they leakage unimpeded from Zn(bt)$_2$ layer. By this reason in BAlq/Zn(bt)$_2$ structure Zn(bt)$_2$ acts the role only of ETL.
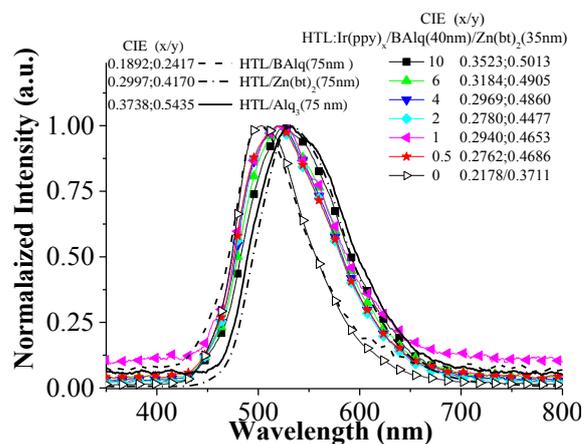
Fig. 4. Normalized electroluminescence spectra of devices HTL/Balq(75nm), HTL/Zn(bt)2(75nm), HTL/Alq3(75nm), and HTL:Ir(ppy)3(x wt.%) /Balq(40)/Zn(bt)2(35nm) (at different concentrations x), viewed in the normal direction at a benchmark of 18 V DC, and their CIE (x;y) chromaticity coordinates.

The El spectra of doped devices did not include any PVK and TPD emissions that points out the effective charge trapping on the Ir(ppy)$_3$ and/or

effective energy transfer from host to the complex guest. The increasing of the dopant concentration x caused a decreasing of the relative intensity of the bluish-green emission of BAlq at 496 nm, and red shifting of λ_{max} and CIE (x;y) coordinates from 504 nm and 0,2178;0, 3711 (bluish-green) for undoped device to 525 nm and 0,3523; 0,5013 (greenish-yellow) for device doped with 10 wt.% of $Ir(ppy)_3$. Devices doped with 4 wt.%≤ x ≤ 6 wt.% demonstrated CIE (x;y) coordinates in the range from 0.2969; 0.4860 to 0.3184; 04905 which were a lot closer to these of the ideal green color 0.3; 0.6 in comparison with these (0.3738; 0.5435) displayed by OLED with ElL of Alq_3.
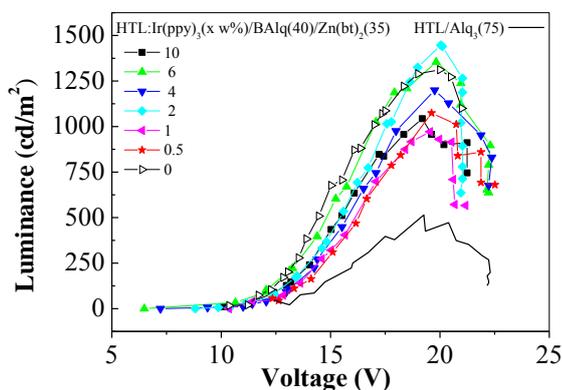
Fig. 5. Electroluminescence – voltage characteristics of devicesHTL:$Ir(ppy)_3$ (x wt.%)/BAlq(40nm)/Zn(bt)$_2$ (35nm) and HTL/Aq$_3$(75nm).
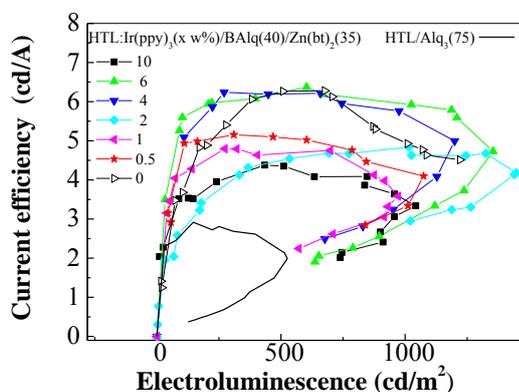
Fig. 6. Current efficiency as a function of electroluminescence of devices HTL:$Ir(ppy)_3$ (x wt.%)/BAlq(40nm)/Zn(bt)$_2$ (35nm) and HTL/Aq$_3$(75nm).

The influence of the dopant concentration on intensity of electroluminescence as a function of applied voltage and on current efficiency as a function of electroluminescence are shown in Fig. 5. and Fig. 6. We established that with increasing of the dopant concentration from 0 to 1.0 wt.% the threshold voltage of all devices initially increased

from 10.2 to 11.4 V and then decreased to 8 V at 10 wt.% (Fig. 5.). At the same time the electroluminescence (at one and same voltage) (Fig. 5.) and current efficiency (at one and the same electroluminescence) (Fig. 6.) had just the opposite behavior: initially decreased from 0 to 1.0 wt.%, then increased from 1.0 wt..% to 6.0 wt..% and over 6.0 wt..% again decreased.

These results on the one hand and the absence of any PVK and TPD emission in El spectra of doped devices - on the other, show the charge trapping in the Ir complex, rather than the energy transfer, as the dominant mechanism in investigated OLEDs. At the low concentration of the dopant in host matrix the mobility limitation of a charge from one dopant site to another appears that leads to a rise of the threshold voltage. Further increasing of dopant concentration increases the charges mobility since the distance between the $Ir(ppy)_3$ molecules decreases. When the dopant concentration falls beyond a certain value, its molecules start to aggregate which causes the degradation of device performance again.

The best performance had devices doped in the range of 4 to 6 wt.% of $Ir(ppy)_3$ with their electroluminescence of 1200 – 1350 cd/m^2 at 18 V DC and current efficiency of nearly 6.25 cd/A in the range of 100 to 1200 cd/m^2 of electroluminescence. For comparison the device with ElL of Alq_3 demonstrated two times lower EL (485 cd/m^2) and current efficiency (2.75 cd/A) at the same conditions.

CONCLUSION

In summary we propose the OLED structure: HTL/BAlq/Zn(bt)$_2$ hole transporting layer doped with green phosphorescent complex $Ir(ppy)_3$. Devices containing from 4 wt.% - 6 wt.% $Ir(ppy)_3$ emit pure green light with intensity 1200 – 1350 cd/m^2 (at 18 V DC) and 6.25 cd/A current efficiency in wide range of electroluminescence (100 - 1200 cd/m^2). The CIE coordinates of emitted light in these concentration limits are in the range of 0.2969; 0.4860 - 0.3184; 04905 and they are very close to these of the ideal green color 0.3; 0.6, which is recommended for the display's manufacturing.

REFERENCES

1. M. Baldo, D. O´Brian, Y. You, A. Shoustikov, S. Sibley, M. Thompson and S. Forrest, *Nature,* **395**, 151 (1998).
2. M. Baldo, M. Thompson and S. Forrest, *Nature,* **403**, 750 (2000).
3. Y.-L. Tung, S.-W. Lee, Y. Chi, Y.-T. Tao, C.-H. Chien, Y.-M. Cheng, P.-T. Chou, S.-M. Peng and C.-S. Liu, *J. Mater. Chem.,* **15**, 460 (2005).
4. H. Xie, M. Liu, O. Wang, X. Zhang, C. Lee, L. Hung, S. Lee, P. Teng, H. Kwong, H. Zheng and C. Che, *Adv. Mater.,* **13**, 1245 (2001).
5. Y. You, C.-G. An, D. Lee, J. Kim and S. Park, *J. Mater. Chem.,* **16**, 4706 (2006).
6. G. Zhou, X. Wang, W. Wong, X. Yu, H. Kwok and Z. Lin, *J. Organomet.Chem.,* **692,** 3461 (2007).
7. C. Adachi, M. Baldo, S. Forrest and M. Thompson, *J. Appl. Phys.* **90,** 4058 (2001).
8. M. Ikai, S. Tokito, Y. Sakamoto, T. Suzuki and Y. Taga, *Appl. Phys. Lett.,* **79**, 156 (2001).
9. C. Adachi, S. Lamansky, M. Baldo, R. Kwong, M. Thompson and S. Forrest, *Appl. Phys. Lett.,* **78**, 1622 (2001).
10. W. Holzer, A. Penzkofer and T. Tsuboi, *Chem. Phys.,* **308**, 93 (2005).
11. L. Han, D. Zhang, J. Wang, Z. Lan and R. Yang, *Dyes and Pigments* **113**, 649 (2015).
12. M. Kolombo and H. Gudel, *Inorg. Chem.,* **32**, 3081 (1993).
13. Y. Kawamura, K. Goushi, J. Brooks, J. Brown, H. Sasabe and C. Adachi, *Appl. Phys. Lett.,* **86,** 071104-3 (2005).
14. X. Gong, J. Ostrowski, D. Moses, G. Guillermo, C. Bazanand A. Heeger, *Adv. Funct. Mater.,* **13**, 439 (2003).
15. M. Baldo, S. Lamansky, P. Burrows, M. Thompson and S. Forrest, *Appl. Phys. Lett.,* **75**, 4 (1999).
16. A. Kawakami, H. Bekku, E. Otsuki, R. Wada, H. Kita, H. Taka, H. Sato and H. Usui, *JJAP,* **47** (2), 1284 (2008).
17. C. Qiu, H. Peng, Z. Xie, H. Chen, M. Wong and H.-S. Kwok *SID 04 DIGEST* www.cdr.ust.hk/publications/research_pub/.../**SID** P_107.
18. S.-K. Kwon, K. Thangaraju, S.-O. Kim, Kang Y. and Y.-H. Kim, The Efficient Green Emitting Iridium(III) Complexes and Phosphorescent Organic Light Emitting Diode Characteristics, Organic Light Emitting Diode, Marco Mazzeo (Ed.), InTech (2010), http://www.intechopen. com/books/organic-light-emitting-diode/the-efficient-green-emitting-iridium-iii-complexes-and-phosphorescent-organic-light-emitting-diode-c.
19. Haldi, B. Domercq, B. Kippelen, R. Hreha, J.-Y. Cho and S. Marder *Appl. Phys. Lett.,* **92**, 253502 (2008).
20. M. Ikai, S. Tokito, Y. Sakamoto, T. Suzuki, and Y. Taga, *Appl. Phys .Lett.,* **79**, 156 (2001).
21. Y.-R. Li, S.-L. Zhao, F.-J. Zhang, Z. Xu and D.-D. Song *Appl. Surf. Sci.*, **255,** 2404 (2008).
22. Y.-B. Li, Y.-B. Hou, F. Teng and Xu X.-R. *Chin. Phys. Lett.,* **21** (7), 1362 (2004).
23. I. Glowacki and Z. Szamel, *Org. Electron.*, **24,** 288 (2015).
24. X.-H. Yang, F. Jaiser, D. Neher, in: Highly Efficient OLEDs with Phosphorescent Materials H. Yersin (Ed.) WILEY-VCH Verlag GmbH & Co. KGaA, Weinheim, 2008. p.251.
25. I. King, P. Spellane and R. Watts, *J. Am. Chem. Soc.*, **107,** 1431 (1985).

ЯРКО ЗЕЛЕН ФОСФОРЕСЦЕНТЕН ОРГАНИЧЕН СВЕТО ДИОД С ДОТИРАН ТРАНСПОРТИРАЩ ПОЛОЖИТЕЛНИТЕ ЗАРЯДИ СЛОЙ

П. Иванов, П. Петрова, Р. Томова

Институт по Оптически Материали и Технологии "Акад. Йордан Малиновски"
Българска Академия на Науките, ул. Акад. Г. Бончев, бл.109, 1113, София, България

(Резюме)

Разработена е структура на органичен свето диод (ОЛЕД) HTL/BAlq/Zn(bt)₂, в която слоят осигуряващ придвижването на положителните заряди (HTL) е дотиран с фосфоресцентния иридиев комплекс Tris[2-phenylpyridinato-C^2,N]iridium(III) - Ir(ppy)₃. Изследвано е влиянието на концентрацията на допанта върху запалващото напрежение, силата на тока, интензитета и цвета на излъчваната светлина. Установено е, че при концентраци на Ir(ppy)₃ от 4 до 6 тегл.% ОЛЕДите излъчват светлина с интензитет 1200 – 1350 cd/m^2 (при напрежение 18 V) и демонстрират стабилна токова ефективност от 6.25 cd/A в широк диапазон от стойности на интензитета на светлината 100 - 1200 cd/m^2. В тези концентрационни граници цветът на излъчваната светлина е с CIE (x;y) координати 0.2969; 0.4860 - 0.3184; 04905, които са много близки до тези на идеалния зелен цвят 0.3; 0.6, препоръчван за производството на дисплеи. Това прави предлаганата ОЛЕД структура обещаваща за приложение в това направление.

Vacuum co-deposition of organic solar cell structures

G. Georgieva[1], D. Dimov[2], G. Dobrikov[3], D. Karashanova[2], A. Kirilov[4], F. Markova[4], E. Bubev[4], A. Georgiev[4], R. Yordanov[3], and I. Zhivkov[1, 2,*]

[1]*Faculty of Chemistry, Centre for Materials Research, Brno University of Technology, Purkynova 118, 612 00 Brno, Czech Republic*
[2]*Institute of Optical Materials and Technologies "Acad. J. Malinowski", Bulgarian Academy of Sciences, Acad. G. Bonchev Str. bl. 101/109, 1113 Sofia, Bulgaria*
[3]*Department of Electronics, Faculty of Electronic Engineering andTechnologies, Technical University - Sofia, 8 Kliment Ohridski blvd., 1000 Sofia, Bulgaria*
[4]*Department of Organic and Physical Chemistry, 1756 Sofia, 8 "St. Kliment Ohridski" Blvd, University of Chemical Technology and Metallurgy, Bulgaria.*

An algorithm for calculation the mass ratio between evaporated components in vacuum co-deposition is presented. The algorithm is demonstrated via preparation of organic solar cells. Zinc phthalocyanine (ZnPc) based solar cell samples of types ITO|PEDOT:PSS|ZnPc:C_{60}|Al were prepared in a clean room conditions. The active bulk heterojunction (BHJ) organic composite ZnPc:C_{60} film was prepared with mass ratio of 4.2:1. The surface morphology was characterized by SEM. Photoelectrical measurements were carried out on the samples prepared, demonstrating the advantages of the composite material with respect to the single ZnPc layer. The algorithm developed allows further precise optimization of the BHJ cells to be performed.

Keywords: vacuum co-deposition, organic electronics, solar cells.

INTRODUCTION

Thin films of low molecular weight semiconductors are usually prepared by variety of complex techniques, including physical or chemical vapour deposition, organic molecular beam epitaxy or solution-based deposition techniques. The performance of small molecular organic devices is highly sensitive to the film morphology and processing conditions. Often, the solution-deposited active layers of devices (e.g. spin coated films) exhibit a high portion of microcrystallites and aggregates. The vapour deposition techniques provide high-quality crystalline films characterized by improved charge-transport properties compared with those of solution-deposited films. The vacuum technique has the advantage of dry film deposition process excluding the usage of solvents. Moreover this technique provides more opportunities to control important film parameters as film thickness and uniformity. As a consequence the films deposited exhibit more stable and reproducible properties with a comparison to solution deposited films.

In the last decades it has been shown that the charge separation on the donor acceptor interface considerable increases the efficiency [1].

The simplest way to provide the charge separation in the organic substances is the formation of bi-layer donor/acceptor structure [2]. In case of insoluble donor and acceptor materials the vacuum deposition suggests possible solution for bi-layer structure formation.

Further increase of the efficiency was achieved introducing p-i-n structures. Pfeiffer and co-workers [3, 4] have developed p-i-n technology using high vacuum deposition process. Efficiency of 3.6% has been obtained.

The exciton diffusion length in the organic semiconductors is about 10 nm but the optimized light absorption requires film thicknesses of about 100 nm. This discrepancy makes the bi-layer structure less effective.

This problem is overcome later developing the BHJ structure. BHJ comprises an active layer with mixed donor and acceptor species to allow for much thicker films to better absorb sunlight [5]. Vacuum co-deposition allows easier way to obtain BHJ composite layer, grown from insoluble

*To whom all correspondence should be sent:
E-mail: zhivkov@fch.vutbr.cz

components.

Also the optimization of the organic solar cells needs a variety of additional layers to be deposited like hole transporting layer (HTL), electron transporting layer (ETL), electron blocking layer (EBL), etc. Such a comprehensive multilayer structure is usually obtained by subsequent vacuum deposition of separate layers without breaking the vacuum.

Following the strategy of the multilayer devices a tandem solar cell was developed [6, 7]

The ultimate goal of stacking PHJ solar cells in a tandem configuration is to have many interfaces for efficient exciton dissociation while maintaining a summative thick film for absorption of light. One may also absorbs a broader spectrum of light through the use of different donor/acceptor materials with different absorption characteristics. [2]. Producing multilayer structure by 'wet' process technology is not reproducible. The deposition of the subsequent layers should not dissolve the sublayers. This problem is successfully overcome by vacuum technology giving in this way the open field for the multilayer and tandem type devices. In all these cases the vacuum preparation of BHJ suffers from precise control of the components, which is maintained by controlling the deposition rates.

This work aimed to develop an algorithm for *in situ* determination of the mass ratio between components in BHJ composite based solar cells during the vacuum co-deposition process.

EXPERIMENTAL

Calculation of the deposition parameters

The co-deposition process is controlled by two channels Quartz Crystal Microbalance (QCM) where the *in situ* thickness measurement is based on Sauerbrey's equation [8]. To keep a correct ratio between the evaporated components a precise determination of the film densities (D_A, D_B), tooling (U_A, U_B) have to be done according to the QCM manual [9].

The calculation assumes two QCM sensors for independent measurements of the deposition rate as depicted on Fig 1. After correct setting of the aforementioned parameters for both materials and a choice of desired mass ratio ($M_{A/B}^H$) and total film thickness (T_{AB}^H) the following relations could be derived:

$$M_{A/B}^H = \frac{U_A}{U_B} M_{A/B}^S \tag{1}$$

$$M_{A/B}^S = \frac{M_A^S}{M_B^S} \tag{2}$$

$$M_A^S = D_A T_A^S \qquad\qquad M_B^S = D_B T_B^S \tag{3, 4}$$

$$T_A^H = U_A T_A^S \qquad T_B^H = U_B T_B^S \tag{5, 6}$$

$$T_{AB}^H = T_A^H + T_B^H \tag{7}$$
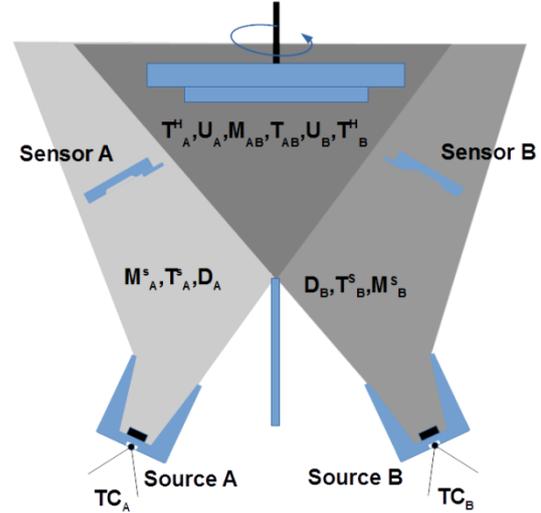
Fig. 1. Schematic draw of the co-deposition process. The parameters, denoted on the scheme are explained in the equations.

Solving this set of equations the unknown parameters, namely the mass ratio of materials A and B, which could be obtained at the sensors ($M_{A/B}^S$), mass of material A at the sensor A (M_A^S), mass of material B at the sensor B (M_B^S), thicknesses of films (T_A^S, T_B^S), deposited at sensor A and B, respectively, and the thicknesses of films (T_A^H, T_B^H), deposited on the holder during a separate deposition of material A or B, respectively, are determined. The parameters T_A^H and T_B^H are more essential as they appear as thickness reading on the QCM display after finishing the co-deposition process.

By the choice of a proper rate of deposition for material A, at the position of the holder (R_A^H), the time of the deposition t and the corresponding deposition rate for material B at the position of the holder (R_B^H) could be calculated by equations:

$$t = \frac{T_A^H}{R_A^H} \qquad R_B^H = \frac{T_B^H}{t} \tag{8, 9}$$

After setting of R_A^H and R_B^H as a given rates for the QCM PID regulators the co-deposition process could start. It is useful to calculate the rate ratio $R_{A/B}^H = \frac{R_A^H}{R_B^H}$ and plot it as a function of t during

the deposition process. As the PID controlled R_A^H and R_B^H always oscillate the $R_{A/B}^H$ parameter could be used to introduce *in situ* corrections. A computer software for co-deposition process control was developed by the authors

Methods

The samples for photoelectrical measurement (patterned ITO Ossila substrates) were preliminary cleaned. On some of the substrates PEDOT:PSS film was deposited by spin coating at 5500 rpm for 60 seconds. Subsequent annealing for 10 minutes at 150°C on air and 10 minutes at 150°C in nitrogen atmosphere was applied to remove the residual moisture.

The organic composite and electrode films were prepared in a clean room class C (M. Braun Inertgas-Systeme GmbH, Garching, Germany). $ZnPc:C_{60}$ composite thin films were deposited by co-evaporation of ZnPc and C_{60} onto Ossila substrates through a proper deposition mask. The deposition was performed in a vacuum system from two thermally heated sources at evaporation temperatures of about 500 and 430ºC, respectively.

The calculations based on the aforementioned set of equations show that for a given composite $ZnPc:C_{60}$ film with thickness of 130 nm and a mass ratio of 4.2 the ratio between the evaporated rates of the two components have to be set at 3.3. These calculations are based on the experimentally obtained for ZnPc and C_{60} densities of 1.25 and 1.36 g/cm^3, respectively, and tooling factors of 0.29 and 0.21, respectively. Assuming ZnPc deposition rate of 5 Å/s, the C_{60} rate of 1.5 Å/s was obtained. These calculations demonstrate the importance of the algorithm developed. ZnPc and C_{60} deposition rates were controlled by two independent channels of quartz crystal microbalance (Inficon SQC 310C).

The solar cell samples of type ITO|PEDOT:PSS|ZnPc:C_{60}|Al were measured in nitrogen atmosphere. For comparison I-V characteristics of ITO|ZnPc|Al sample with single ZnPc layer were also determined. During the measurement the samples were exposed to a light according to the standard AM 1.5, produced by solar simulator LS0916 LOT Oriel class AAA. The light intensity of about 830 mW.cm^{-2} was controlled by a calibrated reference silicon cell RR200O (ReRa Solutions BV; Nijmegen, Netherlands). The current voltage (*IV*) characteristics were measured by Keithley 6487 electrometer (Keithley Instruments Inc., Cleveland, OH, U.S.A.).

The morphology of the films was investigated by scanning electron microscope (SEM) Philips 515 at accelerating voltage of 25 kV. The samples for SEM characterization were deposited on microscopic glasses. Before the SEM study the sample surface was covered consecutively by carbon and palladium/gold films.

Thickness of the layers was measured by Decktak XT profilometer.

RESULTS AND DISCUSSION

Film deposition

Fig. 2 presents typical rates in a co-deposition process for a preparation of $ZnPc:C_{60}$ composite as an active BHJ layer with organic solar cell application. Right ordinate presents the rate R_{ZnPc}/R_{C60} ratio, calculated during the deposition process. The calculation of the rate ratio is useful for *in situ* corrections of the PID parameters to achieve more precise co-deposition control. It could be seen that the ratio between the evaporated rates is more sensitive towards the deviation of the given parameters than the evaporated rates themselves. Presented in the figure mean values of the rates and their standard deviations are calculated after finishing of the deposition process. It is seen from the figure that a precise automatic control of the rates with a standard deviation of ±0.1Å/s is achieved.
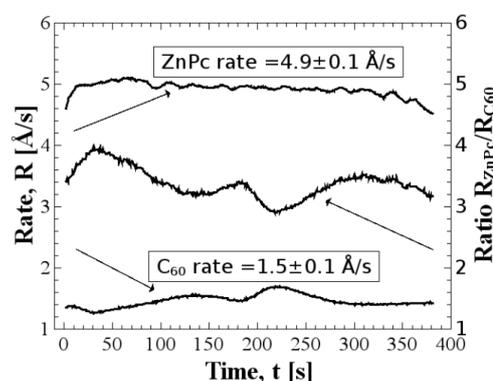
Fig. 2. Typical rates in the co-deposition process for preparation $ZnPc:C_{60}$ composite as an active BHJ layer in organic solar cell. Right ordinate presents the R_{ZnPc} /R_{C60} ratio, calculated during the deposition process.

Surface morphology

Surface morphology SEM image of vacuum deposited C_{60} film is presented in Fig. 3. The film exhibits smooth and flat surface. This surface morphology could be more probably related to a disordered film structure.

In Fig. 4 surface morphology SEM image of vacuum deposited ZnPc film is presented. This

surface morphology could be more probably related to a disordered film structure with formed ZnPc agglomerate. The agglomerates of approximate $10 \div 30$ nm size are probably formed after the film growth by recrystallization.
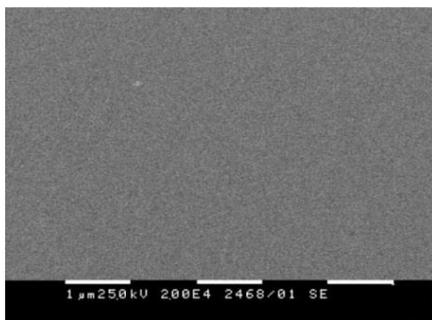
Fig. 3. SEM image of vacuum deposited C60 film. Thickness: 45±3 nm.
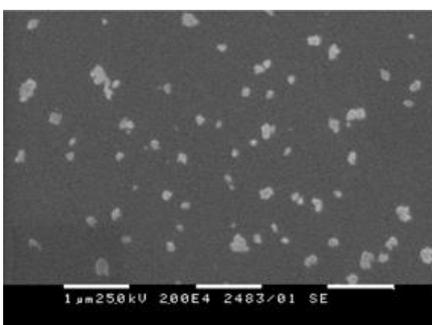
Fig. 4. SEM image of vacuum deposited ZnPc film. Thickness: 75±2 nm.
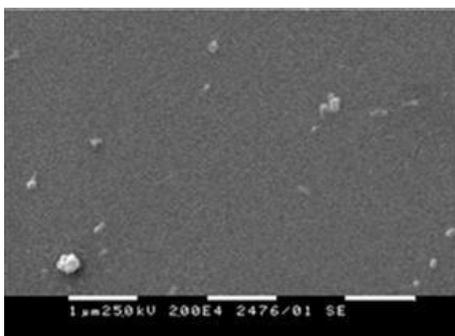
Fig. 5. SEM image of vacuum deposited ZnPc:C_{60} composite film. Thickness:147.0±0.4 nm.

Surface morphology SEM image of vacuum deposited ZnPc:C_{60} composite film is presented in Fig. 5. Again a smooth film surface with some agglomerates of approximate $10 \div 30$ nm size is seen. In this case the concentration of the more ordered particles is less than the case of pure ZnPc. This surface morphology expresses some intermediate state between pure C_{60} and ZnPc film surfaces, which is an expected result. As the evaporation conditions are kept uniform during the

whole time of deposition of about 400 s it could be expected that the surface morphology pictures could be related to the BHJ structure of the film.

Photoelectrical measurements

I-V characteristics of ITO|ZnPc|Al and ITO|PEDOT:PSS|ZnPc:C_{60}|Al structures were measured in dark, and under light illumination as described above. For sake of clarity the characteristics were plotted in semi logarithmic scale.
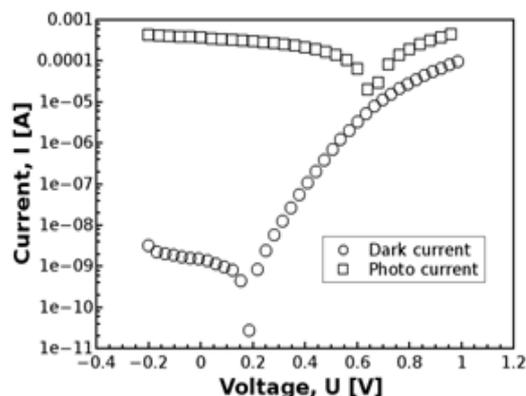
Fig. 6. *I-V* characteristics of ITO|ZnPc|Al samples measured in dark and under light exposure with light according to standard AM 1.5.
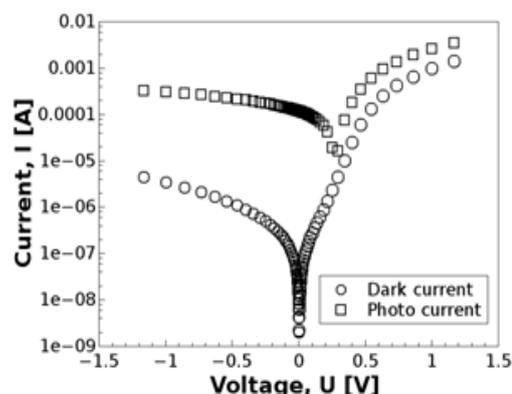
Fig. 7. *I-V* characteristics of ITO|PEDOT:PSS| ZnPc:C_{60}|Al samples measured in dark and under light exposure with light according to standard AM 1.5.

The dark *I-V* characteristic of ITO|ZnPc|Al structure (Fig. 6.) measured in both directions of the voltage scale shows typical asymmetric curve, which is clearly related to a diode behaviour. The dark current measurements indicate formation of a contact barrier at about 0.2 V. This barrier could be related to the ITO|ZnPc interface as no HTL is used. The photocurrent measured from the same structure in reverse voltage direction is higher more than 5 orders of magnitude than the dark one, and

Table1. Photoelectrical parameters of the measured structures

structure	I_{sc}	V_{oc}	FF	η	R_{sh}	R_s
	mA	mV	%	%	$\Omega.cm^2$	$m\Omega.cm^2$
ITO|ZnPc|Al	0.016	607	34.9	0.07	67605	735839
ITO|PEDOT:PSS|ZnPc:C_{60}|Al	0.14	398	34.4	0.44	4493	38343

the open circuite voltage (V_{oc}) of 0.6 V is measured. It should be taken in mind that the curve consists also the dark current contact barrier of 0.2 V. Therefore the final value of V_{oc} = 0.6 - 0.2 = 0.4 V could be obtained.Although the current changes more than 5 orders of magnitude under the light illumination the efficiency (η) is very low (Table 1). This effect could be related to the weak charge carrier separation on the ZnPc|Al interface. The relative high value of the shunt resistance (R_{sh}) could be related to the high resistivity of ZnPc film and the high value of the serial resistance (R_s) could be connected with the contact barriers.

Dark current characteristics of ITO|PEDOT:PSS|ZnPc:C_{60}|Al structures measured in both directions of the voltage scale are presented in Fig. 7. The weaker asymmetry of the curves comparing with the previous case could be related to the decreased contact barriers – the sample decreases his diode properties.

The difference between the dark and photocurrent in reverse direction is only 1.5 orders of magnitude but the I_{sh} increases almost an order of magnitude (Table 1). V_{oc} is about 0.4 V which could be connected with the reduced contact barrier due to the presence of PEDOT:PSS as HTL. This effect is also expressed in the reduced, more than 10 times R_s. This is a clear evidence that the PEDOT:PSS layer decreases the contact barrier. It should be mentioned here that R_{sh} decreases more than 10 times, which obviously results in lower photo generated power. As the R_{sh} could be more related to the BHJ layer than the whole solar cell structure, more optimization of ZnPc:C_{60} composite should take place. It could be expected that decreasing the C_{60} concentration will lead to an increase in R_{sh} in a way to improve the solar cell parameters.

CONCLUSION

An algorithm for determination of the mass ratio between two components of a composite material during the vacuum co-deposition process was developed. A vacuum co-deposition of ZnPc:C_{60} composite BHJ layer was obtained.

This surface morphology express some intermediate state between pure C_{60} and ZnPc film surfaces, which could evidence a formation of a composite. The photoelectrical measurements clearly display an improved photoelectrical properties of the BHJ ZnPc:C_{60} composite with respect to pure ZnPc film. The lower value of R_{sh} indicates the decreased resistivity of the BHJ layer which leads to big reduction of the photo generated power. On the base of the algorithm developed further optimization of the co-deposited BHJ ZnPc:C_{60} composite should take place.

REFERENCES

1. N. S. Sariciftci, *Sciences*, **258**, 1474 (1992).
2. J. Bernede, *J. Chil. Chem. Soc*, **53**, 1549 (2008).
3. M. Pfeiffer, A. Beyer, B. Ploinnings, A. Nallau, T. Fritz, K. Leo, D. Schlettwein, S. Hiller, D. Wohrle, *Sol. Energ. Mat. & Solar Cells*, **63**, 83 (2000).
4. J. Drechsel, B. Maenning, F. Kozlowski, M. Pfeiffer, K. Leo, *Appl. Phys. Lett.,* **86**, 244102 (2005).
5. H. Derouiche, J. Bernède, J. L'Hyver, *Dyes and Pigments,* **63**, 277 (2004).
6. M. Zhang, H. Wang, C.W. Tang, *Org. Electron.*, **13**, 249 (2012).
7. M. Riede, C. Uhrich, J. Widmer, R. Timmreck, D. Wynands, G. Schwartz, W.M. Gnehr, D. Hildebrandt, A. Weiss, J. Hwang, S. Sundarraj, P. Erk, M. Pfeiffer, K. Leo, *Adv. Funct. Mater.,* **21**, 3019 (2011).
8. G. Sauerbrey, *Z. Phys.,* **155**, 20 (1959).
9. http://products.inficon.com/GetAttachment.axd?attaName=70d0f95f-e67d-4974-8253-a82e3cd0934b (last accessed, Nov. 2016)

ПОЛУЧАВАНЕ НА ОРГАНИЧНИ СЛЪНЧЕВИ ЕЛЕМЕНТИ ЧРЕЗ СЪВМЕСТНО ВАКУУМНО ОТЛАГАНЕ ОТ ДВА ИЗТОЧНИКА

Г. Георгиева[1], Д. Димов[2], Г. Добриков[3], Д. Карашанова[2], А. Кирилов[4], Ф. Маркова[4], Е. Бубев[4], А. Георгиев[4], Р. Йорданов[3], И. Живков[1, 2]

[1] *Химически факултет, Център по материалознание, Технологичен университет - Бърно, Пуркиньова 118, 612 00 Бърно, Чешка република*

[2] *Институт по оптически материали ”Акад. Й. Малиновски”, Българска академия на науките, Акад. Г. Бончев. бл. 101/109, 1113 София, България*

[3] *Катедра по Микроелектроника, Факултет по електронна техника и технологии, Технически университет - София, бул. „Кл. Охридски“, 1000 София, България*

[4] *Катедра по органична химия и физикохимия, 1756 София, бул. :Кл. Охридски“ 8, Химикотехнологичен и металургичен университет, София, България.*

(Резюме)

Представен е алгоритъм за определяне на масовото съотношение между компоненти при съвместно вакуумно изпарение от два източника. Алгоритъмът е демонстиран при приготвяне на органични слънчеви клетки от типа ITO|PEDOT:PSS|ZnPc:C_{60}|Al на основата на цинков фталоцианин (ZnPc). Активният органичен ZnPc:C_{60} слой, формиращ обемния хетропреход се получава при съотношение на компонентите 4.2:1. Повърхностната морфология е характеризирана чрез СЕМ. Проведените фотоелектрични измервания показват предимствата на композитния материал в сравнение със свойствата на еднокомпонентния ZnPc слой. Алгоритъмът позволява по-нататъшно оптимизиране на слънчевите клетки с обемни хетеропреходи.

Design of organic solar cells based on a squarine dye as electron donor

S. Kitova*, D. Stoyanova, J. Dikova, M. Kandinska[1], A. Vasilev[1] and V. Mankov

Institute of Optical Materials and Technologies "Acad. J .Malinowski",
Bulgarian Academy of Sciences, Acad. G. Bonchev Str., Bl.109, 1113 Sofia, Bulgaria
[1]Sofia University "St. Kliment Ohridski, Faculty of Chemistry and Pharmacy,
James Bourchier Blvd., 1164 Sofia, Bulgaria

Optical modelling based on transfer matrix method has been carried out to design small molecule BHJ organic solar cells with better performance. The active layers represent blends of in-house synthesized squaraine dye Sq1 as electron donor and soluble fullerene derivative $PC_{61}BM$ ((6,6)-phenyl C_{61} butyric acid methyl ester) as acceptor. The solar photon absorption in $Sq1/PC_{61}BM$ layers with different weight ratio has been simulated and the possible maximum short circuit photocurrent (J_{sc}^{max}) in devices with standard and inverted architecture has been calculated. It is found that the inverted device stacks show larger calculated J_{sc}^{max} compared to the standard device structure. Modelling of the optical field distribution in the different device stacks proved that this enhancement originates from an increased absorption of incident light in the active layer, and hence from the increased exciton generation rate. Simultaneously, it is established that the effect of the ZrO_2 optical spacer to the increase of J_{sc}^{max} is less expressed in inverted device stacks than in standard ones. Finally, the results obtained are discussed with a view to finding the optimal design of real BHJ cells based on $Sq1/ PC_{61}MB$ active layers.

Keywords: bulk heterojunction organic solar cells, inverted solar cell, squaraine dye, optical modelling

INTRODUCTION

Recently, the organic solar cells (OSCs) based on polymer or low molecular weight semiconductors are subject of continuously growing interest as promising low-cost alternative of Si-solar cells that still dominate the market [1]. Contemporary OSCs devices are based on a heterojunction that results from the contact between electron donor (D) and electron acceptor (A) materials. D/A heterojunctions can be created with two main types of architecture: bilayer heterojunction and bulk heterojunction (BHJ) that is now regarded as the most promising approach to obtain high performance devices [1].

The most key element of the multilayered OSCs structure are the active layers, composed by two components – donor and acceptor. In BHJ cells the active layer represents a blend of donor and acceptor that provides larger D/A interface where generation of charge carriers takes place [2]. Till now, the best efficiency OSCs contain fullerene C_{60} and especially its soluble derivative PCBM ((6,6)-phenyl C_{61} butyric acid methyl ester) as acceptor, which seem without alternative in the near future

[3]. As per the type of the electronic donors the organic cells are conditionally divided into polymer and low-molecular (M below 100) ones. Juxtaposing the properties of these two classes of organic semiconductors reveals that the low-molecular ones possess higher purity, better reproduction of the main physicochemical and optical properties, higher carrier mobility, better defined molecular structure and exactly determined molecular weight [1, 4]. All the pointed advantages have generated unprecedented interest and intensive research in the recent years, aiming at development and exploring of new electron donors for producing the so-called "small molecule" OSCs. However, even though the highest power conversion efficiency (PCE) of 9.96 % was obtained very recently it is still considerable lower than that of inorganic solar devices [5]. Obviously, further research efforts are needed to obtain cells with better performance and prolonged lifetime. This requires the optimization of several factors which determine the cell efficiency, such as molecular structure of the donor materials and their optical and electrical properties, active layer nanomorphology, ratio between the donor and acceptor moieties in the BHJ film, concentration of

---

* To whom all correspondence should be sent:
E-mail: skitova@iomt.bas.bg

the blend D/A solution and last but not least the device architecture [6].

In our previous work [7] the potentiality of a synthesized by us symmetrical n-hexyl substituted squaraine dye (labeled as Sq1) for using as electron donor component in BHJ organic solar cells with conventional structure (here referred to as ''standard'') has been studied from the optical point of view. The soluble n-type fullerene $PC_{61}MB$ was chosen as acceptor. The results of optical modelling performed indicate that the optimal thickness of the blended $Sq1/PC_{61}MB$ active layer is about 100 nm, which provides an efficient overlapping of the total absorption with solar spectrum in the range between 580 and 900 nm [7]. It is known, however that due to the short exciton diffusion length and low charge carrier mobility of organic materials, the thickness of the active layers should be considerably smaller [8]. To compensate the lower absorption in the thinner active layers a smart design strategy has been applied [9], consisting of the insertion of optical spacers [10] and the use of different contact materials which reduce the parasitic absorptions [11]. Moreover, to improve the charge collection, functional layers are inserted to modify the interfaces between the active layers and the respective electrodes [1]. Following the above strategy we have found that the insertion of ZnO or C60 spacer layer with optimal thicknesses significantly enhances J_{sc}^{max} for active layers thinner than 50 nm, which is mainly due to the improved light absorption by a factor of 5 to 10. Simultaneously, the optical effect of inserted PEDOT:PSS hole transporting layer was found to be negligible for thicknesses of Sq1/PCMB layers below 100 nm [7].

Recently, there have been extensive investigations on the so-called "inverted architecture" of polymer solar cells (PSCs), where the polarity of charge collection is the opposite of the conventional design [12, 13]. The implementation of the inverted cell structure requires the introduction of a buffer layer from metal oxide, mostly ZrO_2, ZnO, TiO_2 etc., for improving the function of the transparent ITO electrode as cathode, and a substitution of Al electrode with higher work function metal like Au, Ag, Pt, etc., which serves as anode [13]. Compared with conventional PSCs, the inverted type devices demonstrate better long-term ambient stability by avoiding the need for the corrosive and hygroscopic PEDOT:PSS and low-work-function metal cathode, both of which are detrimental to device lifetime [14]. It has also been shown that the inverted design

provides superior solar cell performance, which was attributed to different absorption profiles with reduced parasitic absorption in polymer:fullerene solar cells [15]. However, the efficiency of this architecture in small molecule organic cells has hardly been investigated.

In the present work, the potential photovoltaic performance of BHJ solar cells with $Sq1/PC_{61}BM$ active layer and different design was projected by optical modelling based on transfer matrix method. For the purpose the simulated solar photon absorption in blended with different weight ratio $Sq1/PC_{61}BM$ active layers and the calculated maximum short circuit current J_{sc}^{max} for cells with standard and inverted architecture were compared. Besides, the impact of ZrO_2 and MoO_3 optical spacers on the calculated J_{sc}^{max} values were also estimated.

EXPERIMENTAL DETAILS

The symmetrical n-hexyl substituted squaraine dye 2-(5-(((2,2-diphenylhydrazono) methyl)-1-hexyl-1H-pyrrol-2-yl)-4-(5-(2,2-diphenyl-hydrazono)-ylidenemethyl)-1-hexyl-2H-pyrrol-1-ium)-3-oxocyclobut-1-enolate, labeled as Sq1) was in-house synthesized [7] by optimizing a method proposed recently in the literature [16, 17].

Single Sq1 dye and blended $Sq1/PC_{61}MB$ films with different weight ratios (1:1, 1:2, 1:3) were prepared from solution of the compounds in chloroform by spin coating in glove box. The experimental details are described in [7]. Optical constants of the blended $Sq1/PC_{61}BM$ films were determined with a high accuracy on the basis of three spectrophotometric measurements at normal incidence of light - transmittance T and reflectance R_f and R_m of the films, deposited on transparent (BK7) and opaque (Si wafers) substrates, respectively [18].

Optical modeling of a BHJ device stack was carried out using the transfer matrix formalism, based on the Fresnel formulas for the several interfaces occurring in the cell. This approach has been explained in full detail in the literature [19, 20]. In our work a Matlab script developed by Burkhard and Hoke, which treats the case of normal incidence of light, was applied [21]. The absorption distribution for each wavelength over the film thickness has been calculated in the wavelength range 350 – 900 nm.

Knowing the power of incoming AM 1.5 solar spectrum, the exciton generation rate per unit volume G(x) at each position x is described by

$$G(x) = \int_{\lambda 1}^{\lambda 1} \frac{\lambda}{hc} Q_{act(x,\lambda)} d\lambda$$

where the Q(x, λ) is the time average of the energy dissipation per unit time at the position x and wavelength λ, h is Plank's constant and c is the speed of light [19]. Further integration over the film thickness results in the total number of absorbed photons. The possible maximum short circuit current density J_{sc}^{max} was calculated assuming that each absorbed photon results in a collected electron i.e. the internal quantum efficiency, IQE, equals one [21].

The two types of architectures of the modelled solar cells are shown in Fig. 1. In the standard device configuration (Fig. 1a), the active layer is sandwiched between PEDOT:PSS and ZrO_2 covered with Al. For the inverted devices (Fig. 1b), the active layer is embedded between the electrons selective ZrO_2 and the holes selective MoO_3 layers,
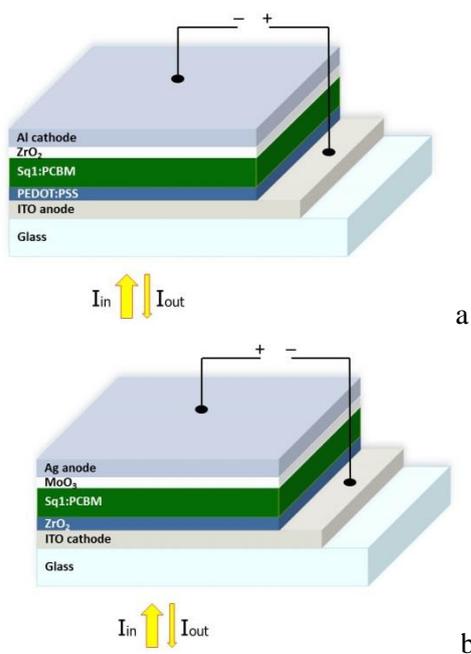
Fig. 1. Scheme of BHJ organic solar cells with:
a) standard structure; b) inverted structure.

covered with Ag metal contacts. The optical modelling was performed for both BHJ cell structures, where the light enters through the glass substrate, sequentially passing the buffers and active layers. Then the light is reflected back from the metal electrode and finally leaves the solar cell partly at the front again. In all calculations the thicknesses of ITO and Ag electrodes were set to 100 nm and those of PEDOT:PSS to 60 nm. We have used literature data for the optical constants of ITO, Al and ZrO_2 [22]. The optical constants of PEDOT:PSS, Ag and MoO_3 films were determined

experimentally by applying the same procedure as for Sq1 dye. For the purpose 50 nm thick films were spin coated or thermally evaporated in vacuum (10^{-4} Pa) on glass substrates and Si wafers.

RESULTS

As a first step in our study the optimal $Sq1/PC_{61}BM$ weight ratio in the blended active layers was experimentally determined. This is because of the fact that, as noted above, the ratio between the donor and acceptor moieties in the BHJ film affects strongly the device performance. Fig. 2 presents the absorption spectra of 100 nm films with different $Sq1/PC_{61}BM$ weight proportions (1:1, 1:2 and 1:3). As seen, the spectrum of the all samples studied shows absorption of light across a broad range of wavelengths - from ultraviolet to near infrared, with a maximum at 775 nm. The absorption in the range 350 – 600 nm is due to the presence of $PC_{61}MB$ in the blended films whilst the main absorption peak is due to electron excitations in the squaraine dye molecules. Reasonably, the height of the main peak decreases with decreasing the content of Sq1 in the blended films studied, being the lowest for 1:3 proportions of the donor/acceptor constituents. Further, the photovoltaic potential of $Sq1/PC_{61}BM$ active layers was followed in simple standard cells, ITO/PEDOT:PSS(~60nm)/Sq1:PC$_{61}$BM(~100nm)/Al(~100nm). The current density–voltage (J-V) curves obtained for cells with different $Sq1/PC_{61}BM$ ratio in the active layers are shown in Fig. 3. It is seen that the weakest photovoltaic response is observed for the active layer with 1:1 ratio of the donor and acceptor moieties. Obviously, this film has very low potential for using as active layer it the cells studied, despite its higher absorption. The two other $Sq1/PC_{61}BM$ films (1:2 and 1:3) have almost the same relatively stronger response which was the reason to continue our investigation with them.
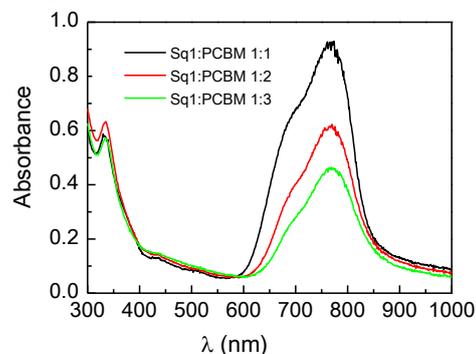
Fig. 2. Absorption spectra of 100 nm thick $Sq1/PC_{61}MB$ films with different D/A weight ratio.
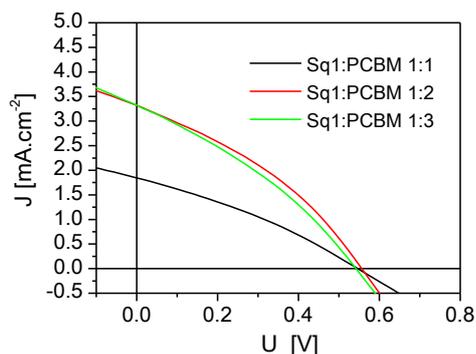
Fig. 3. J-V curves for conventional BHJ cells at different weight ratio of the Sq1/PC$_{61}$MB active layers.
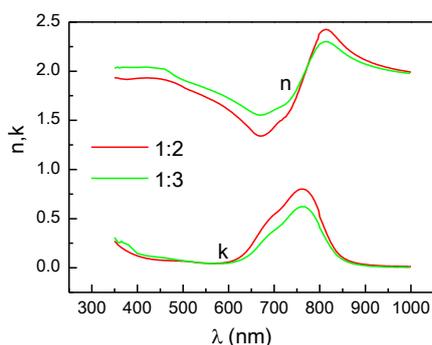
Fig. 4. Refractive index (n) and extinction coefficient (k) spectra of blended Sq1/PC$_{61}$BM films.

Fig. 4 shows the spectral dispersions of refractive index (n) and extinction coefficient (k) for blended Sq1/PC$_{61}$BM layers with 1:2 and 1:3 weight ratio. On their basis, the optical absorption profiles for standard and inverted devices, each with 100 nm thick Sq1/PC$_{61}$BM active layer, were calculated and can be compared in Fig. 5. Fig. 5a presents spectral dependence of total absorption within the active layer, while the exciton generation rate G_x under AM 1.5G illumination versus position in the active layer is shown in Fig. 5b. In the calculations the photon to exciton conversion efficiency is assumed to be one meaning that every single photon absorbed in the active layer initially creates an exciton. It is seen that the inverted structure can harvest more photons from solar spectra than the standard devices. Besides, the generation profile is shifted towards the back metal electrode and the formation of exited states near the back electrode is considerably larger for inverted cell geometry. Hence, the systematical optical modeling studies showed that the inversion of the multilayered cell structure causes both the slight shift of the maximum of the electric field towards the back electrode and the increase of the overall modulus throughout the whole active layer.
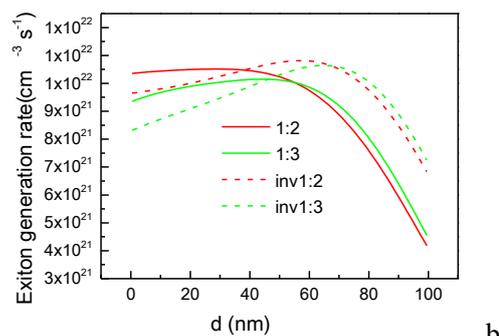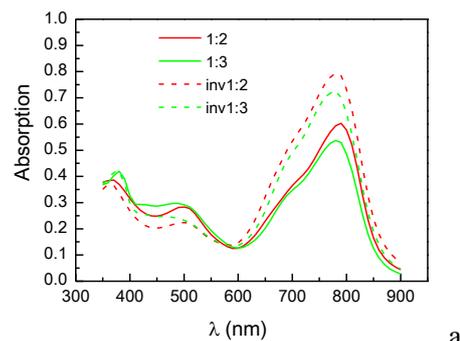
Fig. 5. Comparison of calculated optical absorption profiles for devices with standard and inverted structure. The thicknesses of buffer layers ZrO$_2$ and MoO$_3$ were set to 20 nm. a) Fraction of incident light absorbed in 100 nm thick Sq1/PC$_{61}$MB active layer in dependence of wavelength; b) Exciton generation rate in 100 nm thick active layer under AM 1.5G illumination as a function of position within the active layer;
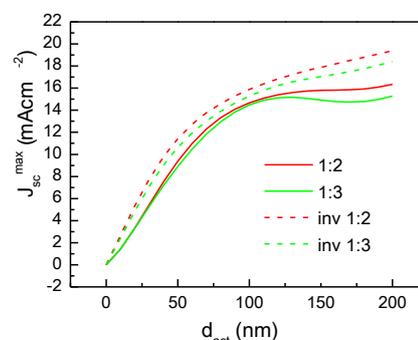
Fig. 6. Calculated J$_{sc}^{max}$ as a function of active layer thickness for the same device structures (as in Fig. 5) under 100 mW cm^{-2} AM 1.5G spectral illumination.

Assuming an IQE=1, the maximum short circuit current density J$_{sc}^{max}$ under AM 1.5G illumination in dependence of Sq1/PC$_{61}$MB layer thickness is depicted in Fig. 6 for both device structures. As seen, the inverted device stack always has a higher J$_{sc}^{max}$ than the standard one, regardless of the active layer thickness, demonstrating the advantage of the inverted device structure. It should be noted here that these calculations consider the optical properties of the solar cells and not the electrical

necessities of low sheet resistance or prevention of pin hole formation. Nevertheless, they represent a
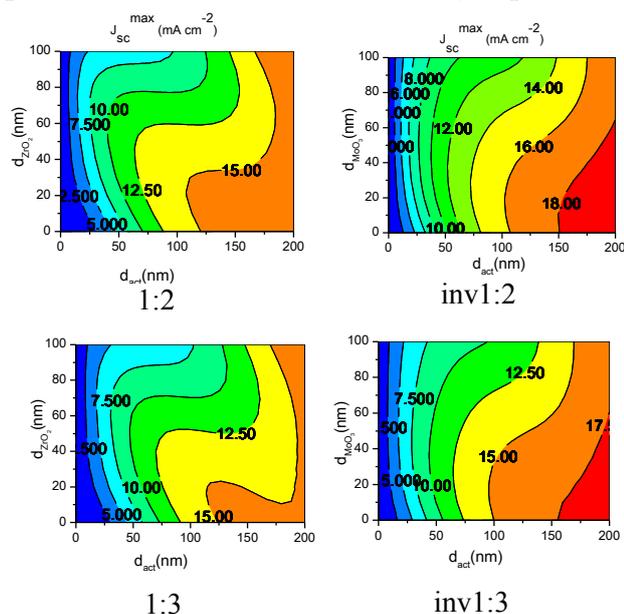
Fig. 7. Calculated short-circuit current density J_{sc}^{max} contours under 100 mW cm^{-2} AM 1.5G spectral illumination as a function of active layers and optical spacer thicknesses for: a) standard device with ZrO$_2$ optical spacer and b) inverted device with MoO$_3$ optical spacer.

considerable potential improvement of the photocurrent in devices with inverted structure. The dependence of calculated J_{sc}^{max} on the thicknesses of the active layers and optical spacer is illustrated in Fig. 7 for standard device with ZrO$_2$ spacer/Al electrode and inverted device with MoO$_3$ spacer/Ag electrode. According to the simulation results presented, the values of J_{sc}^{max} are less dependent on the spacer thickness in the device with inverted structure. On the whole, the effect of optical spacer to the increase in J_{sc}^{max} is higher in devices with standard architecture.

CONCLUSIONS

Optical modelling based on transfer matrix method has been performed to predict and improve the performance of BHJ solar cells with standard and inverted architecture, based on a symmetrical n-hexyl substituted squariane dye Sq1 as electron donating component in the active layer. The results obtained demonstrate that the inverted device stacks, comprising bulk heterojunction composed of Sq1 donor and PC$_{61}$BM acceptor with 1:2 and 1:3 proportions, show larger short circuit currents compared to the standard device structure. Obviously, this enhancement originates from the increased absorption of incident light and the

subsequent raise of exciton generation rate within the active layer. This statement is confirmed by the results from modelling of the optical field distribution in device stacks with both types of architecture. On the other hand, the simulations performed show that the impact of the optical spacer on the increase of J_{sc}^{max} is less expressed in the cells with inverted design than in standard ones.

Finally, it is worth to mention that the experimental verification of the results obtained is in progress and will be forthcoming in a separate paper.

REFERENCES

1. A. Mishra, and P. Bauerle, *Angew. Chem. Int. Ed.*, **51,** 2020 (2012).
2. S. Uchida, J. Xue, B. P. Rand, S. R. Forrest, *Appl. Phys. Lett.*, **84,** 4218 (2004).
3. B. Walker, C. Kim, and T. Nguyen, *Chem. Mater.,* **23,** 470 (2011).
4. X. Xiao, G. Wei, S. Wang, G. Zimmerman, Ch. Renshaw, M. Thompson, and S. Forrest, *Adv. Mater.,* **24,** 1956 (2012).
5. B. Kan, Q. Zhang, M. Li, X. Wan, W. Ni, G. Long, Y. Wang, X. Yang, H. Feng, Y. Chen, *J. Am. Chem. Soc.* **136.** 15529 (2014).
6. T. Razykov, C. Ferekides, D. Morel, E. Stefanakos, H. Ullal, H. Upadhyaya, *Solar Energy,* **85,** 1580 (2011).
7. S. Kitova, D. Stoyanova, J. Dikova, M. Kandinska, A. Vasilev, and S. Angelova, *J. Phys.:Conf. Ser.,* **558,** 012052 (2014).
8. G. Burkhard, E. Hoke, and M. McGehee, *Adv. Mater.,* **22,** 3293 (2010).
9. J. Gilot, I. Barbu, M. Wienk, and R. Janssen, *Appl. Phys.Lett.,* **91,** 113520 (2007).
10. Y. Long, *Solar Energy Mater. & Solar Cells* **94,** 744 (2010).
11. Z. He, Ch. Zhong, Sh. Su, M. Xu, H. Wu, and Y. Cao, *Nat. Photonics* **6,** 591 (2012).
12. A. Zhao, S. Tan, L. Ke, P. Lui, A. Kyaw, X. Sun, G. Lo, and D. Kwong, *Solar Energy Mater. & Solar Cells* **94,** 985 (2010).
13. B. Hsieh, Y. Cheng, P. Li, Ch. Chen, M. Dubosc, R. Liang, and Ch. Hsu, *J. Am. Chem. Soc.,* **132,** 4887 (2010).
14. M. Morana, H.Azimi, G. Dennler, H. Egelhaaf, M. Scharber, K. Forberich, J. Hauch, R. Gaudiana, D. Waller, Z. Zhu, K. Hingerl, S. Bavel, J. Loos, and K. Brabec, *Adv. Funct. Mater.,* **20,** 1180 (2010).
15. A. Becke, *Chem. Phys.,* **98,** 5648 (1993).
16. A. Silvestri, M. Irwin, L. Beverina, A. Facchetti, G. Pagani, and T. Marks, *J. Am. Chem. Soc.*, **130,** 17640 (2008).
17. D. Bagnis, L. Beverina, H. Huang, F. Silvestri, Y. Yao, H .Yan, G. Pagani, T. Marks, and A, Facchetti, *J. Am. Chem. Soc.,* **132,** 4074 (2010).

18. Tz. Babeva, S. Kitova, and I. Konstantinov, *Appl. Opt.,* **40,** 2682 (2001).
19. L. Pettersson, L. Roman, and O. Inganä, *J. Appl. Phys.,* **86,** 487 (1999).
20. P. Peumans, A. Yakimov, and R. Forrest, *J. Appl. Phys.,* **93**, 3693 (2003).
21. A. Burkhard, E. Hoke, and M. McGehee, *Adv. Mater.,* **22,** 3293 (2010).
22. Y. Liu, J. Hsieh, and S. Tung, *Thin Solid Films,* **510,** 32 (2006).

ДИЗАЙН НА ОРГАНИЧНИ СЛЪНЧЕВИ КЛЕТКИ НА ОСНОВАТА НА СКУАРИЛИЕВО БАГРИЛО КАТО ЕЛЕКТРОНЕН ДОНОР

Сн. Китова, Д. Стоянова, Ю. Дикова, М. Кандинска, А. Василев, В. Манков

Институт по оптически материали и технологии "Акад. Й. Малиновски",
Българска Академия на науките,ул. "Акад. Г. Бончев", бл. 109, 1113 София, България
[1]Софийски Университет "Св. Климент Охридски", Факултет по химия и фармация,
бул. Джеймс Баучер, 1164 Sofia, Bulgaria

(Резюме)

Проведено е оптично моделиране по метода на обърнатата матрица с цел проектиране на нискомолекулни органични слънчеви клетки с обемен хетеропреход и подобрени характеристики. Активният слой представлява смес от синтезирано от нас скуарилиево багрило Sq1 като донор на електрони и разтворим дериват на фулерена $PC_{61}BM$ ((6,6)-phenyl C_{61} butyric acid methyl ester) като електронен акцептор. Симулирана е абсорбцията на слънчева светлина в активните слоеве с различно $Sq1/PC_{61}BM$ съотношение и са пресметнати възможните максимални стойности на тока на късо съединение (J_{sc}^{max}) в клетки със стандартна и обърната архитектура. Получените резултати показват, че по-високи стойности на J_{sc}^{max} могат да се очакват при клетките с обърната структура. Моделирането на разпределението на оптичното поле в клетките с различен дизайн потвърди, че това увеличение се дължи на повишената абсорбция на падащата светлина в активния слой и следователно на по-високата концентрация на екситоните. Установено е също така, че влиянието на оптичния спейсър от ZrO_2 върху повишаването на стойностите на J_{sc}^{max} е по-силно изразено в стандартните моделни клетки. Резултатите от проведеното изследване са дискутирани с оглед намирането на оптимален дизайн на реални слънчеви клетки с обемен хетеропреход на основата на $Sq1/ PC_{61}MB$ активни слоеве.

BULGARIAN CHEMICAL COMMUNICATIONS

Instructions about Preparation of Manuscripts

General remarks: Manuscripts are submitted in English by e-mail or by mail (in duplicate). The text must be typed double-spaced, on A4 format paper using Times New Roman font size 12, normal character spacing. The manuscript should not exceed 15 pages (about 3500 words), including photographs, tables, drawings, formulae, etc. Authors are requested to use margins of 3 cm on all sides. For mail submission hard copies, made by a clearly legible duplication process, are requested. Manuscripts should be subdivided into labelled sections, e.g**. Introduction, Experimental, Results and Discussion**, *etc.*

The title page comprises headline, author's names and affiliations, abstract and key words.

Attention is drawn to the following:

a) **The title** of the manuscript should reflect concisely the purpose and findings of the work. Abbreviations, symbols, chemical formulas, references and footnotes should be avoided. If indispensable, abbreviations and formulas should be given in parentheses immediately after the respective full form.

b) **The author**'s first and middle name initials, and family name in full should be given, followed by the address (or addresses) of the contributing laboratory (laboratories). **The affiliation** of the author(s) should be listed in detail (no abbreviations!). The author to whom correspondence and/or inquiries should be sent should be indicated by asterisk (*).

The abstract should be self-explanatory and intelligible without any references to the text and containing not more than 250 words. It should be followed by key words (not more than six).

References should be numbered sequentially in the order, in which they are cited in the text. The numbers in the text should be enclosed in brackets [2], [5, 6], [9-12], etc., set on the text line. References, typed with double spacing, are to be listed in numerical order on a separate sheet. All references are to be given in Latin letters. The names of the authors are given without inversion. Titles of journals must be abbreviated according to Chemical Abstracts and given in italics, the volume is typed in bold, the initial page is given and the year in parentheses. Attention is drawn to the following conventions:

a) The names of all authors of a certain publications should be given. The use of "et *al.*" in the list of references is not acceptable.

b) Only the initials of the first and middle names should be given.

In the manuscripts, the reference to author(s) of cited works should be made without giving initials, e.g. "Bush and Smith [7] pioneered...". If the reference carries the names of three or more authors it should be quoted as "Bush *et al.* [7]", if Bush is the first author, or as "Bush and co-workers [7]", if Bush is the senior author.

Footnotes should be reduced to a minimum. Each footnote should be typed double-spaced at the bottom of the page, on which its subject is first mentioned.

Tables are numbered with Arabic numerals on the left-hand top. Each table should be referred to in the text. Column headings should be as short as possible but they must define units unambiguously. The units are to be separated from the preceding symbols by a comma or brackets.

Note: The following format should be used when figures, equations, *etc.* are referred to the text (followed by the respective numbers): Fig., Eqns., Table, Scheme.

Schemes and figures. Each manuscript (hard copy) should contain or be accompanied by the respective illustrative material as well as by the respective figure captions in a separate file (sheet). As far as presentation of units is concerned, SI units are to be used. However, some non-SI units are also acceptable, such as °C, ml, l, etc.

The author(s) name(s), the title of the manuscript, the number of drawings, photographs, diagrams, etc., should be written in black pencil on the back of the illustrative material (hard copies) in accordance with the list enclosed. Avoid using more than 6 (12 for reviews, respectively) figures in the manuscript. Since most of the illustrative materials are to be presented as 8-cm wide pictures, attention should be paid that all axis titles, numerals, legend(s) and texts are legible.

The authors are asked to submit **the final text** (after the manuscript has been accepted for publication) in electronic form either by e-mail or mail on a 3.5'' diskette (CD) using a PC Word-processor. The main text, list of references, tables

and figure captions should be saved in separate files (as *.rtf or *.doc) with clearly identifiable file names. It is essential that the name and version of the word-processing program and the format of the text files is clearly indicated. It is recommended that the pictures are presented in *.tif, *.jpg, *.cdr or *.bmp format, the equations are written using "Equation Editor" and chemical reaction schemes are written using ISIS Draw or ChemDraw programme. The authors are asked to submit the final text with a list of three potential reviewers. The Editorial Board of the journal is not obliged to accept these proposals.

EXAMPLES FOR PRESENTATION OF REFERENCES

REFERENCES

1. D. S. Newsome, *Catal. Rev.-Sci. Eng.,* **21**, 275 (1980).
2. C.-H. Lin, C.-Y. Hsu, *J. Chem. Soc. Chem. Commun.,* 1479 (1992).
3. R. G. Parr, W. Yang, Density Functional Theory of Atoms and Molecules, Oxford Univ. Press, New York, 1989.
4. V. Ponec, G. C. Bond, Catalysis by Metals and Alloys (Stud. Surf. Sci. Catal., vol. 95), Elsevier, Amsterdam, 1995.
5. G. Kadinov, S. Todorova, A. Palazov, in: New Frontiers in Catalysis (Proc. 10th Int. Congr. Catal., Budapest, 1992), L. Guczi, F. Solymosi, P. Tetenyi (eds.), Akademiai Kiado, Budapest, 1993, Part C, p. 2817.
6. G. L. C. Maire, F. Garin, in: Catalysis. Science and Technology, J. R. Anderson, M. Boudart (eds), vol. 6, Springer-Verlag, Berlin, 1984, p. 161.
7. D. Pocknell, *GB Patent* 2 207 355 (1949).
8. G. Angelov, PhD Thesis, UCTM, Sofia, 2001.
9. JCPDS International Center for Diffraction Data, Power Diffraction File, Swarthmore, PA, 1991.
10. CA 127, 184 762q (1998).
11. P. Hou, H. Wise, *J. Catal.,* in press.
12. M. Sinev, private communication.
13. http://www.chemweb.com/alchem/articles/1051611477211.html.

CONTENTS

СЪДЪРЖАНИЕ